



## รายงานวิจัยฉบับสมบูรณ์

โครงการ การประดิษฐ์เซรามิกเฟอร์โรอิเล็กทริกที่อุณหภูมิต่ำด้วย  
วิธีการเผาไหม้

โดย ผู้ช่วยศาสตราจารย์ ดร. อีระชัย บงการณ  
มหาวิทยาลัยนเรศวร

มิถุนายน 2557

## รายงานวิจัยฉบับสมบูรณ์

โครงการ การประดิษฐ์เซรามิกเฟอร์ไรต์อิเล็กทรอนิกส์ที่อุณหภูมิต่ำด้วย  
วิธีการเผาไหม้

ผู้ช่วยศาสตราจารย์ ดร. อีระชัย บงการณ  
มหาวิทยาลัยนเรศวร

สนับสนุนโดยสำนักงานกองทุนสนับสนุนการวิจัย  
และ คณะวิทยาศาสตร์ มหาวิทยาลัยนเรศวร

(ความเห็นในรายงานนี้เป็นของผู้วิจัย สกว. ไม่จำเป็นต้องเห็นด้วยเสมอไป)

### กิตติกรรมประกาศ

งานวิจัยนี้สำเร็จได้ด้วยดีเนื่องจากการสนับสนุนทุนวิจัยจาก สำนักงานกองทุนสนับสนุนการวิจัย (สกว.) ขอขอบคุณ คณะวิทยาศาสตร์ มหาวิทยาลัยนเรศวรที่อำนวยความสะดวกในการใช้เครื่องมือ สถานที่ ขอขอบคุณ ผู้ช่วยศาสตราจารย์ ดร.นราธิป วิทยากร วิทยาลัยนาโนเทคโนโลยี พระจอมเกล้าลาดกระบัง สจล. ที่สนับสนุนเครื่องมือวิเคราะห์ รวมไปถึงการช่วยเหลือที่ดีจากผู้ร่วมวิจัย ขอขอบคุณนักศึกษาทุกคนที่ช่วยกันทำงานอย่างเข้มแข็ง สุดท้ายขอขอบคุณ บิดา มารดาที่เป็นกำลังใจ และ ให้การสนับสนุนด้วยดีตลอดมา

ผู้ช่วยศาสตราจารย์ ดร.ธีระชัย บงการณ  
หัวหน้าโครงการ

## บทคัดย่อ

รหัสโครงการ: RSA5480021

ชื่อโครงการ: การประดิษฐ์เซรามิกเพอร์โรอิเล็กทริกที่อุณหภูมิต่ำด้วยวิธีการเผาไหม้

ชื่อนักวิจัยและสถาบัน: ผู้ช่วยศาสตราจารย์ ดร. วีระชัย บงการณ  
ภาควิชาฟิสิกส์ คณะวิทยาศาสตร์ มหาวิทยาลัยนเรศวร

E-mail Address: researchcmu@yahoo.com, theerachaib@nu.ac.th

ระยะเวลาดำเนินงาน: 3 ปี (15 มิถุนายน 2554 ถึง 14 มิถุนายน 2557)

## บทคัดย่อ

ศึกษาลักษณะเฉพาะของเซรามิกเพอร์โรอิเล็กทริก  $1-x(\text{Bi}_{0.5}\text{Na}_{0.5})\text{TiO}_3-x\text{ATiO}_3$  [ $A = \text{Ba}^{2+}, \text{Ca}^{2+}$  และ  $\text{Sr}^{2+}$ ] หรือ BNTBT100x, BNTCT100x และ BNTST100x โดยที่  $x = 0-0.12$ ,  $0-0.08$  และ  $0-0.12$  ตามลำดับ ที่เตรียมด้วยวิธีการเผาไหม้ พบว่าเซรามิก BNTBT100x มีโครงสร้างแบบผสมของรอมโบอีตรอลและเททระโนล สำหรับเซรามิก BNTBT2 และ BNTBT4 ค่าความหนาแน่น ค่าความหดตัวเชิงเส้น และค่าคงที่ไดอิเล็กทริกสูงสุดมีค่าเพิ่มขึ้นเมื่ออุณหภูมิซินเตอร์เพิ่มขึ้นจนถึง 1150 องศาเซลเซียส หลังจากนั้นจะเกิดการระเหยของ  $\text{Bi}^{3+}$  และ  $\text{Na}^+$ . ในขณะที่เซรามิก BNTBT6 BNTBT8 BNTBT10 และ BNTBT12 ค่าความหนาแน่น ค่าความหดตัวเชิงเส้น และค่าคงที่ไดอิเล็กทริกสูงสุดมีค่าเพิ่มขึ้นเมื่ออุณหภูมิซินเตอร์เพิ่มขึ้นจนถึง 1200 องศาเซลเซียส หลังจากนั้นจะพบเฟสแปลกปลอม เซรามิก BNTBT8 ซินเตอร์ที่อุณหภูมิ 1200 องศาเซลเซียส มีค่าคงที่ไดอิเล็กทริกที่อุณหภูมิคูรีสูงสุด ค่าความหนาแน่นสูงสุด โดยมีค่าประมาณ 7400 และ  $5.80 \text{ g/cm}^3$  และมี ค่า  $P_r$  และ  $E_c$  (ใช้สนามไฟฟ้าเพิ่ม 40 kV) เท่ากับ  $28.10 \mu\text{C/cm}^3$  และ  $21.02 \text{ kV/cm}$  ตามลำดับ เซรามิก BNTCT100x มีโครงสร้างแบบรอมโบอีตรอลในทุกๆ ตัวอย่าง ค่าความหนาแน่นเพิ่มขึ้นเมื่ออุณหภูมิซินเตอร์เพิ่มขึ้นจนถึง 1150 องศาเซลเซียส หลังจากนั้นความหนาแน่นมีค่าลดลงเมื่ออุณหภูมิซินเตอร์เพิ่มขึ้น ในขณะที่การหดตัวเชิงเส้นมีค่าเพิ่มขึ้นเมื่ออุณหภูมิซินเตอร์เพิ่มขึ้น เซรามิก BNTCT2 ซินเตอร์ที่อุณหภูมิ 1150 องศาเซลเซียส มีค่าคงที่ไดอิเล็กทริกที่อุณหภูมิคูรีสูงสุด และค่าความหนาแน่นสูงสุด โดยมีค่าประมาณ 3208 และ  $5.57 \text{ g/cm}^3$  และมี ค่า  $P_r$  และ  $E_c$  (ใช้สนามไฟฟ้าเพิ่ม 40 kV) เท่ากับ  $17.4 \mu\text{C/cm}^3$  และ  $30.13 \text{ kV/cm}$  ตามลำดับ เซรามิก BNTST100x มีโครงสร้างแบบคิวบิกในทุกๆ ตัวอย่าง ค่าความหนาแน่น และการหดตัวเชิงเส้นมีค่าเพิ่มขึ้นเมื่ออุณหภูมิซินเตอร์เพิ่มขึ้นเพิ่มขึ้น นอกจากนั้นเซรามิก BNTST20 ซินเตอร์ที่อุณหภูมิ 1200 องศาเซลเซียส มีค่าคงที่ไดอิเล็กทริกที่อุณหภูมิคูรีสูงสุด และค่าความหนาแน่นสูงสุด โดยมีค่าประมาณ 4725 และ  $5.57 \text{ g/cm}^3$  ตามลำดับ และมี ค่า  $P_r$  และ  $E_c$  (ใช้สนามไฟฟ้าเพิ่ม 40 kV) เท่ากับ  $17.19 \mu\text{C/cm}^3$  และ  $29.61 \text{ kV/cm}$  ตามลำดับ

คำหลัก: วิธีการเผาไหม้, เพอร์โรอิเล็กทริก, โครงสร้างจุลภาค, สมบัติไดอิเล็กทริก, การก่อเกิดเฟส



### Abstract

**Project Code:** RSA5480021

**Project Title:** Low Temperature Fabrication of Ferroelectric Ceramics by Combustion Method

**Investigator:** Assistant Professor Dr. Theerachai Bongkarn

Department of Physics, Faculty of Science, Naresuan University

**E-mail Address:** researchcmu@yahoo.com, theerachaib@nu.ac.th

**Project Period:** 3 years (15 June 2011 – 14 June 2014)

### Abstract

Characterization of lead-free ferroelectric  $1-x(\text{Bi}_{0.5}\text{Na}_{0.5})\text{TiO}_3-x\text{ATiO}_3$  [ $A = \text{Ba}^{2+}$ ,  $\text{Ca}^{2+}$  and  $\text{Sr}^{2+}$ ] or BNTBT100x, BNTCT100x, BNTST100x with  $x = 0-0.12$ ,  $0-0.08$  and  $0-0.12$  ceramics prepared via combustion method was studied. BNTBT100x ceramics showed mixed of rhombohedral and tetragonal phase. The density, linear shrinkage and maximum dielectric constant of BNTBT2 and BNTBT4 ceramics increased with increasing sintering temperatures up to  $1150^\circ\text{C}$  and then evaporations of  $\text{Bi}^{3+}$  and  $\text{Na}^+$  occurred. While, the density, linear shrinkage and maximum dielectric constant of BNTBT6 BNTBT8 BNTBT10 and BNTBT12 ceramics increased with increasing sintering temperatures up to  $1200^\circ\text{C}$  and then the impurity phases were detected at higher sintering temperatures. Moreover, the BNTBT8 ceramics sintered at  $1200^\circ\text{C}$  showed the highest dielectric constant at  $T_c$  and highest density of  $7400$  and  $5.80\text{ g/cm}^3$ . The  $P_r$  and  $E_c$  (using electric field at  $40\text{ kV}$ ) were  $28.10\text{ }\mu\text{C/cm}^3$  and  $21.02\text{ kV/cm}$ , respectively. BNTCT100x ceramics exhibited the rhombohedral phase in all the samples. The density of BNTCT100x ceramics increased with increasing sintering temperatures up to  $1150^\circ\text{C}$  and thereafter they decreased. The linear shrinkage of BNTCT100x ceramics increased with increasing sintering temperatures. Moreover, the BNTCT2 ceramics sintered at  $1150^\circ\text{C}$  showed the highest dielectric constant at  $T_c$  and highest density of  $3208$  and  $5.57\text{ g/cm}^3$ . The  $P_r$  and  $E_c$  (using electric field at  $40\text{ kV}$ ) were  $17.4\text{ }\mu\text{C/cm}^3$  and  $30.13\text{ kV/cm}$ , respectively. BNTST100x ceramics exhibited the cubic phase in all the samples. The density and linear shrinkage of BNTST100x ceramics increased with increasing sintering temperatures. Moreover, the BNTST20 ceramics sintered at  $1200^\circ\text{C}$  showed the highest dielectric constant at  $T_c$  and highest density of  $4725$  and  $5.57\text{ g/cm}^3$ . The  $P_r$  and  $E_c$  (using electric field at  $40\text{ kV}$ ) were  $17.19\text{ }\mu\text{C/cm}^3$  and  $29.61\text{ kV/cm}$ , respectively.

**Key words:** combustion method, ferroelectric, microstructure, dielectric properties, phase formation

## สารบัญ

บทที่	หน้า
1 บทนำ.....	1
ความเป็นมาของปัญหา.....	1
จุดมุ่งหมายของการศึกษา.....	3
ขอบเขตของงานวิจัย.....	3
2 เอกสารและงานวิจัยที่เกี่ยวข้อง.....	4
เฟอร์โรอิเล็กทริก (Ferroelectric).....	4
สมบัติพิโซอิเล็กทริก (Piezoelectric property).....	8
พาราอิเล็กทริก (Paraelectric).....	9
เครื่องวิเคราะห์การเลี้ยวเบนของรังสีเอกซ์ (X-Ray Diffractometer).....	10
กล้องจุลทรรศน์อิเล็กตรอนแบบส่องกราด(Scanning Electron Microscope).....	14
หลักการเกิดภาพของกล้องจุลทรรศน์อิเล็กตรอนแบบส่องกราด.....	14
การซินเตอร์.....	16
การหาความหนาแน่น (Density).....	20
การเตรียมเซรามิกด้วยวิธีการเผาไหม้.....	21
งานวิจัยที่เกี่ยวข้อง.....	23
3 อุปกรณ์และวิธีการทดลอง.....	32
สารเคมีที่ใช้ในการทดลอง.....	32
อุปกรณ์ที่ใช้ในการเตรียมสาร.....	32
เครื่องมือที่ใช้ในการทดลอง.....	32
เครื่องมือที่ใช้ในการวิเคราะห์ผลการทดลอง.....	33
วิธีการทดลอง.....	33

## สารบัญ (ต่อ)

บทที่	หน้า
4 ผลการวิจัย.....	39
ผลการตรวจสอบลักษณะเฉพาะของผงผลิตภัณฑ์โซเดียมไททาเนต ผงผลิตภัณฑ์ไททาเนต ผงผลิตภัณฑ์แคลเซียมไททาเนต และผงผลิตภัณฑ์ สทธรอนเซียม ไททาเนต.....	39
ผลการตรวจสอบลักษณะเฉพาะของเซรามิกผลิตภัณฑ์โซเดียมไททาเนต- แบเรียมไททาเนต เซรามิกผลิตภัณฑ์โซเดียมไททาเนต-แคลเซียม ไททาเนต และเซรามิกผลิตภัณฑ์โซเดียมไททาเนต-สทธรอนเซียม ไททาเนต.....	42
5 บทสรุป.....	102
สรุปการตรวจสอบผงผลิตภัณฑ์โซเดียมไททาเนต ผงผลิตภัณฑ์แบเรียมไททาเนต ผงผลิตภัณฑ์แคลเซียมไททาเนต และผงผลิตภัณฑ์สทธรอนเซียมไททาเนต.....	102
สรุปการตรวจสอบเซรามิกผลิตภัณฑ์โซเดียมไททาเนต-แบเรียมไททาเนต (1-x) BNT-xBT; BNTBT100x.....	102
สรุปการตรวจสอบเซรามิกผลิตภัณฑ์โซเดียมไททาเนต-แบเรียมไททาเนต (1-x) BNT-xCT; BNTCT100x.....	103
สรุปการตรวจสอบเซรามิกผลิตภัณฑ์โซเดียมไททาเนต-แบเรียมไททาเนต (1-x) BNT-xST; BNTST100x.....	103
บรรณานุกรม.....	105
Output.....	110
ภาคผนวก.....	114

## สารบัญภาพ

ภาพ	หน้า
1 แผนภาพแสดงการแบ่งกลุ่มฟิสิกส์อิเล็กทรอนิกส์และกลุ่มย่อย.....	4
2 ความต่างเฟสระหว่างกระแสลับ (I) และศักย์ไฟฟ้า (V) ของวัสดุไดอิเล็กทริก (a)กรณีไม่มีการสูญเสียพลังงาน (b) กรณีมีการสูญเสียพลังงาน.....	7
3 วงรอบฮิสเทอรีซิสระหว่างโพลาริเซชันกับสนามไฟฟ้าในสารเฟอร์โรอิเล็กทริก	8
4 ปฏิกิริยาการนำฟิสิกส์อิเล็กทรอนิกส์ในวัสดุ (ก) แบบตรง (ข) แบบผกผัน.....	9
5 วงรอบฮิสเทอรีซิสระหว่างโพลาริเซชันกับสนามไฟฟ้าใน (a) สารแอนติเฟอร์โร- อิเล็กทริก (b) สารพาราอิเล็กทริก.....	10
6 แบบจำลองสำหรับการพิสูจน์กฎของแบรกก์ .....	12
7 แสดงพฤติกรรมการขึ้นเตอรแบบสถานะของแข็งทั่ว ๆ ไปในรูปแบบของ ความสัมพันธ์ระหว่างความหนาแน่นกับอุณหภูมิและเวลาที่ใช้ในการเผา	17
8 แสดงพัฒนาการของโครงสร้างจุลภาคที่เกิดจากการขึ้นเตอรแบบสถานะ ของแข็ง (a) อนุภาคฝังยัดกันอยู่แบบหลวม ๆ หลังการอัดขึ้นรูป (b) การขึ้นเตอรช่วงเริ่มต้น (c) การขึ้นเตอรช่วงกลาง และ (d) การขึ้นเตอรช่วง สุดท้าย.....	18
9 การเปลี่ยนแปลงของกระบวนการเผาไหม้.....	22
10 ค่าคงที่ไดอิเล็กทริกของเซรามิก BNBT ที่โพล ( $\epsilon_{33}^T$ ) และไม่ได้โพล ( $\epsilon_{33}$ ).....	23
11 ค่าคงที่ไดอิเล็กทริกและการสูญเสียไดอิเล็กทริกของเซรามิก BNBT-5 ( $x =$ 0.05).....	24
12 วงรอบฮิสเทอรีซิสของเซรามิก BNBT-5 (a) ที่อุณหภูมิห้อง (b) ที่อุณหภูมิ 160 องศาเซลเซียส.....	24
13 ความสัมพันธ์ของปริมาณ $\text{Bi}_{0.5}\text{Na}_{0.5}\text{TiO}_3$ และ $\text{BaTiO}_3$ ในระบบ $(\text{Bi}_{0.5}\text{Na}_{0.5})_{1-x}$ $\text{Ba}_x\text{TiO}_3$ โดยที่ $F_\alpha$ คือเฟสเฟอร์โรอิเล็กทริกที่มีโครงสร้างแบบรอมโบฮีดรอล $F_\beta$ คือเฟสเฟอร์โรอิเล็กทริกที่มีโครงสร้างแบบเททราโกนอล AF คือ เฟสแอนติเฟอร์โรอิเล็กทริกที่มีโครงสร้างแบบรอมโบฮีดรอล P คือเฟส พาราอิเล็กทริก	25

14	รูปแบบการเลี้ยวเบนของรังสีเอกซ์ของเซรามิก (1-x)BNT-xBT.....	26
----	---	----

## สารบัญภาพ (ต่อ)

ภาพ	หน้า	
15	แสดงภาพถ่ายจากกล้องจุลทรรศน์อิเล็กตรอนแบบส่องกราด (SEM) ของเซรามิก (1- x)BNT-xBT ที่เผาขึ้นเตอร์ที่ 1200 องศาเซลเซียส โดย (a) x = 0 และ (b) x = 0.06.....	26
16	แสดงค่า $d_{33}$ , $k_p$ , $\epsilon_r$ และ $\tan\delta$ ของเซรามิก(1- x)BNT-xBT .....	27
17	ค่าคงที่ไดอิเล็กทริกของเซรามิก (1-x)BNT-xBT ที่ปริมาณ x ต่างๆ.....	28
18	ค่าคงที่พิโซอิเล็กทริกและค่าสัมประสิทธิ์ไฟฟ้าเชิงกลของเซรามิก (1- x)BNT-xBT ที่ปริมาณ x ต่างๆ.....	28
19	ค่าคงที่แลตทิซและค่าแลตทิซแสดงความเป็นรอมโบอีดรัล ( $90^\circ - \alpha$ ) ของเซรามิกBNCT100x และ BNST100x ที่ปริมาณ x ต่างๆ .....	29
20	ค่าคงที่ไดอิเล็กทริกของเซรามิก BNST100x ที่ปริมาณ x ต่างๆ (a) x=0.04 (b) x=0.08, (c) x=0.14, (d) x=0.20 และ (e) x=0.24 โดยวัดที่ความถี่10kHz	30
21	ค่าคงที่พิโซอิเล็กทริก, $d_{33}$ ของ BNBT100x, BNST100x และ BNCT100x ที่ปริมาณ x ต่างๆ.....	31
22	แสดงขั้นตอนการขึ้นเตอร์เซรามิกเซรามิกมิกบิสมาทโซเดียมไททานต-แคลเซียมไททานต (BNTCT) เซรามิกบิสมาทโซเดียมไททานต-สทอนเซียมไททานต (BNTST) และเซรามิกบิสมาทโซเดียมไททานต-แบเรียมไททานต (BNTBT)	38
23	รูปแบบการเลี้ยวเบนของรังสีเอกซ์ของผงผลึกบิสมาทโซเดียมไททานต ( $\text{Bi}_{0.5}\text{Na}_{0.5}\text{TiO}_3$ ) ผงผลึกแบเรียมไททานต( $\text{BaTiO}_3$ ) ผงผลึกแคลเซียมไททานต( $\text{CaTiO}_3$ ) และผงผลึกสทอนเซียมไททานต( $\text{SrTiO}_3$ ) ที่เตรียมด้วยวิธีเผาไหม้.....	40
24	ภาพถ่ายบริเวณผิวหน้าของผงผลึกต่างๆ โดยที่ (ก) ผงผลึกบิสมาทโซเดียมไททานต (ข) ผงผลึกแบเรียมไททานต (ค) ผงผลึกแคลเซียมไททานต และ (ง) ผงผลึกสทอนเซียมไททานต.....	41

## สารบัญภาพ (ต่อ)

ภาพ	หน้า
25 รูปแบบการเลี้ยวเบนของรังสีเอกซ์ของเซรามิก BNTBT2 ที่อุณหภูมิซินเตอร์ต่างๆ	43
26 รูปแบบการเลี้ยวเบนของรังสีเอกซ์ของเซรามิก BNTBT4 ที่อุณหภูมิซินเตอร์ต่างๆ	44
27 รูปแบบการเลี้ยวเบนของรังสีเอกซ์ของเซรามิก BNTBT6 ที่อุณหภูมิซินเตอร์ต่างๆ	45
28 รูปแบบการเลี้ยวเบนของรังสีเอกซ์ของเซรามิก BNTBT8 ที่อุณหภูมิซินเตอร์ต่างๆ	46
29 รูปแบบการเลี้ยวเบนของรังสีเอกซ์ของเซรามิก BNTBT10 ที่อุณหภูมิซินเตอร์ ต่างๆ.....	47
30 รูปแบบการเลี้ยวเบนของรังสีเอกซ์ของเซรามิก BNTBT12 ที่อุณหภูมิซินเตอร์ ต่างๆ.....	48
31 รูปแบบการเลี้ยวเบนของรังสีเอกซ์ของเซรามิก BNTBT100x (a) $x = 0.02$ ซินเตอร์ที่อุณหภูมิ 1150 องศาเซลเซียส (b) $x = 0.04$ ซินเตอร์ที่อุณหภูมิ 1150 องศาเซลเซียส (c) $x = 0.06$ ซินเตอร์ที่อุณหภูมิ 1200 องศาเซลเซียส (d) $x = 0.08$ ซินเตอร์ที่อุณหภูมิ 1200 องศาเซลเซียส (e) $x = 0.10$ ซินเตอร์ ที่อุณหภูมิ 1200 องศาเซลเซียส และ (f) $x = 0.12$ ซินเตอร์ที่อุณหภูมิ 1200 องศาเซลเซียส.....	49
32 ภาพถ่ายบริเวณผิวหน้าของเซรามิก BNTBT2 ที่อุณหภูมิซินเตอร์ต่างๆ (ก) 1050 องศาเซลเซียส (ข) 1100 องศาเซลเซียส และ (ค) 1150 องศาเซลเซียส.....	52
33 ภาพถ่ายบริเวณผิวหน้าของเซรามิก BNTBT4 ที่อุณหภูมิซินเตอร์ต่างๆ (ก) 1050 องศาเซลเซียส (ข) 1100 องศาเซลเซียส และ (ค) 1150 องศาเซลเซียส.....	53
34 ภาพถ่ายบริเวณผิวหน้าของเซรามิก BNTBT6 ที่อุณหภูมิซินเตอร์ต่างๆ (ก) 1050 องศาเซลเซียส (ข) 1100 องศาเซลเซียส (ค) 1150 องศาเซลเซียส (ง) 1200 องศาเซลเซียส และ (จ) 1210 องศาเซลเซียส.....	54
35 ภาพถ่ายบริเวณผิวหน้าของเซรามิก BNTBT8 ที่อุณหภูมิซินเตอร์ต่างๆ (ก) 1050 องศาเซลเซียส (ข) 1100 องศาเซลเซียส (ค) 1150 องศาเซลเซียส (ง) 1200 องศาเซลเซียส และ (จ) 1210 องศาเซลเซียส.....	55

## สารบัญภาพ (ต่อ)

ภาพ	หน้า
36 ภาพถ่ายบริเวณผิวหน้าของเซรามิก BNTBT10 ที่อุณหภูมิซินเตอร์ต่างๆ (ก) 1050 องศาเซลเซียส (ข) 1100 องศาเซลเซียส (ค) 1150 องศาเซลเซียส (ง) 1200 องศาเซลเซียส และ (จ) 1210 องศาเซลเซียส.....	56
37 ภาพถ่ายบริเวณผิวหน้าของเซรามิก BNTBT12 ที่อุณหภูมิซินเตอร์ต่างๆ (ก) 1050 องศาเซลเซียส (ข) 1100 องศาเซลเซียส (ค) 1150 องศาเซลเซียส (ง) 1200 องศาเซลเซียส และ (จ) 1210 องศาเซลเซียส.....	57
38 ภาพถ่ายบริเวณรอยหักของเซรามิก BNTBT8 ซินเตอร์ที่อุณหภูมิต่างๆ (ก) 1050 องศาเซลเซียส (ข) 1100 องศาเซลเซียส (ค) 1150 องศาเซลเซียส และ (ง) 1200 องศาเซลเซียส.....	58
39 ค่าคงที่ไดอิเล็กตริกของเซรามิก BNTBT2 ซินเตอร์ที่อุณหภูมิต่างๆ.....	62
40 ค่าคงที่ไดอิเล็กตริกของเซรามิก BNTBT4 ซินเตอร์ที่อุณหภูมิต่างๆ.....	63
41 ค่าคงที่ไดอิเล็กตริกของเซรามิก BNTBT6 ซินเตอร์ที่อุณหภูมิต่างๆ.....	63
42 ค่าคงที่ไดอิเล็กตริกของเซรามิก BNTBT8 ซินเตอร์ที่อุณหภูมิต่างๆ.....	64
43 ค่าคงที่ไดอิเล็กตริกของเซรามิก BNTBT10 ซินเตอร์ที่อุณหภูมิต่างๆ.....	64
44 ค่าคงที่ไดอิเล็กตริกของเซรามิก BNTBT12 ซินเตอร์ที่อุณหภูมิต่างๆ.....	65
45 ค่าคงที่ไดอิเล็กตริกของเซรามิก BNTBT100x ซินเตอร์ที่อุณหภูมิ 1050 – 1200 องศาเซลเซียส.....	65
46 $T_d$ และ $T_m$ ของเซรามิก BNTBT100x ซินเตอร์ที่อุณหภูมิ 1150 องศาเซลเซียส	66
47 วงรอบฮิสเทอรีซิสของเซรามิก BNTBT8 ที่ค่าสนามไฟฟ้าต่างๆ.....	68
48 รูปแบบการเลี้ยวเบนของรังสีเอกซ์ของเซรามิก BNTCT2 ที่อุณหภูมิซินเตอร์ ต่างๆ.....	71
49 รูปแบบการเลี้ยวเบนของรังสีเอกซ์ของเซรามิก BNTCT4 ที่อุณหภูมิซินเตอร์	72

ต่างๆ.....

## สารบัญภาพ (ต่อ)

ภาพ	หน้า
50 รูปแบบการเลี้ยวเบนของรังสีเอกซ์ของเซรามิก BNTCT6 ที่อุณหภูมิซินเตอร์ต่างๆ	73
51 รูปแบบการเลี้ยวเบนของรังสีเอกซ์ของเซรามิก BNTCT8 ที่อุณหภูมิซินเตอร์ ต่างๆ.....	74
52 ภาพถ่ายบริเวณผิวหน้าของเซรามิก BNTCT2 ที่อุณหภูมิซินเตอร์ต่างๆ (ก) 1050 องศาเซลเซียส (ข) 1100 องศาเซลเซียส (ค) 1150 องศาเซลเซียส และ (ง) 1200 องศาเซลเซียส.....	76
53 ภาพถ่ายบริเวณผิวหน้าของเซรามิก BNTCT4 ที่อุณหภูมิซินเตอร์ต่างๆ (ก) 1050 องศาเซลเซียส (ข) 1100 องศาเซลเซียส (ค) 1150 องศาเซลเซียส และ (ง) 1200 องศาเซลเซียส.....	76
54 ภาพถ่ายบริเวณผิวหน้าของเซรามิก BNTCT6 ที่อุณหภูมิซินเตอร์ต่างๆ (ก) 1050 องศาเซลเซียส (ข) 1100 องศาเซลเซียส (ค) 1150 องศาเซลเซียส และ (ง) 1200 องศาเซลเซียส.....	77
55 ภาพถ่ายบริเวณผิวหน้าของเซรามิก BNTCT8 ที่อุณหภูมิซินเตอร์ต่างๆ (ก) 1050 องศาเซลเซียส (ข) 1100 องศาเซลเซียส (ค) 1150 องศาเซลเซียส และ (ง) 1200 องศาเซลเซียส.....	77
56 ภาพถ่ายบริเวณรอยหักของเซรามิก BNTCT2 ซินเตอร์ที่อุณหภูมิต่างๆ (ก) 1050 องศาเซลเซียส (ข) 1100 องศาเซลเซียส (ค) 1150 องศาเซลเซียส และ (ง) 1200 องศาเซลเซียส.....	78
57 ค่าคงที่ไดอิเล็กทริกของเซรามิก BNTCT2 ซินเตอร์ที่อุณหภูมิต่างๆ.....	81
58 ค่าคงที่ไดอิเล็กทริกของเซรามิก BNTCT4 ซินเตอร์ที่อุณหภูมิต่างๆ.....	81
59 ค่าคงที่ไดอิเล็กทริกของเซรามิก BNTCT6 ซินเตอร์ที่อุณหภูมิต่างๆ.....	82
60 ค่าคงที่ไดอิเล็กทริกของเซรามิก BNTCT8 ซินเตอร์ที่อุณหภูมิต่างๆ.....	82
61 วงรอบฮิสเทอรีซิสของเซรามิก BNTBT8 ที่ค่าสนามไฟฟ้าต่างๆ.....	84
62 รูปแบบการเลี้ยวเบนของรังสีเอกซ์ของเซรามิก BNTST10 ที่อุณหภูมิซินเตอร์	



ต่าง ๆ.....	87
-------------	----

## สารบัญภาพ (ต่อ)

ภาพ	หน้า
63 รูปแบบการเลี้ยงเบนของรังสีเอกซ์ของเซรามิก BNTST20 ที่อุณหภูมิซินเตอร์ต่าง ๆ.....	88
64 รูปแบบการเลี้ยงเบนของรังสีเอกซ์ของเซรามิก BNTST30 ที่อุณหภูมิซินเตอร์ต่าง ๆ.....	89
65 รูปแบบการเลี้ยงเบนของรังสีเอกซ์ของเซรามิก BNTST40 ที่อุณหภูมิซินเตอร์ต่าง ๆ.....	90
66 ภาพถ่ายบริเวณผิวหน้าของเซรามิก BNTST10 ที่อุณหภูมิซินเตอร์ต่าง ๆ (ก) 1050 องศาเซลเซียส (ข) 1100 องศาเซลเซียส (ค) 1150 องศาเซลเซียส และ (ง) 1200 องศาเซลเซียส.....	92
67 ภาพถ่ายบริเวณผิวหน้าของเซรามิก BNTST20 ที่อุณหภูมิซินเตอร์ต่าง ๆ (ก) 1050 องศาเซลเซียส (ข) 1100 องศาเซลเซียส (ค) 1150 องศาเซลเซียส และ (ง) 1200 องศาเซลเซียส.....	92
68 ภาพถ่ายบริเวณผิวหน้าของเซรามิก BNTST30 ที่อุณหภูมิซินเตอร์ต่าง ๆ (ก) 1050 องศาเซลเซียส (ข) 1100 องศาเซลเซียส (ค) 1150 องศาเซลเซียส และ (ง) 1200 องศาเซลเซียส.....	93
69 ภาพถ่ายบริเวณผิวหน้าของเซรามิก BNTST40 ที่อุณหภูมิซินเตอร์ต่าง ๆ (ก) 1050 องศาเซลเซียส (ข) 1100 องศาเซลเซียส (ค) 1150 องศาเซลเซียส และ (ง) 1200 องศาเซลเซียส.....	93
70 ภาพถ่ายบริเวณรอยหักของเซรามิก BNTST20 ซินเตอร์ที่อุณหภูมิต่าง ๆ (ก) 1050 องศาเซลเซียส (ข) 1100 องศาเซลเซียส (ค) 1150 องศาเซลเซียส และ (ง) 1200 องศาเซลเซียส.....	94
71 ค่าคงที่ไดอิเล็กทริกของเซรามิก BNTST10 ซินเตอร์ที่อุณหภูมิต่าง ๆ.....	97
72 ค่าคงที่ไดอิเล็กทริกของเซรามิก BNTST20 ซินเตอร์ที่อุณหภูมิต่าง ๆ.....	97
73 ค่าคงที่ไดอิเล็กทริกของเซรามิก BNTST30 ซินเตอร์ที่อุณหภูมิต่าง ๆ.....	98

74	ค่าคงที่ได้อิเล็กทรอนิกส์ของเซรามิก BNTST40 ซินเตอร์ที่อุณหภูมิต่างๆ.....	98
----	---	----

### สารบัญภาพ (ต่อ)

ภาพ		หน้า
75	วงรอบฮิสเทอรีซิสของเซรามิก BNTST20 ที่ค่าสนามไฟฟ้าต่างๆ.....	99
76	วงรอบฮิสเทอรีซิสของเซรามิก BNTST30 ที่ค่าสนามไฟฟ้าต่างๆ.....	100

## สารบัญตาราง

ตาราง	หน้า
1 แสดงค่าแลตทิซแสดงความเป็นรอมโบอีตรอล ค่าคงที่แลตทิซและอัตราส่วน $c/a$ ของเซรามิก BNTBT100x .....	50
2 แสดงขนาดเกรนเฉลี่ย ความหนาแน่น และการหดตัวเชิงเส้นของเซรามิก BNTBT100x ที่อุณหภูมิซินเตอร์ต่างๆ.....	59
3 แสดงขนาดเกรนเฉลี่ย ความหนาแน่น และการหดตัวเชิงเส้นของเซรามิก BNTBT100x ซินเตอร์ที่อุณหภูมิ 1150 องศาเซลเซียส.....	60
4 แสดงอุณหภูมิ depolarization ( $T_d$ ) อุณหภูมิคูรี ( $T_m$ ) ค่าคงที่ไดอิเล็กทริก ( $\epsilon_r$ ) ที่ $T_m$ ค่าสูญเสียไดอิเล็กทริก ( $\tan \delta$ ) ที่ $T_m$ ของเซรามิก BNTBT100x ที่ อุณหภูมิซินเตอร์ต่างๆ.....	67
5 แสดงค่าคงที่พิโซอิเล็กทริก ( $d_{33}$ ) โพลาริเซชันอิ่มตัว ( $P_s$ ) โพลาริเซชันคงค้าง ( $P_r$ ) และสนามไฟฟ้าลบล้าง ( $E_c$ ) ของเซรามิก BNTBT8.....	69
6 แสดงขนาดเกรนเฉลี่ย ความหนาแน่น การหดตัวเชิงเส้น และ แลตทิซพารามิเตอร์ $a_R$ ของเซรามิกBNTBT100x ที่อุณหภูมิซินเตอร์ต่างๆ.....	79
7 แสดงอุณหภูมิ depolarization ( $T_d$ ) อุณหภูมิคูรี ( $T_m$ ) ค่าคงที่ไดอิเล็กทริก ( $\epsilon_r$ ) ที่ $T_m$ ค่าสูญเสียไดอิเล็กทริก ( $\tan \delta$ ) ที่ $T_m$ ของเซรามิก BNTCT100x .....	83
8 แสดงค่าคงที่พิโซอิเล็กทริก ( $d_{33}$ ) โพลาริเซชันอิ่มตัว ( $P_s$ ) โพลาริเซชันคงค้าง ( $P_r$ ) และสนามไฟฟ้าลบล้าง ( $E_c$ ) ของเซรามิก BNTCT2.....	85
9 แสดงขนาดเกรนเฉลี่ย ความหนาแน่น การหดตัวเชิงเส้น และแลตทิซพารามิเตอร์ $a_R$ ของเซรามิกBNTST100x ที่อุณหภูมิซินเตอร์ต่างๆ.....	95
10 .....	
แสดงค่าคงที่พิโซอิเล็กทริก ( $d_{33}$ ) โพลาริเซชันอิ่มตัว ( $P_s$ ) โพลาริเซชันคงค้าง ( $P_r$ ) และสนามไฟฟ้าลบล้าง ( $E_c$ ) ของเซรามิกBNTST20 และ BNTST30.....	101

## บทที่ 1

### บทนำ

#### ความเป็นมาของปัญหา

เซรามิกเฟอร์โรอิเล็กทริก (ferroelectric ceramics) กลุ่มที่มีโครงสร้างแบบเพอร์รอฟสไกต์ (perovskite,  $ABO_3$ ) มีความสำคัญมากที่สุดต่อการประยุกต์ใช้ในอุตสาหกรรมการผลิตตัวเก็บประจุที่มีค่าคงตัวไดอิเล็กทริก (dielectric constant,  $\epsilon_r$ ) สูง ทรานสดิวเซอร์ (transducer) โซนาร์ (sonar) ตัวกรองสัญญาณ และเซนเซอร์ (sensor) เป็นต้น เนื่องจากสารกลุ่มนี้มีสมบัติทางไฟฟ้าที่ดีมาก ซึ่งสารเฟอร์โรอิเล็กทริกที่นิยมนำมาประยุกต์ใช้งานดังกล่าวส่วนมากมักจะเป็นสารในกลุ่มที่มีตะกั่วเป็นองค์ประกอบ เช่น เลดเซอร์โคเนตทาเนต (PZT) เลดแมกนีเซียมไนโอเบต (PMN) เลดแลนแทนนัมเซอร์โคเนตไทเทเนียม (PLZT) เป็นต้น อย่างไรก็ตาม เนื่องจากสารเหล่านี้มีตะกั่วเป็นองค์ประกอบหลักทำให้เป็นอันตรายต่อสิ่งมีชีวิตและสิ่งแวดล้อม [1, 2, 3] และในปัจจุบันได้มีการรณรงค์เรื่องการงดใช้อุปกรณ์อิเล็กทรอนิกส์ที่มีส่วนประกอบของสารมีพิษ เช่น ตะกั่ว หรือปรอท ทำให้มีการหันมาใช้สารไร้ตะกั่วแทน จุดนี้เองที่ทำให้นักวิจัยจำนวนมากทุ่มเท ศึกษา วิจัย และพัฒนาสารไร้ตะกั่วด้วยวิธีการต่างๆ ซึ่งสารเฟอร์โรอิเล็กทริกที่นิยมนำมาพัฒนามาก็คือ บิสมัทโซเดียมไททาเนต (Bismuth Sodium Titanate; BNT) แบเรียมไททาเนต (Barium Titanate; BT) แคลเซียมไททาเนต (Calcium Titanate; CT) สตรอนเทียมไททาเนต (Strontium Titanate; ST) เป็นต้น [4, 5, 6, 7]

เซรามิกบิสมัทโซเดียมไททาเนต ( $Bi_{0.5}Na_{0.5}TiO_3$ ; BNT) เป็นวัสดุเฟอร์โรอิเล็กทริก ที่ไม่มีตะกั่วเป็นส่วนประกอบ ได้รับความสนใจเนื่องจากมีค่าโพลาไรเซชันสูงประมาณ  $38 \mu C/cm^2$  มีอุณหภูมิคูรี ( $T_c$ ) สูงอยู่ที่ประมาณ 320 องศาเซลเซียส โดยที่อุณหภูมิห้อง BNT มีโครงสร้างแบบเพอร์รอฟสไกต์เฟอร์โรอิเล็กทริกแบบโรตารอน และเกิดการเปลี่ยนเฟสจากเฟอร์โรอิเล็กทริกไปเป็นแอนติเฟอร์โรอิเล็กทริกที่อุณหภูมิ ประมาณ 230 องศาเซลเซียส ถึงแม้ว่าผลึกเดี่ยวของเซรามิก BNT จะมีสมบัติพิโซอิเล็กทริกที่ดี ( $\sim 83 \text{ pC/N}$ ) แต่เซรามิก BNT มีค่าสนามไฟฟ้าลบล้าง ( $E_c$ ) สูงประมาณ 73 kV/cm ซึ่งทำให้โพลได้ยาก [4, 8, 9]

การปรับปรุงสมบัติทางไฟฟ้าและลดค่าสนามไฟฟ้าลบล้าง ( $E_c$ ) ของเซรามิก BNT สามารถทำได้ด้วยการเจือสาร  $Ba^{2+}, Ca^{2+}$  และ  $Sr^{2+}$  (BNTBT, BNTCT และ BNTST) ได้พบว่าเซรามิกในระบบ  $(1-x)(Bi_{0.5}Na_{0.5})TiO_3-xBaTiO_3$  โดยที่  $x = 0 - 0.12$  แสดงสมบัติพิโซอิเล็กทริก

$d_{33}$  ที่สูง ( $\sim 174$  pC/N) และค่าคงที่ไดอิเล็กตริกสูงสุดที่อุณหภูมิห้อง  $\epsilon_r$  ( $\sim 1840$ ) นอกจากนั้นยังมีค่าสัมประสิทธิ์ไฟฟ้าเชิงกล  $k_p$  สูง ( $\sim 0.28$ ) [10, 11] และสามารถโพลได้ง่ายขึ้นเนื่องจากมีค่าสนามไฟฟ้าลบล้างประมาณ 4 - 11.2 kV/cm [12, 13] เซรามิกในระบบ  $(1-x)(\text{Bi}_{0.5}\text{Na}_{0.5})\text{TiO}_3$ - $x\text{CaTiO}_3$  โดยที่  $x = 0 - 0.08$  พบว่าเซรามิกมีสมบัติใกล้เคียงกับเซรามิก BNT แต่อุณหภูมิคูรี  $T_c$  เพิ่มขึ้นทำให้ช่วงอุณหภูมิในการนำไปประยุกต์ใช้งานเพิ่มขึ้น [14, 15] และเซรามิกในระบบ  $(1-x)(\text{Bi}_{0.5}\text{Na}_{0.5})\text{TiO}_3$ - $x\text{SrTiO}_3$  โดยที่  $x = 0 - 0.40$  แสดงสมบัติพิโซอิเล็กตริกดีที่สุดที่สุด คือมีค่า  $d_{33}$  เท่ากับ 133 pC/N [16, 17]

เซรามิก BNTBT, BNTCT และ BNTST สามารถเตรียมด้วยวิธีผสมออกไซด์ โดยการเผาแคลไซน์ที่อุณหภูมิ 800 องศาเซลเซียส และซินเตอร์ที่อุณหภูมิ 1050 - 1200 องศาเซลเซียส ซึ่งเป็นที่ทราบกันดีว่าการซินเตอร์เซรามิกด้วยวิธีนี้ ต้องทำที่อุณหภูมิสูง จึงทำให้เกิดการระเหยของ  $\text{Bi}^{3+}$  และ  $\text{Na}^+$  [18] ส่งผลทำให้สมบัติต่างๆของเซรามิกเปลี่ยนแปลงไป ทำให้ไม่เหมาะสมกับการนำไปใช้จริงในเชิงอุตสาหกรรม ในขณะที่วิธีการเผาไหม้ (combustion method) เป็นวิธีที่ได้รับความนิยมมากสำหรับการเตรียมเซรามิก [19, 20, 21, 22, 23, 24] เนื่องจากเป็นวิธีที่มีความสะดวก ไม่ยุ่งยาก มีต้นทุนต่ำ และสามารถลดอุณหภูมิในการเผาแคลไซน์และซินเตอร์ลงได้ โดยอาศัยการปลดปล่อยพลังงานความร้อนจากการเผาไหม้ที่เกิดจากปฏิกิริยาเคมีของเชื้อเพลิง เช่น ยูเรีย ไกลซีน [25] และเซรามิกที่เตรียมได้ด้วยวิธีนี้จะมีคุณภาพดีและมีสมบัติต่างๆ ตามต้องการ

ในงานวิจัยนี้ เราจึงมุ่งศึกษาการเตรียมเซรามิกเฟอร์โรอิเล็กตริกชนิดไร้สารตะกั่วที่มีเซรามิกบิสมาทไซด์แบบไททานเตเป็นองค์ประกอบหลัก  $1-x(\text{Bi}_{0.5}\text{Na}_{0.5})\text{TiO}_3$ - $x\text{ATiO}_3$  [ $A = \text{Ba}^{2+}$ ,  $\text{Ca}^{2+}$  และ  $\text{Sr}^{2+}$ ] โดยที่  $x = 0 - 0.12$ ,  $0 - 0.08$  และ  $0 - 0.40$  ตามลำดับ ด้วยวิธีการเผาไหม้และศึกษาลักษณะเฉพาะของเซรามิกที่เตรียมได้เช่น โครงสร้างผลึก โครงสร้างจุลภาค ความหนาแน่น และสมบัติทางไฟฟ้า เป็นต้น

### จุดมุ่งหมายของการศึกษา

1. เพื่อศึกษาเงื่อนไขที่เหมาะสมในการเตรียมเซรามิกบิสมาทโชเดียมไททานเตเป็นองค์ประกอบหลัก  $1-x(\text{Bi}_{0.5}\text{Na}_{0.5})\text{TiO}_3-x\text{ATiO}_3$  [ $A = \text{Ba}^{2+}$ ,  $\text{Ca}^{2+}$  และ  $\text{Sr}^{2+}$ ] โดยที่  $x = 0-0.12$ ,  $0-0.08$  และ  $0-0.40$  ตามลำดับ ด้วยวิธีการเผาไหม้
2. เพื่อศึกษาผลของปริมาณสารเจือ  $\text{Ba}^{2+}$ ,  $\text{Ca}^{2+}$  และ  $\text{Sr}^{2+}$  ที่มีต่อโครงสร้างผลึก โครงสร้างจุลภาค และสมบัติไฟฟ้า ของเซรามิกที่เตรียมได้
3. เพื่อศึกษาผลของอุณหภูมิซินเตอร์ที่มีต่อโครงสร้างผลึก โครงสร้างจุลภาค และสมบัติไฟฟ้า ของเซรามิกที่เตรียมได้

### ขอบเขตของงานวิจัย

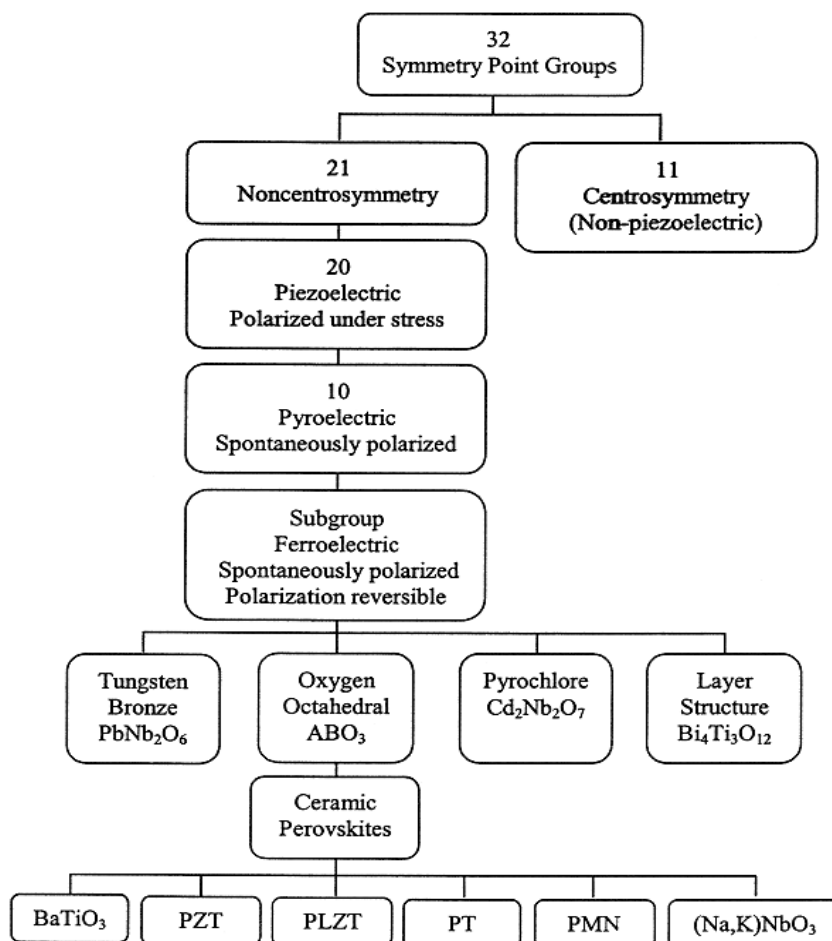
1. เตรียมผงผลึกบิสมาทโชเดียมไททานเต (BNT) ผงผลึกแบเรียมไททานเต (BT) ผงผลึกแคลเซียมไททานเต (CT) และผงผลึกสตรอนเชียมไททานเต (ST) ด้วยวิธีการเผาไหม้ โดยใช้อุณหภูมิในการเผาแคลไซน์ 650 – 1200 องศาเซลเซียส เป็นเวลา 2 – 4 ชั่วโมง
2. เตรียมเซรามิกบิสมาทโชเดียมไททานเตเป็นองค์ประกอบหลัก  $1-x(\text{Bi}_{0.5}\text{Na}_{0.5})\text{TiO}_3-x\text{ATiO}_3$  [ $A = \text{Ba}^{2+}$ ,  $\text{Ca}^{2+}$  และ  $\text{Sr}^{2+}$ ] โดยที่  $x = 0 - 0.12$ ,  $0 - 0.08$  และ  $0 - 0.40$  ตามลำดับ จากผงผลึกที่เตรียมได้จากข้อ 1 โดยใช้อุณหภูมิในการเผาซินเตอร์ 1050 – 1250 องศาเซลเซียส
3. ศึกษาสมบัติต่างๆ เช่น สมบัติทางกายภาพ โครงสร้างผลึก โครงสร้างจุลภาค และสมบัติไฟฟ้าของเซรามิกที่เตรียมได้จากข้อ 2

## บทที่ 2

### เอกสารและงานวิจัยที่เกี่ยวข้อง

#### เฟอร์โรอิเล็กทริก (Ferroelectric)

สารเฟอร์โรอิเล็กทริกเป็นสารที่ไม่มีความสมมาตรกับจุดศูนย์กลางของหน่วยเซลล์ทำให้ผลรวมของการเคลื่อนตัวของประจุบวกและลบ จึงทำให้สามารถสร้างไดโพลขึ้นมาได้โดยไม่ต้องได้รับแรงกล ซึ่งสามารถแยกสารเฟอร์โรอิเล็กทริกออกจากวัสดุไดอิเล็กทริก ด้วยการตกค้างหรือรีมานนท์โพลาไรเซชัน (remanent polarization:  $P_R$ ) เมื่อสนามไฟฟ้าที่ใส่เข้าไปมีค่าเป็นศูนย์ [26]



ภาพ 1 แผนภาพแสดงการแบ่งกลุ่มพิโซอิเล็กทริกและกลุ่มย่อย [26]

โดยปกตินั้นโพลาริเซชัน ( $P$ ) เป็นผลมาจากสนามไฟฟ้าซึ่งจัดเรียงขั้วคู่อะตอม (atomic dipole) หรือขั้วโมเลกุล (molecular dipole) อย่างเป็นระเบียบ ในสารหลายชนิดโพลาริเซชันเป็นสัดส่วนโดยตรงกับสนามไฟฟ้า เมื่อสนามไฟฟ้า  $\vec{E}$  มีความเข้มข้น

$$\vec{P} = \epsilon_0 \chi_e \vec{E} \quad (1)$$

เมื่อ  $\chi_e$  เป็นค่าคงที่เรียกว่าสภาพรับได้ทางไฟฟ้า (electric susceptibility) ของตัวกลาง ค่าของ  $\chi_e$  ขึ้นกับโครงสร้างทางจุลภาค (microscopic structure) ของสารที่พิจารณาและ  $\epsilon_0$  เป็นสภาพยอมของสุญญากาศ (permittivity of a vacuum) มีค่าคงที่ประมาณ  $8.854 \times 10^{-12}$  F/m โปรดสังเกตว่าสนามไฟฟ้า  $E$  ในสมการ (1) นี้เป็นสนามไฟฟ้าทั้งหมด ซึ่งอาจเกิดจากส่วนของประจุอิสระและส่วนของโพลาริเซชันที่สนาม  $\vec{E}$  ผลิตขึ้นเอง

$\chi_e$  ไม่มีทิศทาง และการขจัดไฟฟ้า (electric displacement:  $D$ ) มาจากการกระจายประจุอิสระเท่านั้น ซึ่งมีความสัมพันธ์ตามสมการ (2)

$$\vec{D} = \epsilon_0 \vec{E} + \vec{P} \quad (2)$$

จากสมการ (1) และ (2) จะได้ความสัมพันธ์เป็น

$$\vec{D} = \epsilon_0 \vec{E} + \epsilon_0 \chi_e \vec{E} = \epsilon_0 (1 + \chi_e) \vec{E} \quad (3)$$

ดังนั้นไม่เพียงแต่  $P$  เท่านั้นที่ขึ้นกับ  $\vec{E}$  แต่  $\vec{D}$  ก็ขึ้นกับ  $\vec{E}$  ด้วยเช่นกัน

$$\vec{D} = \epsilon \vec{E} \quad (4)$$

$$\epsilon = \epsilon_0 (1 + \chi_e) \quad (5)$$

เรียก  $\epsilon$  ว่าสภาพยอม (Permittivity) ของวัสดุ



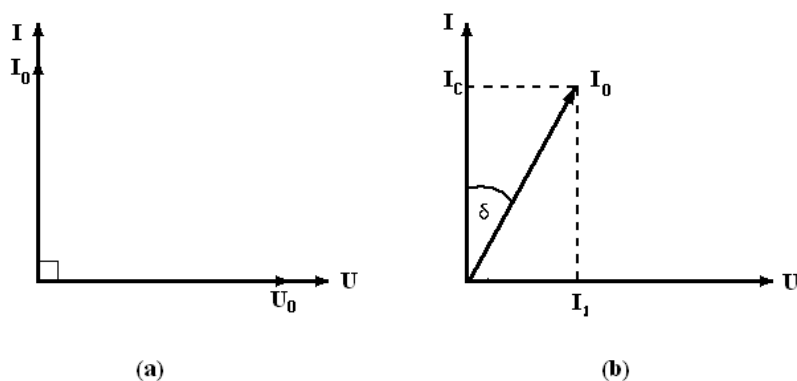
ในสุญญากาศ ไม่มีสารใดก่อให้เกิดโพลาไรซ์ ดังนั้นสภาพรับไว้ได้ทางไฟฟ้าจึงเป็นศูนย์ และสภาพยอม ( $\epsilon$ ) จะมีค่าเท่ากับ  $\epsilon_0$  และจากสมการ (5) จะได้

$$\epsilon_r = 1 + \chi_e = \frac{\epsilon}{\epsilon_0} \quad (6)$$

เมื่อ  $\epsilon_r$  คือสภาพยอมสัมพัทธ์ (relative permittivity) หรือ ค่าคงที่ไดอิเล็กทริกในวัสดุ เฟอร์โรอิเล็กทริก ส่วนใหญ่ค่าคงที่ไดอิเล็กทริก  $\epsilon_r$  จะมีค่าสูง ดังนั้น  $\bar{P} \gg \epsilon_0 \bar{E}$  และ  $D \approx P$

เมื่อป้อนไฟฟ้ากระแสสลับให้กับวัสดุไดอิเล็กทริก สนามไฟฟ้าจากแหล่งกำเนิดเป็นเหตุให้เกิดไดโพลภายในวัสดุไดอิเล็กทริก ในกรณีอุดมคติ ไดโพลภายในวัสดุไดอิเล็กทริกสามารถสลับทิศทางได้ตามความถี่ของแหล่งกำเนิด กรณีกระแสสลับ ( $I$ ) และศักย์ไฟฟ้า ( $V$ ) มีความต่างเฟสกันอยู่ 90 องศา ดังภาพ 3 (a) ทำให้ผลคูณสเกลาร์ (scalar product) ของ  $I$  และ  $V$  เท่ากับศูนย์ ดังนั้นจึงไม่มีการสูญเสียพลังงานของวัสดุไดอิเล็กทริก (dielectric loss:  $\tan \delta$ ) เกิดขึ้น แต่ในความเป็นจริงการสลับทิศทางของไดโพลจะก่อให้เกิดความต้านทานภายในเนื้อวัสดุเอง ทำให้เกิดการสูญเสียพลังงานขึ้น ซึ่งกรณีนี้กระแสไฟฟ้ากับศักย์ไฟฟ้ามีความต่างเฟสกันน้อยกว่า 90 องศา ดังภาพ 4 (b) โดยการสูญเสียพลังงานที่เกิดขึ้นนั้น สามารถวัดได้จากการทดลองและเป็นอัตราส่วนของสภาพยอมจินตภาพ (imaginary permittivity:  $\epsilon''$ ) และสภาพยอมจริง (real permittivity:  $\epsilon'$ ) ดังสมการที่ (7)

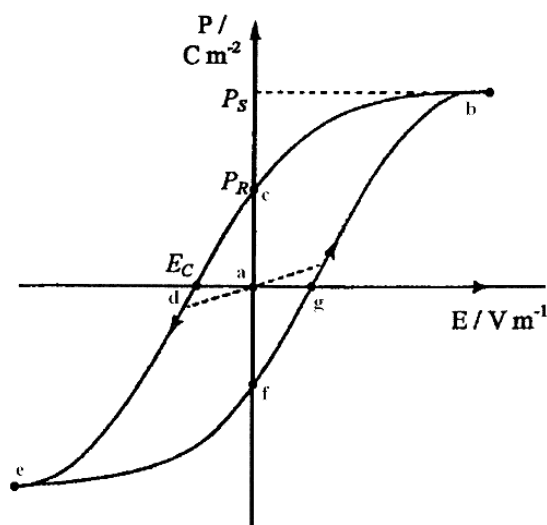
$$\tan \delta = \frac{\epsilon''}{\epsilon'} \quad (7)$$



ภาพ 2 ความต่างเฟสระหว่างกระแสลับ ( $I$ ) และศักย์ไฟฟ้า ( $V$ ) ของวัสดุไดอิเล็กทริก  
(a) กรณีไม่มีการสูญเสียพลังงาน (b) กรณีมีการสูญเสียพลังงาน [26]

ในวัสดุเฟอร์โรอิเล็กทริกการสลับทิศทางของไดโพลตามความถี่ของแหล่งกำเนิด ได้ ความสัมพันธ์ระหว่างการโพลาไรเซชันและสนามไฟฟ้า (polarization versus field) ซึ่ง ความสัมพันธ์จะพบในรูปของวงรอบฮิสเทอรีซิส (hysteresis loop) ดังภาพ 5 เมื่อให้สนามไฟฟ้า เข้าไปครั้งแรกการเกิดโพลาไรเซชันเพิ่มมากขึ้นอย่างรวดเร็ว จนกระทั่งถึงจุดอิ่มตัว (saturation polarization) คือจุด b ซึ่งการเกิดโพลาไรเซชันมีค่ามากที่สุด ไดโพลทั้งหมดจะเรียงตัวขนานกัน และหากเพิ่มสนามไฟฟ้าไปมากกว่านั้น ก็ไม่มีผลต่อการเกิดโพลาไรเซชัน เมื่อสนามไฟฟ้ามีค่า ลดลงแทนที่การโพลาไรเซชันจะถอยกลับไปตามเส้นทางเดิมเหมือนตอนเริ่มต้น ( $P = 0$ ) แต่กลับ ไปสู่ทิศทางที่แตกต่างกัน แม้ว่าจะไม่มีการให้สนามไฟฟ้า ( $E = 0$ ) แก่วัสดุเฟอร์โรอิเล็กทริกก็ตาม แต่ ยังคงมีโพลาไรซ์หลงเหลืออยู่ หรือรีมานেন্ট โพลาไรเซชัน (remanent value:  $P_R$ ) ที่จุด C

ถ้าเราต้องการกำจัดโพลาไรเซชันที่ยังหลงเหลืออยู่ เราต้องให้สนามไฟฟ้าย้อนกลับ ทิศทางเดิม (นั่นคือ  $-E$ ) โพลาไรเซชันจะลดลงสู่ศูนย์ที่จุด d ซึ่งเรียกจุดนี้ว่าสนาม โคเออร์ซีฟ (coercive field:  $E_C$ ) ถ้าเราพยายามให้สนามไฟฟ้าในทิศทางลบนี้สูงขึ้นอีก ในที่สุดก็จะ ถึงจุดอิ่มตัว ที่จุด C ขั้วไดโพลทั้งหมดชี้ไปทางขวา เมื่อถึงขั้นตอนนี้ ถ้าไม่ป้อนกระแสไฟฟ้าให้กับ วัสดุเฟอร์โรอิเล็กทริก แล้วปล่อยให้วัสดุที่มีโพลาไรเซชันเพิ่มขึ้นไปทางขวายังจุด f เพื่อให้ครบวงจร ต้องป้อนกระแสไฟฟ้าอีกครั้งในทิศทางบวก โพลาไรเซชันจะกลับสู่ศูนย์ที่จุด g และในที่สุดก็จะมุ่ง ไปสู่จุดอิ่มตัวที่จุด b

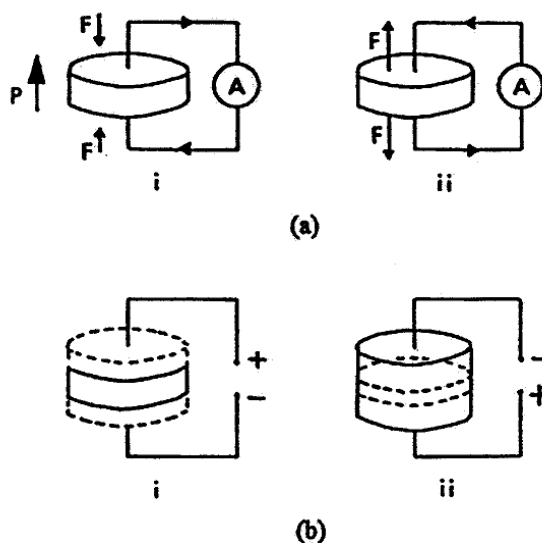


ภาพ 3 วงรอบฮิสเทอรีซิสระหว่างโพลาไรเซชันกับสนามไฟฟ้าในสารเฟอร์โรอิเล็กทริก [26]

#### สมบัติพิโซอิเล็กทริก (Piezoelectric property) [27]

คำว่า “พิโซ” มาจากภาษากรีก แปลว่า “กด” ดังนั้นพิโซอิเล็กทริก จึงหมายความว่า ความสามารถของวัสดุในการเปลี่ยนแรงกดที่ได้รับให้เป็นกระแสไฟฟ้า ซึ่งแรงกดที่ได้รับเป็นแรงทางกลทำให้เกิดความเครียดในผลึกขึ้น จึงเกิดการเรียงตัวไปทางเดียวกันเรียกว่าการโพลาไรเซชัน และการให้กระแสออกมา โดยสภาพพิโซอิเล็กทริกถูกค้นพบครั้งแรก โดย Jacques และ Pierre เมื่อประมาณ ค.ศ. 1880 ในสารประกอบผลึกเชิงเดี่ยว เช่น ควอตซ์ (quartz) และ Rochelle salt ( $\text{NaKC}_4\text{H}_4\text{O}_6 \cdot 4\text{H}_2\text{O}$ )

สภาพพิโซอิเล็กทริกสามารถเกิดขึ้นได้ 2 แบบ คือ แบบตรง (Direct piezoelectric effect) และแบบผกผันได้ (Converse piezoelectric effect) กล่าวคือ สภาพพิโซอิเล็กทริกแบบตรงสามารถเปลี่ยนแรงทางกลให้เป็นไดโพลได้ ดังภาพ 4(a) ในทำนองกลับกันสภาพพิโซอิเล็กทริกแบบผกผันสามารถเปลี่ยนแรงไฟฟ้าให้เป็นแรงกลได้ ภาพ 4(b) ซึ่งระดับการเกิดโพลาไรเซชันจะขึ้นกับความเครียดที่เกิดจากแรงที่ได้รับ นอกจากนี้ทิศทางของสนามไฟฟ้าที่ให้แก่วัสดุชนิดนี้จะเป็นตัวกำหนดว่าวัสดุจะขยายหรือหดลง

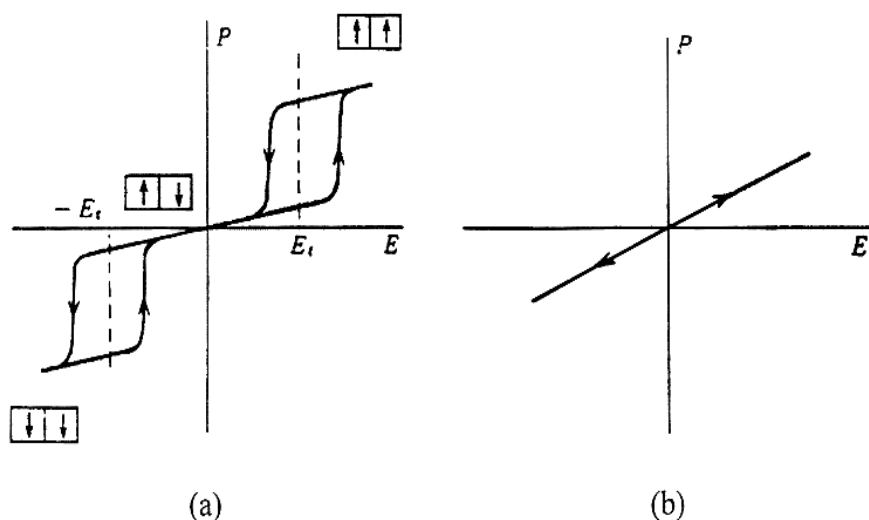


ภาพ 4 ปรากฏการณ์พิโซอิเล็กทริกในวัสดุ (a) แบบตรง (b) แบบผั้กลับ [27]

หน่วยเซลล์ (Unit cell) ของโครงสร้างผลึกในวัสดุมีความสำคัญมากต่อสภาพพิโซอิเล็กทริก กล่าวคือ สภาพพิโซอิเล็กทริกจะเกิดขึ้นได้ในวัสดุที่ไม่มีความสมมาตรกับจุดศูนย์กลางของหน่วยเซลล์เท่านั้น ดังนั้น จึงสามารถแบ่งกลุ่มผลึก 32 กลุ่ม เป็น 2 ประเภทใหญ่ ๆ คือประเภทแรกเป็นสารที่มีความสมมาตรกับจุดศูนย์กลางของหน่วยเซลล์มีทั้งหมด 11 กลุ่ม อีกประเภทหนึ่งเป็นสารที่ไม่มีความสมมาตรกับจุดศูนย์กลางของหน่วยเซลล์ มีทั้งหมด 21 กลุ่ม ใน 21 กลุ่ม เป็นสารที่ไม่มีความสมมาตรกับจุดศูนย์กลางของหน่วยเซลล์ดังกล่าว นั้น มี 20 กลุ่ม ที่มีสมบัติเป็นสารพิโซอิเล็กทริก และในสาร 20 กลุ่มนี้มีกลุ่มย่อยที่เป็นสารเฟอร์โรอิเล็กทริก ดังภาพ 1 ซึ่งข้อแตกต่างของวัสดุทั้ง 2 ชนิดนี้ คือความสามารถในการเกิดโพลาไรเซชัน โดยสารพิโซอิเล็กทริกไม่สามารถเกิดโพลาไรเซชันด้วยตนเองได้ แต่จะเกิดเมื่อให้แรงกลต่อผลึกเท่านั้น ในขณะที่สารเฟอร์โรอิเล็กทริกสามารถเกิดโพลาไรเซชันด้วยตนเองได้แม้จะไม่มีแรงกลมากระทำ

#### พาราอิเล็กทริก (Paraelectric) [28]

เฟสพาราอิเล็กทริกเกิดขึ้นที่อุณหภูมิสูงกว่าอุณหภูมิเฟสเฟอร์โรอิเล็กทริกและเฟสแอนติเฟอร์โรอิเล็กทริก ซึ่งสารพาราอิเล็กทริกจะประพฤติตัวเป็นฉนวนตามปกติ มีโครงสร้างที่สมมาตร จึงไม่สามารถเกิดโพลาไรเซชันได้ด้วยตนเอง เมื่อมีการป้อนสนามไฟฟ้าให้กับสารพาราอิเล็กทริก ทำให้เกิดโพลาไรเซชันขึ้น แต่เมื่อหยุดป้อนสนามไฟฟ้าเข้าไป ผลก็คือไม่มีการเกิดโพลาไรเซชันขึ้นอีก ซึ่งเขียนความสัมพันธ์ได้ดังภาพ 5



ภาพ 5 วงรอบฮิสเทอรีซิสระหว่างโพลาไรเซชันกับสนามไฟฟ้าใน

(a) สารแอนติเฟอร์โรอิเล็กทริก (b) สารพาราอิเล็กทริก [28]

### เครื่องวิเคราะห์การเลี้ยวเบนของรังสีเอกซ์ (X-Ray Diffractometer) [29]

เป็นเครื่องมือวิเคราะห์วัสดุพื้นฐานแบบไม่ทำลาย (Non-destructive analysis) เพื่อศึกษาเกี่ยวกับโครงสร้างผลึก การจัดเรียงตัวของอะตอมในโมเลกุลของสารประกอบต่าง ๆ ทั้งในเชิงคุณภาพและปริมาณ โดยอาศัยหลักการเลี้ยวเบนและการกระเจิงของรังสีเอกซ์และความรู้เกี่ยวกับวิธาระบบโครงสร้างผลึก

รังสีเอกซ์ เป็นคลื่นแม่เหล็กแม่เหล็กไฟฟ้าซึ่งมีอำนาจการทะลุทะลวงสูง มีความยาวคลื่นสั้นอยู่ในช่วงระหว่าง 0.1 – 100 อังสตรอม การเกิดอันตรกิริยาของรังสีเอกซ์กับสสารนั้นก่อให้เกิดปรากฏการณ์ต่าง ๆ โดยปรากฏการณ์ดังกล่าวล้วนเป็นลักษณะเฉพาะของสารแต่ละชนิด ซึ่งหลักการดังกล่าวเหล่านี้เราจึงสามารถนำมาใช้วิเคราะห์สารได้ดังนี้

1. ใช้วิเคราะห์องค์ประกอบของธาตุต่าง ๆ ในสารทั้งในเชิงปริมาณและคุณภาพ
2. ใช้ศึกษาหาโครงสร้างอิเล็กทรอนิกส์ ซึ่งสามารถให้ข้อมูลเกี่ยวกับการเกิดพันธะเคมี
3. ใช้ศึกษาเกี่ยวกับโครงสร้างผลึก หรือโมเลกุลของสารด้วยการใช้เทคนิคการเลี้ยวเบนของรังสีเอกซ์

รังสีเอกซ์มีทั้งที่เกิดเองตามธรรมชาติจากการสลายตัวของนิวเคลียสธาตุกัมมันตรังสีและที่มนุษย์ผลิตขึ้นจากกลไกทางอิเล็กทรอนิกส์ กล่าวคือ เมื่ออะตอมได้รับการกระตุ้นด้วยอิเล็กตรอนที่มีพลังงานสูงวิ่งชนอะตอม ทำให้เกิดอันตรกิริยา ระดับพลังงานของอิเล็กตรอนชั้นวงโคจรต่าง ๆ

ของอะตอมมีค่าสูงขึ้นเกิดภาวะเข้าสู่ปกติ โดยมวลของอะตอมไม่เปลี่ยนแปลงปรากฏการณ์ดังกล่าวเป็นกระบวนการปลดปล่อยพลังงานส่วนเกิน ในรูปคลื่นแม่เหล็กไฟฟ้าหรือโฟตอนออกมาในลักษณะพัลส์ (pulse) จากอะตอมทุกครั้งที่ได้รับการกระตุ้น คลื่นแม่เหล็กไฟฟ้าที่ปลดปล่อยออกมานี้เรียกว่า “รังสีเอกซ์” ซึ่งแบ่งได้ 2 ชนิด ตามกระบวนการของการปลดปล่อยพลังงานส่วนเกินจากอะตอมบริเวณชั้นโคจรอิเล็กตรอน คือ

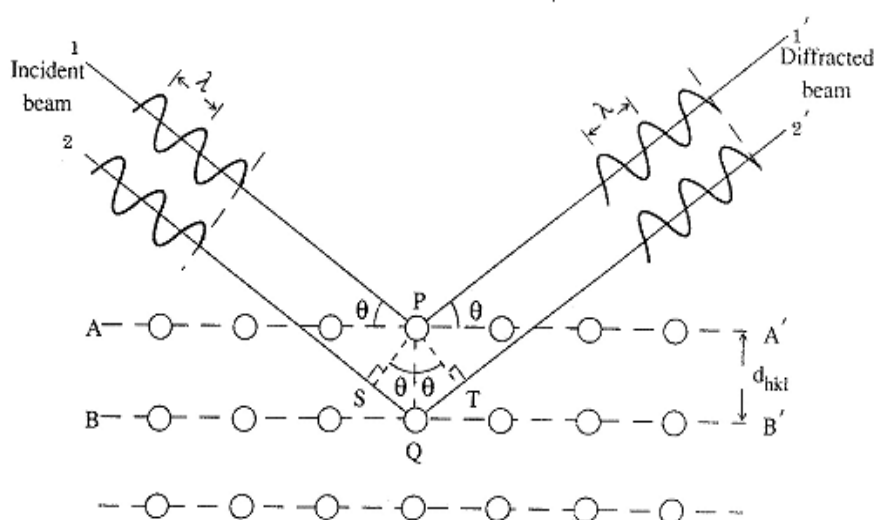
รังสีเอกซ์เฉพาะตัว มีลักษณะเป็นรังสีเอกซ์ที่มีพลังงานเดียว (monochromatic X-ray) เพราะเกิดจากการลดระดับพลังงานที่แน่นอน ปรากฏการณ์ของการเกิดรังสีเอกซ์ชนิดนี้เกิดขึ้นเมื่ออิเล็กตรอนหรืออนุภาคที่มีประจุชนิดอื่น ๆ หรือโฟตอนพลังงานสูงเคลื่อนที่เข้าชนอิเล็กตรอนในวงโคจรชั้นในของอะตอม แล้วถ่ายโอนพลังงานให้อิเล็กตรอน อิเล็กตรอนชั้นในวงโคจรได้รับพลังงานเพิ่มสูงขึ้นกว่าพลังงานยึดเหนี่ยวของชั้นวงโคจร ทำให้หลุดจากวงโคจรเกิดที่ว่างของอิเล็กตรอนในชั้นวงโคจรชั้นใน ทำให้อะตอมอยู่ในภาวะที่ถูกกระตุ้นและจะลดระดับพลังงานลงสู่ภาวะปกติในช่วงระยะเวลาอันสั้นโดยอิเล็กตรอนของวงโคจรในชั้นถัดไปจะลดระดับพลังงานลงมาให้เท่ากับพลังงานยึดเหนี่ยวของวงโคจรชั้นในด้วยการปลดปล่อยพลังงานส่วนเกินออกมาในรูปรังสีเอกซ์ แล้วเข้ามาแทนที่ช่องว่างของวงโคจรชั้นใน พลังงานส่วนเกินนี้จะมีค่าเท่ากับความต่างระดับพลังงานยึดเหนี่ยวเฉพาะวงโคจรของอิเล็กตรอน และชนิดของธาตุนั้น ๆ จึงมีพลังงานเฉพาะค่า

รังสีแบบต่อเนื่องมีลักษณะเป็นรังสีเอกซ์ที่มีพลังงานต่อเนื่องกระจายจากค่าต่ำสุดถึงสูงสุด ปรากฏการณ์ของการเกิดรังสีเอกซ์ต่อเนื่องเกิดจากอิเล็กตรอนพลังงานสูงเคลื่อนเข้าสู่สนามคูลอมบ์ (coulomb field) บริเวณใกล้นิวเคลียส ความหนาแน่นของสนามไฟฟ้าสถิตย์บริเวณดังกล่าวทำให้อิเล็กตรอนสูญเสียพลังงานอย่างรวดเร็วและปล่อยรังสีเอกซ์ออกมา

ก่อนที่อิเล็กตรอนปฐมภูมิจะทำอันตรกิริยากับสนามไฟฟ้าบริเวณใกล้นิวเคลียสที่เกิดจากประจุของอะตอม อิเล็กตรอนจะสูญเสียพลังงานบางส่วน อันเนื่องจากการกระเจิงของอิเล็กตรอน ดังนั้นพลังงานของรังสีเอกซ์ที่เกิดขึ้น จึงมีค่ากระจายต่อเนื่องจากพลังงานต่ำสุดถึงสูงสุดของอิเล็กตรอนปฐมภูมิ ถ้าอิเล็กตรอนปฐมภูมิมีพลังงานสูงพอที่จะกระตุ้นให้อิเล็กตรอนในวงโคจรชั้นในของอะตอมหลุดออกได้ก็จะเกิดรังสีเอกซ์เฉพาะค่าปะปนซ้อนอยู่กับสเปกตรัมของรังสีเอกซ์ต่อเนื่องด้วยเสมอ

การปลดปล่อยรังสีเอกซ์ออกมาที่ความยาวคลื่นใด ๆ ขึ้นอยู่กับระดับพลังงานที่คายออกมา ซึ่งความยาวคลื่นที่สั้นที่สุดเกิดจากการที่อิเล็กตรอนคายพลังงานที่ได้รับมาทั้งหมดจากแหล่งกำเนิดโดยไม่ขึ้นกับชนิดของเป้าหมายที่ใช้

เมื่อรังสีเอกซ์ตกกระทบบนผิวหน้าของผลึกโดยทำมุม  $\theta$  บางส่วนของรังสีเอกซ์จะเกิดการกระเจิงด้วยชั้นของอะตอมที่ผิวหน้า อีกส่วนหนึ่งของลำรังสีเอกซ์จะผ่านไปยังชั้นที่ 2 ของอะตอม ซึ่งบางส่วนจะกระเจิงและส่วนที่เหลือก็จะผ่านเข้าไปยังชั้นที่ 3 ของอะตอมดังภาพ 6



ภาพ 6 แบบจำลองสำหรับการพิสูจน์กฎของแบรกก์ [29]

ถ้าอะตอมในผลึกมีการจัดเรียงตัวอย่างไม่เป็นระเบียบและมีระยะห่างระหว่างอะตอมเท่า ๆ กันลำรังสีเอกซ์ที่ผ่านเข้าไปในแต่ละชั้นของอะตอมจะเกิดการเลี้ยวเบนเป็นลำขนานกัน สิ่งสำคัญในการเกิดการเลี้ยวเบนของรังสีเอกซ์ขึ้นอยู่กับภาวะ 2 ประการ คือ

1. รังสีที่ตกกระทบบ รังสีเลี้ยวเบน และเส้นตั้งฉากกับผิวหน้าจะต้องอยู่ในระนาบเดียวกัน
2. ระยะห่างระหว่างชั้นของอะตอมควรมีค่าใกล้เคียงกับความยาวคลื่นของรังสีเอกซ์

เมื่อปี ค.ศ. 1912 แบรกก์ได้ยิงลำรังสีเอกซ์แคบ ๆ กระทบบนผิวหน้าผลึกเป็นมุม  $\theta$  เพื่อให้เกิดการเลี้ยวเบนและการกระเจิงเมื่อเกิดอันตรกิริยากับอะตอม O, P และ R ถ้า

$$SQ + QT = n\lambda \quad (8)$$

เมื่อ  $n$  คือ จำนวนเต็ม รังสีที่กระเจิงจะอยู่ในเฟสที่ OCD ผลึกก็จะทำหน้าที่สะท้อนรังสีเอกซ์ จะเห็นว่า

$$SQ = QT = d \sin \theta \quad (9)$$

เมื่อ  $d$  คือ ระยะห่างระหว่างชั้นของผลึก เขียนสมการใหม่ได้ว่า

$$n\lambda = 2d \sin \theta \quad (10)$$

เรียกสมการนี้ว่า สมการของแบรกก์ (Bragg's equation) ซึ่งมีประโยชน์มาก สำหรับการศึกษามีโครงสร้างเป็นระเบียบ เช่น สารที่มีโครงสร้างเป็นผลึกเดี่ยว (single crystal) และผลึกเชิงซ้อน (polycrystalline) เพราะในสารแต่ละชนิดจะมีรูปแบบการเรียงตัวของอะตอมเป็นลักษณะเฉพาะ เมื่อเราทราบถึงค่ามุมที่เกิดการเลี้ยวเบนไปของรังสีเอกซ์เมื่อชนกับอะตอมของสาร เราจะทราบถึงระยะห่างระหว่างแต่ละอะตอมของสารนั้น ๆ จึงเป็นประโยชน์อย่างมากในการวิเคราะห์หาชนิดของสาร (qualitative analysis) รวมไปถึงสมบัติทางกายภาพของสารนั้น ๆ อีกด้วย

การคำนวณหาค่าคงที่แลตทิซ  $c$ ,  $a$  และค่าอัตราส่วน  $c/a$  สามารถกระทำได้โดยอาศัยข้อมูลจากเครื่องเอกซเรย์ดิฟแฟรกชัน และจากสมการที่ (10)

$$\frac{1}{d_{hkl}^2} = \frac{h^2}{a^2} + \frac{k^2}{b^2} + \frac{l^2}{c^2} \quad (11)$$

ในระบบเททระโกนัลนั้น ค่าแลตทิซ  $a$  มีค่าเท่ากับแลตทิซ  $b$  แต่ไม่เท่ากับแลตทิซ  $c$  ( $a = b \neq c$ ) ดังนั้น จากสมการที่ (11) เขียนใหม่ได้เป็น

$$\frac{1}{d_{hkl}^2} = \frac{h^2 + k^2}{a^2} + \frac{l^2}{c^2} \quad (12)$$

หรือ

$$\frac{1}{d_{hkl}^2} = (h^2 + k^2) + \frac{l^2}{(c/a)^2}$$



สำหรับเลดไททาเนตสามารถคำนวณหาค่าอัตราส่วน  $c/a$  ได้โดยนำค่า d-spacing  $d_{002}$  และ  $d_{200}$  มาคำนวณตามสมการ (14)

$$c/a = \frac{d_{002}}{d_{200}} \quad (14)$$

### กล้องจุลทรรศน์อิเล็กตรอนแบบส่องกราด (Scanning Electron Microscope) [30]

เนื่องจากกล้องจุลทรรศน์เลนส์ประกอบทั้งแบบใช้แสงธรรมดาและใช้รังสีแบบอื่น ๆ มีข้อจำกัดในการขยายภาพ เพราะกำลังขยายและกำลังแยกนอกจากจะขึ้นกับลักษณะของเลนส์แล้วยังขึ้นอยู่กับความยาวคลื่นของแสงที่ใช้อีกด้วย กล้องจุลทรรศน์เลนส์ประกอบสามารถมีกำลังแยกขณะส่องดูวัตถุขนาดเล็กสุดได้เพียง 0.2 ไมโครเมตรเท่านั้น ส่วนกำลังขยายรวมก็ไม่เกิน 2,000 เท่า จึงยังมองเห็นวัตถุภายในเซลล์ที่มีขนาดเล็กเป็นจุด ไม่สามารถแยกรายละเอียดได้ว่าส่วนนั้นเป็นอะไร ต่อมาได้มีการนำเอาอิเล็กตรอนซึ่งมีช่วงคลื่นสั้นกว่าคลื่นของแสงมาก เข้ามาใช้ในกล้องจุลทรรศน์แทนคลื่นแสง และใช้เลนส์แม่เหล็กแทนเลนส์กระจก เรียกกล้องดังกล่าวว่า กล้องจุลทรรศน์อิเล็กตรอน

กล้องจุลทรรศน์อิเล็กตรอนแบบส่องกราดเป็นกล้องที่ใช้ศึกษาโครงสร้างหรือองค์ประกอบพื้นผิวของเซลล์เนื้อเยื่อและวัตถุได้ โดยทำให้องค์ประกอบต่าง ๆ ของเซลล์หรือวัตถุให้มีความเข้มของเงาแตกต่างกัน

### หลักการเกิดภาพของกล้องจุลทรรศน์อิเล็กตรอนแบบส่องกราด [30]

อิเล็กตรอนปฐมภูมิ (primary electron) จากแหล่งกำเนิดอิเล็กตรอน (electron gun) จะถูกเร่งด้วยศักย์ไฟฟ้าสูง (1,000 ถึง 3,000 อิเล็กตรอนโวลท์ หรือมากกว่า) ที่สามารถปรับค่าได้ จากนั้นจึงถูกดึงดูดลงสู่เบี่ยงล่างโดยแผ่นอะโนด (anode plate) ภายใต้ภาวะความดันสุญญากาศ  $10^{-5} - 10^{-7}$  ทอร์ และมีชุดคอนเดนเซอร์เลนส์ที่จะปรับลำอิเล็กตรอน (electro beam) ให้มีขนาดเล็กลงเพื่อเป็นการเพิ่มความเข้มของลำอิเล็กตรอน จากนั้นลำอิเล็กตรอนจะวิ่งลงสู่เบี่ยงล่างผ่านเลนส์วัตถุ ซึ่งทำหน้าที่ในการปรับลำอิเล็กตรอนปฐมภูมิให้มีจุดโฟกัสบนผิวตัวอย่างพอดี และลำอิเล็กตรอนที่ตกกระทบผิววัตถุ หรือตัวอย่างจะมีขนาดในช่วง 5 ถึง 200 นาโนเมตร โดยมีชุดขดลวดควบคุมการส่องกราด (scan coil) ของลำอิเล็กตรอนทำหน้าที่ในการควบคุมทิศทางการเคลื่อนที่ของลำอิเล็กตรอนบนผิวตัวอย่าง ซึ่งผู้ใช้สามารถกำหนดได้โดยผ่านทางชุดควบคุม

(control unit) ขณะที่ลำอิเล็กตรอนกระทบผิวตัวอย่างจะเกิดอันตรกิริยา (interaction) ระหว่างอิเล็กตรอนปฐมภูมิกับอะตอมธาตุในวัตถุหรือตัวอย่างและเกิดการถ่ายโอนพลังงานที่ขึ้นความลึกจากพื้นผิวที่ระดับต่าง ๆ ทำให้เกิดการปลดปล่อยสัญญาณอิเล็กตรอน (electron signal) ชนิดต่าง ๆ ออกมา ซึ่งใช้ประโยชน์ในการศึกษาลักษณะผิวของตัวอย่างและวิเคราะห์ธาตุที่มีในตัวอย่างได้ตามลักษณะสัญญาณภาพที่ได้จากสัญญาณอิเล็กตรอนชนิดต่าง ๆ ที่เกิดขึ้น คือ

1. สัญญาณภาพจากอิเล็กตรอนทุติยภูมิ (Secondary Electron Image, SEI) หรือเป็นอิเล็กตรอนพลังงานต่ำ 3-5 อิเล็กตรอนโวลท์ เกิดที่พื้นผิวระดับไม่ลึก (ไม่เกิน 10 นาโนเมตร) โดยเกิดกับธาตุที่มีแรงยึดเหนี่ยวอิเล็กตรอนที่ผิวต่ำ

2. สัญญาณภาพจากอิเล็กตรอนกระเจิงกลับ (Backscattered Electron Image, BEI) หรือเป็นกลุ่มอิเล็กตรอนที่สูญเสียพลังงานให้กับอะตอมในชิ้นงานเพียงบางส่วนและกระเจิงกลับออกมา ซึ่งมีพลังงานสูงกว่าอิเล็กตรอนทุติยภูมิ เกิดที่พื้นผิวระดับลึกกว่า 10 นาโนเมตร โดยเกิดได้ดีกับธาตุที่มีเลขอะตอมสูง

3. สัญญาณภาพจากรังสีเอกซ์ (X-Ray Image, XRI) ชนิดที่เป็นรังสีเอกซ์เฉพาะตัวเป็นคลื่นแม่เหล็กไฟฟ้าที่เกิดจากอิเล็กตรอนในระดับชั้นโคจรต่าง ๆ ( $K, L, M, \dots$ ) ถูกกระตุ้น (excited) หรือได้รับพลังงานมากพอจนหลุดออกจากวงโคจรออกมา ทำให้อะตอมต้องรักษาสถิตของโครงสร้างรวมภายในอะตอม โดยการดึงอิเล็กตรอนจากชั้นวงโคจรถัดไปเข้ามาแทนที่และต้องลดพลังงานส่วนเกินออกมาในรูปคลื่นแม่เหล็กไฟฟ้าเพื่อให้ตัวเองมีพลังงานเท่ากับชั้นโคจรที่แทนที่ ซึ่งคลื่นแม่เหล็กไฟฟ้านี้มีความยาวคลื่นเฉพาะในแต่ละธาตุตามระดับพลังงานของตัวอย่างได้ทั้งเชิงปริมาณและคุณภาพ

สัญญาณภาพจากอิเล็กตรอนเหล่านี้จะถูกเปลี่ยนมาเป็นสัญญาณภาพปรากฏบนจอรับภาพได้โดยต้องเลือกใช้อุปกรณ์ในการวัดให้เหมาะสมกับสัญญาณแต่ละชนิด โดยทั่วไปสัญญาณอิเล็กตรอนทุติยภูมิใช้ตัวตรวจวัดชนิดพลาสติกเรืองแสง (Plastic scintillation detector) สัญญาณภาพจากอิเล็กตรอนกระเจิงกลับจะใช้ตัวตรวจวัดที่เป็นสารกึ่งตัวนำชนิดรอยต่อพีเอ็น (PN junction detector) หรือตัวตรวจวัดชนิดโรบินสัน (Robinson detector) และในสัญญาณภาพจากรังสีเอกซ์จะใช้หัววัดรังสีชนิดสารกึ่งตัวนำประเภทซิลิคอนลิเทียม (lithium drifted silicon, Si(Li)) ทำงานร่วมกับอุปกรณ์ในการวิเคราะห์พลังงานของรังสีเอกซ์เฉพาะตัวซึ่งอุปกรณ์วิเคราะห์นั้นมีทั้งแบบช่องเดียว (Single Channel Analyzer, SCA) และอุปกรณ์วิเคราะห์แบบหลายช่อง (Multi Channel Analyzer, MCA)

## การซินเตอร์ [31]

การซินเตอร์แบบสถานะของแข็ง

การซินเตอร์ (sintering) คือกระบวนการทางความร้อนที่ทำให้อนุภาคเกิดการสร้างพันธะกันอย่างสมดุล โดยมีโครงสร้างหลักเป็นของแข็งที่พัฒนามาจากการเคลื่อนย้ายมวลลักษณะต่างๆ ที่มักจะเกิดขึ้นในระดับของอะตอม การเกิดพันธะเชื่อมต่อกันดังกล่าวทำให้ระบบมีความแข็งแรงสูงขึ้นและมีพลังงานลดลง นอกจากนี้ยังอาจจะกล่าวได้ว่าการซินเตอร์นั้นหมายถึงการกำจัดรูพรุนที่อยู่ระหว่างอนุภาคผงเริ่มต้น โดยอาศัยการหดตัวขององค์ประกอบที่เชื่อมอยู่ติดกันแล้วเกิดการเติบโตไปด้วยกัน โดยมีการสร้างพันธะที่แข็งแรงระหว่างอนุภาคที่อยู่ติดกันขึ้นมาทุกขั้นตอนที่อยู่ระหว่างการเปลี่ยนสภาพชิ้นงานที่ผ่านการอัดขึ้นรูป ไปเป็นโครงสร้างจุลภาคที่ประกอบด้วยการยึดเกาะกันของเกรนต่าง ๆ ล้วนแต่เป็นส่วนหนึ่งของขั้นตอนการซินเตอร์ทั้งสิ้น

แรงขับเคลื่อนสำหรับการซินเตอร์นั้นได้มาจากการลดพื้นที่ผิวและพลังงานของพื้นผิวด้วยการใช้ของแข็งที่เชื่อมยึดกันโดยมีพลังงานขอบเกรนแบบของแข็ง-ของแข็ง ( $\gamma_{gb}$ ) ที่ค่อนข้างต่ำเข้าไปแทนที่กลุ่มอนุภาคผงที่ยึดกันอยู่อย่างหลวม ๆ ซึ่งจะมีพลังงานพื้นผิวแบบของแข็ง-ไอ ( $\gamma_{sv}$ ) ที่สูงมาก ด้วยเหตุนี้เองการผลิตเซรามิกส่วนใหญ่จึงนิยมเลือกใช้อุณหภูมิตั้งต้นที่มีขนาดอนุภาคเล็กเนื่องจากอนุภาคผงที่มีขนาดยิ่งเล็กลงเท่าไรก็จะมีพื้นที่ผิวมากขึ้นเท่านั้น จึงทำให้ระบบมีแรงขับเคลื่อนสำหรับการซินเตอร์ที่สูงขึ้นตามไปด้วย ทำให้ชิ้นงานสามารถเกิดการแน่นตัวได้ดี จึงมีความหนาแน่นสูง หรือทำให้สามารถใช้คุณสมบัติในการเผาที่ต่ำลงได้

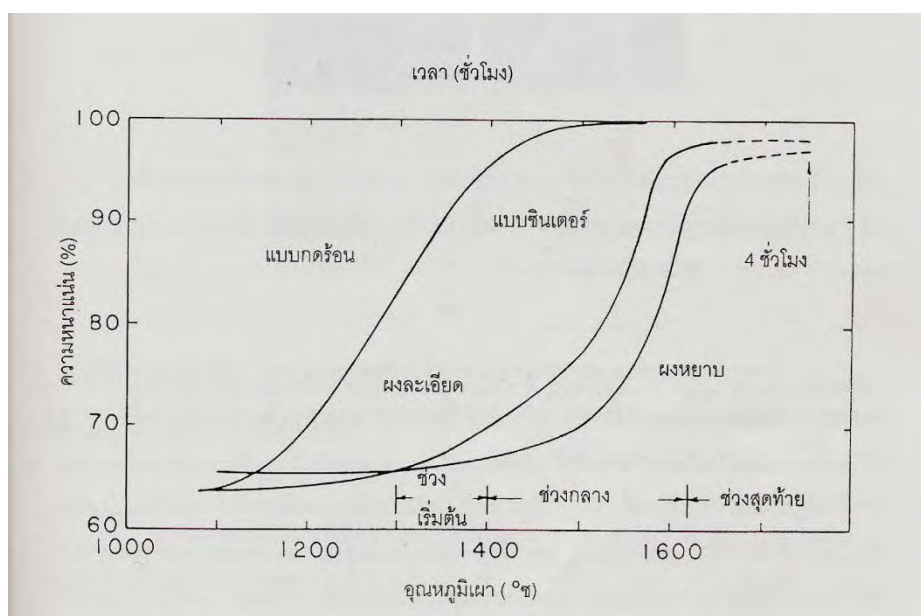
การหดตัวของชิ้นงานเซรามิกขณะที่ทำการซินเตอร์สามารถตรวจสอบได้จากการวัดขนาดหรือหาค่าความหนาแน่นของชิ้นงานขณะที่มีการเปลี่ยนแปลงของอุณหภูมิ และเวลาในการเผา ดังเช่น ตัวอย่างของพฤติกรรมของการซินเตอร์แบบสถานะของแข็ง (solid - state sintering) ทั่ว ๆ ไปที่แสดงดังภาพ 7 ซึ่งประกอบไปด้วย 3 ขั้นตอนหลักที่มีความคาบเกี่ยวต่อเนื่องกันอยู่คือ

1. การซินเตอร์ช่วงเริ่มต้น (initial sintering) จะเกี่ยวข้องกับการจัดเรียงตัวกันใหม่อีกครั้งหนึ่งของอนุภาคผงภายในชิ้นงานและการเกิดพันธะที่แข็งแรง หรือคอ (neck) ขึ้นมาที่บริเวณจุดสัมผัสระหว่างอนุภาคผง ความหนาแน่นสัมพัทธ์ของชิ้นงานในช่วงนี้อาจจะเพิ่มขึ้นจาก 0.5 ไปถึง 0.6 ได้ ส่วนใหญ่ก็เนื่องมาจากการที่อนุภาคผงมีการแพคตัวกันมากยิ่งขึ้นนั่นเอง (ภาพ 8 (b))

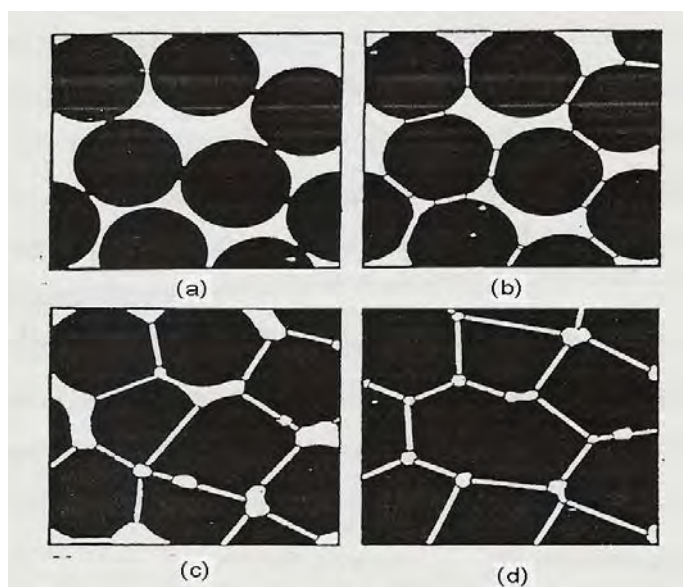
2. การซินเตอร์ช่วงกลาง (intermediate sintering) เป็นช่วงที่ขนาดของคอเริ่มโตขึ้นและปริมาณของความพรุนในชิ้นงานจะเริ่มลดลงอย่างรวดเร็ว เนื่องจากอนุภาคเริ่มเข้ามาใกล้ชิดติดกันมากยิ่งขึ้น ทำให้ชิ้นงานเกิดมีการหดตัวลงอย่างชัดเจน เริ่มมีเกรนและขอบเกรนเกิดขึ้น

พร้อมกับมีการเคลื่อนที่ของสิ่งเหล่านี้ ทำให้เกิดมีการเติบโตของเกรนบางเกรนขึ้น ขั้นตอนนี้จะดำเนินไปเรื่อย ๆ อย่างต่อเนื่องในขณะที่ช่องว่างของรูพรุนจะเริ่มเกิดการเชื่อมต่อกัน (พากรูพรุนเปิด) และจะสิ้นสุดพฤติกรรมนี้ในทันทีเมื่อรูพรุนเกิดการแยกตัวหลุดออกไปอยู่ต่างหาก (พากรูพรุนปิด) การหดตัวของชิ้นงานจะเกิดขึ้นมากที่สุดในการซินเตอร์ช่วงกลางนี้ และอาจจะทำให้ความหนาแน่นสัมพัทธ์ของชิ้นงานมีค่าสูงถึงประมาณ 0.9 ได้ (ภาพ 8 (c))

3. การซินเตอร์ช่วงสุดท้าย (final stage sintering) เป็นช่วงที่รูพรุนในชิ้นงานเริ่มปิดตัวเองลงและค่อย ๆ ถูกกำจัดให้หมดไปจากชิ้นงานอย่างช้า ๆ โดยอาศัยกลไกการแพร่ของอากาศจากรูพรุนออกมาตามแนวของขอบเกรน แล้วหลุดออกไปจากผิวของชิ้นงาน ซึ่งจะทำให้ชิ้นงานเกิดการแน่นตัวเพิ่มขึ้นจากเดิมอีกเพียงเล็กน้อย ขนาดของเกรนจะเพิ่มขึ้นในการซินเตอร์ช่วงสุดท้ายนี้ (ภาพ 8 (d))



ภาพ 7 แสดงพฤติกรรมการซินเตอร์แบบสถานะของแข็งทั่ว ๆ ไปในรูปขอความสัมพันธ์ระหว่างความหนาแน่นกับอุณหภูมิและเวลาที่ใช้ในการเผา [31]



ภาพ 8 แสดงพัฒนาการของโครงสร้างจุลภาคที่เกิดจากการซินเตอร์แบบสถานะของแข็ง  
(a) อนุภาคผงยึดกันอยู่แบบหลวม ๆ หลังการอัดขึ้นรูป (b) การซินเตอร์ช่วงเริ่มต้น (c) การซินเตอร์ช่วงกลาง และ (d) การซินเตอร์ช่วงสุดท้าย [31]

#### การซินเตอร์แบบมีเฟสของเหลว

การซินเตอร์แบบมีเฟสของเหลว (liquid phase sintering) เป็นกระบวนการเผาซินเตอร์ที่มีองค์ประกอบหนึ่งของวัสดุเกิดการหลอมเหลวขึ้นจนกลายสภาพไปเป็นของเหลวในระหว่างที่มีการซินเตอร์ ซึ่งเป็นกระบวนการอันหนึ่งที่นิยมใช้ในการผลิตเซรามิก ด้วยการใช้อุณหภูมิเผาซินเตอร์ที่ต่ำลง เนื่องจากโดยปกติแล้ววัสดุพวกเซรามิกส่วนใหญ่จะมีจุดหลอมเหลวที่สูงมากบางชนิดอาจสูงถึงประมาณ 3000 องศาเซลเซียส ทำให้ต้องมีการใช้พลังงานที่สูงมากในการเผาซินเตอร์ผลิตภัณฑ์เหล่านี้และมีเตาไฟอยู่ไม่กี่ประเภทที่สามารถใช้งานภายใต้เงื่อนไขนี้ได้ นอกจากนี้ยังเป็นการเสี่ยงต่อการเกิดปัญหาเรื่องปฏิกิริยาระหว่างสารในภาชนะที่หลอมตัว กับภาชนะเองได้ง่ายอีกด้วย ดังนั้นจึงมีการพัฒนาเทคนิคการผลิตเซรามิกเหล่านี้ที่อุณหภูมิต่ำลงด้วยการใช้สารช่วยหลอมหรือฟลักซ์ (fluxes) ซึ่งเป็นอนุภาคผงที่เติมลงไปเพื่อทำหน้าที่ช่วยให้ชิ้นงานเกิดการหลอมเหลวที่ต่ำกว่าสารองค์ประกอบหลักของผลิตภัณฑ์มาก จึงเกิดเป็นเฟสที่เป็นของเหลวให้เคลื่อนย้ายที่ในระหว่างการซินเตอร์ได้รวดเร็วยิ่งขึ้น

กระบวนการซินเตอร์แบบมีเฟสของเหลวมีอยู่สองระบบคือ

1. ระบบที่ไม่เป็นเนื้อเดียวกัน เมื่อขึ้นงานได้รับความร้อนจนกระทั่งถึงอุณหภูมิของการซินเตอร์จะมีเฟสที่เป็นของเหลวเกิดขึ้นและคงสภาพอยู่ตลอดช่วงของการซินเตอร์และเมื่อขึ้นงานเริ่ม เย็นตัวลงเฟสที่เป็นของเหลวนี้จะเกิดการแข็ง ตัวแยกเฟสอยู่ในชิ้นงาน
2. ระบบที่มีความเป็นเนื้อเดียวกันเมื่อขึ้นงานได้รับความร้อนจนกระทั่งถึงอุณหภูมิของการซินเตอร์จะมีเฟสที่เป็นของเหลวเกิดขึ้นแล้วค่อย ๆ หายไปช้า ๆ ด้วยการละลายลงไปอยู่ในเมทริกซ์ของชิ้นงาน

กระบวนการซินเตอร์ที่มีเฟสของเหลวประกอบด้วย 4 ระยะหลักดังนี้

1. ระยะที่อนุภาคมีการจัดเรียงตัวกันใหม่ (particle rearrangement stage) หลังจากที่มีการหลอมเหลวเกิดขึ้นอนุภาคของแข็งจะถูกแรงดันรูเล็กจากของเหลวดึงเข้าหากัน ทำให้ชิ้นงานเกิดมีการหดตัวอย่างรวดเร็ว และมีการกำจัดรูพรุนออกไปจากชิ้นงาน
2. ระยะที่อนุภาคมีการแยกออกจากกันแล้วเกิดการตกตะกอนซ้ำ (dissolution reprecipitation stage) มีหลายกรณีที่อนุภาคของแข็งสามารถละลายในเฟสที่เป็นของเหลวได้ในระดับหนึ่ง ซึ่งความโค้งของอนุภาคของแข็งและความดัน ณ จุดสัมผัสระหว่างอนุภาคของแข็งจะช่วยให้เกิดมีการแยกออกจากกันของอนุภาคได้ เมื่อเกิดมีการละลายขึ้น ตัวถูกละลายจะแพร่เข้าสู่จุดที่มีความโค้งตรงกันข้ามภายในโครงสร้างจุลภาค และเกิดการตกตะกอนจนทำให้เกรนบริเวณดังกล่าวมีขนาดโตขึ้นซึ่งตัวที่ตกตะกอนอาจจะไม่ได้เป็นตัวเดียวกันกับอนุภาคของแข็งเริ่มต้นก็ได้ แต่อาจจะเป็นตัวใหม่ที่มียอดประกอบของทั้งที่ได้จากเฟสที่เป็นของแข็งและที่เป็นของเหลวอยู่ร่วมกัน ซึ่งการตกตะกอนในลักษณะดังกล่าวนี้จะทำให้ปริมาณเฟสของเหลวที่เกิดขึ้นในระบบลดลงขณะที่มีการตกตะกอน
3. ระยะที่ของเหลวมีการสมานลักษณะ (liquid assimilation) ในบางกรณีของเหลวจะเข้าไปปะปนอยู่ร่วมกับเฟสที่เป็นของแข็งได้โดยตรงด้วยการเกิดปฏิกิริยาทางเคมีหรืออาจจะเข้าไปแทรกอยู่ด้วยแรงกล จนทำให้เกิดการเป็นของแข็งที่อยู่ในรูปของสารละลายของแข็งที่เกิดจากการดูดซับของเหลวหรือเกิดเฟสใหม่ที่ตกผลึกมาจากสารที่เกิดการหลอม
4. ระยะที่มีการเติบโตของเกรนในสถานะของแข็ง (solid state grain growth stage) เมื่อของเหลวถูกรีดออกมาจากอนุภาคที่อัดกันแน่น หรือมีการแพร่ซึมเข้าไปอยู่ภายในของแข็งจะทำให้เกิดมีขอบเกรนปรากฏขึ้นมา ซึ่งถ้าหากระบบยังมีการซินเตอร์อยู่ก็จะมีพฤติกรรมการเติบโตของเกรนเป็นขั้นตอนหลักที่คอยควบคุมพฤติกรรมของการซินเตอร์ต่อไป

### การหาความหนาแน่น (Density) [32]

ความหนาแน่น หมายถึง ค่ามวลต่อปริมาตรของวัสดุ ณ อุณหภูมิหนึ่งๆ หน่วยของค่าความหนาแน่นสามารถเป็นกรัมต่อมิลลิลิตร, กรัมต่อลูกบาศก์เซนติเมตร, ปอนด์ต่อลูกบาศก์ฟุต, กิโลกรัมต่อลูกบาศก์เมตร เป็นต้น สำหรับส่วนที่จะได้กล่าวถึงต่อไปนี้จะใช้ในหน่วยของกรัมต่อลูกบาศก์เซนติเมตร ซึ่งมีความสำคัญทางด้านเซรามิกอย่างยิ่งคือ การอาศัยค่าความหนาแน่นเป็นตัวชี้วัดถึงประสิทธิภาพในการอัดแน่นตัวของวัสดุในระหว่างขั้นตอนการขึ้นรูป ซึ่งสูตรที่ใช้ในการคำนวณนั้นยังสามารถนำไปสู่การหาค่าความพรุนของวัสดุได้อีกด้วย

การหาค่าความหนาแน่นของชิ้นงานนั้นอาศัยหลักการของอาร์คิมิดีสที่กล่าวไว้ว่า “เมื่อจุ่มของแข็งลงในของเหลวจะมีแรงพยุงเกิดขึ้นบนของแข็งนั้น โดยแรงพยุงที่เกิดขึ้นจะมีค่าเท่ากับน้ำหนักของของเหลวที่ถูกแทนที่ด้วยปริมาตรของของแข็ง” วิธีการนี้ทำได้โดยการหาค่ามวลของวัตถุในอากาศและขณะที่จุ่มอยู่ในน้ำ

$$\text{ความหนาแน่น } \rho = \frac{W_a}{W_a - W_{fl}} \cdot \rho_{fl} \quad (15)$$

เมื่อ	$\rho$	คือ	ค่าความหนาแน่นของชิ้นงาน มีหน่วยเป็นกรัมต่อลูกบาศก์เซนติเมตร
	$\rho_{fl}$	คือ	ค่าความหนาแน่นของของเหลว มีหน่วยเป็นกรัมต่อลูกบาศก์เซนติเมตร
	$W_a$	คือ	น้ำหนักแห้งของชิ้นงาน มีหน่วยเป็นกรัม
	$W_{fl}$	คือ	น้ำหนักแห้งของชิ้นงานในของเหลว มีหน่วยเป็นกรัม

ส่วนการหาความหนาแน่นของของเหลวในกรณีที่ทราบปริมาตรที่แน่นอนของของแข็งลงไป สามารถหาได้จาก

$$\rho_{fl} = G / V \quad (16)$$

โดยที่	$G$	คือ	แรงพยุงที่เกิดขึ้นกับของแข็ง (หน่วยเป็นกรัม) หาได้จากน้ำหนักของชิ้นงานในอากาศลบด้วยน้ำหนักของชิ้นงานในของเหลว
	$V$	คือ	ปริมาตรของของแข็งที่จุ่มลงในของเหลว มีหน่วยเป็นลูกบาศก์เซนติเมตร

สำหรับการหาความหนาแน่นสัมพัทธ์ (relative density :  $\rho_r$ ) นั้น สามารถคำนวณหาได้ตามสมการที่ (17)

$$\rho_r (\%) = \left( \frac{\rho_b}{\rho_{th}} \right) \times 100 \quad (17)$$

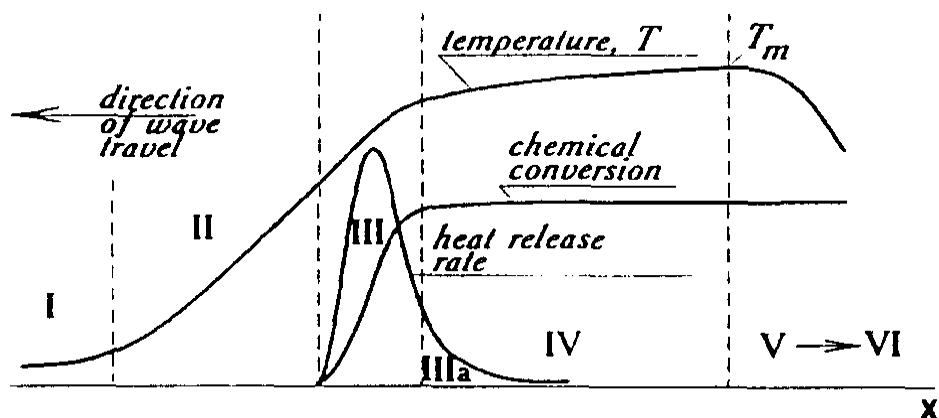
เมื่อ	$\rho_r$	คือ	ค่าความหนาแน่นสัมพัทธ์ มีหน่วยเป็นเปอร์เซ็นต์
	$\rho_b$	คือ	ค่าความหนาแน่นของชิ้นงาน มีหน่วยเป็นกรัมต่อลูกบาศก์เซนติเมตร
	$\rho_{th}$	คือ	ค่าความหนาแน่นในทฤษฎีของสาร มีหน่วยเป็นกรัมต่อลูกบาศก์เซนติเมตร

### การเตรียมเซรามิกด้วยวิธีการเผาไหม้ [33,34]

การใช้ประโยชน์จากการปลดปล่อยพลังงานความร้อนที่ได้จากปฏิกิริยาเคมีในขั้นตอนการผลิต มีการใช้กันมานานแล้วตั้งแต่ศตวรรษที่ผ่านมา เมื่อ Beketov และ Goldshmidt ได้ค้นพบ self-sustaining thermite reaction ซึ่งต่อมาได้ใช้หลักการจุดระเบิดของปฏิกิริยาเคมีในกระบวนการผลิตอย่างมากมาย เช่น ในกระบวนการผลิตเตาหลอมเหล็ก การผลิตเฟอร์โรอัลลอย ฯลฯ อย่างไรก็ตามการพัฒนาทฤษฎีการเผาไหม้ (combustion) ยุคใหม่ไม่ได้มีรูปแบบอย่างที่เคยปฏิบัติมา (ในปี ค.ศ.1930-1940 สำหรับแก๊ส และปี ค.ศ.1950-1960 สำหรับของเหลว) ในปี ค.ศ.1967 ได้มีการค้นพบปรากฏการณ์จุดระเบิดของแข็ง ซึ่งปฏิกิริยาที่เกิดขึ้นจะได้ผลผลิตในสถานะของแข็ง และการพัฒนาวิธีการเผาไหม้บนพื้นฐานของ self-propagation high-temperature (SHS) ได้กระตุ้นให้เกิดการทดลองและการศึกษาทฤษฎีที่เกี่ยวข้องกับกระบวนการเผาไหม้ของสารประกอบอินทรีย์และวัสดุอย่างกว้างขวาง ซึ่งผลของข้อมูลที่ได้จากการทดลองได้กลายเป็นพื้นฐานของเทคโนโลยีการเผาไหม้และการประยุกต์ใช้ในอุตสาหกรรม

กระบวนการเผาไหม้มีการใช้งานกันอย่างกว้างขวาง สำหรับวัสดุขั้นสูงและกระบวนการผลิตเพื่อการประหยัดพลังงาน ในปัจจุบันการควบคุมความเร็วของการจุดระเบิด อุณหภูมิ สัดส่วน และโครงสร้างของผลผลิตทำได้โดยการประยุกต์แนวคิดแผนใหม่ของทฤษฎีการเผาไหม้และโครงสร้างจุลนาโนศาสตร์มหันภาค ของปฏิกิริยาเคมี ซึ่งสามารถอธิบายกระบวนการทั่วไปของการเผาไหม้ ได้ดังภาพ 9



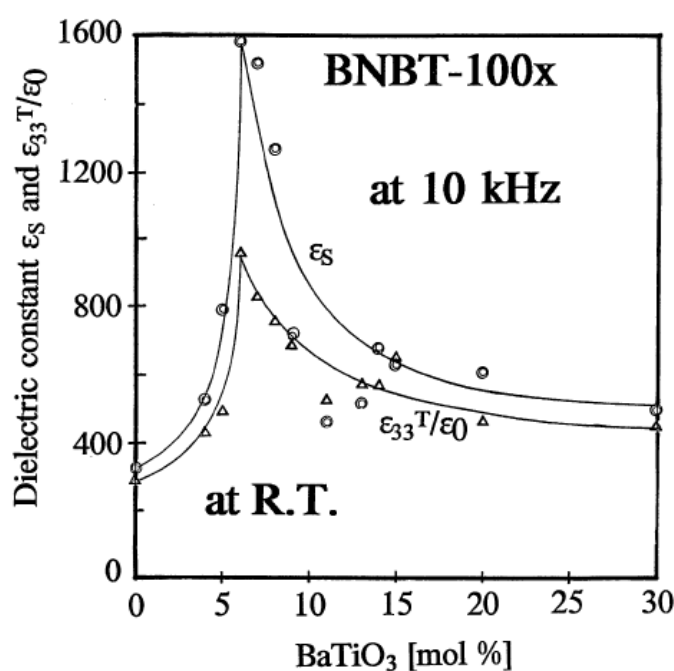


ภาพ 9 การเปลี่ยนแปลงของกระบวนการเผาไหม้ [34]

ช่วงที่หนึ่ง เป็นช่วงเริ่มต้นของปฏิกิริยา ช่วงที่สอง เป็นช่วงก่อนที่จะเกิดปฏิกิริยา ซึ่งช่วงนี้ จะยังไม่มีปฏิกิริยาเกิดขึ้น แต่จะมีการถ่ายเทความร้อนเพิ่มมากขึ้น ช่วงที่สาม เป็นช่วงที่มีความสำคัญต่อโครงสร้างของวัสดุ โดยจะมีการปลดปล่อยพลังงานความร้อนออกมาเมื่อเกิดการจุดระเบิด และความร้อนที่ปลดปล่อยออกมานี้จะแพร่ไปสู่ช่วงต้นของช่วงที่สี่ คือ ช่วงการเปลี่ยนแปลงทางเคมี (chemical conversion) ส่วนที่กว้างที่สุดของช่วงนี้ คือ ส่วนที่มีการเปลี่ยนแปลงเฟสและโครงสร้างของวัสดุ ซึ่งขั้นตอนนี้จะเป็นตัวกำหนดโครงสร้างสุดท้ายและมีบทบาทสำคัญต่อสมบัติของวัสดุ ในช่วงที่ห้าของกระบวนการ เป็นช่วงที่วัสดุเกิดการเย็นตัว และในช่วงนี้อาจมีผลกระทบต่อโครงสร้างของวัสดุ ถ้าการเย็นตัวเกิดขึ้นอย่างช้าๆจะทำให้ได้โครงสร้างของวัสดุที่สมดุล ดังนั้นในกระบวนการเผาไหม้ อัตราการให้ความร้อนจะเป็นตัวกำหนดรูปแบบของการปลดปล่อยความร้อนและถ่ายเทความร้อนไปสู่ช่วงการเปลี่ยนแปลงทางเคมี ส่วนคุณลักษณะของวัสดุที่ได้จะขึ้นอยู่กับเฟส โครงสร้าง เงื่อนไข และอัตราการเย็นตัวของวัสดุ

### งานวิจัยที่เกี่ยวข้อง

T. Takennaka et al. [10] เตรียมเซรามิกบิสมาทโชเดียมไททาเนต-แบเรียมไททาเนต  $[(1-x)(\text{Bi}_{0.5}\text{Na}_{0.5})\text{TiO}_3-x\text{BaTiO}_3]$  โดยที่  $0 \leq x \leq 0.3$  ด้วยวิธีปฏิกิริยาสถานะของแข็งโดยเผาแคลไซน์ที่อุณหภูมิ 800 องศาเซลเซียส และเผาซินเตอร์ที่อุณหภูมิ 1200 องศาเซลเซียส เป็นเวลา 2 ชั่วโมง

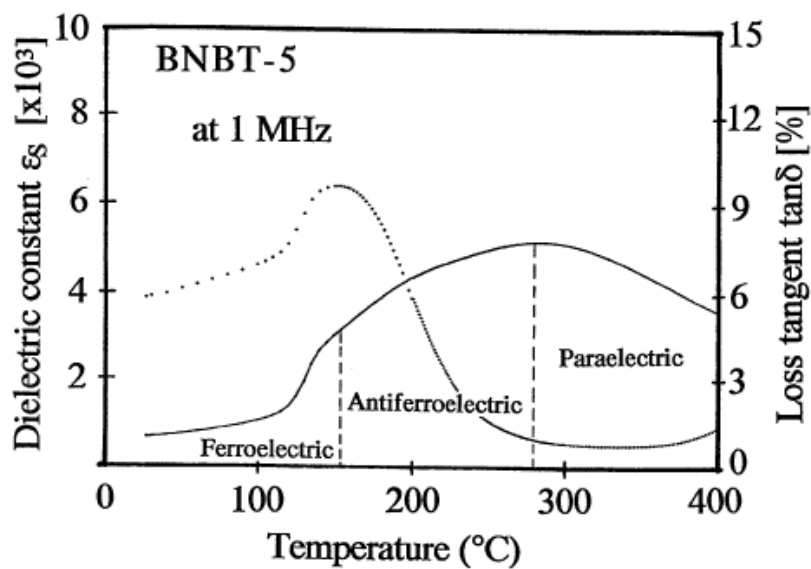


ภาพ 10 ค่าคงที่ได้ไอเล็กทริกของเซรามิก BNBT ที่โพล ( $\epsilon_{33}^T$ ) และไม่ได้โพล ( $\epsilon_s$ ) [10]

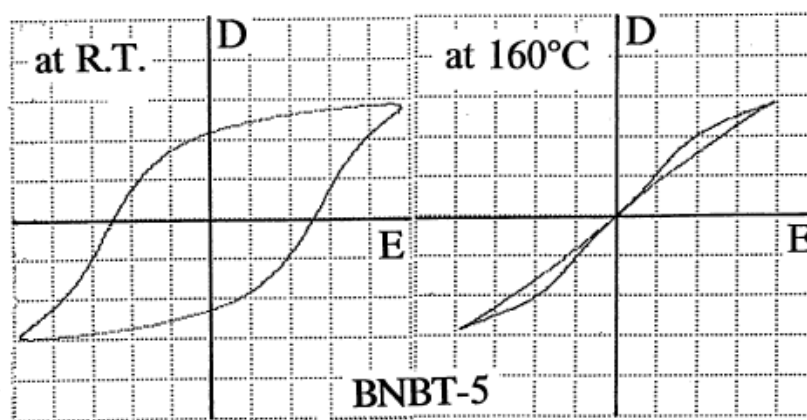
พบว่า เซรามิกมีความหนาแน่นประมาณร้อยละ 90 และบริเวณรอยต่อเฟสระหว่างรอมโบอีตรอลกับเทตระโกนอล เกิดขึ้นที่  $x = 0.06 - 0.07$  ซึ่งปริมาณของ  $x$  ในช่วงนี้จะแสดงค่าคงที่ได้ไอเล็กทริกสูงสุด และตัวอย่างที่โพลจะมีค่าคงที่ได้ไอเล็กทริกลดลงเมื่อเปรียบเทียบกับตัวอย่างที่ไม่ได้โพล ดังแสดงในภาพ 10

เมื่ออุณหภูมิเพิ่มขึ้นเซรามิก BNBT-5 ( $x = 0.05$ ) จะมีการเปลี่ยนแปลงเฟสจากเฟอร์โรอิเล็กทริกเป็นแอนติเฟอร์โรอิเล็กทริกที่อุณหภูมิประมาณ 160 องศาเซลเซียส และจากแอนติเฟอร์โรอิเล็กทริกเป็นพาราอิเล็กทริกที่อุณหภูมิประมาณ 285 องศาเซลเซียส ดังแสดงในภาพ 11 ซึ่งสัมพันธ์กับผลของวงรอบฮีสเทรีซิส ดังแสดงในภาพ 12 นอกจากนี้ยังพบว่าปริมาณของ  $x$  และอุณหภูมิเป็นปัจจัยที่สำคัญต่อการเปลี่ยนแปลงโครงสร้างเฟส ดังแสดงในภาพ 13 และ

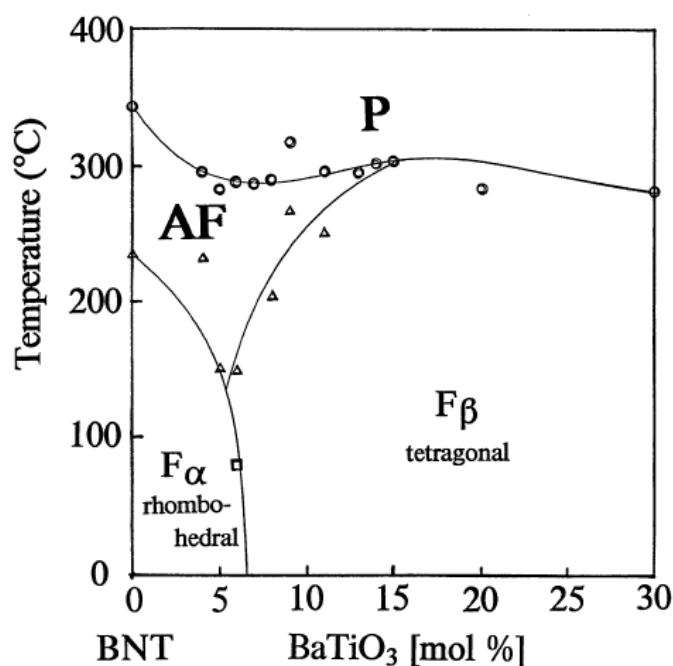
ตัวอย่าง BNBT-6 ( $x = 0.06$ ) มีค่าคงที่พีโซอิเล็กทริกสูงสุดเท่ากับ 125 pC/N สัมประสิทธิ์เชิงกลเท่ากับ 55 และอุณหภูมิคูรีอยู่ที่ประมาณ 288 องศาเซลเซียส



ภาพ 11 ค่าคงที่ไดอิเล็กทริกและการสูญเสียไดอิเล็กทริกของเซรามิก BNBT-5 ( $x = 0.05$ ) [10]

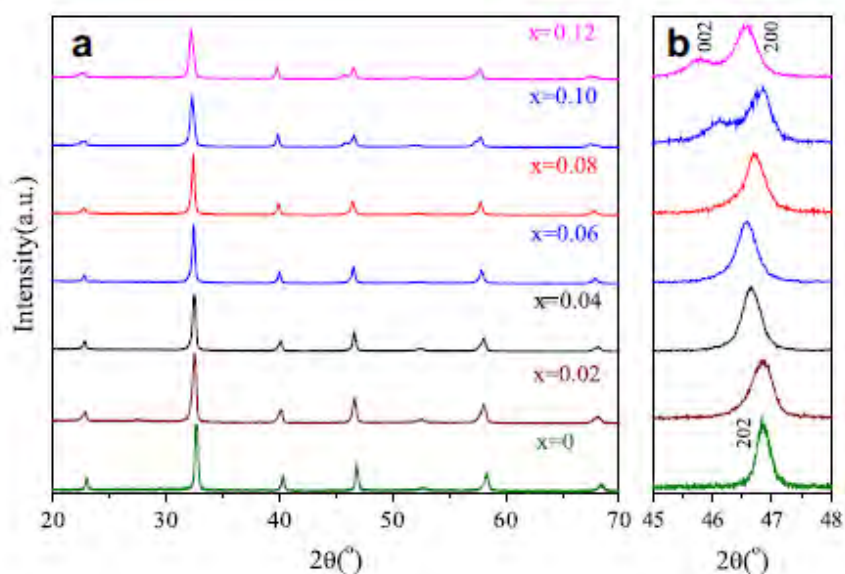


ภาพ 12 วงรอบฮิสเทอรีซิสของเซรามิก BNBT-5 (a) ที่อุณหภูมิห้อง (b) ที่อุณหภูมิ 160 องศาเซลเซียส [10]



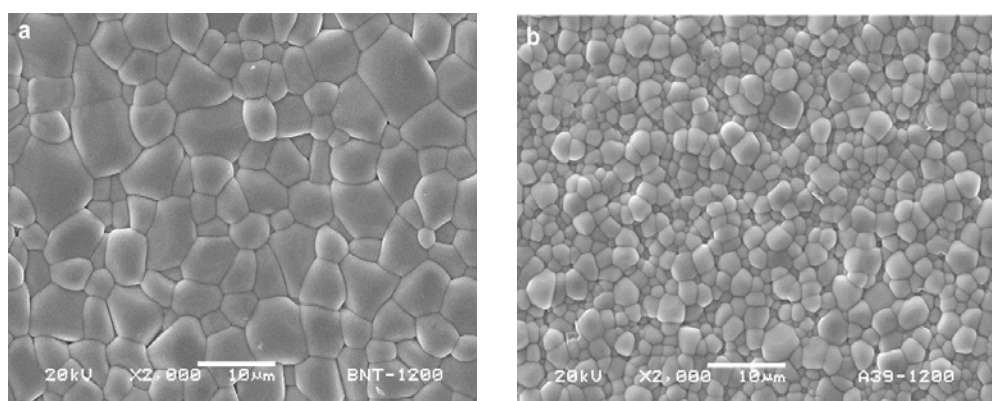
ภาพ 13 ความสัมพันธ์ของปริมาณ  $\text{Bi}_{0.5}\text{Na}_{0.5}\text{TiO}_3$  และ  $\text{BaTiO}_3$  ในระบบ  $(\text{Bi}_{0.5}\text{Na}_{0.5})_{1-x}\text{Ba}_x\text{TiO}_3$  โดยที่  $F_\alpha$  คือเฟสเฟอร์โรอิเล็กทริกที่มีโครงสร้างแบบรอมโบฮีดรอล  $F_\beta$  คือเฟสเฟอร์โรอิเล็กทริกที่มีโครงสร้างแบบเทตระโกนอล AF คือเฟสแอนติเฟอร์โรอิเล็กทริกที่มีโครงสร้างแบบรอมโบฮีดรอล P คือเฟสพาราอิเล็กทริก [10]

D. Lin et al. [35] เตรียมเซรามิกบิสมาทโซเดียมไททานต-แบเรียมไททานต  $[(1-x)(\text{Bi}_{0.5}\text{Na}_{0.5})\text{TiO}_3-x\text{BaTiO}_3]$  โดยที่  $0 \leq x \leq 0.12$  ด้วยวิธีปฏิกิริยาสถานะของแข็งโดยเผาแคลไซน์ที่อุณหภูมิ 850 องศาเซลเซียส และเผาซินเตอร์ที่อุณหภูมิ 1200 องศาเซลเซียส เป็นเวลา 2 ชั่วโมง จากการวิเคราะห์โครงสร้างผลึกด้วยเทคนิคการเลี้ยวเบนแบบรังสีเอกซ์ พบว่า ที่  $x < 0.06$  จะมีโครงสร้างเหมือน BNT ซึ่งเซรามิกจะมีโครงสร้างเป็นแบบรอมโบฮีดรอล เมื่อปริมาณ BT เพิ่มขึ้นเซรามิกจะมีโครงสร้างเป็นแบบเทตระโกนอลมากขึ้น และที่  $x \geq 0.10$  มีโครงสร้างเหมือน BT ซึ่งเซรามิกจะมีโครงสร้างเป็นแบบเทตระโกนอล ดังนั้นบริเวณรอยต่อเฟส (MPB) พบที่  $0.06 < x < 0.10$  ดังภาพ 14

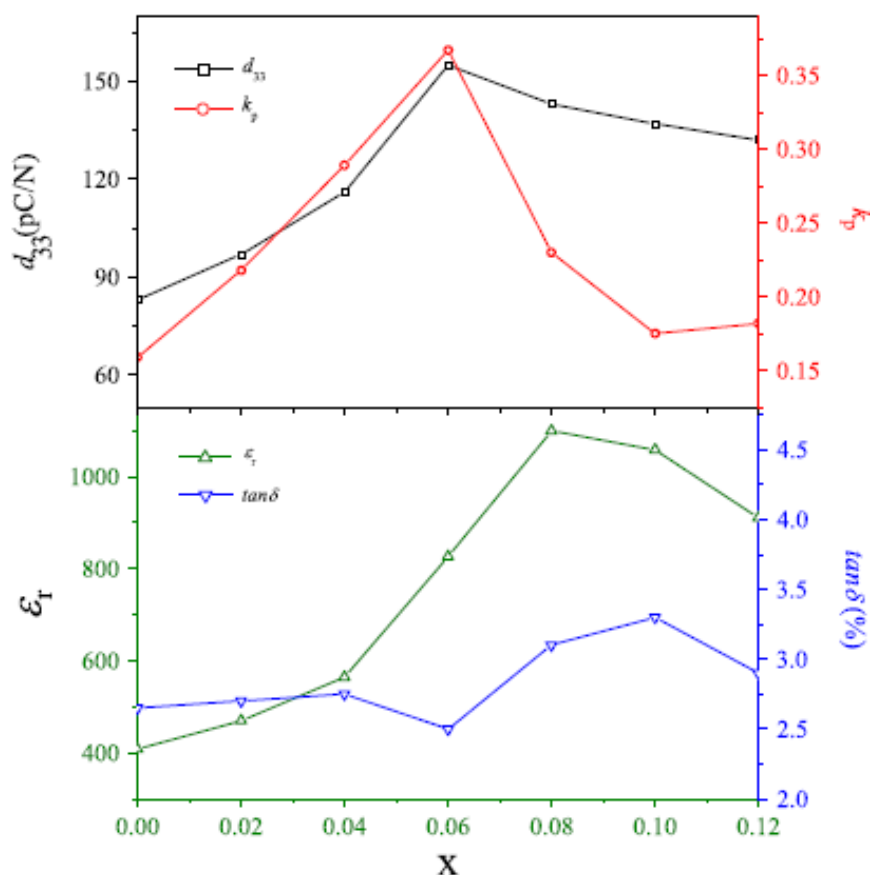


ภาพ 14 รูปแบบการเลี้ยวเบนของรังสีเอกซ์ของเซรามิก  $(1-x)\text{BNT}-x\text{BT}$  [35]

จากภาพ 15 แสดงภาพถ่ายจากกล้องจุลทรรศน์อิเล็กตรอนแบบส่องกราด (SEM) ของเซรามิก  $(1-x)\text{BNT}-x\text{BT}$  พบว่า ค่าความหนาแน่นของเซรามิกที่เตรียมได้มี  $> 97\%$  เมื่อ  $x = 0$  ขนาดเกรนเฉลี่ยเท่ากับ  $4 - 6 \mu\text{m}$  และเมื่อ  $x = 0.06$  ขนาดเกรนเฉลี่ยเท่ากับ  $2 \mu\text{m}$  ดังนั้นขนาดเกรนเฉลี่ยจะมีค่าลดลงเมื่อปริมาณ  $x$  เพิ่มขึ้น และที่  $x = 0.06$  แสดงสมบัติพิโซอิเล็กทริกที่ดีที่สุด มีค่า  $d_{33} = 155 \text{ pC/N}$  and  $k_p = 36.7\%$  ในขณะที่  $x = 0.08$  มีค่าคงที่ได้ิเล็กทริกสูงที่สุด  $\epsilon_r = 1099$  ดังภาพ 16

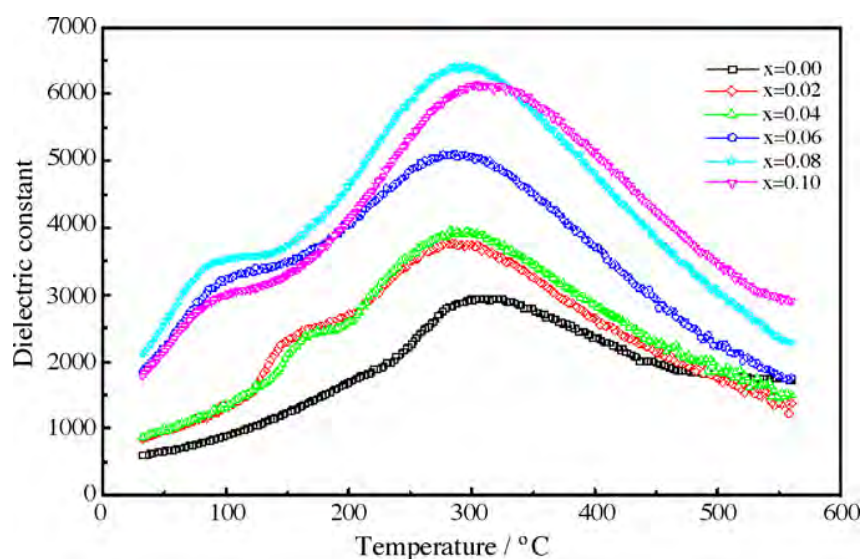


ภาพ 15 แสดงภาพถ่ายจากกล้องจุลทรรศน์อิเล็กตรอนแบบส่องกราด (SEM) ของเซรามิก  $(1-x)\text{BNT}-x\text{BT}$  ที่เผาซินเตอร์ที่ 1200 องศาเซลเซียส โดย (a)  $x = 0$  และ (b)  $x = 0.06$  [35]

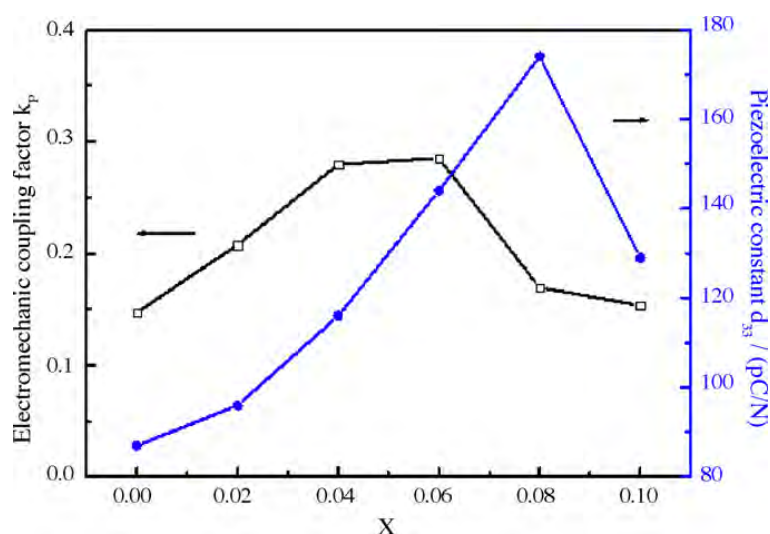


ภาพ 16 แสดงค่า  $d_{33}$ ,  $k_p$ ,  $\epsilon_r$  และ  $\tan\delta$  ของเซรามิก(1-x)BNT-xBT [35]

B.H. Kim et al. [13] เตรียมเซรามิกบิสมาทไทเตียมไททานเต-แบเรียมไททานเต [(1-x)(Bi<sub>0.5</sub>Na<sub>0.5</sub>)TiO<sub>3</sub>-xBaTiO<sub>3</sub>] โดยที่  $0 \leq x \leq 0.10$  ด้วยวิธีอีพิตักษิโดยเผาแคลไซน์ที่อุณหภูมิ 700 องศาเซลเซียส เป็นเวลา 3 ชั่วโมง และเผาซินเตอร์ที่อุณหภูมิ 1200 องศาเซลเซียส เป็นเวลา 3 ชั่วโมง บริเวณรอยต่อเฟส (MPB) พบที่ x เข้าใกล้ 0.06 ซึ่งจะแสดงสมบัติทางไฟฟ้าที่ดี มีค่าคงที่ไดอิเล็กทริก  $\epsilon_r = 1840$ , ค่าคงที่พิโซอิเล็กทริก  $d_{33} = 174$  pC/N เมื่อ  $x = 0.08$  ดังภาพ 17 ในขณะที่  $x = 0.06$  มีค่าสัมประสิทธิ์ไฟฟ้าเชิงกลสูงสุด  $k_p = 0.28$  ดังภาพ 18



ภาพ 17 ค่าคงที่ไดอิเล็กทริกของเซรามิก (1-x)BNT-xBT ที่ปริมาณ x ต่างๆ [13]

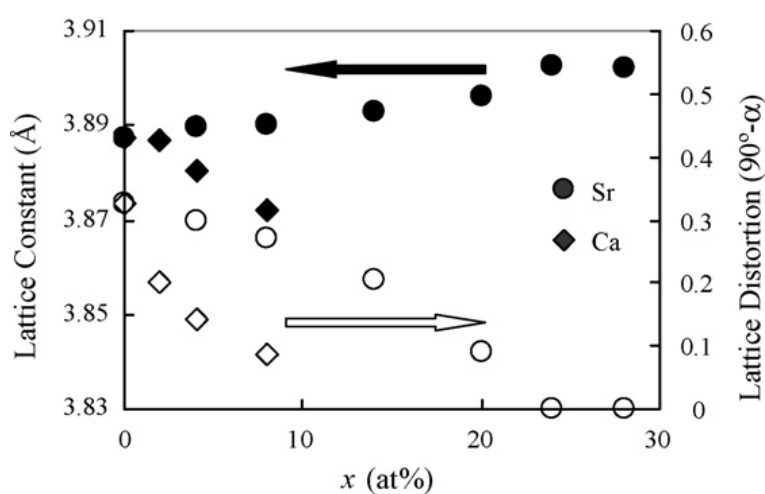


ภาพ 18 ค่าคงที่พิโซอิเล็กทริกและค่าสัมประสิทธิ์ไฟฟ้าเชิงกลของเซรามิก (1-x)BNT-xBT ที่ปริมาณ x ต่างๆ [13]

Y. Hiruma et al. [36] เตรียมเซรามิกบิสมาทโซเดียมไททาเนต-สทรอนเซียมไททาเนต  $[(1-x)(\text{Bi}_{0.5}\text{Na}_{0.5})\text{TiO}_3-x\text{SrTiO}_3]$  โดยที่  $x = 0 - 0.4$  ด้วยวิธีปฏิกิริยาสถานะของแข็งโดยเผาแคลไซต์ที่อุณหภูมิ 800 องศาเซลเซียส เป็นเวลา 2 ชั่วโมง และเผาซินเตอร์ที่อุณหภูมิ 1100 - 1140 องศาเซลเซียส เป็นเวลา 2 ชั่วโมง บริเวณรอยต่อเฟส (MPB) ระหว่างเฟสเฟอร์โรอิเล็กทริกที่มีโครงสร้างเป็นแบบรอมโบฮีดรอล และเฟสพาราอิเล็กทริกที่มีโครงสร้างแบบคิวบิกเทียม

(เทโพโกนอล) พบที่  $x = 0.26 - 0.28$  ซึ่งจะแสดงสมบัติทางไฟฟ้าที่ดี มีค่าคงที่พิโซอิเล็กทริก  $d_{33} = 127$  pC/N เมื่อ  $x = 0.24$

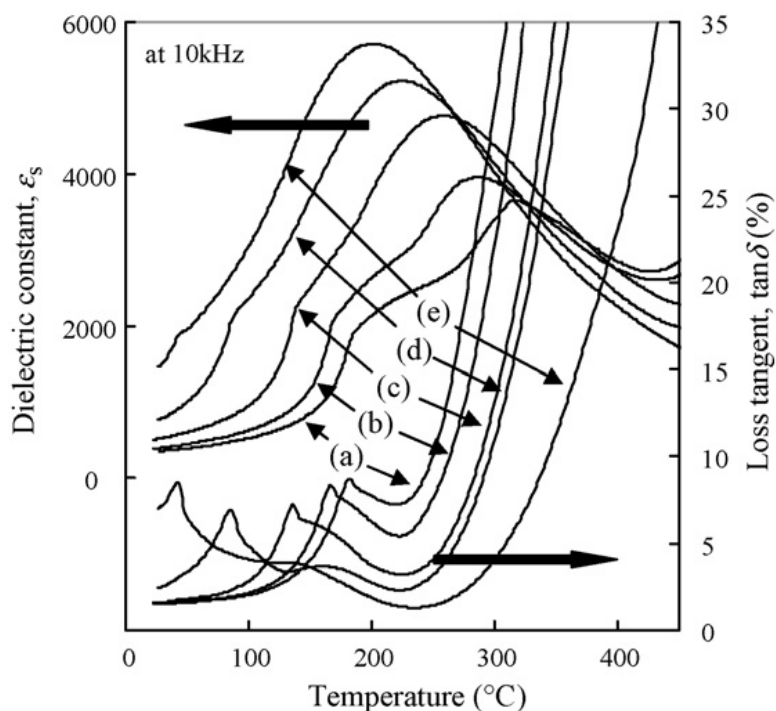
T. Takennaka et al. [37] เตรียมเซรามิกบิสมาทโซเดียมไททานเต โดยเจือสารในระบบ  $1-x(\text{Bi}_{0.5}\text{Na}_{0.5})\text{TiO}_3-x\text{ATiO}_3$  [ $A = \text{Ca}^{2+}$ ,  $\text{Sr}^{2+}$  และ  $\text{Ba}^{2+}$ ] ; BNBT100x, BNST100x และ BNCT100x โดยที่  $x = 0 - 0.08$ ,  $x = 0.28$  และ  $x = 0.20$  ตามลำดับ ด้วยวิธีปฏิกิริยาสถานะของแข็งโดยเผาแคลไซต์ที่อุณหภูมิ 800 องศาเซลเซียส และเผาซินเตอร์ที่อุณหภูมิ 1100 - 1150 องศาเซลเซียส เป็นเวลา 2 ชั่วโมง พบว่า ค่าคงที่แลตทิซและค่าแลตทิซแสดงความเป็นรอมโบอีดรอล ( $90^\circ - \alpha$ ) ของเซรามิก BNCT100x และ BNST100x ที่ปริมาณ  $x$  ต่างๆ พบว่า ค่าคงที่แลตทิซจะมีค่าลดลงเมื่อปริมาณ  $\text{Ca}^{2+}$  เพิ่มขึ้น อาจเนื่องมาจาก  $\text{Ca}^{2+}$  มีขนาดรัศมีอะตอมน้อยกว่าขนาดรัศมีอะตอมเฉลี่ยของ A-site ของเซรามิก BNT สำหรับ  $\text{Sr}^{2+}$  มีขนาดรัศมีอะตอมมากกว่าขนาดรัศมีอะตอมเฉลี่ยของ A-site ของเซรามิก BNT ดังนั้นจึงมีค่าแลตทิซเพิ่มขึ้นเมื่อปริมาณ  $\text{Sr}^{2+}$  เพิ่มขึ้น ดังภาพ 19



ภาพ 19 ค่าคงที่แลตทิซและค่าแลตทิซแสดงความเป็นรอมโบอีดรอล ( $90^\circ - \alpha$ ) ของเซรามิก BNCT100x และ BNST100x ที่ปริมาณ  $x$  ต่างๆ [37]

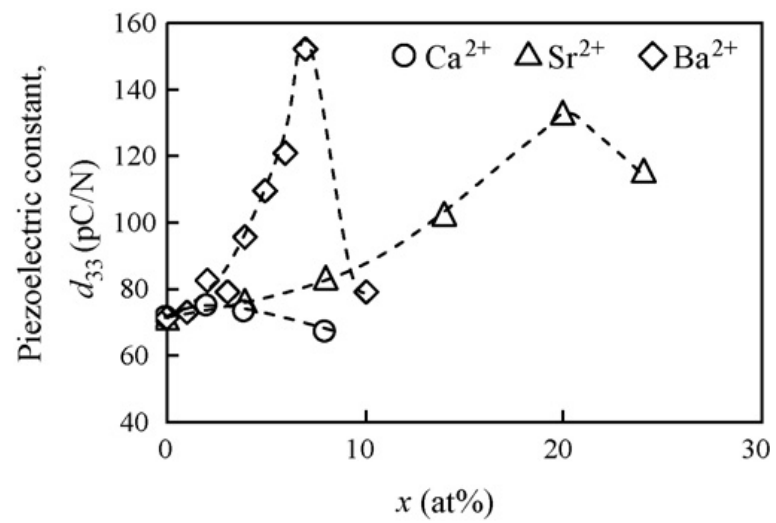
จากภาพ 20 แสดงค่าคงที่ไดอิเล็กทริกของเซรามิก BNST100x ที่ปริมาณ  $x$  ต่างๆ (a)  $x=0.04$  (b)  $x=0.08$ , (c)  $x=0.14$ , (d)  $x=0.20$  และ (e)  $x=0.24$  โดยวัดที่ความถี่ 10 kHz พบว่า อุณหภูมิ  $T_d$  และ  $T_m$  จะเลื่อนต่ำลงเมื่อปริมาณ  $x$  เพิ่มขึ้น สำหรับ BNST-24 อุณหภูมิ  $T_d = 42$  องศาเซลเซียส ในกรณีที่เติม  $\text{Ca}^{2+}$  อุณหภูมิ  $T_m$  จะเลื่อนสูงขึ้นเมื่อ  $x$  เพิ่มขึ้น





ภาพ 20 ค่าคงที่ไดอิเล็กทริกของเซรามิก BNST100x ที่ปริมาณ x ต่างๆ (a)  $x=0.04$   
(b)  $x=0.08$ , (c)  $x=0.14$ , (d)  $x=0.20$  และ (e)  $x=0.24$  โดยวัดที่ความถี่ 10 kHz [37]

สำหรับค่า  $d_{33}$  ของเซรามิก BNT จะมีค่าเท่ากับ 71 pC/N หลังจากเติมสารเจือลงไป ดังภาพ 21 แสดงค่าคงที่พิโซอิเล็กทริก,  $d_{33}$  ของ BNBT100x, BNST100x และ BNCT100x ที่ปริมาณ x ต่างๆ พบว่า มีค่า  $d_{33}$  สูงสุดที่อัตราส่วนดังนี้ BNBT100x;  $x=0.07$ ,  $d_{33} = 152$  pC/N, BNST100x;  $x=0.20$ ,  $d_{33} = 133$  pC/N และ BNCT100x;  $x=0.02$ ,  $d_{33} = 75$  pC/N สรุปอัตราส่วนที่มีคุณสมบัติเหมาะสมในการนำไปประยุกต์ใช้ต่อไปคือ BNCT-2, BNST-20 และ BNBT-6~7 เนื่องจากมีค่าทางไฟฟ้าสูง



ภาพ 21 ค่าคงที่พีโซอิเล็กทริก,  $d_{33}$  ของ BNBT100x, BNST100x และ BNCT100x ที่ ปริมาณ x ต่างๆ [37]

### บทที่ 3

#### วิธีดำเนินงานวิจัย

##### สารเคมีที่ใช้ในการทดลอง

1. ไททาเนียมไดออกไซด์ ( $\text{TiO}_2$ ) ความบริสุทธิ์ 99%
2. แบเรียมคาร์บอเนต ( $\text{BaCO}_3$ ) ความบริสุทธิ์ 99%
3. โซเดียมคาร์บอเนต ( $\text{Na}_2\text{CO}_3$ ) ความบริสุทธิ์ 99%
4. บิสมัทออกไซด์ ( $\text{Bi}_2\text{O}_3$ ) ความบริสุทธิ์ 99%
5. แคลเซียมคาร์บอเนต ( $\text{CaCO}_3$ ) ความบริสุทธิ์ 99.9%
6. สตรอนเชียมคาร์บอเนต ( $\text{SrCO}_3$ ) ความบริสุทธิ์ 99.9%
7. เอทิลแอลกอฮอล์บริสุทธิ์ (Ethanol absolute) ความบริสุทธิ์ 99.7%
8. ยูเรีย
9. โกลซีน

##### อุปกรณ์ที่ใช้ในการเตรียมสาร

1. กระจกปลาสติกใช้ผสมสาร ทำด้วยพอลิเมอร์มีฝาปิดสนิท โดยมีเส้นผ่าศูนย์กลางประมาณ 10 cm ความสูงประมาณ 19.5 cm
2. ลูกบดทรงกลมที่มีเส้นผ่าศูนย์กลางประมาณ 5 mm
3. Magnetic stirrer bar
4. ปีกเกอร์ขนาด 1000 cc
5. กระดาษฟอยล์
6. ช้อนตักสาร
7. ตะแกรงลวด
8. ถ้วย Crucible

##### เครื่องมือที่ใช้ในการทดลอง

1. เครื่องชั่งสารแบบละเอียด ผลิตโดยบริษัท AND รุ่น HM-330
2. เครื่องอัดไฮดรอลิก ใช้สำหรับขึ้นรูปสาร อัดแรงดันได้สูงสุด  $1000 \text{ kg/cm}^3$
3. เครื่องผสมสารแบบบดย่อย แบบลูกบอล (ball milling)

4. เตาเผาสาร Eurotherm อุณหภูมิสูงที่สุดในการเผา 1700 องศาเซลเซียส
5. เครื่อง Hot plate
6. ตู้อบสารยี่ห้อ memmert D06057 Model 100 อุณหภูมิที่ใช้ในการอบประมาณ 200 ° C
7. แม่พิมพ์ (Punch and die) ใช้ในการอัดสาร
8. ครกบดสารทำด้วย Agate

### เครื่องมือที่ใช้ในการวิเคราะห์ผลการทดลอง

1. เครื่องวิเคราะห์การเลี้ยวเบนด้วยรังสีเอกซ์ (X-ray diffractometer; Philip PW3040/60 X' Pert Pro)
2. กล้องจุลทรรศน์อิเล็กตรอนแบบส่องกราด (Scanning Electron Microscopy; LEO 1455 VP)
3. เครื่อง LCR Meter (Agilent 4263B)

### วิธีการทดลอง

#### ตอนที่ 1 การเตรียมผงผลึกบิสมัทโซเดียมไททาเนต (BNT)

1. ชั่งสารตั้งต้นคือ บิสมาทออกไซด์ โซเดียมคาร์บอเนต และไททาเนียมไดออกไซด์ ตามอัตราส่วนโดยโมลที่ได้จากการคำนวณ
2. นำสารที่ชั่งได้ในข้อ 1) มาทำการผสมกันในกระป๋องพลาสติกที่มีลูกบดทรงกลมขนาด 7 มิลลิเมตร จำนวน 200 เม็ด โดยเติมเอทานอลในปริมาณ 200 มิลลิลิตร ซึ่งจะช่วยให้สารทั้งสองเข้ากันได้ดีขึ้น ปิดฝาให้สนิท เสร็จแล้วนำไปวางบนเครื่องบดย่อยแบบลูกบดเป็นเวลา 24 ชั่วโมง
3. เมื่อครบ 24 ชั่วโมงแล้วเทสารลงบนตะแกรงลวดที่วางอยู่บนบีกเกอร์ เพื่อล้างแยกของผสมออกจากเม็ดบด แล้วจึงนำ Magnetic stirrer ใส่ลงสำหรับคนสารให้เข้ากันแล้วนำกระดาษฟอยล์ที่ทำการเจาะรูมาปิดก่อนจะนำไปตั้งที่เครื่อง Hot plate เพื่อทำการแยกเอทานอลออก
4. เมื่อทำการแยกเอทานอลออกจากสารแล้วจึงทำการอบที่ 120 องศาเซลเซียส เป็นเวลา 6 ชั่วโมง
5. นำสารที่แห้งแล้วมาบดอย่างหยาบๆโดยใช้ครกหยก (Agate) จากนั้นนำผงสารที่ได้มาทำการคัดขนาด (Sieving) เพื่อให้ได้ขนาดอนุภาคที่มีความสม่ำเสมอ
6. นำสารมาบดผสมกับไกลซีน โดยใช้อัตราส่วน 1:2 จากนั้นนำผงสารที่ได้มาทำการคัดขนาดอีกครั้งหนึ่ง

7. นำสารที่บดได้ใส่ใน Crucible เปิดฝานำไปเผาแคลไซน์ในเตาที่อุณหภูมิ 750 องศาเซลเซียส เป็นเวลา 2 ชั่วโมง โดยอัตราการขึ้นลงของอุณหภูมิเป็น 5 องศาเซลเซียสต่อนาที

8. นำผงผลึกบิสมาทโซเดียมไททาเนตที่ได้ไปตรวจสอบโครงสร้างผลึก และโครงสร้างจุลภาค ด้วยเทคนิคการเลี้ยวเบนของรังสีเอกซ์ และกล้องจุลทรรศน์อิเล็กตรอนแบบส่องกราด

## ตอนที่ 2 การเตรียมผงผลึกแคลเซียมไททาเนต (CT)

1. ชั่งสารตั้งต้นคือ แคลเซียมคาร์บอเนต และไททาเนียมไดออกไซด์ ตามอัตราส่วนโดยโมลที่ได้จากการคำนวณ

2. นำสารที่ชั่งได้ในข้อ 1) มาทำการผสมกันในกระป๋องพลาสติกที่มีลูกบดทรงกลมขนาด 7 มิลลิเมตร จำนวน 200 เม็ด โดยเติมเอทานอลในปริมาณ 200 มิลลิลิตร ซึ่งจะช่วยให้อาหารทั้งสองเข้ากันได้ดีขึ้น ปิดฝาให้สนิท เสร็จแล้วนำไปวางบนเครื่องบดย่อยแบบลูกบดเป็นเวลา 24 ชั่วโมง

3. เมื่อครบ 24 ชั่วโมงแล้วเทสารลงบนตะแกรงลวดที่วางอยู่บนปิกเกอร์ เพื่อล้างแยกของผสมออกจากเม็ดบด แล้วจึงนำ Magnetic stirrer ใส่ลงสำหรับคนสารให้เข้ากันแล้วนำกระดาษฟอยล์ที่ทำการเจาะรูมาปิดก่อนจะนำไปตั้งที่เครื่อง Hot plate เพื่อทำการแยกเอทานอลออก

4. เมื่อทำการแยกเอทานอลออกจากสารแล้วจึงทำการอบที่ 120 องศาเซลเซียส เป็นเวลา 6 ชั่วโมง

5. นำสารที่แห้งแล้วมาบดอย่างหยาบๆโดยใช้ครกหยก (Agate) จากนั้นนำผงสารที่ได้มาทำการคัดขนาด (Sieving) เพื่อให้ได้ขนาดอนุภาคที่มีความสม่ำเสมอ

6. นำสารมาบดผสมกับไกลซีน โดยใช้อัตราส่วน 1:2 จากนั้นนำผงสารที่ได้มาทำการคัดขนาดอีกครั้งหนึ่ง

7. นำสารที่บดได้ใส่ใน Crucible เปิดฝานำไปเผาแคลไซน์ในเตาที่อุณหภูมิ 1000 องศาเซลเซียส เป็นเวลา 2 ชั่วโมง โดยอัตราการขึ้นลงของอุณหภูมิเป็น 5 องศาเซลเซียสต่อนาที

8. นำผงผลึกแคลเซียมไททาเนตที่เตรียมได้ไปตรวจสอบโครงสร้างผลึก และโครงสร้างจุลภาค ด้วยเทคนิคการเลี้ยวเบนของรังสีเอกซ์ และกล้องจุลทรรศน์อิเล็กตรอนแบบส่องกราด

## ตอนที่ 3 การเตรียมผงผลึกสทรอนเซียมไททาเนต (ST)

1. ชั่งสารตั้งต้นคือ สทรอนเซียมคาร์บอเนต และไททาเนียมไดออกไซด์ ตามอัตราส่วนโดยโมลที่ได้จากการคำนวณ

2. นำสารที่ชั่งได้ในข้อ 1) มาทำการผสมกันในกระป๋องพลาสติกที่มีลูกบดทรงกลมขนาด 7 มิลลิเมตร จำนวน 200 เม็ด โดยเติมเอทานอลในปริมาณ 200 มิลลิลิตร ซึ่งจะช่วยให้อาหารทั้งสองเข้ากันได้ดีขึ้น ปิดฝาให้สนิท เสร็จแล้วนำไปวางบนเครื่องบดย่อยแบบลูกบดเป็นเวลา 24 ชั่วโมง

3. เมื่อครบ 24 ชั่วโมงแล้วเทสารลงบนตะแกรงลวดที่วางอยู่บนปิกเกอร์ เพื่อล้างแยกของผสมออกจากเม็บบด แล้วจึงนำ Magnetic stirrer ใส่ลงสำหรับคนสารให้เข้ากันแล้วนำกระดาษฟอยล์ที่ทำการเจาะรูมาปิดก่อนจะนำไปตั้งที่เครื่อง Hot plate เพื่อทำการแยกเอทานอลออก
4. เมื่อทำการแยกเอทานอลออกจากสารแล้วจึงทำการอบที่ 120 องศาเซลเซียส เป็นเวลา 6 ชั่วโมง
5. นำสารที่แห้งแล้วมาบดอย่างหยาบๆโดยใช้ครกหยก (Agate) จากนั้นนำผงสารที่ได้มาทำการคัดขนาด(Sieving) เพื่อให้ได้ขนาดอนุภาคที่มีความสม่ำเสมอ
6. นำสารมาบดผสมกับยูเรีย โดยใช้อัตราส่วน 1:2 จากนั้นนำผงสารที่ได้มาทำการคัดขนาดอีกครั้งหนึ่ง
7. นำสารที่บดได้ใส่ใน Crucible เปิดฝานำไปเผาแคลไซน์ในเตาที่อุณหภูมิ 1000 องศาเซลเซียส เป็นเวลา 2 ชั่วโมง โดยอัตราการขึ้นลงของอุณหภูมิเป็น 5 องศาเซลเซียสต่อนาที
8. นำผงผลิตภัณฑ์เตรียมไททานेटที่เตรียมได้ไปตรวจสอบโครงสร้างผลึก และโครงสร้างจุลภาค ด้วยเทคนิคการเลี้ยวเบนของรังสีเอกซ์ และกล้องจุลทรรศน์อิเล็กตรอนแบบส่องกราด

#### ตอนที่ 4 การเตรียมผงผลึกแบเรียมไททานेट (BT)

1. ชั่งสารตั้งต้นคือ แบเรียมคาร์บอเนต และไททานเนียมไดออกไซด์ ตามอัตราส่วนโดยโมลที่ได้จากการคำนวณ
2. นำสารที่ชั่งได้ในข้อ 1) มาทำการผสมกันในกระป๋องพลาสติกที่มีลูกบดทรงกลมขนาด 7 มิลลิเมตร จำนวน 200 เม็ด โดยเติมเอทานอลในปริมาณ 200 มิลลิลิตร ซึ่งจะช่วยให้อาหารทั้งสองเข้ากันได้ดีขึ้น ปิดฝาให้สนิท เสร็จแล้วนำไปวางบนเครื่องบดย่อยแบบลูกบดเป็นเวลา 24 ชั่วโมง
3. เมื่อครบ 24 ชั่วโมงแล้วเทสารลงบนตะแกรงลวดที่วางอยู่บนปิกเกอร์ เพื่อล้างแยกของผสมออกจากเม็บบด แล้วจึงนำ Magnetic stirrer ใส่ลงสำหรับคนสารให้เข้ากันแล้วนำกระดาษฟอยล์ที่ทำการเจาะรูมาปิดก่อนจะนำไปตั้งที่เครื่อง Hot plate เพื่อทำการแยกเอทานอลออก
4. เมื่อทำการแยกเอทานอลออกจากสารแล้วจึงทำการอบที่ 120 องศาเซลเซียส เป็นเวลา 6 ชั่วโมง
5. นำสารที่แห้งแล้วมาบดอย่างหยาบๆโดยใช้ครกหยก (Agate) จากนั้นนำผงสารที่ได้มาทำการคัดขนาด(Sieving) เพื่อให้ได้ขนาดอนุภาคที่มีความสม่ำเสมอ
6. นำสารมาบดผสมกับไกลซีน โดยใช้อัตราส่วน 1:2 จากนั้นนำผงสารที่ได้มาทำการคัดขนาดอีกครั้งหนึ่ง

7. นำสารที่บดได้ใส่ใน Crucible เปิดฝาเข้าไปเผาแคลไซน์ในเตาที่อุณหภูมิ 1200 องศาเซลเซียส เป็นเวลา 4 ชั่วโมง โดยอัตราการขึ้นลงของอุณหภูมิเป็น 5 องศาเซลเซียสต่อนาที

8. นำผงผลึกแบเรียมไททาเนตที่เตรียมได้ไปตรวจสอบโครงสร้างผลึก และโครงสร้างจุลภาค ด้วยเทคนิคการเลี้ยวเบนของรังสีเอกซ์ และกล้องจุลทรรศน์อิเล็กตรอนแบบส่องกราด

### ตอนที่ 5 การเตรียมเซรามิกบิสมาทโซเดียมไททาเนต-แคลเซียมไททาเนต (BNTCT)

1. ทำการเตรียมเซรามิกบิสมาทโซเดียมไททาเนต-แคลเซียมไททาเนต (BNTCT) โดยการนำผงผลึกที่ได้จากการเตรียมในตอนต้นที่ 1 และตอนที่ 2 มาผสมกันตามสัดส่วนสมการเคมีดังนี้  $1-x(\text{Bi}_{0.5}\text{Na}_{0.5})\text{TiO}_3-x\text{ATiO}_3$  [ $A = \text{Ca}^{2+}$ ] โดย  $x = 0.0 - 0.08$  แล้วนำผงผลึกผสมที่ได้มาใส่ลงในกระป๋องพลาสติกที่มีลูกบดทรงกลมขนาด 7 มิลลิเมตร จำนวน 200 เม็ด หลังจากนั้นเติมเอทานอลในปริมาณ 200 มิลลิลิตร และผสมสาร binder ลงไปร้อยละ 2 โดยน้ำหนัก ปิดฝาให้สนิทเสร็จแล้วนำไปวางบนเครื่องบดย่อยแบบลูกบดเป็นเวลา 24 ชั่วโมง

2. เมื่อครบ 24 ชั่วโมงแล้วเทสารลงบนตะแกรงลวดที่วางอยู่บนปีกเกอร์ เพื่อล้างแยกของผสมออกจากเม็ดบด แล้วจึงนำ Magnetic stirrer ใส่ลงสำหรับคนสารให้เข้ากันแล้วนำกระดาษฟอยล์ที่ทำการเจาะรูมาปิดก่อนจะนำไปตั้งที่เครื่อง Hot plate เพื่อทำการแยกเอทานอลออก

3. เมื่อทำการแยกเอทานอลออกจากสารแล้วจึงทำการอบที่ 120 องศาเซลเซียส เป็นเวลา 6 ชั่วโมง

4. นำสารที่แห้งแล้วมาบดอย่างหยาบๆโดยใช้ครกหยก (Agate) จากนั้นนำผงสารที่ได้มาทำการคัดขนาด (Sieving) จนได้ผงสารที่ละเอียด

5. นำสารที่คัดขนาดแล้วมาอัดขึ้นรูปด้วยเครื่องอัดไฮดรอลิก และใช้แม่พิมพ์โลหะที่มีขนาดเส้นผ่านศูนย์กลางประมาณ 1.5 เซนติเมตร โดยใช้ผงผลึกบิสมาทโซเดียมไททาเนต-แคลเซียมไททาเนต (BNTCT) 1.2 กรัม ต่อการขึ้นรูป 1 ครั้ง อัดด้วยแรงดันประมาณ 80 MPa

6. นำชิ้นงานที่ขึ้นรูปเสร็จแล้ว (Green body) มาเรียงไว้ในถ้วยอลูมินาที่มีฝาปิดโดยทำการจัดเรียงเป็นชั้นๆ ซึ่งในแต่ละชั้นจะใส่ผงอลูมินา ดังแสดงในภาพ 22

7. ทำการเผาซินเตอร์ที่อุณหภูมิ 1050 - 1200 องศาเซลเซียส เป็นเวลา 2 ชั่วโมง โดยอัตราการขึ้นลงของอุณหภูมิเป็น 5 องศาเซลเซียสต่อนาที

### ตอนที่ 6 การเตรียมเซรามิกบิสมาทโซเดียมไททาเนต-สทรอนเซียมไททาเนต (BNTST)

1. ทำการเตรียมเซรามิกบิสมาทโซเดียมไททาเนต-สทรอนเซียมไททาเนต (BNTST) โดยการนำผงผลึกที่ได้จากการเตรียมในตอนต้นที่ 1 และตอนที่ 3 มาผสมกันตามสัดส่วนสมการเคมีดังนี้

1-  $x(\text{Bi}_{0.5}\text{Na}_{0.5})\text{TiO}_3$ - $x\text{ATiO}_3$  [ $A = \text{Sr}^{2+}$ ] โดย  $x = 0.0 - 0.40$  แล้วนำผงผลิตภัณฑ์ที่ได้มาใส่ลงในกระป๋องพลาสติกที่มีลูกบดทรงกลมขนาด 7 มิลลิเมตร จำนวน 200 เม็ด หลังจากนั้นเติมเอทานอลในปริมาณ 200 มิลลิลิตร และผสมสาร binder ลงไปร้อยละ 2 โดยน้ำหนัก ปิดฝาให้สนิทเสร็จแล้วนำไปวางบนเครื่องบดย่อยแบบลูกบดเป็นเวลา 24 ชั่วโมง

2. เมื่อครบ 24 ชั่วโมงแล้วเทสารลงบนตะแกรงลวดที่วางอยู่บนปิกเกอร์ เพื่อล้างแยกของผสมออกจากเม็ดบด แล้วจึงนำ Magnetic stirrer ใส่ลงสำหรับคนสารให้เข้ากันแล้วนำกระดาษฟอยล์ที่ทำการเจาะรูมาปิดก่อนจะนำไปตั้งที่เครื่อง Hot plate เพื่อทำการแยกเอทานอลออก

3. เมื่อทำการแยกเอทานอลออกจากสารแล้วจึงทำการอบที่ 120 องศาเซลเซียส เป็นเวลา 6 ชั่วโมง

4. นำสารที่แห้งแล้วมาบดอย่างหยาบๆโดยใช้ครกหยก (Agate) จากนั้นนำผงสารที่ได้มาทำการคัดขนาด (Sieving) จนได้ผงสารที่ละเอียด

5. นำสารที่คัดขนาดแล้วมาอัดขึ้นรูปด้วยเครื่องอัดไฮดรอลิก และใช้แม่พิมพ์โลหะที่มีขนาดเส้นผ่านศูนย์กลางประมาณ 1.5 เซนติเมตร โดยใช้ผงผลิตภัณฑ์โซเดียมไททานเตสทรอนเนียมไททานเต (BNTST) 1.2 กรัม ต่อการขึ้นรูป 1 ครั้ง อัดด้วยแรงดันประมาณ 80 MPa

6. นำชิ้นงานที่ขึ้นรูปเสร็จแล้ว (Green body) มาเรียงไว้ในถ้ำยอลูมินาที่มีฝาปิดโดยทำการจัดเรียงเป็นชั้นๆ ซึ่งในแต่ละชั้นจะใส่ผงอลูมินา ดังแสดงในภาพ 22

7. ทำการเผาชิ้นเตอร์ที่อุณหภูมิ 1050 - 1200 องศาเซลเซียส เป็นเวลา 2 ชั่วโมง โดยอัตราการขึ้นลงของอุณหภูมิเป็น 5 องศาเซลเซียสต่อนาที

#### ตอนที่ 7 การเตรียมเซรามิกบิสมาทโซเดียมไททานเต-แบเรียมไททานเต (BNTBT)

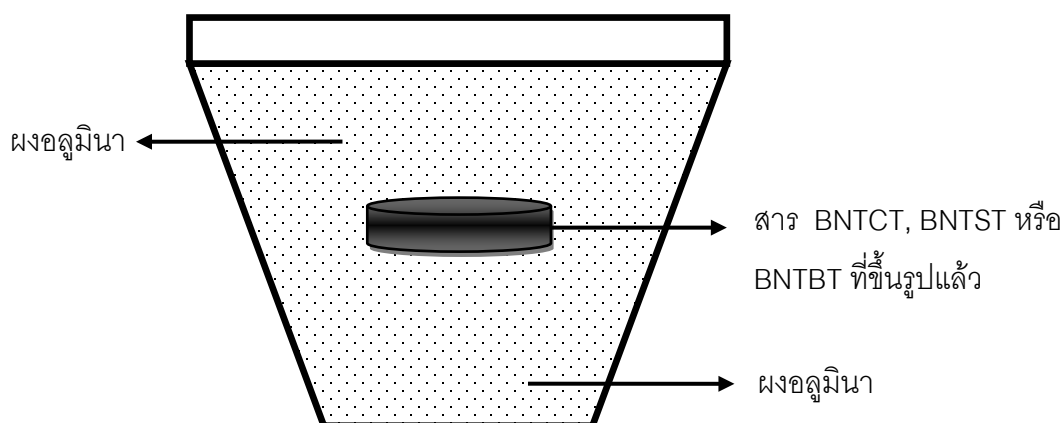
1. ทำการเตรียมเซรามิกบิสมาทโซเดียมไททานเต-แบเรียมไททานเต (BNTBT) โดยการนำผงผลิตภัณฑ์ได้จากการเตรียมในตอนที่ 1 และตอนที่ 4 มาผสมกันตามสัดส่วนสมการเคมีดังนี้  $1-x(\text{Bi}_{0.5}\text{Na}_{0.5})\text{TiO}_3$ - $x\text{ATiO}_3$  [ $A = \text{Ba}^{2+}$ ] โดย  $x = 0.0 - 0.12$  แล้วนำผงผลิตภัณฑ์ที่ได้มาใส่ลงในกระป๋องพลาสติกที่มีลูกบดทรงกลมขนาด 7 มิลลิเมตร จำนวน 200 เม็ด หลังจากนั้นเติมเอทานอลในปริมาณ 200 มิลลิลิตร และผสมสาร binder ลงไปร้อยละ 2 โดยน้ำหนัก ปิดฝาให้สนิทเสร็จแล้วนำไปวางบนเครื่องบดย่อยแบบลูกบดเป็นเวลา 24 ชั่วโมง

2. เมื่อครบ 24 ชั่วโมงแล้วเทสารลงบนตะแกรงลวดที่วางอยู่บนปิกเกอร์ เพื่อล้างแยกของผสมออกจากเม็ดบด แล้วจึงนำ Magnetic stirrer ใส่ลงสำหรับคนสารให้เข้ากันแล้วนำกระดาษฟอยล์ที่ทำการเจาะรูมาปิดก่อนจะนำไปตั้งที่เครื่อง Hot plate เพื่อทำการแยกเอทานอลออก

3. เมื่อทำการแยกเอทานอลออกจากสารแล้วจึงทำการอบที่ 120 องศาเซลเซียส เป็นเวลา 6 ชั่วโมง



4. นำสารที่แห้งแล้วมาบดอย่างหยาบๆโดยใช้ครกหยก (Agate) จากนั้นนำผงสารที่ได้มาทำการคัดขนาด(Sieving) จนได้ผงสารที่ละเอียด
5. นำสารที่คัดขนาดแล้วมาอัดขึ้นรูปด้วยเครื่องอัดไฮดรอลิก และใช้แม่พิมพ์โลหะที่มีขนาดเส้นผ่านศูนย์กลางประมาณ 1.5 เซนติเมตร โดยใช้ผงผลึกบิสมาทโซเดียมไททาเนต-แบเรียมไททาเนต (BNTBT) 1.2 กรัม ต่อการขึ้นรูป 1 ครั้ง อัดด้วยแรงดันประมาณ 80 MPa
6. นำชิ้นงานที่ขึ้นรูปเสร็จแล้ว (Green body) มาเรียงไว้ในถ้วยอลูมินาที่มีฝาปิดโดยทำการจัดเรียงเป็นชั้นๆ ซึ่งในแต่ละชั้นจะใส่ผงอลูมินา ดังแสดงในภาพ 22
7. ทำการเผาซินเตอร์ที่อุณหภูมิ 1050 - 1200 องศาเซลเซียส เป็นเวลา 2 ชั่วโมง โดยอัตราการขึ้นลงของอุณหภูมิเป็น 5 องศาเซลเซียสต่ออนาที



ภาพ 22 แสดงขั้นตอนการซินเตอร์เซรามิกเซรามิกบิสมาทโซเดียมไททาเนต-แคลเซียมไททาเนต (BNTCT) เซรามิกบิสมาทโซเดียมไททาเนต-สทรอนเซียมไททาเนต (BNTST) และเซรามิกบิสมาทโซเดียมไททาเนต-แบเรียมไททาเนต (BNTBT)

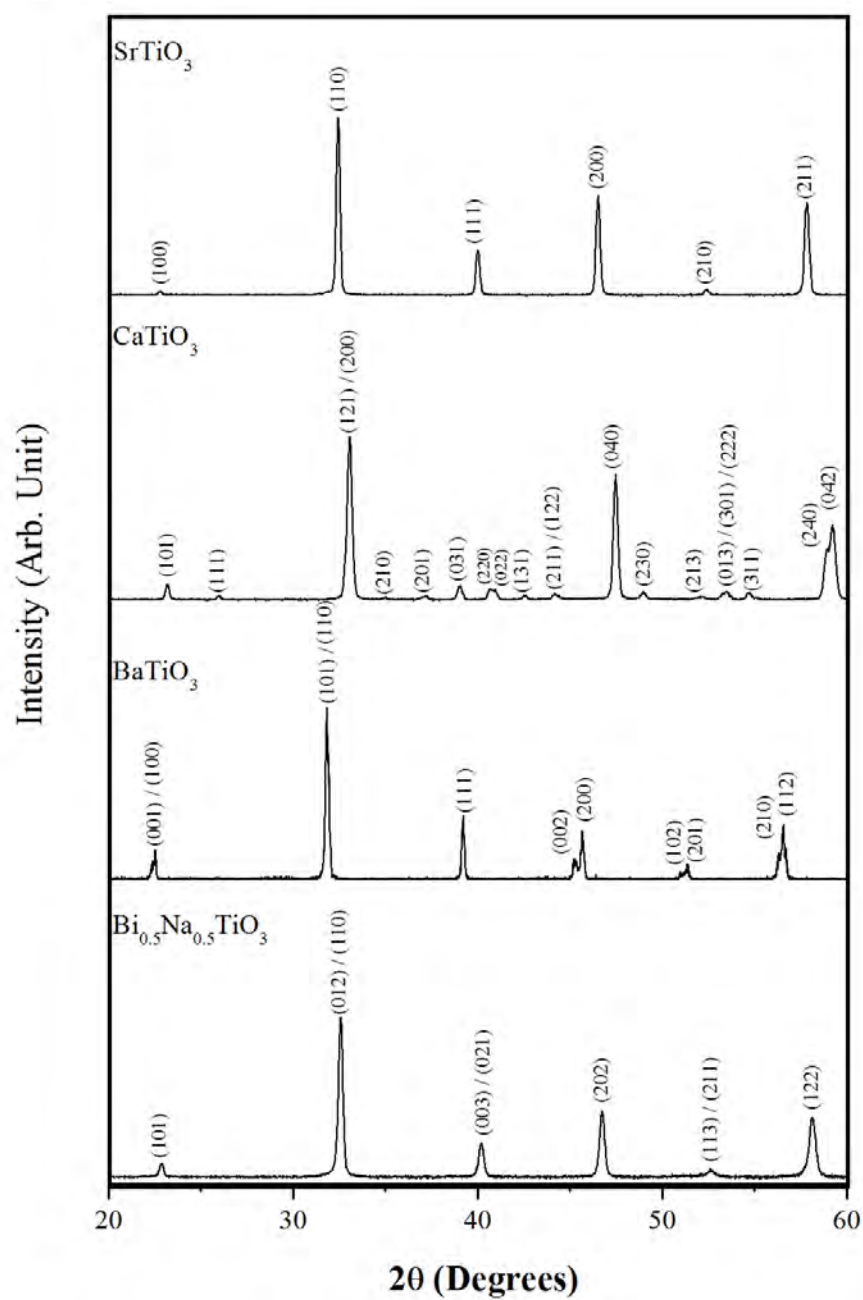
## บทที่ 4

### ผลการวิจัย

ผลการตรวจสอบลักษณะเฉพาะของผงผลึกบิส്മัทโซเดียมไททาเนต ผงผลึกแบเรียมไททาเนต ผงผลึกแคลเซียมไททาเนต และผงผลึกสทรอนเซียมไททาเนต

#### 1. ผลการวิเคราะห์โครงสร้างผลึกด้วยเทคนิคการเลี้ยวเบนของรังสีเอกซ์ (X-ray diffractometer: XRD)

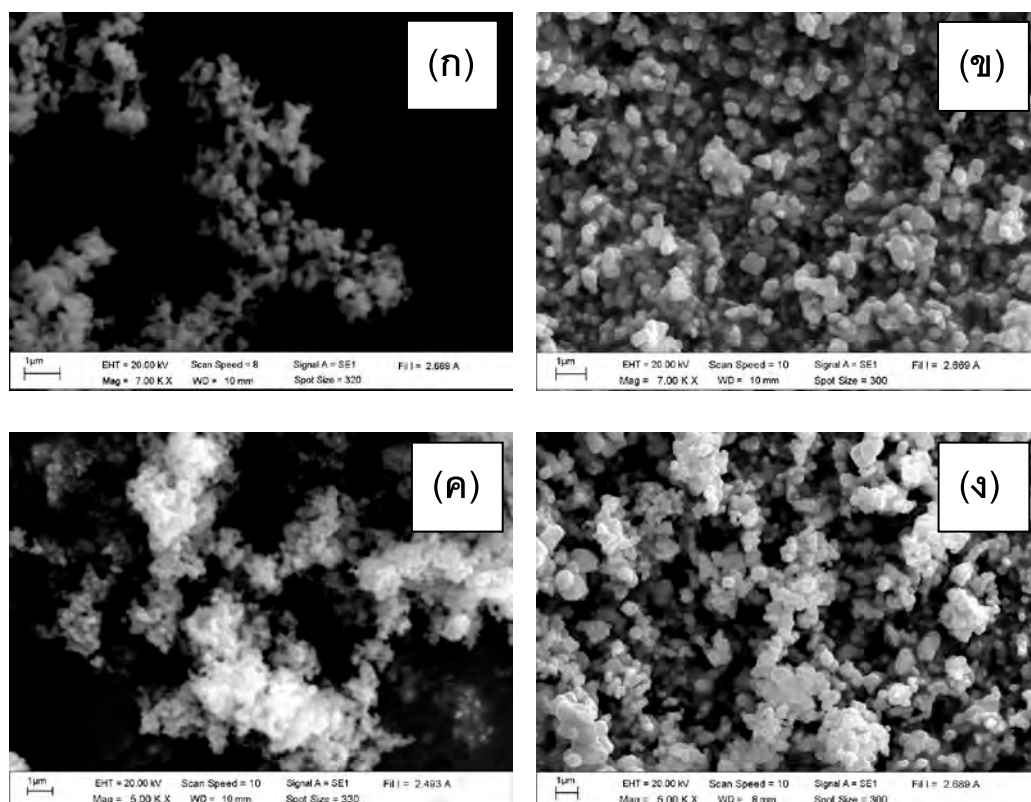
การตรวจวิเคราะห์โครงสร้างผลึกด้วยรูปแบบการเลี้ยวเบนของรังสีเอกซ์ของผงผลึกบิส്മัทโซเดียมไททาเนต ( $\text{Bi}_{0.5}\text{Na}_{0.5}\text{TiO}_3$ ; BNT) ผงผลึกแบเรียมไททาเนต ( $\text{BaTiO}_3$ ; BT) ผงผลึกแคลเซียมไททาเนต ( $\text{CaTiO}_3$ ; CT) และผงผลึกสทรอนเซียมไททาเนต ( $\text{SrTiO}_3$ ; ST) แสดงดังภาพ 23 พบว่ารูปแบบการเลี้ยวเบนของผงผลึก BNT ที่เผาแคลไซน์ที่อุณหภูมิ 650 องศาเซลเซียส เป็นเวลา 2 ชั่วโมง มีโครงสร้างเป็นแบบรอมโบอีดรอลและตรงกับแฟ้มข้อมูลของ JCPDS หมายเลข 36-0340 และไม่พบพีคที่บ่งบอกถึงสารเจือปนใดๆ ส่วนรูปแบบการเลี้ยวเบนของผงผลึก BT ที่เผาแคลไซน์ที่อุณหภูมิ 1200 องศาเซลเซียส เป็นเวลา 4 ชั่วโมง มีโครงสร้างเป็นแบบเทตระโกนอลและพีคที่ปรากฏตรงกับแฟ้มข้อมูลของ JCPDS หมายเลข 03-0752 และไม่พบเฟสแปลกปลอมของสารเจือปนใดๆ สำหรับรูปแบบการเลี้ยวเบนของผงผลึก CT ที่เผาแคลไซน์ที่อุณหภูมิ 1000 องศาเซลเซียส เป็นเวลา 1 ชั่วโมง พบว่ามีโครงสร้างเป็นแบบออโรมบิคสัมพันธ์กับแฟ้มข้อมูล JCPDS หมายเลข 42-0423 และไม่พบพีคที่บ่งบอกถึงสารเจือปนใดๆ และรูปแบบการเลี้ยวเบนของผงผลึก ST ที่เผาแคลไซน์ที่อุณหภูมิ 1200 องศาเซลเซียส เป็นเวลา 4 ชั่วโมง พบว่ามีโครงสร้างเป็นแบบคิวบิกสัมพันธ์กับแฟ้มข้อมูล JCPDS หมายเลข 05-0634 และไม่พบเฟสแปลกปลอมของสารเจือปนใดๆ



ภาพ 23 รูปแบบการเลี้ยวเบนของรังสีเอกซ์ของผงผลึกบิสมาทไทเดียมไททานเตต ( $\text{Bi}_{0.5}\text{Na}_{0.5}\text{TiO}_3$ ) ผงผลึกแบเรียมไททานเตต( $\text{BaTiO}_3$ ) ผงผลึกแคลเซียมไททานเตต ( $\text{CaTiO}_3$ ) และผงผลึกสตรอนเชียมไททานเตต( $\text{SrTiO}_3$ ) ที่เตรียมด้วยวิธีเผาไหม้

## 2. ผลการวิเคราะห์ด้วยกล้องจุลทรรศน์อิเล็กตรอนแบบส่องกราด (Scanning Electron Microscope: SEM)

ศึกษาโครงสร้างจุลภาคของผงผลึกบิสมาทไททาเนต ( $\text{Bi}_{0.5}\text{Na}_{0.5}\text{TiO}_3$ ; BNT) ผงผลึกแบเรียมไททาเนต ( $\text{BaTiO}_3$ ; BT) ผงผลึกแคลเซียมไททาเนต ( $\text{CaTiO}_3$ ; CT) และผงผลึกสทรอนเชียมไททาเนต ( $\text{SrTiO}_3$ ; ST) แสดงในภาพ 24 พบว่าผงผลึก BNT, BT, CT และ ST ที่ได้จากการเผาแคลไซต์ที่อุณหภูมิ 650, 1200, 1000 และ 1200 องศาเซลเซียส มีขนาดอนุภาคเฉลี่ยประมาณ 0.42, 0.80, 0.50 และ 1.00 ไมโครเมตร ตามลำดับ โดยอนุภาคส่วนใหญ่ของผงผลึกทั้ง 3 ชนิด มีลักษณะคล้ายเป็นทรงกลมและมีการเกาะกลุ่มกัน



ภาพ 24 ภาพถ่ายบริเวณผิวหน้าของผงผลึกต่างๆ โดยที่ (ก) ผงผลึกบิสมาทไททาเนต (ข) ผงผลึกแบเรียมไททาเนต (ค) ผงผลึกแคลเซียมไททาเนต และ (ง) ผงผลึกสทรอนเชียมไททาเนต

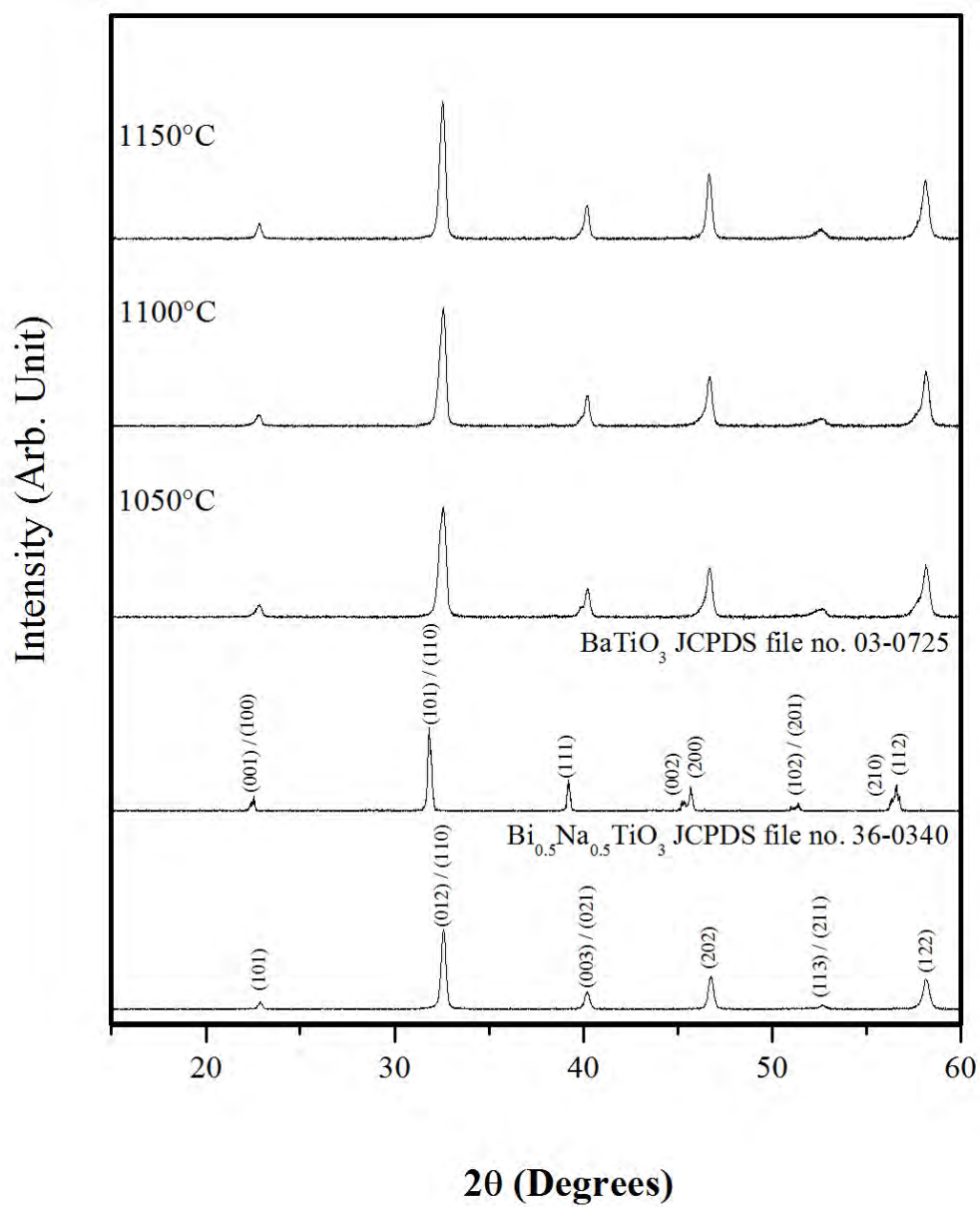
ผลการตรวจสอบลักษณะเฉพาะของเซรามิกบิสมาทโซเดียมไททาเนต-แบเรียมไททาเนต เซรามิกบิสมาทโซเดียมไททาเนต-แคลเซียมไททาเนต และเซรามิกบิสมาทโซเดียมไททาเนต-สทรอนเชียมไททาเนต

1. ผลการตรวจสอบลักษณะเฉพาะของเซรามิกบิสมาทโซเดียมไททาเนต-แบเรียมไททาเนต (1-x)BNT-xBT; BNTBT100x

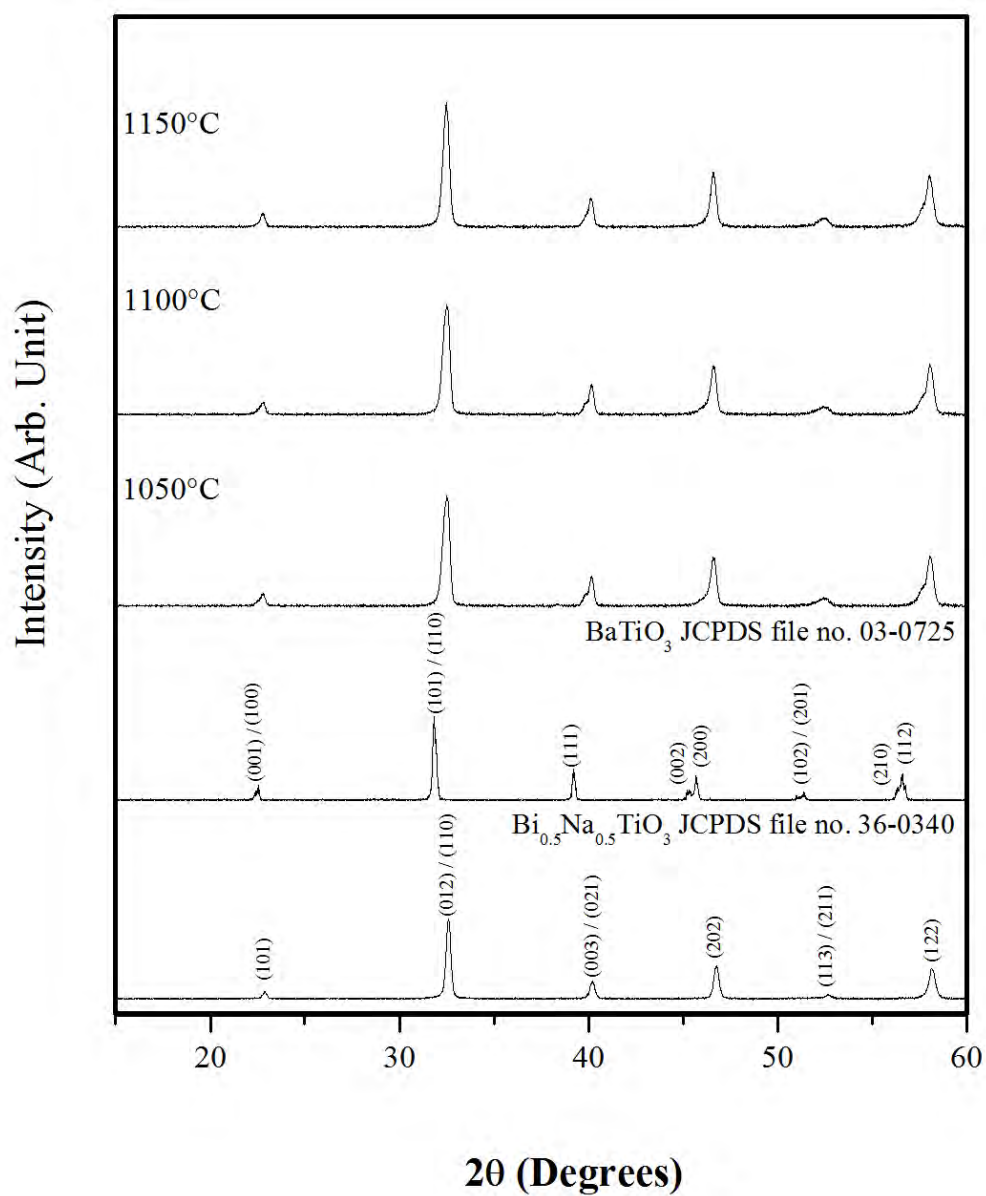
1.1 ผลการวิเคราะห์โครงสร้างผลึกด้วยเทคนิคการเลี้ยวเบนของรังสีเอกซ์ (X-ray diffractometer: XRD)

นำผงผลึก BNT และ BT มาผสมกันตามสัดส่วนโดยโมลโดยใช้อัตราส่วน  $x = 0.02, 0.04, 0.06, 0.08, 0.10$  และ  $0.12$  (BNTBT2, BNTBT4, BNTBT6, BNTBT8, BNTBT10 และ BNTBT12) เพื่อนำมาอัดเม็ดและเผาซินเตอร์ที่อุณหภูมิระหว่าง 1050-1200 องศาเซลเซียส โดยทั่วไปเซรามิก BNT มีโครงสร้างรอมโบอีตรอลซึ่งตรงกับแฟ้มข้อมูลของ JCPDS หมายเลข 36-0340 โดยมีพีคคู่ของ (003)/(021) เกิดขึ้น ที่มุมระหว่าง 38-42 องศา และมีพีคเดี่ยวของ (202) เกิดขึ้นที่มุมระหว่าง 45-48 องศา [8, 38] ในขณะที่เซรามิก BT มีโครงสร้างเทตระโกนอลซึ่งตรงกับแฟ้มข้อมูลของ JCPDS หมายเลข 03-0725 โดยมีพีคเดี่ยวของ (111) เกิดขึ้นที่มุมระหว่าง 38-42 องศา และมีพีคคู่ของ (002)/(200) เกิดขึ้นที่มุมระหว่าง 45-48 องศา [5] จากการศึกษาโครงสร้างผลึกของเซรามิก BNTBT2, BNTBT4, BNTBT6, BNTBT8, BNTBT10 และ BNTBT12 ด้วยรูปแบบการเลี้ยวเบนของรังสีเอกซ์ โดยเผาซินเตอร์ที่อุณหภูมิระหว่าง 1050-1210 องศาเซลเซียส ดังแสดงในภาพ 25, ภาพ 26, ภาพ 27, ภาพ 28, ภาพ 29 และภาพ 30 ตามลำดับ พบว่าในกรณีที่  $x = 0.02$  และ  $0.04$  (BNTBT2 และ BNTBT4) ซินเตอร์ที่อุณหภูมิมากกว่า 1150 องศาเซลเซียส เซรามิกหายไป เนื่องจากที่อุณหภูมิซินเตอร์สูงๆ เกิดการระเหยของ  $\text{Bi}^{3+}$  และ  $\text{Na}^+$  (ภาพ 25 และ 26) ในขณะที่  $x > 0.04$  (BNTBT6, BNTBT8, BNTBT10 และ BNTBT12) พบว่าการระเหยของ  $\text{Bi}^{3+}$  และ  $\text{Na}^+$  ทำให้เกิดเฟสแปลกปลอมของ  $\text{BaO}_{4.977}$  Ti และ  $\text{Ba}_2\text{BiO}_4$  เมื่อซินเตอร์ที่อุณหภูมิสูงกว่า 1200 ดังแสดงในภาพ 27 – 30

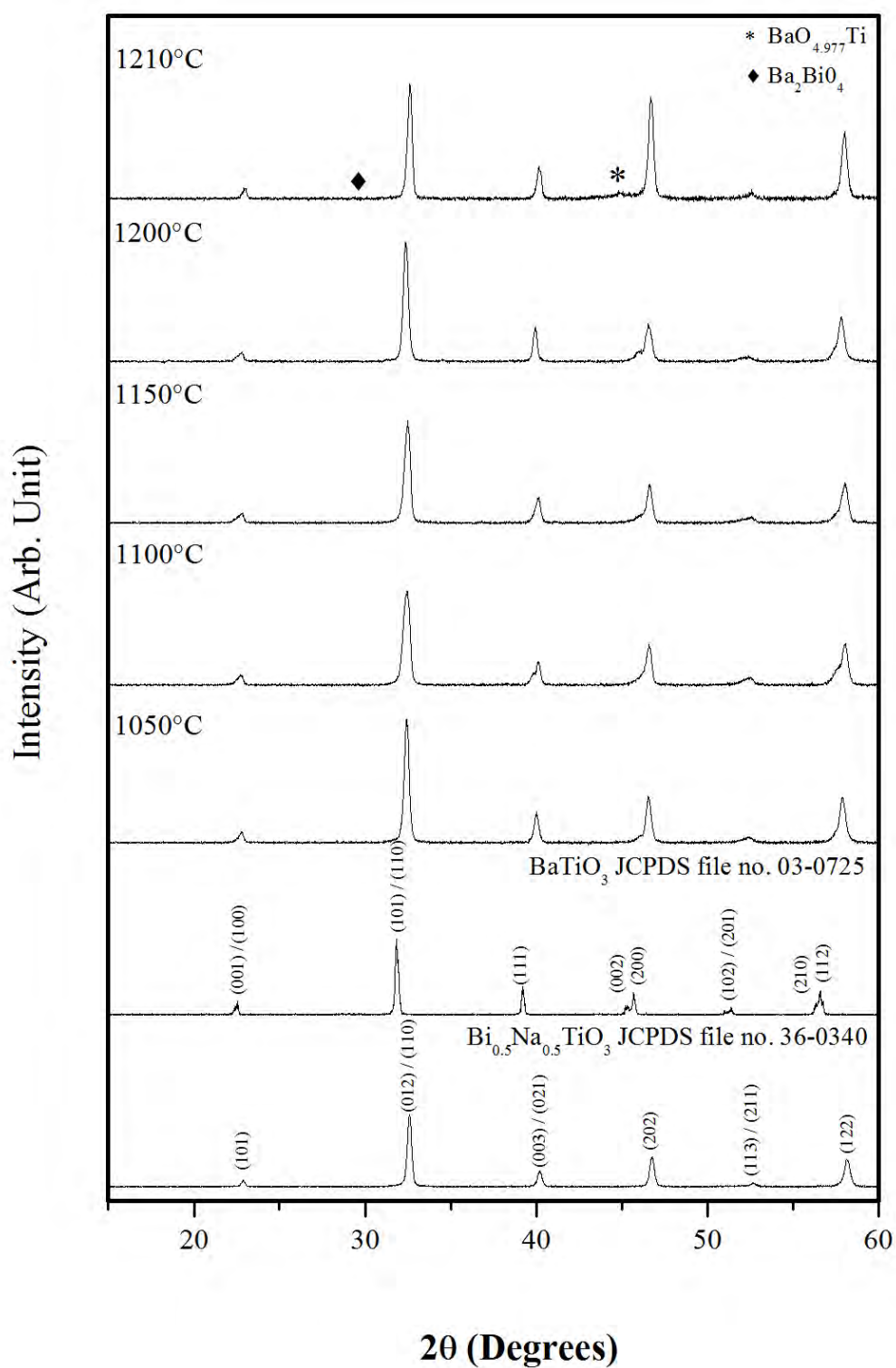
ที่  $x \leq 0.04$  เซรามิก BNTBT2 และ BNTBT4 พบว่ามีโครงสร้างเป็นแบบรอมโบอีตรอลซึ่งเหมือนกับ BNT เมื่อปริมาณ BT เพิ่มขึ้น เซรามิกมีความเป็นเทตระโกนอลลิต์มากขึ้น ในขณะที่  $x \geq 0.10$  เซรามิก BNTBT10 และ BNTBT12 มีโครงสร้างเป็นแบบเทตระโกนอลซึ่งเหมือนกับ BT และสอดคล้องกับงานวิจัยอื่นๆ [12, 13, 35, 37] ดังแสดงในภาพ 31 และที่  $x = 0.06$  และ  $0.08$  เซรามิก BNTBT6 และ BNTBT8 จะมีโครงสร้างร่วมระหว่างเทตระโกนอลและรอมโบอีตรอลเกิดขึ้น โดยสังเกตจากพีคของ (002)/(200) และ (003)/(021) เกิดขึ้นที่มุมระหว่าง 45-48 องศาและ 39-41 องศา ตามลำดับ



ภาพ 25 รูปแบบการเลี้ยวเบนของรังสีเอกซ์ของเซรามิก BNTBT2 ที่อุณหภูมิซินเตอร์  
ต่างๆ

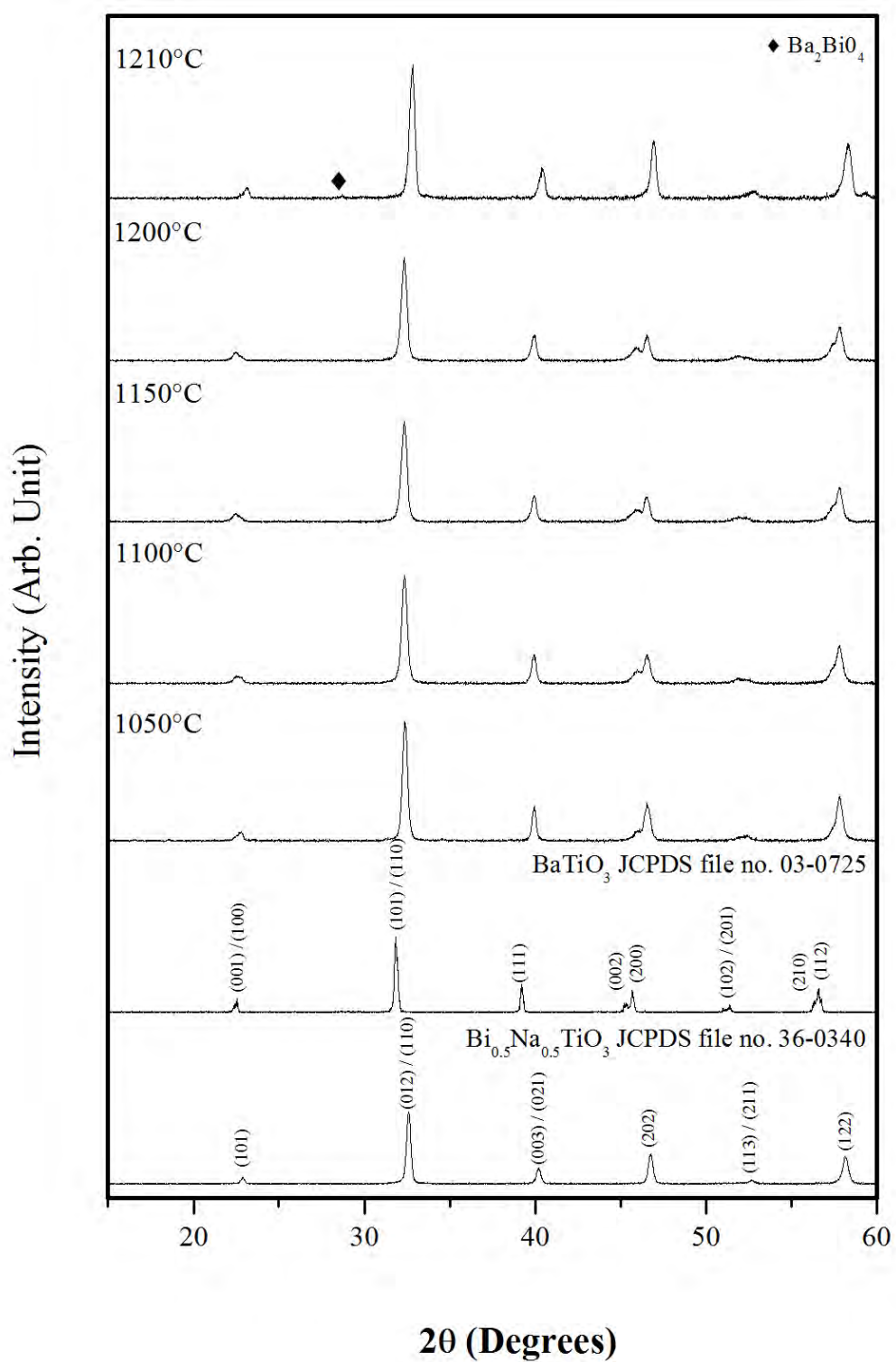


ภาพ 26 รูปแบบการเลี้ยวเบนของรังสีเอกซ์ของเซรามิก BNTBT4 ที่อุณหภูมิซินเตอร์  
ต่างๆ

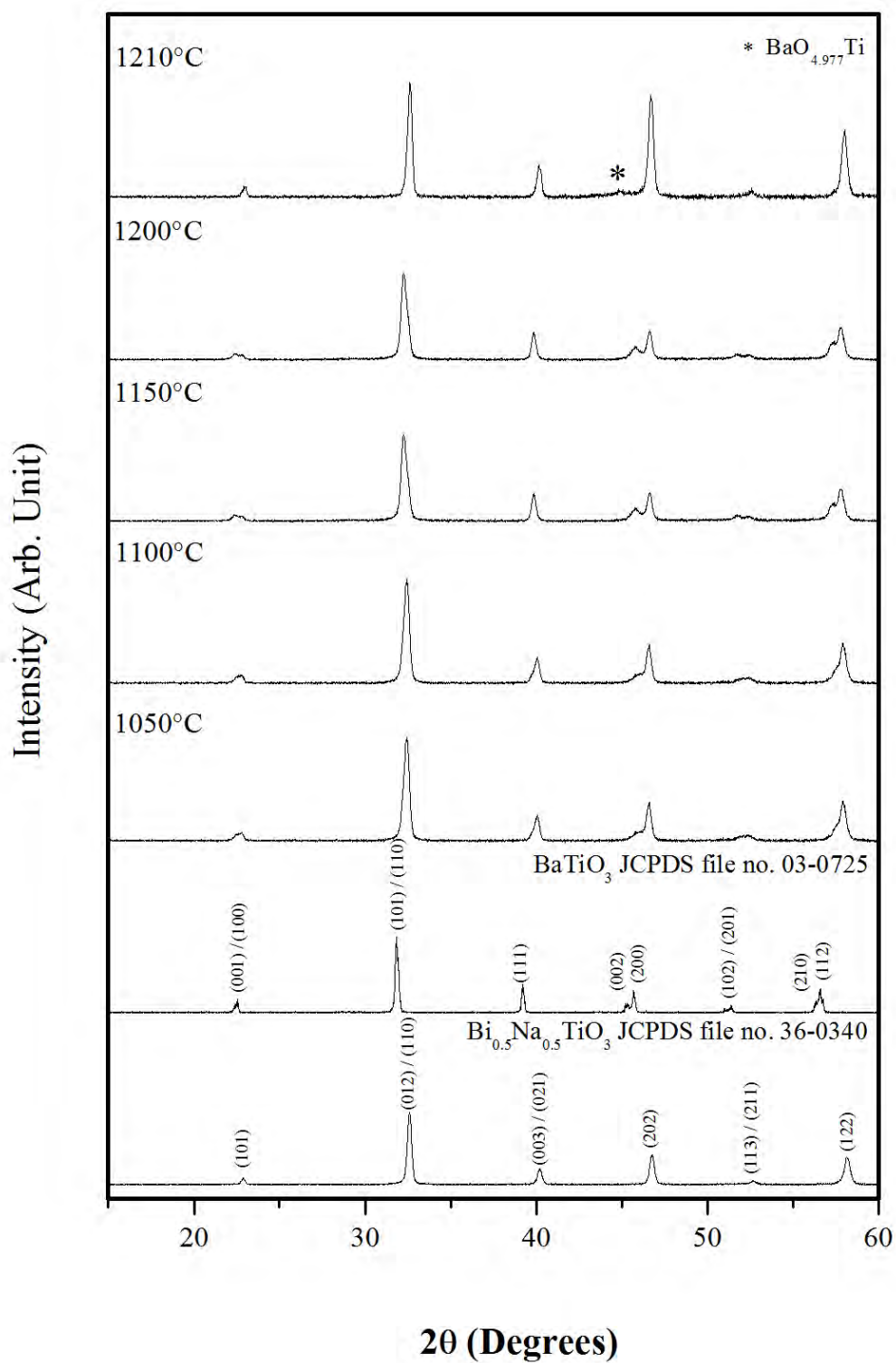


ภาพ 27 รูปแบบการเลี้ยวเบนของรังสีเอกซ์ของเซรามิก BNTBT6 ที่อุณหภูมิซินเตอร์ต่างๆ

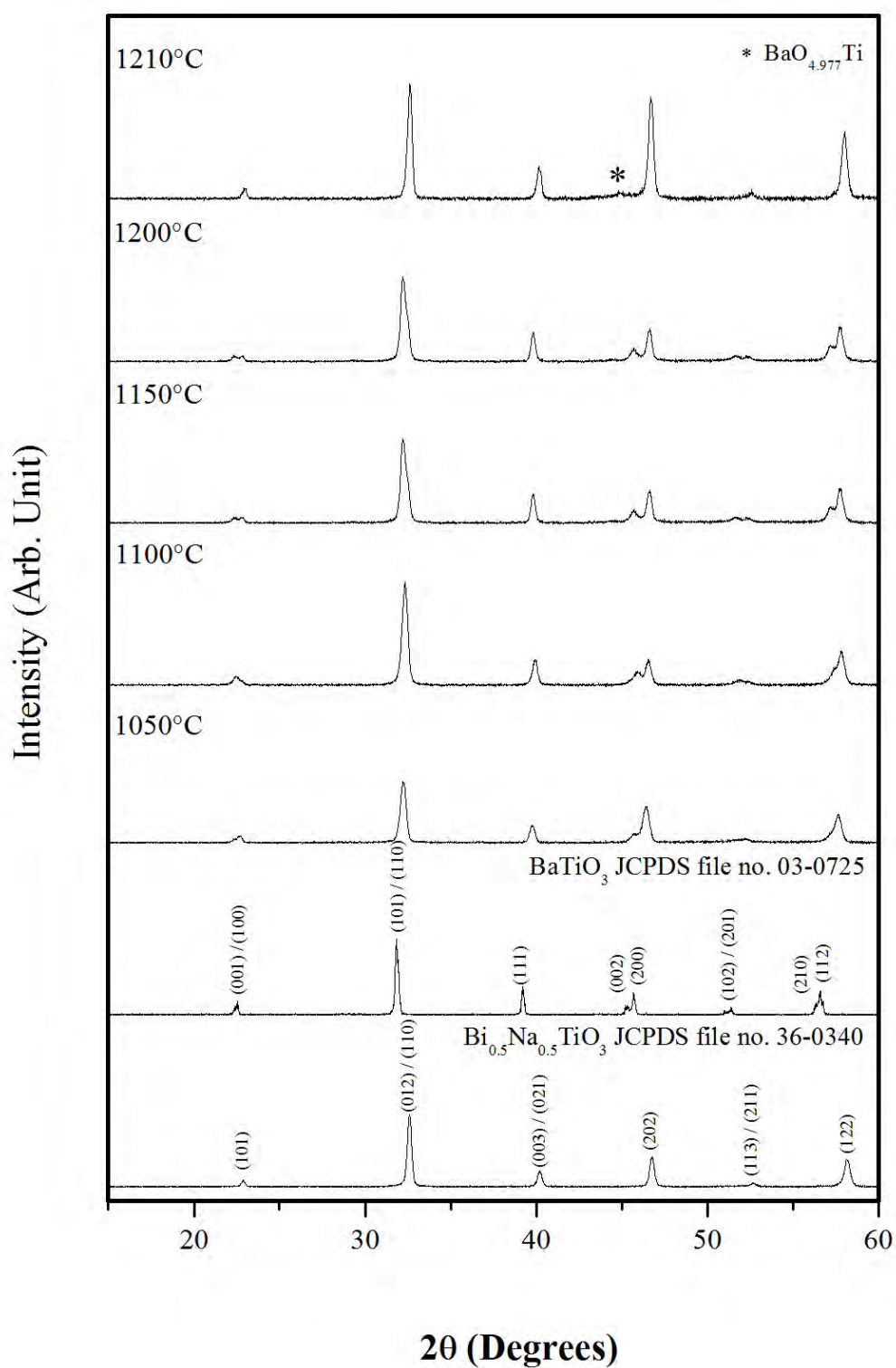




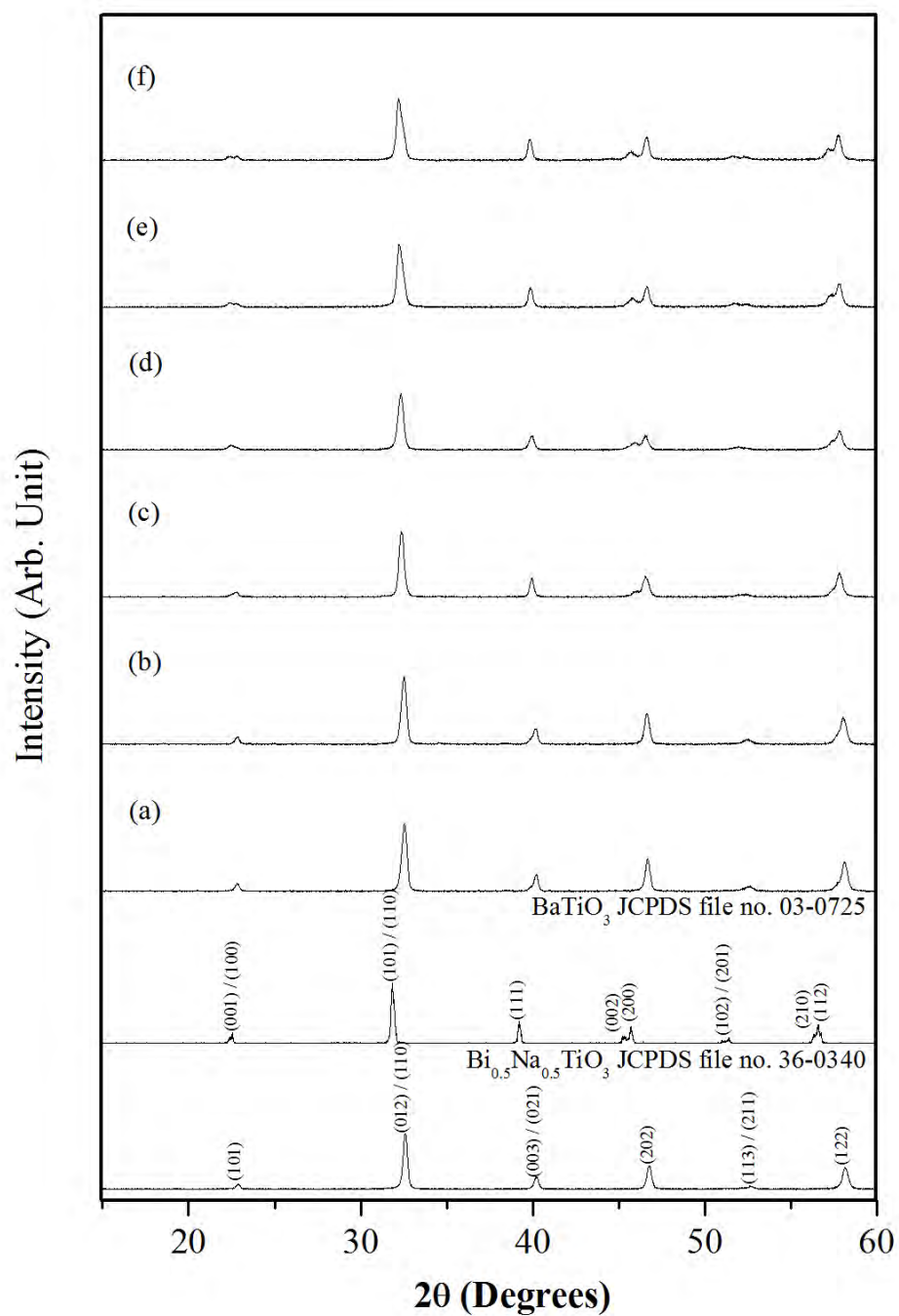
ภาพ 28 รูปแบบการเลี้ยวเบนของรังสีเอกซ์ของเซรามิก BNTBT8 ที่อุณหภูมิซินเตอร์  
ต่างๆ



ภาพ 29 รูปแบบการเลี้ยวเบนของรังสีเอกซ์ของเซรามิก BNTBT10 ที่อุณหภูมิซินเตอร์ต่างๆ



ภาพ 30 รูปแบบการเลี้ยวเบนของรังสีเอกซ์ของเซรามิก BNTBT12 อุณหภูมิที่ขึ้นเตา  
ต่างๆ



ภาพ 31 รูปแบบการเลี้ยวเบนของรังสีเอกซ์ของเซรามิก BNTBT100<sub>x</sub> (a)  $x = 0.02$  ซินเตอร์ที่อุณหภูมิ 1150 องศาเซลเซียส (b)  $x = 0.04$  ซินเตอร์ที่อุณหภูมิ 1150 องศาเซลเซียส (c)  $x = 0.06$  ซินเตอร์ที่อุณหภูมิ 1200 องศาเซลเซียส (d)  $x = 0.08$  ซินเตอร์ที่อุณหภูมิ 1200 องศาเซลเซียส (e)  $x = 0.10$  ซินเตอร์ที่อุณหภูมิ 1200 องศาเซลเซียส และ (f)  $x = 0.12$  ซินเตอร์ที่อุณหภูมิ 1200 องศาเซลเซียส

ตาราง 1 แสดงค่าแลตทิซแสดงความเป็นรอมโบอีตรอล ค่าคงที่แลตทิซและอัตราส่วน  $c/a$  ของเซรามิก BNTBT100x

x	โครงสร้าง	แลตทิซพารามิเตอร์			อัตราส่วน
		$a_R$ (Å)	$a_T$ (Å)	$c_T$ (Å)	
0.02	รอมโบอีตรอล	3.8853	-	-	-
0.04	รอมโบอีตรอล	3.9033	-	-	-
0.06	รอมโบอีตรอล+เทตระโกนอล	3.9054	3.9035	3.9205	1.0043
0.08	รอมโบอีตรอล+เทตระโกนอล	3.9067	3.8950	3.9412	1.0118
0.10	เทตระโกนอล	-	3.8967	3.9577	1.0156
0.12	เทตระโกนอล	-	3.8982	3.9666	1.0175

คำนวณหาค่าแลตทิซแสดงความเป็นรอมโบอีตรอล ( $a_R$ ) จากสมการ

$$a_R = \frac{1}{3} \sqrt{3(a_H)^2 + c_H^2}$$

โดยที่  $a_H$  คือค่าแลตทิซพารามิเตอร์  $a$  ของโครงสร้างเฮกซะโกนอล และ  $c_H$  คือค่าแลตทิซพารามิเตอร์  $c$  ของโครงสร้างเฮกซะโกนอล และคำนวณหาค่าคงที่แลตทิซ  $a$  และ  $c$  ของโครงสร้างเทตระโกนอล ( $a_T$  และ  $c_T$ ) และอัตราส่วน  $c/a$  จากสมการที่ 12 พบว่าที่  $0.02 \leq x \leq 0.08$  ค่าแลตทิซแสดงความเป็นรอมโบอีตรอล  $a_R$  มีค่าเพิ่มขึ้นเมื่อปริมาณ BT เพิ่มขึ้น และที่  $0.06 \leq x \leq 0.12$  ค่าคงที่แลตทิซ  $a_T$ ,  $c_T$  และอัตราส่วน  $c/a$  มีแนวโน้มเพิ่มขึ้น เมื่อปริมาณ BT เพิ่มขึ้น เนื่องจากการแทนที่ของ BT ในโครงสร้างเพอรวอฟสไกต์ของ BNT บริเวณ A – site โดยมีรัศมีไอออนของ  $Ba^{2+}$  (161 pm)  $Na^+$  (139 pm) และ  $Bi^{3+}$  (140 pm) พบว่า  $Ba^{2+}$  มีขนาดรัศมีไอออนใหญ่กว่าขนาดรัศมีไอออนเฉลี่ยของ A – site จึงเป็นสาเหตุให้ค่าแลตทิซพารามิเตอร์ต่างๆมีค่าเพิ่มขึ้นเมื่อปริมาณ BT เพิ่มขึ้น ดังแสดงในตาราง 1 ทั้งนี้ผลที่ได้สอดคล้องกับงานวิจัยของ L.V. Yinong และคณะ [12]

## 1.2 ผลการวิเคราะห์ด้วยกล้องจุลทรรศน์อิเล็กตรอนแบบส่องกราด (Scanning Electron Microscope: SEM)

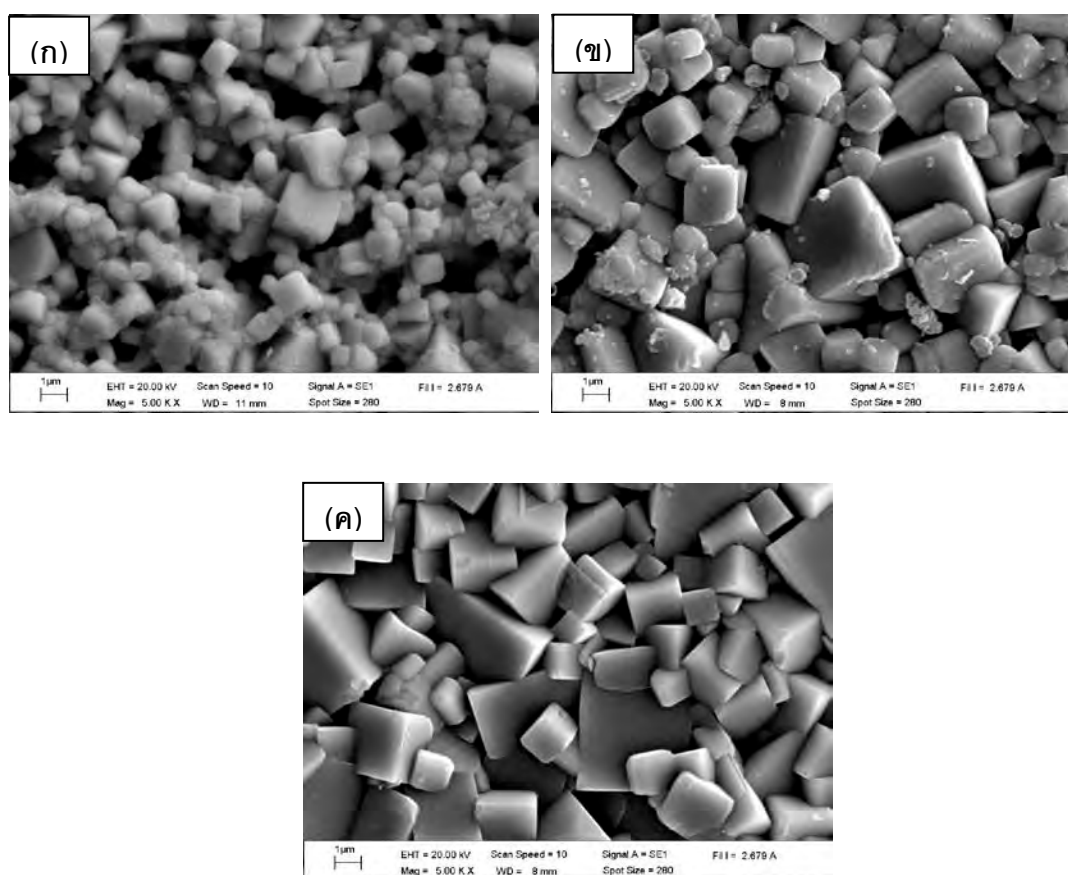
ศึกษาโครงสร้างจุลภาคของเซรามิก BNTBT2, BNTBT4, BNTBT6, BNTBT8, BNTBT10 และ BNTBT12 ที่อุณหภูมิซินเตอร์ต่างๆ โดยถ่ายภาพบริเวณผิวหน้าด้วยกล้องจุลทรรศน์อิเล็กตรอนแบบส่องกราด ดังแสดงในภาพ 32, ภาพ 33, ภาพ 34, ภาพ 35, ภาพ 36 และภาพ 37 ตามลำดับ พบว่าเมื่ออุณหภูมิซินเตอร์เพิ่มขึ้นขนาดเกรนเฉลี่ยมีค่าเพิ่มขึ้น ดังแสดงในตาราง 2 เมื่อสังเกตภาพถ่ายบริเวณผิวหน้าของเซรามิก BNTBT2 และ BNTBT4 พบว่าซินเตอร์ที่อุณหภูมิต่ำ ( $\leq 1100$  องศาเซลเซียส) มีรูพรุนเป็นจำนวนมาก ดังแสดงในภาพ 32 (ก) และ(ข) และเมื่ออุณหภูมิซินเตอร์เพิ่มขึ้นจนถึง 1150 องศาเซลเซียส เกรนมีขนาดใหญ่ขึ้นและมีการเปลี่ยนแปลงรูปร่างของเกรนคล้ายเป็นทรงสี่เหลี่ยมมุมฉาก ดังแสดงในภาพ 32 (ค) สำหรับเซรามิก BNTBT6, BNTBT8, BNTBT10 และ BNTBT12 พบว่าที่อุณหภูมิซินเตอร์ต่ำๆผลที่ได้คล้ายกับเซรามิก BNTBT2 และ BNTBT4 ในขณะที่อุณหภูมิสูงกว่า 1200 พบว่าเกรนเริ่มหลอมละลาย (ภาพ 34, ภาพ 35, ภาพ 36 และภาพ 37) ซึ่งผลที่ได้จาก SEM สอดคล้องกับผลที่ได้จาก XRD ที่อุณหภูมิซินเตอร์เดียวกัน พบว่าเมื่อปริมาณ x เพิ่มขึ้น ขนาดของเกรนเฉลี่ยมีแนวโน้มลดลงจาก  $1.60 - 2.33 \mu\text{m}$  ดังแสดงในตาราง 3

ภาพ 38 แสดงรูปถ่ายรอยหักของเซรามิก BNTBT8 ซินเตอร์ที่อุณหภูมิต่างๆ พบว่า ที่อุณหภูมิต่ำกว่าหรือเท่ากับ 1100 องศาเซลเซียส เป็นรอยหักชนิดหักตามเกรน และพบรูพรุนแบบเปิด ในขณะที่อุณหภูมิซินเตอร์สูงขึ้น เซรามิกจะหักแบบผ่าเกรนแสดงให้เห็นว่ามีความหนาแน่นมาก แต่อย่างไรก็ตามยังพบรูพรุนแบบปิด ด้วยเหตุนี้ทำให้เซรามิกที่ซินเตอร์ที่อุณหภูมิสูงกว่า 1200 องศาเซลเซียสมีความหนาแน่นน้อยลง

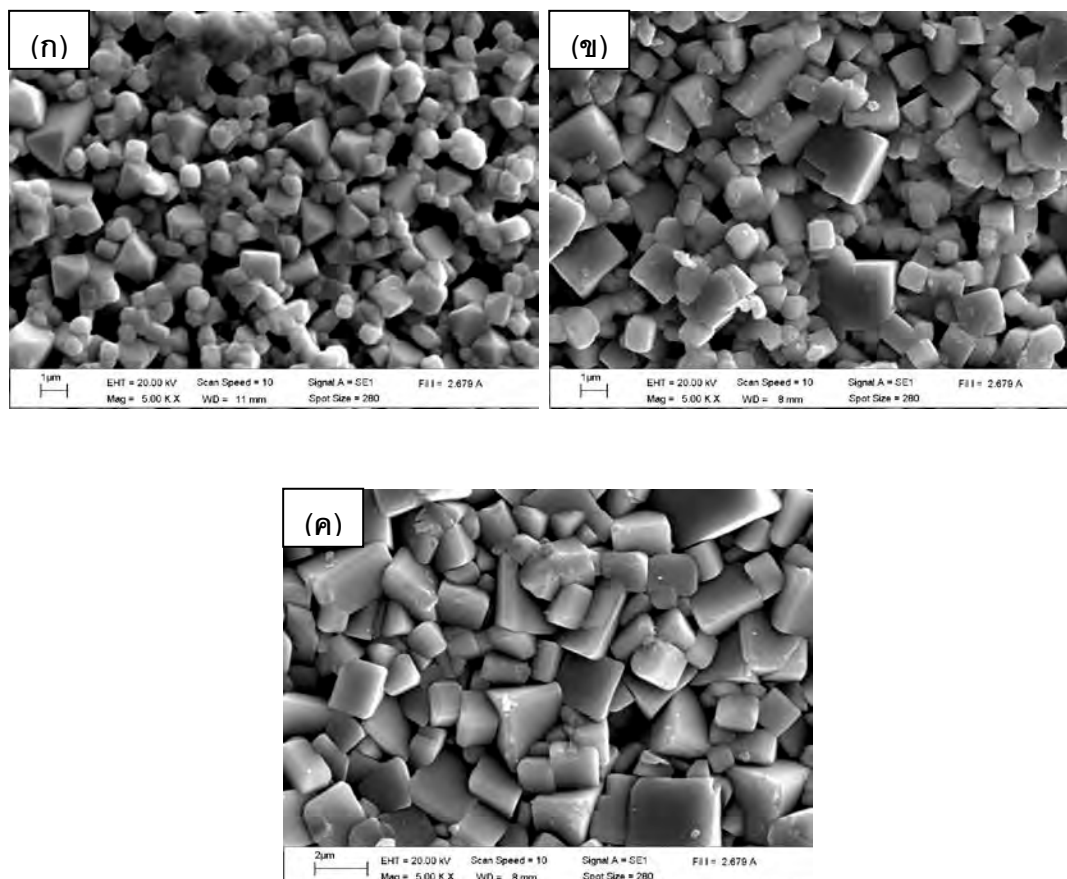
## 1.3 ผลการคำนวณหาค่าความหนาแน่นและการหดตัวเชิงเส้น

ค่าความหนาแน่นและค่าร้อยละการหดตัวของเซรามิก BNTBT2, BNTBT4, BNTBT6, BNTBT8, BNTBT10 และ BNTBT12 ที่อุณหภูมิซินเตอร์ต่างๆ แสดงดังตาราง 2 พบว่าเซรามิก BNTBT2 และ BNTBT4 มีค่าความหนาแน่นและการหดตัวเชิงเส้นของเซรามิกเพิ่มขึ้นเมื่ออุณหภูมิซินเตอร์เพิ่มขึ้นจนถึง 1150 องศาเซลเซียส หลังจากนั้นไม่สามารถหาค่าได้ สำหรับเซรามิก BNTBT6, BNTBT8, BNTBT10 และ BNTBT12 พบว่า ค่าความหนาแน่นเพิ่มขึ้นเมื่ออุณหภูมิซินเตอร์เพิ่มขึ้นจนถึง 1200 องศาเซลเซียส หลังจากนั้นจะลดลงเมื่ออุณหภูมิซินเตอร์เพิ่มขึ้น และการหดตัวเชิงเส้นเพิ่มขึ้นเมื่ออุณหภูมิซินเตอร์เพิ่มขึ้น (แสดงดังตาราง 2)

ค่าความหนาแน่นและการหดตัวเชิงเส้นสูงสุดของเซรามิก BNTBT100x ที่ปริมาณ x ต่างๆ จากตัวอย่างซินเตอร์ที่อุณหภูมิ 1050 - 1200 องศาเซลเซียส พบว่าค่าความหนาแน่นของเซรามิกมีค่ามีค่าใกล้เคียงกันอยู่ระหว่าง 5.70 - 5.78 g/cm<sup>3</sup> สำหรับการหดตัวเชิงเส้นของเซรามิกมีค่าอยู่ระหว่างร้อยละ 14.5 – 16.4 ดังแสดงในตาราง 3 ค่าความหนาแน่นสูงสุดมีค่ามากที่สุดคือ 5.78 g/cm<sup>3</sup> ที่เซรามิก BNTBT8

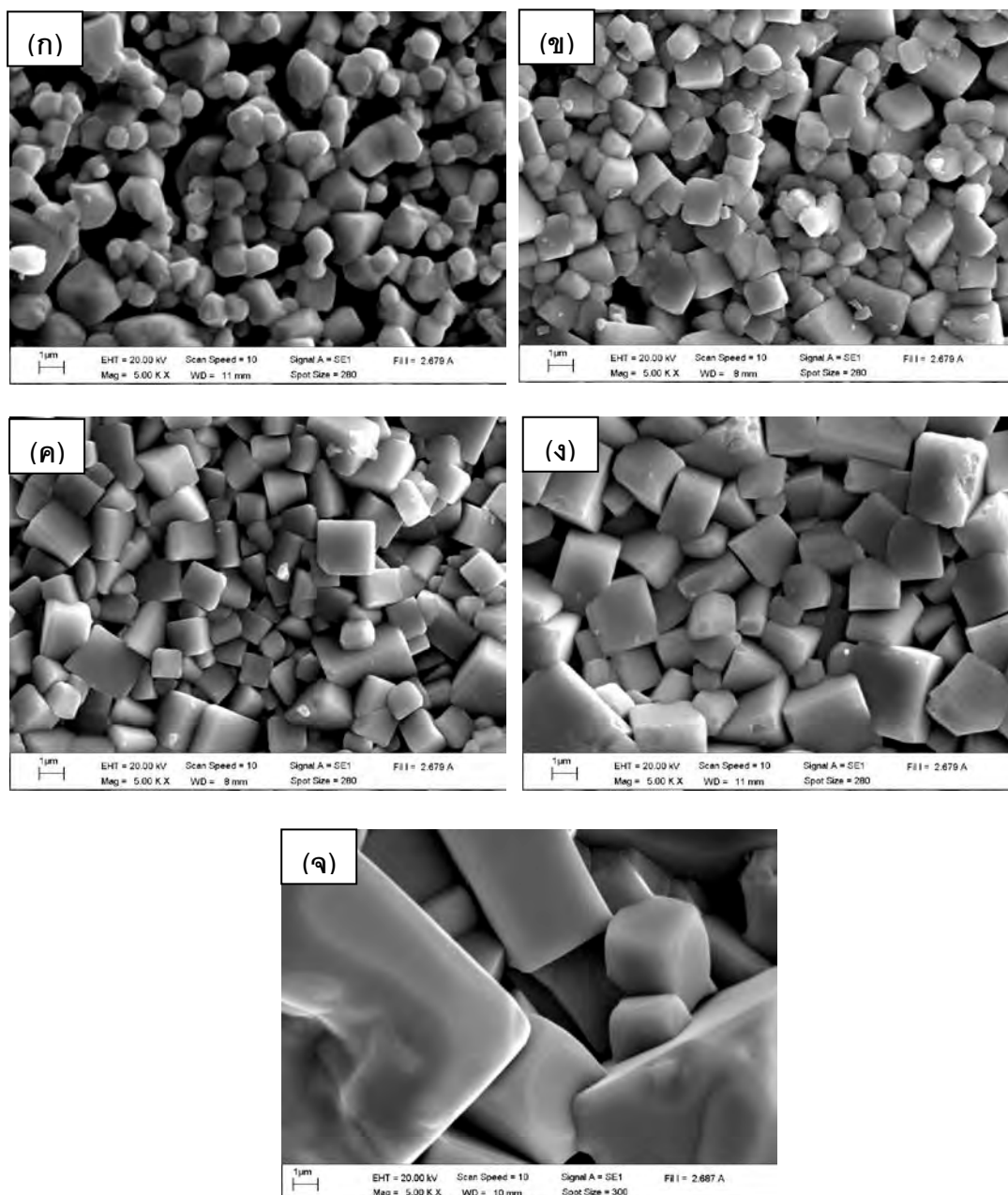


ภาพ 32 ภาพถ่ายบริเวณผิวหน้าของเซรามิก BNTBT2 ที่อุณหภูมิซินเตอร์ต่างๆ (ก) 1050 องศาเซลเซียส (ข) 1100 องศาเซลเซียส และ (ค) 1150 องศาเซลเซียส

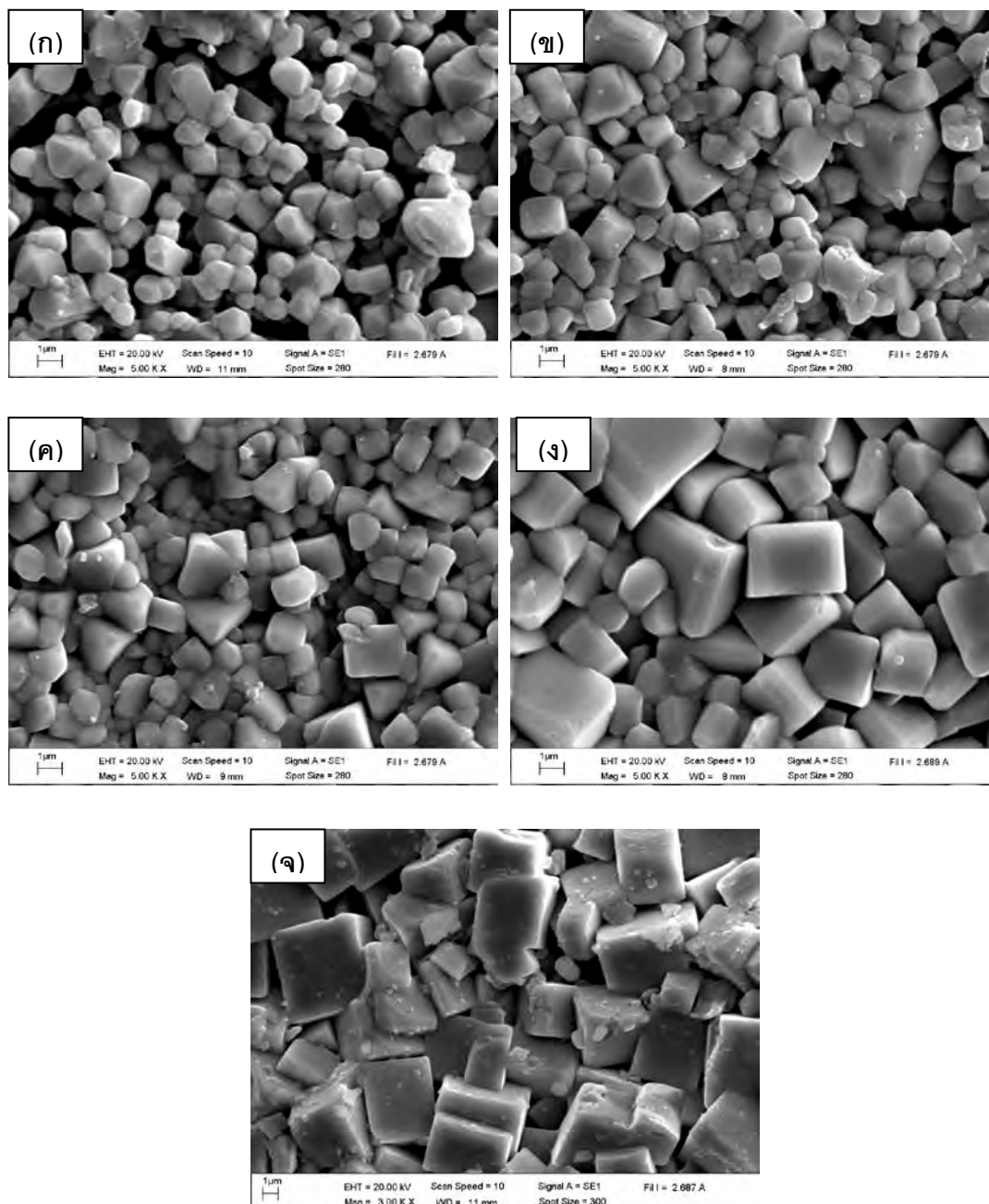


ภาพ 33 ภาพถ่ายบริเวณผิวหน้าของเซรามิก BNTBT4 ที่อุณหภูมิซินเตอร์ต่างๆ (ก) 1050 องศาเซลเซียส (ข) 1100 องศาเซลเซียส และ (ค) 1150 องศาเซลเซียส

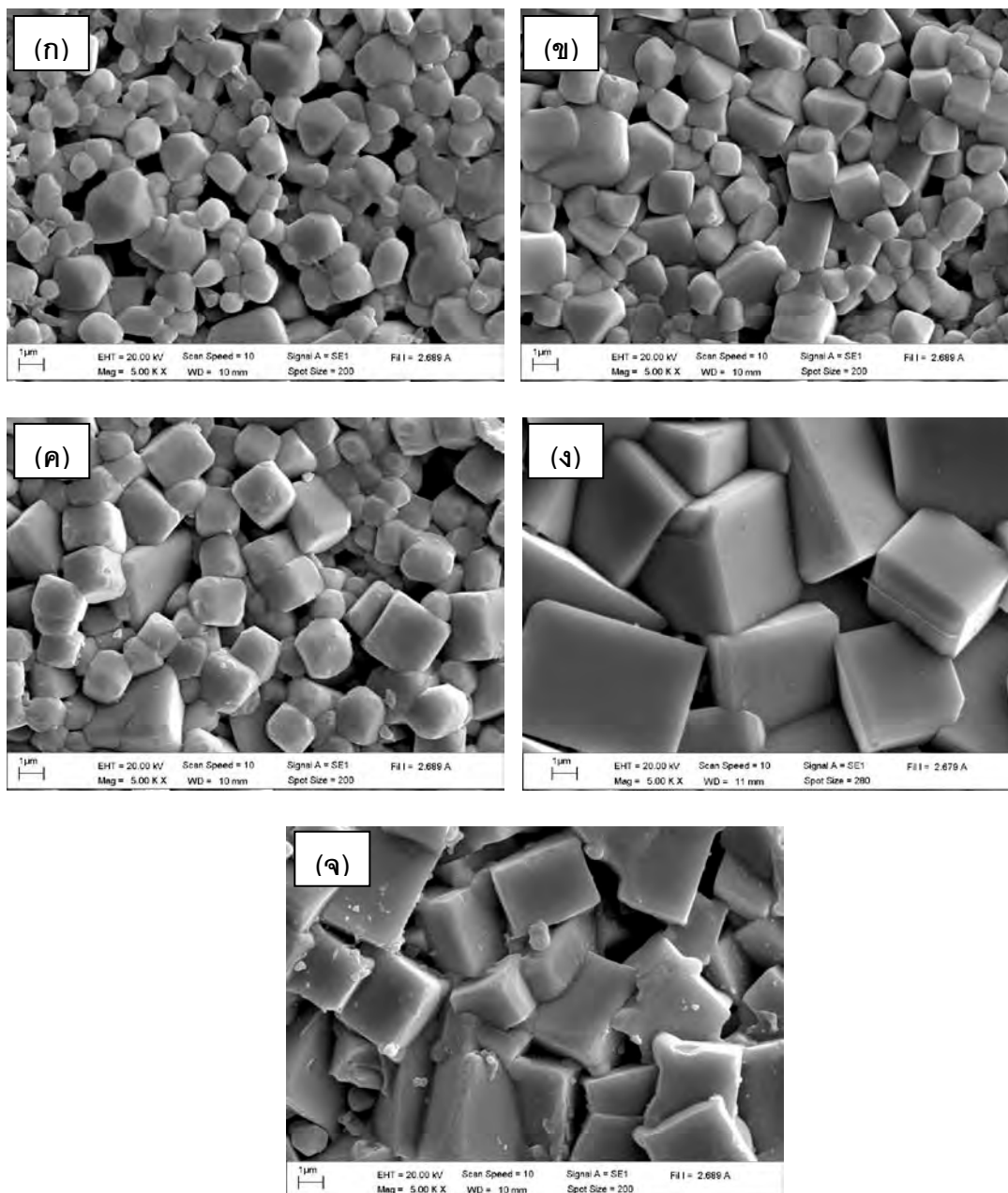




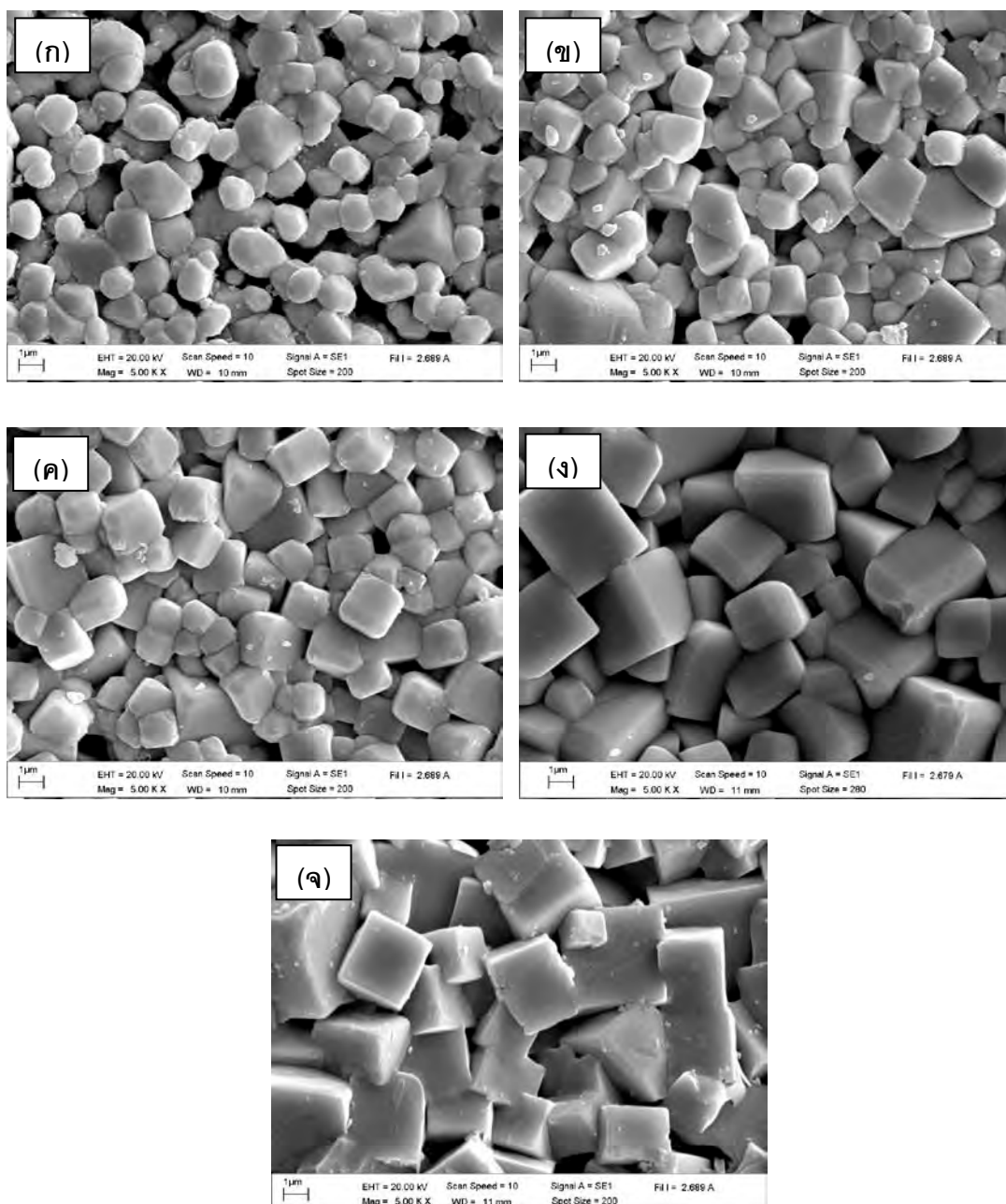
ภาพ 34 ภาพถ่ายบริเวณผิวหน้าของเซรามิก BNTBT6 ที่อุณหภูมิซินเตอร์ต่างๆ (ก) 1050 องศาเซลเซียส (ข) 1100 องศาเซลเซียส (ค) 1150 องศาเซลเซียส (ง) 1200 องศาเซลเซียส และ (จ) 1210 องศาเซลเซียส



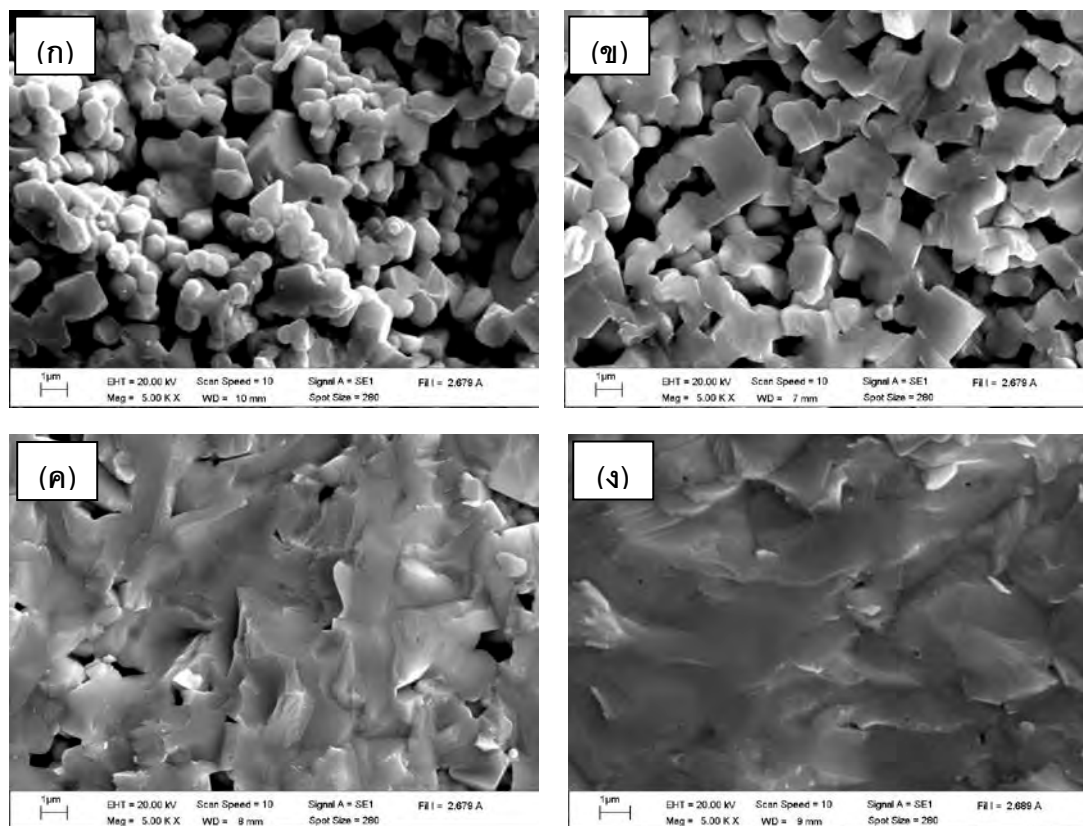
ภาพ 35 ภาพถ่ายบริเวณผิวหน้าของเซรามิก BNTBT8 ที่อุณหภูมิซินเตอร์ต่างๆ (ก) 1050 องศาเซลเซียส (ข) 1100 องศาเซลเซียส (ค) 1150 องศาเซลเซียส (ง) 1200 องศาเซลเซียส และ (จ) 1210 องศาเซลเซียส



ภาพ 36 ภาพถ่ายบริเวณผิวหน้าของเซรามิก BNTBT10 ที่อุณหภูมิซินเตอร์ต่างๆ (ก) 1050 องศาเซลเซียส (ข) 1100 องศาเซลเซียส (ค) 1150 องศาเซลเซียส (ง) 1200 องศาเซลเซียส และ (จ) 1210 องศาเซลเซียส



ภาพ 37 ภาพถ่ายบริเวณผิวหน้าของเซรามิก BNTBT12 ที่อุณหภูมิซินเตอร์ต่างๆ (ก) 1050 องศาเซลเซียส (ข) 1100 องศาเซลเซียส (ค) 1150 องศาเซลเซียส (ง) 1200 องศาเซลเซียส และ (จ) 1210 องศาเซลเซียส



ภาพ 38 ภาพถ่ายบริเวณรอยหักของเซรามิก BNTBT8 ซินเตอร์ที่อุณหภูมิต่างๆ (ก) 1050 องศาเซลเซียส (ข) 1100 องศาเซลเซียส (ค) 1150 องศาเซลเซียส และ (ง) 1200 องศาเซลเซียส

ตาราง 2 แสดงขนาดเกรนเฉลี่ย ความหนาแน่น และการหดตัวเชิงเส้นของเซรามิก BNTBT100x ที่อุณหภูมิซินเตอร์ต่างๆ

เซรามิก	อุณหภูมิซินเตอร์ (°C)	ขนาดเกรนเฉลี่ย ( $\mu\text{m}$ )	ความหนาแน่น ( $\text{g/cm}^3$ )	การหดตัวเชิงเส้น (%)
BNTBT2	1050	1.42	5.47	6.9
	1100	1.73	5.58	12.1
	1150	2.05	5.71	15.8
BNTBT4	1050	1.21	5.49	9.2
	1100	1.57	5.62	13.8
	1150	1.75	5.73	16.4
BNTBT6	1050	1.15	5.59	9.2
	1100	1.51	5.64	10.2
	1150	1.63	5.74	14.8
	1200	2.19	5.79	16.1
	1210	-	5.10	17.1
BNTBT8	1050	1.04	5.62	9.5
	1100	1.41	5.69	12.1
	1150	1.60	5.78	15.1
	1200	2.09	5.80	16.8
	1210	-	-	-
BNTBT10	1050	1.67	5.48	9.2
	1100	2.07	5.62	11.7
	1150	2.33	5.72	14.8
	1200	5.05	5.77	15.4
	1210	-	-	-

ตาราง 2 (ต่อ)

เซรามิก	อุณหภูมิซินเตอร์ (°C)	ขนาดเกรนเฉลี่ย ( $\mu\text{m}$ )	ความหนาแน่น ( $\text{g/cm}^3$ )	การหดตัวเชิงเส้น (%)
BNTBT12	1050	1.66	5.47	9.0
	1100	2.09	5.59	12.2
	1150	2.29	5.70	14.5
	1200	3.99	5.75	16.1
	1210	-	-	-

ตาราง 3 แสดงขนาดเกรนเฉลี่ย ความหนาแน่น และการหดตัวเชิงเส้นของเซรามิก  
BNTBT100x ซินเตอร์ที่อุณหภูมิ 1150 องศาเซลเซียส

เซรามิก	ขนาดเกรนเฉลี่ย ( $\mu\text{m}$ )	ความหนาแน่น ( $\text{g/cm}^3$ )	การหดตัวเชิงเส้น (%)
BNTBT2	2.05	5.71	15.8
BNTBT4	1.75	5.73	16.4
BNTBT6	1.63	5.74	14.8
BNTBT8	1.60	5.78	15.1
BNTBT10	2.33	5.72	14.8
BNTBT12	2.29	5.70	14.5

#### 1.4 ผลที่ได้จากการวัดค่าคงที่ไดอิเล็กทริกและค่าสูญเสียไดอิเล็กทริก

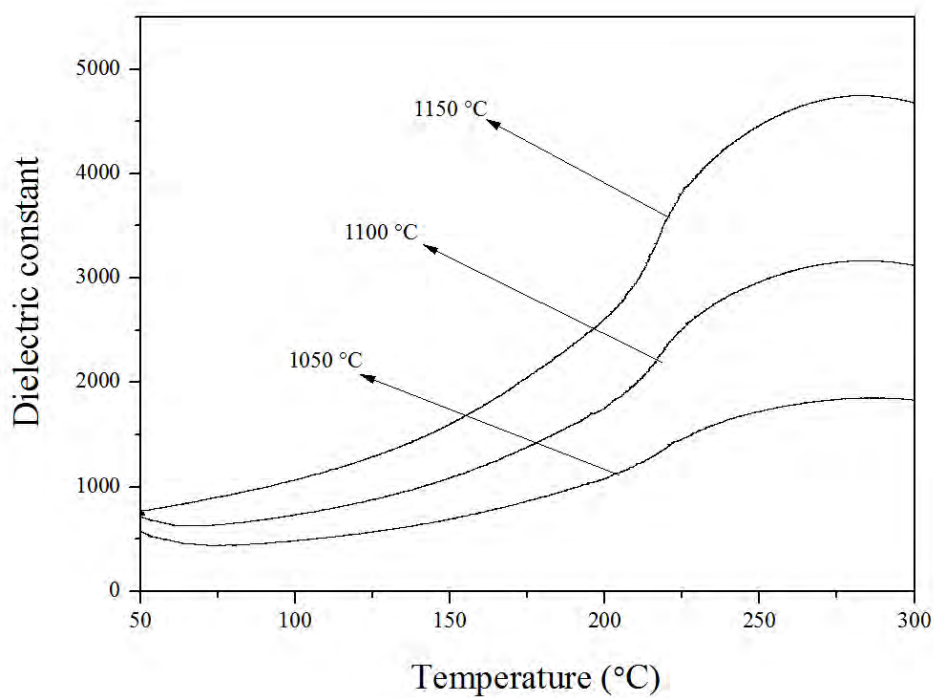
ศึกษาผลจากการวัดค่าคงที่ไดอิเล็กทริกและค่าสูญเสียไดอิเล็กทริกของเซรามิก BNTBT2, BNTBT4, BNTBT6, BNTBT8, BNTBT10 และ BNTBT12 ที่อุณหภูมิซินเตอร์ต่างๆ โดยใช้ความถี่ 1 kHz ดังแสดงในภาพ 39, ภาพ 40, ภาพ 41, ภาพ 42, ภาพ 43 และ ภาพ 44 ตามลำดับ พบว่ามีพีคเกิดขึ้น 2 พีค โดยพีคแรกเกิดขึ้นในช่วงอุณหภูมิ depolarization ( $T_d$ ) ประมาณ 110 - 224 องศาเซลเซียส สามารถหาได้จากอุณหภูมิที่มีค่าการสูญเสียไดอิเล็กทริกพีคแรก ซึ่งสอดคล้องกับการเปลี่ยนเฟสจากเฟอร์โรอิเล็กทริกไปเป็นแอนติเฟอร์โรอิเล็กทริก และพีคที่สองเกิดขึ้นในช่วงอุณหภูมิคูรี ( $T_m$ ) ประมาณ 260 - 288 องศาเซลเซียส สามารถหาได้จากอุณหภูมิที่มีค่าคงที่ไดอิเล็กทริกสูงสุด ซึ่งสอดคล้องกับการเปลี่ยนเฟสจากแอนติเฟอร์โรอิเล็กทริกเป็นพาราอิเล็กทริก การเปลี่ยนเฟสดังกล่าวมีการรายงานโดยงานวิจัยของ T. Takenaka [10] ในกรณีที่  $x = 0.02$  และ  $0.04$   $T_d$  เพิ่มขึ้นในขณะที่  $T_m$  ลดลงเมื่ออุณหภูมิซินเตอร์เพิ่มขึ้น ดังแสดงในตาราง 4 ค่าคงที่ไดอิเล็กทริกและการสูญเสียไดอิเล็กทริกเพิ่มขึ้นเมื่ออุณหภูมิซินเตอร์เพิ่มขึ้นจนถึง 1150 องศาเซลเซียส หลังจากนั้นไม่สามารถวัดค่าได้เนื่องจากเซรามิกระเหิดจนหมดไปที่อุณหภูมิสูง ดังแสดงในภาพ 39, 40 และตาราง 4 สำหรับที่  $x \geq 0.06$   $T_d$  และ  $T_m$  ลดลงเมื่ออุณหภูมิซินเตอร์เพิ่มขึ้น ดังแสดงในตาราง 4 ค่าคงที่ไดอิเล็กทริกและการสูญเสียไดอิเล็กทริกเพิ่มขึ้นเมื่ออุณหภูมิซินเตอร์เพิ่มขึ้นจนถึง 1200 องศาเซลเซียส หลังจากนั้นไม่สามารถวัดค่าได้เนื่องจากเซรามิกเปราะและแตกที่อุณหภูมิสูง ดังแสดงในภาพ 41, 42, 43, 44 และตาราง 4

จากภาพ 45 แสดงค่าคงที่ไดอิเล็กทริกของเซรามิก BNTBT100x ซินเตอร์ที่อุณหภูมิที่มีค่าความหนาแน่นสูงสุด พบว่าค่าคงที่ไดอิเล็กทริกเพิ่มขึ้นเมื่อปริมาณ  $x$  เพิ่มขึ้นถึง 0.08 หลังจากนั้นจะมีค่าลดลงเมื่อปริมาณ  $x$  เพิ่มขึ้น ที่  $x \leq 0.06$   $T_d$  มีค่าลดลงหลังจากนั้นจะมีค่าเพิ่มขึ้นเมื่อปริมาณ  $x$  เพิ่มขึ้น ในขณะที่  $T_m$  มีแนวโน้มลดลงเมื่อปริมาณ  $x$  เพิ่มขึ้น ดังแสดงในรูป 46 ในกรณีที่  $T_d$  ของเซรามิก BNTBT6 มีค่าต่ำสุด อาจะเกิดจากเมื่อเข้าใกล้บริเวณ MPB มีการบิดเบี้ยวของ oxygen octahedron [35]

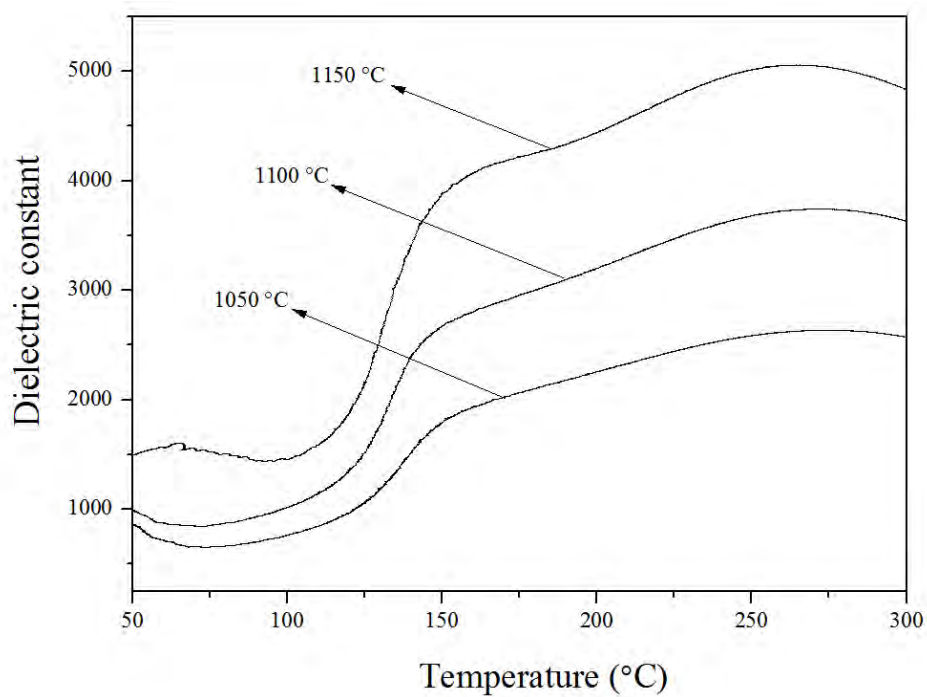
จากภาพ 46 แสดงความสัมพันธ์ของ  $T_d$  และ  $T_m$  ของเซรามิก BNTBT100X ที่ปริมาณ  $x$  ต่างๆ ซินเตอร์ที่อุณหภูมิ 1150 องศาเซลเซียส พบว่าในกรณีที่  $x = 0.02, 0.10$  และ  $0.12$  มีค่า  $T_d$  และ  $T_m$  เข้าใกล้กันมาก ส่งผลให้เส้นกราฟไดอิเล็กทริกของเซรามิกเหล่านี้มองเห็นเป็นพีคเดียวอาจจะเกิดจากการรวมกันของพีค  $T_d$  และ  $T_m$  ที่อยู่ใกล้กันมากๆ (ภาพ 45) สำหรับที่  $x = 0.04, 0.06$  และ  $0.08$  มีค่า  $T_d$  และ  $T_m$  ห่างกันมาก ส่งผลให้เส้นกราฟไดอิเล็กทริกของเซรามิกเหล่านี้มองเห็นเป็นพีคสองพีค อาจจะเกิดพีค  $T_d$  และ  $T_m$  ที่อยู่ใกล้กันมากๆ ทำให้มองเห็นพีคทั้ง



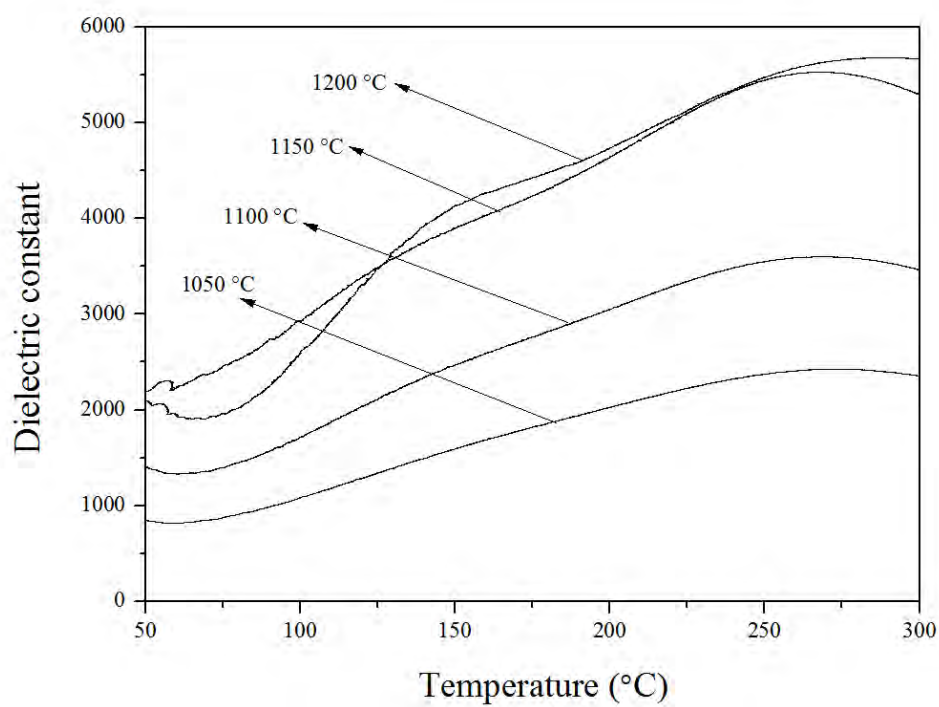
สองแยกออกจากกันอย่างชัดเจน (ภาพ 45) ซึ่งผลที่ได้สอดคล้องกับงานวิจัยของ C. Xu และคณะ [35]



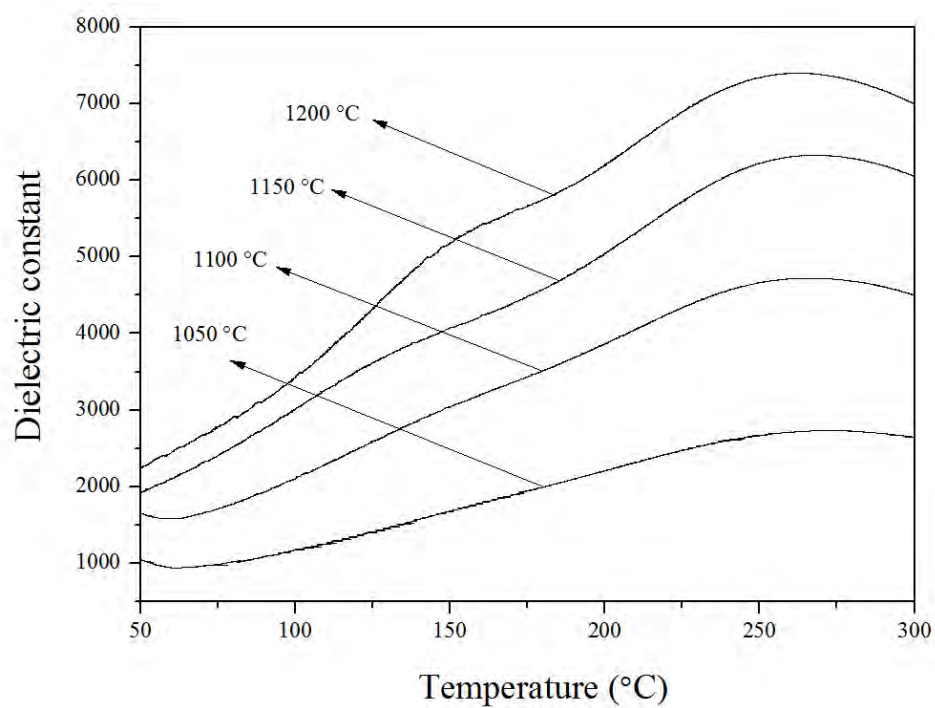
ภาพ 39 ค่าคงที่ได้ไอเล็กทริกของเซรามิก BNTBT2 ซินเตอร์ที่อุณหภูมิต่างๆ



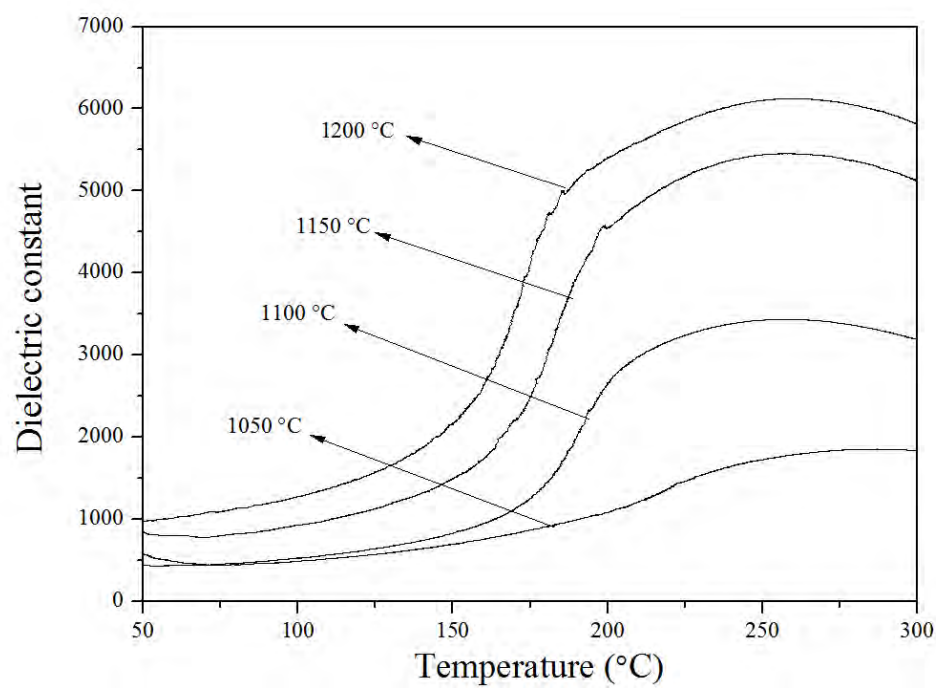
ภาพ 40 ค่าคงที่ได้ไอเล็กทริกของเซรามิก BNTBT4 ซินเตอร์ที่อุณหภูมิต่างๆ



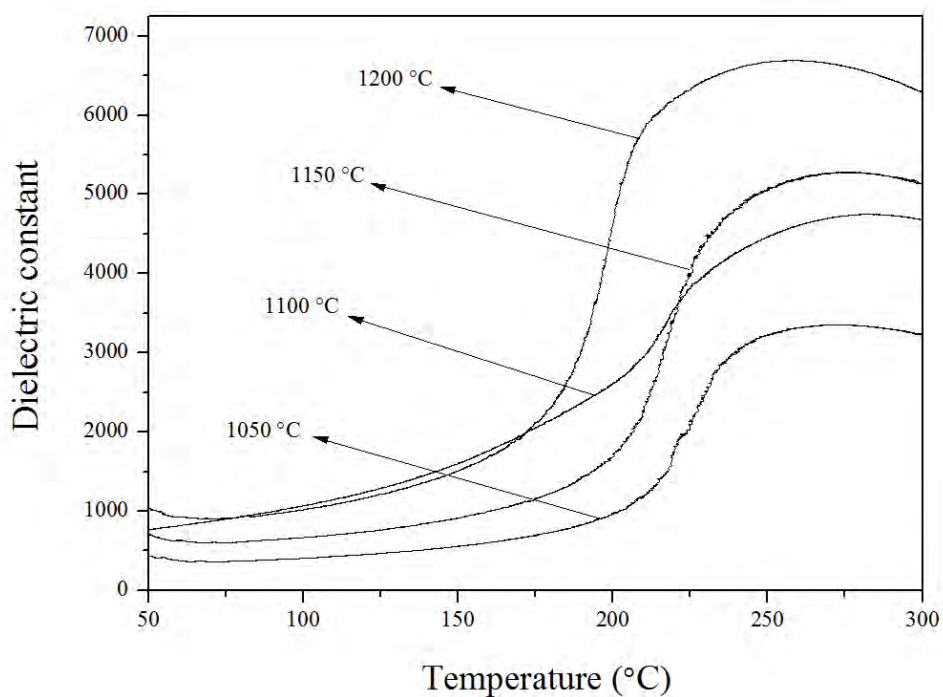
ภาพ 41 ค่าคงที่ได้ไอเล็กทริกของเซรามิก BNTBT6 ซินเตอร์ที่อุณหภูมิต่างๆ



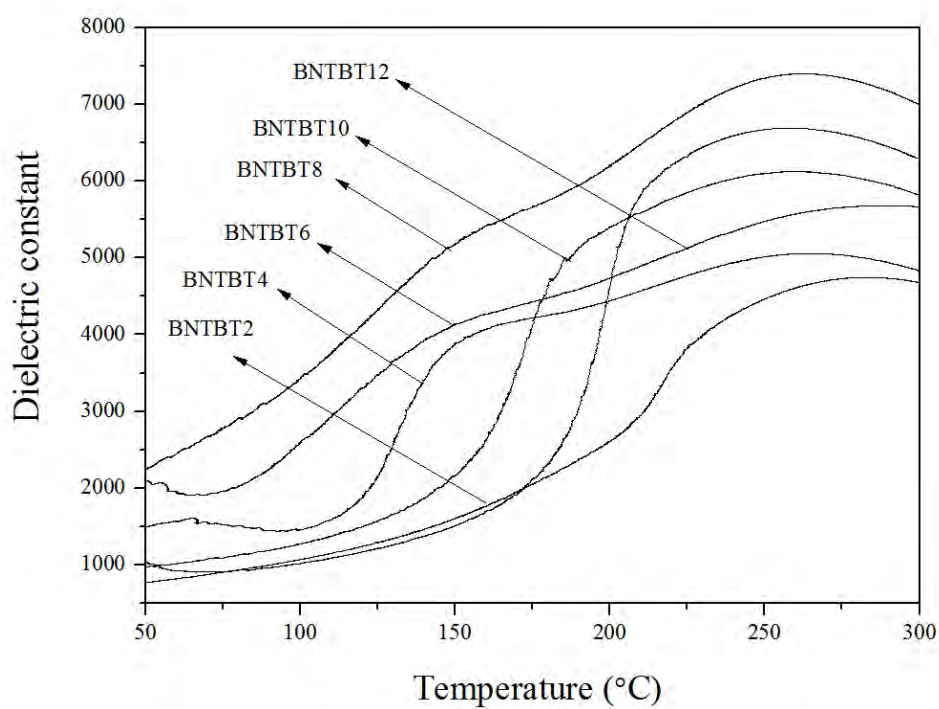
ภาพ 42 ค่าคงที่ได้อิเล็กทรอนิกส์ของเซรามิก BNTBT8 ซินเตอร์ที่อุณหภูมิต่างๆ



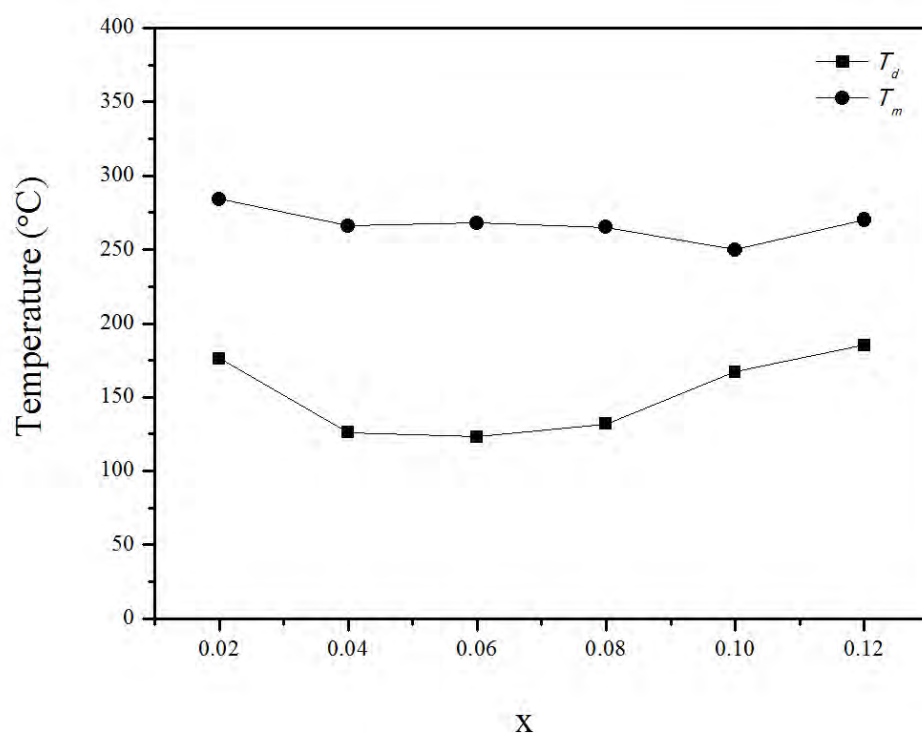
ภาพ 43 ค่าคงที่ได้อิเล็กทรอนิกส์ของเซรามิก BNTBT10 ซินเตอร์ที่อุณหภูมิต่างๆ



ภาพ 44 ค่าคงที่ไดอิเล็กทริกของเซรามิก BNTBT12 ซินเตอร์ที่อุณหภูมิต่างๆ



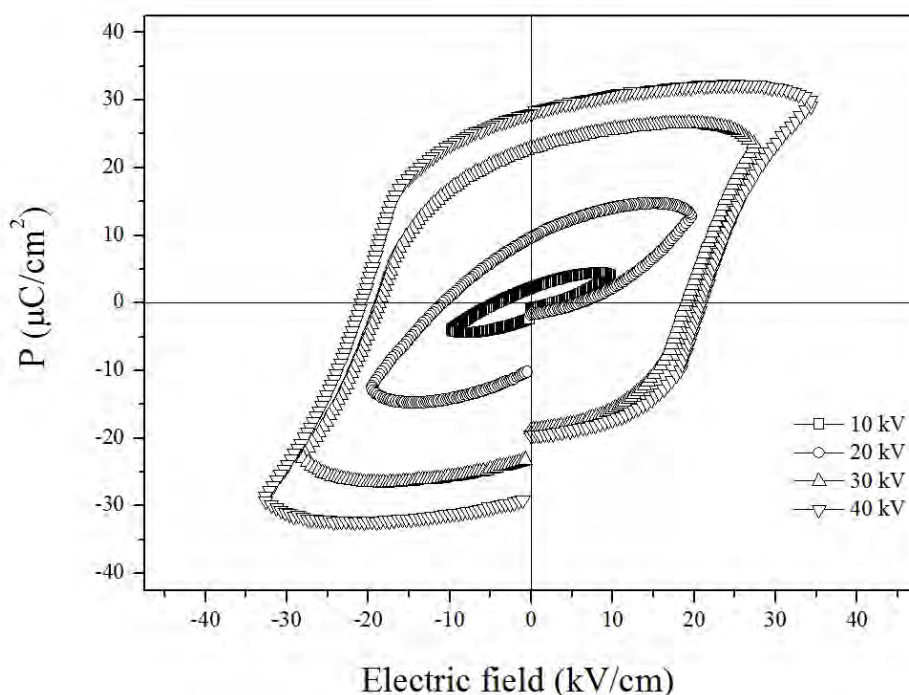
ภาพ 45 ค่าคงที่ไดอิเล็กทริกของเซรามิก BNTBT100x ซินเตอร์ที่อุณหภูมิ 1150 – 1200 องศาเซลเซียส



ภาพ 46  $T_d$  และ  $T_m$  ของเซรามิก BNTBT100x ซินเตอร์ที่อุณหภูมิ 1150 องศาเซลเซียส

ตาราง 4 แสดงอุณหภูมิ depolarization ( $T_d$ ) อุณหภูมิคูรี ( $T_m$ ) ค่าคงที่ไดอิเล็กทริก ( $\epsilon_r$ ) ที่  $T_m$  ค่าสูญเสียไดอิเล็กทริก ( $\tan \delta$ ) ที่  $T_m$  ของเซรามิก BNTBT100x ที่อุณหภูมิซินเตอร์ต่างๆ

เซรามิก	อุณหภูมิซินเตอร์ (°C)	$T_d$ (°C)	$T_m$ (°C)	$\epsilon_r$ ที่ $T_m$	$\tan \delta$ ที่ $T_m$
BNTBT2	1050	162	287	1853	0.0292
	1100	168	286	3165	0.0607
	1150	176	284	4747	0.0758
BNTBT4	1050	125	275	2637	0.0255
	1100	125	271	3743	0.0215
	1150	126	266	5574	0.0298
BNTBT6	1050	145	272	2427	0.0451
	1100	131	270	3600	0.0252
	1150	123	268	5530	0.0334
	1200	110	288	5682	0.1762
BNTBT8	1050	151	270	2730	0.3464
	1100	145	268	4721	0.0157
	1150	132	265	6327	0.0120
	1200	130	263	7400	0.0372
BNTBT10	1050	192	282	1855	0.0291
	1100	184	225	3249	0.0389
	1150	167	250	5440	0.0329
	1200	103	260	6125	0.0453
BNTBT12	1050	224	275	3350	0.0376
	1100	220	282	4747	0.0753
	1150	185	270	5272	0.0504
	1200	130	260	6692	0.0423



ภาพ 47 วงรอบฮิสเทอรีซิสของเซรามิก BNTBT8 ที่ค่าสนามไฟฟ้าต่างๆ

### 1.5 ผลการวัดค่าโพลาริเซชัน ( $P_r$ ) และค่าคงที่เพียโซอิเล็กทริก ( $d_{33}$ )

การศึกษาสมบัติเพียโซอิเล็กทริกของเซรามิก BNTBT8 ที่มีความหนาแน่นสูงสุด โดยการวัดวงรอบฮิสเทอรีซิส (hysteresis loop) ที่สนามไฟฟ้าต่างๆ แสดงดังภาพ 47 พบว่าโพลาริเซชันอิ่มตัว ( $P_s$ ) โพลาริเซชันคงค้าง ( $P_r$ ) และค่าสนามไฟฟ้าลบกลับ ( $E_c$ ) ของเซรามิกมีแนวโน้มเพิ่มขึ้นเมื่อสนามไฟฟ้าที่ให้แก่เซรามิกมีค่าเพิ่มขึ้น แสดงดังตาราง 5 โดยมีค่าสูงสุดเท่ากับ  $29.94 \mu\text{C}/\text{cm}^2$ ,  $28.10 \mu\text{C}/\text{cm}^2$  และ  $21.02 \text{ kV}/\text{cm}$  ตามลำดับ เมื่อใช้สนามไฟฟ้า  $40 \text{ kV}/\text{cm}$  จากงานวิจัยก่อนหน้านี้ การเจือสาร BT ในเซรามิก BNT ช่วยทำให้ค่าโพลาริเซชันคงค้างสูงขึ้น และสนามไฟฟ้าลบกลับต่ำกว่าเซรามิก BNT [12, 13]

การศึกษาสมบัติเพียโซอิเล็กทริกของเซรามิก BNTBT8 ที่มีความหนาแน่นสูงสุด โดยการวัดค่าคงที่เพียโซอิเล็กทริก  $d_{33}$  ทำการโพลลิง (polling) ภายใต้สนามไฟฟ้า  $35 \text{ kV}/\text{cm}$  ใน silicone oil ที่อุณหภูมิ  $80^\circ\text{C}$  เป็นเวลา 15 นาที เท่ากับ  $169 \text{ pC}/\text{N}$  แสดงดังตาราง 5 นอกจากนี้แล้วค่าเพียโซอิเล็กทริกของเซรามิก BNTBT8 ที่ได้จากงานวิจัยนี้ มีค่าสูงกว่าค่าที่ได้จากงานวิจัยที่เคยศึกษามาก่อน [37]

ตาราง 5 แสดงค่าคงที่พิโซอิเล็กทริก ( $d_{33}$ ) โพลาริเซชันอิมิตัว ( $P_s$ ) โพลาริเซชันคงค้าง ( $P_r$ ) และสนามไฟฟ้าลบ้าง ( $E_c$ ) ของเซรามิก BNTBT8

เซรามิก	$d_{33}$	สนามไฟฟ้า	โพลาริเซชัน อิมิตัว	โพลาริเซชัน คงค้าง	สนามไฟฟ้า ลบ้าง
	(pC/N)	(KV/cm)	( $\mu\text{C}/\text{cm}^2$ )	( $\mu\text{C}/\text{cm}^2$ )	(KV/cm)
BNTBT8	169	10	4.01	2.21	2.89
		20	12.65	9.62	6.10
		30	23.57	22.82	19.05
		40	29.94	28.10	21.02



## 2. ผลการตรวจสอบลักษณะเฉพาะของเซรามิกบิสมาทโซเดียมไททาเนต-แคลเซียมไททาเนต (1-x)BNT-xCT; BNTCT100x

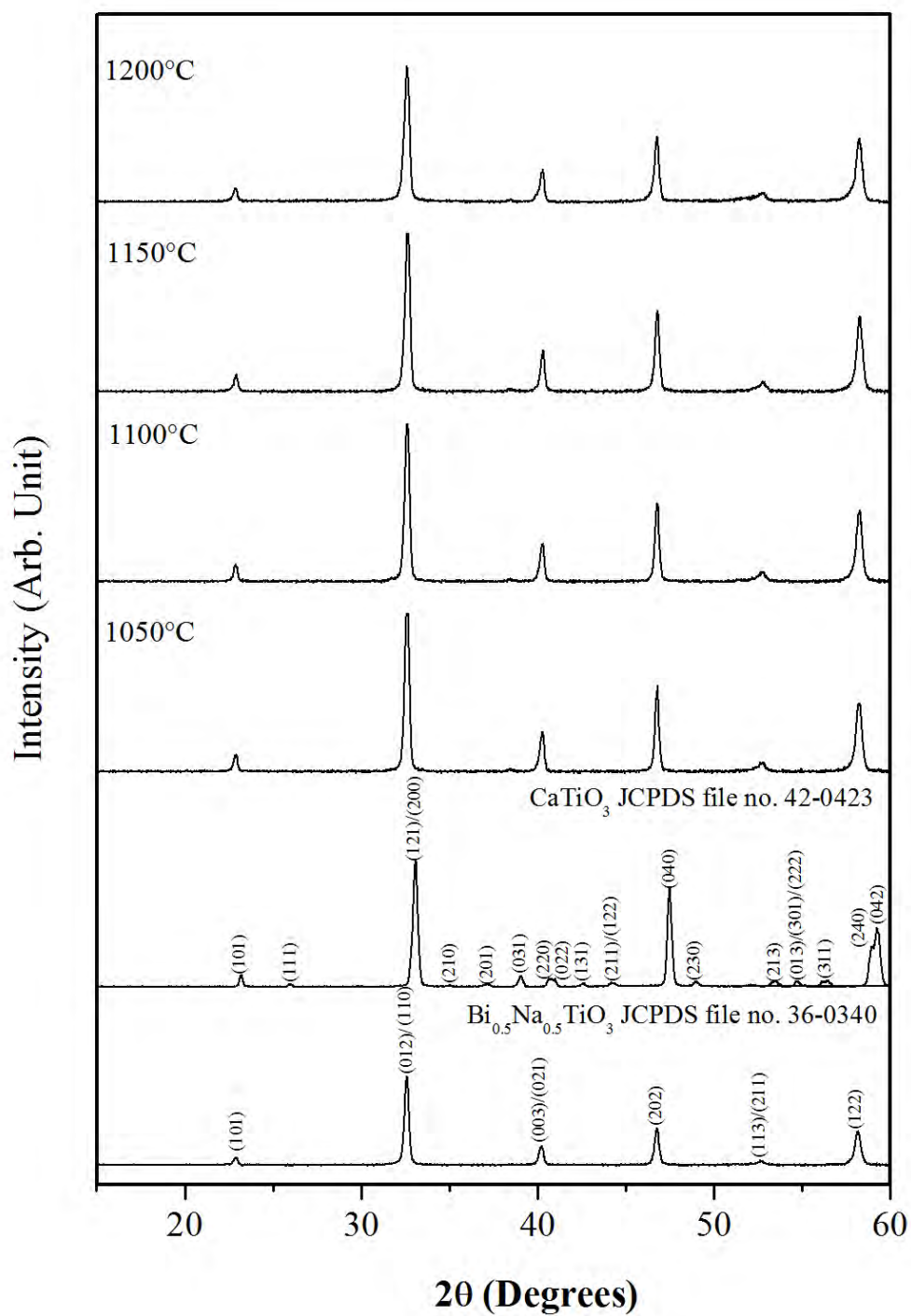
### 2.1 ผลการวิเคราะห์โครงสร้างผลึกด้วยเทคนิคการเลี้ยวเบนของรังสีเอกซ์ (X-ray diffractometer: XRD)

นำผงผลึก BNT และ CT มาผสมกันตามสัดส่วนโดยโมลโดยใช้อัตราส่วน  $x = 0.02, 0.04, 0.06$  และ  $0.08$  (BNTCT2, BNTCT4, BNTCT6 และ BNTCT8) เพื่อนำมาอัดเม็ดและเผาซินเตอร์ที่อุณหภูมิระหว่าง 1050-1200 องศาเซลเซียส โดยทั่วไปเซรามิก BNT มีโครงสร้างรอมโบอีตรอลซึ่งตรงกับแฟ้มข้อมูลของ JCPDS หมายเลข 36-0340 [8, 35] ในขณะที่เซรามิก CT มีโครงสร้างแบบอโรธอมบิคซึ่งตรงกับแฟ้มข้อมูลของ JCPDS หมายเลข 42-0423 [6] จากการศึกษารูปภาพโครงสร้างผลึกของเซรามิก BNTCT2, BNTCT4, BNTCT6 และ BNTCT8 ด้วยรูปแบบการเลี้ยวเบนของรังสีเอกซ์ โดยเผาซินเตอร์ที่อุณหภูมิระหว่าง 1050-1200 องศาเซลเซียส ดังแสดงในภาพ 48, ภาพ 49, ภาพ 50 และภาพ 51 ตามลำดับ พบว่าเซรามิกมีโครงสร้างแบบรอมโบอีตรอลซึ่งเหมือนกับ BNT โดยสังเกตจากพีคคู่ของ (003)/(021) เกิดขึ้น ที่มุมระหว่าง 38-42 องศา และมีพีคเดี่ยวของ (202) เกิดขึ้นที่มุมระหว่าง 45-48 องศา และสอดคล้องกับงานวิจัยที่ศึกษามาก่อน [14, 15] และเมื่ออุณหภูมิเพิ่มขึ้นเซรามิกมีความเป็นรอมโบอีตรอลมากขึ้น

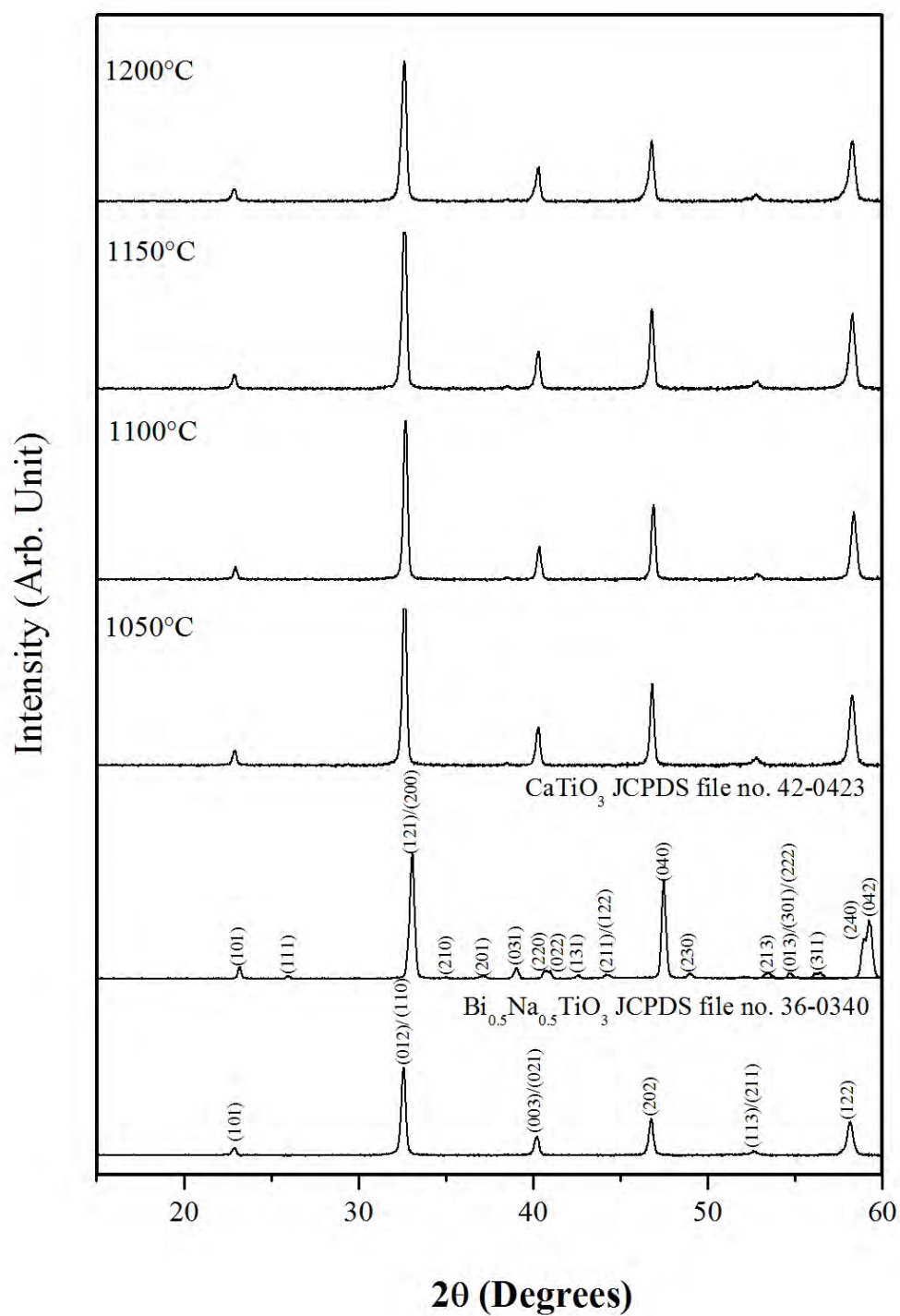
คำนวณหาค่าแลตทิซแสดงความเป็นรอมโบอีตรอล ( $a_R$ ) จากสมการ

$$a_R = \frac{1}{3} \sqrt{3(a_H)^2 + c_H^2}$$

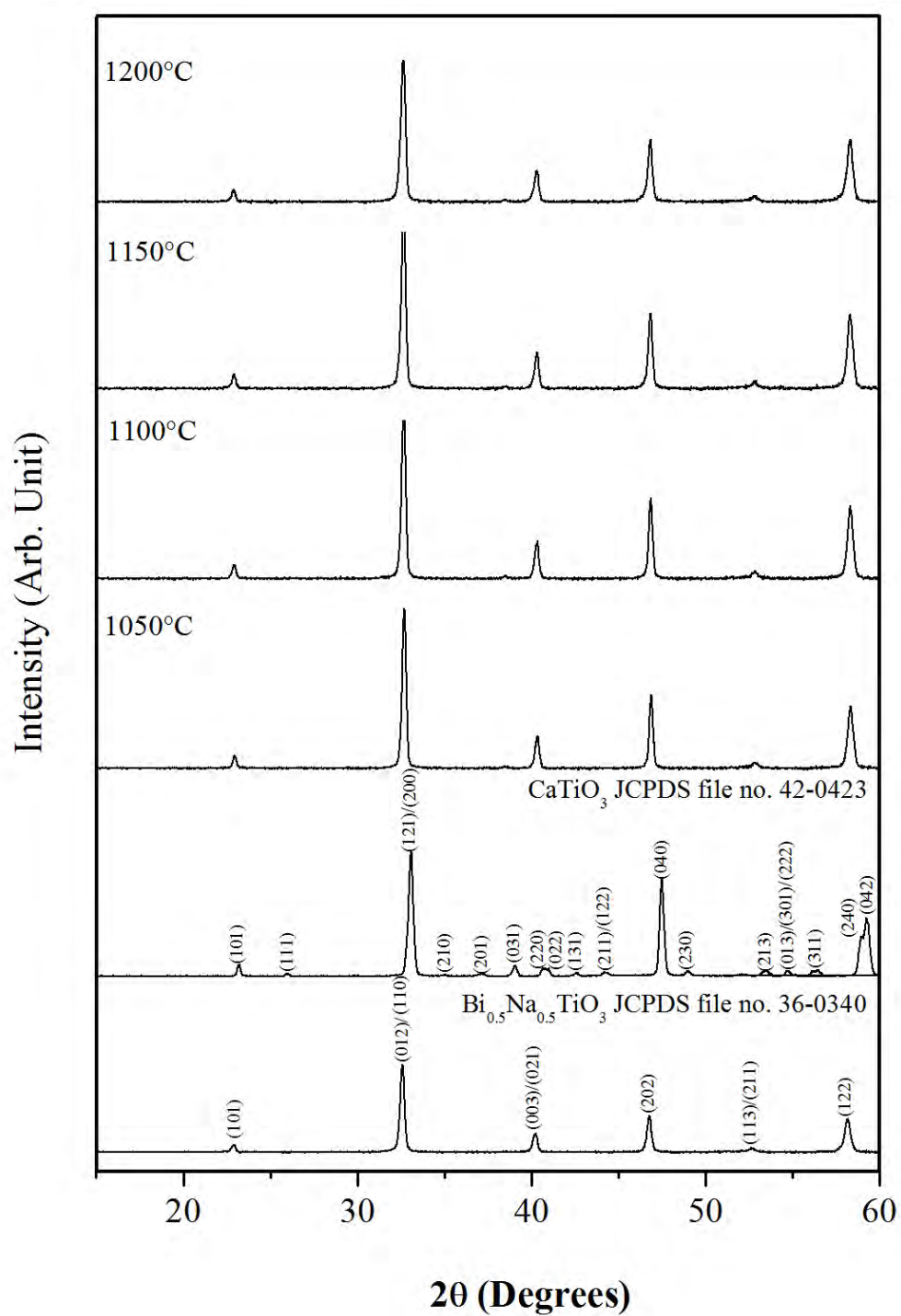
โดยที่  $a_H$  คือค่าแลตทิซพารามิเตอร์  $a$  ของโครงสร้างเฮกซะโกนอล และ  $c_H$  คือค่าแลตทิซพารามิเตอร์  $c$  ของโครงสร้างเฮกซะโกนอล พบว่าค่าแลตทิซแสดงความเป็นรอมโบอีตรอล  $a_R$  มีค่าอยู่ระหว่าง 3.8664 – 3.8860 Å เมื่อซินเตอร์ที่อุณหภูมิระหว่าง 1050 – 1200 องศาเซลเซียส และแลตทิซแสดงความเป็นรอมโบอีตรอล  $a_R$  มีค่าเพิ่มขึ้นเมื่อปริมาณ CT เพิ่มขึ้น เนื่องจากการแทนที่ของ CT ในโครงสร้างเพอร์อฟสไกต์ของ BNT บริเวณ A – site โดยมีรัศมีไอออนของ  $\text{Ca}^{2+}$  (134 pm)  $\text{Na}^+$  (139 pm) และ  $\text{Bi}^{3+}$  (140 pm) พบว่า  $\text{Ca}^{2+}$  มีขนาดรัศมีไอออนเล็กกว่าขนาดรัศมีไอออนเฉลี่ยของ A – site จึงเป็นสาเหตุให้ค่าแลตทิซพารามิเตอร์มีค่าลดลงเมื่อปริมาณ CT เพิ่มขึ้น และผลที่ได้สอดคล้องกับงานวิจัยของ L.V. Yinong และคณะ [12] ดังแสดงในตาราง 6



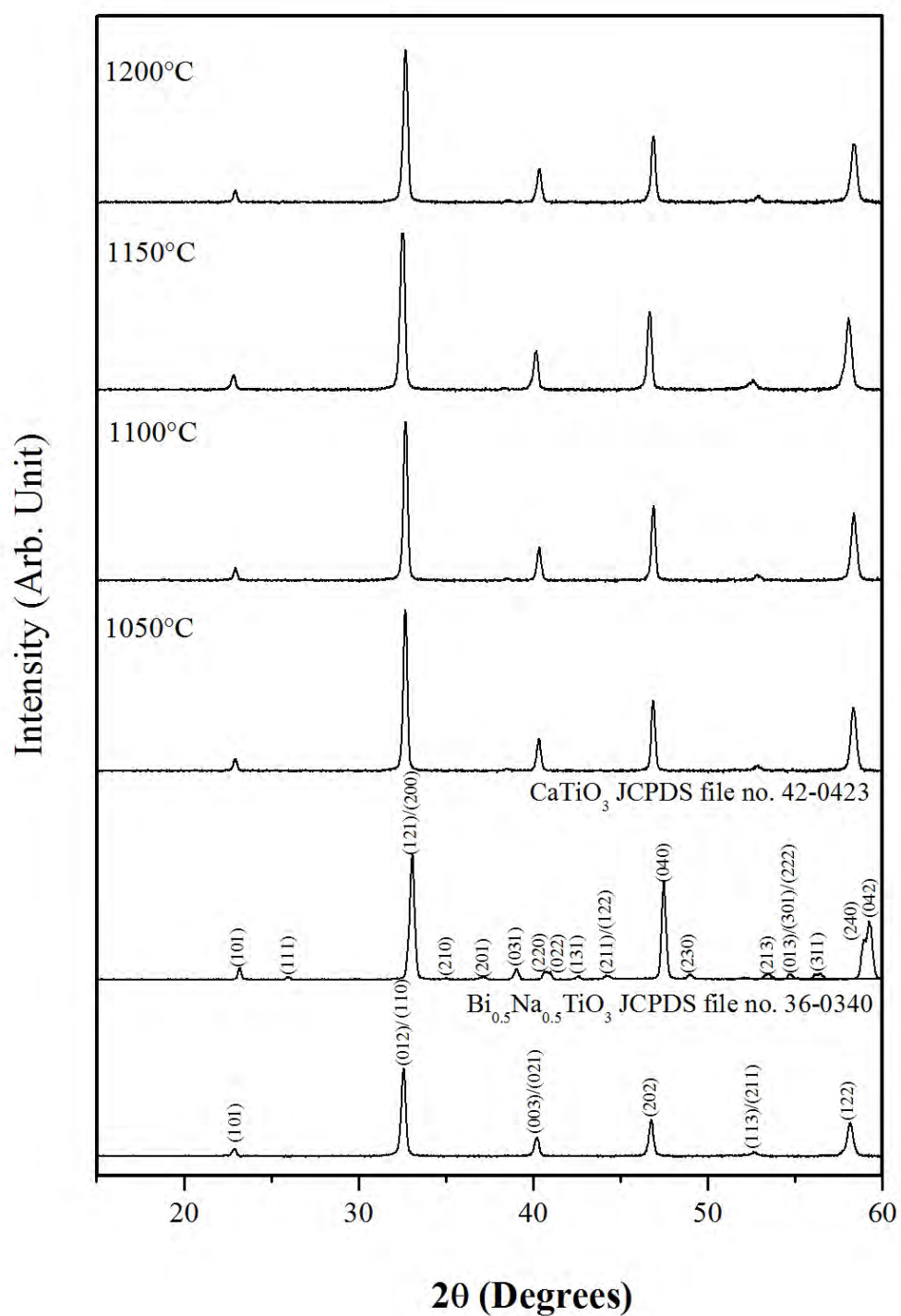
ภาพ 48 รูปแบบการเลี้ยวเบนของรังสีเอกซ์ของเซรามิก BNTCT2 ที่อุณหภูมิซินเตอร์  
ต่างๆ



ภาพ 49 รูปแบบการเลี้ยวเบนของรังสีเอกซ์ของเซรามิก BNTCT4 ที่อุณหภูมิซินเตอร์  
ต่างๆ



ภาพ 50 รูปแบบการเลี้ยวเบนของรังสีเอกซ์ของเซรามิก BNTCT6 ที่อุณหภูมิซินเตอร์  
ต่างๆ



ภาพ 51 รูปแบบการเลี้ยวเบนของรังสีเอกซ์ของเซรามิก BNTCT8 ที่อุณหภูมิซินเตอร์  
ต่างๆ

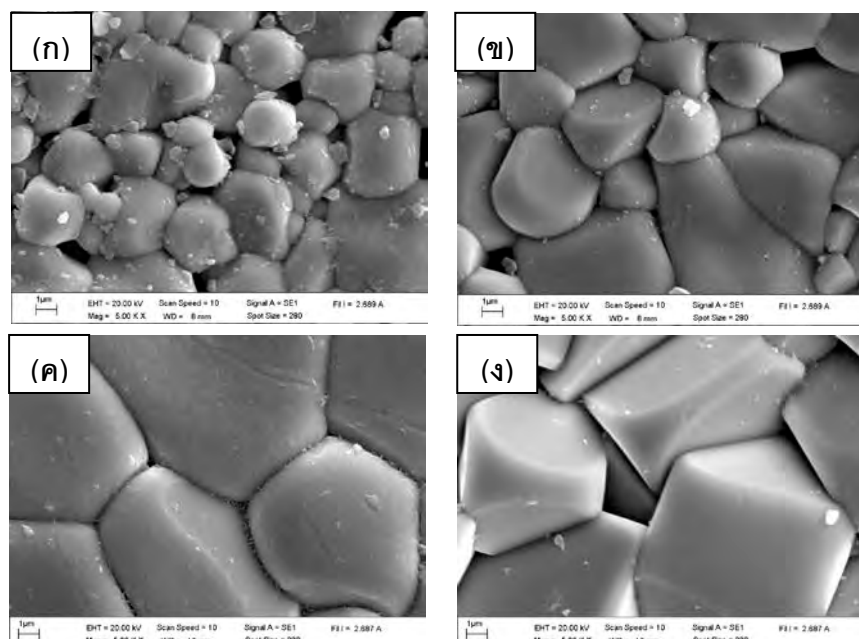
## 2.2 ผลการวิเคราะห์ด้วยกล้องจุลทรรศน์อิเล็กตรอนแบบส่องกราด (Scanning Electron Microscope: SEM)

ศึกษาโครงสร้างจุลภาคของเซรามิก BNTCT2, BNTCT4, BNTCT6 และ BNTCT8 ซินเตอร์ที่อุณหภูมิต่างๆ โดยถ่ายภาพบริเวณผิวหน้าด้วยกล้องจุลทรรศน์อิเล็กตรอนแบบส่องกราด ดังแสดงในภาพ 52, ภาพ 53, ภาพ 54 และ ภาพ 55 พบว่ารูปร่างเกรนส่วนใหญ่ของเซรามิกมีลักษณะคล้ายเป็นทรงกลมและสีเหลี่ยมมุมฉาก จากภาพ 52 พบว่าเซรามิก BNTCT2 ซินเตอร์ที่อุณหภูมิต่ำกว่า 1100 องศาเซลเซียส เซรามิกมีรูพรุนมาก (ภาพ 52 (ก) และ (ข)) หลังจากนั้นพบว่ารูพรุนลดลงและเกรนมีขนาดเพิ่มขึ้นเมื่ออุณหภูมิซินเตอร์เพิ่มขึ้น ดังแสดงในภาพ 52 (ค) และ (ง) สำหรับเซรามิก BNTCT 4, BNTCT6 และ BNTCT8 ขนาดเกรนเฉลี่ยมีแนวโน้มเพิ่มขึ้นเมื่ออุณหภูมิซินเตอร์เพิ่มขึ้น ดังแสดงในตาราง 6 นอกจากนั้นพบว่าเมื่อปริมาณ x เพิ่มขึ้น ขนาดเกรนเฉลี่ยมีค่าอยู่ระหว่าง 2.43 – 8.28 ไมโครเมตร (ตาราง 6)

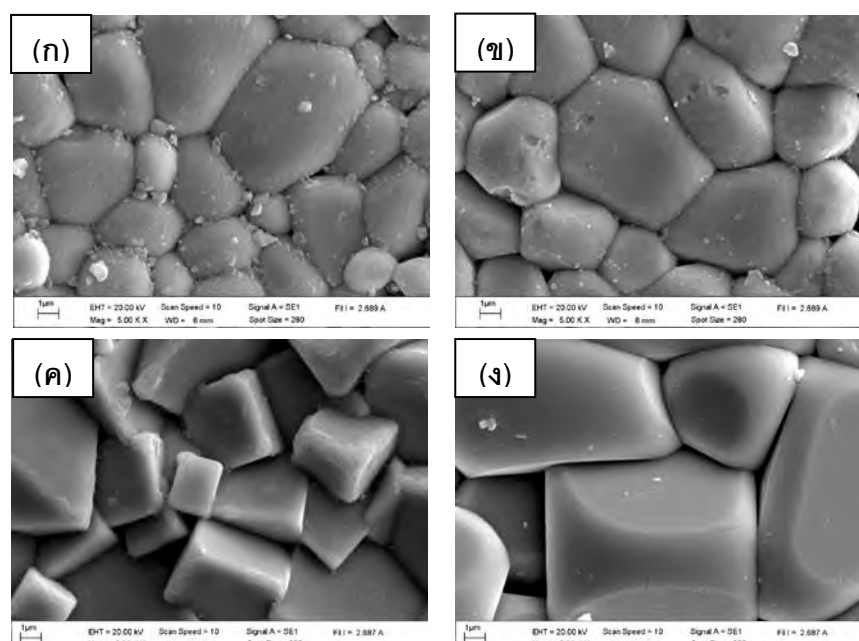
ภาพ 56 แสดงรูปถ่ายรอยหักของเซรามิก BNTCT2 ซินเตอร์ที่อุณหภูมิต่างๆ พบว่า ที่อุณหภูมิน้อยกว่าหรือเท่ากับ 1100 องศาเซลเซียส เป็นรอยหักชนิดหักตามเกรน และพบรูพรุนแบบเปิด ในขณะที่อุณหภูมิซินเตอร์สูงขึ้น เซรามิกจะหักแบบผ่าเกรนแสดงให้เห็นว่ามีความหนาแน่นมาก แต่อย่างไรก็ตามยังพบรูพรุนแบบปิด ด้วยเหตุนี้ทำให้เซรามิกที่ซินเตอร์ที่อุณหภูมิ 1200 องศาเซลเซียสมีความหนาแน่นน้อยลง

## 2.3 ผลการคำนวณหาค่าความหนาแน่นและการหดตัวเชิงเส้น

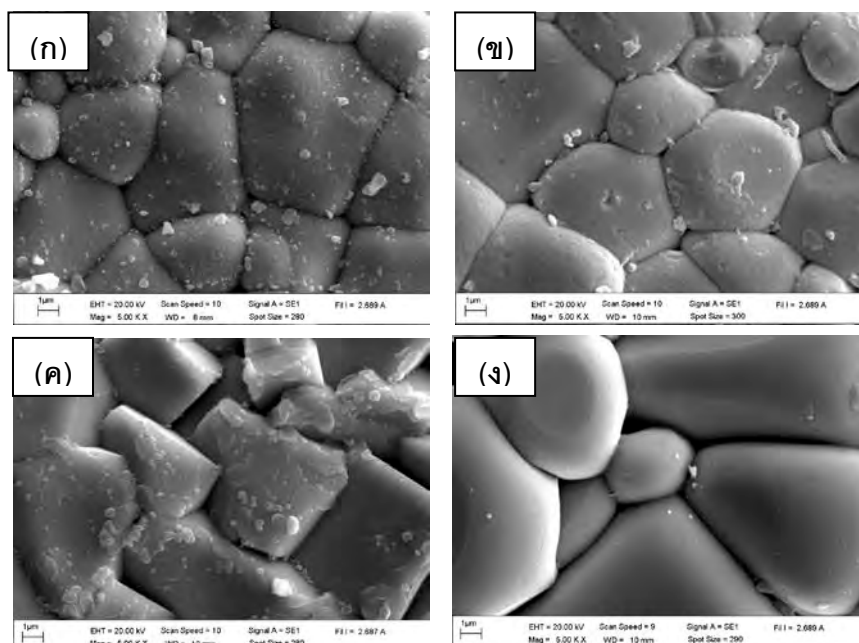
ค่าความหนาแน่นและค่าร้อยละการหดตัวของเซรามิก BNTCT2, BNTCT4, BNTCT6 และ BNTCT8 ที่อุณหภูมิซินเตอร์ต่างๆ ดังแสดงในตาราง 6 พบว่าเซรามิกมีค่าความหนาแน่นเพิ่มขึ้นเมื่ออุณหภูมิซินเตอร์เพิ่มขึ้นจนถึง 1150 องศาเซลเซียส หลังจากนั้นความหนาแน่นมีค่าลดลงเมื่ออุณหภูมิซินเตอร์เพิ่มขึ้น และการหดตัวเชิงเส้นของเซรามิกเพิ่มขึ้นเมื่ออุณหภูมิซินเตอร์เพิ่มขึ้น (ตาราง 5) เมื่อปริมาณ x เพิ่มขึ้น ค่าความหนาแน่นมีค่าลดลง ในขณะที่ค่าการหดตัวเชิงเส้น มีค่าอยู่ระหว่าง 12.5 – 14.4 % ดังแสดงในตาราง 6



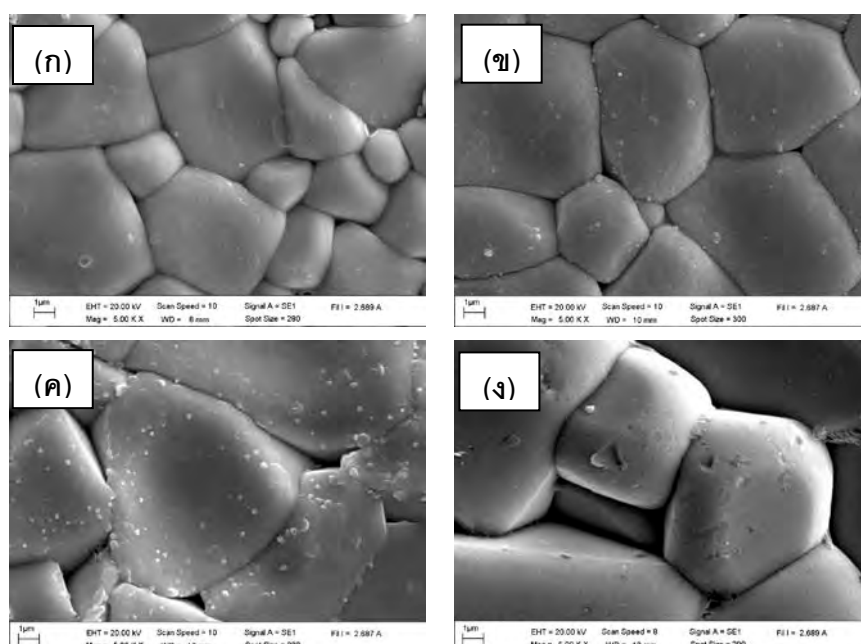
ภาพ 52 ภาพถ่ายบริเวณผิวหน้าของเซรามิก BNTCT2 ที่อุณหภูมิซินเตอร์ต่างๆ (ก) 1050 องศาเซลเซียส (ข) 1100 องศาเซลเซียส (ค) 1150 องศาเซลเซียส และ (ง) 1200 องศาเซลเซียส



ภาพ 53 ภาพถ่ายบริเวณผิวหน้าของเซรามิก BNTCT4 ที่อุณหภูมิซินเตอร์ต่างๆ (ก) 1050 องศาเซลเซียส (ข) 1100 องศาเซลเซียส (ค) 1150 องศาเซลเซียส และ (ง) 1200 องศาเซลเซียส

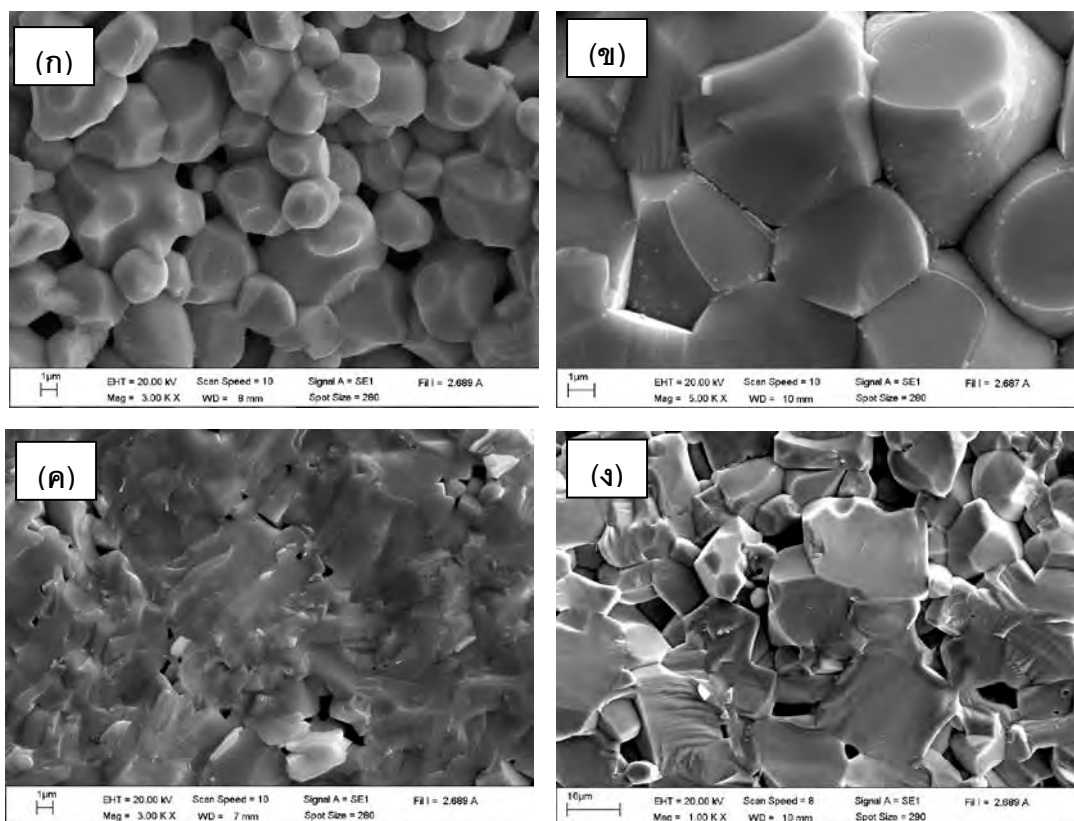


ภาพ 54 ภาพถ่ายบริเวณผิวหน้าของเซรามิก BNTCT6 ที่อุณหภูมิซินเตอร์ต่างๆ (ก) 1050 องศาเซลเซียส (ข) 1100 องศาเซลเซียส (ค) 1150 องศาเซลเซียส และ (ง) 1200 องศาเซลเซียส



ภาพ 55 ภาพถ่ายบริเวณผิวหน้าของเซรามิก BNTCT8 ที่อุณหภูมิซินเตอร์ต่างๆ (ก) 1050 องศาเซลเซียส (ข) 1100 องศาเซลเซียส (ค) 1150 องศาเซลเซียส และ (ง) 1200 องศาเซลเซียส





ภาพ 56 ภาพถ่ายบริเวณรอยหักของเซรามิก BNTCT2 ที่อุณหภูมิซินเตอร์ต่างๆ (ก) 1050 องศาเซลเซียส (ข) 1100 องศาเซลเซียส (ค) 1150 องศาเซลเซียส และ (ง) 1200 องศาเซลเซียส

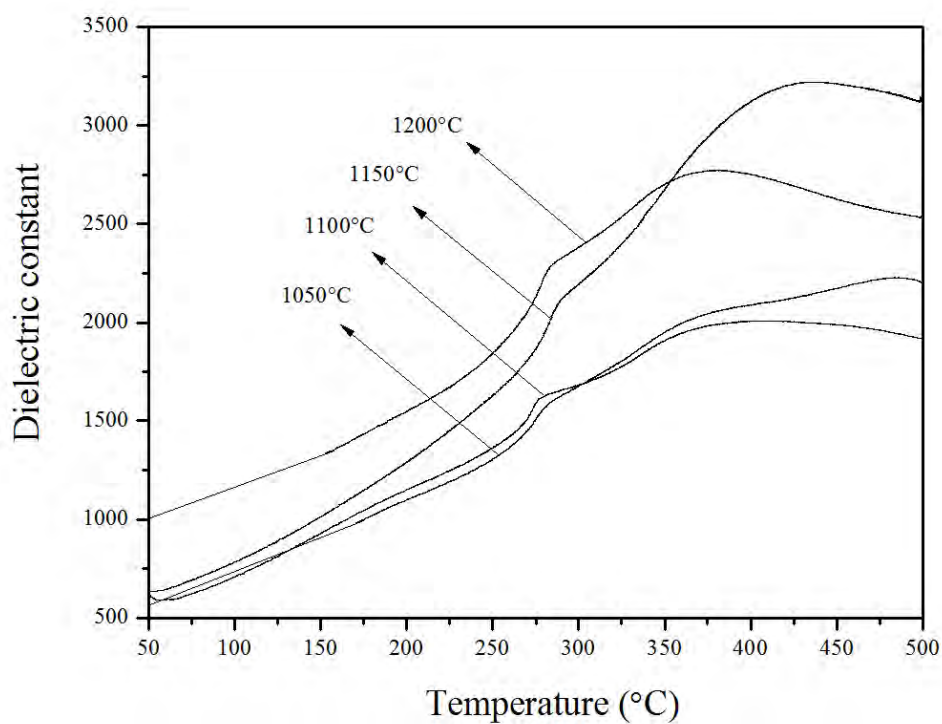
ตาราง 6 แสดงขนาดเกรนเฉลี่ย ความหนาแน่น การหดตัวเชิงเส้น และ แลตทิซพารามิเตอร์  $a_R$  ของเซรามิก BNTCT100x ที่อุณหภูมิซินเตอร์ต่างๆ

เซรามิก	อุณหภูมิซินเตอร์ (°C)	ขนาดเกรนเฉลี่ย ( $\mu\text{m}$ )	ความหนาแน่น ( $\text{g/cm}^3$ )	การหดตัวเชิงเส้น (%)	แลตทิซพารามิเตอร์ $a_R$ (Å)
BNTCT2	1050	2.43	5.19	12.7	3.8782
	1100	4.28	5.37	12.9	3.8746
	1150	6.71	5.57	13.0	3.8776
	1200	8.28	5.45	13.4	3.8765
BNTCT4	1050	3.00	5.10	12.6	3.8758
	1100	3.71	5.24	12.9	3.8766
	1150	4.85	5.55	13.6	3.8724
	1200	8.14	5.41	13.5	3.8753
BNTCT6	1050	3.85	4.99	12.5	3.8722
	1100	4.05	5.17	12.8	3.8757
	1150	5.65	5.50	13.7	3.8719
	1200	8.57	5.40	13.8	3.8707
BNTCT8	1050	5.28	4.80	12.8	3.8709
	1100	5.85	5.09	13.1	3.8664
	1150	5.71	5.30	13.8	3.8860
	1200	6.42	5.40	14.4	3.8706

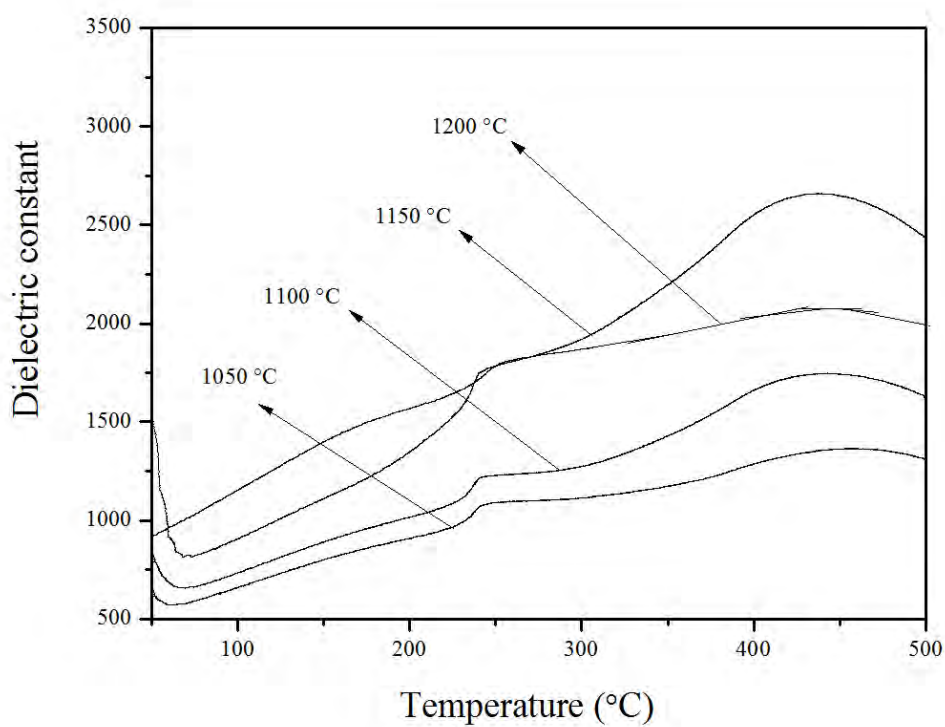
## 2.4 ผลที่ได้จากการวัดค่าคงที่ไดอิเล็กทริกและค่าสูญเสียไดอิเล็กทริก

ศึกษาผลจากการวัดค่าคงที่ไดอิเล็กทริกและค่าสูญเสียไดอิเล็กทริกของเซรามิก BNTCT2, BNTCT4, BNTCT6 และ BNTCT8 ที่อุณหภูมิซินเตอร์ต่างๆ โดยใช้ความถี่ 1 kHz ดังแสดงในภาพ 57, ภาพ 58, ภาพ 59 และ ภาพ 60 ตามลำดับ พบว่ามีพีคเกิดขึ้น 2 พีค โดยพีคแรกเกิดขึ้นในช่วงอุณหภูมิ depolarization ( $T_d$ ) ประมาณ 119 - 287 องศาเซลเซียส ซึ่งสอดคล้องกับการเปลี่ยนเฟสจากเฟร์โรอิเล็กทริกไปเป็นแอนติเฟร์โรอิเล็กทริก และพีคที่สองเกิดขึ้นในช่วงอุณหภูมิคูรี ( $T_m$ ) ประมาณ 369 - 494 องศาเซลเซียส สามารถหาได้จากอุณหภูมิที่มีค่าคงที่ไดอิเล็กทริกสูงสุด ซึ่งสอดคล้องกับการเปลี่ยนเฟสจากแอนติเฟร์โรอิเล็กทริกเป็นพาราอิเล็กทริก การเปลี่ยนเฟสดังกล่าวมีการรายงานโดยงานวิจัยของ T. Takenaka [14] ค่าคงที่ไดอิเล็กทริกเพิ่มขึ้นเมื่ออุณหภูมิซินเตอร์เพิ่มขึ้นจนถึง 1150 องศาเซลเซียส หลังจากนั้นลดลงเมื่ออุณหภูมิเพิ่มขึ้น ดังแสดงในภาพ 57, ภาพ 58, ภาพ 59 และ ภาพ 60 และการสูญเสียไดอิเล็กทริกเพิ่มขึ้นเมื่ออุณหภูมิซินเตอร์เพิ่มขึ้นดังแสดงในตาราง 7

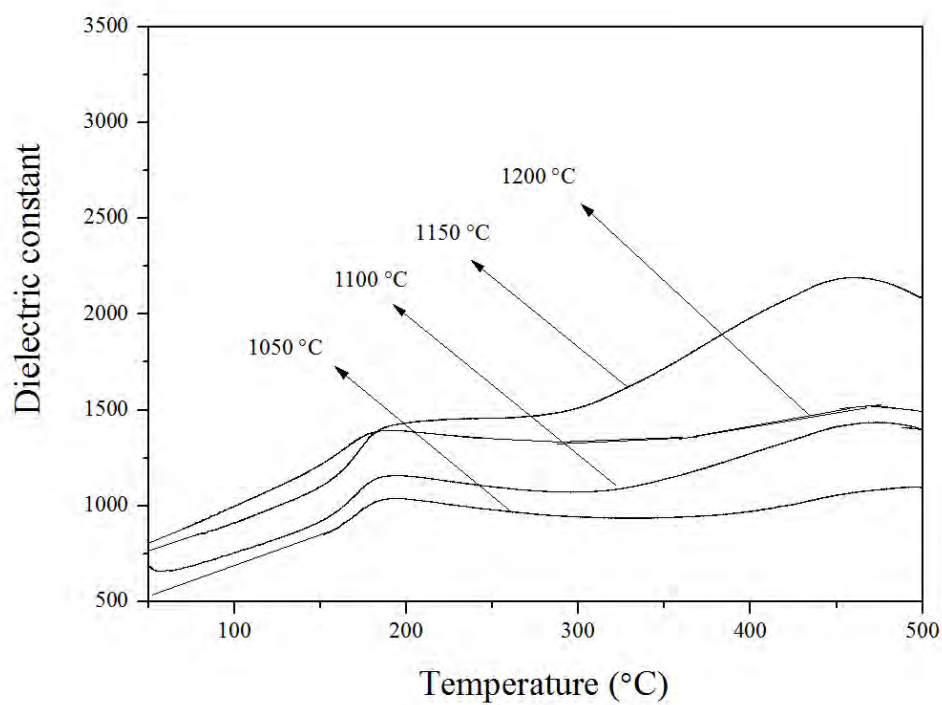
ที่อุณหภูมิซินเตอร์เดียวกันพบว่า  $T_d$  มีค่าลดลงในขณะที่  $T_m$  มีค่าเพิ่มขึ้นเมื่อปริมาณ x เพิ่มขึ้น ดังแสดงในตาราง 7 จากงานวิจัยของ Yuan E.Z. และคณะ [14] พบว่าการเติม CT ในเซรามิก BNT ทำให้  $T_d$  มีค่าลดลง เนื่องจาก  $\text{Ca}^{2+}$  มีขนาดเล็กและมีค่า polarizability ต่ำ จึงทำให้ความเป็นเฟร์โรอิเล็กทริกของ BNT ลดลงเมื่อเติม CT เป็นสาเหตุให้เกิดการเปลี่ยนเฟสจาก ferroelectric macrodomains ไปเป็น polar nanodomains สำหรับการสูญเสียไดอิเล็กทริกมีค่าเพิ่มขึ้นเมื่อปริมาณ x เพิ่มขึ้น ค่าคงที่ไดอิเล็กทริกมีแนวโน้มลดลงเมื่อ x เพิ่มขึ้น ค่าคงที่ไดอิเล็กทริกสูงสุดเท่ากับ 3208 ที่  $x = 0.02$  ซินเตอร์ที่อุณหภูมิ 1500 องศาเซลเซียส ซึ่งผลที่ได้สอดคล้องกับผลของค่าความหนาแน่น และผลจากการเตรียมเซรามิก BNTCT100x ด้วยวิธีการเผาไหม้สามารถเตรียมได้ที่อุณหภูมิซินเตอร์ต่ำกว่าวิธีผสมออกไซด์ [15]



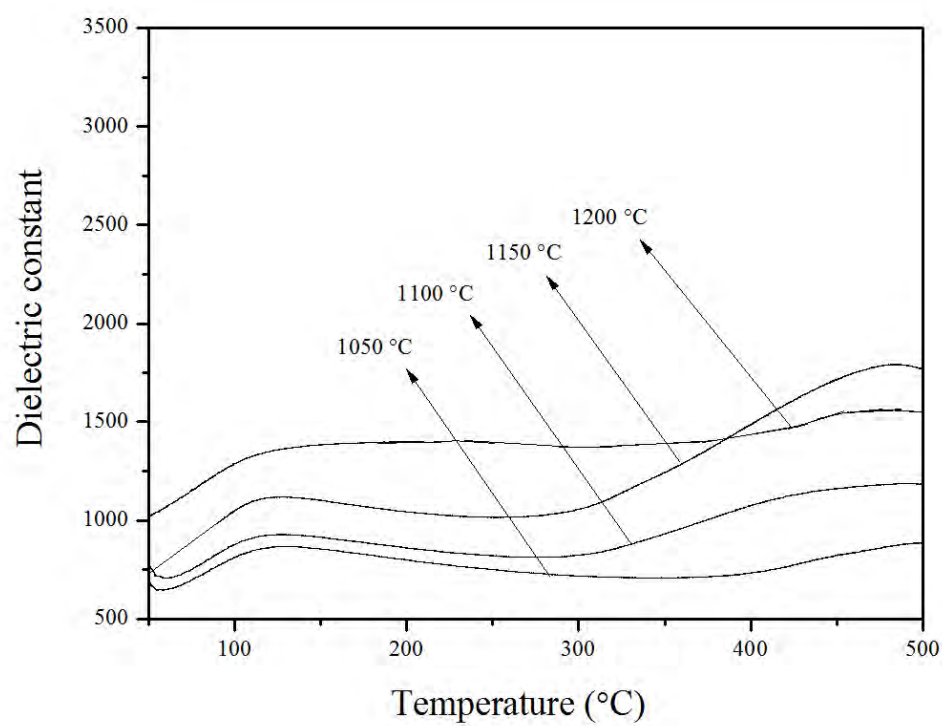
ภาพ 57 ค่าคงที่ได้อิเล็กทรอนิกส์ของเซรามิก BNTCT2 ซินเตอร์ที่อุณหภูมิต่างๆ



ภาพ 58 ค่าคงที่ได้อิเล็กทรอนิกส์ของเซรามิก BNTCT4 ซินเตอร์ที่อุณหภูมิต่างๆ



ภาพ 59 ค่าคงที่ได้อิเล็กทริกของเซรามิก BNTCT6 ซินเตอร์ที่อุณหภูมิต่างๆ



ภาพ 60 ค่าคงที่ได้อิเล็กทริกของเซรามิก BNTCT8 ซินเตอร์ที่อุณหภูมิต่างๆ

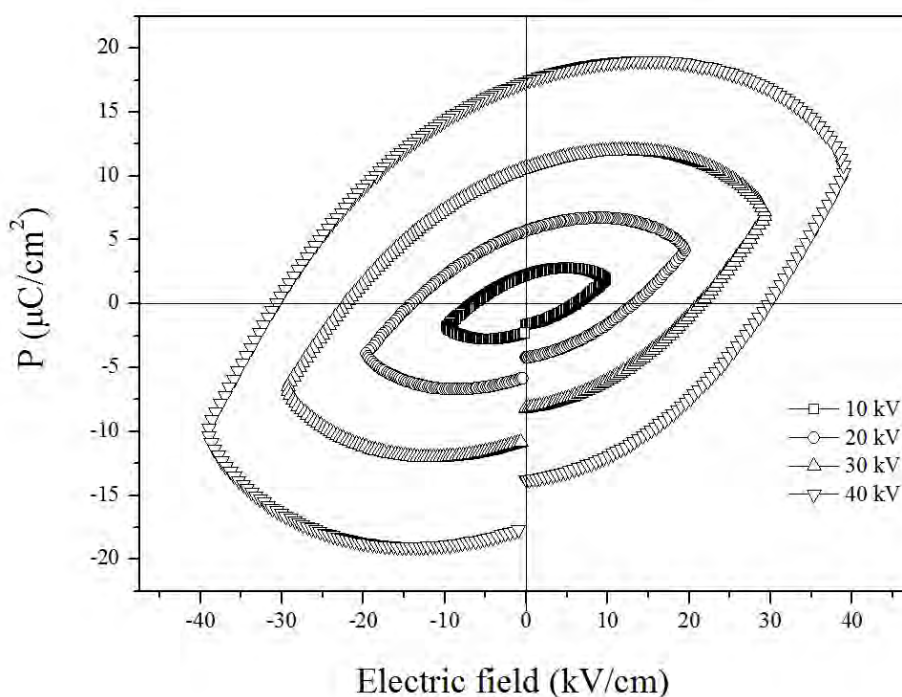
ตาราง 7 แสดงอุณหภูมิ depolarization ( $T_d$ ) อุณหภูมิคูรี ( $T_m$ ) ค่าคงที่ไดอิเล็กทริก ( $\epsilon_r$ ) ที่  $T_m$  ค่าสูญเสียไดอิเล็กทริก ( $\tan \delta$ ) ที่  $T_m$  ของเซรามิก BNTCT100x

เซรามิก	อุณหภูมิซินเตอร์ ( $^{\circ}\text{C}$ )	$T_d$ ( $^{\circ}\text{C}$ )	$T_m$ ( $^{\circ}\text{C}$ )	$\epsilon_r$ ที่ $T_m$	$\tan \delta$ ที่ $T_m$
BNTCT2	1050	287	389	1999	0.0367
	1100	280	478	2219	0.0450
	1150	284	429	3208	0.0505
	1200	286	369	2777	0.0625
BNTCT4	1050	246	488	1370	0.0464
	1100	243	429	1743	0.0557
	1150	247	430	2066	0.0604
	1200	239	432	2664	0.0692
BNTCT6	1050	189	488	1105	0.0491
	1100	184	474	1435	0.0595
	1150	190	462	2191	0.0629
	1200	181	474	1522	0.0753
BNTCT8	1050	120	494	892	0.0506
	1100	115	485	1188	0.0553
	1150	119	479	1801	0.0662
	1200	119	473	1549	0.0723

## 2.5 ผลการวัดค่าโพลาริเซชัน ( $P_r$ ) และค่าคงที่พีโซอิเล็กทริก ( $d_{33}$ )

การศึกษาสมบัติเพียโรอิเล็กทริกของเซรามิก BNTCT2 ที่มีความหนาแน่นสูงสุด โดยการวัดวงรอบฮิสเทอรีซิส (hysteresis loop) ที่สนามไฟฟ้าต่างๆ แสดงดังภาพ 61 พบว่า โพลาริเซชันอิ่มตัว ( $P_s$ ) โพลาริเซชันคงค้าง ( $P_r$ ) และค่าสนามไฟฟ้าลบกลับ ( $E_c$ ) ของเซรามิกมีแนวโน้มเพิ่มขึ้นเมื่อสนามไฟฟ้าที่ให้แก่เซรามิกมีค่าเพิ่มขึ้น แสดงดังตาราง 8 โดยมีค่าสูงสุดเท่ากับ  $10.27 \mu\text{C}/\text{cm}^2$ ,  $17.4 \mu\text{C}/\text{cm}^2$  และ  $30.13 \text{ kV}/\text{cm}$  ตามลำดับ เมื่อใช้สนามไฟฟ้า  $40 \text{ kV}/\text{cm}$  ดังนั้น การเจือสาร CT ในเซรามิก BNT ช่วยทำให้ค่าสนามไฟฟ้าลบกลับลดลง (เซรามิก BNT;  $E_c = 73 \text{ kV}/\text{cm}$ ) ดังแสดงในตาราง 8

การศึกษาสมบัติเพียโซอิเล็กทริกของเซรามิก BNTCT2 ที่มีความหนาแน่นสูงสุด โดยการวัดค่าคงที่เพียโซอิเล็กทริก  $d_{33}$  ทำการโพลลิง (polling) ภายใต้สนามไฟฟ้า  $35 \text{ kV}/\text{cm}$  ใน silicone oil ที่อุณหภูมิ  $80$  องศาเซลเซียส เป็นเวลา  $15$  นาที เท่ากับ  $40 \text{ pC}$ / ดังแสดงในตาราง 8



ภาพ 61 วงรอบฮิสเทอรีซิสของเซรามิก BNTCT2 ที่ค่าสนามไฟฟ้าต่างๆ

ตาราง 8 แสดงค่าคงที่พีโซอิเล็กทริก ( $d_{33}$ ) โพลาริเซชันอิมิตัว ( $P_s$ ) โพลาริเซชันคงค้าง ( $P_r$ ) และสนามไฟฟ้าลบกลับ ( $E_c$ ) ของเซรามิก BNTCT2

เซรามิก	$d_{33}$	สนามไฟฟ้า	โพลาริเซชันอิมิตัว	โพลาริเซชันคงค้าง	สนามไฟฟ้าลบกลับ
	(pC/N)	(KV/cm)	( $\mu\text{C}/\text{cm}^2$ )	( $\mu\text{C}/\text{cm}^2$ )	(KV/cm)
BNTCT2	40	10	1.95	2.23	6.18
		20	4.16	5.68	13.48
		30	6.89	10.61	21.42
		40	10.27	17.4	30.13



### 3. ผลการตรวจสอบลักษณะเฉพาะของเซรามิกบิสมาทโซเดียมไททาเนต-สทรอนเซียมไททาเนต (1-x)BNT-xST; BNTST100x

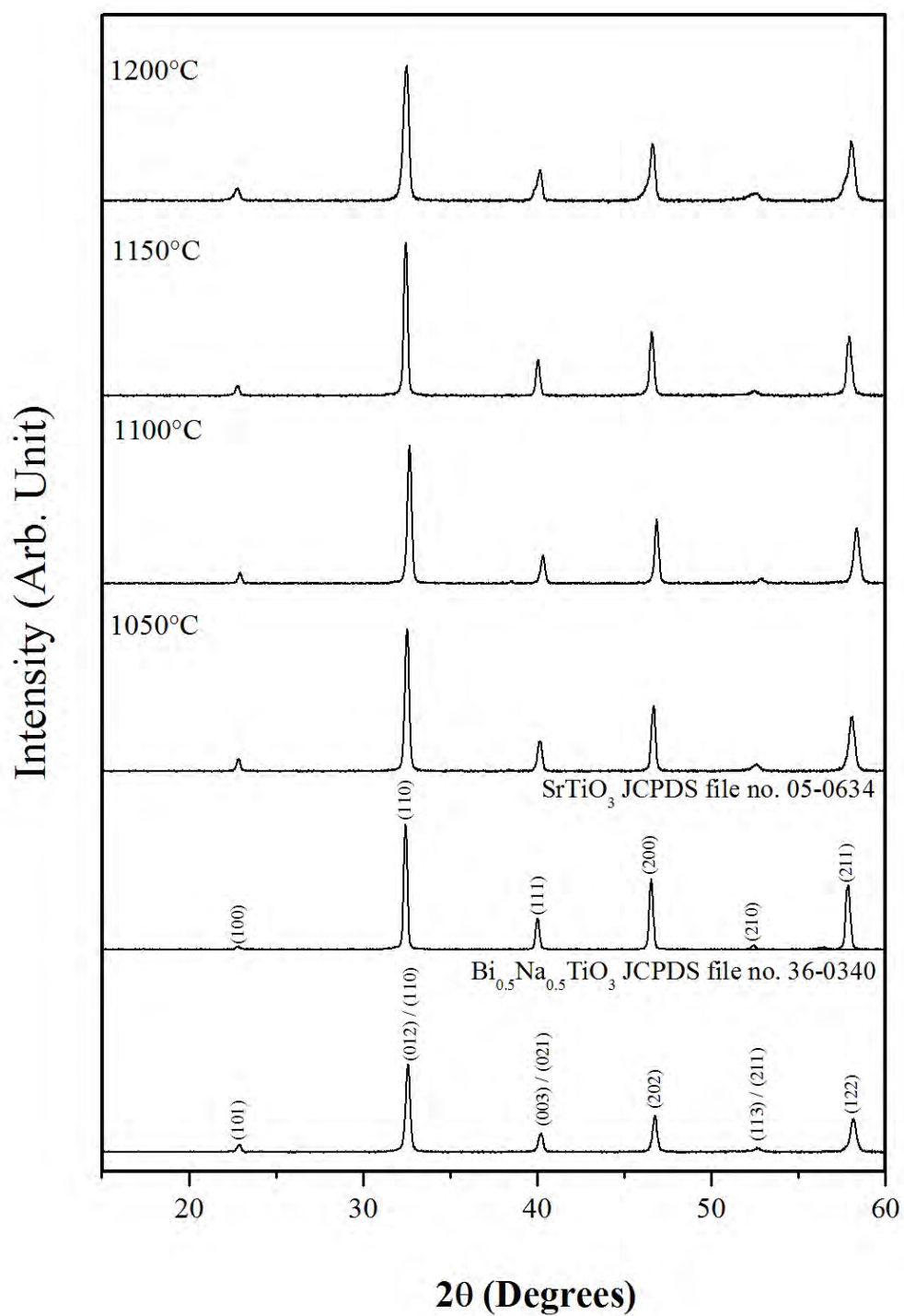
#### 3.1 ผลการวิเคราะห์โครงสร้างผลึกด้วยเทคนิคการเลี้ยวเบนของรังสีเอกซ์ (X-ray diffractometer: XRD)

นำผงผลึก BNT และ ST มาผสมกันตามสัดส่วนโดยโมลโดยใช้อัตราส่วน  $x = 0.10, 0.20, 0.30$  และ  $0.40$  (BNTST10, BNTST20, BNTST30 และ BNTST40) เพื่อนำมาอัดเม็ดและเผาซินเตอร์ที่อุณหภูมิระหว่าง 1050-1200 องศาเซลเซียส โดยทั่วไปเซรามิก BNT มีโครงสร้างรวมโบฮีตรอลซึ่งตรงกับแฟ้มข้อมูลของ JCPDS หมายเลข 36-0340 [8, 38] ในขณะที่เซรามิก ST มีโครงสร้างแบบคิวบิกตรงกับแฟ้มข้อมูลของ JCPDS หมายเลข 05-0634 [7] จากการศึกษาโครงสร้างผลึกของเซรามิก BNTST10, BNTST20, BNTST30 และ BNTST40 ด้วยรูปแบบการเลี้ยวเบนของรังสีเอกซ์ โดยเผาซินเตอร์ที่อุณหภูมิระหว่าง 1050-1200 องศาเซลเซียส ดังแสดงในภาพ 62 ภาพ 63 ภาพ 64 และภาพ 65 ตามลำดับ พบว่าเซรามิกมีโครงสร้างร่วมระหว่างรวมโบฮีตรอลกับคิวบิก ซึ่งสอดคล้องกับงานวิจัยที่ศึกษามาก่อน [16, 36]

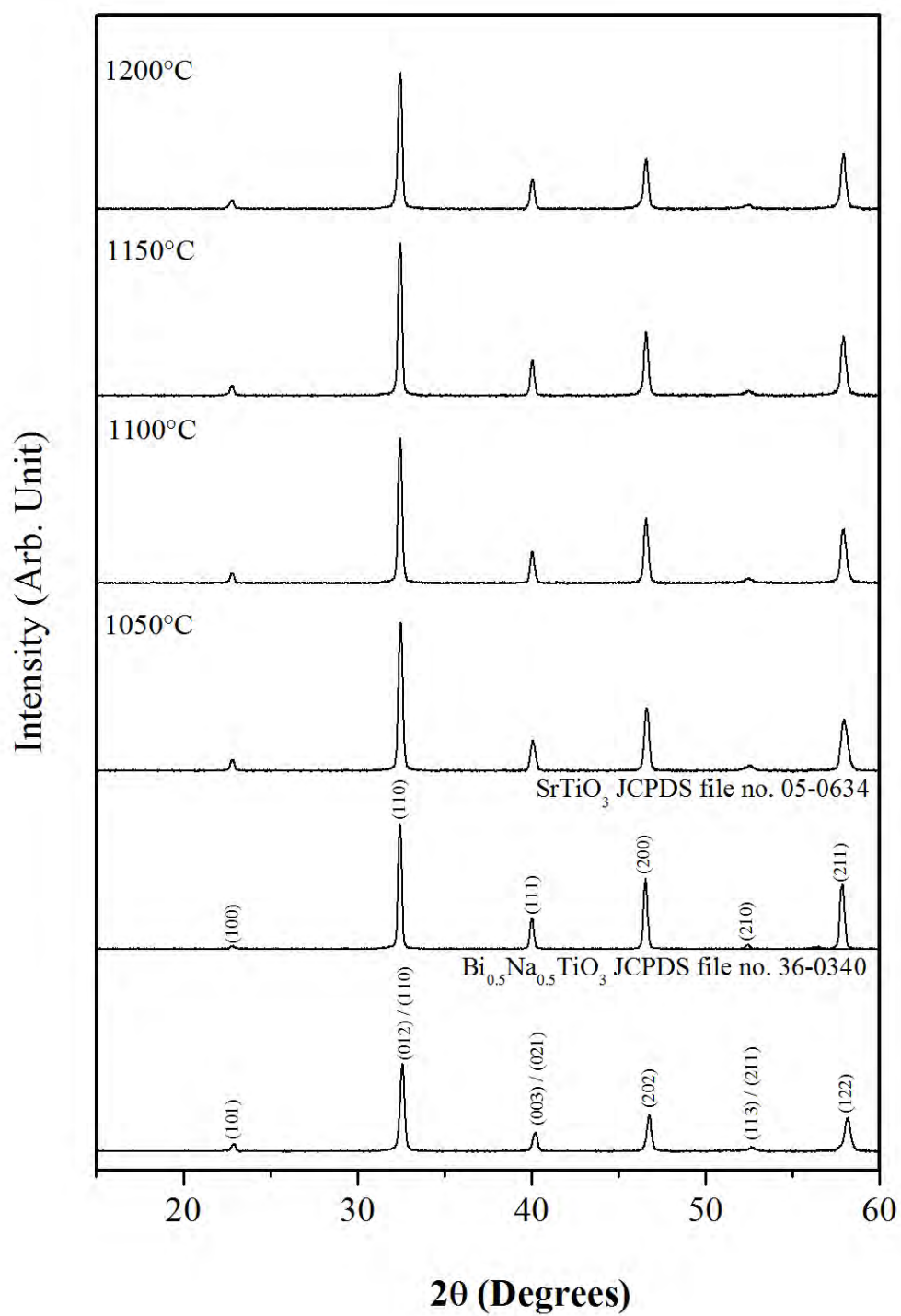
คำนวณหาค่าแลตทิซแสดงความเป็นรวมโบฮีตรอล ( $a_R$ ) จากสูตร

$$a_R = \frac{1}{3} \sqrt{3(a_H)^2 + c_H^2}$$

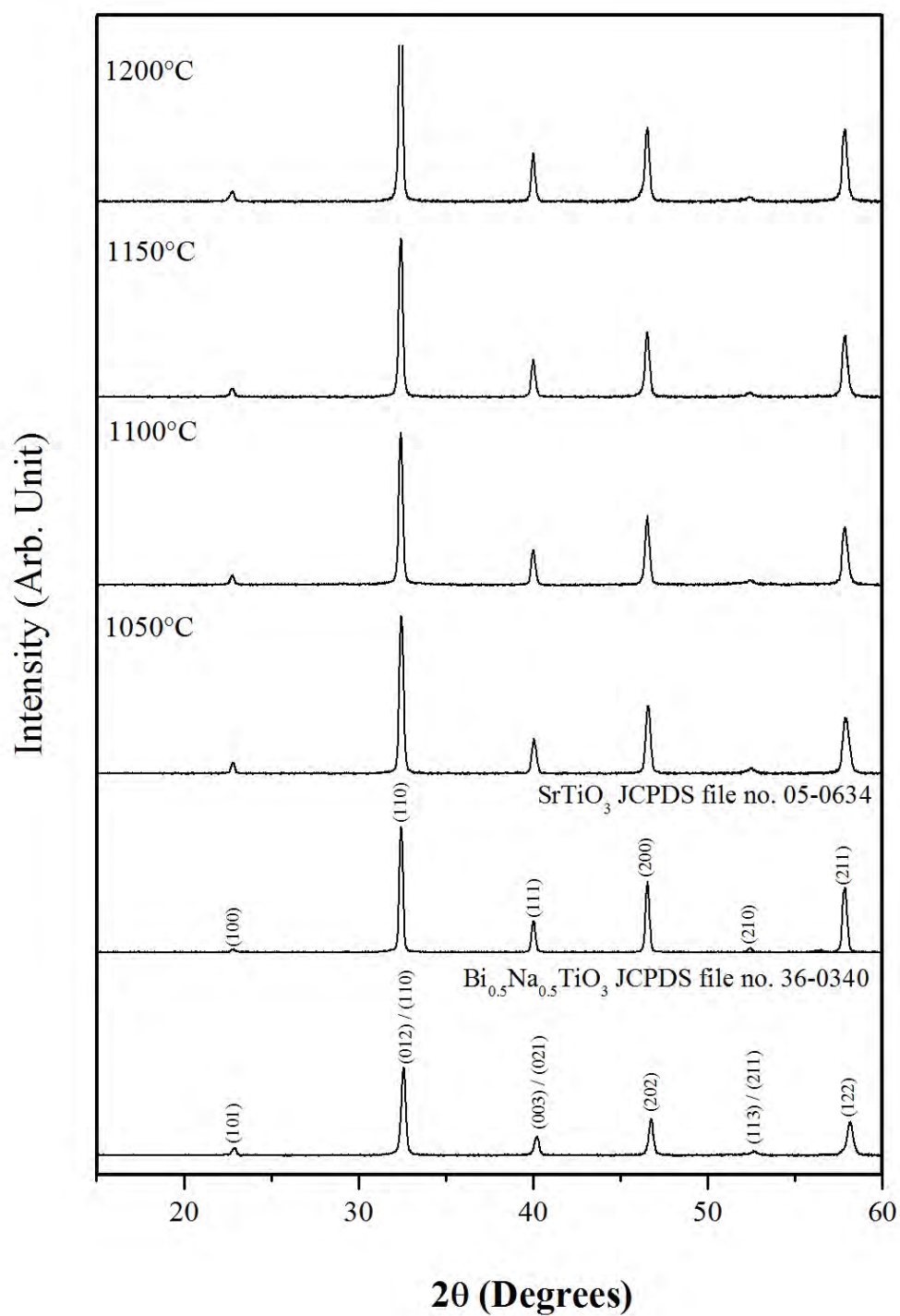
โดยที่  $a_H$  คือค่าแลตทิซพารามิเตอร์  $a$  ของโครงสร้างเฮกซะโกนอล และ  $c_H$  คือค่าแลตทิซพารามิเตอร์  $c$  ของโครงสร้างเฮกซะโกนอล พบว่าค่าแลตทิซแสดงความเป็นรวมโบฮีตรอล  $a_R$  มีค่าอยู่ระหว่าง 3.9601 – 3.8702 Å เมื่อซินเตอร์ที่อุณหภูมิระหว่าง 1050 – 1200 องศาเซลเซียส และแลตทิซแสดงความเป็นรวมโบฮีตรอล  $a_R$  มีค่าเพิ่มขึ้นเมื่อปริมาณ ST เพิ่มขึ้น เนื่องจากการแทนที่ของ ST ในโครงสร้างเพอร์อฟสไกต์ของ BNT บริเวณ A – site โดยมีรัศมีไอออนของ  $\text{Sr}^{2+}$  (144 pm)  $\text{Na}^+$  (139 pm) และ  $\text{Bi}^{3+}$  (140 pm) พบว่า  $\text{Sr}^{2+}$  มีขนาดรัศมีไอออนใหญ่กว่าขนาดรัศมีไอออนเฉลี่ยของ A – site จึงเป็นสาเหตุให้ค่าแลตทิซพารามิเตอร์มีค่าเพิ่มขึ้นเมื่อปริมาณ ST เพิ่มขึ้น และผลที่ได้สอดคล้องกับงานวิจัยของ L.V. Yinong และคณะ [12] ดังแสดงในตาราง 9



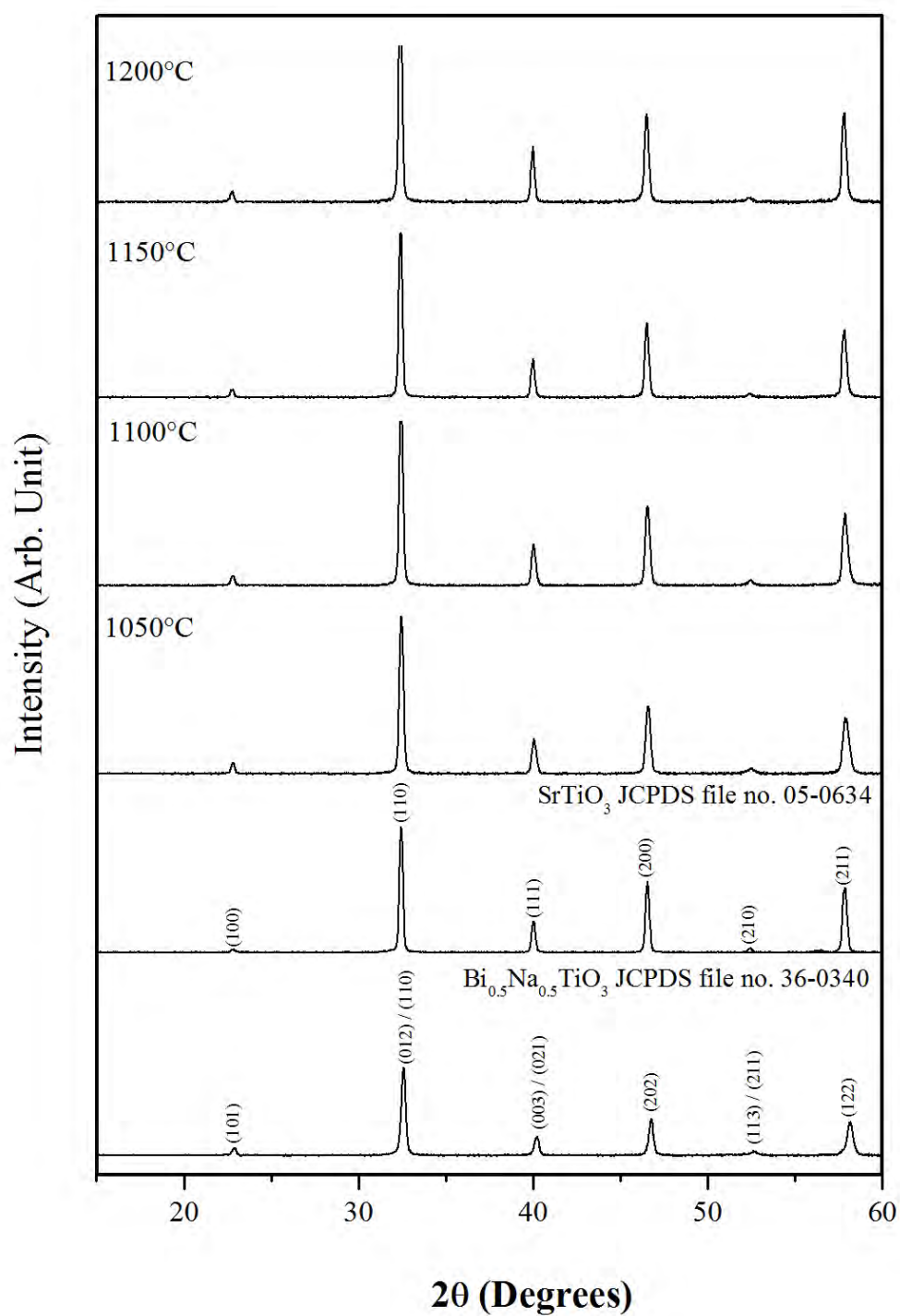
ภาพ 62 รูปแบบการเลี้ยวเบนของรังสีเอกซ์ของเซรามิก BNTST10 ที่อุณหภูมิซินเตอร์  
ต่างๆ



ภาพ 63 รูปแบบการเลี้ยวเบนของรังสีเอกซ์ของเซรามิก BNTST20 ที่อุณหภูมิซินเตอร์  
ต่างๆ



ภาพ 64 รูปแบบการเลี้ยวเบนของรังสีเอกซ์ของเซรามิก BNTST30 ที่อุณหภูมิซินเตอร์  
ต่างๆ



ภาพ 65 รูปแบบการเลี้ยวเบนของรังสีเอกซ์ของเซรามิก BNTST40 ที่อุณหภูมิซินเตอร์  
ต่างๆ

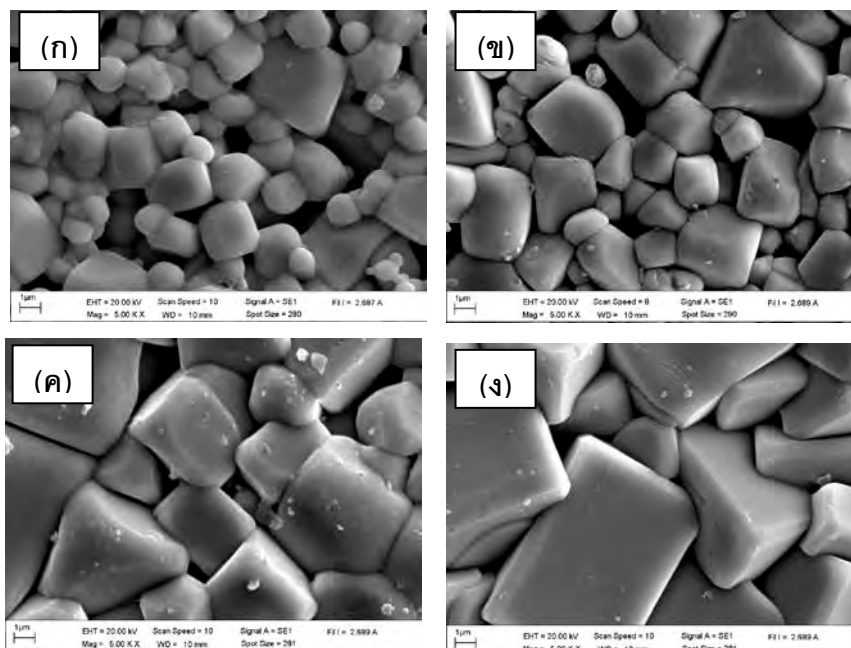
### 3.2 ผลการวิเคราะห์ด้วยกล้องจุลทรรศน์อิเล็กตรอนแบบส่องกราด (Scanning Electron Microscope: SEM)

ศึกษาโครงสร้างจุลภาคของเซรามิก BNTST10, BNTST20, BNTST30 และ BNTS40T8 ซินเตอร์ที่อุณหภูมิต่างๆ โดยถ่ายภาพบริเวณผิวหน้าด้วยกล้องจุลทรรศน์อิเล็กตรอนแบบส่องกราด ดังแสดงในภาพ 66, ภาพ 67, ภาพ 68 และ ภาพ 69 พบว่ารูปร่างเกรนส่วนใหญ่ของเซรามิกมีลักษณะคล้ายเป็นทรงกลมและสีเหลืองมูมจาก จากภาพ 66 พบว่าเซรามิก BNTBT10 ซินเตอร์ที่อุณหภูมิต่ำกว่า 1100 องศาเซลเซียส เซรามิกมีรูพรุน (ภาพ 66 (ก) และ (ข)) หลังจากนั้นพบว่าเกรนมีรูพรุนลดลงและเกรนมีขนาดเพิ่มขึ้นเมื่ออุณหภูมิซินเตอร์เพิ่มขึ้น ดังแสดงในภาพ 66 (ค) และ (ง) สำหรับเซรามิก BNTST 20, BNTST30 และ BNTST40 มีผลคล้ายกับเซรามิก BNTST10 และขนาดเกรนเฉลี่ยมีค่าเพิ่มขึ้นเมื่ออุณหภูมิซินเตอร์เพิ่มขึ้น ดังแสดงในตาราง 9 นอกจากนี้พบว่าเมื่อปริมาณ x เพิ่มขึ้นขนาดเกรนเฉลี่ยมีค่าอยู่ระหว่าง 0.85 – 10.12 ไมโครเมตร (ตาราง 9)

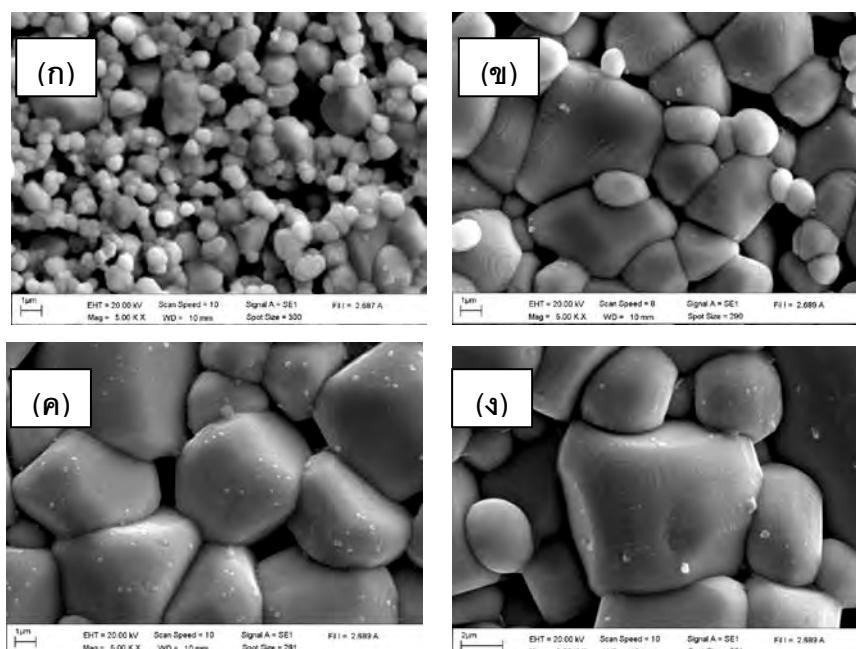
ภาพ 70 แสดงรูปถ่ายรอยหักของเซรามิก BNTST20 ซินเตอร์ที่อุณหภูมิต่างๆ พบว่า ที่อุณหภูมิน้อยกว่าหรือเท่ากับ 1100 องศาเซลเซียส เป็นรอยหักชนิดหักตามเกรน และพบรูพรุนแบบเปิด ในขณะที่อุณหภูมิซินเตอร์สูงขึ้น เซรามิกจะหักแบบผ่าเกรนแสดงให้เห็นว่ามีความหนาแน่นมากขึ้น

### 3.3 ผลการคำนวณหาค่าความหนาแน่นและร้อยละความหดตัว

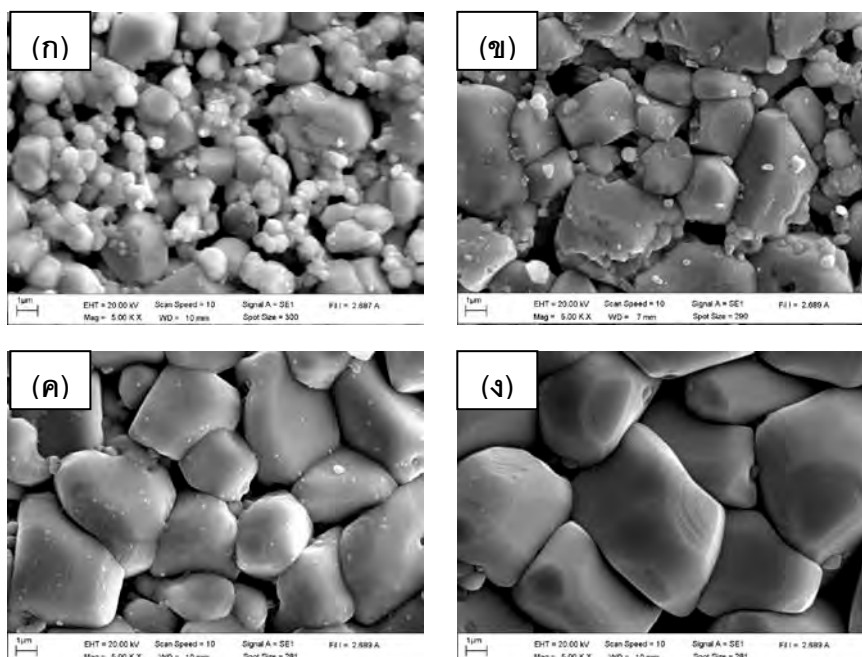
ค่าความหนาแน่นและค่าร้อยละการหดตัวของเซรามิก BNTST10, BNTST20, BNTST30 และ BNTST40 ที่อุณหภูมิซินเตอร์ต่างๆ แสดงดังตาราง 9 พบว่าเซรามิกมีค่าความหนาแน่นและการหดตัวเชิงเส้นของเซรามิกเพิ่มขึ้นเมื่ออุณหภูมิซินเตอร์เพิ่มขึ้น (ตาราง 9) และเมื่อปริมาณ x เพิ่มขึ้น ค่าความหนาแน่นมีค่าลดลง ในขณะที่ค่าการหดตัวเชิงเส้น มีค่าอยู่ระหว่าง 12.4 – 14.7 % ดังแสดงในตาราง 9



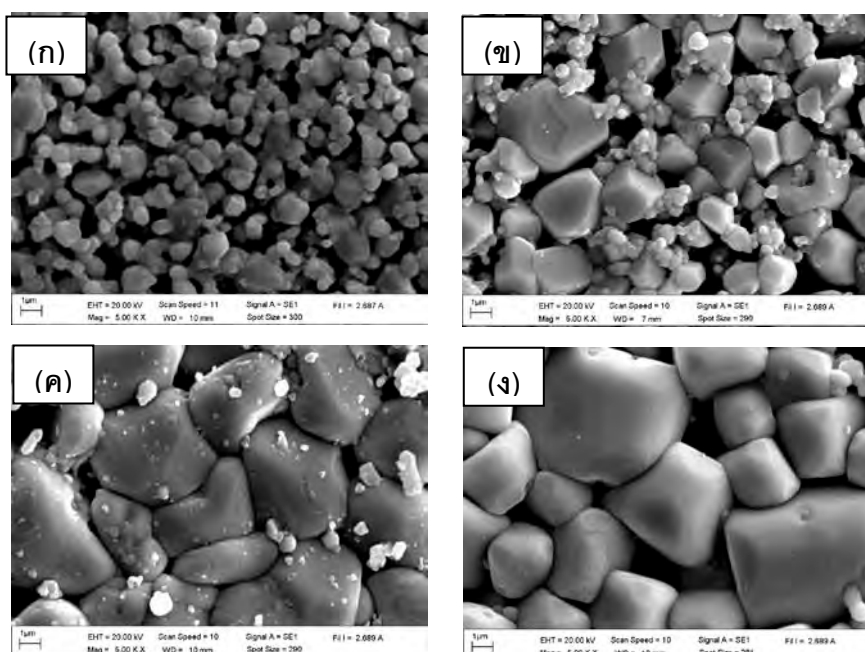
ภาพ 66 ภาพถ่ายบริเวณผิวหน้าของเซรามิก BNTST10 ที่อุณหภูมิซินเตอร์ต่างๆ (ก) 1050 องศาเซลเซียส (ข) 1100 องศาเซลเซียส (ค) 1150 องศาเซลเซียส และ (ง) 1200 องศาเซลเซียส



ภาพ 67 ภาพถ่ายบริเวณผิวหน้าของเซรามิก BNTST20 ที่อุณหภูมิซินเตอร์ต่างๆ (ก) 1050 องศาเซลเซียส (ข) 1100 องศาเซลเซียส (ค) 1150 องศาเซลเซียส และ (ง) 1200 องศาเซลเซียส

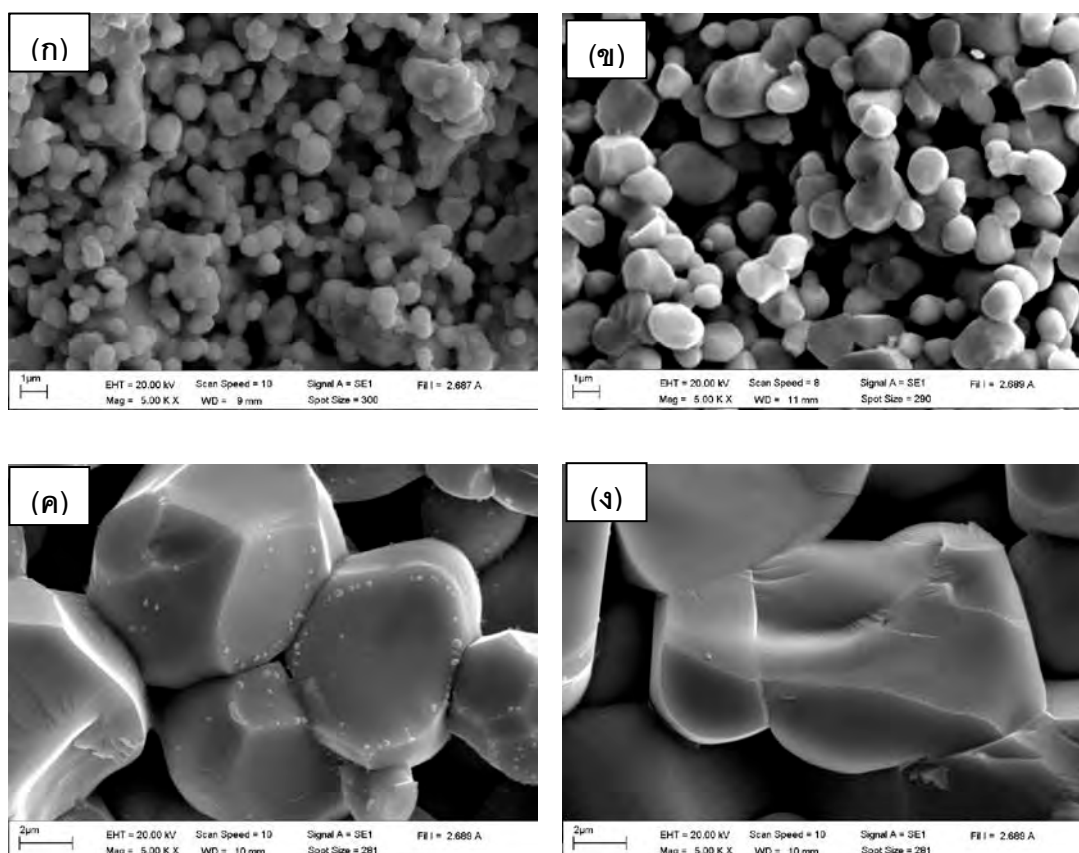


ภาพ 68 ภาพถ่ายบริเวณผิวหน้าของเซรามิก BNTST30 ที่อุณหภูมิซินเตอร์ต่างๆ (ก) 1050 องศาเซลเซียส (ข) 1100 องศาเซลเซียส (ค) 1150 องศาเซลเซียส และ (ง) 1200 องศาเซลเซียส



ภาพ 69 ภาพถ่ายบริเวณผิวหน้าของเซรามิก BNTST40 ที่อุณหภูมิซินเตอร์ต่างๆ (ก) 1050 องศาเซลเซียส (ข) 1100 องศาเซลเซียส (ค) 1150 องศาเซลเซียส และ (ง) 1200 องศาเซลเซียส





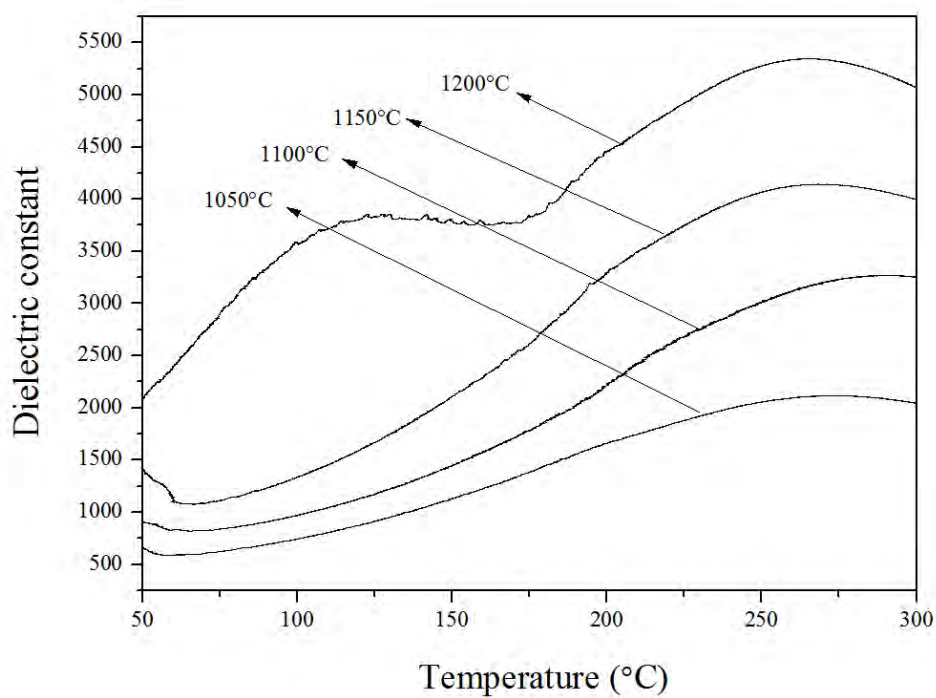
ภาพ 70 ภาพถ่ายบริเวณรอยหักของเซรามิก BNTST20 ที่อุณหภูมิซินเตอร์ต่างๆ (ก) 1050 องศาเซลเซียส (ข) 1100 องศาเซลเซียส (ค) 1150 องศาเซลเซียส และ (ง) 1200 องศาเซลเซียส

ตาราง 9 แสดงขนาดเกรนเฉลี่ย ความหนาแน่น การหดตัวเชิงเส้น และแลตทิซพารามิเตอร์  $a_R$  ของเซรามิก BNTST100x ที่อุณหภูมิซินเตอร์ต่างๆ

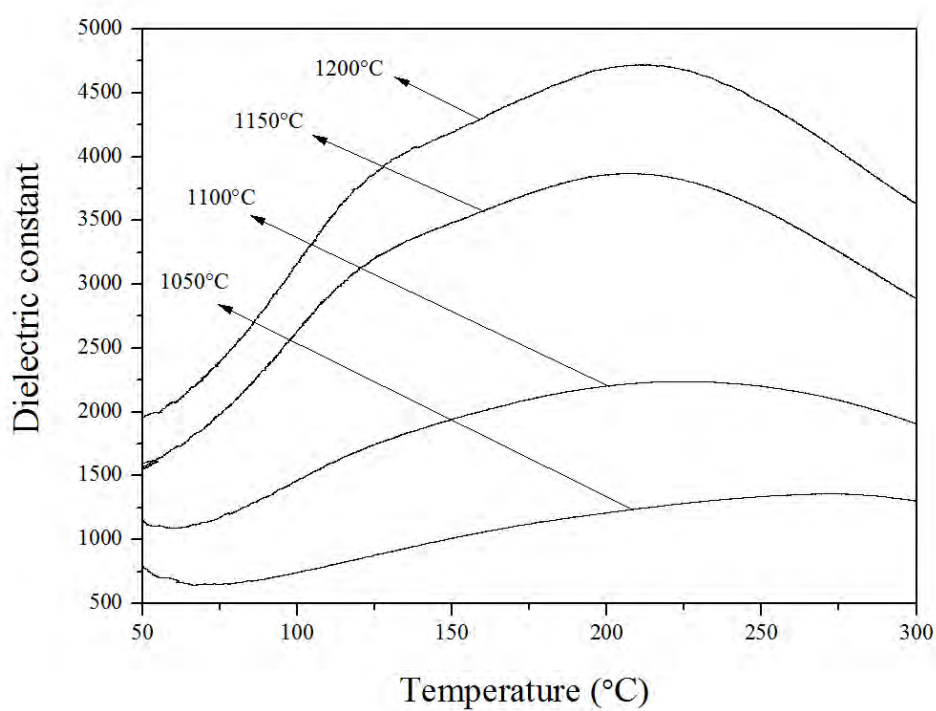
เซรามิก	อุณหภูมิซินเตอร์ (°C)	ขนาดเกรนเฉลี่ย ( $\mu\text{m}$ )	ความหนาแน่น ( $\text{g/cm}^3$ )	การหดตัวเชิงเส้น (%)	แลตทิซพารามิเตอร์ $a_R$ (Å)
BNTST10	1050	1.71	4.99	12.4	3.8858
	1100	2.00	5.17	12.7	3.8702
	1150	4.28	5.41	13.0	3.8891
	1200	6.05	5.61	13.2	3.8865
	1250	10.12	5.40	13.7	3.8940
BNTST20	1050	1.14	4.90	12.7	3.8941
	1100	2.85	5.14	13.1	3.8971
	1150	4.85	5.45	13.4	3.8959
	1200	5.42	5.59	13.7	3.8944
	1250	8.75	5.44	14.4	3.9011
BNTST30	1050	1.42	4.81	13.0	3.8957
	1100	2.14	5.21	13.3	3.9025
	1150	3.42	5.43	13.6	3.8961
	1200	5.57	5.56	13.9	3.9008
	1250	8.50	5.45	14.5	3.9088
BNTST40	1050	0.85	4.73	13.2	3.9601
	1100	2.28	4.95	13.8	3.8994
	1150	4.28	5.44	14.1	3.9001
	1200	5.12	5.47	14.8	3.9079
	1250	7.56	5.45	14.7	3.9090

### 3.4 ผลที่ได้จากการวัดค่าคงที่ไดโพลีทริกและค่าสูญเสียไดโพลีทริก

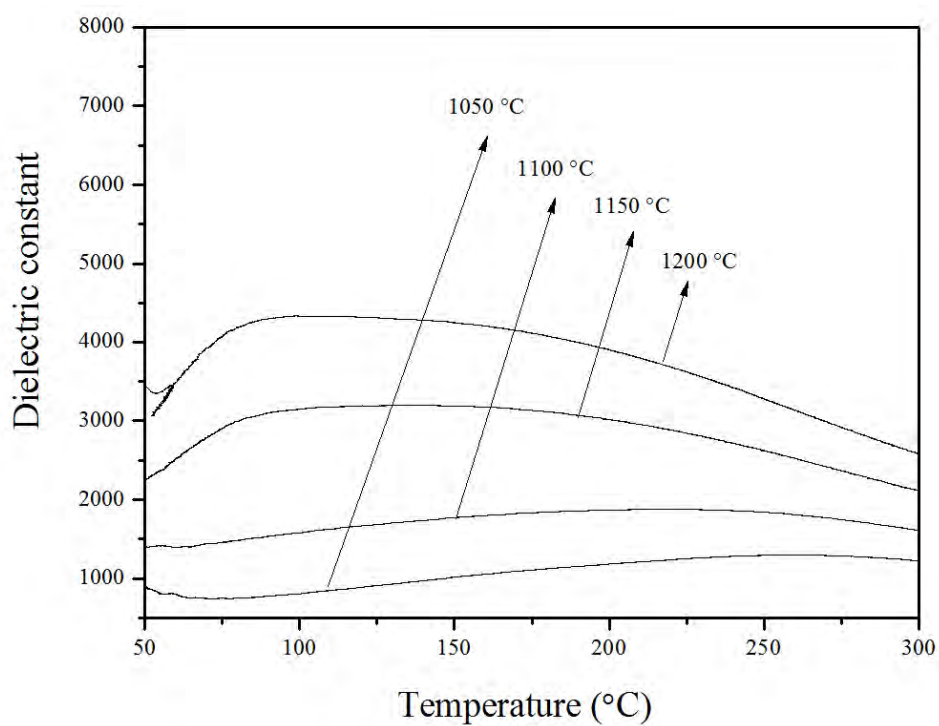
ศึกษาผลจากการวัดค่าคงที่ไดโพลีทริกและค่าสูญเสียไดโพลีทริกของเซรามิก BNTST10, BNTST20, BNTST30 และ BNTST40 ที่อุณหภูมิซินเตอร์ต่างๆ โดยใช้ความถี่ 1 kHz ดังแสดงในภาพ 71, 72, 73 และ ภาพ 74 ตามลำดับ ค่าคงที่ไดโพลีทริกของเซรามิก BNTST10 และ BNTST20 ที่อุณหภูมิซินเตอร์ต่างๆ พบว่ามีพีคเกิดขึ้น 2 พีค โดยพีคแรกเกิดขึ้นในช่วงอุณหภูมิ depolarization ( $T_d$ ) ประมาณ 119 - 287 องศาเซลเซียส ซึ่งสอดคล้องกับการเปลี่ยนเฟสจากเฟร์โรอิเล็กทริกไปเป็นแอนติเฟร์โรอิเล็กทริก และพีคที่สองเกิดขึ้นในช่วงอุณหภูมิคูรี ( $T_m$ ) ประมาณ 369 - 494 องศาเซลเซียส สามารถหาได้จากอุณหภูมิที่มีค่าคงที่ไดโพลีทริกสูงสุด ซึ่งสอดคล้องกับการเปลี่ยนเฟสจากแอนติเฟร์โรอิเล็กทริกเป็นพาราอิเล็กทริก การเปลี่ยนเฟสดังกล่าวมีการรายงานโดยงานวิจัยของ T. Takenaka [37] ค่าคงที่ไดโพลีทริกเพิ่มขึ้นเมื่ออุณหภูมิซินเตอร์เพิ่มขึ้นจนถึง 1200 องศาเซลเซียส หลังจากนั้นลดลงเมื่ออุณหภูมิเพิ่มขึ้น ดังแสดงในภาพ 71 และ ภาพ 72 และการสูญเสียไดโพลีทริกเพิ่มขึ้นเมื่ออุณหภูมิซินเตอร์เพิ่มขึ้นดังแสดงในตาราง ในกรณีเซรามิก BNTST30 และ BNTST40 ที่อุณหภูมิซินเตอร์ต่างๆ พบว่ามีพีคเกิดขึ้นพีคเดียว โดยเกิดขึ้นในช่วงอุณหภูมิคูรี ( $T_m$ ) ประมาณ 369 - 494 องศาเซลเซียส สามารถหาได้จากอุณหภูมิที่มีค่าคงที่ไดโพลีทริกสูงสุด ซึ่งสอดคล้องกับการเปลี่ยนเฟสจากแอนติเฟร์โรอิเล็กทริกเป็นพาราอิเล็กทริก การเปลี่ยนเฟสดังกล่าวมีการรายงานโดยงานวิจัยของ T. Takenaka [37] ค่าคงที่ไดโพลีทริกเพิ่มขึ้นเมื่ออุณหภูมิซินเตอร์เพิ่มขึ้นจนถึง 1200 องศาเซลเซียส หลังจากนั้นลดลงเมื่ออุณหภูมิเพิ่มขึ้น ดังแสดงในภาพ 73 และ ภาพ 74



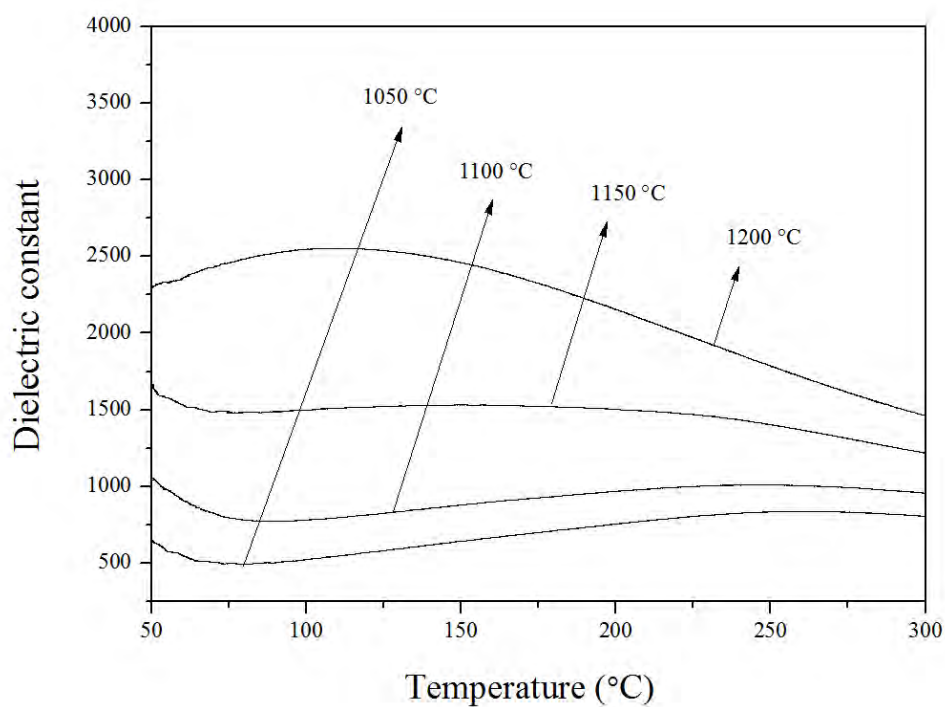
ภาพ 71 ค่าคงที่ได้ิเล็กทริกของเซรามิก BNTST10 ที่อุณหภูมิซินเตอร์ต่าง ๆ



ภาพ 72 ค่าคงที่ได้ิเล็กทริกของเซรามิก BNTST20 ที่อุณหภูมิซินเตอร์ต่าง ๆ



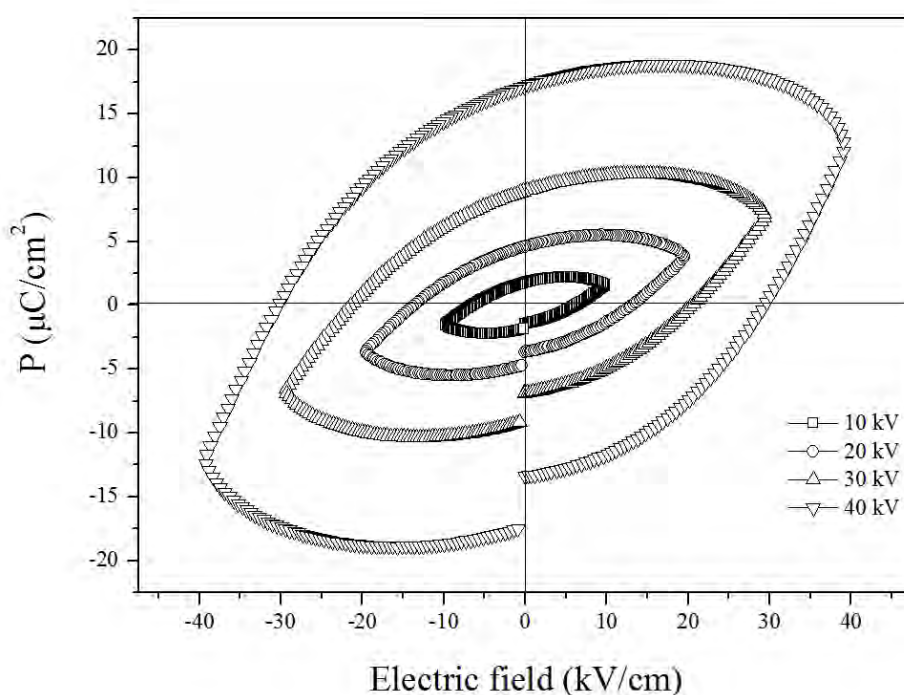
ภาพ 73 ค่าคงที่ไดอิเล็กตริกของเซรามิก BNTST30 ที่อุณหภูมิซินเตอร์ต่างๆ



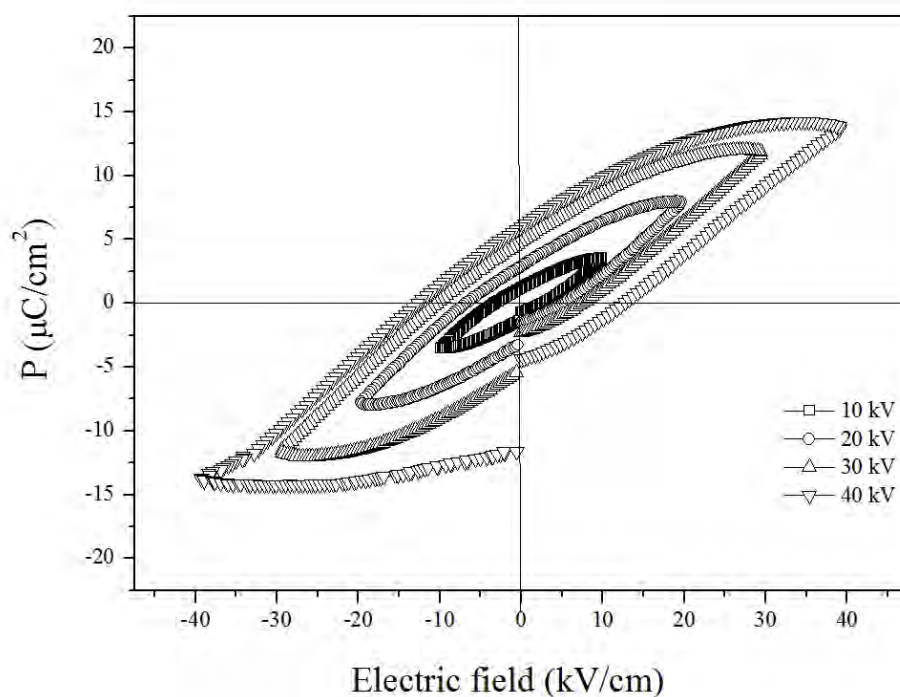
ภาพ 74 ค่าคงที่ไดอิเล็กตริกของเซรามิก BNTST40 ที่อุณหภูมิซินเตอร์ต่างๆ

### 3.5 ผลการวัดค่าโพลาริเซชัน ( $P_r$ ) และค่าคงที่พิโซอิเล็กทริก ( $d_{33}$ )

การศึกษสมบัติเพโรอิเล็กทริกของเซรามิก BNTST20 และ BNTST30 ที่มีความหนาแน่นสูงสุดโดยการวัดวงรอบฮิสเทอรีซิส (hysteresis loop) ที่สนามไฟฟ้าต่างๆ แสดงดังภาพ 75 และ 76 พบว่าโพลาริเซชันอิ่มตัว ( $P_s$ ) โพลาริเซชันคงค้าง ( $P_r$ ) และค่าสนามไฟฟ้าลบกลับ ( $E_c$ ) ของเซรามิกมีแนวโน้มเพิ่มขึ้นเมื่อสนามไฟฟ้าที่ให้แก่เซรามิกมีค่าเพิ่มขึ้น แสดงดังตาราง 10 โดยมีค่าสูงสุดสำหรับ BNTST20 เท่ากับ  $12.04 \mu\text{C}/\text{cm}^2$ ,  $17.19 \mu\text{C}/\text{cm}^2$  และ  $29.61 \text{ kV}/\text{cm}$  ตามลำดับ และ BNTST30 เท่ากับ  $13.81 \mu\text{C}/\text{cm}^2$ ,  $6.03 \mu\text{C}/\text{cm}^2$  และ  $12.71 \text{ kV}/\text{cm}$  เมื่อใช้สนามไฟฟ้า  $40 \text{ kV}/\text{cm}$  ดังนั้นการเจือสาร ST ในเซรามิก BNT ช่วยทำให้ค่าสนามไฟฟ้าลบกลับลดลง (เซรามิก BNT;  $E_c = 73 \text{ kV}/\text{cm}$ ) แสดงดังตาราง 11 และที่  $x > 0.40$  พบว่าจะแสดงความเป็นพาราอิเล็กทริก [15]



ภาพ 75 วงรอบฮิสเทอรีซิสของเซรามิก BNTST20 ที่ค่าสนามไฟฟ้าต่างๆ



ภาพ 76 วงรอบฮิสเทอรีซิสของเซรามิก BNTST30 ที่ค่าสนามไฟฟ้าต่างๆ

การศึกษาสสมบัติเพียโซอิเล็กทริกของเซรามิก BNTST20 ที่มีความหนาแน่นสูงสุดโดยการวัดค่าคงที่เพียโซอิเล็กทริก  $d_{33}$  ทำการโพลลิง (polling) ภายใต้สนามไฟฟ้า 35 kV/cm ใน silicone oil ที่อุณหภูมิ 80 องศาเซลเซียส เป็นเวลา 15 นาที เท่ากับ 90 pC/N แสดงดังตาราง ดังนั้นการเติม ST ในเซรามิก BNT ช่วยทำให้ค่าคงที่เพียโซอิเล็กทริกเพิ่มขึ้น ( $d_{33} = 71$  pC/N)

ตาราง 10 แสดงค่าคงที่พีโซอิเล็กทริก ( $d_{33}$ ) โพลาริเซชันอิมพัลส์ ( $P_s$ ) โพลาริเซชันคงค้าง ( $P_r$ ) และสนามไฟฟ้าลบกลับ ( $E_c$ ) ของเซรามิก BNTST20 และ BNTST30

เซรามิก	$d_{33}$	สนามไฟฟ้า	โพลาริเซชันอิมพัลส์	โพลาริเซชันคงค้าง	สนามไฟฟ้าลบกลับ
	(pC/N)	(KV/cm)	( $\mu\text{C}/\text{cm}^2$ )	( $\mu\text{C}/\text{cm}^2$ )	(KV/cm)
BNTST20	90	10	1.57	1.79	6.2
		20	3.72	4.61	13.23
		30	6.88	8.97	20.67
		40	12.04	17.19	29.61
BNTST30		10	3.46	1.19	2.82
		20	7.88	2.89	5.29
		30	11.84	4.84	7.56
		40	13.81	6.03	12.71



## บทที่ 5

### บทสรุป

#### สรุปการตรวจสอบผงผลึกบิสมาทโซเดียมไททาเนต ผงผลึกแบเรียมไททาเนต ผงผลึกแคลเซียมไททาเนต และผงผลึกสทรอนเซียมไททาเนต

จากผลการวิเคราะห์ด้วยเทคนิคการเลี้ยวเบนของรังสีเอกซ์ของผงผลึกบิสมาทโซเดียมไททาเนต (BNT) ผงผลึกแบเรียมไททาเนต (BT) ผงผลึกแคลเซียมไททาเนต (CT) และผงผลึกสทรอนเซียมไททาเนต (ST) โดยเผาแคลไซน์ที่อุณหภูมิ 650, 1200, 1100 และ 1200 องศาเซลเซียส เป็นเวลา 2, 4, 2 และ 4 ชั่วโมง ตามลำดับ พบว่าสามารถเตรียมผงผลึกบิสมาทโซเดียมไททาเนต ผงผลึกแบเรียมไททาเนต ผงผลึกแคลเซียมไททาเนต และผงผลึกสทรอนเซียมไททาเนต ที่มีความบริสุทธิ์สูงและไม่พบเฟสแปลกปลอมของสารเจือปนใดๆ

ผลการตรวจสอบโครงสร้างจุลภาคของผงผลึกบิสมาทโซเดียมไททาเนต ผงผลึกแบเรียมไททาเนต ผงผลึกแคลเซียมไททาเนต และผงผลึกสทรอนเซียมไททาเนต พบว่าอนุภาคส่วนใหญ่ของผงผลึกทั้ง 3 ชนิด มีลักษณะรูปร่างคล้ายเป็นทรงกลมและมีการเกาะกลุ่มกัน

#### สรุปการตรวจสอบของเซรามิกบิสมาทโซเดียมไททาเนต-แบเรียมไททาเนต (1-x)BNT-xBT; BNTBT100x

จากผลการวิเคราะห์ด้วยเทคนิคการเลี้ยวเบนของรังสีเอกซ์ของเซรามิก BNTBT2, BNTBT4, BNTBT6, BNTBT8, BNTBT10 และ BNTBT12 ที่  $x \leq 0.04$  เซรามิก BNTBT2 และ BNTBT4 พบว่ามีโครงสร้างเป็นแบบรอมโบอีดรอลซึ่งเหมือนกับ BNT เมื่อปริมาณ BT เพิ่มขึ้น เซรามิกมีความเป็นเทระโกนอลมากขึ้น ในขณะที่  $x \geq 0.10$  เซรามิก BNTBT10 และ BNTBT12 มีโครงสร้างเป็นแบบเทระโกนอลซึ่งเหมือนกับ BT โดยที่ปริมาณ  $x$  น้อยกว่า 0.06 ใช้อุณหภูมิซินเตอร์ 1050 – 1150 และที่ปริมาณ  $x$  มากกว่า 0.06 ใช้อุณหภูมิซินเตอร์ที่ 1050-1210 องศาเซลเซียส พบว่าเซรามิก BNTBT100x เมื่อซินเตอร์ที่อุณหภูมิสูงกว่า 1200 องศาเซลเซียส พบเฟสแปลกปลอมของ  $\text{Bi}^{2+}$  และ  $\text{Na}^{2+}$  เนื่องจากการระเหยของสารตั้งต้น ผลจากการตรวจสอบโครงสร้างจุลภาคพบว่ารูปร่างเกรนส่วนใหญ่มีลักษณะคล้ายทรงกลมและสีเหลี่ยมมุมฉาก เกรนมีขนาดใหญ่ขึ้น เมื่ออุณหภูมิซินเตอร์สูงขึ้น แต่ที่อุณหภูมิซินเตอร์เดียวกันเมื่อปริมาณ  $x$  เพิ่มขึ้น ขนาดเกรนเฉลี่ยของเซรามิกมีแนวโน้มลดลง และเซรามิก BNTBT2 และ BNTBT4 มีค่าความ

หนาแน่น ค่าความหดตัวเชิงเส้น และค่าคงที่ไดอิเล็กทริก ณ อุณหภูมิคูรีสูงสุด ซึ่งได้จากตัวอย่างที่เผาซินเตอร์ที่อุณหภูมิ 1150 องศาเซลเซียส ในขณะที่เซรามิก BNTBT6, BNTBT8, BNTBT10 และ BNTBT12 ได้จากตัวอย่างที่เผาซินเตอร์ที่อุณหภูมิ 1200 องศาเซลเซียส นอกจากนั้นเซรามิก BNTBT100x มีค่าคงที่ไดอิเล็กทริกสูงสุด (7400) ค่าความหนาแน่นสูงสุด ( $5.80 \text{ g/cm}^3$ ) ค่าคงที่พิโซอิเล็กทริก (169 pC/N) และใช้สนามไฟฟ้าเพิ่ม 40 kV) มีค่าโพลาริเซชันคงค้างสูงสุด ( $28.10 \mu\text{C/cm}^2$ ) และค่าสนามไฟฟ้าลบล้าง ( $21.02 \text{ kV/cm}$ ) ที่เซรามิก BNTBT8 ซินเตอร์ที่อุณหภูมิ 1200 องศาเซลเซียส และเซรามิกที่เตรียมได้ด้วยวิธีการเผาใหม่มีค่าสมบัติทางไฟฟ้าสูงกว่าเซรามิกที่เตรียมด้วยวิธีผสมออกไซด์

#### **สรุปการตรวจสอบของเซรามิกบิสมาทโซเดียมไททาเนต-แคลเซียมไททาเนต (1-x)BNT-xCT; BNTCT100x**

จากผลการวิเคราะห์ด้วยเทคนิคการเลี้ยวเบนของรังสีเอกซ์ของเซรามิก BNTCT2, BNTCT4, BNTCT6 และ BNTCT8 ซินเตอร์ที่อุณหภูมิ 1050 -1200 องศาเซลเซียส จากผลการวิเคราะห์ด้วยเทคนิคการเลี้ยวเบนรังสีเอกซ์ของเซรามิก BNTCT100x พบว่ามีโครงสร้างแบบรวมไบสตรอลในทุกๆตัวอย่าง และผลจากการตรวจสอบโครงสร้างจุลภาคพบว่ารูปร่างเกรนส่วนใหญ่ของเซรามิกมีลักษณะคล้ายทรงกลมและสีเหลี่ยมมุมฉาก เมื่ออุณหภูมิเพิ่มขึ้นขนาดเกรนเฉลี่ยมีค่าเพิ่มขึ้น ในขณะที่ เมื่อปริมาณ x เพิ่มขึ้นขนาดเกรนเฉลี่ยมีแนวโน้มไม่คงที่ ค่าความหนาแน่นเพิ่มขึ้นเมื่ออุณหภูมิซินเตอร์เพิ่มขึ้นจนถึง 1150 องศาเซลเซียส หลังจากนั้นความหนาแน่นมีค่าลดลงเมื่ออุณหภูมิซินเตอร์เพิ่มขึ้น ในขณะที่การหดตัวเชิงเส้นมีค่าเพิ่มขึ้นเมื่ออุณหภูมิซินเตอร์เพิ่มขึ้น มีค่าคงที่ไดอิเล็กทริกสูงสุด (3208) และค่าความหนาแน่นสูงสุด ( $5.57 \text{ g/cm}^3$ ) ค่าคงที่พิโซอิเล็กทริก (40 pC/N) และใช้สนามไฟฟ้าเพิ่ม 40 kV) มีค่าโพลาริเซชันคงค้างสูงสุด ( $17.4 \mu\text{C/cm}^2$ ) และค่าสนามไฟฟ้าลบล้าง ( $30.13 \text{ kV/cm}$ ) ที่เซรามิก BNTCT2 ซินเตอร์ที่อุณหภูมิ 1150 องศาเซลเซียส

#### **สรุปการตรวจสอบของเซรามิกบิสมาทโซเดียมไททาเนต-สทรอนเซียมไททาเนต (1-x)BNT-xST; BNTST100x**

จากผลการวิเคราะห์ด้วยเทคนิคการเลี้ยวเบนของรังสีเอกซ์ของเซรามิก BNTST10, BNTST20, BNTST30 และ BNTST40 ซินเตอร์ที่อุณหภูมิ 1050 -1200 องศาเซลเซียส จากผลการวิเคราะห์ด้วยเทคนิคการเลี้ยวเบนรังสีเอกซ์ของเซรามิก BNTST100x พบว่ามีโครงสร้างแบบคิวบิกในทุกๆตัวอย่าง และผลจากการตรวจสอบโครงสร้างจุลภาคพบว่ารูปร่างเกรนส่วนใหญ่ของเซรามิก

มีลักษณะคล้ายทรงกลมและสีเหลืองมุกจาก เมื่ออุณหภูมิเพิ่มขึ้นขนาดเกรนเฉลี่ยมีค่าเพิ่มขึ้น ในขณะที่ เมื่อปริมาณ  $x$  เพิ่มขึ้นขนาดเกรนเฉลี่ยมีแนวโน้มไม่คงที่ ค่าความหนาแน่น และการหดตัวเชิงเส้นมีค่าเพิ่มขึ้นเมื่ออุณหภูมิซินเตอร์เพิ่มขึ้นเพิ่มขึ้น ค่าคงที่ไดอิเล็กทริกสูงสุด (4725) ค่าความหนาแน่นสูงสุด ( $5.57 \text{ g/cm}^3$ ) ค่าคงที่พิโซอิเล็กทริก ( $90 \text{ pC/N}$ ) และ(ใช้สนามไฟฟ้าเพิ่ม 40 kV) มีค่าโพลาริเซชันคงค้างสูงสุด ( $17.19 \text{ } \mu\text{C/cm}^3$ ) และค่าสนามไฟฟ้าบล้าง ( $29.61 \text{ kV/cm}$ ) ที่เซรามิก BNTST20 ซินเตอร์ที่อุณหภูมิ 1200 องศาเซลเซียส และเซรามิกที่เตรียมได้ด้วยวิธีการเผาไหม้มีค่าสมบัติทางไฟฟ้าสูงกว่าเซรามิกที่เตรียมด้วยวิธีผสมออกไซด์

บรรณานุกรม

## บรรณานุกรม

- [1] Forrester, J. S., Zobec, J. S., Phelan, D. and Kisi, E. H. (2004). Syntensis of  $\text{PbTiO}_3$  ceramics using mechanical alloying and solid state sintering. **Journal of solid state sintering**, 177, 3553-3559.
- [2] Cross, E. (2004). Materials science-lead-free at last. **Nature**, 423, 24-25.
- [3] Meader, M. D., Damjanovic, D. and Setter, N. (2004). Lead free piezoelectric materials. **Journal of Electroceramic**, 13, 385-392.
- [4] Suchanicz, J., Roleder, K., Kania, A. and Handerek, J. (1988). Electrostrictive strain and pyroeffect in the region of phase coexistence in  $\text{Na}_{0.5}\text{Bi}_{0.5}\text{TiO}_3$ . **Ferroelectrics**, 77, 107-110.
- [5] Panya, P. and Bongkarn, T. (2009). Fabrication of perovskite Barium Titanate ceramics via combustion route. **Ferroelectrics**, 383, 102-110.
- [6] Liou, Y. -C., Wu, C. -T., Huang, Y. -L. and Chung T.-C. (2009). Effect of CuO on  $\text{CaTiO}_3$  perovskite ceramics prepared using a direct sintering process. **Journal of Nuclear Material**, 393, 492-496.
- [7] Li, L., Zhao, J. and Gui, Z. (2004). The thermal sensitivity and dielectric properties of  $\text{SrTiO}_3$  based ceramics. **Ceramics International**, 30, 1073-1078.
- [8] Qu, Y., Shan, D. and Song, J. (2005). Effect of A-site substitution on crystal component and dielectric properties in  $\text{Bi}_{0.5}\text{Na}_{0.5}\text{TiO}_3$  ceramics. **Materials Science and Engineering B**, 121, 148-151.
- [9] Park, S. -E., Chung, S. -J. and Kim, I. T. (1996). Ferroic phase transitions in  $(\text{Na}_{1/2}\text{Bi}_{1/2})\text{TiO}_3$  crystals. **Journal of the American Ceramic Society**, 79, 1290-1296.
- [10] Takenaka, T., Maruyama, K. and Sakata, K. (1991).  $(\text{Bi}_{1/2}\text{Na}_{1/2})\text{TiO}_3$ - $\text{BaTiO}_3$  system for lead-free piezoelectric ceramics. **Japanese Journal of Applied Physics**, 30, 2236-2239.

- [11] Cernea, M., Andronesco, E., Radu, R., Fochi, F. and Galassi, C. (2010). Sol-gel synthesis and characterization of BaTiO<sub>3</sub>-doped (Bi<sub>0.5</sub>Na<sub>0.5</sub>)TiO<sub>3</sub> piezoelectric ceramics. **Journal of Alloys and Compounds**, 490, 690-694.
- [12] Liu, Y., Lv, Y., Xu, M., Shi, S., Xu, H. and Yang, X. (2007). Structure and Electric properties of (1-x)(Bi<sub>1/2</sub>Na<sub>1/2</sub>)TiO<sub>3</sub>-xBaTiO<sub>3</sub> System. **Journal of Wuhan University of Technology-Materials**, 22, 315-319.
- [13] Kim, B. -H., Han, S. -J., Kim, J. -H., Lee, J. -H., Ahn, B. -K. and Xu, Q. (2007). Electric properties of (1-x)(Bi<sub>1/2</sub>Na<sub>1/2</sub>)TiO<sub>3</sub>-xBaTiO<sub>3</sub> synthesized by emulsion method. **Ceramics International**, 33, 447-452.
- [14] Yuan, Y., Li, E.Z., Li, B., Tang, B. and Zhou, X. H. (2011). Effects of Ca and Mn additions on the microstructure and dielectric properties of (Bi<sub>0.5</sub>Na<sub>0.5</sub>)TiO<sub>3</sub> ceramics. **Jouurnal of Electronic Materials**, 40, 2234-2239.
- [15] Yuan, Y., Zhoh, X. H., Zhao, C. J., Li, B. and Zhang, S.R. (2010). High-temperature capacitor based on Ca-doped Bi<sub>0.5</sub>Na<sub>0.5</sub>TiO<sub>3</sub>-BaTiO<sub>3</sub> ceramics. **Jouurnal of Electronic Materials**, 39, 2471-2475.
- [16] Krauss, W., Schutz, D., Mautner, F. A., Feteira, A. and Reichmann, K. (2010). Piezoelectric properties and phase transition temperatures of the solid solution of (1-x)Bi<sub>0.5</sub>Na<sub>0.5</sub>TiO<sub>3</sub>-xSrTiO<sub>3</sub>. **Journal of the European Ceramics Society**, 30, 1827-1832.
- [17] Fu, Z., Zhu, R., Wu, D. and Li, A. (2009). Preparation of (1-x%)(Na<sub>0.5</sub>Bi<sub>0.5</sub>)TiO<sub>3</sub>-x%SrTiO<sub>3</sub> thin films by a sol-gel method for dielectric tunable applications. **Journal Sol-Gel Science and Technology**, 49, 29-34.
- [18] Takenaka, T., Nagata, H. and Hiruma, Y. (2008). Current developments and prospective of Lead-Free piezoelectric ceramics. **Japanese Journal of Applied Physics**, 47, 3787-3801
- [19] Thongtha, A. and Bongkarn, T. (2010). Fabrication and characterization of perovskite SrZrO<sub>3</sub> ceramics through a combustion technique. **Key Engineering Materials**, 421-422, 223-226.

- [20] Thongtha, A., Angsukased, K. and Bongkarn, T. (2008). Effects of calcination temperatures on phase and morphology evolution of  $(\text{Ba}_{0.25}\text{Sr}_{0.75})(\text{Zr}_{0.75}\text{Ti}_{0.25})\text{O}_3$  powders synthesized via solid-state reaction and combustion technique. **Advanced Materials Research**, 55-57, 197-200.
- [21] Sittiketkorn, P., Thountom, S. and Bongkarn, T. (2008). Effect of calcination temperatures on phase formation and microstructure of Lead Titanate powders synthesized via combustion technique, **NU Science Journal**, 5, 143-150.
- [22] Sittiketkorn, P., Ramaneepikool, S. and Bongkarn, T. (2010). The Effects of firing temperature on phase formation and microstructure of  $\text{Pb}_{0.975}\text{Sr}_{0.025}\text{TiO}_3$  ceramics synthesized via the combustion technique. **Ferroelectrics**, 403, 158-165.
- [23] Thongtha, A., Angsukased, K. and Bongkarn, T. (2010). Fabrication of  $(\text{Ba}_{1-x}\text{Sr}_x)(\text{Zr}_x\text{Ti}_{1-x})\text{O}_3$  ceramics prepared using the combustion technique. **Smart Materials and structures**, 19, 124001.
- [24] Wattanawikkam C. and Bongkarn, T. (2009). The influence of calcinations temperature on phase and morphology of BST powders synthesis via solid state reaction method and combustion technique. **Ferroelectric**, 282, 42-48.
- [25] Patil, K. C., Aruna, S. T. and Ekambaram, S. (1997). Combustion synthesis. **Current Opinion in Solid State & Materials Science**, 2, 158-165.
- [26] Moulson, A. J. and. Herbert, J. M. (2003). **Electroceramics: materials, properties, applications**. England: West Sussex PO19 8SQ.
- [27] Haertling, G.H. (1999). Ferroelectric ceramics: History and technology. **Journal of the American Ceramic Society**, 82, 797-818.
- [28] Comyn, T. (1998). **Piezoelectric PZT-based ceramics: Principle and applications**. USA: APC international.
- [29] บัญชา ธนบุญสมบัติ. (2544). **การศึกษาวัสดุโดยเทคนิคดิฟแฟรกชัน**. กรุงเทพฯ: สมาคมส่งเสริมเทคโนโลยี.

- [30] กฤษณา ศิวเลิศมกุล. (2545). กล้องจุลทรรศน์อิเล็กตรอนแบบส่องกราดและอุปกรณ์วิเคราะห์ธาตุรังสีเอกซ์. ใน **เครื่องมือวิจัยทางวัสดุศาสตร์: ทฤษฎีและการทำงานเบื้องต้น** (หน้า 289-305). กรุงเทพฯ: สำนักพิมพ์จุฬาลงกรณ์มหาวิทยาลัย.
- [31] สุกานดา เจียรศิริสมบุญ. (1992). กระบวนการประดิษฐ์สำหรับเซรามิกชั้นสูง. ใน **เอกสารประกอบการสอนรายวิชา ว.วศ. 210443**. เชียงใหม่: ภาควิชาฟิสิกส์ คณะวิทยาศาสตร์ มหาวิทยาลัยเชียงใหม่.
- [32] ปราณี รัตนวลิตโรจน์. (2543). การหาความหนาแน่นด้วยเครื่องชั่งไฟฟ้า. ใน **เครื่องมือวิจัยทางวัสดุศาสตร์: ทฤษฎีและการทำงานเบื้องต้น**. กรุงเทพฯ: สำนักพิมพ์จุฬาลงกรณ์มหาวิทยาลัย.
- [33] Anuradha, T.V., Ranganathan, S., Mimani, T. and Patil, K.C. (2001). Combustion synthesis of nanostructured barium titanate. **Scripta Materialia**, 44, 2237-2241.
- [34] Merzhanov, A.G., Borovinskaya, I.P. and Nauk, D. A. (1985). Self-propagating high temperature synthesis. **Combustion Science and Technology**, 43, 127-165.
- [35] Lin, D., Kwok, K.W. and Xu, C. (2008). Structure electrical properties and depolarization temperature of  $(\text{Bi}_{0.5}\text{Na}_{0.5})\text{TiO}_3\text{--BaTiO}_3$  lead-free piezoelectric ceramics. **Solid. State. Sci**, 10, 934-940.
- [36] Hiruma, Y., Imai, Y., Watanabe, Y., Nagata, H. and Takenaka, T. (2008). Large electrostrain near the phase transition temperature of  $(\text{Bi}_{0.5}\text{Na}_{0.5})\text{TiO}_3\text{--SrTiO}_3$  ferroelectric ceramics. **Applied Physics Letters**, 92, 262904.
- [37] Watanabe, Y., Hiruma, Y., Nagata, H. and Takenaka, T. (2008). Phase transition temperatures and electrical properties of divalent ions ( $\text{Ca}^{2+}$ ,  $\text{Sr}^{2+}$  and  $\text{Ba}^{2+}$ ) substituted  $(\text{Bi}_{1/2}\text{Na}_{1/2})\text{TiO}_3$  ceramics. **Ceramics International**, 34, 761-764.
- [38] Chou, C. –S., Yang, R. –Y., Chen. J. –H. and Chou, S. –W. (2010). The optimum conditions for preparing the lead-free piezoelectric ceramics of  $\text{Bi}_{0.5}\text{Na}_{0.5}\text{TiO}_3$  using the Taguchi method. **Powder Technology**, 199, 264-271.



# 1. Output จากโครงการวิจัยที่ได้รับทุนจาก สกว.

ผลงานตีพิมพ์ในวารสารวิชาการระดับนานาชาติจำนวนทั้งสิ้น 28 เรื่อง

1. Panadda Sittiketkorn, Arrak Klinbumrung and Theerachai Bongkarn, "Influence of Excess  $\text{Bi}_2\text{O}_3$  and  $\text{Na}_2\text{CO}_3$  on Crystal Structure and Microstructure of Bismuth Sodium Titanate Ceramics" Key Engineering Materials, 474-476(2011)1711-1714. (Indexed by Elsevier: SCOPUS)
2. Atthakorn Thongtha, and Theerachai Bongkarn, "Optimum Sintering Temperature for Fabrication of  $0.8\text{Bi}_{0.5}\text{Na}_{0.5}\text{TiO}_3 - 0.2\text{Bi}_{0.5}\text{K}_{0.5}\text{TiO}_3$  Lead-Free Ceramics by Combustion Technique" Key Engineering Materials, 474-476(2011)1754-1759. (Indexed by Elsevier: SCOPUS)
3. Ukrit Chaimongkon, Atthakorn Thongtha and Theerachai Bongkarn "The Effect of Firing Temperatures and Barium Content on Phase Formation, Microstructure and Dielectric Properties of Lead Barium Titanate Ceramics Prepared via the Combustion Technique" Current Applied Physics, 11(2011)S70-S76. (Impact Factor: 2012 = 1.814)
4. Rattiphorn Sumang and Theerachai Bongkarn "The Influences of Firing Temperatures and Excess PbO on Crystal Structure and Microstructure of  $(\text{Pb}_{0.25}\text{Sr}_{0.75})\text{TiO}_3$  Ceramics" Journal of Materials Science. 46(2011)6823-6829. (Impact Factor: 2012 = 2.163)
5. Panadda Sittiketkorn and Theerachai Bongkarn "The Preparation of Lead Strontium Titanate Ceramics by the Combustion" Ferroelectrics 414(2011)170-179. (Impact Factor: 2012 = 0.415)
6. Atthakorn Thongtha, Chakkaphan Wattanawikkam and Theerachai Bongkarn "Phase Formation and Dielectric Properties of  $(\text{Pb}_{0.925}\text{Ba}_{0.075})(\text{Zr}_{1-x}\text{Ti}_x)\text{O}_3$  Ceramics Prepared by the Solid State Reaction Method" Phase Transitions, 84(2011)952-959. (Impact Factor: 2012 = 0.863)
7. Chakkaphan Wattanawikkam, Naratip Vittakorn and Theerachai Bongkarn "Low Temperature Fabrication of Lead-free KNN-LS-BS Ceramics via the Combustion Method" Ceramics International, 39(2013)S399-S403. (Impact Factor: 2012 = 1.789)
8. Chittakorn Kornphom, Artid Laowaniwatana and Theerachai Bongkarn "The Effects of Sintering Temperatures and Content of x on Phase Formation, Microstructure and Dielectric Properties of  $(1-x)(\text{Bi}_{0.4871}\text{Na}_{0.4871}\text{La}_{0.0172}\text{TiO}_3) - x(\text{BaZr}_{0.05}\text{Ti}_{0.95}\text{O}_3)$  Ceramics Prepared via the Combustion Technique" Ceramics International, 39(2013)S421-S426. (Impact Factor: 2012 = 1.789)

9. Phongthorn Julphunthong, Suphornpun Chootin and Theerachai Bongkarn "Phase Formation and Electrical Properties of  $\text{Ba}(\text{Zr}_x\text{Ti}_{1-x})\text{O}_3$  Ceramics Synthesized Through a Novel Combustion Technique" *Ceramics International*, 39(2013)S415-S419. (Impact Factor: 2012 = 1.789)
10. Panadda Sittiketkorn and Theerachai Bongkarn "Effects of Sintering Temperature on Phase Formation, Microstructure and the Dielectric Properties of BNT – BT Ceramics near MPB Prepared using the Combustion Technique" *Ferroelectric Letters* 40(2013)77-84. (Impact Factor: 2012 = 0.613)
11. Peerapong Panya, Chakkaphan Wattanawikkam, Artid Laowanidwatana, Naratip Vittayakorn and Theerachai Bongkarn "Optimum Conditions for Fabrication High-Density KNN-LS-BF Ceramics by Combustion Method" *Integrated Ferroelectrics* 148(2013)161-170. (Impact Factor: 2012 = 0.375)
12. Peerapong Panya, Chakkaphan Wattanawikkam, Suphornpun Chootin and Theerachai Bongkarn "Effect of Firing Conditions on Phase Formation, Microstructure and Dielectric Properties of KNN-LS-BN Ceramics Fabricated by Combustion Technique" *Ferroelectrics* 454(2013)119-128. (Impact Factor: 2012 = 0.415)
13. Phongthorn Julphunthong, Sujiphat Janaun and Theerachai Bongkarn "The Effects of Firing Temperatures and Dwell Time on Phase and Morphology Evolution of  $\text{LaNi}_{0.6}\text{Fe}_{0.4}\text{O}_3$  Ceramics Prepared via the Combustion Technique" *Ferroelectrics* 454(2013)135-144. (Impact Factor: 2012 = 0.415)
14. Chittakorn Kornphom, Pamornnarumol Bhupaijit, Naratip Vittayakorn, and Theerachai Bongkarn "Fabrication of 0.62[0.75PMN-0.25PYbN]-0.38PT Ceramics Using One Step Calcination via Combustion Technique" *Ferroelectrics* 456(2013)89-97. (Impact Factor: 2012 = 0.415)
15. Rattiphorn Sumang, Fuangfa Sutamma, Suphornpun Chootin and Theerachai Bongkarn "Influence of Firing Temperatures on Crystal Structure and Microstructure of  $\text{LiNbO}_3$  Ceramics" *Integrated Ferroelectrics* 149(2013)1-8. (Impact Factor: 2012 = 0.375)
16. Rattiphorn Sumang, Naratip Vittayakorn and Theerachai Bongkarn "The Effect of Excess  $\text{PbO}$  on Crystal Structure, Microstructure and Dielectric Properties of  $(\text{Pb}_{0.50}\text{Sr}_{0.50})\text{TiO}_3$  Ceramics" *Ferroelectrics* 456(2013)98-106. (Impact Factor: 2012 = 0.415)
17. Chamaiporn Wicheanrat, Artid Laowanidwatana and Theerachai Bongkarn "Influences of Excess  $\text{Bi}_2\text{O}_3$  and  $\text{K}_2\text{CO}_3$  on Crystal Structure, Microstructure and Dielectric Properties

- of Bismuth Potassium Titanate Ceramics” Integrated Ferroelectrics 149(2013)9-17.  
(Impact Factor: 2012 = 0.375)
18. Atthakorn Thongtha, Sariya Tupmongkol, Artid Laowanidwatana and Theerachai Bongkarn “Combustion Synthesis and Characterization of Perovskite  $(\text{Pb}_{0.75}\text{Ca}_{0.13}\text{Sm}_{0.08})(\text{Ti}_{0.98}\text{Mn}_{0.02})\text{O}_3$  Ceramics” Ferroelectrics 455(2013)6-14. (Impact Factor: 2012 = 0.415)
  19. Atthakorn Thongtha, Artid Laowanidwatana and Theerachai Bongkarn “Phase Formation, Microstructure and Dielectric Properties of Bismuth Potassium Titanate Ceramic Fabricated using the Combustion Technique” Integrated Ferroelectrics 149(2013)32-38. (Impact Factor: 2012 = 0.375)
  20. Panadda Sittiketkorn, Pongkiti Wongtey, Naratip Vittayakorn and Theerachai Bongkarn “The Effect of Firing Temperatures on  $(\text{Pb}_{0.75}\text{Ba}_{0.25})(\text{Zr}_{0.70}\text{Ti}_{0.30})\text{O}_3$  Ceramics Prepared via the Combustion Technique” Integrated Ferroelectrics 149(2013)39-48. (Impact Factor: 2012 = 0.375)
  21. Atthakorn Thongtha, Artid Laowanidwatana and Theerachai Bongkarn “Phase Evolution, Microstructure and Dielectric Properties of  $\text{CaCu}_3\text{Ti}_4\text{O}_{12}$  Ceramics Fabricated by Combustion Technique” Ferroelectrics 457(2013)23-29. (Impact Factor: 2012 = 0.415)
  22. Panadda Sittiketkorn, Artid Laowanidwatana, Naratip Vittayakorn and Theerachai Bongkarn “Influence of Sintering Temperature on Phase Formation, Microstructure and Dielectric Properties of Calcium and Strontium Doped BNT Ceramics Prepared via Combustion Technique” Ferroelectrics 455(2013)54-61. (Impact Factor: 2012 = 0.415)
  23. Phongthorn Julphunthong, Suphornpun Chootin, Benjawan Suansawan and Theerachai Bongkarn “Influence of Firing Temperatures on Phase Formation and Microstructure of  $\text{La}_{0.92}\text{Mg}_{0.18}\text{Fe}_{0.90}\text{O}_3$  Ceramics Synthesized via the Combustion Route” Integrated Ferroelectrics 148(2013)116-123. (Impact Factor: 2012 = 0.375)
  24. Phongthorn Julphunthong, Boonyaphas Phengraek, Artid Laowanidwatana and Theerachai Bongkarn “Low Temperature Fabrication of Dense Calcium Titanate Ceramics via Combustion Technique” Integrated Ferroelectrics 150(2014)107-115. (Impact Factor: 2012 = 0.375)
  25. Krailas Mathrmool, Aniruj Akkarapongtrakul, Supattra Sukkum and Theerachai Bongkarn “Low Temperature Fabrication of Lead-Free KNN-BNT Ceramics via the Combustion Technique” Ferroelectrics 458(2014)136-145. (Impact Factor: 2012 = 0.415)
  26. Chittakron Kronphom, Saranporn Paowsawat and Theerachai Bongkarn “Phase Formation, Microstructure and Electrical Properties of KNN-BZT Ceramics Fabricated

via Combustion Technique" *Ferroelectrics* 458(2014)127-135. (Impact Factor: 2012 = 0.415)

27. C. Kornphom, C. Panich and T. Bongkarn "Phase formation and piezoelectric properties of  $(\text{Pb}_{0.95}\text{Ba}_{0.05})(\text{Zr}_{1-x}\text{Ti}_x)\text{O}_3$  ceramics fabricated by solid state reaction technique" *Materials Research Innovations* 18(S2)(2014)146-150. (Impact Factor: 2012 = 0.321)
28. P. Julphunthong and T. Bongkarn "Phase formation, microstructure and dielectric properties of  $\text{Bi}_{0.5}(\text{Na}_{0.74}\text{K}_{0.16}\text{Li}_{0.10})_{0.5}\text{TiO}_3\text{-Ba}(\text{Zr}_{0.5}\text{Ti}_{0.95})\text{O}_3$  ceramics prepared via combustion technique" *Materials Research Innovations* 18(S2)(2014)151-156. (Impact Factor: 2012 = 0.321)

## 2. การนำผลงานวิจัยไปใช้ประโยชน์

### - เชิงพาณิชย์

โครงการวิจัยนี้ได้สร้างองค์ความรู้ใหม่เกี่ยวกับการประดิษฐ์เซรามิกเพอร์โรอิเล็กทริกที่อุณหภูมิต่ำด้วยวิธีการเผาไหม้ ซึ่งสามารถนำไปประยุกต์ใช้ในเชิงพาณิชย์ และเป็นองค์ความรู้พื้นฐานของอุตสาหกรรมได้เป็นอย่างดี

### - เชิงนโยบาย

ผลงานที่ได้จากโครงการวิจัยนี้ได้ ใช้เป็นตัวกำหนดทิศทางการวิจัยที่จะทำต่อในอนาคต และใช้เป็นส่วนช่วยในการกำหนดหัวข้อวิจัยในมุมมองอื่นๆ สำหรับนักศึกษา และผู้ร่วมวิจัยในสาขาอื่นๆ ซึ่งเป็นประโยชน์ในการเชื่อมโยงองค์ความรู้ให้เกิดหลากหลายมากขึ้น

### - เชิงสาธารณะ

โครงการวิจัยนี้ได้เกิดเครือข่ายงานวิจัยกับหลากหลายภาคส่วนด้วยกันทั้งในองค์กรภายในมหาวิทยาลัยและองค์กรนอกมหาวิทยาลัย เช่น ศาสตราจารย์ ดร. กอบวุฒิ รุจิจนากุล จากห้องปฏิบัติการอิเล็กทรอนิกส์เซรามิก จาก ภาควิชาฟิสิกส์ คณะวิทยาศาสตร์ มหาวิทยาลัยเชียงใหม่ ความร่วมมือกับ ผู้ช่วยศาสตราจารย์ ดร.นราธิป วิทยากร จากภาควิชาเคมี คณะวิทยาศาสตร์ สถาบันเทคโนโลยีพระจอมเกล้าเจ้าคุณทหารลาดกระบัง ผู้วิจัยได้มีโครงการความร่วมมือกับนักวิจัยต่างประเทศหลายท่าน อาทิเช่น Prof. Dr. Steven J. Milne จาก Institute for Materials Research, University of Leeds ประเทศอังกฤษ Prof. Dr. Tadashi Takenaka จาก Department of Electrical Engineering, Tokyo University of Science ประเทศญี่ปุ่น และ Prof. Dr. David P. Cann จากห้องปฏิบัติการอิเล็กทรอนิกส์เซรามิก มหาวิทยาลัยโอเรกอน ประเทศสหรัฐอเมริกา

### - เชิงวิชาการ

ผลงานวิจัยที่เกิดขึ้นบางส่วนนำไปประยุกต์ใช้สอนในกระบวนวิชาเซรามิกไฟฟ้า ในระดับบัณฑิตศึกษา นอกจากนั้นประสบการณ์ที่ได้จากงานวิจัยยังสามารถนำไปประยุกต์ อบรมเจ้าหน้าที่และ ผู้ช่วยวิจัยให้มีทักษะและความชำนาญมากยิ่งขึ้น ก่อให้เกิดองค์ความรู้ในองค์กร

ผลงานวิจัยส่วนใหญ่สามารถตีพิมพ์ในวารสารระดับนานาชาติ รวมไปถึงการเสนอผลงานวิจัยในงานประชุมวิชาการที่เกี่ยวข้องทั้งในระดับชาติและนานาชาติ อีกทั้งยังเกิดนักวิจัยรุ่นใหม่ขึ้น

ภาคผนวก

## Influence of Excess $\text{Bi}_2\text{O}_3$ and $\text{Na}_2\text{CO}_3$ on Crystal Structure and Microstructure of Bismuth Sodium Titanate Ceramics

Panadda Sittiketkorn<sup>a</sup>, Arrak Klinbumrung<sup>b</sup> and Theerachai Bongkarn<sup>\*c</sup>

<sup>a</sup>Department of Physics, Faculty of Science, Naresuan University, Phitsanulok, Thailand

<sup>b</sup>Division of Material Science, Faculty of Science, Phayao University, Phayao, Thailand

<sup>\*c</sup> Department of Physics, Faculty of Science, Naresuan University, Phitsanulok, Thailand

<sup>a</sup>may\_panat@hotmail.com, <sup>b</sup>arrakin@hotmail.com, <sup>\*c</sup>researchcmu@yahoo.com

**Keywords:** Bismuth Sodium Titanate, Excess  $\text{Bi}_2\text{O}_3$ , Excess  $\text{Na}_2\text{CO}_3$ , Crystal structure, Microstructure

### Abstract

This study investigated the influence of excess  $\text{Bi}_2\text{O}_3$  and  $\text{Na}_2\text{CO}_3$  on the crystal structure, microstructure and dielectric properties of  $(\text{Bi}_{0.5}\text{Na}_{0.5})\text{TiO}_3$  (BNT) ceramics. The BNT ceramics were synthesized using the solid-state reaction method with various excess  $\text{Bi}_2\text{O}_3$  and  $\text{Na}_2\text{CO}_3$  levels (0, 1, 2, 3 and 4 mol%). The X-ray characterization revealed that all samples had a rhombohedral structure. A pure perovskite phase was obtained in all samples. The lattice parameter  $a$  tended to increase with increased excess  $\text{Bi}_2\text{O}_3$  and  $\text{Na}_2\text{CO}_3$  content in the calcined powders and sintered ceramics. The average particle size increased while, the average grain size tended to decreased with increased of excess  $\text{Bi}_2\text{O}_3$  and  $\text{Na}_2\text{CO}_3$  content. The depolarization temperature ( $T_d$ ) and the Curie temperature ( $T_c$ ) were slightly decreased with the increase of excess  $\text{Bi}_2\text{O}_3$  and  $\text{Na}_2\text{CO}_3$  content. The dielectric properties were related to the density.

### Introduction

Bismuth sodium titanate  $[(\text{Bi}_{0.5}\text{Na}_{0.5})\text{TiO}_3]$  BNT is a type of perovskite-type ferroelectric, which has been considered to be a good candidate for lead-free ceramics because of its relatively large remanant polarization ( $P_r = 38 \mu\text{C}/\text{cm}^2$ ) at room temperature and high Curie temperature ( $T_c = 320^\circ\text{C}$ ) [1,2]. Therefore, BNT ceramics have been applied for use in capacitor and actuator devices [2,3]. However, in fabricated BNT ceramics, the  $\text{Bi}_2\text{O}_3$  and  $\text{Na}_2\text{CO}_3$  are always evaporated during the firing process at high temperatures. Evaporation of  $\text{Bi}_2\text{O}_3$  and  $\text{Na}_2\text{CO}_3$  change the properties of the ceramics due to the change of stoichiometry. Moreover, it is well known that the optimum amount of excess  $\text{Bi}_2\text{O}_3$  and  $\text{Na}_2\text{CO}_3$  lead to ceramics with a high density and good electrical properties, which is important in device applications [4-6].

So, in this work, some excess  $\text{Bi}_2\text{O}_3$  and  $\text{Na}_2\text{CO}_3$  were added during the batch preparation to compensate for the  $\text{Bi}_2\text{O}_3$  and  $\text{Na}_2\text{CO}_3$  loss in the samples, which were prepared by the solid-state reaction method. The effect of the amount of excess  $\text{Bi}_2\text{O}_3$  and  $\text{Na}_2\text{CO}_3$  on the phase formation, microstructure and dielectric properties of BNT ceramics were also investigated.

### Experimental

$\text{Bi}_{0.5}\text{Na}_{0.5}\text{TiO}_3$  (BNT) was fabricated using an established mixed oxide method. An excess of  $\text{Bi}_2\text{O}_3$  and  $\text{Na}_2\text{CO}_3$ , equivalent to 0, 1, 2, 3 and 4 mol% were added. The raw materials  $\text{Bi}_2\text{O}_3$ ,  $\text{Na}_2\text{CO}_3$  and  $\text{TiO}_2$  were weighed and mixed by ball milling in ethanol using zirconia balls for 24 h. The mixed powders were dried at  $120^\circ\text{C}$  for 6 h. After sieving, the mixing powders were calcined at  $800^\circ\text{C}$  for 2 h. The calcined powders were reground by wet ball milling with 2 wt% binder for 24 h. The obtained powders were pressed into pellets with a diameter of 15 mm prior to sintering at  $1200^\circ\text{C}$  for 2 h. X-ray diffraction (XRD) was performed to examine the phase constitution of the specimens at room temperature. The microstructures of the BNT samples were examined using scanning electron microscopy (SEM). The densities of the sintered ceramics were measured by the

Archimedes's method. Dielectric measurements were performed using a LCR meter (Agilent 4263B), and the measuring frequency was 1 kHz.

### Results and discussion

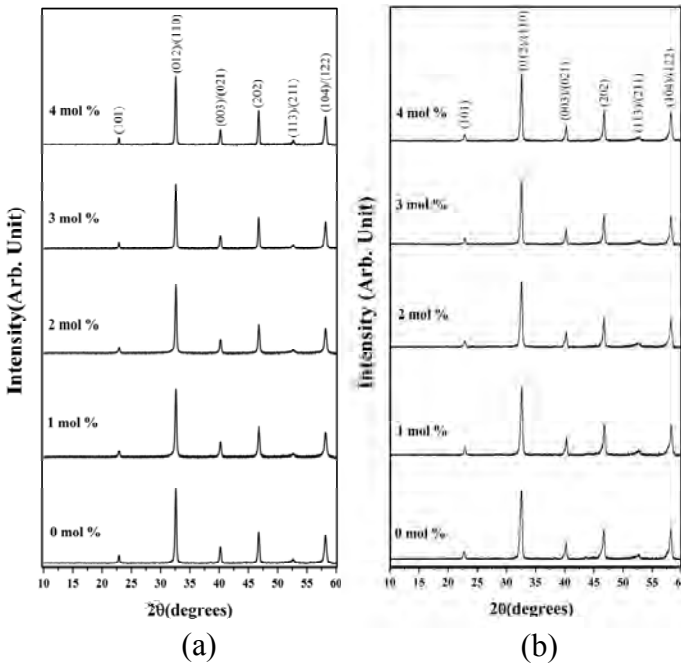


**Fig. 1** XRD patterns of (a) calcined powders and (b) sintered ceramics made from starting powders containing different amounts of excess  $\text{Bi}_2\text{O}_3$  and  $\text{Na}_2\text{CO}_3$ .

The XRD patterns of BNT calcined powders and sintered ceramics at various  $\text{Bi}_2\text{O}_3$  and  $\text{Na}_2\text{CO}_3$  content are shown in Fig. 1(a) and 1(b). The BNT powders and ceramics index in the rhombohedral structure, could be matched with the JCPDS file number 36-0340 [7]. The pure perovskite phase of BNT calcined powders and sintered ceramics were obtained in all samples.

The lattice parameter  $a$  of the BNT rhombohedral structure was calculated by the following equation [8].

$$a_R = \frac{1}{3} \sqrt{3(a_H^2) + c^2} \quad (1)$$

$a_H$  and  $c$  are the lattice parameter of the hexagonal structure, and  $a_R$  is the lattice parameter of the rhombohedral structure.

**Table 1** Lattice parameter  $a$ , average particle size and grain size, shrinkage and density of BNT calcined powders and sintered ceramics

Excess	Calcined powders		Sintered ceramics			
$\text{Bi}_2\text{O}_3$ and $\text{Na}_2\text{CO}_3$	Lattice parameter $a$	Average particle size	Lattice parameter $a$	Average grain size	Shrinkage	Density
(mol%)	(Å)	(μm)	(Å)	(μm)	(%)	(g/cm <sup>3</sup> )
0	3.8797	0.20	3.8720	11.33	20.9	5.90
1	3.8798	0.24	3.8722	1.96	21.0	5.91
2	3.8801	0.32	3.8755	1.83	18.6	5.98
3	3.8824	0.27	3.8798	1.53	9.5	5.63
4	3.8844	1.89	3.8840	1.43	7.7	5.58



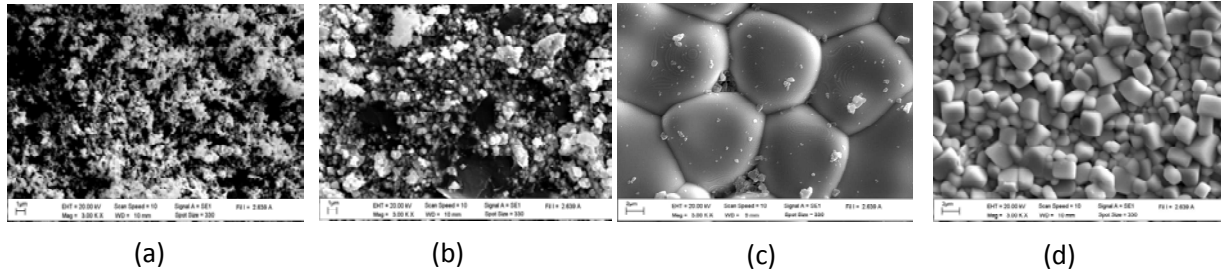


**Fig. 2** SEM photomicrographs of the calcined powders with excess  $\text{Bi}_2\text{O}_3$  and  $\text{Na}_2\text{CO}_3$ ; (a) 0 mol%, (b) 3 mol% and sintered ceramics with excess  $\text{Bi}_2\text{O}_3$  and  $\text{Na}_2\text{CO}_3$ ; (d) 0 mol%, (e) 2 mol%.

The lattice parameter  $a$  of the BNT calcined powders and sintered ceramics tended to increase with the increase of excess  $\text{Bi}_2\text{O}_3$  and  $\text{Na}_2\text{CO}_3$  content (Table 1).

The calcined powders exhibited an almost spherical morphology and have a porous agglomerated form as shown in Fig. 2 (a), and (b). The average particle size increased from 0.20 to 1.89  $\mu\text{m}$  with an increase excess of  $\text{Bi}_2\text{O}_3$  and  $\text{Na}_2\text{CO}_3$  content. The grain sizes were nearly spherical in shape (Fig. 2 (c) and (d)). When the excess  $\text{Bi}_2\text{O}_3$  and  $\text{Na}_2\text{CO}_3$  increased, the grain size changed from a spherical morphology to a nearly cubic shape. The average grain sizes rose from 1.43 to 11.33  $\mu\text{m}$ . The average particle size increased while, the average grain size tended to decrease with the increase of excess  $\text{Bi}_2\text{O}_3$  and  $\text{Na}_2\text{CO}_3$  content (Table 1).

The shrinkage and density of BNT sintered ceramics are listed in Table 1. The shrinkage increased with an increase of excess  $\text{Bi}_2\text{O}_3$  and  $\text{Na}_2\text{CO}_3$  content. The density increased with the increase of excess  $\text{Bi}_2\text{O}_3$  and  $\text{Na}_2\text{CO}_3$  content and reached a maximum at 2 mol% and then dropped in value when the excess  $\text{Bi}_2\text{O}_3$  and  $\text{Na}_2\text{CO}_3$  content was higher than 2 mol%, as seen in Table 1.

Fig. 3 exhibits the dielectric constant ( $\epsilon_r$ ) different excess  $\text{Bi}_2\text{O}_3$  and  $\text{Na}_2\text{CO}_3$  contents. The  $\epsilon_r$  peak exhibited two dielectric anomalies at  $T_d$  and  $T_c$ .  $T_d$  which is the depolarization temperature, and corresponds to the transition from the ferroelectric state to an anti-ferroelectric state,  $T_c$  is Curie temperature and relates the transition from an anti-ferroelectric state to a paraelectric state [8].

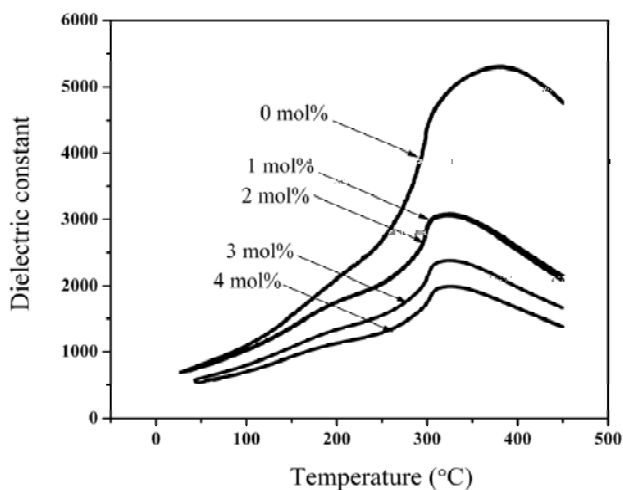


**Fig. 3** Dielectric constant of BNT ceramics at various  $\text{Bi}_2\text{O}_3$  and  $\text{Na}_2\text{CO}_3$  content, measured at 1 kHz.

The  $T_d$  and  $T_c$  decreased from 217 to 181°C and from 376 to 317°C with the increase of excess  $\text{Bi}_2\text{O}_3$  and  $\text{Na}_2\text{CO}_3$  contents (Table 2). The  $\epsilon_r$  at  $T_c$  decreased with the increase of excess  $\text{Bi}_2\text{O}_3$  and  $\text{Na}_2\text{CO}_3$  contents as seen in Fig. 3. The dielectric loss at  $T_c$  tended to decreased with increased excess  $\text{Bi}_2\text{O}_3$  and  $\text{Na}_2\text{CO}_3$  contents up to 2 mol% and increased after further excess  $\text{Bi}_2\text{O}_3$  and  $\text{Na}_2\text{CO}_3$  contents (Table 2).

**Table 2** The dielectric properties of BNT ceramics

Excess Bi <sub>2</sub> O <sub>3</sub> and Na <sub>2</sub> CO <sub>3</sub> (mol%)	T <sub>d</sub> (°C)	T <sub>c</sub> (°C)	Dielectric constant at T <sub>c</sub>	Loss tangent at T <sub>c</sub>
0	217	376	5301	0.252
1	203	325	3082	0.021
2	190	323	3062	0.013
3	186	317	2369	0.019
4	181	328	1993	0.02

### Summary

The excess of Bi<sub>2</sub>O<sub>3</sub> and Na<sub>2</sub>CO<sub>3</sub> affected phase formation, microstructure, density, and dielectric properties. The lattice parameter *a* tended to increase with an increased excess Bi<sub>2</sub>O<sub>3</sub> and Na<sub>2</sub>CO<sub>3</sub> content in the calcined powders and sintered ceramics. The average particle size increased while, the average grain size tended to decrease with increased excess Bi<sub>2</sub>O<sub>3</sub> and Na<sub>2</sub>CO<sub>3</sub> content. At T<sub>c</sub>, a high density, dielectric constants and low dielectric loss were discovered in the sample with excess 2 mol% of Bi<sub>2</sub>O<sub>3</sub> and Na<sub>2</sub>CO<sub>3</sub> content.

### Acknowledgment

This work was financially supported by the Thailand Research Fund (TRF), Commission on Higher Education (CHE). The authors wish to thank the Science Lab Center, Faculty of Science, Naresuan University for supporting facilities. Thanks are also given to Mr. Don Hindle for his help in editing the manuscript.

### References

- [1] G.A. Smolenskii, V.A. Isupov, A.I. Agranovskaya and N.N. Krainik: Phys. Solid State, Vol. 2 (1961), p. 2651.
- [2] K. Rolede, J. Suchanicz and A. Kania: Ferroelectrics, Vol. 89 (1989), p. 1.
- [3] J. Hao, X. Wang, R. Chen and L. Li: Mater. Chem. Phys., Vol. 90 (2005), p. 282.
- [4] R. Zuoa, S. Sua, Y. Wua, J. Fua, M. Wanga and L. Li: Mater. Chem. Phys., Vol. 110 (2008), p. 311.
- [5] D. Shan, Y. Qu and J. Song: Mater. Sci. Eng. B, Vol. 121 (2005), p. 148.
- [6] D. Xiao, H. Yan, P. Yu, J. Zhu, D. Lin and G. Li: Mater. Des., Vol. 26 (2005), p. 474.
- [7] Powder diffraction files no. 36-0340: International Center for Diffraction data. New ton Square: PA; 2003.
- [8] D. Lin, C. Xu and Q. Zheng: J. Mater. Sci., Vol. 20 (2009), p. 393.

## **Advanced Materials and Computer Science**

doi:10.4028/www.scientific.net/KEM.474-476

### **Influence of Excess $\text{Bi}_2\text{O}_3$ and $\text{Na}_2\text{Co}_3$ on Crystal Structure and Microstructure of Bismuth Sodium Titanate Ceramics**

doi:10.4028/www.scientific.net/KEM.474-476.1711

# Optimum Sintering Temperature for Fabrication of $0.8\text{Bi}_{0.5}\text{Na}_{0.5}\text{TiO}_3$ - $0.2\text{Bi}_{0.5}\text{K}_{0.5}\text{TiO}_3$ Lead-Free Ceramics by Combustion Technique

Atthakorn Thongtha<sup>a</sup> and Theerachai Bongkarn<sup>\*b</sup>

Department of Physics, Faculty of Science, Naresuan University, Phitsanulok, 65000, THAILAND

<sup>a</sup>Jerran99\_@hotmail.com, <sup>\*b</sup>researchcmu@yahoo.com

**Keywords:** Sintering, Microstructure, Morphotropic phase boundary, BNKT, Combustion technique

**Abstract.** The effect of sintering temperatures (1050-1200 °C) on the phase formation, microstructure and dielectric properties of a binary system lead-free ceramic bismuth sodium titanate–bismuth potassium titanate were investigated.  $0.8\text{Bi}_{0.5}\text{Na}_{0.5}\text{TiO}_3$ - $0.2\text{Bi}_{0.5}\text{K}_{0.5}\text{TiO}_3$ ; BNKT ceramics were successfully fabricated using the combustion technique. XRD results showed the rhombohedral-tetragonal morphotropic phase boundary (MPB). The SEM results showed the average grain size (0.51-2.59 μm) of the samples increased with the increase of sintering temperatures. The sample sintered at the optimum temperature of 1150 °C exhibited the maximum density, shrinkage, dielectric constant at Curie temperature and remanent polarization ( $P_r$ ) which were around 5.65 g/cm<sup>3</sup>, 17.75%, 5014 and 1.6 μC/cm<sup>2</sup>, respectively. The dielectric constant was related to the XRD results and density of the sintered ceramic.

## Introduction

Recently,  $\text{Bi}_{0.5}\text{Na}_{0.5}\text{TiO}_3$  (BNT) and  $\text{Bi}_{0.5}\text{K}_{0.5}\text{TiO}_3$  (BKT) are two attractive lead-free materials, which were considered to be the significant attention to replace the widely used lead-containing perovskite materials because there are a relative large remanent polarization and high Curie temperature [1-5]. Among the (1-x)BNT–xBKT system, it possesses a rhombohedral-tetragonal morphotropic phase boundary (MPB) at  $x = 0.16$ – $0.20$  [2]. Furthermore, many previous researches exhibited the outstanding electrical properties at  $x=0.20$  [1-3].

Presently, the combustion technique is interesting because it can decrease the calcination and sintered temperature [6,7], obtain a highly dense and the good electrical properties [6,8]. Besides, it is well known that the optimal sintered condition lead to obtain the ceramics with high dielectric constant and polarization. However, a detailed study of the fabrication and characterization of  $0.8\text{Bi}_{0.5}\text{Na}_{0.5}\text{TiO}_3$ - $0.2\text{Bi}_{0.5}\text{K}_{0.5}\text{TiO}_3$ ; BNKT ceramics via the combustion technique has not been reported in the literature. Thus, the BNKT ceramics were prepared via the combustion technique in this work. The effect of sintering temperatures on the phase formation, microstructure, dielectric and ferroelectric properties of BNKT ceramics were also investigated

## Experimental

Bismuth sodium potassium titanate [ $0.8\text{Bi}_{0.5}\text{Na}_{0.5}\text{TiO}_3$ - $0.2\text{Bi}_{0.5}\text{K}_{0.5}\text{TiO}_3$ ; BNKT] powders were synthesized by the combustion technique. For preparation ( $\text{Bi}_{0.5}\text{Na}_{0.5}\text{TiO}_3$ ; BNT powder, the raw materials of  $\text{Bi}_2\text{O}_3$  (99%),  $\text{Na}_2\text{CO}_3$  (99%) and  $\text{TiO}_2$  (99%) were weighed. A thoroughly ground mixture of raw materials were ground by a ball milling procedure (zirconia milling media under ethanol for 24 h). Drying was carried out at 120 °C for 4 h. The raw powders were well-mixed with fuel (glycine) in an agate mortar before the calcination step. Afterwards, the uncalcined powders of BNT were calcined at 650 °C with a dwell time of 1 h and a heating/cooling rate of 5 °C/min. For synthesis ( $\text{Bi}_{0.5}\text{K}_{0.5}\text{TiO}_3$ ; BKT powder, the raw materials of  $\text{Bi}_2\text{O}_3$  (99%),  $\text{K}_2\text{CO}_3$ , (99%) and  $\text{TiO}_2$  (99%) were weighed in the required stoichiometric ratio and the raw materials were mixed by a ball milling procedure. The processing of BKT powders is similar to BNT powders, but the uncalcined powders of BKT were calcined at 850 °C for 2 h.

The calcined powders of BNT and BKT were weighed and mixed in the required stoichiometric ratio with a 2 wt.% binder solution and reground by ball milling for 24 h. The mixed calcined powders were then pressed into disks with a diameter of 15 mm at a pressure of 80 MPa. The pellets

were sintered between 1050 and 1200 °C for 2 h and cooled in a furnace. X-ray diffraction (XRD; Philip PW3040/60 X' Pert Pro) was employed to identify the phase formed and the optimum temperature for the optimum formation of BNKT ceramics. The morphological features of the product were imaged using scanning electron microscopy (SEM; LEO 1455 VP). The density of the sintered ceramics was measured by the Archimedes method. The average grain sizes were determined by using the mean linear intercept method. The raw data were obtained by measuring the grain sizes over 300 grains. Silver paste was coated and fired at 600 °C for 5 min to form electrodes. The dielectric property as a function of temperature was also observed using a LCR impedance analyzer (Agilent 4263B). The polarization hysteresis (P-E) loops were measured by using a ferroelectric test system (Radiant Technologies, Inc.).

## Results and discussion

The XRD diffraction patterns of sintered ceramics with various sintering temperatures are shown in Fig. 1. BNKT ceramics are identified as a pure perovskite phase below 1175 °C. The peak of  $\text{Bi}_2\text{O}_3$  was detected at 1200 °C, which may be due to the vaporization of  $\text{K}^+$  at high temperatures. Generally, the rhombohedral symmetry is characterized by a (003)/(021) peak splitting between 38° and 42° and a single (202) peak between 45° and 48° [1]. While, the tetragonal symmetry, it is identified by a single (111) peak between 38° and 42° and a (002)/(200) peak splitting between 45° and 48° [1]. In case of this work, the tetragonal and rhombohedral symmetry of BNKT at the sintering temperature  $\geq 1125$  °C are characterized by the (002)/(200) and (003)/(021) peaks splitting in the  $2\theta$  range of 45-48° and 38-42°, respectively. So, it can be inferred that this composition lies in the MPB, where the rhombohedral and tetragonal phases coexist, which could be matched with JCPDS file number 36-0339 and 36-0340 and corresponded to previous work [1,3]. While, the peak splitting of (003)/(021) between 38° and 42° and (002)/(200) between 45° and 48° were not distinctively appeared at the sintering temperature  $\leq 1100$  °C. This result may be due to the BNKT ceramics were not fully crystallized at low sintered temperature ( $\leq 1100$  °C).

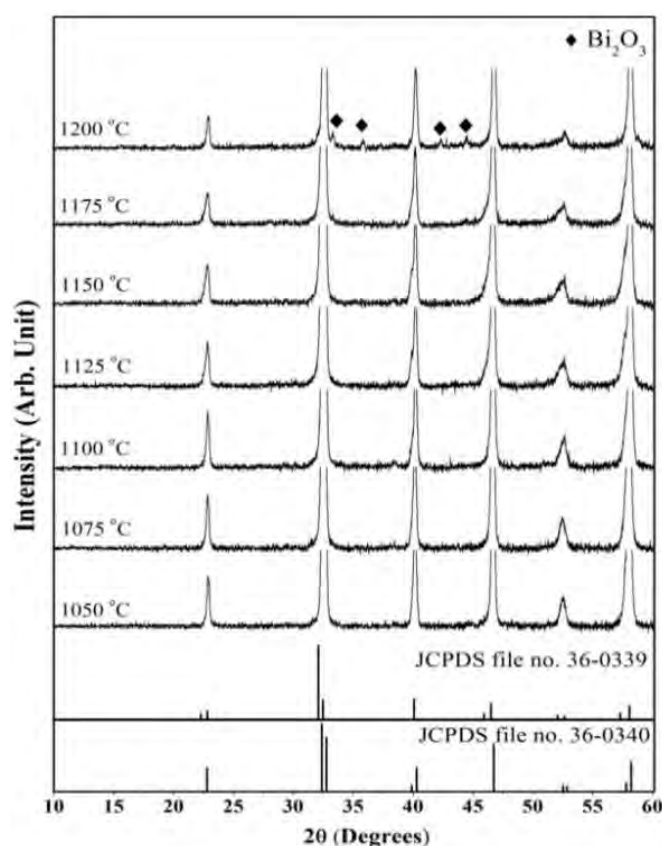


**Fig. 1** X-ray patterns of BNKT ceramic at various sintering temperatures in the  $2\theta$  range of 10° to 60°.



Fig. 2 illustrated the morphological changes in the BNKT surface of the sintered ceramics as a function of sintered temperatures. The point touches between particles grew into necks which exhibited the primary state of sintering at the sintering temperature  $\leq 1100$  °C, as shown in Fig. 3 (a). The increasing of sintered temperature up to  $1100$  °C caused still no evident change in the microstructure except for a slight increase in the grain size. When the sintering temperature increased higher than  $1100$  °C and reached its highest at  $1150$  °C, the grain growth became increasingly active. At the same time, the pore structure was also decreased and led to an obvious change in the feature of grain size. While, the porosity of samples sintered  $> 1150$  °C increased as shown in Fig. 3 (d). The grain growth exhibited an almost similarly rectangular morphology, as shown in Fig. 3 (b)-(d). The average grain sizes increased from  $0.51$  to  $2.59$   $\mu\text{m}$  when the sintering temperatures increased from  $1050$  to  $1200$  °C, as shown in Table 1.

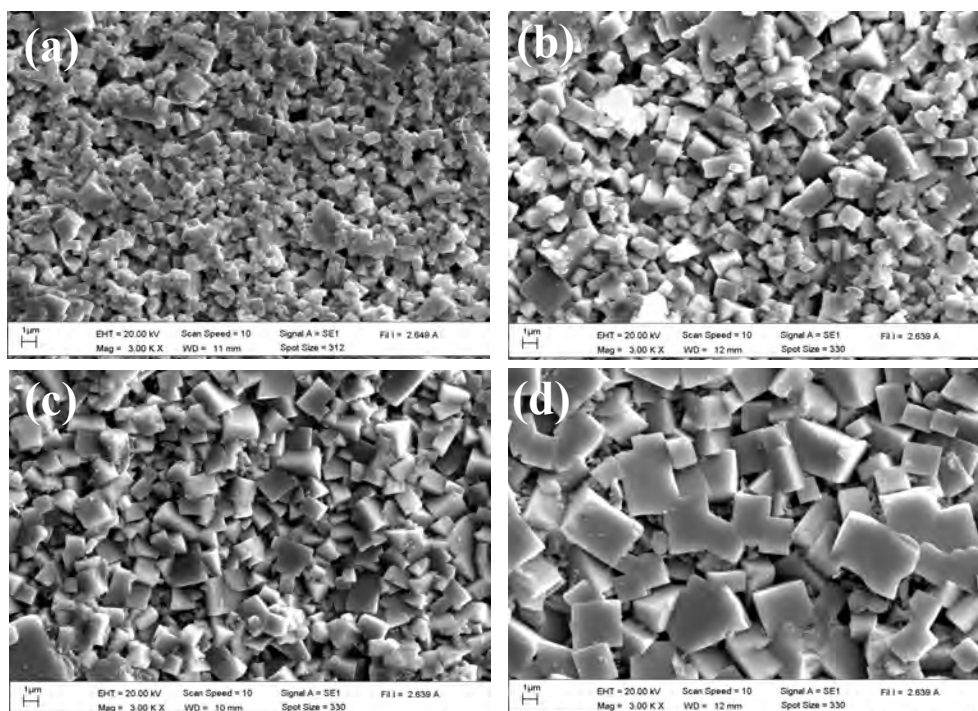


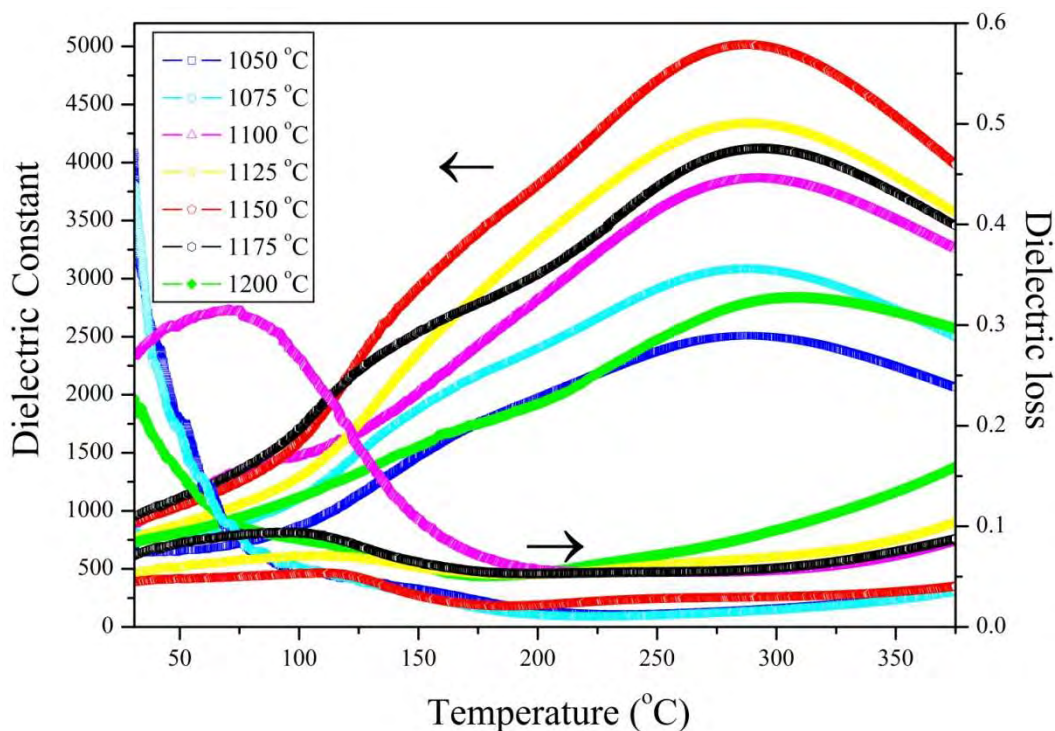
**Fig. 2** SEM photographs of BNKT ceramics sintered at; (a)  $1075$  °C, (b)  $1125$  °C, (c)  $1150$  °C and (d)  $1200$  °C

The measured density with a variation of the sintering temperatures is shown in Table 1. The density first increased and reached its highest at  $1150$  °C and then dropped value when the sintering temperature was higher than  $1150$  °C, as shown in Table 1. It was noticed that the density decreased when the sintered temperature was higher than an optimal temperature in the sintering process. The maximum density was around  $5.65$   $\text{g}/\text{cm}^3$  or  $\sim 94.5\%$  of the theoretical density obtained from the sample sintered at  $1150$  °C for 2 h. During the sintering process, the densification mechanisms during treatment corresponded to the XRD results and the grain growth, especially at the final stage of sintering. The density decreases when the sintering temperature is higher than the optimal temperature may be due to distending from the trapped gas in the pores. The gas-filled pores combined and grew because of the grain growth [9]. The percent of shrinkage of the pellet samples was listed in Table 1. The tendency of percent shrinkage was the same trend with the density as a function of sintered temperatures. The percent shrinkage first increased and reached its highest at  $1150$  °C. Then, the percent shrinkage of ceramics decreased as the sintered temperature increased above  $1150$  °C.

**Table 1** The average grain size, density and shrinkage of BNKT samples

Sintered temperature (°C)	Average grain size (μm)	Density (g/cm <sup>3</sup> )	Relative density (%)	Shrinkage (%)
1050	0.51±0.06	4.99	83.5	10.17
1075	0.66±0.09	5.17	86.5	12.53
1100	1.02±0.12	5.41	90.5	15.67
1125	1.13±0.16	5.61	93.8	17.10
1150	1.18±0.18	5.65	94.5	17.75
1175	1.58±0.20	5.46	91.3	16.17
1200	2.59±0.37	5.02	84.0	10.81

Fig. 3 shows the temperature dependence of the dielectric constant ( $\epsilon_r$ ) and dielectric loss tangent of BNKT ceramics which were measured at 10 kHz. The samples sintered at temperature  $\leq 1100$  °C, the dielectric constant showed a broadened peak around 260 °C, which was due to the phase transition from an antiferroelectric to paraelectric state [1,10]. While, the samples sintered  $> 1100$  °C, the dielectric constant showed 2 broadened peaks. The first broadened peak of various sintered samples showed an anomaly in the similar range of temperature as shown in Table 2, which was due to the phase transition from the ferroelectric to antiferroelectric state [1,10]. The second broadened peaks of each condition were above 265 °C, which was caused by an antiferroelectric-paraelectric transformation process [1,10]. At Curie temperature, the maximum dielectric constant was observed in the samples, which first increased and reached its highest at 1150 °C and then dropped value when the sintering temperature was higher than 1150 °C. The dielectric loss at  $T_c$  was shown in Table 2. In case of the samples sintered at temperature  $\leq 1100$  °C, showed only a peak may be caused from the fully crystalline have not still formed. These results corresponded to the XRD results and density.

**Fig. 3** Temperature dependence of the dielectric constant and dielectric loss tangent of BNKT ceramics measured at 10 kHz.

The maximum density ceramic which obtained by sintered at 1150 °C, were used to investigate ferroelectric properties. Fig. 4 showed the P-E hysteresis loop of BNKT sample with difference electric fields strengths at room temperature. It is clearly seen that the shape of hysteresis different greatly with the electric fields strength. A near-linear relationship of P-E is observed at 5 kV/cm electric fields strength. This result is due to the fact that the electric field is not large enough to switch any domains. The polarization nonlinearity is improved in both regions of the positive and negative fields at 10 kV/cm electric fields. These demonstrated that the electric field strength of 10 kV/cm is of enough energy to constrain realignment of some domains in the direction of the applied fields. The largest of symmetric hysteresis loop is revealed at 35 kV/cm electric field strength, which displays the remanent polarization ( $P_r$ ) of 1.6  $\mu\text{C}/\text{cm}^2$  and coercive field  $E_c$  of 10.1 kV/cm. Due to the limiting of the based instrument, the saturated hysteresis loop has not been still obtained at 35 kV/cm electric field strength when compared with previous works [1-2].

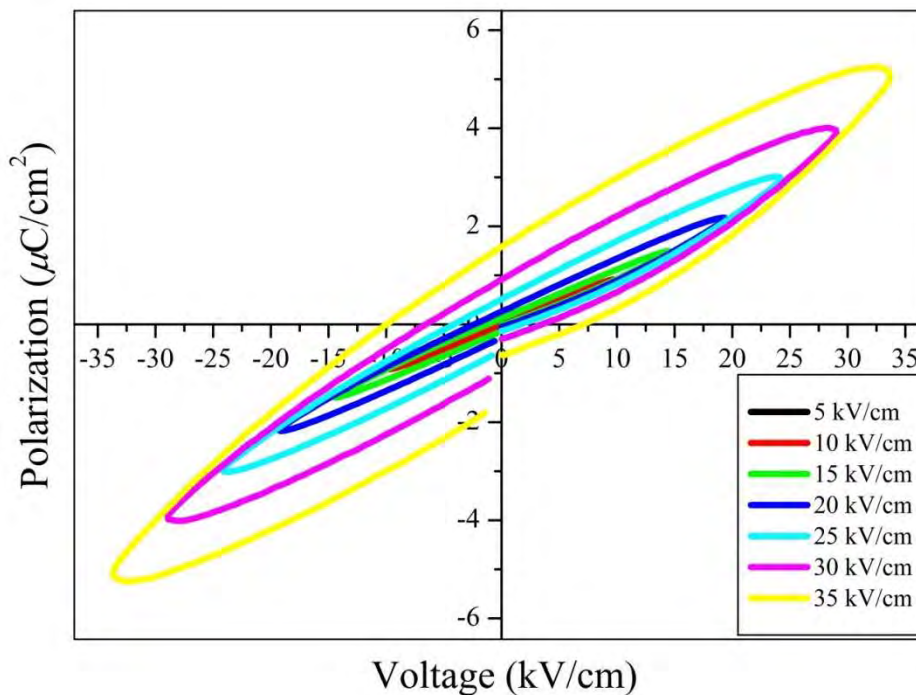


**Fig. 4** P-E hysteresis loop of BNKT ceramic sintered at 1150 °C.

**Table 2** Range of depolarization temperature ( $T_d$ ), curie temperature ( $T_c$ ), dielectric constant ( $\epsilon_r$ ), and loss tangent ( $\tan \delta$ ) of BNKT ceramics at various sintering temperature.

Sintered temperature (°C)	Range of $T_d$ (°C)	$T_c$ (°C)	$\epsilon_r$ (at $T_c$ )	$\tan \delta$ (at $T_c$ )
1050	-	261	2508	0.0170
1075	-	263	3085	0.0153
1100	-	254	3859	0.0541
1125	110-180	269	4336	0.0675
1150	105-176	280	5014	0.0293
1175	104-175	274	4123	0.0575
1200	100-170	276	2840	0.1013



## Summary

High density and dielectric properties of BNKT ceramics can be obtained successfully by the combustion method. The sintering temperatures directly affect crystal structure, microstructure, density and dielectric properties of the sintered ceramics. The range of the average grain size increased with the increase of sintering temperatures. The maximum densities ~95% of the theoretical density, dielectric constant at  $T_c$  and percent of shrinkage were received from the ceramics sintered at the optimal temperature of 1150 °C for 2 h. The remanent polarization ( $1.6 \mu\text{C}/\text{cm}^2$ ) and coercive field (10.1 kV/cm) were also obtained from the sample sintered at 1150 °C.

## Acknowledgments

This work was supported financially by the Thailand Research Fund (TRF), Commission on Higher Education (CHE), The Science Achievement Scholarship of Thailand, Faculty of Science, Naresuan University. Thanks also to the Science Lab Center, Faculty of Science, Naresuan University for support facilities. Acknowledgements also to Mr. Don Hindle, for his helpful correction of the manuscript.

## References

- [1] M. Otonicar, S.D. Skapin, M. Spreitzer and D. Suvorov: J Eur. Ceram. Soc., Vol. 30 (2010), p. 971.
- [2] A. Sasaki, T. Chiba, Y. Mamyia and E. Otsuki: Jpn. J. Appl. Phys., Vol. 38 (1999), p. 5564.
- [3] H. Xie, L. Jin, D. Shen, X. Wang and G. Shen: J. Cryst. Growth, Vol. 311 (2009), p. 3626.
- [4] O. Elkechai, M. Manier and J. P. Mercurio: Phys. Status Solidi (A), Vol. 157 (1996), p 499.
- [5] K. Yoshii, Y. Hiruma, H. Nagata and T. Takenaka: Jpn. J. Appl. Phys., Vol. 45 (2006), p. 4493.
- [6] A. Thongtha and T. Bongkarn: Ferroelectrics, Vol. 383 (2009), p. 33.
- [7] A. Thongtha and T. Bongkarn: Key Eng. Mater., Vol. 421-422 (2010), p. 223.
- [8] P. Julphunthong and T. Bongkarn: Curr. Appl. Phys., (In Press).
- [9] R.M. German: Sintering Theory and Practice (New York, Wiley 1996).
- [10] X.J. Yi, H.C. Chen, W.W. Cao, M.L. Zhao, D.M. Yang, G.P. Ma, C.H. Yang and J.R. Han: J. Cryst. Growth, Vol. 281 (2005), p. 364.

## **Advanced Materials and Computer Science**

doi:10.4028/www.scientific.net/KEM.474-476

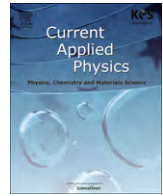
### **Optimum Sintering Temperature for Fabrication of**

**$0.8\text{Bi}_{0.5}\text{Na}_{0.5}\text{TiO}_3$ -**

**$0.2\text{Bi}_{0.5}\text{K}_{0.5}\text{TiO}_3$  Lead-Free Ceramics by**

### **Combustion Technique**

doi:10.4028/www.scientific.net/KEM.474-476.1754



# The effects of firing temperatures and barium content on phase formation, microstructure and dielectric properties of lead barium titanate ceramics prepared via the combustion technique

Ukrit Chaimongkon, Atthakorn Thongtha, Theerachai Bongkarn\*

Department of Physics, Faculty of Science, Naresuan University, Pitsanulok-Nakonsawan Rd, Phitsanulok 65000, Thailand

## ARTICLE INFO

### Article history:

Received 25 June 2010

Received in revised form

9 February 2011

Accepted 14 March 2011

Available online 21 March 2011

### Keywords:

Lead barium titanate

Microstructure

Phase formation

Dielectric constant

Combustion technique

## ABSTRACT

This work concentrated on the phase formation, microstructure and dielectric properties of  $(\text{Pb}_{1-x}\text{Ba}_x)\text{TiO}_3$ ; PBT ceramics with  $0.2 \leq x \leq 0.8$  prepared by the combustion technique under various calcination ( $600\text{--}1200\text{ }^\circ\text{C}$ ) and sintering temperatures ( $1125\text{--}1275\text{ }^\circ\text{C}$ ) for 2 h. It was found that the PBT powders indexed in a tetragonal structure. The impurity phases of lead oxide ( $\text{PbO}$ ), lead dioxide ( $\text{PbO}_2$ ), titanium dioxide ( $\text{TiO}_2$ ) and barium carbonate ( $\text{BaCO}_3$ ) were detected in the powders calcinated below  $1000\text{ }^\circ\text{C}$ ,  $1050\text{ }^\circ\text{C}$ ,  $1100\text{ }^\circ\text{C}$  and  $1150\text{ }^\circ\text{C}$  for  $x = 0.2, 0.4, 0.6$  and  $0.8$ , respectively. The XRD results corresponded to the DTA-TGA investigations. The sintered pellets showed pure perovskite in all samples. The lattice parameter  $a$  tended to decrease, while the lattice parameter  $c$  tended to increase with increased firing temperatures. The tetragonality, the average particles size, and the average grain size increased when the firing temperatures increased. The dielectric constant was depended on the sintering temperature. The Curie temperature decreased when  $x$  increased. The combustion fuel (urea) performed an important role for reducing soak time and improved the density and dielectric properties.

© 2011 Elsevier B.V. All rights reserved.

## 1. Introduction

Lead titanate,  $\text{PbTiO}_3$ ; PT is a perovskite-type ferroelectric material with excellent dielectric, pyroelectric and piezoelectric properties. At room temperature, PT exhibits a tetragonal perovskite structure. PT has a very high Curie temperature of  $490\text{ }^\circ\text{C}$  [1,2]. The Curie point of PT can be shifted to a lower temperature by substituting barium for lead [3,4]. The lead barium titanate,  $(\text{Pb}_{1-x}\text{Ba}_x)\text{TiO}_3$ ; PBT is indexed with a tetragonal structure at room temperature and a cubic structure above its Curie temperatures [5]. The Curie temperature of PBT materials drop monotonically with the Ba content, from  $490\text{ }^\circ\text{C}$  at  $x = 0$  to  $120\text{ }^\circ\text{C}$  at  $x = 1$ . PBT ceramics also exhibit a large positive temperature coefficient of resistance (PTCR) near the Curie temperature [4].

After a survey of the literature, the PBT ceramics were prepared by the solid state reaction method [3] and the polymerized citrate method [6]. For the solid state reaction method, the raw materials were calcined above  $500\text{ }^\circ\text{C}$  for 24 h and at  $950\text{ }^\circ\text{C}$  for a further 24 h. This procedure was repeated twice and then the samples were

sintered at specific temperatures (from  $950$  to  $1250\text{ }^\circ\text{C}$ ) for 24 h [3]. P.R. Arya et al. prepared PBT nano powder by the polymerized citrate method. The precursor was obtained from a mixture of a stoichiometric amount of barium carbonate, lead nitrate in ethylene glycol-citric acid-Ti-isopropoxide solution. The polymerization occurred by keeping the mixed solution in an oven at  $135 \pm 5\text{ }^\circ\text{C}$  for 20 h. The precursor was calcinated at  $500\text{ }^\circ\text{C}$  for 24 h and at  $800\text{ }^\circ\text{C}$  for 8 h. The particle size of the calcined powders was in the range of  $40\text{--}60\text{ nm}$ . A large dielectric constant ( $60\text{--}80$ ) and low dielectric loss ( $0.005$ ) were also obtained [6]. Chemical synthesis can provide homogenous nanosized oxides of high purity at lower reaction temperatures but they have a high material costs and are intricate and complicated to prepare [4,6,7]. It is well-known that the most fundamental, practical, routine technique which provides more product is the solid state reaction method [3,8]. However, PBT ceramics, which are synthesized by solid state reaction, require complicated processes and use a long soak time ( $>140\text{ h}$ ). Thus, a technique which is simple and has low material cost was required for PBT ceramics fabrication.

Recently, our previous work has successfully fabricated different oxides ceramics such as:  $\text{BaZrO}_3$  [9],  $\text{SrZrO}_3$  [10],  $\text{BaTiO}_3$  [11],  $\text{CaZrO}_3$  [12],  $\text{Ba}(\text{Ti}_{1-x}\text{Zr}_x)\text{O}_3$  [13],  $(\text{Ba}_{1-x}\text{Sr}_x)(\text{Zr}_x\text{Ti}_{1-x})\text{O}_3$  [14] by the combustion technique. This technique involves a self-sustained

\* Corresponding author. Tel.: +66 869253326; fax: +66 55963528.

E-mail address: [researchcmu@yahoo.com](mailto:researchcmu@yahoo.com) (T. Bongkarn).

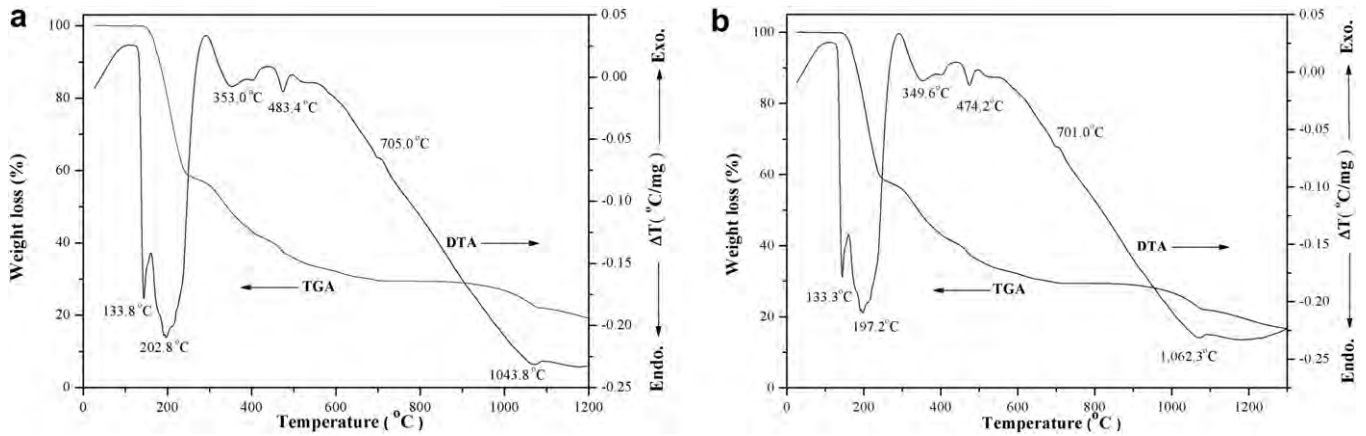


Fig. 1. TGA-DTA curves for the mixture of raw materials and urea with; (a) PBT40 and (b) PBT60.

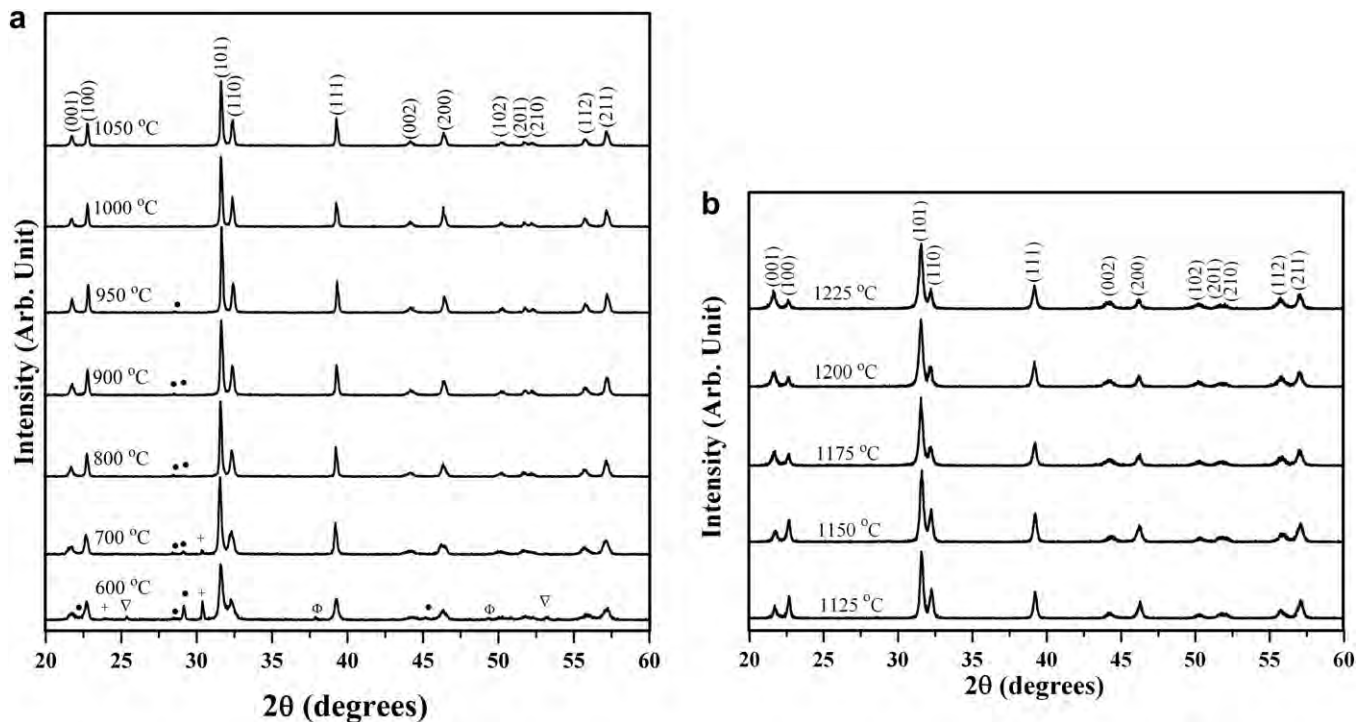
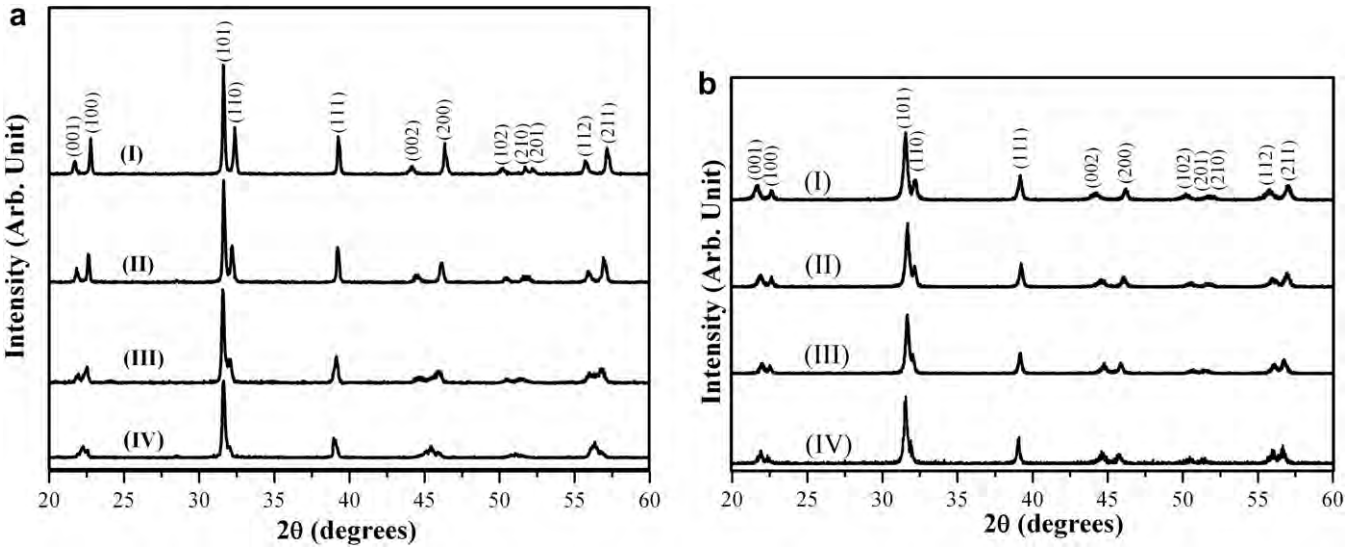


Fig. 2. (a) XRD patterns of PBT20 powders calcined at various temperatures for 2 h; (Φ) PbO, (●) PbO<sub>2</sub>, (+) BaCO<sub>3</sub> and (▽) TiO<sub>2</sub>, (b) XRD patterns of PBT20 ceramics sintered at various temperatures.

reaction between the reactive materials and the fuel (e.g., urea) which supplies a liquid medium at the start of the reaction. The reaction can react easily in a liquid system because the diffusion coefficient is higher than in the solid medium [9,15]. The combustion technique can reduce the soak time, obtain a high density and has good electrical properties [9–16]. Furthermore, from a survey of the literature, (Pb<sub>1-x</sub>Ba<sub>x</sub>)TiO<sub>3</sub> ceramics, prepared by the combustion method, have not been studied. Thus, in this work, (Pb<sub>0.8</sub>Ba<sub>0.2</sub>)TiO<sub>3</sub> [PBT20], (Pb<sub>0.6</sub>Ba<sub>0.4</sub>)TiO<sub>3</sub> [PBT40], (Pb<sub>0.4</sub>Ba<sub>0.6</sub>)TiO<sub>3</sub> [PBT60], and (Pb<sub>0.2</sub>Ba<sub>0.8</sub>)TiO<sub>3</sub> [PBT80] ceramics were prepared via the combustion method. The effects of firing temperatures and the change of the *x* content on the phase formation, microstructure, and dielectric properties of PBT were also investigated and compared with previous work.

## 2. Experimental

Lead barium titanate ceramics were prepared via the combustion technique. The appropriate amounts of PbO (99% purity), BaCO<sub>3</sub> (98.5% purity) and TiO<sub>2</sub> (99% purity) were mixed by ball milling for 24 h with ethanol using zirconia balls. After drying at 120 °C and sieving, the mixture of raw materials and the fuel, urea, in a ratio of 1:2 by weight, were well-mixed in an agate mortar [9–14,17]. Then, the mixed powders were calcined using various calcination temperatures ranging from 600 to 1200 °C for 2 h at a heating/cooling rate of 5 °C/min. The reaction of the uncalcined PBT powders and urea fuel taking place during the heat treatment, were investigated by thermogravimetric analysis and differential thermal analysis (TGA-DTA). The calcined powders were pressed



**Fig. 3.** (a) XRD patterns of PBT powders; (I) PBT20 calcined at 1000 °C, (II) PBT40 calcined at 1050 °C, (III) PBT60 calcined at 1100 °C and (IV) PBT80 calcined at 1150 °C (b) XRD patterns of PBT ceramics; (I) PBT20 sintered at 1200 °C, (II) PBT40 sintered at 1200 °C, (III) PBT60 sintered at 1225 °C and (IV) PBT80 sintered at 1250 °C.

into pellets with a diameter of 15 mm at a pressure of 60 MPa and sintered for 2 h over a range of temperatures between 1125 and 1275 °C. The calcined powders and sintered ceramics were characterized with respect to phase identification and lattice parameters by using an X-ray diffractometer (XRD). The morphological features of the product were imaged using scanning electron microscopy (SEM) and transmission electron microscopy (TEM). The average particle size and average grain size were determined by using a mean linear intercept method. The densities of the

sintered pellets were measured via the Archimedes method. The dielectric constant at 1 kHz was observed by an LCR meter.

3. Results and discussion

The TGA-DTA traces of urea and the uncalcined powders of PBT40 are illustrated in Fig. 1(a). It exhibited three distinct weight losses. The first weight loss occurred between 122 and 223 °C and was associated with endothermic peaks at 133.8 and 202.8 °C.

**Table 1**  
% perovskite phase, average particle size, average grain size, density, Curie temperature, and dielectric properties of PBT.

Calcined powders				Sintered ceramics					
x	Calcination temperature (°C)	% perovskite phase	Average particle size (μm)	Sintering temperature (°C)	Average grain size (μm)	density (g/cm <sup>3</sup> )	T <sub>c</sub> (°C)	Dielectric constant at T <sub>c</sub>	Dielectric loss at T <sub>c</sub>
0.2	600	44.0	0.37	1125	1.04	7.11	435	2036	15.54
	700	82.5	0.38	1150	1.12	7.19	430	2613	12.72
	800	93.5	0.53	1175	1.52	7.20	430	8131	31.93
	900	94.2	0.60	1200	1.94	7.31	418	42,920	7.36
	950	97.2	0.63	1225	2.31	7.11	415	20,910	9.19
	1000	100.0	0.68						
	1050	100.0	0.97						
	1100	100.0	1.37						
0.4	600	39.3	0.42	1125	0.70	6.79	370	1150	0.56
	700	60.8	0.45	1150	0.81	6.86	365	1830	0.55
	800	88.5	0.52	1175	0.96	6.94	361	3673	0.54
	900	97.3	0.74	1200	1.14	7.01	357	7852	1.43
	950	97.4	0.78	1225	1.30	6.52	354	6252	1.20
	1000	97.5	0.90						
	1050	100.0	0.94						
	1100	100.0	1.37						
0.6	700	46.8	0.27	1175	1.15	6.04	292	1795	0.15
	800	77.7	0.45	1200	1.35	6.17	290	2540	0.21
	900	88.1	0.72	1225	1.74	6.58	290	3374	0.28
	950	89.8	0.73	1250	3.91	6.49	286	3173	0.17
	1000	90.2	0.80	1275	7.51	6.39	280	2650	0.16
	1050	96.6	0.85						
	1100	100.0	0.86						
	1150	100.0	0.87						
0.8	800	80.2	0.42	1175	1.12	5.94	223	887	0.02
	900	80.4	0.45	1200	1.38	5.95	212	1062	0.02
	950	86.0	0.52	1225	1.37	6.04	210	1317	0.02
	1000	86.5	0.74	1250	2.35	6.20	208	1845	0.03
	1050	88.5	0.78	1275	2.52	6.19	207	1732	0.04
	1100	89.9	0.91						
	1150	100.0	0.94						
	1200	100.0	1.37						



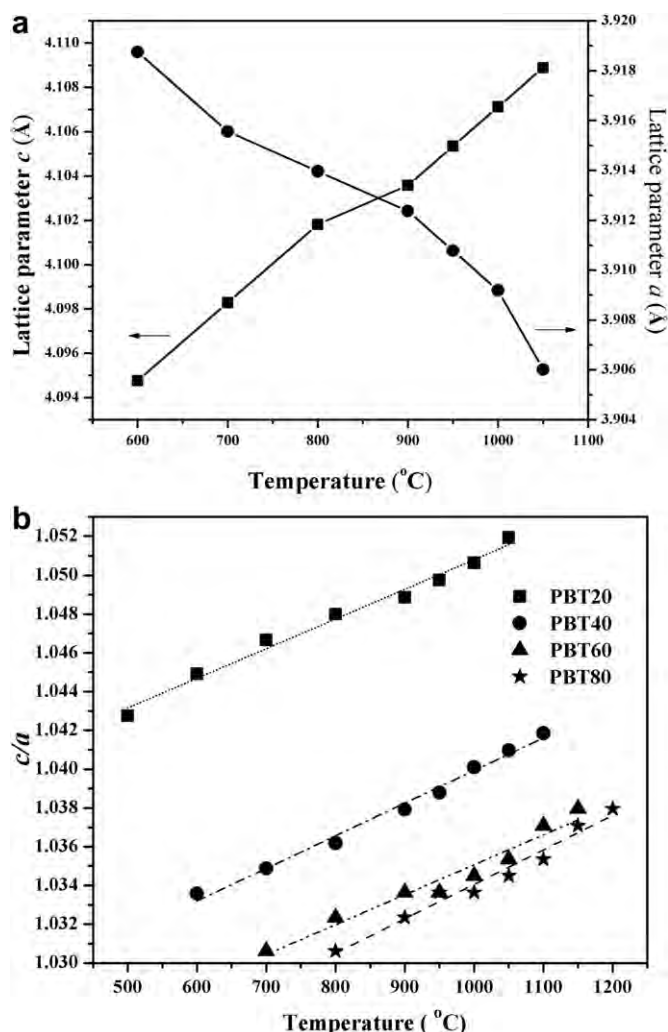


Fig. 4. (a) Plot of the lattice parameter *c* and *a* of PBT20 powders, (b) *c/a* ratio of PBT powders at various calcined temperatures.

These DTA peaks can be attributed to the melting of the urea which normally occurs at about 135 °C [15] as is shown in Formula (1). The second weight loss was found at less than 497 °C, and related to endothermic peaks at 353.0 °C and 483.4 °C in the DTA curve. This weight loss was due to the rapid vaporization of water and gas which was the result of the decomposition of ammonia as exhibited in Formula (2) [10,15,18]. The combustion reaction process occurred during these two steps. The molten urea and the decomposition of the ammonia supplied a liquid environment, in which the diffusion coefficient was higher than in the solid medium. This caused the raw materials to have a more uniform distribution. Furthermore, the energy obtained from the combustion of urea (as shown in Formula (1)) and the oxidation–reduction reaction between ammonia and NO (as shown in Formula (2)) was also released. The combustion energy reduced the particle size of the powder. These results affected the chemical reaction and accelerated the reaction in the next step.



The last weight loss was discovered above 550 °C, which correlated with a small endotherm around 705.0 °C and the

endothermic peak at 1043.8 °C. These may be ascribed as the beginning and completion points of the reaction of the raw materials. Fig. 1(b) shows the TGA-DTA simultaneous analysis of a powder mixed in stoichiometric proportions of PBT60 and urea. It was found that, the results of PBT60 were similar to PBT40 but the reaction process of the PBT60 could be completed at around 1062.3 °C. These results were used to identify the range of different calcination temperatures.

XRD patterns of PBT20 powder calcined at various temperatures are plotted in Fig. 2(a). The X-ray analysis indicated that PBT20 calcined from 600 to 1050 °C, has mainly a set peak with a major peak at (101). The crystal structure belonged to a tetragonal phase, which could be matched with JCPDS file number 74-2492 [19]. The starting materials (PbO, BaCO<sub>3</sub>, TiO<sub>2</sub>) and the impurity phase (PbO<sub>2</sub>), were found in the PBT20 powders calcined below 1000 °C. Above 1000 °C the second phases disappeared and the sample showed a pure perovskite phase. The results of PBT40, PBT60 and PBT80 were similar to PBT20, but the purity phase of PBT40, PBT60 and PBT80 was obtained from powders calcined at higher temperatures than 1050, 1100 and 1150 °C as shown in Fig. 3(a).

The relative amounts of the perovskite phase were calculated by measuring major peak intensities of the perovskite phase. The percentage of perovskite is described by the following equation:

$$\% \text{ perovskite phase} = \left( \frac{I_{\text{perov}}}{I_{\text{perov}} + I_{\text{PbO}} + I_{\text{PbO}_2} + I_{\text{BaCO}_3} + I_{\text{TiO}_2}} \right) \times 100 \quad (3)$$

This equation is well-known and widely employed in connection with the preparation of complex perovskite structure materials [17,20], where  $I_{\text{perov}}$ ,  $I_{\text{PbO}}$ ,  $I_{\text{PbO}_2}$ ,  $I_{\text{BaCO}_3}$  and  $I_{\text{TiO}_2}$  refer to the intensity of the (101) perovskite peak, and the intensities of the highest PbO, PbO<sub>2</sub>, BaCO<sub>3</sub> and TiO<sub>2</sub>, respectively. The percent of the perovskite phase of PBT powders with various calcination temperatures was computed and is listed in Table 1. The percentage of the perovskite phase increased with an increase in the calcination temperatures and the highest percentage was observed in powders calcined above 1000, 1050, 1100 and 1150 °C for PBT20, PBT40, PBT60 and PBT80, respectively. The XRD results of PBT corresponded to the results of DTA-TGA. Xing et al. [3] prepared the pure PBT powders via the solid state reaction method, by calcining at 500 °C and again at 950 °C and using a soak time longer than 140 h. The calcination temperatures in this work were between 1000 and 1150 °C, and the soak time was only for 2 h. This indicated that the combustion technique is an alternate way to save energy and time.

The lattice parameters (*c* and *a*) of PBT20 powders with different calcined temperatures (600–1050 °C) were computed from the (100), (001), (200) and (002) reflective peaks of XRD patterns and are shown in Fig. 4(a). The lattice parameter *c* increased, while the lattice parameter *a* decreased with an increase in the calcination temperatures. The results were similar with PBT40, PBT60 and PBT80. The tetragonality (*c/a*) of PBT powders with different calcination temperatures is exhibited in Fig. 4(b). The tetragonality of PBT powders increased with an increase in the calcination temperatures. At the same calcination temperature, the tetragonality decreased with the increase of the barium ion content (Fig. 4(b)). This result was similar to previous work [21].

Fig. 5(a), (b) and (c) shows the SEM micrographs of PBT20 powders at different calcined temperatures. The synthesized PBT20 powders consisted of ultra-fine particulates. The particles were highly agglomerated and basically irregular in shape with a substantial variation in particle size. The obtained particle size of PBT powders increased as the calcination temperatures increased (Table 1). The results were similar to PBT40, PBT60, and PBT80.

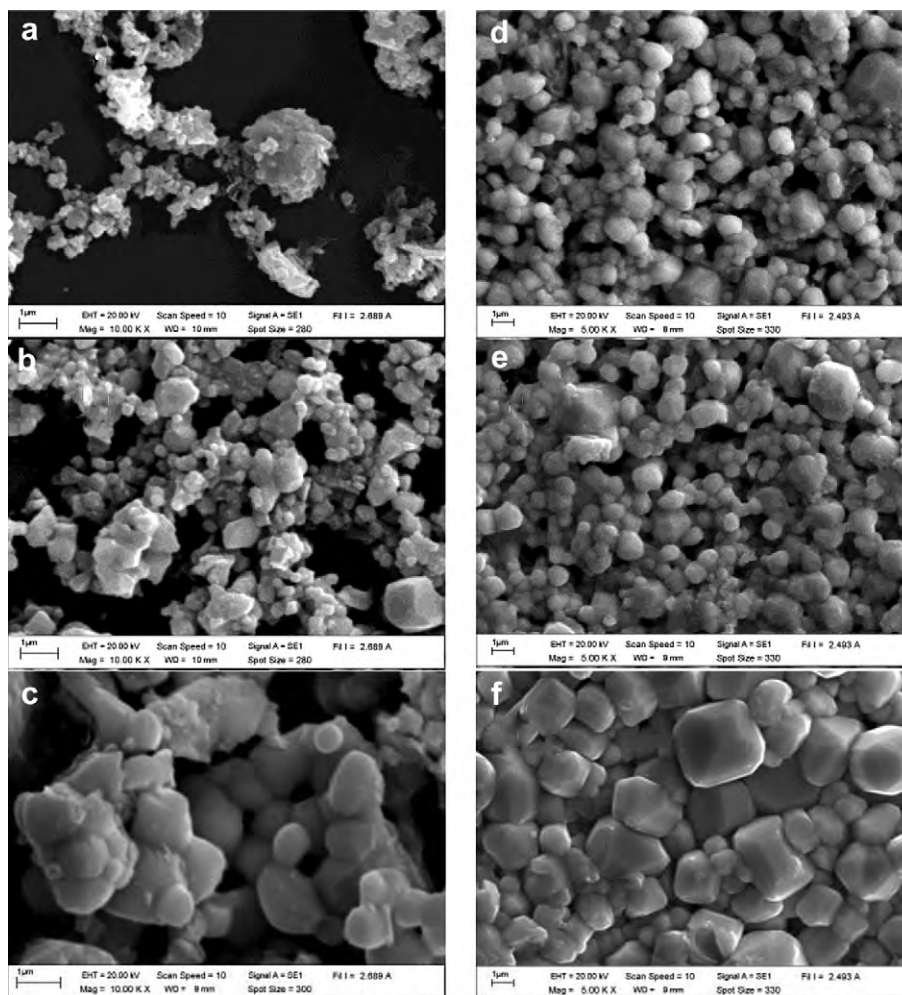


**Fig. 5.** SEM morphology of calcined powders; (a) PBT40 calcined at 700 °C, (b) PBT40 calcined at 900 °C, (c) PBT40 calcined at 1100 °C and sintered ceramics; (d) PBT80 sintered at 1175 °C, (e) PBT80 sintered at 1200 °C and (f) PBT80 sintered at 1250 °C.

At the same calcination temperature, the effect of the barium content had no influence on particle sizes.

The pure phase of PBT20, PBT40, PBT60, and PBT80 powders calcined at 1000, 1050, 1100, and 1150 °C was observed by TEM as shown in Fig. 6. The details of the aggregated particles can be seen in the high magnification images. The powders of PBT have irregular shaped particles and have a porous agglomerated form. The agglomerated particles of PBT20, PBT40, PBT60, and PBT80 exhibited a diameter of around 450, 480, 600, and 625 nm. The

almost fine particles of PBT have a similar spherical shape. The size of the fine primary particles is in the range of 25–85, 28–90, 32–98 nm and 36–103 nm with an average value size around 54, 60, 70, and 77 nm, obtained from PBT20, PBT40, PBT60, and PBT80, respectively. These indicated that the combustion technique produced nano-powders of PBT powders. However, TEM results were different in their values when compared with the particle size from the SEM image. This may have been caused by the agglomeration affects in the SEM results.

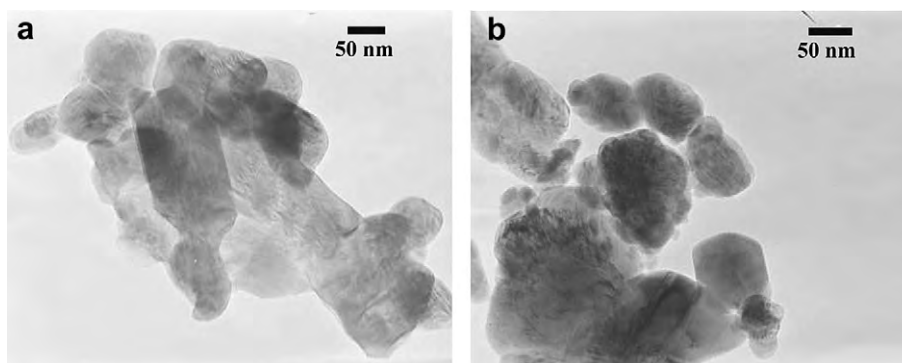


**Fig. 6.** TEM micrographs of (a) original magnification  $\times 120,000$  of PBT40 powder calcined at 1050 °C and (b) original magnification  $\times 100,000$  of PBT80 powder calcined at 1150 °C.

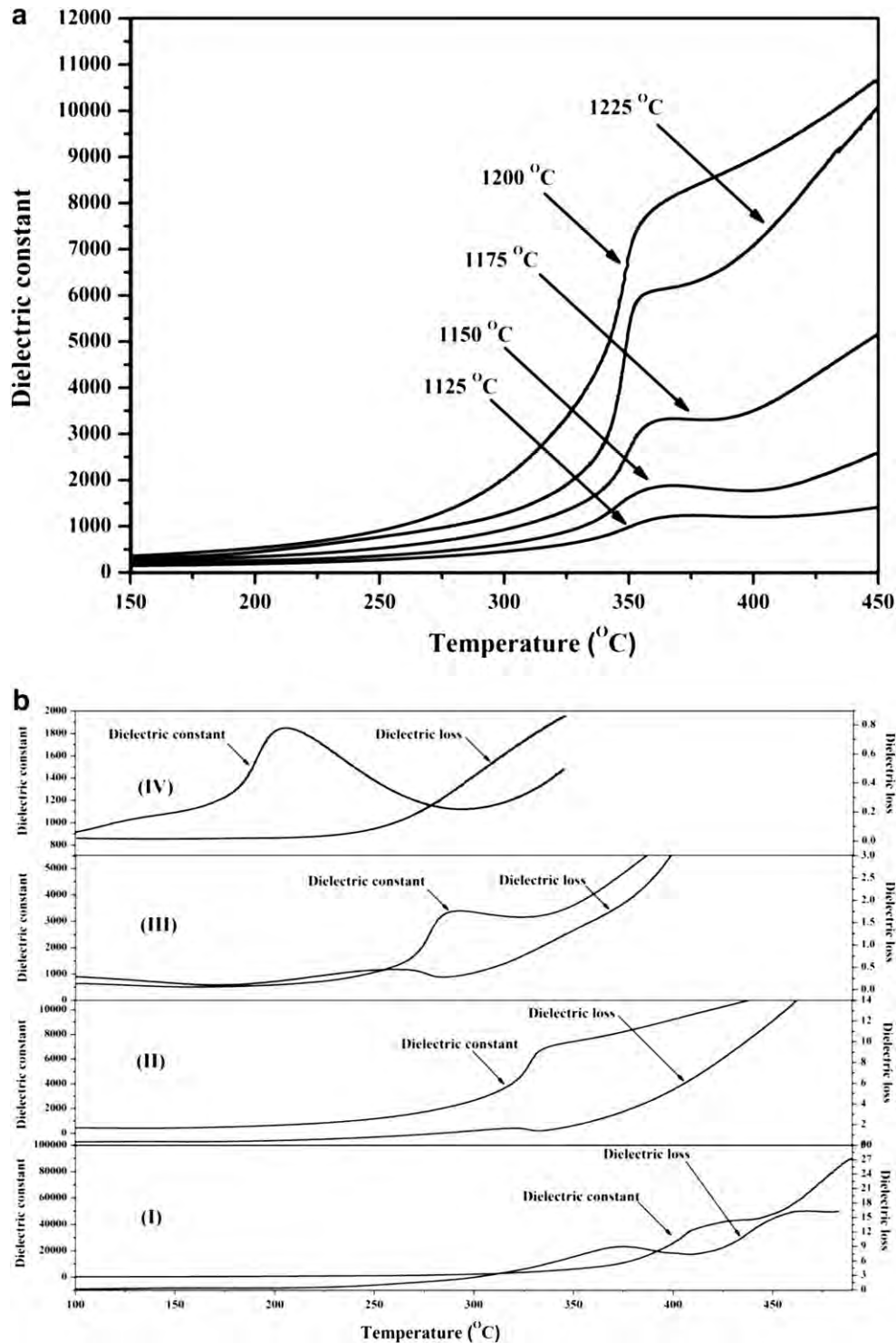


**Fig. 7.** (a) Dielectric constant of PBT40 with different sintering temperature measured at various temperatures (b) Dielectric constant of PBT different  $x$  measured at with various temperatures (I) PBT20 sintered at 1200  $^{\circ}\text{C}$ , (II) PBT40 sintered at 1200  $^{\circ}\text{C}$ , (III) PBT60 sintered at 1225  $^{\circ}\text{C}$  and (IV) PBT80 sintered at 1250  $^{\circ}\text{C}$ .

The powders calcined at 1000, 1050, 1100, and 1150  $^{\circ}\text{C}$  for PBT20, PBT40, PBT60, and PBT80 were pressed into pellets. Thereafter, the pellets were sintered between 1125  $^{\circ}\text{C}$  and 1275  $^{\circ}\text{C}$  for 2 h. The XRD patterns of PBT20 sintered at various temperatures are plotted in Fig. 2(b). They suggest that the PBT ceramics consist of a pure tetragonal perovskite structure in all samples. The XRD results of PBT40, PBT60, and PBT80 were similar to PBT20 (Fig. 3(b)). The tendency of lattice parameters  $c$ ,  $a$  and  $c/a$  ratio was

similar to the calcination step but the  $c/a$  of sintered ceramics were lower than the calcined powders.

The SEM photomicrographs of the PBT80 ceramics at various sintered temperatures are shown in Fig. 5(d), (e) and (f). The grains were similar in shape, with significant variations in size (1.12–2.52  $\mu\text{m}$ ). Micrographs showed a few pores in pellets sintered at 1175 and 1200  $^{\circ}\text{C}$  and then disappeared at 1250  $^{\circ}\text{C}$ . The microstructure becomes denser as the sintering temperatures increases



as indicated by the grain packing and increases in grain boundary thickness. The grain sizes increased with an increase in the sintering temperatures (Table 1). The results were similar to PBT20, PBT40, and PBT60. At the same sintering temperature, the Ba ion content had no effect on the grain size.

The density of PBT ceramics at various temperatures (1125–1275 °C) measured by the Archimedes method, is listed in Table 1. The density increased with the increase of sintering temperatures up to an optimal point at 1200, 1200, 1225, and 1250 °C for PBT20, PBT40, PBT60, and PBT80, respectively. At higher than optimal temperatures, a decrease in the density of the PBT ceramics occurred (Table 1). This may be due to PbO evaporation at high temperature [21–23]. The maximum densities of samples were above 96.5% of theoretical density. This proved that high-density PBT ceramics could be produce by the combustion technique. At the same sintering temperature, the densities decreased when the Ba content increased.

Fig. 7(a) shows the dielectric constant of PBT40 at various temperatures. The dielectric constant curve has a peak at about 360 °C. This peak can be attributed to the Curie temperature ( $T_c$ ) – the transition temperature from the ferroelectric (FE) to the paraelectric (PE) phase.  $T_c$  tends to decrease with the increasing of sintering temperature. This result was similar to PBT20, PBT60, and PBT80 as is listed in Table 1. At  $T_c$ , the maximum dielectric constant increased with the increasing of sintering temperatures up to 1200, 1200, 1225, and 1250 °C for PBT20, PBT40, PBT60, and PBT80, respectively. Above the proper sintering temperature, the dielectric constant decreased as listed in Table 1. The dielectric constant corresponded with the density results. The dielectric loss at  $T_c$  is also shown in Table 1. The dielectric constant at different Ba ion contents is plotted in Fig. 7(b). When the Ba ion contents increased, the  $T_c$  monotonically shifted toward lower temperatures as shown in Table 1. At  $T_c$ , the dielectric constant decreased from 42920 to 1845 and the dielectric loss decreased from 7.36 to 0.02 when the Ba ion content increased from  $x = 0.2$  to  $x = 0.8$ . These were due to the natural dielectric properties of lead titanate (PT) and barium titanate (BT). The PT ceramics have a higher dielectric constant and dielectric loss, while the BT ceramics have lower values [24]. The results agreed with previous work [6].

#### 4. Conclusions

A high density, above 96.5% in PBT ceramics, can be prepared via the combustion technique when calcined between 1000 and 1150 °C and sintered between 1200 and 1250 °C for only 2 h, which is a much shorter time than is required by the solid state reaction method. The firing temperatures and Ba ion content have a strong influence on the phase formation, microstructure, tetragonality, and dielectric properties of PBT ceramics. The pure tetragonal perovskite phase appeared above 1000, 1050, 1100 and 1150 °C with  $x = 0.2, 0.4, 0.6$  and  $0.8$ , respectively. The tetragonality of the PBT powder and ceramics increased with an increase in the calcination and sintering temperatures. The average particle and average grain size tended to increase with increasing firing temperatures. The density of the PBT pellets corresponded to the dielectric constant. The  $T_c$  of PBT ceramics depended on the sintering temperature and Barium ion content.

#### Acknowledgments

This work was financially supported by the Thailand Research Fund (TRF) and Commission on Higher Education (CHE). Thanks also to Department of Physics, Faculty of Science, Naresuan University for supporting facilities. Acknowledgments also to Mr. Don Hindle for helpful comments and corrections of the manuscript.

#### References

- [1] S.W. Lee, K.B. Shim, K.H. Auh, P. Knott, Ferroelectric anomaly in the differential thermal analysis of PbTiO<sub>3</sub> glass, *Mater. Lett.* 38 (1999) 31–36.
- [2] J. Tartaj, C. Moure, P. Durán, Influence of seeding on the crystallization kinetics of PbTiO<sub>3</sub> from gel-derived precursors, *Ceram. Int.* 27 (2001) 741–747.
- [3] X. Xing, J. Deng, Z. Zhu, G. Liu, Solid solution Ba<sub>1-x</sub>Pb<sub>x</sub>TiO<sub>3</sub> and its thermal expansion, *J. Alloys. Compd.* 353 (2003) 1–4.
- [4] O.Z. Yanchevskii, O.I. V'yunov, A.G. Belousov, Fabrication and properties of semiconducting barium lead titanate ceramics containing low-melting glass additions, *Inorg. Mater.* 39 (2003) 645–651.
- [5] W.D. Yung, S.M. Haile, Characterization and microstructure of highly preferred oriented lead barium titanate thin films on MgO (100) by sol–gel process, *Thin Solid Films* 510 (2006) 55–61.
- [6] P.R. Arya, P. Jha, G.N. Subbanna, A.K. Ganguli, Polymeric citrate precursor route to the synthesis of nano-sized barium lead titanates, *Mater. Res. Bull.* 38 (2003) 617–628.
- [7] R.E. Vold, R. Biederman, G.A. Rossetti, A. Sacco, Hydrothermal synthesis of lead doped barium titanate, *J. Mater. Sci.* 36 (2001) 2019–2026.
- [8] P. Panya, T. Bongkarn, Dependence of firing temperatures on phase formation, microstructure and phase transition of (Pb<sub>1-x</sub>Ba<sub>x</sub>)TiO<sub>3</sub> ceramics, *Ferroelectrics* 403 (2010) 1–9.
- [9] A. Thongtha, T. Bongkarn, Phase formation and microstructure of barium zirconate ceramics prepared using the combustion technique, *Ferroelectrics* 383 (2009) 33–39.
- [10] A. Thongtha, T. Bongkarn, Fabrication and characterization of perovskite SrZrO<sub>3</sub> ceramics through a combustion technique, *Key. Eng. Mater.* 421–422 (2010) 223–226.
- [11] P. Panya, T. Bongkarn, Fabrication of perovskite barium titanate ceramics using combustion route, *Ferroelectrics* 383 (2009) 102–110.
- [12] A. Thongtha, T. Bongkarn, Effect of firing temperatures on phase and morphology evolution of CaZrO<sub>3</sub> ceramics synthesized using the combustion technique, *Ferroelectrics* 403 (2010) 3–10.
- [13] P. Bongkarn, Phase formation, microstructure and dielectric properties of Ba(Zr<sub>0.1</sub>Ti<sub>0.9</sub>)O<sub>3</sub> ceramics prepared via the combustion technique, *Curr. Appl. Phys.* 11 (2011) S60–S65.
- [14] A. Thongtha, K. Angsukased, T. Bongkarn, Fabrication of (Ba<sub>1-x</sub>Sr<sub>x</sub>)(Zr<sub>x</sub>Ti<sub>1-x</sub>)O<sub>3</sub> ceramics prepared using the combustion technique, *Smart Mater. Struct.* 19 (2010) 124001.
- [15] D. Xue, J. Xu, C. Yan, Chemical synthesis of NaTaO<sub>3</sub> powder at low-temperature, *Mater. Lett.* 59 (2005) 2920–2922.
- [16] K.C. Patil, S.T. Aruna, S. Ekambaram, Combustion synthesis, *Curr. Opin. Solid State Mater. Sci.* 2 (1997) 156–165.
- [17] T. Bongkarn, W. Tangkawsakul, Low temperature preparation of antiferroelectric PZ and PBZ powders using the combustion technique, *Ferroelectrics* 383 (2009) 50–56.
- [18] C.C. Hwang, T.Y. Wu, J. Wan, J.S. Tsai, Development of a novel combustion synthesis method for synthesizing of ceramic oxide powders, *Mater. Sci. Eng. B* 111 (2004) 49–56.
- [19] Powders Diffraction File No. 74-2492. International Center Diffraction Data, Newton Square, PA, 2003.
- [20] R. Sumang, T. Bongkarn, The effect of calcinations temperatures on the phase formation and microstructure of (Pb<sub>1-x</sub>Sr<sub>x</sub>)TiO<sub>3</sub> powders, *Key Eng. Mater.* 421–442 (2010) 243–246.
- [21] R. Sumang, T. Bongkarn, Effect of sintering temperature on the crystal structure, microstructure and phase transition of (Pb<sub>1-x</sub>Sr<sub>x</sub>)TiO<sub>3</sub> ceramics, *Func. Mater. Lett.* 4 (2009) 193–197.
- [22] A. Garg, D.C. Agrawal, Effect of net PbO content on mechanical and electro-mechanical properties of lead zirconate titanate ceramics, *Mater. Sci. Eng. B* 56 (1999) 46–50.
- [23] L.B. Kong, J. Ma, PZT ceramics formed directly from oxides via reactive sintering, *Mater. Lett.* 51 (2001) 95–100.
- [24] B. Jaffe, W.R. Cook Jr., H. Jaffe, *Piezoelectric Ceramics*. Academic Press, London and New York, 1971.

# The influences of firing temperatures and excess PbO on the crystal structure and microstructure of $(\text{Pb}_{0.25}\text{Sr}_{0.75})\text{TiO}_3$ ceramics

Rattiphorn Sumang · Theerachai Bongkarn

Received: 17 December 2010 / Accepted: 16 May 2011 / Published online: 1 June 2011  
© Springer Science+Business Media, LLC 2011

**Abstract** Polycrystalline samples of  $(\text{Pb}_{0.25}\text{Sr}_{0.75})\text{TiO}_3$  (PST75) were prepared by the solid-state reaction method. The effects of firing temperatures and excess PbO on PST75 ceramics were investigated. The PST75 was calcined between 600 and 1000 °C for 3 h and the sintering temperature ranged between 1050 and 1250 °C for 2 h. The optimized calcination and sintering conditions were identified as 950 and 1250 °C, respectively. The lattice parameter  $c$  increased, while the lattice parameter  $a$  decreased with increased firing temperatures. The average particle size and average grain size increased with increased firing temperatures. After the addition of PbO—excess 0, 1, 3, 5, and 10 wt%—in the PST75 samples, the lattice parameter  $a$  decreased. The average particle size and the average grain size increased with the increase of PbO. The porous microstructure slightly decreased with an increasing amount of PbO—up to 3 wt%—then slightly increased with the higher excess PbO. The density was improved by adding 3 wt% of excess PbO. A low dielectric loss was observed from the 3 wt% excess PbO sample.

## Introduction

$(\text{Pb}_x\text{Sr}_{1-x})\text{TiO}_3$  (PST) is a complete solid solution of  $\text{PbTiO}_3$  (PT) and  $\text{SrTiO}_3$  (ST). Nomura and Sawada [1] studied the PT:ST solid solution system and found an easy formation for a good homogeneous composition. With the addition of ST to PT, the Curie temperature decreases linearly and the phase transition from tetragonal to cubic

occurs at  $x \approx 0.65$  at room temperature. Somiya et al. [2] studied the PST solid solution with  $0.7 < x < 0.8$ . These are the most suitable for microwave applications due to their high dielectric constant and extremely high dielectric tenability of 70% under 2 kV/cm at 1 kHz with a very low dielectric loss value of less than 0.001 [3].

Various fabrication techniques such as sol–gel [3, 4], coprecipitation [5], complex polymerization [6], and the precursor solution [7] have been used to study PST ceramics. All these methods use high-purity inorganic or organic chemicals with a homogeneity and precise composition as starting materials but the production costs are high with only small quantities synthesized. The conventional solid-state reaction method is more economical for large batch processing of these ferroelectric materials [8, 9]. A previous work showed that PST ceramics could be prepared by conventional methods using high sintering temperatures above 1200 °C [4, 10, 11]. This created problems with vaporization of PbO during sintering because of the low melting point of PbO, which is about 850 °C. This can cause lead deficiency which may produce large pores in the microstructure and have a subsequent effect on densification. The addition of excess PbO is one of the techniques developed to counteract this problem. For example, the optimum density of Bi-doped PT [12], PBZ [13], PBT [14], PZT [15] ceramics, can be improved by the addition of excess PbO. Therefore, the effect of firing temperatures and excess PbO on the crystal structure and microstructure of  $(\text{Pb}_{0.25}\text{Sr}_{0.75})\text{TiO}_3$  ceramics synthesized by a solid-state reaction method were investigated in this study.

## Experimental

Ceramic composition of  $(\text{Pb}_{0.25}\text{Sr}_{0.75})\text{TiO}_3$ ; PST75 was prepared by the solid-state reaction method. Lead oxide

R. Sumang · T. Bongkarn (✉)  
Department of Physics, Faculty of Science, Naresuan University,  
Phitsanulok 65000, Thailand  
e-mail: researchcmu@yahoo.com

(99.9% PbO), strontium carbonate (99%  $\text{SrCO}_3$ ), and titanium oxide (99.5%  $\text{TiO}_2$ ) powders were used as starting materials. The starting powders were weighed in the required stoichiometric ratio and then ball-milled in ethanol for 24 h. After the drying process, the mixed powders were calcined from 600 to 1000 °C with a 5 °C/min heating/cooling rate for 3 h to discover the optimum calcinations temperature. The calcined powders were mixed with 4 wt% binder and then ball-milled again in ethanol for 24 h. Subsequently, the calcined powders were pressed into disks with a diameter of 15 mm at a pressure of 80 MPa. The disk samples were then sintered from 1050 to 1250 °C for 2 h to discover the optimum sintering temperature. In order to compensate for the PbO loss during the process of calcination and sintering, excess PbO was added. The excess PbO was subdivided into 0, 1, 3, 5, and 10 wt% at calcination and sintering temperatures of 950 and 1250 °C, respectively.

The reactions of the uncalcined PST75 powders taking place during heat treatment were investigated by differential thermal analysis (DTA) and thermo gravimetric analysis (TGA). The structure phase of the calcined powders and sintered ceramics was identified using an X-ray diffractometer (XRD). The typical size of the crystallites was determined from scanning electron microscopy (SEM). The apparent density of the samples was measured by the Archimedes method with distilled water as the fluid medium. Silver electrodes were constructed on two major surfaces of the polished samples and dielectric measurements were performed using a LCR meter (Agilent 4263B).

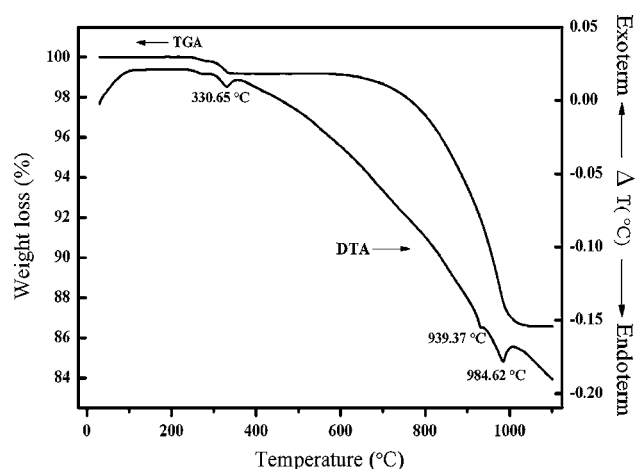


**Fig. 1** The DTA–TGA curves for the mixture of PbO,  $\text{SrCO}_3$ , and  $\text{TiO}_2$  powders

## Results and discussion

The DTA–TGA simultaneous analysis of the powders mixed in stoichiometric proportions of PST75 is displayed in Fig. 1. The sharp decrease curve of the TGA, between 250 and 320 °C, indicated a major weight loss due to the process of getting rid of the left over burned plastic during the ball milling and related to a small endothermic peak at 331 °C in the DTA curve. The second weight loss was

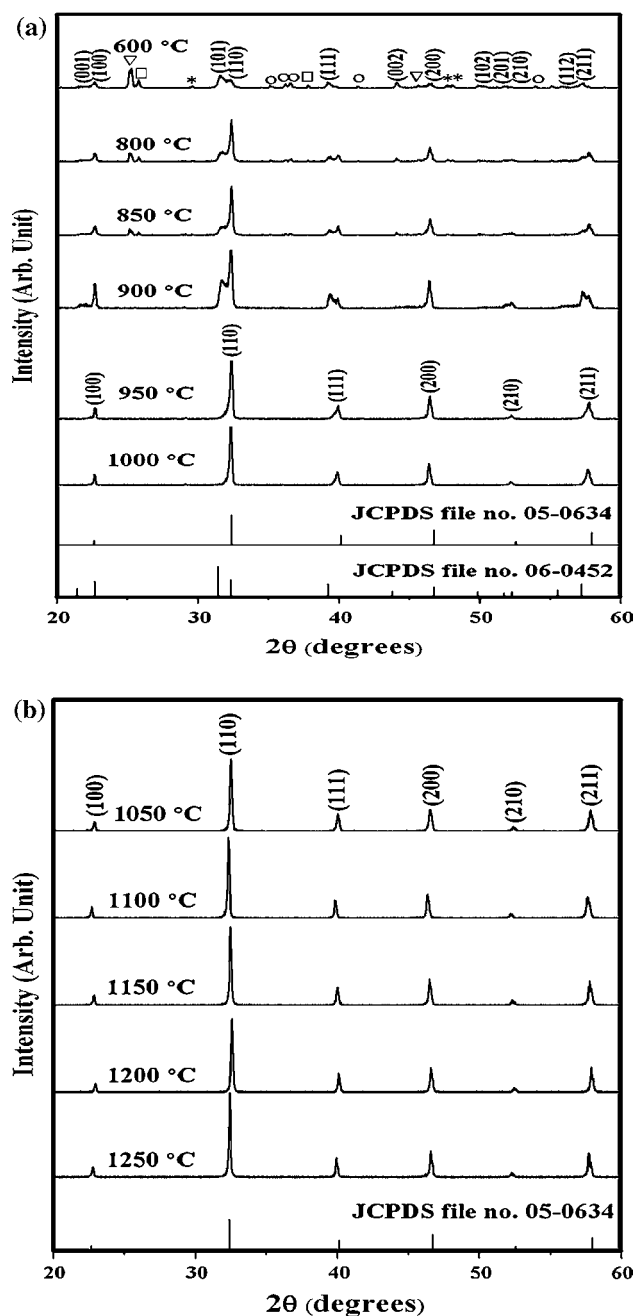


**Fig. 2** XRD pattern of PST75 **a** calcined powders and **b** sintered ceramics with different firing temperatures (*asterisk* PbO), (*inverted triangle*  $\text{SrCO}_3$ ), (*square*  $\text{TiO}_2$ ), and (*circle* TiO)

observed above 600 °C, which related to the endothermic peak at 939 and 985 ° on the DTA curve. These temperatures caused many chemical reactions between the PbO, SrCO<sub>3</sub>, and TiO<sub>2</sub>. From previous works reported, synthesizing pure PbTiO<sub>3</sub> based on the solid-state reaction between PbO and TiO<sub>2</sub> typically occurs at temperatures higher than 630 °C [16], while the pure perovskite phase of SrTiO<sub>3</sub> is produced by the solid-state reaction between SrCO<sub>3</sub> and TiO<sub>2</sub> at temperatures above 1300 °C [17]. Chen et al. [18] prepared pure PST powders via the solid-state reaction method by calcining at 900 °C for 2 h. Therefore, the reaction between PbO, SrCO<sub>3</sub>, and TiO<sub>2</sub> of PST75 should begin at a temperature higher than 600 °C but not greater than 1300 °C. These data were used to define the range of calcination temperatures.

The XRD patterns of PST75 calcined powders and sintered ceramics at various temperatures are shown in Fig. 2a, b. The XRD pattern shows a major X-ray reflection peak in the perovskite PST75 phase, indicating the polycrystalline nature of the powder with (110) as the major peak. For the powders calcined at <950 °C, the index of the tetragonal structure matched JCPDS file number 06-0452 [19] and an X-ray peak of precursors (PbO, SrCO<sub>3</sub>) and impurities (TiO<sub>2</sub>, TiO) appeared. The pure cubic perovskite phase was discovered in powders calcined ≥950 °C, which were matched with JCPDS file number 05-0634 [20] and earlier reports [9, 10]. Crystallinity of the calcined powders was improved by increasing the calcination temperature, as indicated by the increase in intensity of the X-ray diffraction peak. The relative amounts of the perovskite phase were calculated by measuring major peak intensities of the perovskite phase. The percentage of perovskite is described by the following equation:

% perovskite phase

$$= \left( \frac{I_{\text{perov}}}{I_{\text{perov}} + I_{\text{PbO}} + I_{\text{SrCO}_3} + I_{\text{TiO}_2} + I_{\text{TiO}}} \right) \times 100 \quad (1)$$

This well-known equation is widely employed in the preparation of complex perovskite structure materials [9, 21].  $I_{\text{perov}}$ ,  $I_{\text{PbO}}$ ,  $I_{\text{SrCO}_3}$ ,  $I_{\text{TiO}_2}$ , and  $I_{\text{TiO}}$  refer to the intensity of the (101) perovskite peak and the intensities of the highest PbO, SrCO<sub>3</sub>, TiO<sub>2</sub>, and TiO peaks, respectively.

The percentage of the perovskite phase of the PST75 calcined powders was increased from 10 to 96 when the calcination temperature increased from 600 to 900 °C. When increasing the calcination temperature above 950 °C, the percent of the perovskite phase of the samples reached a hundred percent, Table 1. The  $a$ -,  $c$ -axis lattice constants of PST75 calcined powders at different temperatures were calculated from the (001)/(100) and (002)/(200) XRD peaks and are shown in Fig. 3. When the calcined temperatures increased, the  $a$ -axis parameter of the tetragonal structure increased whereas the  $c$ -axis parameter

**Table 1** % perovskite phase, lattice parameter, unit cell volume, average particle size, average grain size, density, shrinkage, and dielectric properties of the PST75 with different firing temperatures

Calcination temperature (°C)	Calcined powder			Sintering temperature (°C)	Sintered ceramic						
	Perovskite phase (%)	$c/a$ ratio	Unit cell volume (Å <sup>3</sup> )		Average particle size (μm)	Lattice parameter $a$ (Å)	Average grain size (μm)	Density (g/cm <sup>3</sup> )	Shrinkage (%)	Dielectric constant at $T_{\text{room}}$	Dielectric loss at $T_{\text{room}}$
600	10	1.051	63.36	0.12	1050	3.9040	0.30	5.78	3.3	768	0.67
800	52	1.050	62.73	0.14	1100	3.9032	0.42	5.88	5.3	1704	3.53
850	64	1.049	62.70	0.17	1150	3.9016	0.50	5.92	8.6	1743	2.11
900	96	1.047	62.48	0.21	1200	3.8984	0.57	5.94	10.6	1914	1.17
950	100	1.000	59.81	0.24	1250	3.8960	0.59	5.99	13.3	1930	0.39
1000	100	1.000	59.03	0.38							



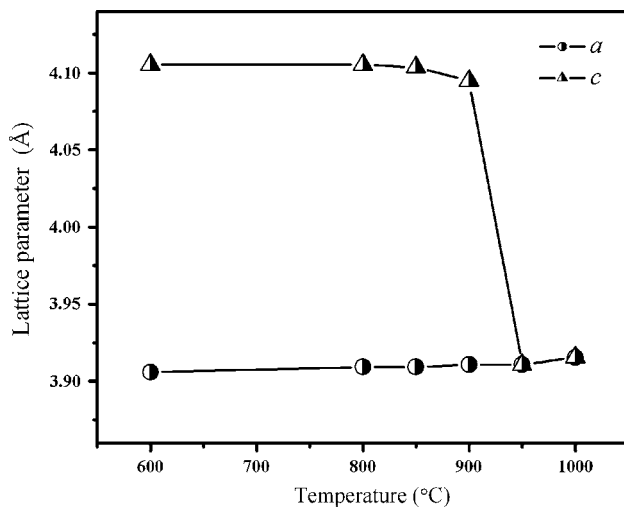


**Fig. 3** Lattice parameters of PST75 powders at different calcination temperatures

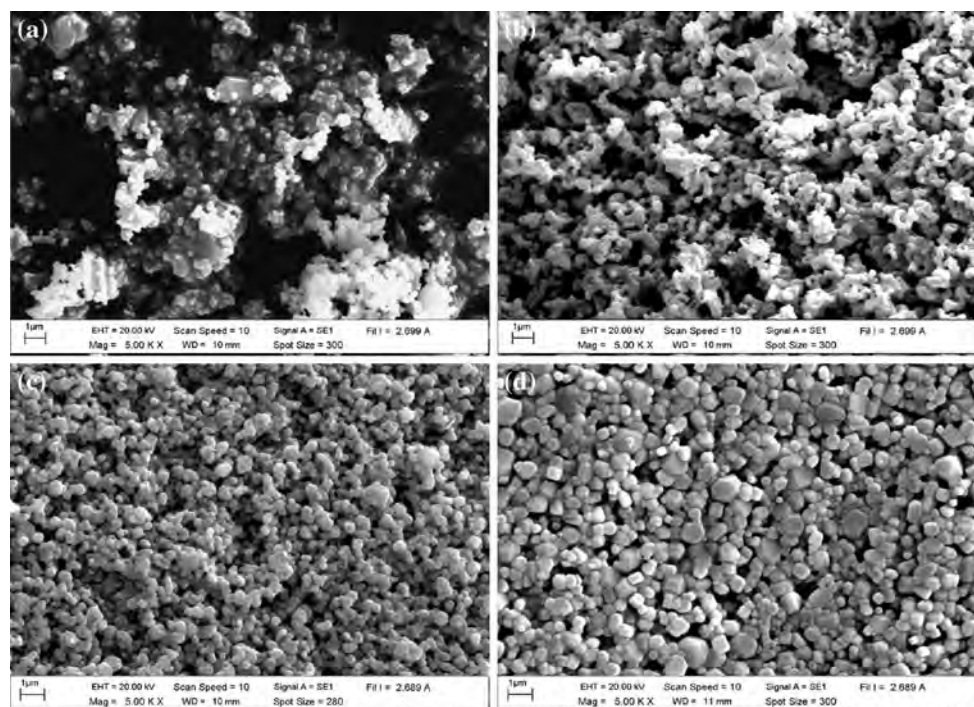
decreased. The  $c/a$  ratio and unit cell volume of PST75 decreased with increasing calcined temperatures, as listed in Table 1. In Fig. 2b, the sintered pellets show a pure perovskite phase. The diffraction patterns of PST75 could be indexed with respect to a cubic structure. The  $a$ -axis lattice constantly decreased with increased sintering temperatures, see Table 1. These indicate that the calcination and sintering temperatures have a direct bearing on the phase formation and lattice parameters.

Figure 4a, b shows SEM photomicrographs of PST75 calcined powders at different temperatures. In general, the particles have a spherical morphology. The average particle size increased from 0.12 to 0.38  $\mu\text{m}$ , when the calcination temperature was increased from 600 to 1000  $^{\circ}\text{C}$ , Table 1. Figure 4c, d shows the microstructure of PST75 ceramics at different sintering temperatures. It was found that increasing sintering temperatures helped grain size growth, Table 1. A similar result was found in Nb-doped PZT and  $\text{Pb}(\text{Zr}_{0.44}\text{Ti}_{0.56})\text{O}_3$  ceramics [22, 23]. A porous microstructure with a small grain size was observed in the PST75 sintered at 1050  $^{\circ}\text{C}$ . When sintering temperatures increased from 1050 to 1250  $^{\circ}\text{C}$ , the porosity of the PST75 ceramics decreased. However, when the sintering temperature was higher than 1250  $^{\circ}\text{C}$ , the PST75 ceramics became very fragile.

The densities and shrinkage of the PST75 ceramics are listed in Table 1. The density and shrinkage increased with increased sintering temperatures, and the maximum value was 5.99  $\text{g}/\text{cm}^3$  and 13.3% obtained from ceramics sintered at 1250  $^{\circ}\text{C}$ .

The dielectric constant and dielectric loss of PST75 sintered ceramics as a result of temperature are listed in Table 1. The dielectric constant of the samples increased when sintering temperatures increased from 1050 to 1250  $^{\circ}\text{C}$ . The dielectric loss increased at first and then dropped as the sintering temperature  $>1100$   $^{\circ}\text{C}$ .

To compensate for PbO loss from evaporation during calcination and sintering, some excess PbO is usually added during the batch preparation. The batch is then



**Fig. 4** SEM photomicrographs of PST75 at different firing temperatures: **a** 600  $^{\circ}\text{C}$  and **b** 950  $^{\circ}\text{C}$  of calcined powders, **c** 1050  $^{\circ}\text{C}$  and **d** 1250  $^{\circ}\text{C}$  of sintered ceramics

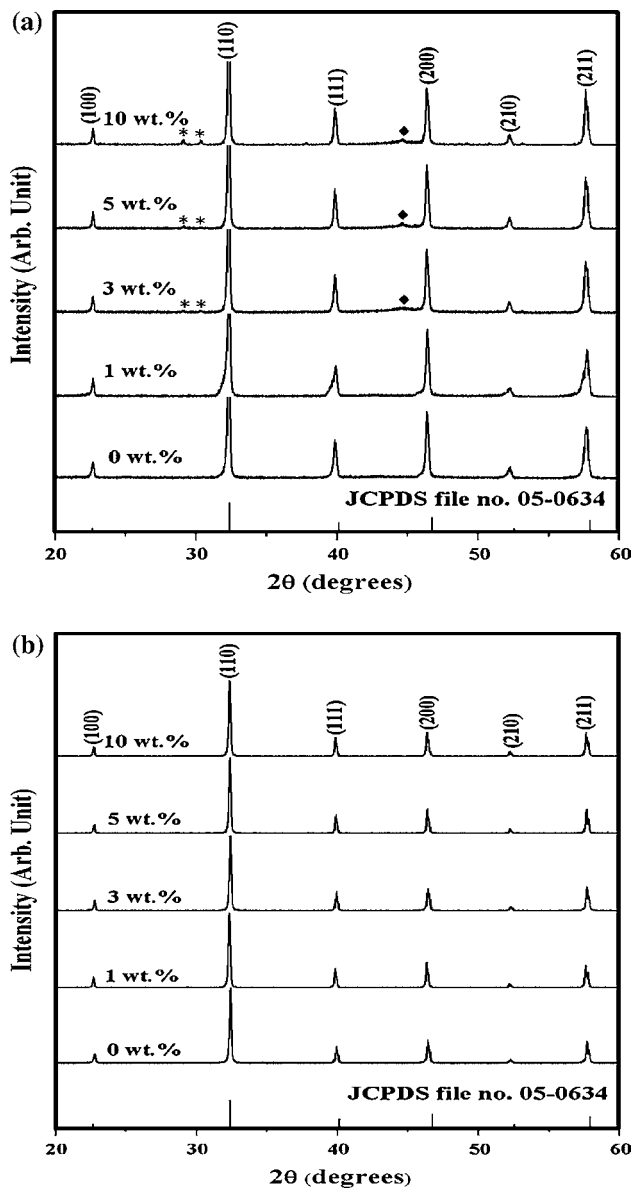


**Fig. 5** XRD pattern of PST75 **a** calcined powders and **b** sintered ceramics with different amounts of excess PbO (asterisk PbO) and (diamond PbO<sub>2</sub>)

calcined and sintered at 950 and 1250 °C, respectively. The X-ray diffraction patterns of PST75 calcined powders, containing different amounts of PbO, are shown in Fig. 5a. The crystal structure of the PST75 system was proposed as a cubic phase. The impurity phase of PbO and PbO<sub>2</sub> was found in the  $\geq 3$  wt% excess PbO sample. The impurity phases occurred because of too much lead for the proper reaction during calcinations [13, 14]. The percentage of the perovskite phase decreased from 100 to 92 when excess PbO was higher than 1 wt%, see Table 2. The impurity phase was not obtained in any of the ceramics samples, see Fig. 5b. This indicated that the excess PbO exceeded that required to maintain compositional control (assumed) in the PST75 powders and was eliminated from the sample by volatilization during sintering at 1250 °C. The perovskite phase in the ceramics reached a hundred percent in all samples. The lattice parameter  $a$  of PST75 in the calcined powders and sintered ceramics decreased from 3.9159 to 3.9127 Å and 3.8960 to 3.8864 Å, when increasing excess PbO from 0 to 10 wt%, as listed in Table 2. In the case of the PbTiO<sub>3</sub>, the sample deficient in PbO exhibited an increase of lattice parameter  $a$  [24]. The decrease of lattice parameter  $a$  in this study indicated that the excess PbO was utilized to compensate for PbO-volatility.

The SEM photomicrographs of PST75 calcined powders with various PbO excess are shown in Fig. 6a–c. These powders exhibited an almost spherical morphology and agglomeration. The average particles size increased from 0.24 to 0.59  $\mu\text{m}$  with increased PbO content from 0 to 10 wt%, see Table 2. Figure 7a–c reveals the SEM photomicrograph of PST75 sintered pellets. The grain growth of the PST75 continuously increased with increased excess PbO, changing from 0.59 to 0.76  $\mu\text{m}$ , as listed in Table 2. The PbO may be combined into the ceramics and therefore less liquid phases exist in the grain boundaries. This would hinder the grain growth [14]. A porous microstructure was also found on the surface of the samples without (0 wt%) and with 1 wt% PbO content. With the addition of 3 wt% excess PbO, the porosity decreased, due to a liquid phase

**Table 2** % perovskite phase, lattice parameter  $a$ , average particle size, average grain size, density, and dielectric properties of the PST75 samples with different excess PbO contents

Excess PbO (wt%)	Calcined powder			Sintered ceramic				
	Perovskite phase (%)	Lattice parameter $a$ (Å)	Average particle size ( $\mu\text{m}$ )	Lattice parameter $a$ (Å)	Average grain size ( $\mu\text{m}$ )	Density ( $\text{g}/\text{cm}^3$ )	Dielectric constant at $T_{\text{room}}$	Dielectric loss at $T_{\text{room}}$
0	100	3.9159	0.24	3.8960	0.59	5.99	1930	0.39
1	100	3.9151	0.26	3.8919	0.61	6.01	1975	0.33
3	97	3.9143	0.38	3.8917	0.63	6.26	2325	0.08
5	93	3.9135	0.47	3.8903	0.64	5.78	2457	0.19
10	92	3.9127	0.59	3.8864	0.76	5.75	2242	0.20

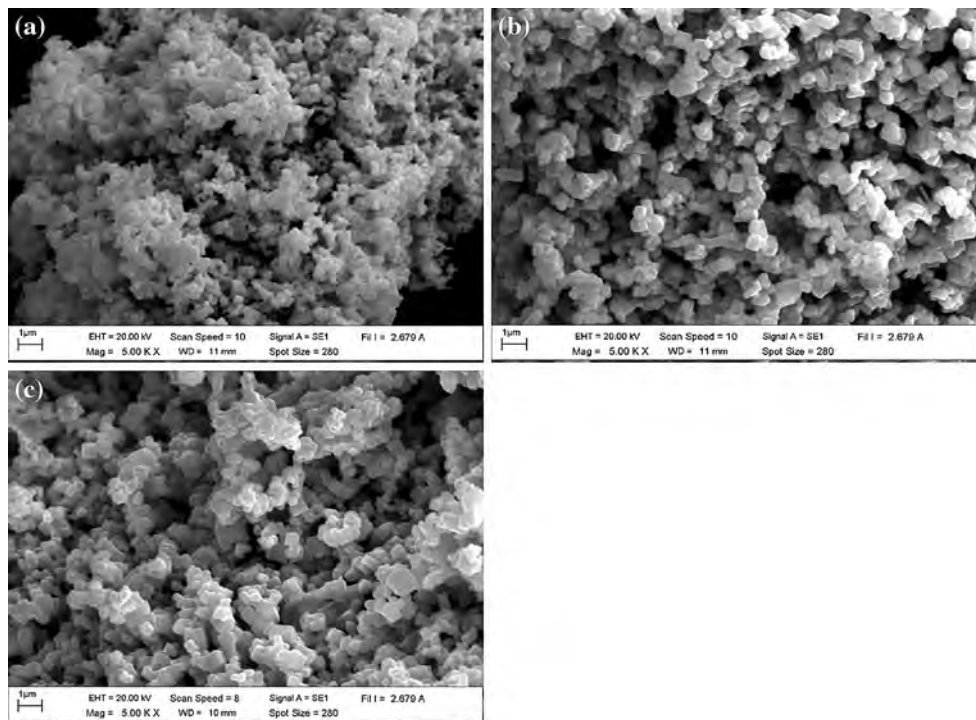


**Fig. 6** SEM photomicrographs of PST75 made from starting with different excess PbOs: **a** 0 wt%, **b** 3 wt%, and **c** 5 wt% of calcined powders

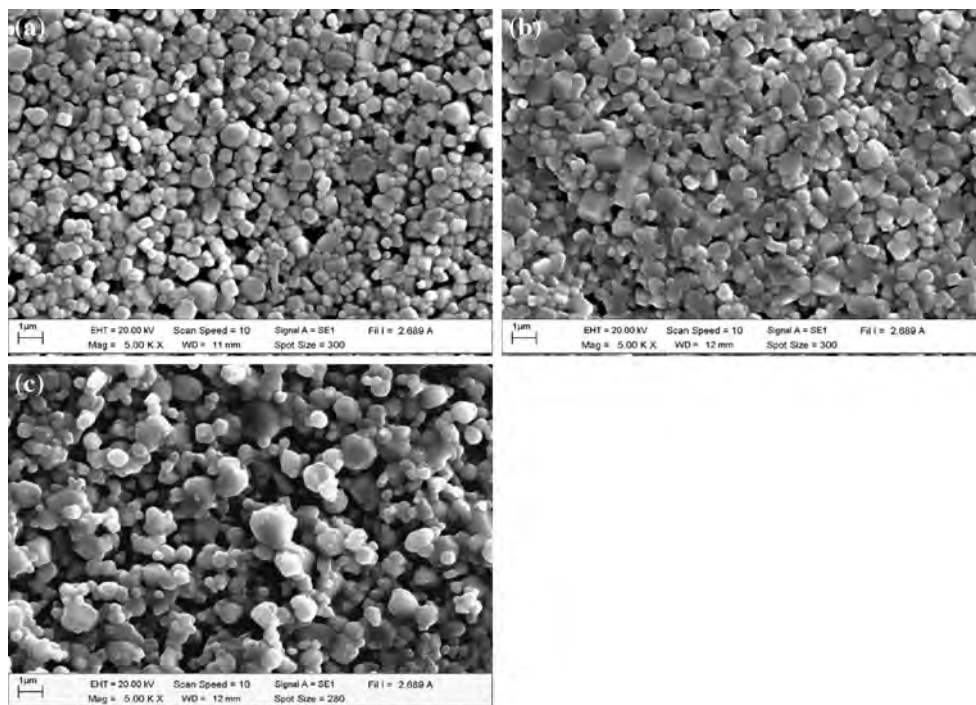


**Fig. 7** SEM photomicrographs of PST75 made from starting with different excess PbOs: **a** 0 wt%, **b** 3 wt%, and **c** 5 wt% of sintered ceramics

which formed between the perovskite grains. The porosity increased with an increase of excess PbO. This could be caused by the loss of PbO from the compact pellet which increased its porosity.

The densities of the PST75 ceramics are listed in Table 2. The density increases with increased PbO, reaches a maximum value at 3 wt% excess PbO, and slightly decreases above >3 wt% excess PbO. The density results can be



correlated to the microstructure since the high density for 3 wt% excess PbO samples showed high degrees of close grain packing, whereas the low density of the sample with >3 wt% excess PbO contained many pores. Thus, the porosity of the samples has a marked effect on density. The increases and decreases in the densities of the PST75 ceramics are due to the degree of porosity. The density and porosity depend on the amount of PbO in the liquid phase. In the presence of excess PbO, the densification of the samples takes place by a rapid rearrangement of the particles surrounded by the liquid phase. This process becomes more intense if a sufficient liquid phase is present to allow an easy rearrangement of the grains. Consequently, the densification should be proportional to the amount of liquid PbO. In this study, the amount of liquid PbO was not enough to fill in the pores of the sample without excess PbO (0 wt%) and with excess PbO 1 wt% and appeared on the porous microstructure of the surface of these samples. When the excess PbO was raised to 3 wt%, the effect of decreasing porosity concentration resulted in higher densification. However, a large amount of the PbO liquid phase can produce an initial rapid densification but a lower final density because of void formation due to PbO evaporation. As a consequence the porosity of the pellet increases [12, 25]. In this study, the reduction in density for the 5 and 10 wt% samples is consistent with an excessive amount of PbO in these samples. In the previous study, excess PbO 1 wt% was added to the Pb-based samples (PBZ, PBT, PCT) to obtain a higher densification [13, 14, 26]. In this study, the calcination and sintering were performed at a higher temperatures so a higher excess PbO content (3 wt%) was added in the PST samples to compensate for the vaporization of PbO.

The dielectric constant and dielectric loss of the PST75 ceramics with various excess PbO content are listed in Table 2. The dielectric constant increased with an increased PbO until 5 wt% and then decreased with higher excess PbO. However, the lowest dielectric loss was observed from the 3 wt% excess PbO samples. The dielectric constant and dielectric loss of the excess PbO samples (Table 2) were higher and lower than the samples without excess PbO (Table 1). This indicated that the electrical properties of lead-containing ceramics produced by the solid-state reaction method can be improved by the addition of excess PbO.

## Conclusions

Firing temperatures and excess PbO have a strong influence on the crystal structure, microstructure, and lattice parameter of PST75 ceramics. The optimal calcination and sintering conditions were found to be 950 and 1250 °C, respectively. The PST75 powders calcined below <950 °C were indexed with a tetragonal structure, while the pure

cubic perovskite phase was discovered in powders calcined at  $\geq 950$  °C. For the ceramic samples, the lattice parameter  $a$  decreased while grain size increased with increasing sintering temperatures. The maximum density of the ceramics was discovered in the pellets sintered at 1250 °C. Furthermore, the particle size and average grain size increased with an increase of excess PbO. Appropriate amounts of the liquid phase can decrease porosity. The density can be improved by adding 3 wt% of excess PbO.

**Acknowledgments** This study was financially supported by the Thailand Research Fund (TRF), Commission on Higher Education (CHE) and The Royal Golden Jubilee Ph.D. Program. The authors wish to thanks the Science Lab Center, Faculty of Science, Naresuan University for supporting facilities. Thanks are also given to Mr. Don Hindle for his help in editing the manuscript.

## References

1. Nomura S, Sawada S (1955) *J Phys Soc Jpn* 10:108
2. Somiya Y, Bhalla AS, Cross LE (2001) *Int J Inorg Mater* 3:709
3. Kang DH, Kim HJ, Park JH, Yoon KH (2001) *Mater Res Bull* 36:265
4. Jain M, Majumder SB, Guo R, Bhalla AS, Katiyar RS (2002) *Mater Lett* 56:692
5. Zhang F, Karaki T, Adachi M (2005) *Powder Technol* 159:13
6. Leal SH, Escote MT, Pontes FM, Leite ER, Joya MR, Pizani PS, Longo E, Varela JA (2009) *J Alloys Compd* 475:940
7. Sen S, Choudhary RNP (2007) *Appl Phys A* 87:727
8. Zhou L, Zimmermann A, Zeng YP, Aldinger F (2004) *J Mater Sci Mater Electron* 15:145
9. Sumang R, Bongkarn T (2010) *Key Eng Mater* 421:243
10. Rivera I, Kumar A, Mendoza F, Katiyar RS (2008) *Physica B* 403:2423
11. Sumang R, Bongkarn T (2009) *Funct Mater Lett* 2:193
12. Amaranda L, Miclea C, Tanasoiu C (2002) *J Eur Ceram Soc* 22:1269
13. Bongkarn T, Rujijanagul G, Milne SJ (2005) *Mater Lett* 59:1200
14. Sumang R, Bongkarn T (2009) *Ferroelectrics* 383:57
15. Song Z, Gao J, Zhu X, Wang L, Fu X, Lin C (2001) *J Mater Sci* 36:4285. doi:10.1023/A:1017999223329
16. Udornporn A, Ananta S (2004) *Mater Lett* 58:1154
17. Tagawa H, Igarashi K (1986) *J Am Ceram* 69:310
18. Chen H, Yang C, Zhang J, Pei Y, Zhao Z (2009) *J Alloys Compd* 486:615
19. Powder Diffraction File No. 06-0452, International Center for Diffraction Data, Newton Square, PA, 2003
20. Powder Diffraction File No. 06-0634, International Center for Diffraction Data, Newton Square, PA, 2003
21. Vittayakorn N, Rujijanagul G, Tunkasiri T, Xiaoli T, Cann DP (2003) *J Mater Res* 18:2882
22. Chu SY, Chen TY, Tsai IT (2003) *Integr Ferroelectr* 58:1293
23. Yimnirun R, Tipakontitkul R, Ananta S (2006) *Int J Mod Phys B* 20:2415
24. Selbach SM, Tybell T, Einarsrud M, Grande T (2011) *Appl Phys Lett* 98:091912
25. Kong LB, Ma J, Huang H, Zhang RF (2002) *J Alloy Compd* 345:238
26. Zhang Y, Kuang A, Chan HLW (2003) *Microelectr Engine* 66:918



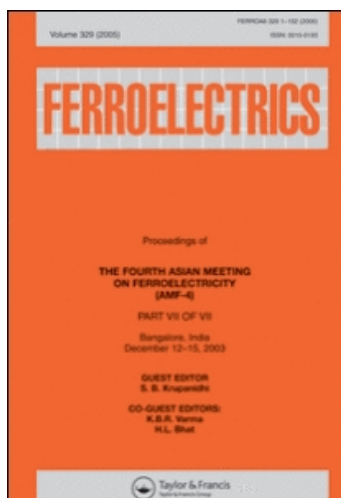
This article was downloaded by: [Bongkarn, Theerachai]

On: 22 June 2011

Access details: Access Details: [subscription number 938846547]

Publisher Taylor & Francis

Informa Ltd Registered in England and Wales Registered Number: 1072954 Registered office: Mortimer House, 37-41 Mortimer Street, London W1T 3JH, UK



## Ferroelectrics

Publication details, including instructions for authors and subscription information:

<http://www.informaworld.com/smpp/title~content=t713617887>

## The Preparation of Lead Strontium Titanate Ceramics by the Combustion Method

Panadda Sittiketkorn<sup>a</sup>; Theerachai Bongkarn<sup>a</sup>

<sup>a</sup> Department of Physics, Faculty of Science, Naresuan University, Phitsanulok, Thailand

Online publication date: 21 June 2011

**To cite this Article** Sittiketkorn, Panadda and Bongkarn, Theerachai(2011) 'The Preparation of Lead Strontium Titanate Ceramics by the Combustion Method', *Ferroelectrics*, 414: 1, 170 – 179

**To link to this Article:** DOI: 10.1080/00150193.2011.577335

**URL:** <http://dx.doi.org/10.1080/00150193.2011.577335>

PLEASE SCROLL DOWN FOR ARTICLE

Full terms and conditions of use: <http://www.informaworld.com/terms-and-conditions-of-access.pdf>

This article may be used for research, teaching and private study purposes. Any substantial or systematic reproduction, re-distribution, re-selling, loan or sub-licensing, systematic supply or distribution in any form to anyone is expressly forbidden.

The publisher does not give any warranty express or implied or make any representation that the contents will be complete or accurate or up to date. The accuracy of any instructions, formulae and drug doses should be independently verified with primary sources. The publisher shall not be liable for any loss, actions, claims, proceedings, demand or costs or damages whatsoever or howsoever caused arising directly or indirectly in connection with or arising out of the use of this material.

# The Preparation of Lead Strontium Titanate Ceramics by the Combustion Method

PANADDA SITTIKETKORN  
AND THEERACHAI BONGKARN\*

Department of Physics, Faculty of Science, Naresuan University, Phitsanulok,  
65000, Thailand

*In this work,  $(\text{Pb}_{1-x}\text{Sr}_x)\text{TiO}_3$  (PST) ceramics with  $0.25 \leq x \leq 0.75$  were successfully prepared by the combustion method. The calcination and sintering temperatures were  $800^\circ\text{C}$ – $1050^\circ\text{C}$  and  $1050^\circ\text{C}$ – $1250^\circ\text{C}$  for 2 h, respectively. A single perovskite phase of the PST powders was found with calcination temperatures above  $1000^\circ\text{C}$ . The samples were indexed in a tetragonal system when  $x = 0.25$ . The lattice parameter  $c$  and  $c/a$  ratio increased while, the lattice parameter  $a$  decreased with increasing firing temperatures. For  $x = 0.75$ , the samples were indexed in a cubic phase and the lattice parameter  $a$  decreased with an increase in the firing temperatures. The samples were indexed in a tetragonal and cubic phase coexist when  $x = 0.50$ . The pure perovskite phase was found in all the sintered pellet samples. The average particle size and average grain size tended to increase with increasing calcining and sintering temperatures. The maximum density was 7.67, 6.52 and  $5.59\text{ g/cm}^3$  obtained from the samples sintered at  $1150^\circ\text{C}$  with  $x = 0.25$ , 0.50 and 0.75, respectively.*

**Keywords** Lead strontium titanate; phase formation; microstructure; combustion technique

## Introduction

Lead strontium titanate  $(\text{Pb}_{1-x}\text{Sr}_x)\text{TiO}_3$  (PST) is a complete solid solution of  $\text{PbTiO}_3$  (PT) and  $\text{SrTiO}_3$  (ST). The Curie temperature of PST is composition-dependent because it could be adjusted from  $-220$  to  $490^\circ\text{C}$  by the ratio of ST and PT. At room temperature, the PST solid solution is in a ferroelectric phase when the Sr content is less than 0.60, and in paraelectric phase when the Sr content is in the range of 0.60–1.00. Due to its large electric field-dependent dielectric constant at a temperature near the Curie temperature, PST is highly suitable for electronic and microelectronic applications: such as microwave devices, frequency tuning devices, capacitors, sensors, etc. [1–3].

There are several processing techniques for preparing PST ceramics such as: the coprecipitation technique [3], the sol-gel technique [4] and the conventional mixed-oxide method [5]. F. Zhang *et al.* fabricated lead strontium titanate ceramics via the coprecipitation technique [3]. The nitrates of the raw materials were dissolved in ethanol and then coprecipitated by an oxalic acid dehydrate. The precipitate powders were calcined at  $600^\circ\text{C}$  for 1 h. By this method, nanosized PST powders with an average size of 10 nm

---

Received June 20, 2010; in final form July 11, 2010.

\*Corresponding author. E-mail: researchcmu@yahoo.com

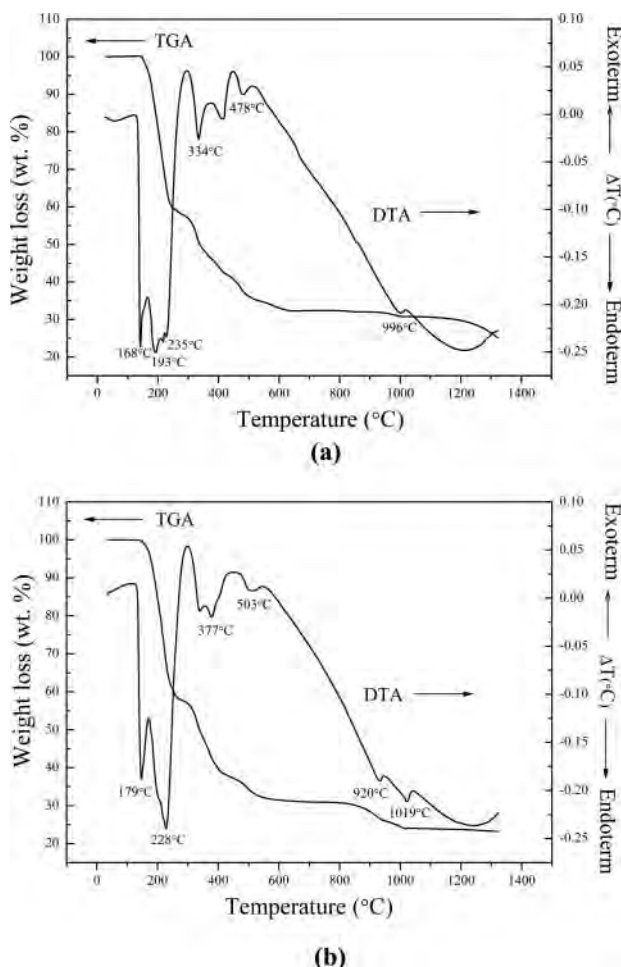


**Figure 1.** TGA-DTA curves of raw materials and urea: (a)  $x = 0.25$  and (b)  $x = 0.75$ .

were obtained. Jiwei Zhai *et al.* synthesized  $(\text{Pb}_{1-x}\text{Sr}_x)\text{TiO}_3$  by the sol-gel technique [4]. Lead acetate trihydrate and strontium acetate were mixed in a ratio of predetermined number, and then dissolved into heated glacial acetic acid. This was followed by the addition of titanium isopropoxide with constant stirring. The grain size of PST was systematically reduced with the increase in strontium doping and the dielectric constant of PST decreased with the increase in Sr content.  $(\text{Pb}_{1-x}\text{Sr}_x)\text{TiO}_3$  ( $x = 0.70, 0.75$  and  $0.80$ ) were prepared by the conventional mixed-oxide method using calcination temperatures at  $1100^\circ\text{C}$  for 3 h. [1]. Dielectric tenability of 3, 15, and 70% measured under 20 kV/cm bias field at 10 kHz were obtained from  $x = 0.70, 0.75$  and  $0.80$ . It is well known that ceramics which are synthesized by wet chemical synthesis can provide homogenous nanosized oxides of high purity at lower reaction temperatures but they have a high cost for starting materials and they are intricate and complicated [6]. The solid state reaction method requires high temperatures and the resulting powders exhibit many undesirable characteristics: large particle size and wide particle size distribution [7]. The combustion method is interesting because it helps to decrease the temperature in the preparation and results in a small particle size. The

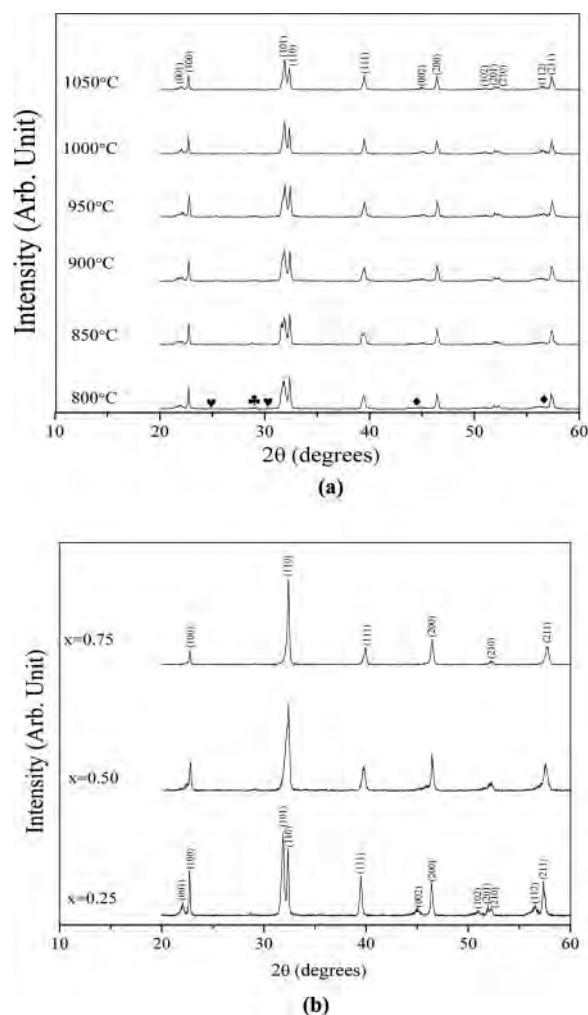


**Figure 2.** XRD patterns of PST powders (a)  $x = 0.25$  at various calcination temperatures; (♣) PbO, (♥) TiO<sub>2</sub> and (♦) SrCO<sub>3</sub> and (b) calcined at 1000°C with different Sr content.

combustion reaction method also has interesting characteristics such as: its simplicity, its relatively low cost, and the fact that it usually results in products with the desired structure and composition [8]. Thus, in this work, (Pb<sub>1-x</sub>Sr<sub>x</sub>)TiO<sub>3</sub> (PST) ceramics with  $0.25 \leq x \leq 0.75$  were prepared via the combustion method and the effect of firing temperatures on its phase formation and microstructure were investigated.

## Experimental

(Pb<sub>1-x</sub>Sr<sub>x</sub>)TiO<sub>3</sub> (PST) ceramics with  $0.25 \leq x \leq 0.75$  were fabricated using an established combustion method. PbO, SrCO<sub>3</sub> and TiO<sub>2</sub> powders were used as starting materials. The raw materials were ball milled with stabilized zirconia balls and ethanol for 24 h. The mixed powders were dried at 120°C for 6 h. Prior to sieving, the powders and urea were

Table 1

The percentage perovskite, average particle size, lattice parameter  $a$ ,  $c$ ,  $c/a$  ratio, average grain size, density and shrinkage of PST samples

x	Calcination temperature (°C)	The percentage perovskite (%)	Average particle size (μm)	Sintered temperature (°C)	Lattice parameter			The c/a ratio	Average grain size (μm)	Shrinkage (%)	Density (g/cm <sup>3</sup> )
					a (Å)	c (Å)					
0.25	800	85.8	0.19	1050	3.9149	4.0199	1.0268	0.50	3.7	7.46	
	850	94.0	0.20	1100	3.9132	4.0239	1.0282	0.98	9.9	7.55	
	900	95.4	0.25	1150	3.9110	4.0254	1.0292	2.52	15.7	7.67	
	950	97.8	0.28	1200	3.9087	4.0286	1.0306	3.05	19.0	6.64	
	1000	100.0	0.34	1250	3.9066	4.0342	1.0326	5.96	10.7	6.60	
0.50	1050	100.0	0.35								
	800	84.8	0.20	1050	—	—	—	0.66	1.6	5.97	
	850	95.0	0.25	1100	—	—	—	0.72	4.5	6.16	
	900	96.3	0.27	1150	—	—	—	0.89	9.9	6.52	
	950	98.0	0.30	1200	—	—	—	1.27	10.3	6.22	
0.75	1000	100.0	0.35	1250	—	—	—	4.55	2.8	5.99	
	1050	100.0	0.36								
	800	86.7	0.21	1050	3.9145	—	—	0.49	1.6	5.46	
	850	87.4	0.27	1100	3.9122	—	—	0.50	1.2	5.47	
	900	97.3	0.30	1150	3.9011	—	—	0.54	9.0	5.59	
	950	98.2	0.33	1200	3.9080	—	—	0.67	12.3	5.42	
	1000	100.0	0.35	1250	3.9072	—	—	1.56	5.7	5.40	
	1050	100.0	0.37								

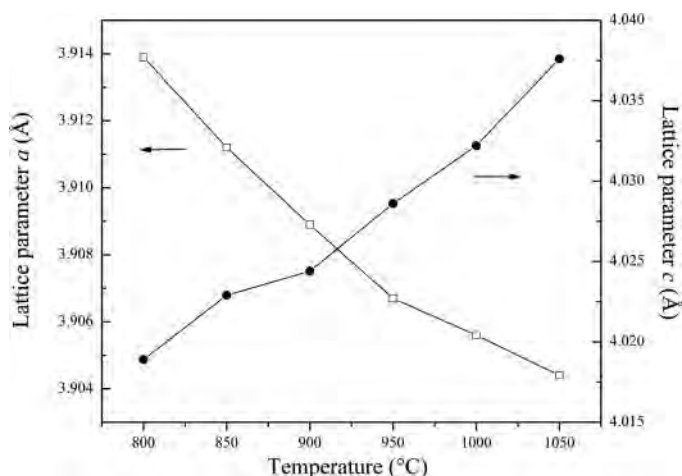


**Figure 3.** The lattice parameter *a* and *c* of PST powders  $x = 0.25$  at various calcination temperatures.

mixed in an agate mortar, then calcined between 800 and 1050°C for 2 h. The calcined powders were reground by wet ball milling with a 2 wt% binder for 24 h. The obtained powders were pressed into the pellets with a diameter of 15 mm prior to sintering between 1050 and 1250°C for 2 h. X-ray diffraction (XRD) was performed to examine the phase constitution of the specimens at room temperature. The microstructure of the PST samples were examined using scanning electron microscopy (SEM). The densities of the sintered ceramics were measured by the Archimedes's method and the average grain size was determined by using a mean linear intercept method.

## Results and Discussion

Figure 1 shows the TGA and DTA curves of raw materials and urea: (a)  $x = 0.25$  and (b)  $x = 0.75$ . For  $x = 0.25$ , demonstrated a three-stage weight loss: the first was in the

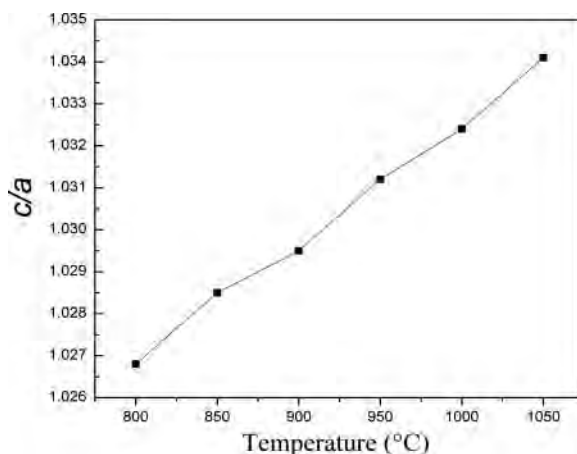


**Figure 4.** The *c/a* ratio of PST powders  $x = 0.25$  at various calcination temperatures.

temperature range from room temperature to 250°C, the second occurred from 300 to 500°C and the third at around 900°C. The first weight loss was believed to have been caused by the melting of the urea [9]. It was related to the endothermic peaks in the DTA curves at 168, 193 and 235°C. The second weight loss was caused by the evaporation of water and gas [10]. This was associated with endothermic peaks at 334 and 478°C. The third corresponded to an endothermic peak at 996°C, which may represent the reaction of PbO, SrCO<sub>3</sub> and TiO<sub>2</sub>. For  $x = 0.75$ , demonstrated a three-stage weight loss: the first and second one were similar with  $x = 0.25$ , the third one was around 800°C. The first weight loss was related to the endothermic peaks in the DTA curves at 179 and 228°C. The second weight loss was associated with endothermic peaks at 377 and 503°C. The third corresponded to an endothermic reaction caused by the decomposition of intermediate carbonate leading to the formation of single phase PST. The peak was related to a small endothermic peak at 920°C, and the last one around 1019°C. Based on the results of the DTA and TGA, a series of calcinations for the PST powders were carried out from 800 to 1050°C for 2 h, at a heating/cooling rate of 5°C/min.

The XRD patterns of the PST powders, formed with different calcined temperatures and Sr content are given in Fig. 2 (a) and (b). It was found that the PST powders with  $x = 0.25$  indexed in a tetragonal structure, which matched with JCPDS file number 06-0452. While, the PST powders with  $x = 0.75$  indexed in a cubic structure, which matched with JCPDS file number 39-1395 and corresponded with the previous works [11, 12]. The PST powders with  $x = 0.50$ , indexed as a mixed phase between the tetragonal and the cubic phase [13]. The XRD pattern of the tetragonal phase is known to contain the doublet reflections of (001)(100), (101)(110), (002)(200), (201)(210) and (112)(211). The XRD pattern of the cubic phase, these doublet reflections are merged and change to the singlet peak of (100), (110), (200), (210) and (211). In this study, the doublet reflections of (101)(110), (201)(210) and (112)(211) of the PST powders with  $x = 0.50$  merged to the singlet peak. While, (001)(100) and (002)(200) were still in the combine step, the doublet peaks of the tetragonal phase were shifted toward each other and the intensity of the (001) and (002) peaks were reduced to a background level. Unfortunately, they still did not absolutely merge. These observations confirmed that the tetragonal and cubic phase coexist in PST powders with  $x = 0.50$ . In previous work, the different crystal structures of PST ceramics with  $x = 0.50$  prepared by conventional mixed oxide method have been reported [11, 12]. X. Xing *et al.* [12] and M. Jain *et al.* [11] proposed that the crystal structures belonged to tetragonal and cubic phase, respectively.

In the samples calcined below 1000°C, the precursors of the PbO, TiO<sub>2</sub> and SrCO<sub>3</sub> phase were detected (Fig. 2 (a)). A high purity of the tetragonal perovskite phase was discovered in the powders calcined above 1000°C in all compositions and are illustrated in Fig. 2 (b). This temperature was lower than the calcination temperature in the solid state reaction method by around 100°C [5]. The relative percentage in the perovskite and impurity phases was determined by measuring the major XRD peak intensities of the perovskite and impurity phases. The percentage of the perovskite phase is described by the following equation:

$$\% \text{ perovskite phase} = \left( \frac{I_{\text{perov}}}{I_{\text{perov}} + I_{\text{PbO}} + I_{\text{TiO}_2} + I_{\text{SrCO}_3}} \right) \times 100 \quad (1)$$

This equation is a well-known equation which is widely employed in the preparation of complex perovskite structure materials [14]. Here  $I_{\text{perov}}$ ,  $I_{\text{PbO}}$ ,  $I_{\text{TiO}_2}$  and  $I_{\text{SrCO}_3}$  refer to the intensity of the (101) perovskite peak and the intensities of the highest PbO, TiO<sub>2</sub> and

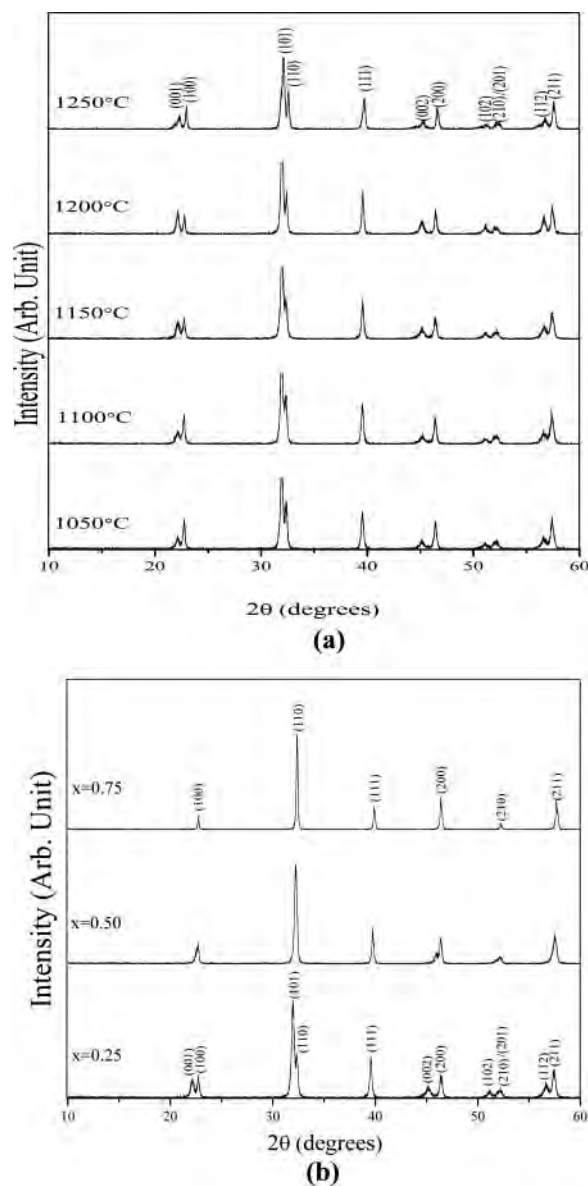


**Figure 5.** XRD patterns of PST ceramics (a)  $x = 0.25$  at various sintering temperatures and (b) sintered at 1150°C with different Sr content.

$\text{SrCO}_3$  peaks. The percentage of the perovskite phase of PST compounds are calculated and demonstrated in Table 1. The purity of the perovskite phase rose with increasing calcination temperatures and 100% of the perovskite phase was found above 1000°C. Figure 3 shows that the lattice parameter  $a$  and  $c$  of the PST powders  $x = 0.25$  at various calcination temperatures. The lattice parameter  $c$  increased correspondingly with increasing calcination temperatures, while the lattice parameter  $a$  decreased with increasing calcination temperatures. Thus, the  $c/a$  ratio was increased with the increasing the calcination temperatures



as seen in Fig 4. For  $x = 0.75$ , while the lattice parameter  $a$  decreased from 3.9145 to 3.9072 Å with an increase in the calcining temperatures. Figure 5 (a) shows the XRD pattern of the PST ceramics with 0.25 at different sintering temperatures. The pure perovskite phase was found in all the sintered pellet samples. Figure 5 (b) shows the XRD patterns of the PST ceramics with different Sr content using a sintering temperature of 1150°C. For  $x = 0.25$  the lattice parameter  $c$  and  $c/a$  ratio increased, while the lattice parameter  $a$  decreased with increasing sintering temperatures. For  $x = 0.75$  the lattice parameter  $a$  decreased with increasing sintering temperatures (Table 1).

The SEM photomicrographs of PST calcined powders and sintered ceramics are illustrated in Fig. 6. These powders exhibited an almost spherical morphology and have a porous agglomerated form as shown in Fig. 6 (a), (b) and (c). The particle size, which is calculated from the cutting lines in SEM (Table 1). The average particle size tended to increase with an increased calcination temperatures, while the average particle size tended to increase with increased Sr content. Figure 6 (d), (e) and (f) show the microstructure of PST ceramics with different Sr content at a sintering temperature of 1150°C. The grains are nearly spherical in shape. At the same sintering temperature, the average grain size tended

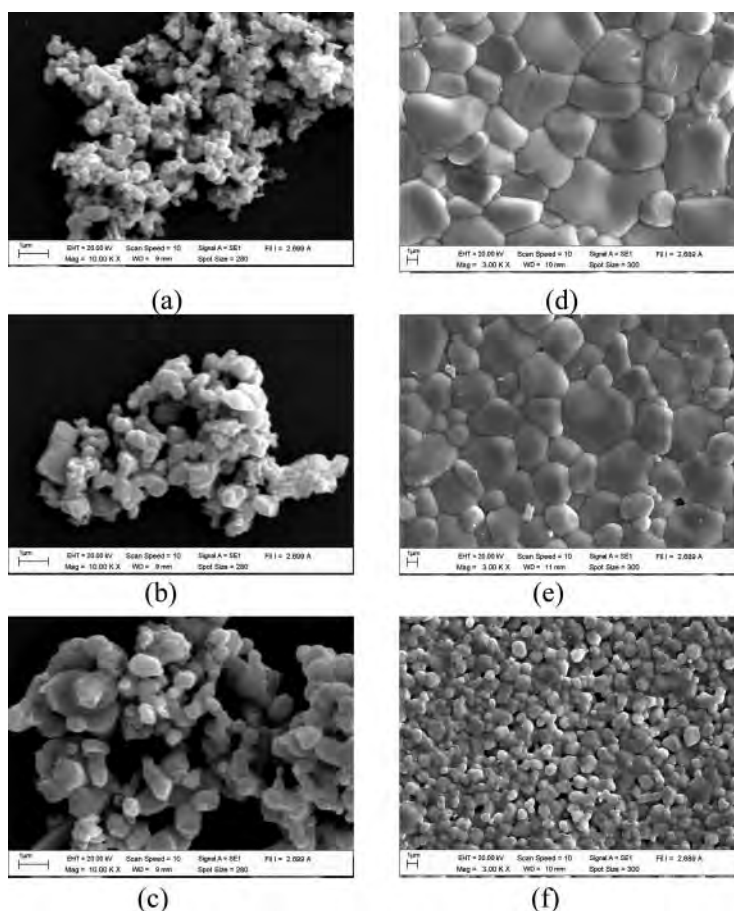


**Figure 6.** SEM morphology of PST calcined powders with  $x = 0.25$ ; (a) 800°C, (b) 900°C and (c) 1050°C, and ceramics sintered at 1250°C; (d)  $x = 0.25$ , (e)  $x = 0.50$  and (f)  $x = 0.75$ .

to decrease with an increase of Sr content. The average grain size tended to increase with an increase sintering temperatures (Table 1).

The variation of the measured shrinkage and density of PST ceramics with different sintering temperatures and Sr content are shown in Table 1. The shrinkage increased with increased sintering temperatures up to 1200°C and decreased with higher sintering temperatures. The density increased with increased sintering temperatures up to 1150°C and decreased with higher sintering temperatures. At the same sintering temperature, the density tended to decrease with increased Sr content. In this study, for  $x = 0.50$ , the maximum density (97%) were obtained from the samples sintered at 1150°C. While, the maximum density (95%) of the PST ceramics with  $x = 0.50$  prepared via the mixed oxide method were obtained from the samples sintered at 1200°C [5]. The combustion method, produced denser ceramics at lower sintering temperatures.

## Conclusions

A high density of  $(\text{Pb}_{1-x}\text{Sr}_x)\text{TiO}_3$  (PST) ceramics with  $0.25 \leq x \leq 0.75$  were successfully obtained via the combustion method. The purest tetragonal perovskite phase was discovered in powders calcined above 1000°C in all compositions. The structural phase of PST ceramics were in a tetragonal phase for  $x = 0.25$  and a cubic phase for  $x = 0.75$ . The samples were in a mixed phase between—tetragonal and cubic phase—at  $x = 0.50$ . The average particle size and average grain size tended to increase with increasing calcination and sintering temperatures. The average particle size tended to increase, while average grain size tended to decrease with an increased Sr content in all the samples. The maximum density of 97% was obtained from the samples sintered at 1150°C, which is lower than the conventional mixed oxide method by around 50°C. The firing temperatures and Sr content have directly affected the phase formation, microstructure, density and shrinkage of the PST ceramics.

## Acknowledgments

This work was financially supported by the Thailand Research Fund (TRF), Commission on Higher Education (CHE). The authors wish to thanks the Science Lab Center, Faculty of Science, Naresuan University for supporting facilities. Thanks are also given to Mr. Don Hindle for his help in editing the manuscript.

## References

1. Y. Somiya, A. S. Bhalla, and L. E. Cross, Study of  $(\text{Sr}, \text{Pb})\text{TiO}_3$  ceramics on dielectric and physical properties. *Int. J. Inorg. Mater.* **3**, 709–714 (2001).
2. T. Fujii and M. Adachi, Preparation of  $(\text{Pb}, \text{Sr})\text{TiO}_3$  films by sol-gel technique. *Jpn. J. Appl. Phys.* **44**, 692–694 (2005).
3. F. Zhang, T. Karaki, and M. Adachi, Preparation and Curie temperatures of nanosized  $(\text{Pb}, \text{Sr})\text{TiO}_3$  powders. *Jpn. J. Appl. Phys.* **44**, 6995–6997 (2005).
4. J. Zhai, X. Yao, Z. Xu, and H. Chen, Enhancement of ferroelectricity in the compositionally graded  $(\text{Pb}, \text{Sr})\text{TiO}_3$  thin films derived by a sol-gel process. *J. Crystal Growth.* **286**, 37–41 (2006).
5. I. Rivera, A. Kumar, F. Mendoza, and R. S. Katiyar, Investigation of dielectric, electrical and optical properties of  $\text{Pb}_{0.5}\text{Sr}_{0.5}\text{TiO}_3$  ceramic. *Physica B.* **403**, 2423–2430 (2008).
6. A. M. Azad and S. Subramaniam, Temperature dependence of the dielectric response of  $\text{BaZrO}_3$  by immittance spectroscopy. *Mater Res Bull.* **37**, 11–21 (2002).

7. M. Viviani, M. Buscaglia, V. Buscaglia, M. Leoni, and P. Nanni, Barium perovskites as humidity sensing materials. *J Eur Ceram Soc.* **21**, 1981–1984 (2001).
8. T. Bongkarn and W. Tangkawsakul, Low temperature preparation of antiferroelectric PZ and PBZ powders using the combustion technique. *Ferroelectrics*. **383**, 50–56 (2009).
9. D. Xue, J. Xu, and C. Yan, Chemical synthesis of  $\text{NaTaO}_3$  powder at low-temperature. *Mater Lett.* **59**, 2920–2922 (2005).
10. T. Bongkarn and A. Thongtha, Fabrication and characterization of perovskite  $\text{SrZrO}_3$  ceramics through a combustion technique. *Key Eng Mater.* **421–422**, 223–226 (2010).
11. M. Jain, Y. I. Yuzyuk, R. S. Katiyar, Y. Somiya, and A. S. Bhalla, Local symmetry breaking in  $\text{Pb}_x\text{Sr}_{1-x}\text{TiO}_3$  ceramics and composites studied by Raman spectroscopy. *J Appl Phys.* **98**, 2–7 (2005).
12. X. Xing, J. Chen, J. Deng, and G. Liu, Solid solution  $\text{Pb}_{1-x}\text{Sr}_x\text{TiO}_3$  and its thermal Expansion. *J. Alloys Compd.* **360**, 286–289 (2003).
13. S. H. Leal, M. T. Escote, F. M. Pontes, E. R. Joya, P. S. Pizani, E. Longo, and J. A. Varela, Structure transition on  $\text{Pb}_{1-x}\text{Sr}_x\text{TiO}_3$  produced by chemical method. *J. Alloys Compd.* **475**, 940–945 (2009).
14. T. Bongkarn, A. Thongtha, and A. Angsukased, Influences of firing temperature on phase and morphology evolution of  $(\text{Ba}_{0.5}\text{Sr}_{0.5})(\text{Zr}_{0.75}\text{Ti}_{0.25})\text{O}_3$  ceramics synthesized via solid-state reaction method. *Key Eng Mater.* **421–422**, 247–250 (2010).

This article was downloaded by: [Naresuan University]

On: 14 November 2012, At: 20:57

Publisher: Taylor & Francis

Informa Ltd Registered in England and Wales Registered Number: 1072954 Registered office: Mortimer House, 37-41 Mortimer Street, London W1T 3JH, UK



## Phase Transitions: A Multinational Journal

Publication details, including instructions for authors and subscription information:

<http://www.tandfonline.com/loi/gpht20>

### Phase formation and dielectric properties of $(\text{Pb}_{0.925}\text{Ba}_{0.075})(\text{Zr}_{1-x}\text{Ti}_x)\text{O}_3$ ceramics prepared by the solid-state reaction method

Atthakorn Thongtha<sup>a</sup>, Chakkaphan Wattanawikkam<sup>a</sup> & Theerachai Bongkarn<sup>a</sup>

<sup>a</sup> Department of Physics, Faculty of Science, Naresuan University, Phitsanulok 65000, Thailand

Version of record first published: 25 Jul 2011.

To cite this article: Atthakorn Thongtha, Chakkaphan Wattanawikkam & Theerachai Bongkarn (2011): Phase formation and dielectric properties of  $(\text{Pb}_{0.925}\text{Ba}_{0.075})(\text{Zr}_{1-x}\text{Ti}_x)\text{O}_3$  ceramics prepared by the solid-state reaction method, Phase Transitions: A Multinational Journal, 84:11-12, 952-959

To link to this article: <http://dx.doi.org/10.1080/01411594.2011.599563>

PLEASE SCROLL DOWN FOR ARTICLE

Full terms and conditions of use: <http://www.tandfonline.com/page/terms-and-conditions>

This article may be used for research, teaching, and private study purposes. Any substantial or systematic reproduction, redistribution, reselling, loan, sub-licensing, systematic supply, or distribution in any form to anyone is expressly forbidden.

The publisher does not give any warranty express or implied or make any representation that the contents will be complete or accurate or up to date. The accuracy of any instructions, formulae, and drug doses should be independently verified with primary sources. The publisher shall not be liable for any loss, actions, claims, proceedings, demand, or costs or damages whatsoever or howsoever caused arising directly or indirectly in connection with or arising out of the use of this material.

## Phase formation and dielectric properties of $(\text{Pb}_{0.925}\text{Ba}_{0.075})(\text{Zr}_{1-x}\text{Ti}_x)\text{O}_3$ ceramics prepared by the solid-state reaction method

Atthakorn Thongtha, Chakkaphan Wattanawikkam and Theerachai Bongkarn\*

*Department of Physics, Faculty of Science, Naresuan University, Phitsanulok 65000, Thailand*

*(Received 11 December 2010; final version received 21 June 2011)*

Lead barium zirconate titanate  $[(\text{Pb}_{0.925}\text{Ba}_{0.075})(\text{Zr}_{1-x}\text{Ti}_x)\text{O}_3]$  ceramics with  $0 \leq x \leq 1$  were prepared by the solid-state reaction method. The calcination temperatures were between  $800^\circ\text{C}$  and  $1000^\circ\text{C}$  for 1 h and the sintering temperature was  $1200^\circ\text{C}$  for 3 h. It was found that the structure of the calcined powders and sintered pellets was in an orthorhombic phase for  $x=0$ ; a rhombohedral phase for  $x=0.25$  and a tetragonal phase for  $0.5 \leq x \leq 1$ . The  $c/a$  ratio increased with an increase in the  $x$  content. The average particle size and density slightly decreased with an increase in the  $x$  content, while the average grain size, linear shrinkage, and Curie temperature increased when the  $x$  content increased.

**Keywords:** lead barium zirconate titanate; microstructure; phase transition; crystal structure; dielectric properties

### 1. Introduction

Lead barium zirconate  $(\text{Pb}_{1-x}\text{Ba}_x)\text{ZrO}_3$  (PBZ) is one of the perovskite structure materials discovered by Roberts [1,2] in 1950. The investigation of the structural phase at room temperature indicated that: PBZ with  $0 \leq x \leq 0.175$  has an orthorhombic anti-ferroelectric phase; PBZ with  $0.175 < x \leq 0.35$  has a rhombohedral ferroelectric phase; and PBZ with  $0.35 < x \leq 1$  has a cubic paraelectric phase [3–6]. The Curie temperature of the PBZ materials decreased with the increase of  $x$ , from  $230^\circ\text{C}$  for  $x=0$  to  $50^\circ\text{C}$  for  $x=0.35$  [7]. The maximum dielectric constant at Curie temperature was observed at  $x=0.25$  and a relaxor ferroelectric behavior was exhibited at  $x=0.30$  [7]. For  $x \leq 0.10$ , the electric field induced an anti-ferroelectric-to-ferroelectric phase transition which gave a large increase in volume [3,8,9]. Specifically, the anti-ferroelectric-to-ferroelectric phase transition of  $(\text{Pb}_{0.925}\text{Ba}_{0.075})\text{ZrO}_3$  ceramics exhibited high expansion, which makes this ceramic an interesting candidate for application in large-displacement actuator devices [3].

Lead barium titanate  $(\text{Pb}_{1-x}\text{Ba}_x)\text{TiO}_3$  (PBT) with  $0 \leq x \leq 1$  is a perovskite ferroelectric material which has a tetragonal structure at room temperature [10–14]. It changes from a ferroelectric to a paraelectric phase when it receives a certain Curie temperature. The Curie temperature of PBT materials drops monotonically with an increase of  $x$ , from  $490^\circ\text{C}$  at

---

\*Corresponding author. Email: researchcmu@yahoo.com

$x=0$  to  $120^\circ\text{C}$  at  $x=1$  [15].  $(\text{Pb}_{0.925}\text{Ba}_{0.075})\text{TiO}_3$  has a high Curie temperature ( $\sim 457^\circ\text{C}$ ) [13,14]. It has been considered for use in high-temperature electric and optical devices.

Lead barium zirconate titanate (PBZT) ceramic is a solid system composed of orthorhombic anti-ferroelectric, rhombohedral ferroelectric, cubic paraelectric PBZ, and ferroelectric PBT. Recently, Ujma et al. [16–18] studied the dielectric properties of  $(\text{Pb}_{0.75}\text{Ba}_{0.25})(\text{Zr}_{0.70}\text{Ti}_{0.30})\text{O}_3$  ceramic which is the solid solution of rhombohedral ferroelectric PBZ and tetragonal ferroelectric PBT. They found typical relaxor behavior. The magnitude of the dielectric constant decreased and the maximum shifted to higher temperatures with increased frequency. After a survey of the literature, it was found that the dielectric properties and phase transition of a solid solution of orthorhombic anti-ferroelectric PBZ and tetragonal ferroelectric PBT have not been studied. Therefore, in this study, the phase formation, microstructure, phase transition, and dielectric properties of  $(\text{Pb}_{0.925}\text{Ba}_{0.075})(\text{Zr}_{1-x}\text{Ti}_x)\text{O}_3$  (PBZT) ceramics with  $0 \leq x \leq 1$  were investigated. The PBZT ceramics were prepared by the solid-state reaction method. The structural phase, microstructure, dielectric constant, and dielectric loss with a variation of frequencies of the PBZT ceramics were characterized by a X-ray diffractometer (XRD), scanning electron microscopy (SEM), and LCR meter.

## 2. Experimental

The  $(\text{Pb}_{0.925}\text{Ba}_{0.075})(\text{Zr}_{1-x}\text{Ti}_x)\text{O}_3$  ceramics with  $0 \leq x \leq 1$  were prepared by a conventional solid-state reaction method. The raw materials of  $\text{PbO}$ ,  $\text{BaCO}_3$ ,  $\text{ZrO}_2$ , and  $\text{TiO}_2$  were weighed and mixed by ball milling in ethanol using zirconia balls for 24 h. After drying and sieving, they were calcined between  $800^\circ\text{C}$  and  $1000^\circ\text{C}$  for 1 h. The calcined powders were reground by ball milling and mixed with 2 wt% binder for 24 h. The calcined powders were then dried, crushed, and sieved. The powders were isostatically pressed at 80 MPa into 15 mm diameter pellets. Finally, the pellets were sintered at  $1200^\circ\text{C}$  for 3 h. In order to minimize the loss of lead due to vaporization, the  $\text{PbO}$  atmosphere during the sintering process was maintained using lead titanate and lead zirconate as the spacer powders. The crystal structure and microstructure of the calcined and sintered samples were characterized by an XRD and SEM, respectively. The average particle size and average grain size were determined using a mean linear intercept method. The Archimedes displacement method with distilled water was employed to evaluate the sample's density. Silver paste was coated and fired at  $550^\circ\text{C}$  for 5 min to form electrodes. Dielectric constants with various frequencies were also measured by an LCR meter.

## 3. Results and discussion

Figure 1 shows the XRD pattern of PBZT powders with  $0 \leq x \leq 1$ . The pure perovskite phase was observed for all compositions. For  $x=0$ , the structural phase, indexed in an orthorhombic phase, matched the JCPDS file number 35-0739 [19] and corresponded to previous works [3,5,7,20]. For  $x=0.25$ , the structural phase belonged to the rhombohedral phase which matched the JCPDS file number 29-0775 [21]. For  $0.5 \leq x \leq 1$ , the samples indexed in the tetragonal phase matched JCPDS file number 06-0452 [22], as shown in Figure 1(a). To investigate the range of the rhombohedral structure, the XRD patterns of  $x=0.05, 0.1, 0.2, 0.3, 0.4$ , and  $0.45$  were also studied, as shown in Figure 1(b). The structural phase changed from orthorhombic to rhombohedral and rhombohedral to tetragonal when  $x=0.05$  and  $0.4$ , respectively. The XRD results from the sintered pellets

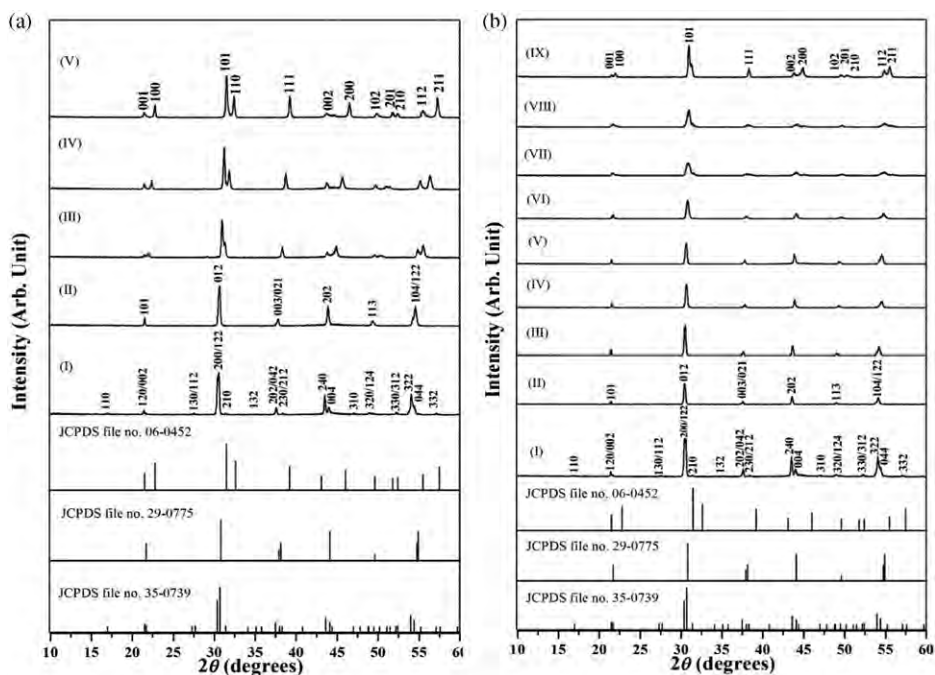


Figure 1. (a) XRD pattern of PBZT powders with (I)  $x = 0$  calcined at  $1000^{\circ}\text{C}$ , (II)  $x = 0.25$  calcined at  $950^{\circ}\text{C}$ , (III)  $x = 0.5$  calcined at  $900^{\circ}\text{C}$ , (IV)  $x = 0.75$  calcined at  $850^{\circ}\text{C}$ , and (V)  $x = 1$  calcined at  $800^{\circ}\text{C}$ . (b) XRD pattern of PBZT powders with (I)  $x = 0$  calcined at  $1000^{\circ}\text{C}$ , (II)  $x = 0.05$  calcined at  $990^{\circ}\text{C}$ , (III)  $x = 0.1$  calcined at  $980^{\circ}\text{C}$ , (IV)  $x = 0.2$  calcined at  $960^{\circ}\text{C}$ , (V)  $x = 0.25$  calcined at  $950^{\circ}\text{C}$ , (VI)  $x = 0.3$  calcined at  $940^{\circ}\text{C}$ , (VII)  $x = 0.4$  calcined at  $920^{\circ}\text{C}$ , (VIII)  $x = 0.45$  calcined at  $910^{\circ}\text{C}$ , and (IX)  $x = 0.5$  calcined at  $900^{\circ}\text{C}$ .

were similar to the results from the XRD powders, as shown in Figure 2. The lattice parameters  $a$ ,  $b$ , and  $c$  of the PBZT ceramics were calculated by the least square method and are shown in Table 1. For  $0.5 \leq x \leq 1$ , the lattice parameters  $a$  and  $c$  decreased with increased  $x$  values. The  $c/a$  ratio increased while the unit cell volume decreased when the  $x$  values increased, as given in Table 1.

The SEM morphology of the PBZT powders is shown in Figure 3(a)–(c). The particles were agglomerated and were irregular in shape with a variation in particle size. The average particle size of  $0 \leq x \leq 0.75$  showed little difference in their values, while the value in the size of the  $x = 1$  sample rapidly decreased. The average particle size of  $0 \leq x \leq 1$  was between  $0.4$  and  $1.7\ \mu\text{m}$ . The change of the PBZT ceramic surface morphology was a function of increasing  $x$ , as shown in Figure 3(d)–(f). The increase of the average grain sizes was between  $2.3$  and  $3.9\ \mu\text{m}$  when the  $x$  content was increased from  $0$  to  $1$ , as given in Table 1. The measured density and linear shrinkage with the variation of the  $x$  content are shown in Table 1. The increase of the  $x$  content also affected density and linear shrinkage. The density tended to decrease, while the linear shrinkage tended to increase with the increase of  $x$ . The obtained density of all samples was around  $96\%$  of the theoretical density.

Figure 4(a)–(c) illustrates the temperature dependence of the dielectric constant ( $\epsilon_r$ ) of PBZT ceramics at various frequencies. For  $x = 0$ , the dielectric constant showed two peaks. The first peak showed an anomaly around  $105^{\circ}\text{C}$ , which was due to the phase

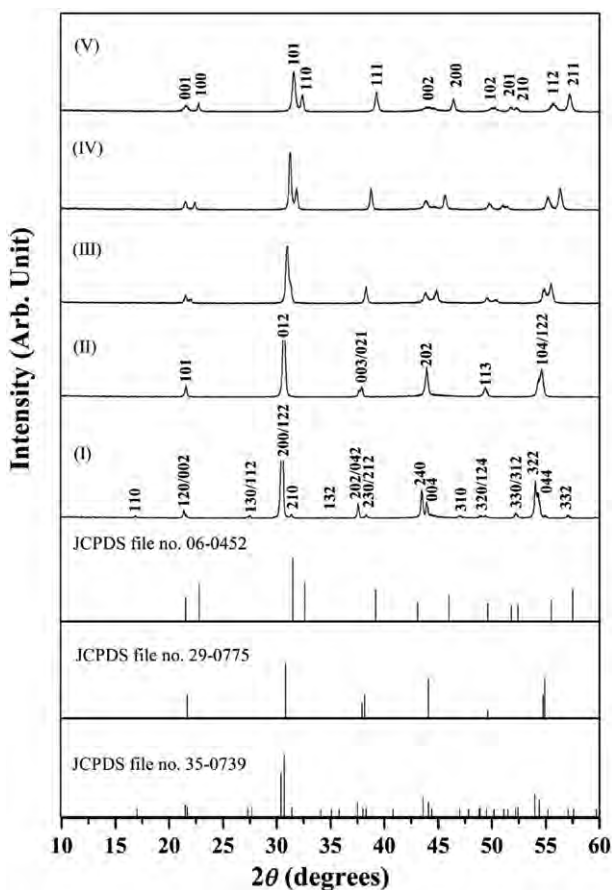


Figure 2. XRD pattern of PBZT ceramics sintered at 1200°C with: (I)  $x=0$ , (II)  $x=0.25$ , (III)  $x=0.5$ , (IV)  $x=0.75$ , and (V)  $x=1$ .

transition from an antiferroelectric to a ferroelectric state. This phase transition was explained and confirmed by previous works [3,6,7,9]. The second peak was at around 202°C, which was caused by a ferroelectric–paraelectric transformation process, as shown in Figure 4(a). When the content of  $x$  increased, the anomalous peak vanished but the ferroelectric–paraelectric phase transition still occurred and the Curie temperature moved toward a higher temperature, as shown in Figure 4(a)–(d). At varied frequencies, the samples with  $x=0$  did not change the Curie temperature, as is demonstrated in Figure 4(a), while  $x \geq 0.25$  effected the shift of Curie temperature, as shown in Figure 4(b) and (c) and is listed in Table 2. The Curie temperature shifted to a higher temperature with increased frequency. The dielectric constant at a Curie temperature of  $x \geq 0.25$  decreased when the frequency increased from 1 to 100 kHz, as shown in Figure 4(b) and (c). This is a typical behavior of relaxor ferroelectrics with  $x \geq 0.25$ . For  $x \geq 0.25$ , the result is similar to previous works describing  $(\text{Pb}_{0.75}\text{Ba}_{0.25})(\text{Zr}_{0.70}\text{Ti}_{0.30})\text{O}_3$  ceramics [16–18]. For the same frequency at 1, 10, and 100 kHz, the dielectric constant at room temperature first increased and reached its highest at  $x=0.75$  and then the value dropped when  $x$  was higher than 0.75, as given in Table 2. The frequency and content of  $x$  affected the dielectric properties.



Table 1. Crystal structure, lattice parameters,  $c/a$  ratio, unit cell volume, grain size, density, and linear shrinkage of PBZT ceramics.

X	Crystal structure	Lattice parameters (Å)			$c/a$ ratio	Unit cell volume (Å <sup>3</sup> )	Grain size (μm)	Bulk density (g cm <sup>-3</sup> )	Theoretical density (%)	Linear shrinkage (%)
		$a$	$b$	$c$						
0	Orthorhombic	5.2459	11.4839	7.8661	—	473.8805	2.3	7.54	95.4	14.24
0.25	Rhombohedral	4.1188	4.1188	4.1188	—	69.8734	2.6	7.51	95.7	16.25
0.5	Tetragonal	4.0426	4.0426	4.1355	1.0225	67.5848	3.0	7.49	96.1	17.09
0.75	Tetragonal	3.9766	3.9766	4.1301	1.0386	65.3107	3.1	7.47	96.5	17.49
1	Tetragonal	3.9115	3.9115	4.1287	1.0555	63.1684	3.9	7.43	96.6	17.74

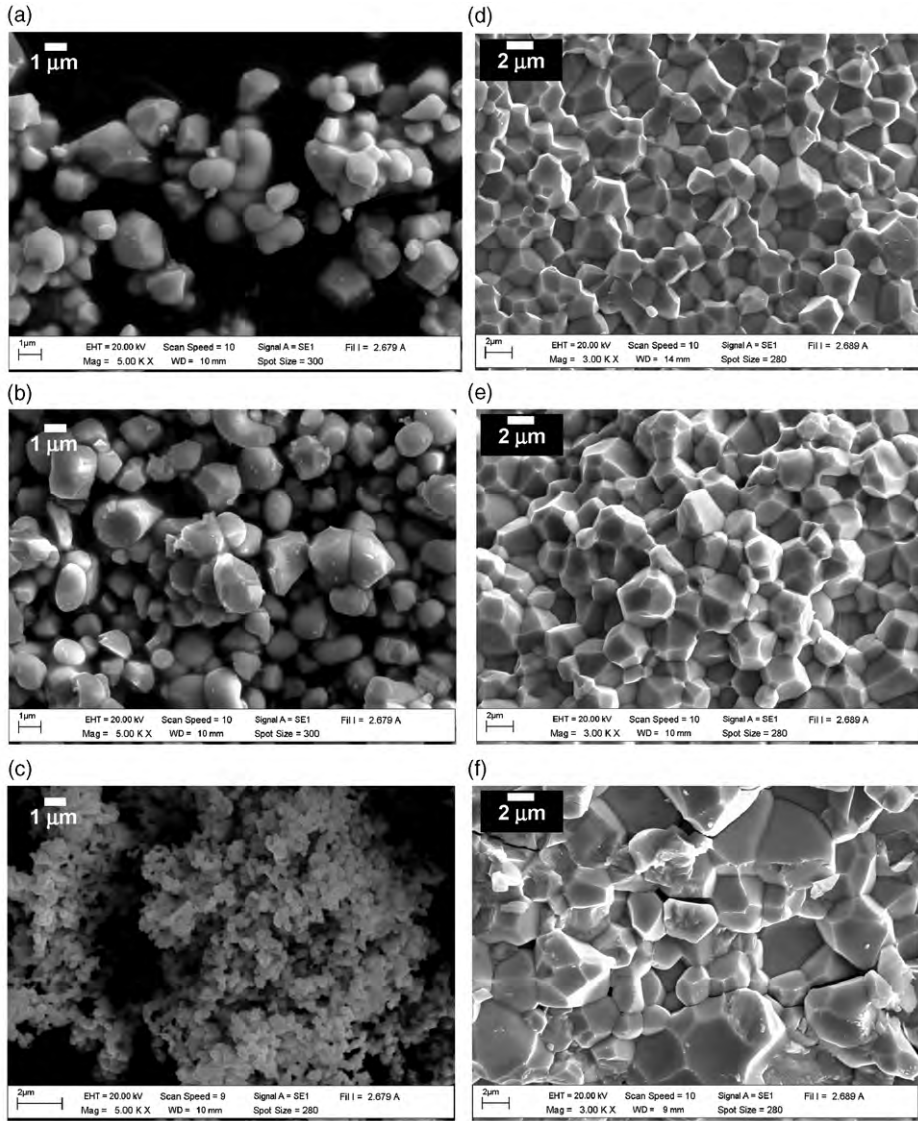


Figure 3. SEM morphology of PBZT powders with: (a)  $x=0.5$  calcined at  $900^{\circ}\text{C}$ , (b)  $x=0.75$  calcined at  $850^{\circ}\text{C}$ , and (c)  $x=1$  calcined at  $800^{\circ}\text{C}$  and PBZT ceramics with: (d)  $x=0.5$ , (e)  $x=0.75$ , and (f)  $x=1$  sintered at  $1200^{\circ}\text{C}$ .

#### 4. Conclusions

The results indicated that the concentration of  $\text{Zr}^{4+}$  and  $\text{Ti}^{4+}$  ions has a significant effect on the phase formation, microstructure, and dielectric properties of PBZT ceramics. The structure phase of  $(\text{Pb}_{0.925}\text{Ba}_{0.075})(\text{Zr}_{1-x}\text{Ti}_x)\text{O}_3$  (PBZT) samples is in an orthorhombic phase for  $x=0$ ; a rhombohedral phase for  $x=0.25$  and a tetragonal phase for  $0.5 \leq x \leq 1$ . The average particle is  $0.4\text{--}1.7\mu\text{m}$  and the average grain size is  $2.3\text{--}3.9\mu\text{m}$ . The linear shrinkage, average grain size, and Curie temperature of the PBZT increased, while the

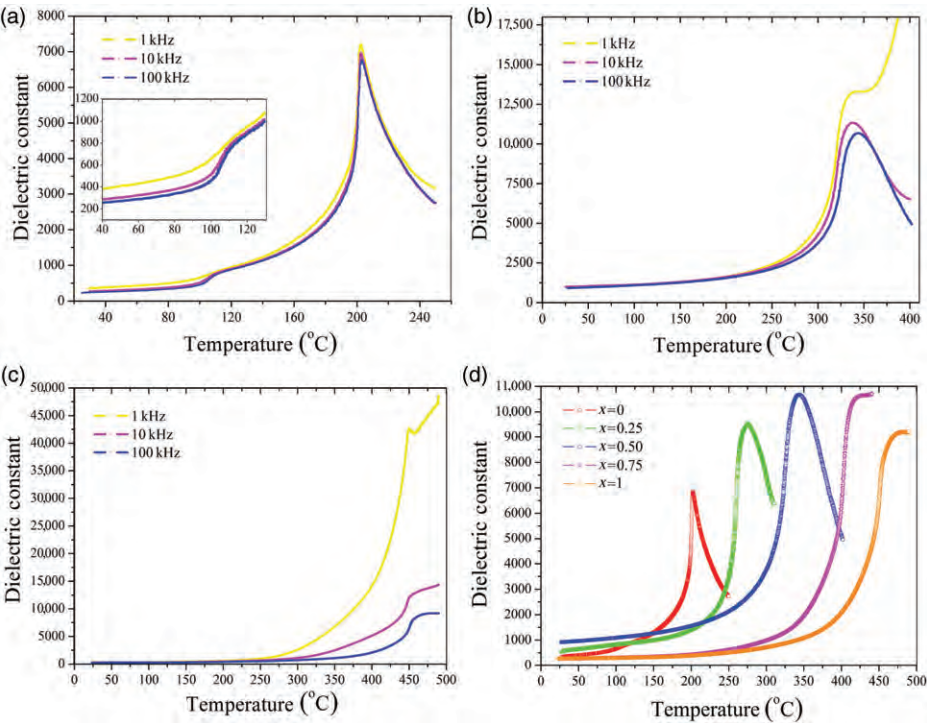


Figure 4. Functional temperature and frequency of the dielectric constant of PBZT ceramics with: (a)  $x=0$ , (b)  $x=0.5$ , (c)  $x=1$ , and (d) PBZT ceramics with  $0 \leq x \leq 1$  measured at 100 kHz.

Table 2. Curie temperature ( $T_c$ ), dielectric constant ( $\epsilon_r$ ), and loss tangent ( $\tan \delta$ ) of PBZT ceramic at room temperature.

$x$	1 kHz			10 kHz			100 kHz		
	$T_c$ (°C)	$\epsilon_r$	$\tan \delta$	$T_c$ (°C)	$\epsilon_r$	$\tan \delta$	$T_c$ (°C)	$\epsilon_r$	$\tan \delta$
0	202	128	0.008	202	126	0.006	202	124	0.005
0.25	272	253	0.032	274	251	0.006	274	250	0.002
0.5	337	878	0.002	338	875	0.002	344	873	0.002
0.75	405	920	0.003	407	917	0.002	410	915	0.002
1	450	268	0.084	452	216	0.051	458	204	0.016

average particle size and density decreased, when the  $x$  content increased. Typical relaxor ferroelectrics were discovered in the PBZT sample with  $x \geq 0.25$ .

### Acknowledgments

This study was financially supported by Thailand Research Fund (TRF) and Commission in Higher Education (CHE). The authors also thank the Department of Physics, Faculty of Science, Naresuan

University for providing facilities. They also acknowledge Mr. Don Hindle for his helpful correction of this article.

## References

- [1] S. Roberts, *Dielectric properties of lead zirconate and barium-lead zirconate*, J. Am. Ceram. Soc. 33 (1950), pp. 63–66.
- [2] S. Roberts, *Piezoelectric effect in lead zirconate*, Phys. Rev. 83 (1951), p. 1078.
- [3] G. Rujijanagul and T. Bongkarn, *Phase transition and linear thermal expansion of  $(\text{Pb}_{1-x}\text{Ba}_x)\text{ZrO}_3$  ceramics*, Phase Trans. 80 (2007), pp. 209–215.
- [4] T. Bongkarn and G. Rujijanagul, *Properties of perovskite lead barium zirconate ceramics*, Ferroelectrics 358 (2007), pp. 67–73.
- [5] B.P. Pokharel, M.K. Datta, and D. Pandey, *Influence of calcination and sintering temperature on the structure of  $(\text{Pb}_{1-x}\text{Ba}_x)\text{ZrO}_3$* , J. Mater. Sci. 34 (1999), pp. 691–700.
- [6] T. Bongkarn, G. Rujijanagul, and S.J. Milne, *Antiferroelectric-ferroelectric phase transitions in  $\text{Pb}_{1-x}\text{Ba}_x\text{ZrO}_3$  ceramics: Effect of PbO content*, Appl. Phys. Lett. 92 (2008), p. 092905.
- [7] B.P. Pokharel and D. Pandey, *Dielectric studies of phase transitions in  $(\text{Pb}_{1-x}\text{Ba}_x)\text{ZrO}_3$* , J. Appl. Phys. 88 (2000), pp. 5364–5373.
- [8] T. Bongkarn, G. Rujijanagul, and S.J. Milne, *Effect of excess PbO on phase formation and properties of  $(\text{Pb}_{0.90}\text{Ba}_{0.10})\text{ZrO}_3$  ceramics*, Mater. Lett. 59 (2005), pp. 1200–1205.
- [9] N. Vittayakorn, T. Bongkarn, and G. Rujijanagul, *Phase transition, mechanical, dielectric and piezoelectric properties of perovskite  $(\text{Pb}_{1-x}\text{Ba}_x)\text{ZrO}_3$  ceramics*, Physica B. 387 (2007), pp. 415–420.
- [10] T. Bongkarn and P. Panya, *Fabrication of lead barium titanate ceramics via conventional solid-state mixed oxide technique*, Adv. Mater. Res. 55–57 (2008), pp. 209–212.
- [11] W.D. Yang and S.M. Haile, *Highly preferred oriented lead barium titanate thin films using acetylacetone as chelating agent in sol-gel process*, Rev. Adv. Mater. Sci. 10 (2005), pp. 143–148.
- [12] X. Xing, J. Deng, Z. Zhu, and G. Liu, *Solid solution  $\text{Ba}_{1-x}\text{Pb}_x\text{TiO}_3$  and its thermal expansion*, J. Alloy. Comp. 353 (2003), pp. 1–4.
- [13] R. Sumang and T. Bongkarn, *Phase formation, microstructure and phase transition of lead barium titanate ceramics: Effect of PbO content*, Ferroelectrics 383 (2009), pp. 57–64.
- [14] P. Panya, S. Ramaneepikool, and T. Bongkarn, *Dependence of firing temperatures on phase formation, microstructure and phase transition of  $(\text{Pb}_{1-x}\text{Ba}_x)\text{TiO}_3$  ceramics*, Ferroelectrics 403 (2010), pp. 204–212.
- [15] O.Z. Yanchevskii, O.I. V'yunov, and A.G. Belousov, *Fabrication and properties of semiconducting barium lead titanate ceramics containing low-melting glass additions*, Inorg. Mater. 39 (2003), pp. 645–651.
- [16] Z. Ujma, M. Adamczyk, and J. Handerek, *Relaxor properties of  $(\text{Pb}_{0.75}\text{Ba}_{0.25})(\text{Zr}_{0.70}\text{Ti}_{0.30})\text{O}_3$  ceramics*, J. Eur. Ceram. Soc. 18 (1998), pp. 2201–2207.
- [17] J. Handerek, M. Adamczyk, and Z. Ujma, *Dielectric and pyroelectric properties of  $(\text{Pb}_{0.75}\text{Ba}_{0.25})(\text{Zr}_{0.70}\text{Ti}_{0.30})\text{O}_3$  [ $x = 0.25 \div 0.35$ ] ceramics exhibiting the relaxor ferroelectrics behaviour*, Ferroelectrics 233 (1999), pp. 253–270.
- [18] M. Adamczyk, Z. Ujma, and J. Handerek, *Relaxor behavior of La-modified  $(\text{Pb}_{0.75}\text{Ba}_{0.25})(\text{Zr}_{0.70}\text{Ti}_{0.30})\text{O}_3$  ceramics*, J. Appl. Phys. 89 (2001), pp. 542–547.
- [19] Powder Diffraction File No. 35-0739, International Centre for Diffraction Data, Newton Square, PA, 2000.
- [20] B.P. Pokharel and D. Pandey, *High temperature x-ray diffraction studies on antiferroelectric and ferroelectric phase transitions in  $(\text{Pb}_{1-x}\text{Ba}_x)\text{ZrO}_3$  ( $x = 0.05, 0.10$ )*, J. Appl. Phys. 90 (2001), pp. 2985–2994.
- [21] Powder Diffraction File No. 29-0775, International Centre for Diffraction Data, Newton Square, PA, 2000.
- [22] Powder Diffraction File No. 06-0452, International Centre for Diffraction Data, Newton Square, PA, 2000.

# Low temperature fabrication of lead-free KNN-LS-BS ceramics via the combustion method

Chakkaphan Wattanawikkam<sup>a,b</sup>, Naratip Vittayakorn<sup>c</sup>, Theerachai Bongkarn<sup>a,b,\*</sup>

<sup>a</sup>Department of Physics, Faculty of Science, Naresuan University, Phitsanulok 65000, Thailand

<sup>b</sup>Research Center for Academic Excellence in the Petroleum, Petrochemicals and Advanced Materials, Naresuan University, Phitsanulok 65000, Thailand

<sup>c</sup>Department of Chemistry, Faculty of Science, King Mongkut's Institute of Technology Ladkrabang, Ladkrabang, Bangkok 10520, Thailand

Available online 17 October 2012

## Abstract

Lead-free piezoelectric 0.992(0.95K<sub>0.5</sub>Na<sub>0.5</sub>NbO<sub>3</sub>–0.05LiSbO<sub>3</sub>)–0.008BiScO<sub>3</sub>; KNN-LS-BS ceramics were successfully prepared using the combustion method. The highest % perovskite phase was found in the sample calcined at 700 °C for 1 h. The structural phase of orthorhombic structure was also detected in this sample. For the sintered ceramics, a pure tetragonal perovskite phase was observed in the samples sintered between 1025 and 1100 °C. The microstructure of ceramics showed a square or rectangular shape and the average grain size increased with increasing of sintering temperature. The density of the ceramics increased with increasing of sintered temperature up to 1075 °C, were it reached 97.5% of theoretical density and then dropped in value when the sintered temperature further increased. The excellent electrical properties of  $\epsilon_r$  at  $T_c$ =6600,  $\tan\delta$  at  $T_c$ =0.04,  $P_r$  (at 40 kV/cm)=19.4  $\mu$ C/cm<sup>2</sup> and  $E_c$  (at 40 kV/cm)=24.1 kV/cm were obtained in the most dense ceramic. The results indicate that the KNN-LS-BS ceramics are promising lead-free piezoelectric materials.

© 2012 Elsevier Ltd and Techna Group S.r.l. All rights reserved.

**Keywords:** A. Sintering; C. Dielectric properties; D. Perovskites; KNN-LS-BS ceramics

## 1. Introduction

In recent years, the most widely used piezoelectric materials are lead-base PZT ceramics due to their excellent electrical properties [1–3]. The use of lead-base ceramics can cause a serious threat to human health and create environmental problems. As a consequence, much of the current research is oriented toward more environmentally friendly lead-free materials [4–6]. An alternative group of lead-free piezoelectric materials are those based on a KNN solid solution which have a high Curie temperature ( $T_c$ ~420 °C) and high piezoelectric constant ( $d_{33}$ ~100 pC/N) [7–10]. Nevertheless, it is extremely difficult for pure KNN to achieve high density by using ordinary sintering methods because their phase stability is limited to 1140 °C for potassium sodium niobate [9]. In order to solve the above problem, additives of LiAO<sub>3</sub>

(A=Na, Ta, Sb) and BiBO<sub>3</sub> (B=Fe, Sc, Al) were added into the KNN ceramics to form a new solid solution, which enhanced the density, dielectric, and piezoelectric properties [11–16]. Among these materials, 0.992(0.95K<sub>0.5</sub>Na<sub>0.5</sub>NbO<sub>3</sub>–0.05LiSbO<sub>3</sub>)–0.008BiScO<sub>3</sub>; KNN-LS-BS has been considered a good candidate for lead-free piezoelectric ceramics because its high piezoelectric constant  $d_{33}$  of 305 pC/N, high dielectric constant of ~6100, and favorable electromechanical planar  $k_p$  of 0.54. Minhong et al. [15] fabricated the KNN-LS-BS via the solid state reaction method. The KNN-LS-BS were calcined at 900 °C for 6 h and sintered at 1090 °C for 3 h. The results suggested that LS-BS can be diffused into a KNN lattice to form a new solid solution in which the KNN-LS-BS ceramics exhibited a structural phase indexed in the tetragonal perovskite ferroelectric phase and whose maximum density was ~96%.

It is well known that the solid state reaction method is relatively simple, yet it is time consuming, needing high firing temperatures, is energy intensive, and the calcined powders are often of a large particle size [17]. Recently, interest has been shown in the combustion method as a

\*Corresponding author at: Department of Physics, Faculty of Science, Naresuan University, Phitsanulok 65000, Thailand.  
Tel.: +6655 963528; fax: +6655 963501.

E-mail address: [researchcmu@yahoo.com](mailto:researchcmu@yahoo.com) (T. Bongkarn).



mean of preparing ferroelectric ceramics. It is not a complicated method, which produces ultra-fine powders, with a high density, and excellent electrical properties, which use lower firing temperatures and have a lower soak time compared to other methods [18–20]. This because the combustion reaction provides heat that can be effectively applied to the starting materials. This energy speeds up the chemical reaction of the materials. In addition, from the literature survey, the ferroelectric properties of KNN-LS-BS ceramics have not been studied. Therefore, the purposes of this paper are to synthesize of KNN-LS-BS ceramics via the combustion method and to investigate the effect of firing temperatures on phase structure, microstructure, density and electrical properties of KNN-LS-BS ceramics.

## 2. Experimental

The raw materials of  $0.992(0.95\text{K}_{0.5}\text{Na}_{0.5}\text{NbO}_3-0.05\text{LiSbO}_3)-0.008\text{BiScO}_3$  samples processed by the combustion method were pure reagent  $\text{K}_2\text{CO}_3$ ,  $\text{Na}_2\text{CO}_3$ ,  $\text{Nb}_2\text{O}_5$ ,  $\text{Li}_2\text{O}_3$ ,  $\text{Sb}_2\text{O}_3$ ,  $\text{Bi}_2\text{O}_3$  and  $\text{Sc}_2\text{O}_3$ . They were weighed and milled for 24 h using planetary milling with a zirconia ball media and ethanol. They were then dried and sieved. The powders were mixed with glycine in a ratio of 1:2. These powders were calcined at 650–750 °C for 0.5–2 h. The calcined powders, milled with 3 wt% PVA aqueous, were uniaxially pressed into discs with a diameter of 15 mm under 80 mPa pressures and subsequently sintered between

1000 and 1100 °C for 3 h. The phase structure and microstructure were studied by the X-ray diffraction (XRD) and scanning electron microscope (SEM). Bulk densities were measured by Archimedes method using distilled water as a medium. The dielectric properties (measured from 30 to 400 °C), and ferroelectric properties were determined by a LCR meter and a ferroelectric test system, respectively.

## 3. Results and discussion

The XRD patterns of KNN-LS-BS powders calcined at 650–750 °C for 0.5–2 h are displayed in Fig. 1(a). The phase structure in all samples is an orthorhombic perovskite structure. The impurity phases of  $\text{NaSbO}_3$  and  $\text{LiSbO}_3$  were detected. At the calcination temperature of 650, 700 and 750 °C, using a dwell time of 1 h, the %perovskite phases were 91.4, 94.3 and 92.2%, respectively. To improve the %perovskite phase, shorter and longer dwell times (0.5 and 2 h) were adopted using a calcination temperature of 700 °C. The sample exhibited a %perovskite of 93.2 and 93.0% when the dwell time was 0.5 and 2 h, which is lower than the powders calcined at 700 °C for 1 h. Therefore, the calcination temperature of 700 °C for 1 h was used for the preparation of the KNN-LS-BS ceramics.

The XRD patterns of KNN-LS-BS ceramics sintered at 1000–1100 °C for 2 h is shown in Fig. 1(b). The structural phase indexed in the tetragonal perovskite phase in all samples. The impurity phase was found in the sample sintered at 1000 °C. While, the pure perovskite structure

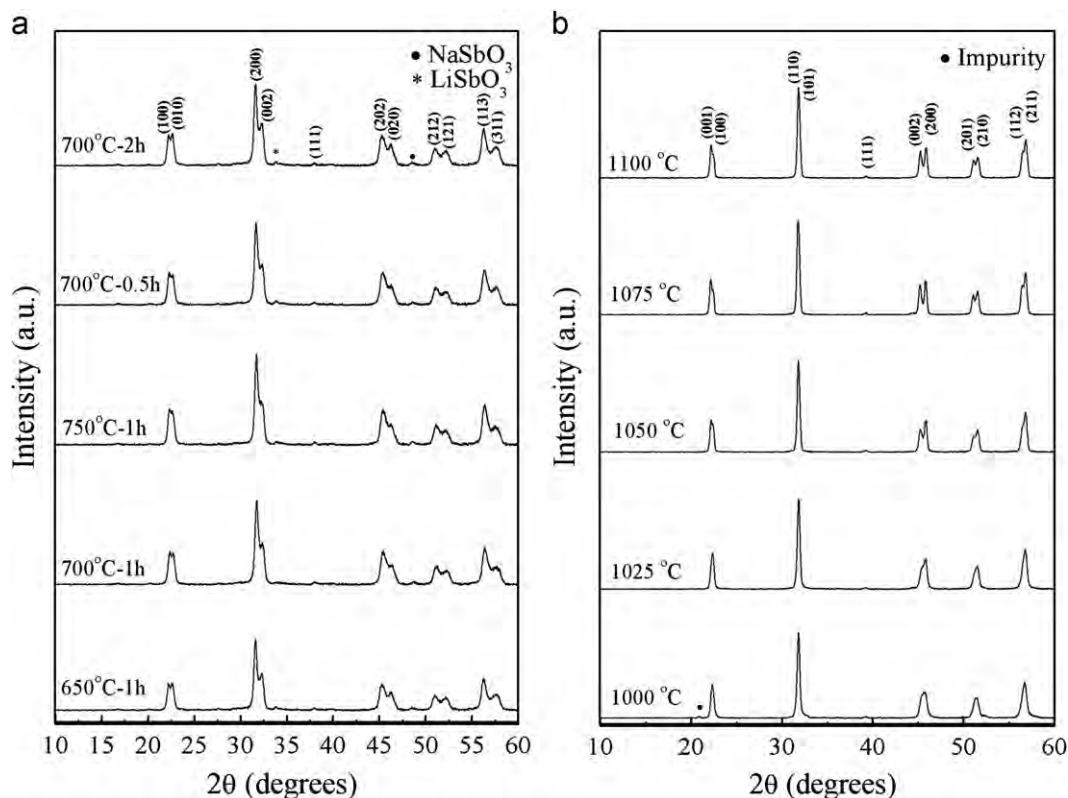


Fig. 1. XRD patterns of (a) KNN-LS-BS powders calcined at 650–750 °C and (b) KNN-LS-BS ceramics sintered at 1000–1100 °C for 2 h.

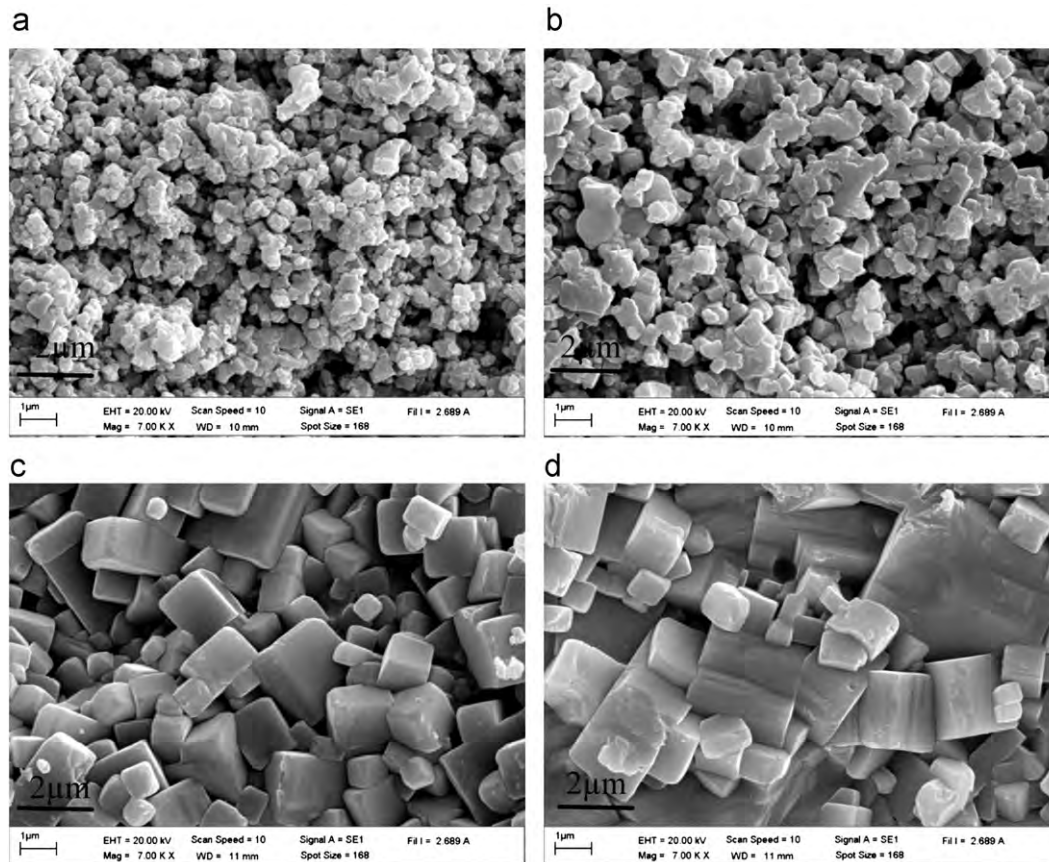


Fig. 2. The natural surface SEM micrographs of KNN-LS-BS ceramics sintered at (a) 1000 °C, (b) 1050 °C, (c) 1075 °C and (d) 1100 °C [15].

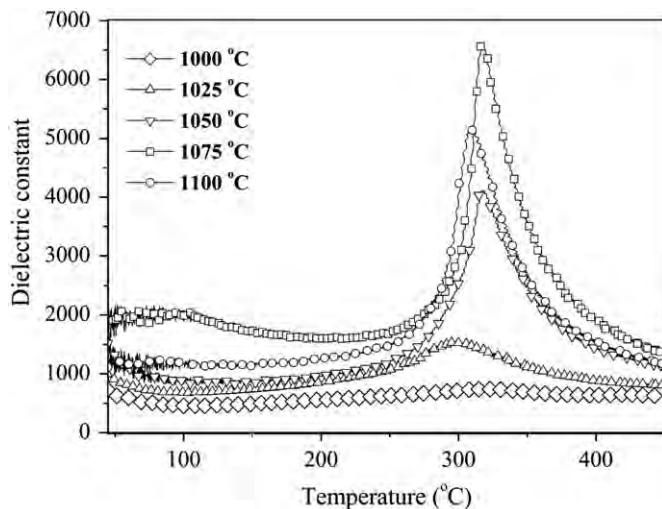


Fig. 3. Temperature dependence of dielectric constant of KNN-LS-BS ceramics sintered at 1000–1100 °C for 2 h.

was obtained in samples sintered at 1025–1100 °C. Moreover, it can be seen that at sintering temperatures of 1050–1100 °C, the obviously separated XRD peaks (such as 0 0 2 and 2 0 0) were observed. These represent the higher crystallinity of ceramics. The lattice parameter  $a$ ,  $c$  and  $c/a$  ratio were calculated and are listed in Table 1. The lattice parameter  $a$

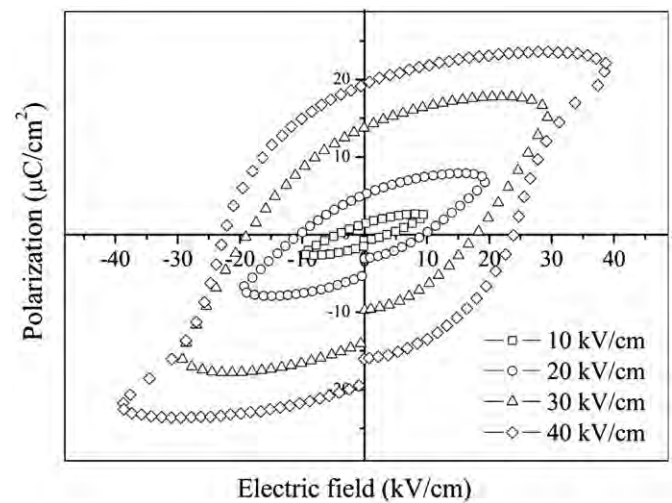


Fig. 4.  $P$ – $E$  hysteresis loops of KNN-LS-BS ceramics sintered at 1075 °C.

decreased, while the lattice parameter  $c$  and  $c/a$  ratio increased with increasing of sintered temperatures.

Fig. 2 shows the natural surface SEM micrograph of KNN-LS-BS pellets sintered at 1000–1100 °C for 2 h. A characteristic square or rectangular morphology of the grain were obtained in all samples. At a low sintering

temperature of 1000–1050 °C, in Fig. 2(a) and (b), many distinct pores occurred. At a higher sintering temperature of 1075 °C, in Fig. 2(c), the porosity decreased and the average grain size extremes increased. When the sintering temperature increased to 1100 °C, in Fig. 2(d), grain boundaries began to melt and the small grains merge together to produce a larger grain. The average value of grain size, as measured by the linear intercept method, increased from 0.32 to 1.32  $\mu\text{m}$  with increasing of sintering temperature from 1000 to 1100 °C, as shown in Table 1.

The linear shrinkage, bulk density ( $\rho$ ) and theoretical density (%T.D.) of KNN-LS-BS ceramics sintered between 1000 and 1100 °C for 2 h are shown in Table 1. The linear shrinkage of ceramics increased from 4.0 to 15.9% when the sintered temperature increased. The density of sintered pellets increased to a maximum of 1075 °C, with a value of 4.56 g/cm<sup>3</sup> or 97.5% of theoretical density. A further increase in the sintering temperature resulted in a drop in value. This may be due to distending from the trapped gas in the pores. The gas-filled pores combined and grew because the grains growth [15]. The density corresponded to the microstructure results. Moreover, the density in this study was higher than the density of ceramics prepared via solid state reaction method [15].

The temperature dependence of the dielectric constant of KNN-LS-BS ceramics under 1 kHz is shown in Fig. 3. For the pellets sintered at 1050–1100 °C, the result exhibited a sharp phase transition peak at around 320 °C representing the ferroelectric tetragonal phase to paraelectric cubic phase transition. This agrees with previous work by Minhong et al. [15]. At 1025 °C, a broad peak of dielectric constant was found. The peak was not clearly observed in the samples sintered at 1000 °C. The Curie temperatures ( $T_c$ ) of ceramics are in a range of 293–320 °C, as seen in Table 1. The dielectric constant at  $T_c$  first increased and reached its highest at 1075 °C, and then dropped as a sintering temperature increased above 1075 °C. The highest dielectric constant (at  $T_c$ ) of 6600 and lowest dielectric loss (at  $T_c$ ) of 0.04 of the KNN-LS-BS ceramics were obtained from the samples sintered at 1075 °C for 2 h, as shown in Table 1. The dielectric properties were in a good agreement with the phase structure, microstructure and density results. This indicated that high quality KNN ceramics could be prepared via the combustion method. In addition, the dielectric constants observed in this study were higher than the ceramics prepared by the solid state reaction method [15].

In order to characterize the ferroelectric properties of KNN-LS-BS ceramics, the room temperature  $P$ – $E$  hysteresis loops of the densest pellets were measured at different electric field strengths as shown in Fig. 4. It can be seen that the shape of the hysteresis loops differed greatly with different electric field strengths. A loop pinching was observed at lower electric fields (10–30 kV/cm), which is linked to a preferred orientation of defect dipole in the materials [15]. At electric fields higher than 30 kV/cm,

Table 1  
Lattice parameters,  $c/a$  ratio, average grain size, linear shrinkage, density, Curie temperature and dielectric properties of KNN-LS-BS ceramics.

Sintered temperature (°C)	Lattice parameters (Å)		$c/a$ ratio	Average grain size ( $\mu\text{m}$ )	Linear shrinkage (%)	Density $\rho$ (g/cm <sup>3</sup> )	%T.D.	$T_c$ (°C)	$\epsilon_r$ at $T_c$	tan $\delta$ at $T_c$
	$a$	$c$								
1000	–	–	–	0.32	4.0	4.20	89.7	–	–	–
1025	–	–	–	0.44	6.6	4.22	90.2	293	1550	0.08
1050	3.9639	4.0080	1.01	0.50	11.3	4.25	90.5	320	4120	0.08
1075	3.9622	4.0151	1.03	1.11	15.6	4.56	97.5	317	6600	0.04
1100	3.9602	4.0206	1.06	1.32	15.9	4.50	96.2	310	5170	0.05



pinching loops vanished and well formed symmetric loops were observed.

At the maximum electric fields of 40 kV/cm, the coercive field ( $E_c$ ) and remnant polarization ( $P_r$ ) of 24.1 kV/cm and 19.4  $\mu\text{C}/\text{cm}^2$  existed.

#### 4. Conclusions

Lead-free KNN-LS-BS ceramics were successfully prepared by the combustion method. The calcination and sintering conditions influenced the phase structure, microstructure, density and dielectric properties of KNN-LS-BS ceramics. The highest % perovskite phase of the calcined powders was detected in samples calcined at 700 °C for 1 h. The tetragonality of the sintered pellets increased with increasing sintering temperature from 1050 to 1100 °C. The microstructure of the ceramics exhibited distinct porosity when the samples were sintered at low temperatures (1000–1050 °C). The melting of the grain boundary was observed in the pellets sintered higher than the appropriate temperature of 1075 °C. The outstanding density and electrical properties of %T.D.=97.5%,  $\epsilon_r$  at  $T_c=6600$ ,  $\tan\delta$  at  $T_c=0.04$ ,  $P_r$  (at 40 kV/cm)=19.4  $\mu\text{C}/\text{cm}^2$  and  $E_c$  (at 40 kV/cm)=24.1 kV/cm were obtained from the samples sintered at 1075 °C for 2 h. These had superior density and better electrical properties than those obtained by using the solid state reaction method.

#### Acknowledgements

This work was financially supported by the Thailand Research Fund (TRF). Thanks also to Department of Physics, Faculty of Science, Naresuan University for supporting facilities. Acknowledgements to Dr. Antony Harfield, for helpful comments and corrections of the manuscript.

#### References

- [1] B. Jaffe, W.R. Cook, H. Jaffe, in: *Piezoelectric Ceramics*, Academic Press, 1971 221–224.
- [2] Z. Yang, X. Zong, H. Li, Y. Chang, Structure and electrical properties of new  $\text{Pb}(\text{Zr,Ti})\text{O}_3\text{--Pb}(\text{Fe}_{2/3}\text{W}_{1/3})\text{O}_3\text{--Pb}(\text{Mn}_{1/3}\text{Nb}_{2/3})$  ceramics, *Materials Letters* 55 (2005) 3476–3480.
- [3] Y. Hou, M. Zhu, F. Gao, H. Wang, H. Yan, C.S. Tiam, Effect of  $\text{MnO}_2$  addition on the structure and electrical properties of  $\text{Pb}(\text{Zn}_{1/3}\text{Nb}_{2/3})_{0.20}(\text{Zr}_{0.50}\text{Ti}_{0.5})_{0.80}\text{O}_3$  ceramics, *Journal of the American Ceramic Society* 87 (2004) 847–854.
- [4] E. Cross, Materials science-lead-free at last, *Nature* 432 (2004) 24–25.
- [5] M.D. Meader, D. Damjanovic, N. Setter, Lead free piezoelectric materials, *Journal of Electroceramics* 13 (2004) 385–392.
- [6] Y. Li, K.C. Moon, P. Wong, Electronic without lead, *Journal of Science* 308 (2005) 1419.
- [7] Y. Saito, H. Takao, T. Tani, T. Nonoyama, K. Takatori, T. Homma, T. Nagaya, M. Nagamura, Lead-free piezoceramics, *Nature* 432 (2004) 84–87.
- [8] E. Ringgaard, T. Wurlizer, Lead-free piezoceramics based on alkali niobium, *Journal of the European Ceramic Society* 25 (2005) 2701–2706.
- [9] W.W. Wolny, European approach to development of new mentally sustainable electroceramics, *Ceramics International* 30 (2004) 1079–1083.
- [10] H. Birol, D. Damjanovic, N. Setter, Preparation and characterization of  $(\text{K}_{0.5}\text{Na}_{0.5})\text{NbO}_3$  ceramics, *Journal of the European Ceramic Society* 26 (2006) 861–866.
- [11] J.G. Wu, D.Q. Xiao, Y.Y. Wang, W.J. Wu, B. Zhang, J.G. Zhu, Z.H. Pu, Q.S. Li, Microstructure and electrical properties of (Li, Ag, Ta, Sb)-modified  $(\text{K}_{0.50}\text{Na}_{0.50})\text{NbO}_3$  lead-free ceramics with good temperature stability, *Journal of Physics D: Applied Physics* 41 (2008) 125405.
- [12] J.G. Wu, D.Q. Xiao, J.G. Zhu, P. Yu, Y.H. Jiang, Compositional dependence of phase structure and electrical properties in  $(\text{K}_{0.42}\text{Na}_{0.58})\text{NbO}_3\text{--LiSbO}_3$  lead-free ceramics, *Journal of Applied Physics* 102 (2007) 114113–114121.
- [13] S. Zhang, R. Xia, R.T. Shrout, G. Zang, J. Wang, Characterization of lead-free  $(\text{K}_{0.5}\text{Na}_{0.5})\text{NbO}_3\text{--LiSbO}_3$  piezoceramic, *Solid State Communications* 141 (2007) 675–679.
- [14] J. Liu, J. Zhu, X. Li, M. Wang, X. Zhu, J. Zhu, D. Xiao, Effects of  $\text{CuO}$  doping on the electrical properties of  $0.98\text{K}_{0.5}\text{Na}_{0.5}\text{NbO}_3\text{--}0.02\text{BiScO}_3$  lead-free piezoelectric ceramics, *Materials Letters* 65 (2011) 948–950.
- [15] J. Minhong, D. Manjiao, L. Huaxin, W. Shi, L. Xinyu, Piezoelectric and dielectric properties of  $\text{K}_{0.5}\text{Na}_{0.5}\text{NbO}_3\text{--LiSbO}_3\text{--BiScO}_3$  lead-free piezoceramics, *Materials Sciences and Engineering B-Solid* 176 (2011) 167–170.
- [16] M.H. Jiang, X.Y. Liu, G.H. Chen, Phase structures and electrical properties of new lead-free  $\text{Na}_{0.5}\text{K}_{0.5}\text{NbO}_3\text{--LiSbO}_3\text{--BiFeO}_3$  ceramics, *Scripta Materialia* 60 (2009) 909–912.
- [17] C.C. Hwang, T.Y. Wu, J. Wan, J.S. Tsai, Development of a novel combustion synthesis method for synthesizing of ceramics oxide powders, *Materials Science and Engineering: B-Solid* 111 (2004) 49–56.
- [18] A. Thongtha, T. Bongkarn, Phase formation and microstructure of barium zirconate ceramics prepared using the combustion technique, *Ferroelectrics* 383 (2009) 33–39.
- [19] N. Phungjit, P. Panya, T. Bongkarn, N. Vittayakarn, The structural phase and microstructures of perovskite  $\text{Ba}(\text{Ti}_{1-x}\text{Zr}_x)\text{O}_3$  ceramics using a combustion route, *Functional Materials Letters* 4 (2009) 169–174.
- [20] C. Wattanawikkam, T. Bongkarn, The influence of calcinations temperature on phase and morphology of BST powders synthesis via solid state reaction method and combustion technique, *Ferroelectrics* 282 (2009) 42–48.

# The effects of sintering temperature and content of $x$ on phase formation, microstructure and dielectric properties of $(1-x)(\text{Bi}_{0.4871}\text{Na}_{0.4871}\text{La}_{0.0172}\text{TiO}_3) - x(\text{BaZr}_{0.05}\text{Ti}_{0.95}\text{O}_3)$ ceramics prepared via the combustion technique

Chittakorn Kornphom<sup>a,b</sup>, Artid Laowanidwatana<sup>a,b</sup>, Theerachai Bongkarn<sup>a,b,\*</sup>

<sup>a</sup>Department of Physics, Faculty of Science, Naresuan University, Phitsanulok 65000, Thailand

<sup>b</sup>Research Center for Academic Excellent in Petroleum, Petrochemicals and Advanced Materials, Naresuan University, Phitsanulok 65000, Thailand

Available online 24 October 2012

## Abstract

$(1-x)(\text{Bi}_{0.4871}\text{Na}_{0.4871}\text{La}_{0.0172}\text{TiO}_3) - x(\text{BaZr}_{0.05}\text{Ti}_{0.95}\text{O}_3)$  ceramics (abbreviated  $(1-x)\text{BNLT} - x\text{BZT}$ ) where  $0.1 \leq x \leq 0.3$  were fabricated by the combustion technique using glycine as fuel. BNLT and BZT powders were calcined at temperatures of 825 °C for 4 h and 925 °C for 6 h, respectively. After that they were mixed with the different compositions. It was found that the optimum sintering temperature of  $(1-x)\text{BNLT} - x\text{BZT}$  ceramic was obtained at 1125 °C for 2 h. This ceramic had the highest density. The structure of the  $(1-x)\text{BNLT} - x\text{BZT}$  ceramics exhibited the co-existence of tetragonal and rhombohedral phases with  $x \leq 0.1$ . The tetragonality increases with the increase of  $x$  content. The average grain size, the density and the Curie temperatures decrease with increasing  $x$  content. The maximum dielectric constant and the highest  $P_r$  were at about 4850 and 12.7  $\mu\text{C}/\text{cm}^2$ , respectively, and were obtained by the 0.85BNLT–0.15BZT sample.

© 2012 Elsevier Ltd and Techna Group S.r.l. All rights reserved.

**Keywords:** Sintering; Ferroelectric properties; Dielectric properties; Perovskites

## 1. Introduction

$\text{Bi}_{0.4871}\text{Na}_{0.4871}\text{La}_{0.0172}\text{TiO}_3$  (abbreviated as BNLT) is a kind of lead-free piezoelectric material which is a ferroelectric with a rhombohedral perovskite structure at room temperature [1]. BNLT ceramic exhibits a good dielectric constant at room temperature (515) [1] and a high piezoelectric coefficient  $d_{33}$  (120 pC/N) [1]. Consequently, this ceramic is appropriate for application as the sensors, actuators and transducers [2].  $\text{Ba}(\text{Zr}_{0.05}\text{Ti}_{0.95})\text{O}_3$  ceramic (abbreviated as BZT) is one of the most studied piezoelectric materials due to its great piezoelectric properties (236 pC/N) with an orthorhombic perovskite structure at room temperature. It also exhibits a high dielectric

constant (14,000) and low loss characteristic (0.05) at Curie temperature of 120 °C [3]. This ceramic has become widely attractive for use as multilayer ceramics capacitors and piezoelectric sensors/actuators [2].

To improve the electrical properties of lead-free piezoelectric materials, a new system of  $(1-x)\text{Bi}_{0.4871}\text{Na}_{0.4871}\text{La}_{0.0172}\text{TiO}_3 - x\text{BaZr}_{0.05}\text{Ti}_{0.95}\text{O}_3$  ( $(1-x)\text{BNLT} - x\text{BZT}$ ) at a composition of around  $0 \leq x \leq 1$  step 0.2 was proposed by Kantha et al. [3]. The  $(1-x)\text{BNLT} - x\text{BZT}$  ceramics were prepared by a two step mixed oxide method for synthesized the BNLT and BZT powders then sintered at temperatures between 1125 and 1400 °C for 2 h. The structure of the  $(1-x)\text{BNLT} - x\text{BZT}$  ceramics changed from a rhombohedral phase to a tetragonal phase when  $\geq 0.2$ . For the  $(1-x)\text{BNLT} - x\text{BZT}$  ceramic  $x \leq 0.2$ , the dielectric permittivity ( $\epsilon_r$ ) curve exhibited two peaks. The first curve was the phase transition temperature ( $T_p$ ), corresponding to a ferroelectric rhombohedral phase which transformed into a ferroelectric tetragonal phase.

\*Corresponding author at: Department of Physics, Faculty of Science, Naresuan University, Phitsanulok 65000, Thailand. Tel.: +66 5596 3528; fax: +66 5596 3501.

E-mail address: [researchcmu@yahoo.com](mailto:researchcmu@yahoo.com) (T. Bongkarn).

The second curve is Curie temperature ( $T_c$ ) and it is related to the transition from a ferroelectric tetragonal phase to a paraelectric cubic phase [3]. A broad dielectric peak was observed to increase from the  $\epsilon_r$  curves with  $x$  content  $\geq 0.4$ . The  $\epsilon_r$  measured at room temperature increased from 675 to 1575 with the increased of  $x$  content from 0 to 0.2. Upon further increasing  $x$ , the  $\epsilon_r$  decreased. Appropriate ferroelectric properties is observed in the composition of  $x=0.2$ . Many changes in the phase formation, phase transition and electrical properties of  $(1-x)\text{BNLT}-x\text{BZT}$  ceramics were observed at around the composition of  $x=0.2$ .

In recent years, our previous work has successfully fabricated lead-free ferroelectric ceramics such as:  $(\text{Bi Na})\text{TiO}_3$  [4],  $\text{BaTiO}_3$  [5],  $\text{BaZrO}_3$  [6],  $\text{Ba}(\text{Ti Zr})\text{O}_3$  [7],  $(\text{Bi Na})\text{TiO}_3-(\text{Bi K})\text{TiO}_3$  [4] via the combustion technique. The technique is simple. It has a low cost and it produces high quality ultra fine powders [8]. The ceramics fabricated by this technique possesses a high density and has good electrical properties [4–8]. Therefore, in the present work, the fabrication of the  $(1-x)\text{BNLT}-x\text{BZT}$  ceramics were prepared by the combustion technique, where a range of  $x$  values was chosen between 0.1 and 0.3 (mole step 0.05 was performed). The effects of sintering temperature on phase formation, microstructure of BNLT–BZT ceramics were investigated. The influence of  $x$  content on the crystal structure and the microstructure were studied. Special emphasis was focused on phase formation and the electrical properties of the composition between the BNLT and BZT systems in order to enhance these ceramics.

## 2. Experimental

The sample,  $(1-x)(\text{Bi}_{0.4871}\text{Na}_{0.4871}\text{La}_{0.0172}\text{TiO}_3)-x(\text{BaZr}_{0.05}\text{Ti}_{0.95}\text{O}_3)$ , (abbreviated as  $(1-x)\text{BNLT}-x\text{BZT}$ ) where  $0.1 \leq x \leq 0.3$ , was prepared by the combustion technique using glycine as fuel. To synthesize  $\text{Bi}_{0.4871}\text{Na}_{0.4871}\text{La}_{0.0172}\text{TiO}_3$  (BNLT) powder, reagent grade oxide and carbonate powders of  $\text{Bi}_2\text{O}_3$  (99%),  $\text{Na}_2\text{CO}_3$  (99%),  $\text{La}_2\text{O}_3$  (99%) and  $\text{TiO}_2$  (99%) were used as starting materials. The compositions of the raw materials were weighed and mixed by a ball-milling method for 24 h in absolute ethanol. The mixed powder was dried and ground using an agate mortar and then sieved into a fine powders. The mixed powder and glycine were mixed with a ratio of 1:2 in an agate mortar and calcined at 825 °C for 4 h. To synthesize the  $\text{BaZr}_{0.05}\text{Ti}_{0.95}\text{O}_3$  (BZT) powder;  $\text{BaCO}_3$  (99%),  $\text{ZrO}_2$  (99%) and  $\text{TiO}_2$  (99%) were used as raw materials. The processing of the BZT was similar to that of the BNLT powders but the uncalcined BZT powders were calcined at the temperatures of 925 °C for 6 h. The two calcined powders were a mixture of different compositions ( $0.1 \leq x \leq 0.3$ ) and reground by the ball-milling method for 24 h. The mixtures were dried and sieved and then were made into pellets 15 mm in diameter using uniaxial pressing in a stainless steel mold. The pellets were sintered between 1050 °C and 1200 °C in an electric furnace at air

atmosphere under controlled heating and a cooling rate of 5 °C/min with a soak time of 2 h. X-ray diffraction (XRD) was employed to identify the phase formed and the optimum temperature for  $(1-x)\text{BNLT}-x\text{BZT}$  ceramics. The sintered ceramics morphologies were imaged using scanning electron microscopy (SEM). The density of the sintered ceramics was measured by the Archimedes method. The average grain size was determined by a mean linear intercept method. The dielectric constant was observed by a LCR meter. The ferroelectric hysteresis ( $P-E$ ) loops were characterized by using a computer controlled modified Sawyer–Tower circuit.

## 3. Results and discussion

The X-ray diffraction patterns of the 0.8BNLT–0.2BZT ceramics sintered at 1050–1200 °C for 2 h are shown in Fig. 1. All patterns of the sintered samples exhibited the tetragonal perovskite phase which matched with JCPDS file no. 03-0725 below 1200 °C. At the sintered temperature of 1200 °C, the second phase of  $\text{Bi}_2\text{Ti}_2\text{O}_7$  occurred. This result may be caused by the evaporation of  $\text{Na}_2\text{O}$  and  $\text{Bi}_2\text{O}_3$ , which has a low melting point [9].

The SEM micrographs of the 0.8BNLT–0.2BZT ceramic surface sintered between 1100 and 1200 °C are presented in Fig. 2. The grain morphology exhibited an almost spherical morphology at low sintering temperature and changes to a polygonal morphology when the sintering temperature increased. At a low sintering temperature (below 1100 °C), the ceramics contained small and loosely bonded grains (Fig. 2(a)). The grain size increased and the porosity decreased when the sample was sintered at temperatures higher than 1100 °C (Fig. 2(b) and (c)). At a sintering temperature of 1200 °C, the ceramic exhibited a rugged surface and the a high porosity, as shown in Fig. 2(d). The

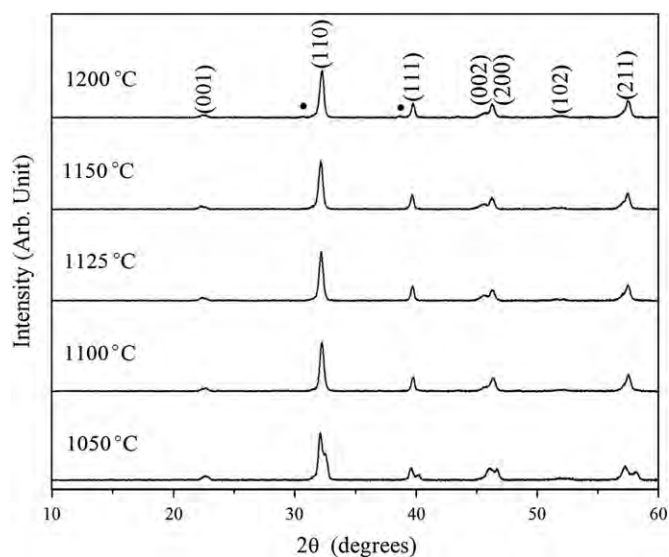


Fig. 1. XRD patterns of 0.8BNLT–0.2BZT ceramics sintered at various temperatures; (●)  $\text{Bi}_2\text{Ti}_2\text{O}_7$ .

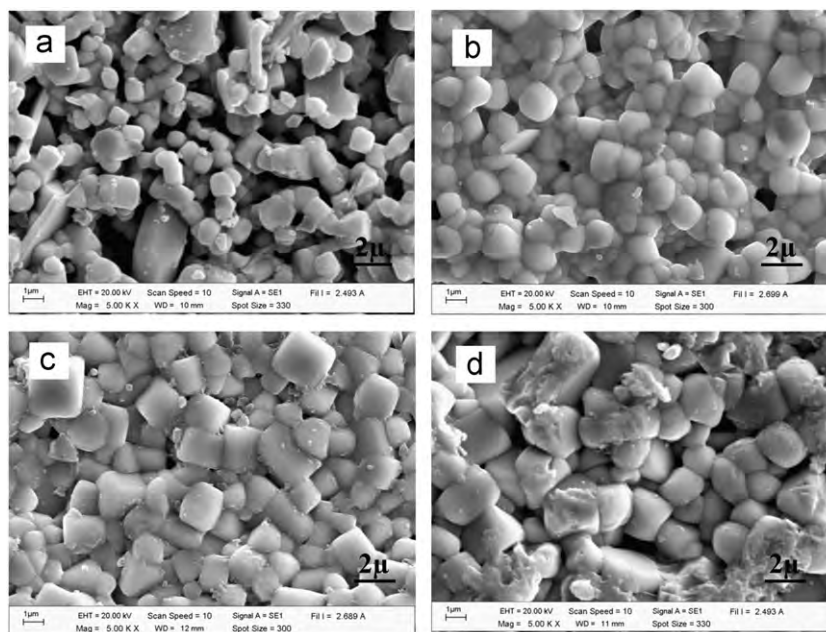


Fig. 2. The SEM micrographs of 0.8BNLT–0.2BZT surface pellet sintered at: (a) 1100, (b) 1125, (c) 1150 and (d) 1200 °C for 2 h.

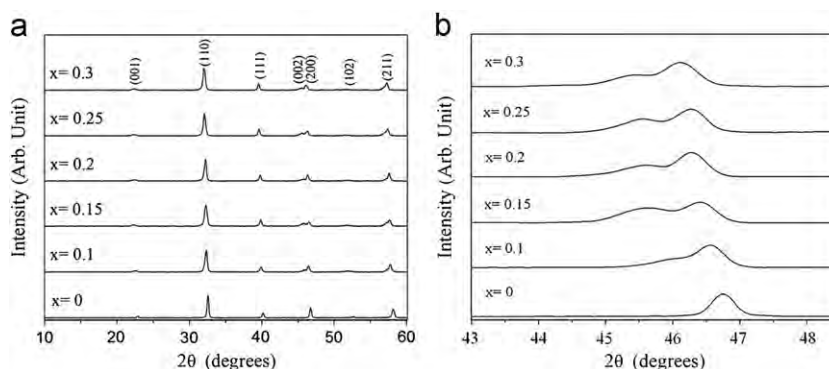


Fig. 3. XRD patterns of  $(1-x)\text{BNLT}-x\text{BZT}$  powders where  $0.1 \leq x \leq 0.3$  sintered at 1125 °C for 2 h: (a) at high scanning rate and (b) at very low scanning rate.

occurrence of a rugged surface and a high porosity at high sintering temperatures indicated that the grain began to melt. This was caused by the evaporation of  $\text{Na}_2\text{O}$  and  $\text{Bi}_2\text{O}_3$  at high sintering temperatures [9]. The microstructure is consistent with the XRD results. The average grain size increased from 0.48 to 1.33  $\mu\text{m}$  when sintering temperature increased from 1100 °C to 1200 °C. The density of the 0.8BNLT–0.2BZT ceramics was increased from 5.57 to 5.79  $\text{g}/\text{cm}^3$  when the sintering temperatures increased up to 1125 °C, whereas the density decreased. The density results were consistent with a microstructure investigation. The optimum conditions for 0.8BNLT–0.2BZT was obtained at a sintering temperature of 1125 °C for 2 h.

To study the effect of  $x$  content on phase formation, microstructure and dielectric properties of  $(1-x)(\text{Bi}_{0.4871}\text{Na}_{0.4871}\text{La}_{0.0172}\text{TiO}_3)-x(\text{BaZr}_{0.05}\text{Ti}_{0.95}\text{O}_3)$  ceramics, the two powders were mixed in ratios of  $0.1 \leq x \leq 0.3$  and then made into pellets and sintered at 1125 °C for 2 h. The X-ray results of  $(1-x)\text{BNLT}-x\text{BZT}$  with  $0.1 \leq x \leq 0.3$

are shown Fig. 3. All the samples exhibited the single perovskite phase (Fig. 3(a)).

The X-ray diffraction patterns of these ceramics also showed a phase change from rhombohedral to tetragonal, with increasing  $x$  content. The difference between these two structures can be seen clearly from Fig. 3(b) which represents the X-ray peaks at  $2\theta$  range between 43° and 48° that measured using a low scanning rate. The peak of (200) is observed in the diffraction pattern for pure BNLT, indicating that this is rhombohedral structures. When adding BZT of  $0.1 \leq x \leq 0.3$ , the peak of (200) split into two peaks of (002)/(200) and the peaks shifted slightly toward low angles. The peak of ceramics for  $x=0.1$  is slightly asymmetrical, featured with inappreciable split of the (200) and (002) peaks, indicating the co-existence structures between rhombohedral and tetragonal phases. Doping of  $x \geq 0.15$  leads to the apparent separation between (200) and (002) peaks, indicating an increase in the tetragonality of the ceramics. In the district



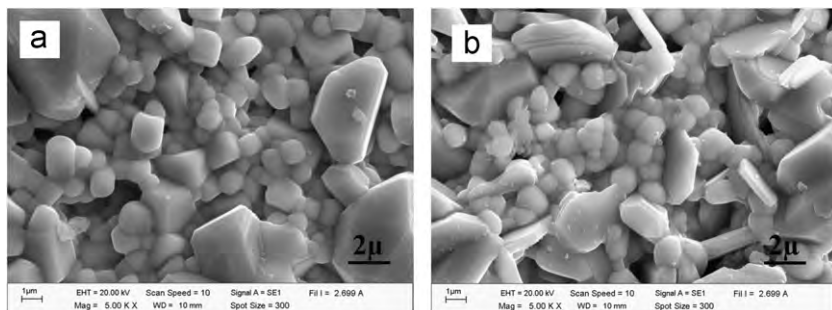


Fig. 4. The SEM micrographs of  $(1-x)\text{BNLT}-x\text{BZT}$  ceramics where  $x=(a)$  0.1 and  $(b)$  0.3 sintered at  $1125^\circ\text{C}$  for 2 h.

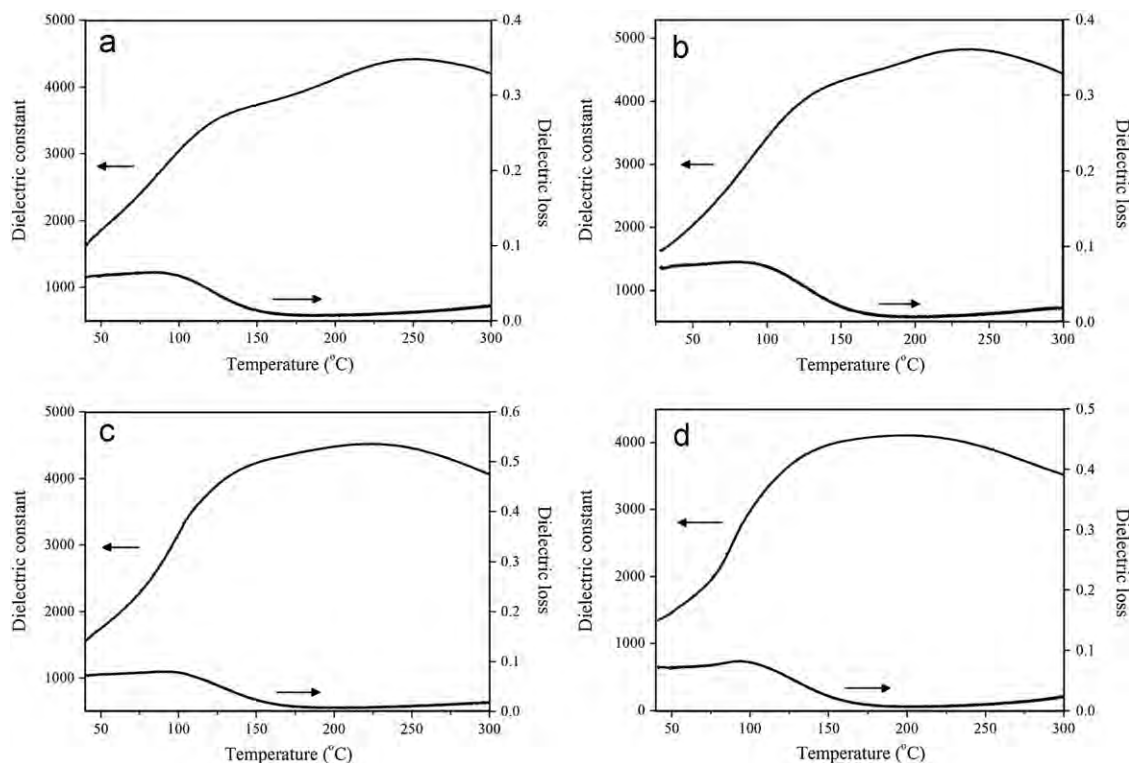


Fig. 5. Temperature dependence of dielectric constant and dielectric loss of  $(1-x)\text{BNLT}-x\text{BZT}$  sintered at  $1125^\circ\text{C}$  for 2 h where  $x=(a)$  0.1  $(b)$  0.15,  $(c)$  0.2 and  $(d)$  0.25.

of the tetragonal structure, the lattice parameters  $a$  and  $c$  of the  $(1-x)\text{BNLT}-x\text{BZT}$  system are listed in Table 1. The lattice parameters  $a$  and  $c$  increased gradually with increasing  $x$  content. The  $c/a$  ratio increased with increasing  $x$  up to 0.2, and then it decreased (Table 1).

Fig. 4 illustrates the SEM photomicrograph of  $(1-x)\text{BNLT}-x\text{BZT}$  ceramics with  $x=0.1$  and 0.3 (Fig. 4(a) and (b)). It can be observed that the grain morphology of the ceramics exhibited an almost spherical morphology combined with a polygonal morphology. The porosity was found on the surface of all the samples. The porosity increased while the grain size decreased when the content of  $x$  increased (Table 1). The reduction in grain

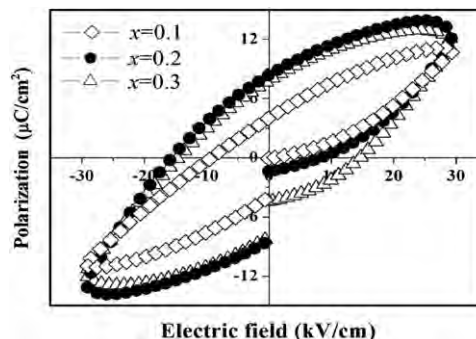


Fig. 6.  $P-E$  hysteresis loops of  $(1-x)\text{BNLT}-x\text{BZT}$  ceramics measured at electric field of 30 kV.

Table 1

Lattice parameters,  $c/a$ , average grain size, density,  $T_p$ ,  $T_c$ , dielectric properties and ferroelectric properties of  $(1-x)\text{BNLT}-x\text{BZT}$  ceramics.

$x$	Lattice Parameters (Å)		$c/a$	Average grain size ( $\mu\text{m}$ )	Density ( $\text{g}/\text{cm}^3$ )	$T_p$ ( $^\circ\text{C}$ )	$T_c$ ( $^\circ\text{C}$ )	$\epsilon_r$ at $T_p$	$\tan \delta$ at $T_p$	$\epsilon_r$ at $T_c$	$\tan \delta$ at $T_c$	$\gamma$	$P_r$ ( $\mu\text{C}/\text{cm}^2$ )	$E_c$ (kV/cm)
	$a$	$c$												
0.1	3.913	3.956	1.0109	1.67	5.82	124	250	3630	0.036	4425	0.0011	1.61	8.3	16.1
0.15	3.917	3.965	1.0122	1.64	5.80	128	240	4450	0.047	4850	0.0067	1.95	12.7	18.6
0.2	3.919	3.984	1.0165	1.60	5.79	150	225	4260	0.021	4550	0.0072	1.98	8.6	14.7
0.25	3.924	3.988	1.0163	1.55	5.78	–	190	–	–	4125	0.0088	1.82	7.1	10.7
0.3	3.934	3.994	1.0152	1.53	5.77	–	175	–	–	3775	0.0368	1.70	4.3	8.4

size may be due to the difference the ionic radius and valency of A-site cations of  $\text{Bi}^{3+}$  (131 pm) and  $\text{Ba}^{2+}$  (156 pm) which plays an important role in the grain growth mechanism. This is because beyond the solubility limit of BZT it may accumulate at the grain boundary. This would result in the inhibition of grain growth [10]. The density of the  $(1-x)\text{BNLT}-x\text{BZT}$  ceramics measured by the Archimedes method is listed in Table 1. The density of the ceramics decreased when the content of  $x$  increased.

The temperature dependence of dielectric permittivity ( $\epsilon_r$ ) and dielectric loss of the  $(1-x)\text{BNLT}-x\text{BZT}$  ceramics as a function of  $x$  at 1 kHz are shown in Fig. 5(a)–(d). For the  $0.1 \leq x \leq 0.2$  samples, the  $\epsilon_r$  peak exhibited two dielectric anomalies at  $T_p$  (low temperature) and  $T_c$  (high temperature) (Fig. 5(a)–(c)). The  $T_p$  is the phase transition temperature, corresponding to a ferroelectric rhombohedral phase which transforms to a ferroelectric tetragonal phase, while,  $T_c$  is Curie temperature and relates the transition from a ferroelectric tetragonal phase to a paraelectric cubic phase [3,10]. For  $x \geq 0.25$  (Fig. 5(d)), the dielectric constant curves exhibited a broad dielectric peak. The transition temperature at  $T_p$  exhibited an unclear phase transformation. The  $T_p$  increases and the  $T_c$  decreases with increasing amount of  $x$ , as shown in Table 1. The dielectric constant at  $T_p$  and  $T_c$  increased when the content of  $x$  was increased up to 0.15 and then dropped. The dielectric loss at  $T_p$  and  $T_c$  are illustrated in Table 1. The maximum dielectric constant at  $T_c$  was observed from the sintered sample with  $x=0.15$ . For the sample with the composition of  $x=0.2$ , the dielectric properties of the sample prepared by the combustion method was higher than that found using the solid-state reaction method [3]. This indicated that the combustion technique is a simple method to prepare high quality  $(1-x)\text{BNLT}-x\text{BZT}$  ceramics. The diffuseness constant ( $\gamma$ ) which is used for explaining the diffuseness of the ferroelectric phase transition, follows a modified Curie–Weiss law [11]. The parameter  $\gamma$  indicates the character of the phase transition: for  $\gamma=1$ , a normal Curie–Weiss law and for  $\gamma=2$ , a complete diffuse phase transition [11]. The values of  $\gamma$  increased from 1.61 to 1.98 when  $x$  content increased from 0.1 to 0.2. For the sample with  $x \geq 0.25$ , the values of  $\gamma$  decreased, as shown in Table 1. Generally, the broadness or diffusiveness occurs mainly due to the change

in composition and the disordered structure in the arrangement of cation in one or more crystallographic site of the structure [11]. From the compositions studied the values of  $\gamma$  are found to be more than 1.6. This indicates that the transitions are of a diffuse type and the materials are highly disordered [11].

The polarization ( $P$ – $E$ ) hysteresis loops of the  $(1-x)\text{BNLT}-x\text{BZT}$  ceramics with  $0.1 \leq x \leq 0.3$  were measured at a maximum electric field of 30 kV/cm is illustrated in Fig. 6. It is evident that the shape of the  $P$ – $E$  loops exhibited a slim loop for all compositions. The remnant polarization ( $P_r$ ) and the coercive field ( $E_c$ ) of  $(1-x)\text{BNLT}-x\text{BZT}$  increased with the increased of  $x$  content up to 0.15. Then, they decreased with a higher content of  $x$  as shown in Table 1.

#### 4. Conclusions

A high quality  $(1-x)\text{BNLT}-x\text{BZT}$  ceramic in the composition of  $0.1 \leq x \leq 0.3$  is obtained successfully by the combustion method. The sintering temperatures and  $x$  content directly affect phase formation, microstructure and the physical properties of the ceramics. The grain size increases with increasing sintered temperatures. The highest density of ceramics was discovered in the sample sintered at 1125  $^\circ\text{C}$  for 2 h. The ceramics exhibited both the rhombohedral and tetragonal phases if  $x$  content  $\leq 0.1$  and the tetragonality increases with the increased of  $x$  content. The average grain size, the density and Curie temperature of the ceramic decrease, as the  $x$  content increasing. The phase transition from rhombohedral to tetragonal appeared in the dielectric curve where  $0.1 \leq x \leq 0.2$ . The maximum dielectric constant at Curie and the highest  $P_r$  were obtained in sample with  $x=0.15$ .

#### Acknowledgments

This work was financially supported by the Thailand Research Fund (TRF). Thanks also to Department of Physics, Faculty of Science, Naresuan University for supporting facilities. Acknowledgments to Mr. Don Hindle, for helpful comments and corrections of the manuscript.

## References

- [1] A. Herabut, A. Safari, Processing and electromechanical properties of  $(\text{Bi}_{0.5}\text{Na}_{0.5})_{(1-1.5x)}\text{La}_x\text{TiO}_3$  ceramics, *Journal of the American Ceramic Society* 80 (1997) 2954–2958.
- [2] J.M. Herbert, *Ferroelectric Transducers and Sensors*, Gordon & Breach, New York, 1982.
- [3] P. Kantha, K. Pengpat, P. Jarupoom, U. Intatha, G. Rujijanagul, T. Tunkasiri, Phase formation and electrical properties of BNLT–BZT lead-free piezoelectric ceramic system, *Current Applied Physics* 9 (2009) 460–466.
- [4] A. Thongtha, T. Bongkarn, Optimum sintering temperature for fabrication of  $0.8\text{Bi}_{0.5}\text{Na}_{0.5}\text{TiO}_3-0.2\text{Bi}_{0.5}\text{K}_{0.5}\text{TiO}_3$  lead-free ceramics by combustion technique, *Key Engineering Materials* 474–476 (2011) 1754–1759.
- [5] A. Thongtha, T. Bongkarn, Phase formation and microstructure of barium zirconate ceramics prepared using the combustion technique, *Ferroelectrics* 383 (2009) 33–39.
- [6] P. Panya, N. Vittayakorn, N. Phungjitt, T. Bongkarn, The structural phase and microstructure of perovskite  $\text{Ba}(\text{Ti}_{1-x}\text{Zr}_x)\text{O}_3$  ceramics using the combustion route, *Functional Materials Letters* 2 (4) (2009) 169–174.
- [7] A. Thongtha, T. Bongkarn, K. Angsukased, Fabrication of  $(\text{Ba}_{1-x}\text{Sr}_x)(\text{Zr}_x\text{Ti}_{1-x})\text{O}_3$  ceramics using the combustion technique, *Smart Materials and Structures* 19 (2010) 1–7.
- [8] P. Julphunthong, T. Bongkarn, Phase formation, microstructure and dielectric properties of  $\text{Ba}(\text{Zr}_{0.1}\text{Ti}_{0.9})\text{O}_3$  ceramics prepared via the combustion technique, *Current Applied Physics* 11 (3) (2011) 60–65.
- [9] P. Sittiketkorn, A. Klinbumrung, T. Bongkarn, Influence of excess  $\text{Bi}_2\text{O}_3$  and  $\text{Na}_2\text{CO}_3$  on crystal structure and microstructure of bismuth sodium titanate ceramics, *Key Engineering Materials* 474–476 (2011) 1711–1714.
- [10] K. Pengpat, S. Hanphimol, S. Eitssayeam, U. Intatha, G. Rujijanagul, T. Tunkasiri, Morphotropic phase boundary and electrical properties of lead-free bismuth sodium lanthanum titanate-barium titanate ceramics, *Journal of Electroceramics* 16 (2006) 301–306.
- [11] S.K. Rout, E. Sinha, S. Panigrahi, Dielectric properties and diffuse phase transition in  $\text{Ba}_{1-x}\text{Mg}_x\text{Ti}_{0.6}\text{Zr}_{0.4}\text{O}_3$  solid solutions, *Materials Chemistry and Physics* 101 (2007) 428–432.

# Phase formation and electrical properties of $\text{Ba}(\text{Zr}_x\text{Ti}_{1-x})\text{O}_3$ ceramics synthesized through a novel combustion technique

Phongthorn Julphunthong<sup>a,b</sup>, Suphornpun Chootin<sup>a,b</sup>, Theerachai Bongkarn<sup>a,b,\*</sup>

<sup>a</sup>Department of Physics, Faculty of Science, Naresuan University, Phitsanulok 65000, Thailand

<sup>b</sup>Research Center for Academic Excellence in Petroleum, Petrochemicals and Advanced Materials, Naresuan University, Phitsanulok 65000, Thailand

Available online 16 October 2012

## Abstract

High quality  $\text{Ba}(\text{Zr}_x\text{Ti}_{1-x})\text{O}_3$  (BZT,  $0.025 \leq x \leq 0.150$ , step=0.025) ceramic has been prepared by the combustion technique. The raw materials were mixed with  $\text{CH}_4\text{N}_2\text{O}$  and calcined at  $1000^\circ\text{C}$  and sintered at  $1375^\circ\text{C}$ . For  $\text{Ba}(\text{Zr}_x\text{Ti}_{1-x})\text{O}_3$  with  $x=0.025$ , the ceramics exhibited orthorhombic structure at room temperature. The crystal structure was transformed to rhombohedral, tetragonal and cubic phase, respectively with increasing zirconium content. The effect of  $x$  on dielectric properties has been studied intensively. It is found that the phase formation, which was affected from zirconium substitution, strongly influences the dielectric behavior. The rhombohedral phase decreases the maximum dielectric constant while the tetragonal phase enhances it. An extrapolation studied revealed the phase transition peaks merged into one peak at  $x \sim 0.094$ . The highest diffuseness constant of 1.95 was observed in BZT with 0.075 mol% zirconium. This was caused by the broadest dielectric peak of ferroelectric phase transition and the imminent diffusion between ferroelectric phase transition peak and Curie phase transition peak. The ferroelectric properties were sensitive to the phase exhibited in BZT system.

© 2012 Elsevier Ltd and Techna Group S.r.l. All rights reserved.

**Keywords:** C. Dielectric properties; C. Ferroelectric properties; Barium zirconate titanate; Perovskite structure

## 1. Introduction

Barium titanate (BT) ceramics have been used extensively as electroceramics materials due to their high dielectric constant and low dielectric loss. The phase transformations of BT occur at  $120^\circ\text{C}$ ,  $0^\circ\text{C}$  and  $-90^\circ\text{C}$  from cubic to tetragonal, tetragonal to orthorhombic and orthorhombic to rhombohedral, respectively [1]. The dropping in maximum dielectric constant is accompanied with the phase transformation at lower temperature.

$\text{Ba}(\text{Zr}_x\text{Ti}_{1-x})\text{O}_3$  (BZT) system, one of the first  $\text{BaTiO}_3$ -based solid solution, has been chosen in the fabrications of ceramic capacitors because  $\text{Zr}^{4+}$  is chemically more stable than  $\text{Ti}^{4+}$ . Moreover, Zr-substitution at Ti-site has been found to be an effective way to decrease the Curie temperature and exhibits several interesting features in

the dielectric behavior and phase formation of  $\text{BaTiO}_3$  ceramics. The Zr-ion substitution affects an increase of rhombohedral to orthorhombic ( $T_{\text{r-o}}$ ) and orthorhombic to tetragonal ( $T_{\text{o-t}}$ ) phase transition temperature but decreases the tetragonal to cubic ( $T_{\text{c}}$ ) phase transition temperature. The pinch phase transitions between three phase transitions merge into one peak where  $x \leq 0.15$  [2,3]. Below 15 mol% zirconium, there are several difference reports about the effects of zirconium substituted on phase formation and dielectric properties of BZT. In term of structural phase, some researchers distinguished BZT belonging to tetragonal structure [3–5] and the tetragonality was decreased by increasing zirconium content [4,5] while several literatures reported that the amount of orthorhombic to rhombohedral phase transformation was increased with increasing zirconium [3,6,7]. In term of dielectric properties, Huang et al. [4] explained that maximum dielectric constant was enhanced by increasing the amount of zirconium. On the other hand, Chen et al. [5] reported that the maximum dielectric constant was depressed by the amount of zirconium substitution. Kuang

\*Corresponding author at: Naresuan University, Department of Physics, Faculty of Science, Phitsanulok 65000, Thailand.

Tel.: +66 5596 3528; fax: +66 5596 3501.

E-mail address: [reseachemu@yahoo.com](mailto:reseachemu@yahoo.com) (T. Bongkarn).



et al. [6] represented the highest maximum dielectric exhibited in BZT with  $x=0.08$ . For BZT with  $x$  less than 0.08, maximum dielectric constant insignificantly relates to the amount of zirconium and in BZT with  $x \geq 0.8$ , it is observed that the maximum dielectric constant tended to increase with increasing zirconium content.

Due to the variation in reports, an accurate investigation of the zirconium content effects on phase formation and dielectric properties in BZT is topical. In addition, our previous work has demonstrated that high quality BZT ceramics such as nano-particles and high density can be produced via the combustion technique [8]. Therefore, this study aims to synthesize  $\text{Ba}(\text{Zr}_x\text{Ti}_{1-x})\text{O}_3$  (BZT,  $0.025 \leq x \leq 0.150$ , step=0.025) ceramics by the combustion technique. The effect of composition on phase formation, dielectric and ferroelectric properties of BZT was extensively investigated.

## 2. Experimental procedure

$\text{Ba}(\text{Zr}_x\text{Ti}_{1-x})\text{O}_3$  or (BZT100 $x$ ) ceramics were prepared via the combustion technique using urea as fuel. The starting materials barium carbonate ( $\text{BaCO}_3$ ), zirconium dioxide ( $\text{ZrO}_2$ ) and titanium dioxide ( $\text{TiO}_2$ ) were weighed based on the stoichiometric compositions of  $\text{Ba}(\text{Zr}_x\text{Ti}_{1-x})\text{O}_3$  (BZT100 $x$ ,  $0.025 \leq x \leq 0.150$ , step=0.025). The weighed raw materials were mixed by ball milling with zirconia media in ethanol for 24 h, and then were dried and the powders were ground using an agate mortar and sieved into a fine powder. The mixed powders and urea ( $\text{CH}_4\text{N}_2\text{O}$ ) were mixed with a ratio of 1:2 in an agate mortar. All compositions were calcined at 1000 °C for 5 h [8]. The calcined ones were again ball-milled in the mixture medium absolute ethanol for 24 h. Disc-shaped specimens with 15 mm in diameter were fabricated using a hydraulic pressing and then the green body were sintered at 1375 °C with soaking time at 2 h [8]. The phase formation behavior and the lattice refinement of all compositions were studied by XRD analytical technique. The bulk densities of the sintered samples were measured by the Archimedes method. The temperature dependence of relative permittivity and dielectric loss of BZT specimens was investigated using LCR meter. The measurement of ferroelectric hysteresis loops was conducted at room temperature by using a ferroelectric tester.

## 3. Results and discussion

The phase formation of BZT ceramics were studied using XRD patterns as shown in Fig. 1 and the results showed that pure perovskite phase was found in all sintered samples (Fig. 1(a)). To determine the phase formation behavior of BZT with the increasing zirconium content, the XRD patterns which measured from 72 to 77° at a very low scanning rate (step size 0.00116°, time/θ 7.42 s, scan speed 0.05152°/s) were investigated (Fig. 1(b)). It can be seen that the diffraction angle also decreases as the zirconium content is raised. This can be explained by

the ionic radius of  $\text{Zr}^{4+}$  (0.072 nm) being larger than  $\text{Ti}^{4+}$  (0.061 nm), so more substitution of  $\text{Zr}^{4+}$  will increase the  $d$  spacing of BZT and cause the diffraction peaks to shift toward a lower angle [4]. At room temperature, the splitting of (133) and (311) diffraction peaks of BZT2.5 ceramics confirms the orthorhombic phase (Refer to ICCD No.01-0812196). When zirconium content was increased to 5 mol%, the two diffraction peaks gradually merged into one peak which was indicated by the rhombohedral phase which was initially diffused and influenced the phase system (Refer to ICCD no. 01-0850368). The diffraction peak exhibited a sharper curve and a nearly symmetric shape, lightly skewed to the left side in BZT7.5. This implies that the tetragonal phase was occurred and slightly diffused in rhombohedral phase of BZT system (Refer to ICCD no. 00-0030725). When zirconium content was increased to 10 mol%, the distinct non-symmetry (skewed to the right side) of the diffraction peak can be explained by the BZT showing a tetragonal phase. Moreover, when zirconium content was higher than 10 mol%, the diffraction peak changed from non-symmetry to near symmetry illustrated the cubic phase influence on BZT system (Refer to ICCD no. 01-0741961). The XRD analysis indicates that a slight change of zirconium content highly influences on the crystal structure of BZT ceramics. The accurate interpretation is derived from high quality samples which were produced via the combustion technique.

The measured density with a variation in zirconium content of BZT is listed in Table 1. The density of the ceramics was in the range of 5.61–5.86 g/cm<sup>3</sup> and the densities insignificantly changed with zirconium content modification. The highest density exhibited in BZT12.5 was 97% of the theoretical density and was higher than the samples which were prepared via the solid-state reaction method [3] and the wet chemical reaction method [7].

The temperature dependence of the dielectric constant of BZT ceramics with various stoichiometric percentage of zirconium is shown in Fig. 2. It was found that as zirconium increased from 2.5 to 5.0 mol%, maximum dielectric constant tended to increase. The reduction of maximum dielectric constant appeared in BZT with 7.5 mol% zirconium. Thereafter, more zirconium doping induced the increasing of maximum dielectric constant again. The increasing of maximum dielectric constant reached maximum value in BZT12.5 thereafter, it decreased in BZT15. The maximum dielectric constant and the loss tangent at Curie point were listed in Table 1. The value of density and maximum dielectric constant of BZT in all compositions in this study were higher when compared to previous works [3,5,7,9] which indicated that high quality BZT ceramics could be prepared via the combustion technique.

The transition temperature from orthorhombic to tetragonal structure ( $T_{o-t}$ ) is obviously observed in BZT2.5, BZT5.0 and BZT7.5 ceramics. The dielectric peak at  $T_{o-t}$  appeared broader with increasing zirconium content. From literature surveyed, by increasing  $x$ ,  $T_{r-o}$  and  $T_{o-t}$  peaks were shifted to higher temperatures. However, the shifted rate of  $T_{r-o}$  peak is

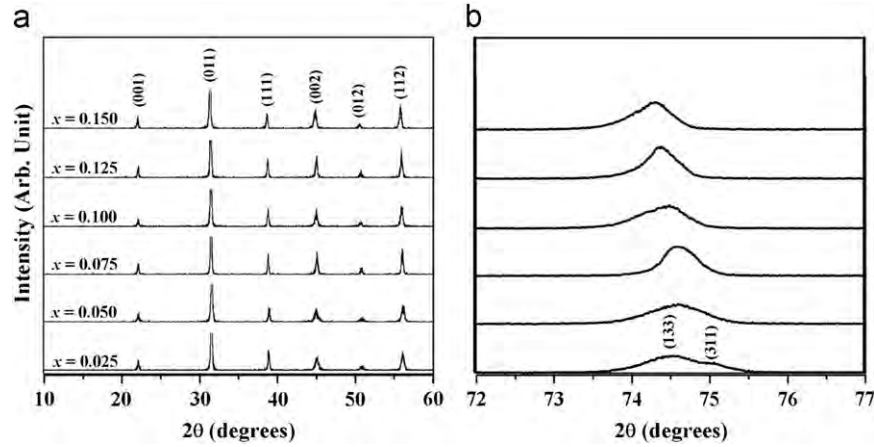
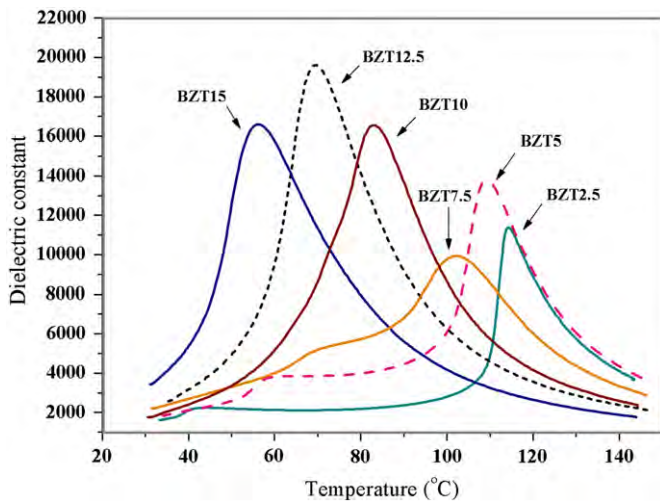
Fig. 1. XRD patterns of Ba(Zr<sub>x</sub>Ti<sub>1-x</sub>)O<sub>3</sub> ceramics where 0.025 ≤ *x* ≤ 0.150.

Table 1

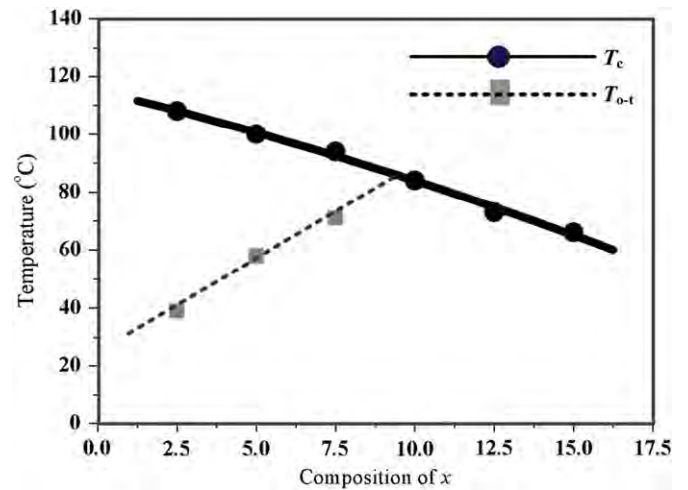
The density,  $T_{o-t}$ ,  $T_c$ , maximum dielectric constant ( $\epsilon_r$ ) and dielectric loss ( $\tan\delta$ ) at  $T_c$ ,  $\gamma$ ,  $P_r$  and  $E_c$  of Ba(Zr<sub>x</sub>Ti<sub>1-x</sub>)O<sub>3</sub> ceramics.

<i>x</i>	Density (g/cm <sup>3</sup> )	$T_{o-t}$ (°C)	$T_c$ (°C)	$\epsilon_r$ at $T_c$	$\tan\delta$ at $T_c$	$\gamma$	$P_r$ (μC/cm <sup>2</sup> )	$E_c$ (kV/cm)
0.025	5.69	39	108	11,380	0.004	1.32	8.31	2.42
0.050	5.64	50	100	13,770	0.006	1.85	8.36	4.51
0.075	5.61	71	94	9930	0.009	1.95	3.61	2.17
0.100	5.78	—	84	16,540	0.013	1.72	7.27	2.34
0.125	5.86	—	73	19,600	0.015	1.76	6.33	2.11
0.150	5.75	—	66	16,600	0.017	1.90	3.12	1.79

Fig. 2. Temperature dependences of dielectric constant of BZT100*x* ceramics where 0.025 ≤ *x* ≤ 0.150.

higher than that of  $T_{o-t}$  peak and two peaks were nearly merged at around *x* of 0.08 [3]. Therefore, the broadening of dielectric curve at  $T_{o-t}$  is caused from higher diffusive  $T_{r-o}$  peak by increased amount of zirconium.

The phase transition temperature  $T_{o-t}$  (exhibited at lower temperature) and  $T_c$  (exhibited at higher temperature) were observed from dielectric loss peak and are listed in Table 1. To investigate the pinch phase transition characteristic, the phase transition temperature  $T_{o-t}$  and

Fig. 3. Phase transition temperature  $T_c$  and  $T_{o-t}$  as function of zirconium content *x* for Ba(Zr<sub>x</sub>Ti<sub>1-x</sub>)O<sub>3</sub> ceramics.

$T_c$  as function of zirconium doping content were plotted (Fig. 3). It is found that the increase of  $T_{o-t}$  and decrease of  $T_c$  showed nonlinear function with increasing zirconium content. The intersection of  $T_{o-t}$  and  $T_c$  phase transitions temperature was observed at around 9.4 mol% of zirconium which displays the two phase transition is pinched into one dielectric peak due to the increased Zr content. Moreover, the function plotted revealed that the interval

between  $T_{o-t}$  and  $T_c$  tended to decrease by increasing zirconium content.

The study of phase transition characteristic exposed the increase and decrease of maximum dielectric constant and broadening of dielectric curve in dielectric result. In this study, BZT with zirconium  $0.025 \leq x \leq 0.075$  showed lower maximum dielectric constant compared with BZT with zirconium  $0.1 \leq x \leq 0.15$ . This can be related to the orthorhombic phase influences on dielectric constant. In case of BZT with 7.5 mol% zirconium, the lowest of maximum dielectric constant with broadest dielectric curve was exhibited. This may be attributed to the rhombohedral phase being the highest diffused as exhibited in the XRD result. Maximum dielectric constant was enhanced immediately again in the BZT sample with zirconium content 10 mol% and reached the highest in BZT with 12.5 mol% zirconium. This demonstrated that tetragonal phase induces increasing dielectric constant. The reduction of BZT with 15 mol% zirconium could be speculated by the cubic phase affected.

A diffuse phase transition is generally characterized by the diffuseness of phase transition ( $\gamma$ ) which was calculated from a modified Curie–Weiss law [8]. The  $\gamma$  values of the BZT prepared via the combustion technique are in the range of 1.32 to 1.95 up on zirconium content as listed in Table 1. The diffuseness was increased when zirconium content increased and reached its highest diffuseness of 1.95 on BZT7.5. This result was supported by two reasons. The first one is the diffusion between  $T_{r-o}$  and  $T_{o-t}$  arouse dielectric curve to broader. Another one reason is the reducing of the interval between  $T_{o-t}$  and  $T_c$  which indicated the phase transition at  $T_{o-t}$  and  $T_c$  more easily diffused. After reaching the highest value, the diffuseness decreased in BZT10 and increased again in BZT12.5 and BZT15. The increment of the  $\gamma$  with increasing zirconium content can be explained by the diffusive phase transition between ferroelectric to paraelectric phase. This result is consistent with the XRD result and the report in literature [5,10,11].

Fig. 4 shows the polarization-electric field characteristics of BZT ceramics at room temperature. It is found that well-behaved hysteresis loops can be observed in all compositions of BZT. The hysteresis loop increasingly swelled with increasing amount of zirconium from BZT2.5 to BZT5. In BZT7.5, the altitude of  $P$ – $E$  loop was decreased and appears slimmer as shown in Fig. 4(a). The loop altitude was raised again in BZT10, and thereafter the altitude and the slope were decreased with increasing zirconium content (Fig. 4(b)). The remanent polarization ( $P_r$ ) and the coercive field ( $E_c$ ) of BZT for all compositions were listed in Table 1. The value of  $P_r$  tended to increase as the amount of zirconium then depreciated for BZT7.5. The remanent polarization was raised again in BZT10 thereafter the  $P_r$  was found to decrease with increasing zirconium content. The reduction of  $P_r$  in BZT7.5 may be due to the diminution of domain wall mobility caused from the mixing phase of rhombohedral and orthorhombic phase. In the case of BZT5, although the diffusion of rhombohedral phase did not cause  $P_r$  to reduce, it affected the value of  $E_c$  which showed the highest. For BZT

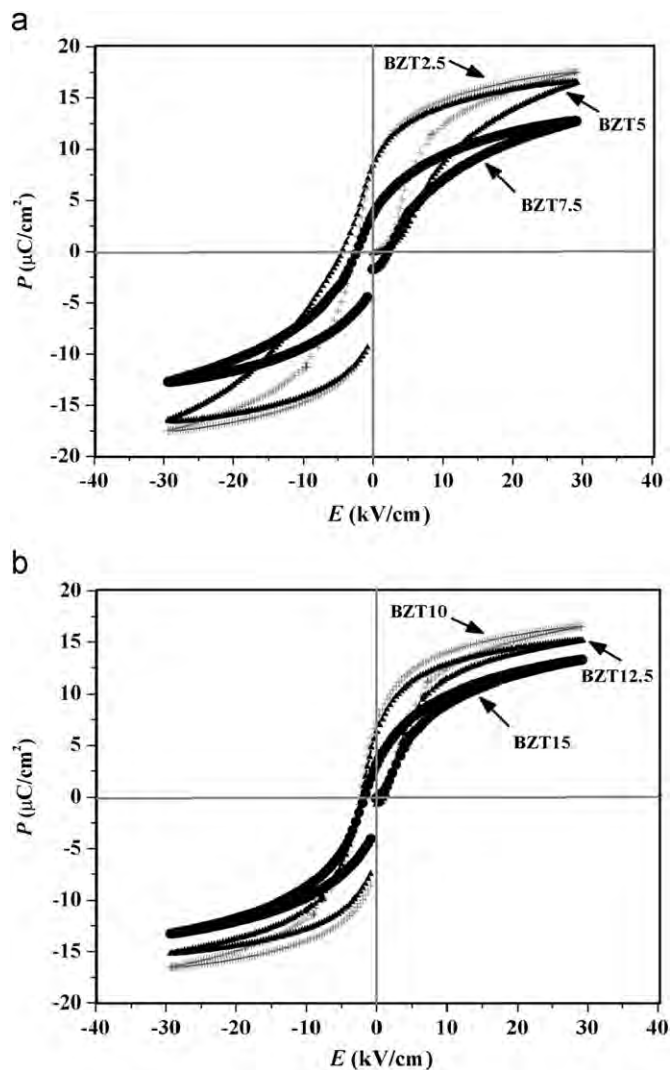


Fig. 4.  $P$ – $E$  hysteresis loop of BZT100 $x$  ceramics (a)  $0.025 \leq x \leq 0.075$  and (b)  $0.10 \leq x \leq 0.150$ .

with  $x \geq 10$ , remanent polarization tended to decrease with increasing zirconium content. This can be explained by the difference of the radius of  $Zr^{4+}$  and  $Ti^{4+}$  [5]. Moreover, the procrastination of Curie temperature approaching to room temperature may cause the decrease of the ferroelectric characteristic [3].

#### 4. Conclusions

The phase formation, dielectric behavior and ferroelectric properties of  $Ba(Zr_xTi_{1-x})O_3$  ceramics with  $0.025 \leq x \leq 0.150$  prepared via the combustion technique were investigated. The X-ray diffraction patterns clearly indicated that the transformation from orthorhombic to rhombohedral, tetragonal or cubic phase is dependent on zirconium content. The dielectric measurement indicated that, by increasing the amount of zirconium substituted,  $T_{r-o}$ ,  $T_{o-t}$  and  $T_c$  phase transition peaks were shifted and the pinched phase transition occurred in BZT with zirconium content

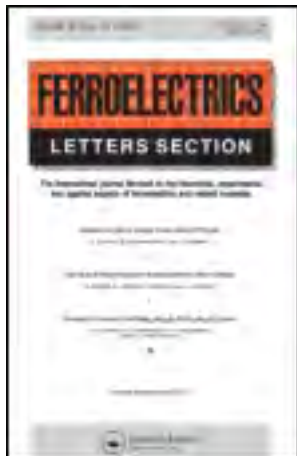
~9.4 mol%. The lowest and the highest maximum dielectric constant were 9930 and 19,600 which were exhibited in BZT with  $x=0.075$  and 0.125, respectively. The diffusion of rhombohedral and tetragonal phase influenced on the decrease and increase of maximum dielectric constant, respectively. In addition, the diffusion of  $T_{r-o}$  to  $T_{o-t}$  dielectric peak and  $T_{o-t}$  to  $T_c$  dielectric peak also caused the reduction in maximum dielectric constant of BZT7.5. Ferroelectric properties were decreased by the diffusion of rhombohedral into orthorhombic phase. The result from XRD investigation, the dielectric behavior analysis and the ferroelectric results were consistent with each other, and hence this work demonstrates the potential for the combustion technique in preparing BZT ceramics.

### Acknowledgments

This work was financially supported by the Thailand Research Fund (TRF). Thanks also to Department of Physics, Faculty of Science, Naresuan University for supporting facilities. Acknowledgments to Dr. Antony Harfield, for helpful comments and corrections of the manuscript.

### References

- [1] A.J. Moulson, J.M. Herbert, *Electroceramics*, Chapman & Hall, U.K., 1993.
- [2] A. Dixit, S.B. Majumder, P.S. Dobal, R.S. Katiyar, A.S. Bhalla, Phase transition studies of sol–gel deposited barium zirconate titanate thin films, *Thin Solid Films* 447–778 (2004) 284–288.
- [3] N. Nanakorn, P. Jalupoom, N. Vaneesorn, A. Thanaboonsombut, Dielectric and ferroelectric properties of  $\text{Ba}(\text{Zr}_x\text{Ti}_{1-x})\text{O}_3$  ceramics, *Ceramics International* 34 (2008) 779–782.
- [4] H.H. Huang, H.H.S. Chiu, N.C. Wu, M.C. Wang, Tetragonality and properties of  $\text{Ba}(\text{Zr}_x\text{Ti}_{1-x})\text{O}_3$  ceramics determined using the Rietveld method, *Metallurgical and Materials Transactions* 39A (2008) 3276–3284.
- [5] H. Chen, C. Yang, C. Fu, J. Shi, J. Zhang, W. Leng, Microstructure and dielectric properties of  $\text{Ba}(\text{Zr}_x\text{Ti}_{1-x})\text{O}_3$  ceramics, *Journal of Materials Science* 19 (2008) 379–382.
- [6] S.J. Kuang, X.G. Tang, L.Y. Li, Y.P. Jiang, Q.X. Liu, Influence of Zr dopant on dielectric properties and Curie temperature of  $\text{Ba}(\text{Zr}_x\text{Ti}_{1-x})\text{O}_3$  ( $0 \leq x \leq 0.12$ ) ceramics, *Scripta Materialia* 61 (2009) 68–71.
- [7] N. Binhayeeniyi, P. Sukvisut, C. Thanachayanont, S. Muensit, Physical and electromechanical properties of barium zirconium titanate synthesized at low-sintering temperature, *Materials Letters* 64 (2010) 305–308.
- [8] P. Julphunthong, T. Bongkarn, Phase formation, microstructure and dielectric properties of  $\text{Ba}(\text{Zr}_{0.1}\text{Ti}_{0.9})\text{O}_3$  ceramics prepared via the combustion technique, *Current Applied Physics* 11 (2011) s60–s65.
- [9] F. Moura, A.Z. Simon, B.D. Stojanovic, Dielectric and ferroelectric characteristics of barium zirconate titanate ceramics prepared from mixed oxide method, *Journal of Alloys and Compounds* 462 (2008) 129–134.
- [10] J.W. Xiong, B. Zeng, W.Q. Cao, Investigation of dielectric and relaxor ferroelectric properties in  $\text{Ba}(\text{Zr}_x\text{Ti}_{1-x})\text{O}_3$  ceramics, *Journal of Electroceramics* 21 (2008) 124–127.
- [11] X.G. Tang, K.H. Chew, H.L.W. Chan, Diffuse phase transition and dielectric tenability of  $\text{Ba}(\text{Zr}_x\text{Ti}_{1-x})\text{O}_3$  relaxor ferroelectric ceramics, *Acta Materialia* 52 (2004) 5177–5183.



## Ferroelectrics Letters Section

Publication details, including instructions for authors and subscription information:

<http://www.tandfonline.com/loi/gfel20>

### Effects of Sintering Temperature on Phase Formation, Microstructure and Dielectric Properties of BNT-BT Ceramics Prepared by Combustion Technique

Panadda Sittiketkorn<sup>a</sup> & Theerachai Bongkarn<sup>a b</sup>

<sup>a</sup> Department of Physics, Faculty of Science, Naresuan University, Phitsanulok, 65000, Thailand

<sup>b</sup> Research Center for Academic Excellence in Petroleum, Petrochemicals and Advanced Materials, Naresuan University, Phitsanulok, 65000, Thailand

To cite this article: Panadda Sittiketkorn & Theerachai Bongkarn (2013) Effects of Sintering Temperature on Phase Formation, Microstructure and Dielectric Properties of BNT-BT Ceramics Prepared by Combustion Technique, *Ferroelectrics Letters Section*, 40:4-6, 77-84, DOI: [10.1080/07315171.2007.830054](https://doi.org/10.1080/07315171.2007.830054)

To link to this article: <http://dx.doi.org/10.1080/07315171.2007.830054>

PLEASE SCROLL DOWN FOR ARTICLE

Taylor & Francis makes every effort to ensure the accuracy of all the information (the "Content") contained in the publications on our platform. However, Taylor & Francis, our agents, and our licensors make no representations or warranties whatsoever as to the accuracy, completeness, or suitability for any purpose of the Content. Any opinions and views expressed in this publication are the opinions and views of the authors, and are not the views of or endorsed by Taylor & Francis. The accuracy of the Content should not be relied upon and should be independently verified with primary sources of information. Taylor and Francis shall not be liable for any losses, actions, claims, proceedings, demands, costs, expenses, damages, and other liabilities whatsoever or howsoever caused arising directly or indirectly in connection with, in relation to or arising out of the use of the Content.

This article may be used for research, teaching, and private study purposes. Any substantial or systematic reproduction, redistribution, reselling, loan, sub-licensing, systematic supply, or distribution in any form to anyone is expressly forbidden. Terms &





# Effects of Sintering Temperature on Phase Formation, Microstructure and Dielectric Properties of BNT–BT Ceramics Prepared by Combustion Technique

PANADDA SITTIKORK<sup>1</sup>  
AND THEERACHAI BONGKARN<sup>1,2,\*</sup>

<sup>1</sup>Department of Physics, Faculty of Science, Naresuan University, Phitsanulok, 65000, Thailand

<sup>2</sup>Research Center for Academic Excellence in Petroleum, Petrochemicals and Advanced Materials, Naresuan University, Phitsanulok, 65000, Thailand

Communicated by Professor Amar S. Bhalla  
(Received in final form February 10, 2013)

*Effects of sintering temperatures on phase formation, microstructure and the dielectric properties of near MPB (1-x)BNT-xBT ceramics ( $x = 0.06$  and  $0.08$ ) were investigated. The (1-x)BNT-xBT ceramics were prepared using a combustion technique. The phase purity, crystal structure and microstructure of the samples were examined using X-ray diffraction (XRD) and scanning electron microscopy (SEM). Pure perovskite, which consists of rhombohedral and tetragonal phases, was found in the samples sintered below  $1200^{\circ}\text{C}$ . The average grain size tended to increase with increased sintering temperature. The density and the dielectric constant at room temperature increased with increasing sintered temperature up to  $1200^{\circ}\text{C}$ , thereafter they decreased. The ceramic composition with  $x = 0.08$  exhibited the highest density ( $\sim 5.80\text{ g/cm}^3$ ) and dielectric constant ( $\sim 2829$ ).*

**Keywords** Phase formation; microstructure; dielectric properties; BNT-BT

## 1. Introduction

Bismuth sodium titanate  $[(\text{Bi}_{0.5}\text{Na}_{0.5})\text{TiO}_3]$  (BNT) is a kind of perovskite-type ferroelectric, that has been considered to be a good candidate for lead-free ceramics because of their relatively large remnant polarization ( $P_r = 38\text{ }\mu\text{C/cm}^2$ ) at room temperature, high Curie temperature ( $T_c = 320^{\circ}\text{C}$ ) and high coercive field ( $E_c = 7.3\text{ kV/mm}$ ) [1–3]. It has been reported that BNT experiences two phases transition: from a ferroelectric rhombohedral phase to an antiferroelectric tetragonal phase and from an antiferroelectric tetragonal phase to a paraelectric cubic phase, resulting in a maximum dielectric constant [2, 4]. To improve its properties, several solid solutions of BNT with  $\text{BaTiO}_3$  (BT),  $\text{SrTiO}_3$  (ST), and

---

\*Corresponding author. E-mail: researchcmu@yahoo.com

CaTiO<sub>3</sub> (CT) *etc.*, have been investigated [4–9]. The addition of BT to BNT improves the piezoelectric and dielectrics properties. Furthermore, the ceramics exhibit a lower coercive field ( $E_c$ ) and larger remnant polarization ( $P_r$ ) [5–12]. Chenggang Xu *et al.* prepared (1-x)(Bi<sub>0.5</sub>Na<sub>0.5</sub>)TiO<sub>3</sub>-xBaTiO<sub>3</sub>; (1-x)BNT-xBT ( $0 \leq x \leq 0.12$ ) ceramics by a conventional solid reaction method. A morphotropic phase boundary (MPB) existed at  $0.06 < x < 0.10$ . The ceramics with  $x = 0.06$  exhibited optimum piezoelectric properties:  $d_{33} = 155$  pC/N and  $k_p = 36.7\%$ . The dielectric constant at room temperatures gave a maximum value of 1099 at  $x = 0.08$  [12]. (1-x)BNT-xBT ( $x = 0-0.10$ ) powders were synthesized by the emulsion method. The prepared emulsion was sprayed into kerosene heated at 170°C. Powder was derived from the emulsion after filtering and drying at 120°C in an oven. The emulsion-derived powder was calcined in the temperature range of 400–800°C for 2–4 h, and sintered at 1150–1200°C for 2–4 h. The powders, consisting of uniform and fine preliminary particles of about 50 nm, were obtained. The dielectric constant at 1 kHz and the piezoelectric constant  $d_{33}$  attained maximum values of 1840 and 174 pC/N, respectively, when  $x = 0.08$ , while the electromechanical coupling factor  $k_p$  exhibited the maximum value of 0.28 when  $x = 0.06$  [11]. It is well known that ceramics which are synthesized by wet chemical synthesis can provide homogenous nano-sized oxides of high purity at lower reaction temperatures but they require high cost starting materials and they are intricate and complicated [2, 11]. The solid state reaction method requires high temperatures and the resulting powders exhibit many undesirable characteristics such as: large particle size and wide particle size distribution [5, 12].

Recently, interest has been shown in the combustion method because it helps to decrease the temperature in the preparation and results in an ultra-fine particle size. The combustion reaction method also has interesting characteristics such as: its simplicity, its relatively low cost, and the fact that it usually results in products with the desired structure and composition [13–16]. Thus, in this work, (1-x)(Bi<sub>0.5</sub>Na<sub>0.5</sub>)TiO<sub>3</sub>-xBaTiO<sub>3</sub>; (1-x)BNT-xBT where  $x = 0.06$  and  $0.08$  ceramics were prepared via the combustion method. The phase formation, microstructure and dielectric properties of the resulting ceramics were also investigated.

## 2. Experimental

(1-x)BNT-xBT where  $x = 0.06$  and  $0.08$  ceramics were synthesized by the combustion method. Reagent-grade oxide and carbonate powders of Bi<sub>2</sub>O<sub>3</sub>, Na<sub>2</sub>CO<sub>3</sub>, BaCO<sub>3</sub> and TiO<sub>2</sub> were used as starting materials. The (1-x)BNT-xBT powders were prepared separately and then blended together. To prepared the BNT powders [15], Bi<sub>2</sub>O<sub>3</sub>, Na<sub>2</sub>CO<sub>3</sub>, and TiO<sub>2</sub> were weighed and mixed by ball-milling in ethanol for 24 h. After drying, the powders were mixed with glycine as a fuel, and then calcined at 650°C for 2 h. BT powders were also prepared from raw materials of BaCO<sub>3</sub> and TiO<sub>2</sub> under the same condition then mixed with urea as a fuel. The mixed powders were calcined at 1200°C for 4 h [16]. The (1-x)BNT-xBT powders were then weighed and blended according to the formula (1-x)BNT-xBT where  $x = 0.06$  and  $0.08$ . After ball-milling in ethanol for 24 h and drying, the blended powders were die-pressed into discs of 10 mm in diameter and 1–2 mm in thickness. The small disc samples were sintered at 1050–1200°C for 2 h. The crystalline phase of the calcined and sintered samples was identified by X-ray diffractometer (XRD). The microstructure evolution was observed using a scanning electron microscope (SEM). Density was measured by the Archimedes method with distilled water. Dielectric properties were investigated using an LCR meter.



### 3. Results and Discussion

The structural phase of the pure BNT calcined powder indexed in a rhombohedral phase, while the pure BT calcined powder indexed in a tetragonal phase. This matched with JCPDS file number 36–0340 and 03–0725, respectively and are shown in Fig. 1(I) and (II) [17, 18]. The structural phase of (1-x)BNT-xBT ceramics with  $x = 0.06$ , indexed as the mixed phase

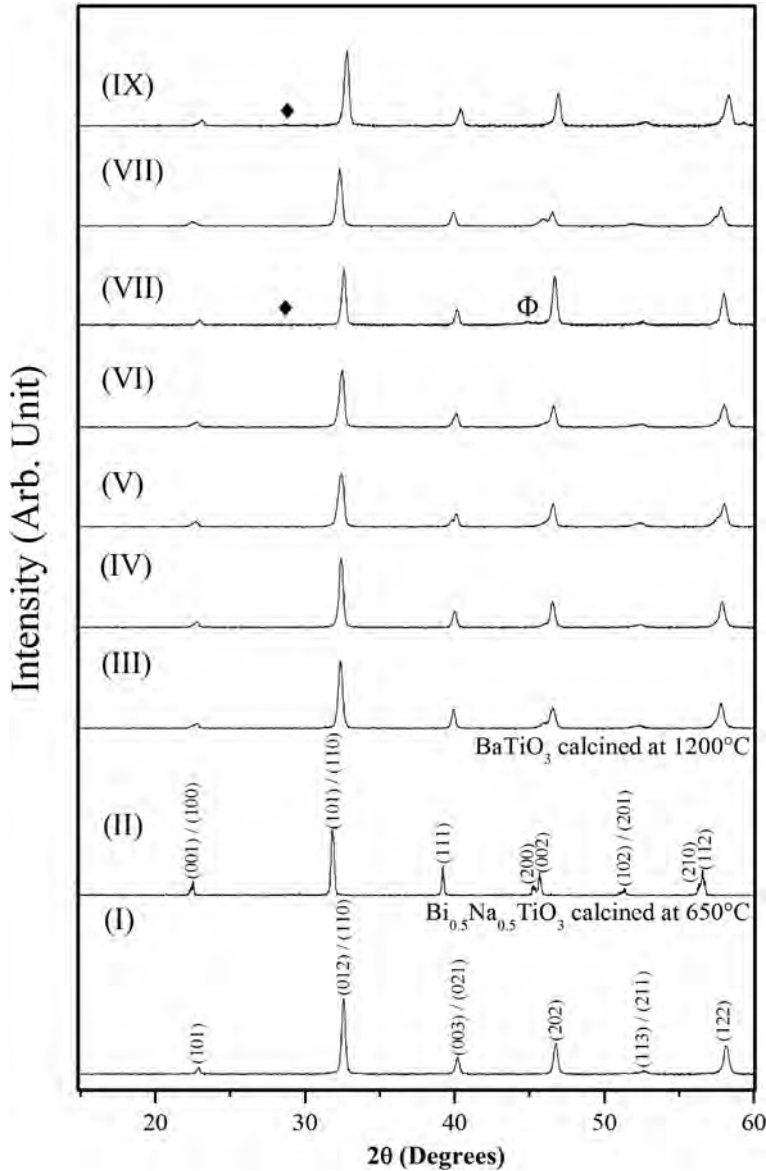


**Figure 1.** XRD patterns of (I) BNT powder, (II) BT powder and (1-x)BNT-xBT ceramics with (III)  $x = 0.06$  sintered at  $1050^{\circ}\text{C}$ , (IV)  $x = 0.06$  sintered at  $1100^{\circ}\text{C}$ , (V)  $x = 0.06$  sintered at  $1150^{\circ}\text{C}$ , (VI)  $x = 0.06$  sintered at  $1200^{\circ}\text{C}$ , (VII)  $x = 0.06$  sintered at  $1210^{\circ}\text{C}$ , (VIII)  $x = 0.08$  sintered at  $1200^{\circ}\text{C}$  and (IX)  $x = 0.08$  sintered at  $1210^{\circ}\text{C}$ ; (♦)  $\text{Ba}_2\text{BiO}_4$  and (Φ)  $\text{BaO}_{4.977}\text{Ti}$ .

between the rhombohedral phase and the tetragonal phase and the purity of the perovskite phase was found in the samples sintered below 1200°C as seen in Fig. 1(III), (IV), (V) and (VI). The peaks of  $\text{Ba}_2\text{BiO}_4$  and  $\text{BaO}_{4.977}\text{Ti}$  were detected in the sample sintered at 1210°C (Fig. 1(VII)), which may be due to vaporization of  $\text{Bi}^{2+}$  and  $\text{Na}^{2+}$  at high temperature [2, 3]. For  $x = 0.08$ , the results were similar with  $x = 0.06$ . However, the tetragonality of  $x = 0.08$  (Fig. 1(VIII)) was higher than  $x = 0.06$  and only the impurity phase of  $\text{Ba}_2\text{BiO}_4$  was detected when sintering temperature was higher than 1200°C as shown in Fig. 1(IX).

Figure 2 shows the SEM micrographs of  $(1-x)\text{BNT}-x\text{BT}$  ceramics with  $x = 0.08$  at various sintered temperatures. These ceramics exhibited a square or rectangular shape which was similar to previous works [9, 11]. At low sintering temperature, many distinct

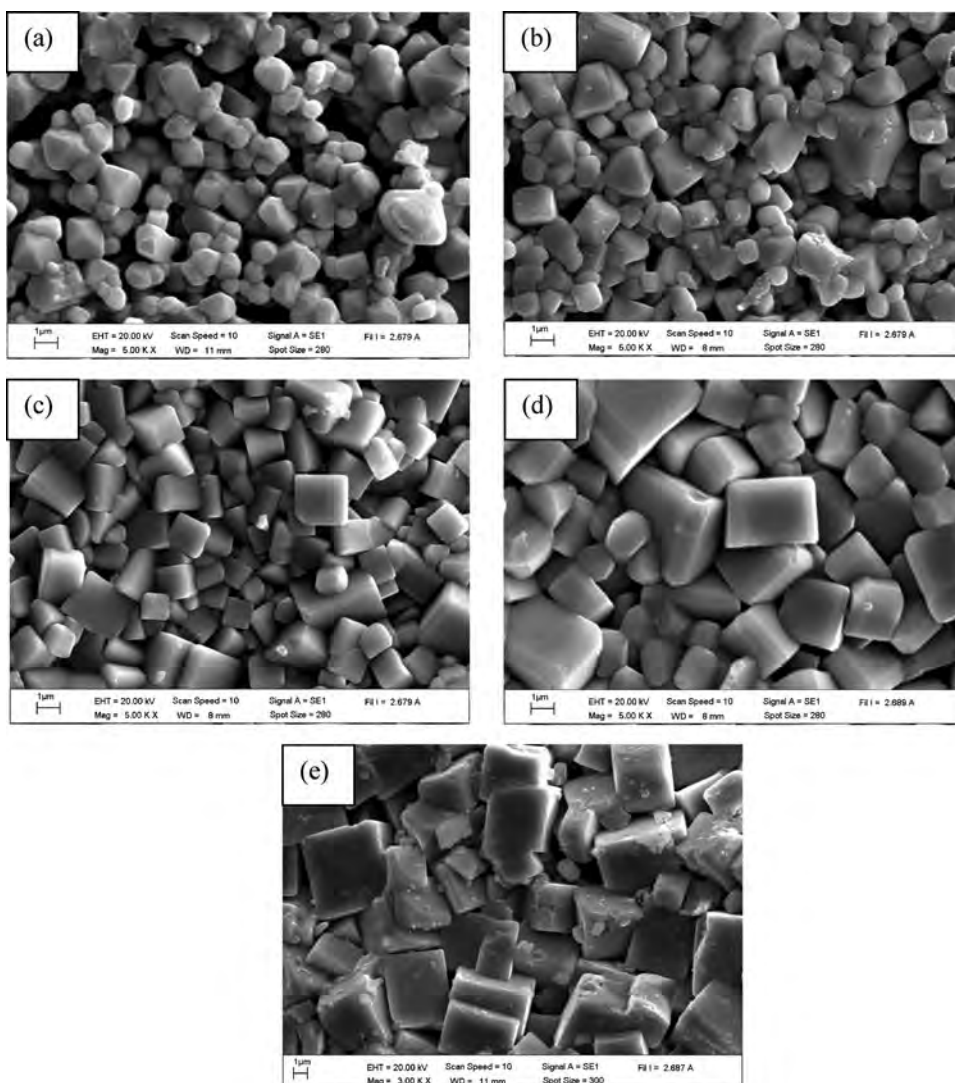


**Figure 2.** The SEM micrographs of  $(1-x)\text{BNT}-x\text{BT}$  ceramics with  $x = 0.08$ : (a) sintered at 1050°C, (b) sintered at 1100°C, (c) sintered at 1150°C, (d) sintered at 1200°C and (e) sintered at 1210°C.

**Table 1**

Average grain size, density, linear shrinkage, and dielectric properties at room temperature of (1-x)BNT-xBT ceramics with  $x = 0.06$  and  $x = 0.08$

x	Sintering temperature (°C)	Average grain size ( $\mu\text{m}$ )	Density ( $\text{g/cm}^3$ )	Linear shrinkage (%)	Dielectric constant at $T_R$	Loss factor at $T_R$
0.06	1050	1.15	5.46	5.50	1401	4.80
	1100	1.51	5.57	10.2	1574	1.60
	1150	1.63	5.74	14.8	1768	0.60
	1200	2.78	5.79	15.8	2383	0.12
	1210	6.09	—	—	—	—
0.08	1050	1.04	5.58	6.2	1526	7.20
	1100	1.41	5.68	12.1	2049	1.20
	1150	1.60	5.78	15.1	2307	0.10
	1200	2.90	5.80	16.1	2829	0.08
	1210	5.10	—	—	—	—

pores occurred in the samples (Fig. 2(a) and (b)). When the sintering temperature increase up to 1200°C (Fig. 2(c) and (d)), the porosity markedly decreased and the average grain size slightly increased. The increase of sintering temperature significantly promoted the grain growth and microstructure densification [3]. However, at a sintering temperature above 1200°C, the grain uniformity decreased and began to melt (Fig. 2(e)) which supported the XRD result. These results were similar to the (1-x)BNT-xBT ceramics with  $x = 0.06$ . The average grain size determined with the linear intercept method is summarized in Table 1. The average grain size increased with an increase sintering temperature. At the same sintering temperature, the average grain size of (1-x)BNT-xBT ceramics when  $x = 0.08$  was smaller than  $x = 0.06$ .

The density and linear shrinkage of all the ceramics increased with an increase in sintering temperatures, up to 1200°C and then decreased with higher sintering temperatures (Table 1). The density attained a maximum value of 5.79 and 5.80  $\text{g/cm}^3$  when  $x = 0.06$  and 0.08, respectively. This was observed from the sample sintered at 1200°C. However, the density of the pellet sintered at 1210°C could not be reported due to its fragility which corresponded to the SEM result.

Figure 3(a) shows the dielectric constant of (1-x)BNT-xBT ceramics with 0.08 at various sintered temperatures, measured at 1 kHz. At 1200°C of sintering temperature, the ceramics exhibited two dielectric anomalies: the lower dielectric peaks  $T_d$  (150°C) and the higher dielectric peaks  $T_m$  (270°C).  $T_d$  is the depolarization temperature which corresponds to the transition from a ferroelectric state to a so-called “anti-ferroelectric” state, while  $T_m$  is the maximum temperature at which  $\epsilon_r$  reaches a maximum value and corresponds to a transition from an “anti-ferroelectric state” to a paraelectric state [9, 11]. At a lower sintering temperature, the dielectric curves broadened even more and the  $T_d$  peaks gradually disappeared. These linked to the lower crystallinity existed at lower sintering temperatures. At room temperature ( $T_R$ ), the dielectric constant and loss factor of the ceramics with  $x = 0.08$  increased and decreased with increased sintering temperature (Table 1). The pellets sintered at 1210°C could not have its dielectric properties measured due to its fragility. The dielectric properties of the ceramics with  $x = 0.06$  were similar to  $x = 0.08$ . At the same

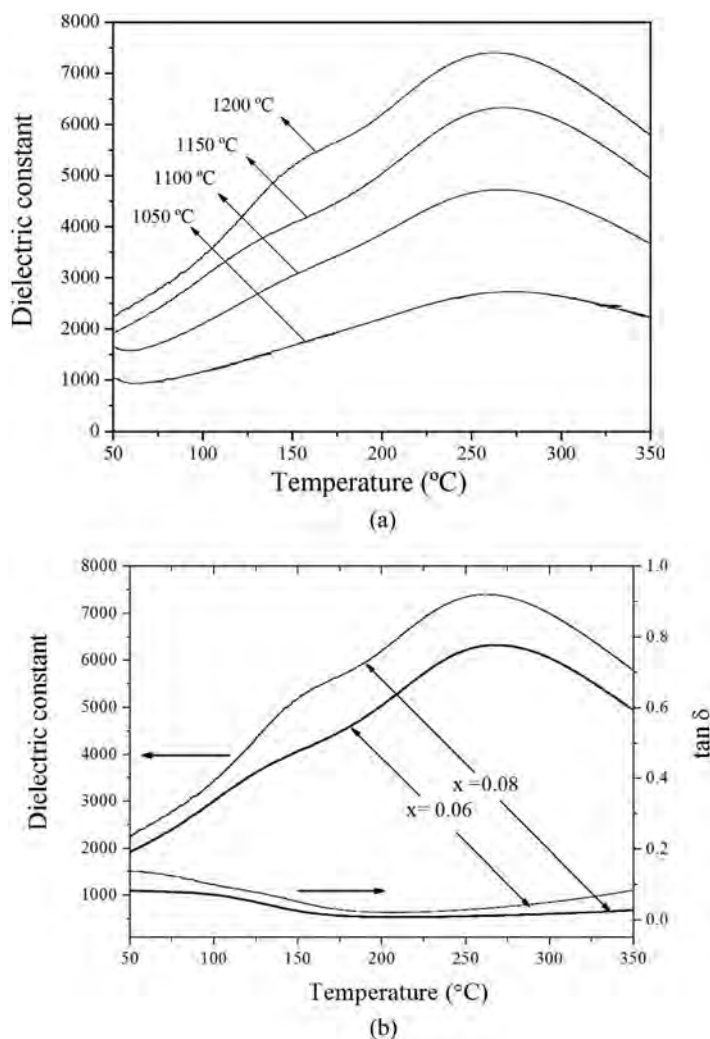


**Figure 3.** (a) Dielectric constant of (1-x)BNT-xBT ceramics with  $x = 0.08$  at various sintering temperatures, measured at 1 kHz and (b) dielectric properties of (1-x)BNT-xBT ceramics with  $x = 0.06$  and  $x = 0.08$  sintered at 1200 °C, measured at 1 kHz.

sintering temperature, the dielectric constant at  $T_c$  and  $T_R$  of the ceramics with  $x = 0.08$  was higher than  $x = 0.06$  as seen in Fig 3(b) and Table 1. The dielectric properties results corresponded with the density and SEM results. The highest dielectric constant and the lowest loss factor of the (1-x)BNT-xBT ceramics were obtained from the sample sintered at 1200 °C, which should be the proper condition when using the combustion technique. It should be noted that the dielectric constant at  $T_R$  of the ceramics with  $x = 0.08$  obtained by using the combustion technique ( $\sim 2829$ ) was higher than the conventional mixed oxide method ( $\sim 1099$ ) [12] or the emulsion method ( $\sim 1840$ ) [11]. These results confirmed that the combustion technique is a simple method for fabricating high quality (1-x)BNT-xBT ceramics.

#### 4. Conclusions

Dense near-MPB (1-x)BNT-xBT ceramic compositions ( $x = 0.06$  and  $0.08$ ) were successfully prepared by the combustion technique. The sintering temperature directly affected the phase formation, microstructure, density and dielectric properties. The optimum morphology, highest density ( $\sim 5.80 \text{ g/cm}^3$ ), highest dielectric constant ( $\sim 2829$ ), and lowest dielectric loss ( $\sim 0.08$ ) were obtained from the (1-x)BNT-xBT ceramics with  $x = 0.08$  sintered at  $1200^\circ\text{C}$ . At higher sintering temperature, the ceramics began to melt and very fragile ceramics were obtained.

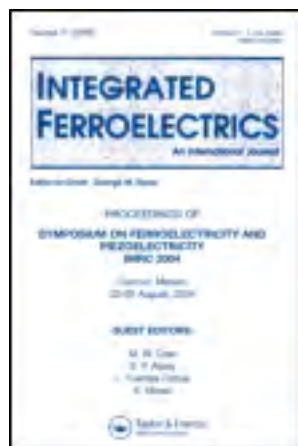
#### Acknowledgments

This work was financially supported by the Thailand Research Fund (TRF), Commission on Higher Education (CHE). The authors wish to thank the Science Lab Center, Faculty of Science, Naresuan University for equipments. Thanks are also given to Mr. Don Hindle for his help in editing the manuscript

#### References

1. C. S. Chou, R. Y. Yang, J. H. Chen, and S. W. Chou, The optimum conditions for preparing the lead-free piezoelectric ceramic of  $\text{Bi}_{0.5}\text{Na}_{0.5}\text{TiO}_3$  using the Taguchi method. *Powder Technol.* **199**, 264–271 (2010).
2. J. Hao, X. Wang, R. Chen, and L. Li, Synthesis of  $(\text{Bi}_{0.5}\text{Na}_{0.5})\text{TiO}_3$  nanocrystalline powders by stearic acid gel method. *Mater. Chem. Phys.* **90**, 282–285 (2005).
3. T. Motohashi, and T. Kimura, Development of texture in  $\text{Bi}_{0.5}\text{Na}_{0.5}\text{TiO}_3$  prepared by reactive-templated grain growth process. *J. Eur. Ceram. Soc.* **27**, 3633–3636 (2007).
4. W. C. Lee, C. Y. Huang, L. K. Tsao, and Y. C. Wu, Chemical composition and tolerance factor at the morphotropic phase boundary in  $(\text{Bi}_{0.5}\text{Na}_{0.5})\text{TiO}_3$ -based piezoelectric ceramics. *J. Eur. Ceram. Soc.* **29**, 1443–1448 (2009).
5. L. Gao, Y. Huang, Y. Hu, and H. Du, Dielectric and ferroelectric properties of  $(1-x)\text{BaTiO}_3$ - $x\text{Bi}_{0.5}\text{Na}_{0.5}\text{TiO}_3$  ceramics. *Ceram. Int.* **33**, 1041–1046 (2007).
6. Y. Watanabe, Y. Hiruma, H. Nagata and T. Takenaka, Phase transition temperatures and electrical properties of divalent ions ( $\text{Ca}^{2+}$ ,  $\text{Sr}^{2+}$  and  $\text{Ba}^{2+}$ ) substituted  $(\text{Bi}_{1/2}\text{Na}_{1/2})\text{TiO}_3$  ceramics. *Ceram. Int.* **34**, 761–764 (2008).
7. Y. Qu, D. Shan, and J. Song, Effect of A-site substitution on crystal component and dielectric properties in  $\text{Bi}_{0.5}\text{Na}_{0.5}\text{TiO}_3$  ceramics. *Mater. Sci. Eng. B.* **121**, 148–151 (2005).
8. R. Zuo, S. Su, Y. Wu, J. Fu, M. Wang and L. Li, Influence of A-site nonstoichiometry on sintering, microstructure and electrical properties of  $(\text{Bi}_{0.5}\text{Na}_{0.5})\text{TiO}_3$  ceramics. *Mater. Chem. Phys.* **110**, 311–315 (2008).
9. M. Cernea, E. Andronescu, R. Radu, F. Fochi, and C. Galassi, Sol–gel synthesis and characterization of  $\text{BaTiO}_3$ -doped  $(\text{Bi}_{0.5}\text{Na}_{0.5})\text{TiO}_3$  piezoelectric ceramics. *J. Alloy. Compd.* **490**, 690–694 (2010).
10. H. Wang, R. Zuo, X. Ji, and Z. Xu, Effects of ball milling on microstructure and electrical properties of sol–gel derived  $(\text{Bi}_{0.5}\text{Na}_{0.5})_{0.94}\text{Ba}_{0.06}\text{TiO}_3$  piezoelectric ceramics. *Mater. Design.* **31**, 4403–4407 (2010).
11. B. H. Kim, S. J. Han, J. H. Kim, J. Lee, B. K. Ahn, and Q. Xu, Electrical properties of  $(1-x)(\text{Bi}_{0.5}\text{Na}_{0.5})\text{TiO}_3$ - $x\text{BaTiO}_3$  synthesized by emulsion method. *Ceram. Int.* **33**, 447–452 (2007).
12. C. Xu, D. Lin, and K. W. Kwok, Structure, electrical properties and depolarization temperature of  $(\text{Bi}_{0.5}\text{Na}_{0.5})\text{TiO}_3$ - $\text{BaTiO}_3$  lead-free piezoelectric ceramics. *Solid State Sci.* **10**, 934–940 (2008).
13. A. Thongtha, A. Laowanidwatana, and Theerachai Bongkarn, Effect of firing temperatures on phase and morphology evolution of  $\text{CaZrO}_3$  ceramics synthesized using the combustion technique. *Ferroelectrics.* **403**, 3–10 (2010).

14. P. Sittiketkorn, S. Ramaneeepikool, and Theerachai Bongkarn, The effects of firing temperatures on phase formation and microstructure of  $\text{Pb}_{0.975}\text{Sr}_{0.025}\text{TiO}_3$  ceramics synthesized via the combustion technique. *Ferroelectrics*. **403**, 158–165 (2010).
15. C. Kronprom, and T. Bongkarn, The preparation of lead-free bismuth sodium titanate ceramics by the combustion method. *Ferroelectrics*. (submitted).
16. P. Panya and T. Bongkarn, Fabrication of perovskite barium titanate ceramics using combustion route. *Ferroelectrics*. **383**, 102–110 (2009).
17. Powder Diffraction File No. 36-0340, International Centre for Diffraction Data, Newton Square, PA (2000).
18. Powder Diffraction File No. 03-0725, International Centre for Diffraction Data, Newton Square, PA (2000).



## Integrated Ferroelectrics: An International Journal

Publication details, including instructions for authors and subscription information:

<http://www.tandfonline.com/loi/ginf20>

### Optimum Conditions for Fabrication High-Density KNN-LS-BF Ceramics by Combustion Method

Peerapong Panya<sup>a b</sup>, Chakkaphan Wattanawikkam<sup>a b</sup>, Artid Laowanidwatana<sup>a b</sup>, Naratip Vittayakorn<sup>c</sup> & Theerachai Bongkarn<sup>a</sup>

<sup>a</sup> Department of Physics, Faculty of Science, Naresuan University, Phitsanulok, 65000, Thailand

<sup>b</sup> Research Center for Academic Excellence in Applied Physics, Naresuan University, Phitsanulok, 65000, Thailand

<sup>c</sup> Materials Science Research Unit, Department of Chemistry, Faculty of Science, King Mongkut's Institute of Technology Ladkrabang, Bangkok, 10520, Thailand

Published online: 07 Dec 2013.

To cite this article: Peerapong Panya, Chakkaphan Wattanawikkam, Artid Laowanidwatana, Naratip Vittayakorn & Theerachai Bongkarn (2013) Optimum Conditions for Fabrication High-Density KNN-LS-BF Ceramics by Combustion Method, Integrated Ferroelectrics: An International Journal, 148:1, 161-170

To link to this article: <http://dx.doi.org/10.1080/10584587.2013.852457>

PLEASE SCROLL DOWN FOR ARTICLE

Taylor & Francis makes every effort to ensure the accuracy of all the information (the "Content") contained in the publications on our platform. However, Taylor & Francis, our agents, and our licensors make no representations or warranties whatsoever as to the accuracy, completeness, or suitability for any purpose of the Content. Any opinions and views expressed in this publication are the opinions and views of the authors, and are not the views of or endorsed by Taylor & Francis. The accuracy of the Content should not be relied upon and should be independently verified with primary sources of information. Taylor and Francis shall not be liable for any losses, actions, claims, proceedings, demands, costs, expenses, damages, and other liabilities whatsoever or howsoever caused arising directly or indirectly in connection with, in relation to or arising out of the use of the Content.

This article may be used for research, teaching, and private study purposes. Any substantial or systematic reproduction, redistribution, reselling, loan, sub-licensing, systematic supply, or distribution in any form to anyone is expressly forbidden. Terms & Conditions of access and use can be found at <http://www.tandfonline.com/page/terms-and-conditions>



# Optimum Conditions for Fabrication High-Density KNN-LS-BF Ceramics by Combustion Method

PEERAPONG PANYA,<sup>1,2</sup>

CHAKKAPHAN WATTANAWIKKAM,<sup>1,2</sup>

ARTID LAOWANIDWATANA,<sup>1,2</sup> NARATIP VITTAYAKORN,<sup>3</sup>

AND THEERACHAI BONGKARN<sup>1,2,\*</sup>

<sup>1</sup>Department of Physics, Faculty of Science, Naresuan University, Phitsanulok, 65000, Thailand

<sup>2</sup>Research Center for Academic Excellence in Applied Physics, Naresuan University, Phitsanulok 65000, Thailand

<sup>3</sup>Materials Science Research Unit, Department of Chemistry, Faculty of Science, King Mongkut's Institute of Technology Ladkrabang, Bangkok 10520, Thailand

*The 0.996(0.95K<sub>0.5</sub>Na<sub>0.5</sub>NbO<sub>3</sub>-0.05LiSbO<sub>3</sub>)-0.004BiFeO<sub>3</sub> (KNN-LS-BF) ceramics were prepared by the combustion method using glycine as a fuel. The raw materials were mixed and calcined at various calcination temperatures (650–750°C) with different dwell time (0.5–3 h). Then, the calcined powders were pressed and sintered at various temperatures (1000–1100°C) with 0.5–4 h dwell time. The highest % perovskite orthorhombic phase was found in powder calcined at 700°C for 1 h. For the sintered pellets, the orthorhombic structure was found in ceramic sintered at 1075°C for 2 h using heating and cooling rate of 10°C/min. The SEM photographs showed square or rectangular morphology. The average grain size increased with the increasing of soak time. The highest density (4.47 g/cm<sup>3</sup>), maximum dielectric constant ( $\epsilon_r = 6180$ ) and lowest dielectric loss ( $\tan\delta = 0.1$ ) at  $T_c$  were obtained in the sample sintered at 1075°C for 3 h. The densest sample showed the  $P_r = 14.3 \mu\text{C}/\text{cm}^3$  and  $E_c = 20.68 \text{ kV}/\text{cm}$  at 40 kV/cm.*

**Keywords** KNN-LS-BF ceramics; dielectric constant; combustion method

## Introduction

Lead-based piezoceramics are widely used because they have excellent piezoelectric properties. However, because of environmental issues associated with lead, the development of lead-free piezoceramics has recently attracted much attention. Recently, solid solutions based on K<sub>0.5</sub>Na<sub>0.5</sub>NbO<sub>3</sub> (abbreviation KNN) have increasingly been studied. Because of its relatively strong piezoelectric properties ( $d_{33} \sim 100 \text{ pC}/\text{N}$ ) and high Curie temperature ( $T_c \sim 420^\circ\text{C}$ ), KNN-based ceramic systems were considered as one of the most promising candidates for lead-free piezoelectric application [1–4]. The major disadvantage of pure KNN was the difficulty in obtaining ceramics with good density [5]. The reason is the evaporation of Na<sub>2</sub>O and K<sub>2</sub>O found at high temperature. To obtain satisfactory density

---

Received December 9, 2012; in final form August 25, 2013.

\*Corresponding author. E-mail: researchcmu@yahoo.com

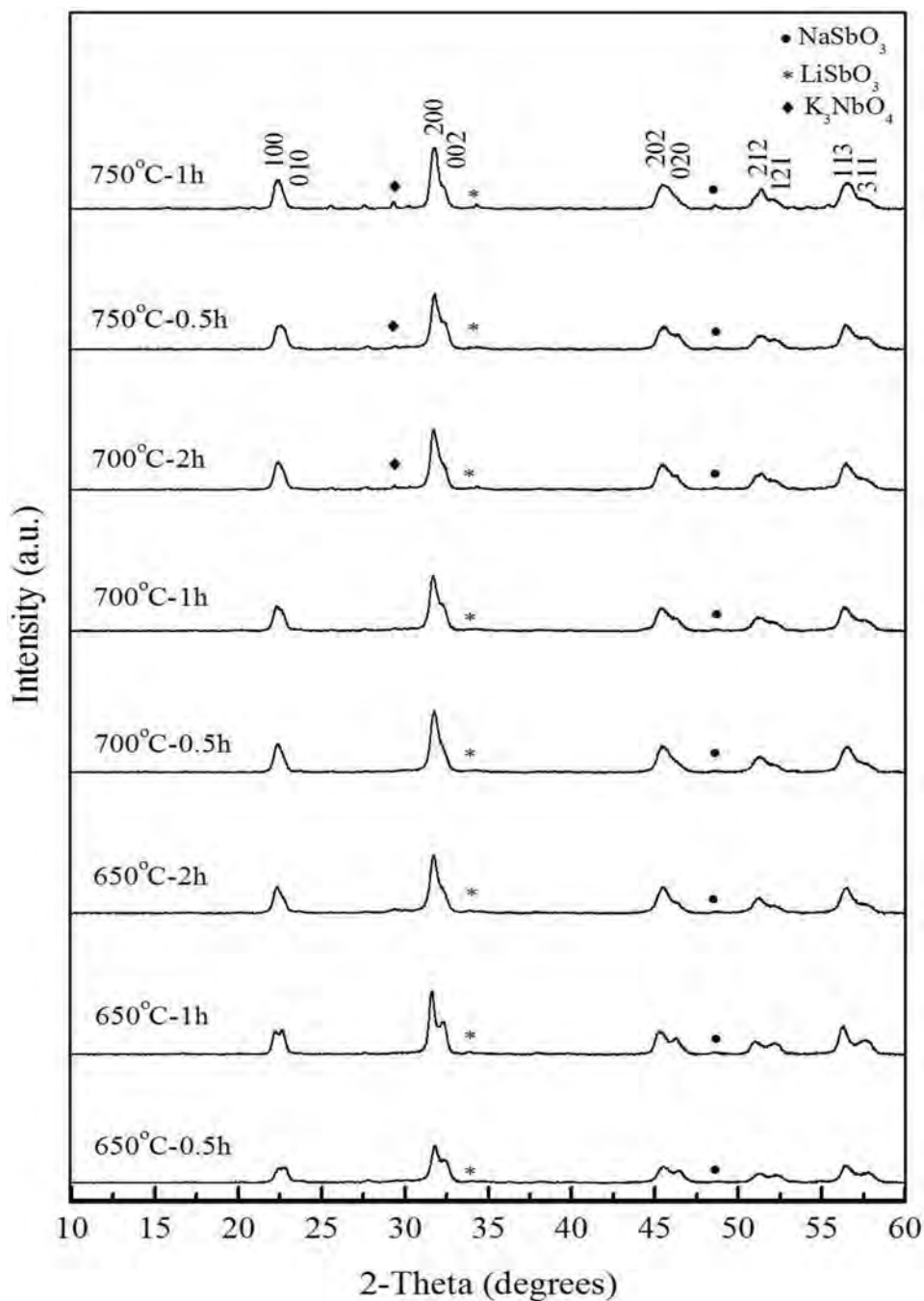


**Figure 1.** The XRD pattern of KNN-LS-BF powders calcined at various temperatures (650–750°C) with 0.5–2 h dwell time and heating/cooling rate of 5°C/min.

**Table 1**

The % perovskite phase of KNN-LS-BF powders calcined at various conditions

Calcination temperatures (°C)	Dwell time (h)	% perovskite phase (%)
650	0.5	80.5
	1	92.8
	2	92.6
700	0.5	95.8
	1	90.2
	2	84.2
750	0.5	82.7
	1	78.1

and electrical properties, number of solid solutions of KNN with ABO<sub>3</sub>-type ferroelectrics perovskite materials such as KNN-LiSbO<sub>3</sub> [6] and KNN-LiSbO<sub>3</sub>-BiFeO<sub>3</sub> [7] have been studied. The solid solution 0.996(0.95KNN-0.05LiSbO<sub>3</sub>)-0.004BiFeO<sub>3</sub> having good density and electrical properties has been obtained. Minhong et al. [7] prepared the high density (>96 %) 0.996(0.95KNN-0.05LiSbO<sub>3</sub>)-0.004BiFeO<sub>3</sub> ceramics by solid state reaction. They found that the dielectric constant at Curie temperature, piezoelectric constant  $d_{33}$  and planar coupling factor  $k_p$  of the sample sintered at 1100°C for 3 h were 5600, 260 pC/N and 0.52, respectively. However, the solid state reaction method required high temperature, the evaporation of Na<sup>+</sup>, K<sup>+</sup>, Bi<sup>3+</sup> and Ni<sup>2+</sup> was present and a large particle size distribution was observed.

The combustion route is a simple preparation process of relatively low cost. Obtained nano-powders can be used for sintering ceramics having high density and excellent electrical properties. The combustion route also reduces the firing temperatures. That saves energy and decreases the ion evaporation [8-9]. Thus, the aim of this work was to investigate the optimum conditions for preparing 0.996(0.95K<sub>0.5</sub>Na<sub>0.5</sub>NbO<sub>3</sub>-0.05LiSbO<sub>3</sub>)-0.004BiFeO<sub>3</sub>; KNN-LS-BF ceramics by the combustion method using glycine as a fuel. The phase formation, microstructure, dielectric and ferroelectric properties of the ceramic systems have also been studied.

## Experimental Procedure

The 0.996(0.95K<sub>0.5</sub>Na<sub>0.5</sub>NbO<sub>3</sub>-0.05LiSbO<sub>3</sub>)-0.004BiFeO<sub>3</sub>; KNN-LS-BF ceramics were prepared by the combustion method using glycine as a fuel. The mixtures of K<sub>2</sub>CO<sub>3</sub>, NaCO<sub>3</sub>, Nb<sub>2</sub>O<sub>5</sub>, LiCO<sub>3</sub>, Sb<sub>2</sub>O<sub>3</sub>, Bi<sub>2</sub>O<sub>3</sub> and Fe<sub>2</sub>O<sub>3</sub> powders were ball milled. Zirconia milling media under ethanol for 24 h was used. Drying was carried out at 120°C. After sieving, the powders and glycine were mixed in the agate mortar. Then the mixture was calcined at various temperatures ranging from 650 to 750°C, with the dwell time of 0.5-2 h and heating/cooling rate of 5°C/min. The calcined powders were then pressed into disks with a diameter of 15 mm at a pressure of 80 MPa. The pellets were sintered at various temperatures from 1000 to 1100°C for 0.5-4 h. The calcined powders were examined by room temperature X-ray diffraction (XRD) to identify the phase and find the optimum calcination temperature. The sintered ceramics morphology was imaged by scanning electron microscopy (SEM). Density of sintered ceramics was measured by Archimedes

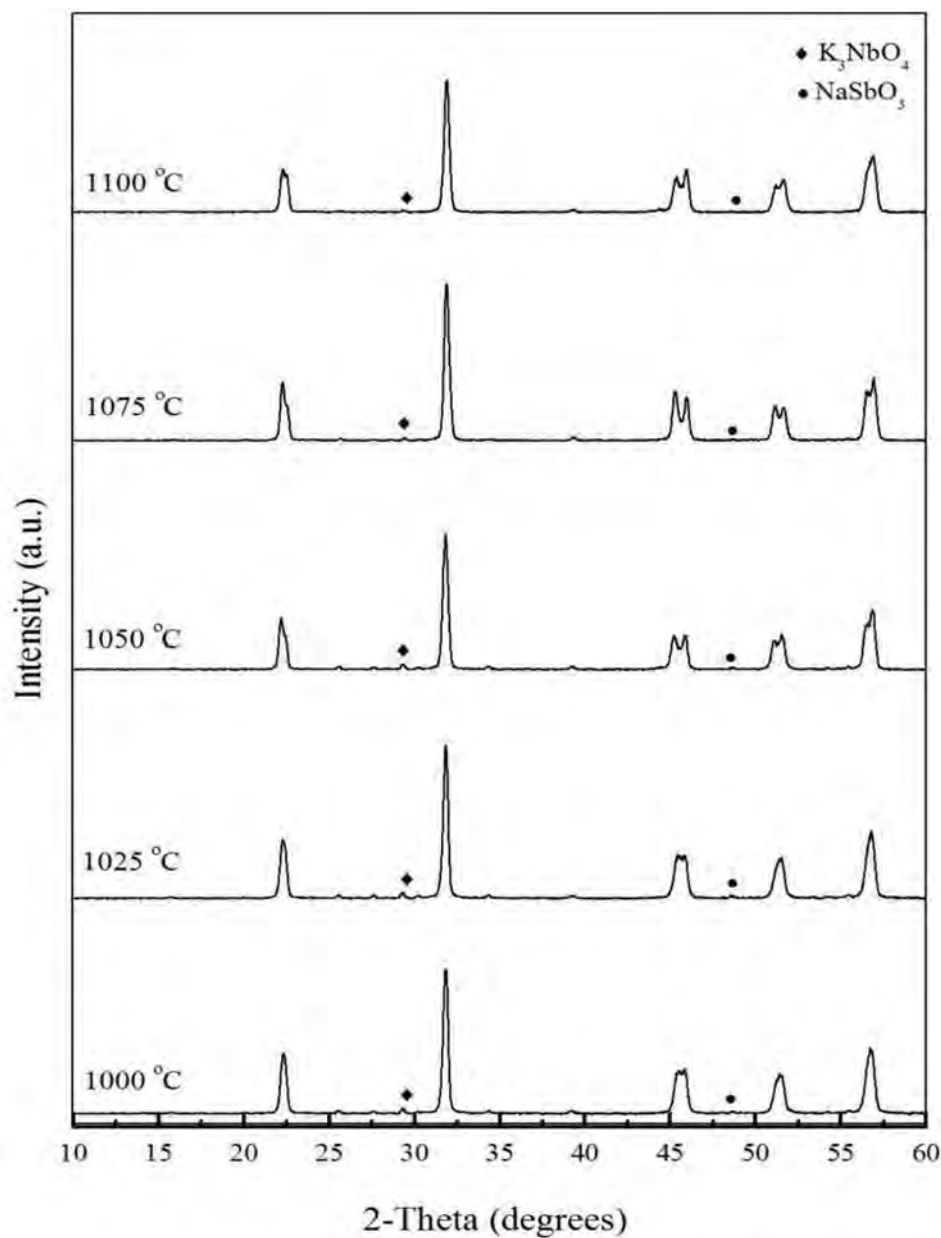


**Figure 2.** The XRD pattern of KNN-LS-BF ceramics sintered at various temperatures (1000–1100 °C) with 2 h dwell time and heating/cooling rate of 5 °C/min.

method. The average grain size was determined by the mean linear intercept method. The capacitance was measured with a LCR meter. The dielectric constant ( $\epsilon_r$ ) was calculated using the geometric area and thickness of the discs. The ferroelectric properties were also studied.

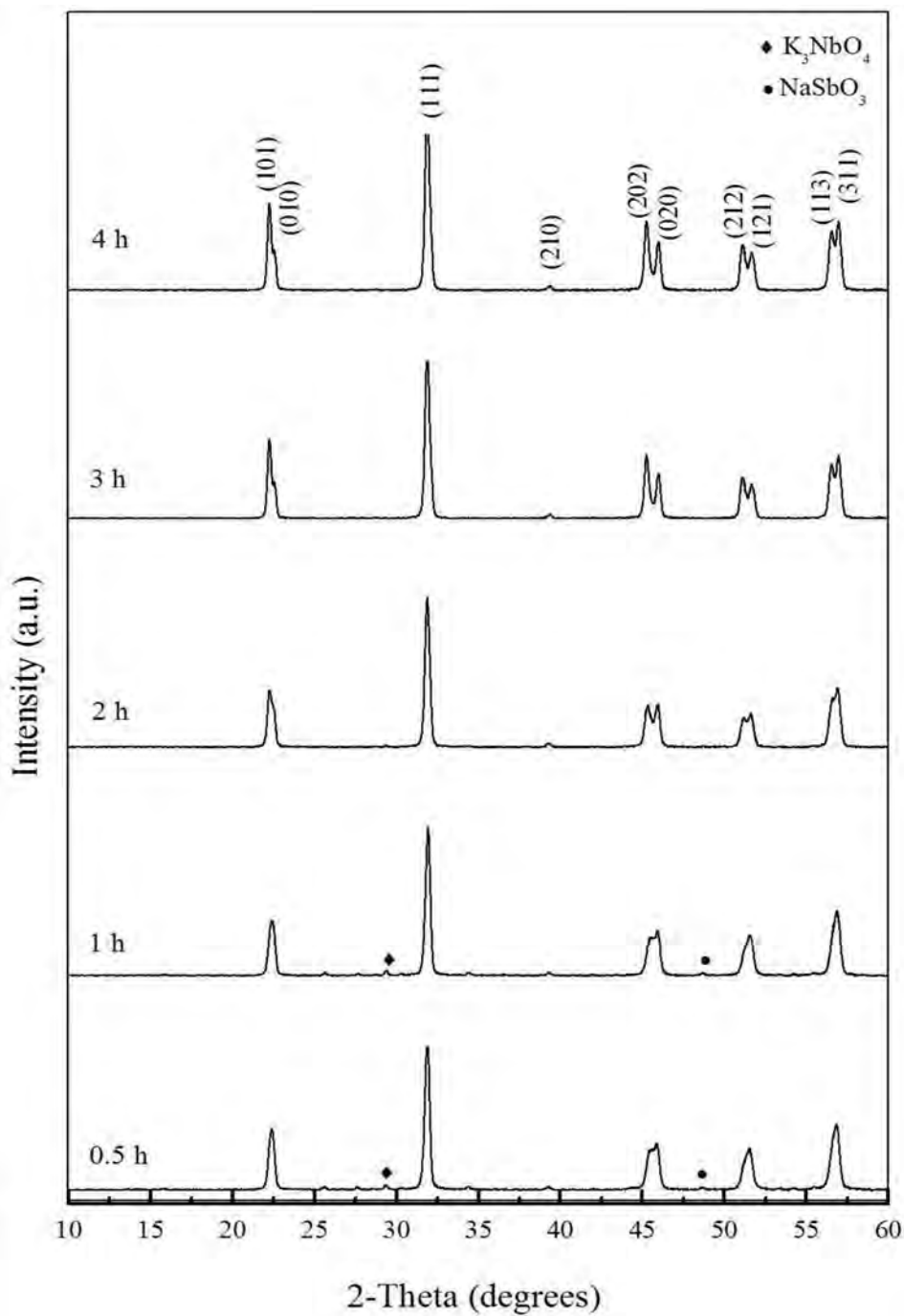


**Figure 3.** The XRD pattern of KNN-LS-BF ceramics sintered at 1075°C with heating/cooling rate of 10°C/min, for 0.5–4 h.

**Table 2**

The % perovskite phase of KNN-LS-BF ceramics sintered at various conditions

Sintering temperature (°C)	Heating/cooling rate (°C)	Dwell time (h)	% perovskite phase (%)
1000	5	2	90.4
1025	5	2	91.6
1050	5	2	92.6
1075	5	2	95.8
1100	5	2	98.0
1075	10	0.5	90.7
1075	10	1	92.2
1075	10	2	100.0
1075	10	3	100.0
1075	10	4	100.0

## Results and Discussion

XRD patterns of KNN-LS-BF powders calcined at various temperatures (650–750°C) with 0.5–2 h soak time and heating/cooling rate of 5°C/min are shown in Fig. 1. The second phase such as NaSbO<sub>3</sub>, LiSbO<sub>3</sub> and K<sub>3</sub>NbO<sub>4</sub> was found in all samples. The % perovskite phase was found between 80.5% and 95.8% (Table 1). The highest percent perovskite phase of KNN-LS-BF powder was 95.8% obtained from powder calcined at 700°C for 0.5 h.

The KNN-LS-BF powder calcined at 700°C for 0.5 h were pressed and sintered at various temperatures (1000–1100°C) for 2 h with heating/cooling rate 5°C/min. The XRD patterns of KNN-LS-BF ceramics are shown in Fig. 2. The minor phase of K<sub>3</sub>NbO<sub>4</sub> and NaSbO<sub>3</sub> was obtained for all samples. The percentage of perovskite phase increased with the increasing of the sintering temperatures (Table 2). The maximum % perovskite phase of 98.0% was found in the sample sintered at 1100°C, but the pellet showed the irregular shape due to the high sintering temperature. The sintering temperature of 1075°C was then chosen for more study. Fig. 3 showed the XRD pattern of KNN-LS-BF ceramics sintered at 1075°C with heating/cooling rate of 10°C/min, for 0.5–4 h. At the dwell time below 2 h

**Table 3**Average grain size, linear shrinkage, density, T<sub>c</sub> and dielectric properties of KNN-LS-BF ceramics sintered at 1075°C for various dwell times

Sintering temperature(°C)	Dwell time(h)	Average grain size (μm)	Linear shrinkage(%)	Density (%)	T <sub>c</sub> (°C)	Dielectric properties at T <sub>c</sub> (°C)	
						ε <sub>r</sub>	tanδ
1075	2	0.68	15.8	96.6	332	3465	0.11
	3	1.12	16.5	98.4	325	6180	0.11
	4	1.23	17.5	97.7	341	5639	0.20

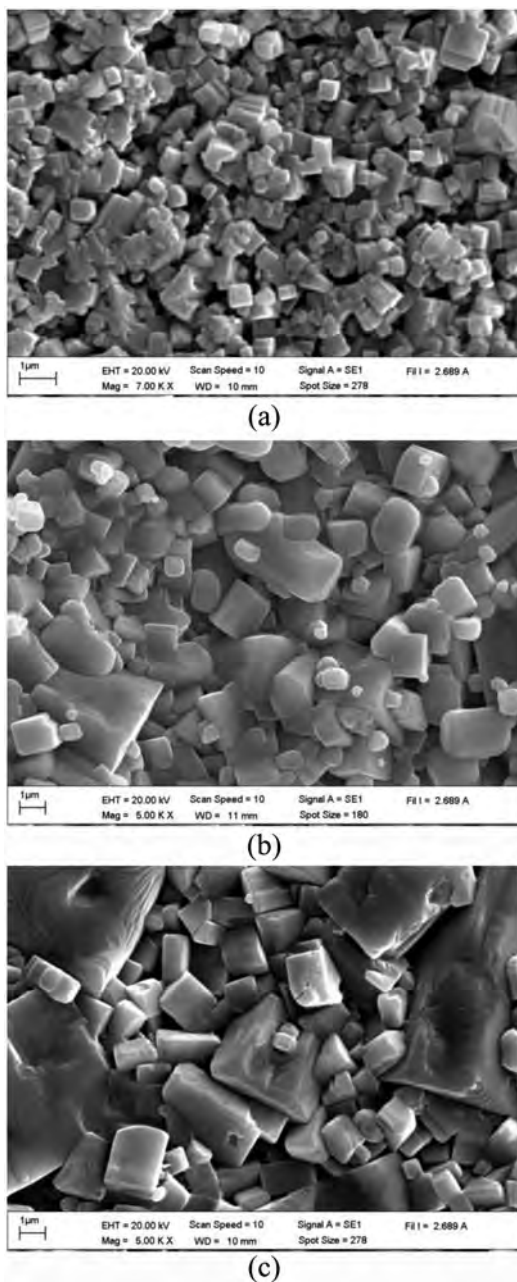


**Figure 4.** SEM photographs of KNN-LS-BF ceramics sintered at 1075°C with heating/cooling rate of 10°C/min for (a) 2 h, (b) 3 h and (c) 4 h.

the minor phase of  $K_3NbO_4$  and  $NaSbO_3$  was detected. However, the samples sintered for 2–4 h were free from the minor phase. The pure orthorhombic phase was obtained. This indicates that the combustion technique can reduce the sintering temperature and dwell time compared with the conventional method [7].

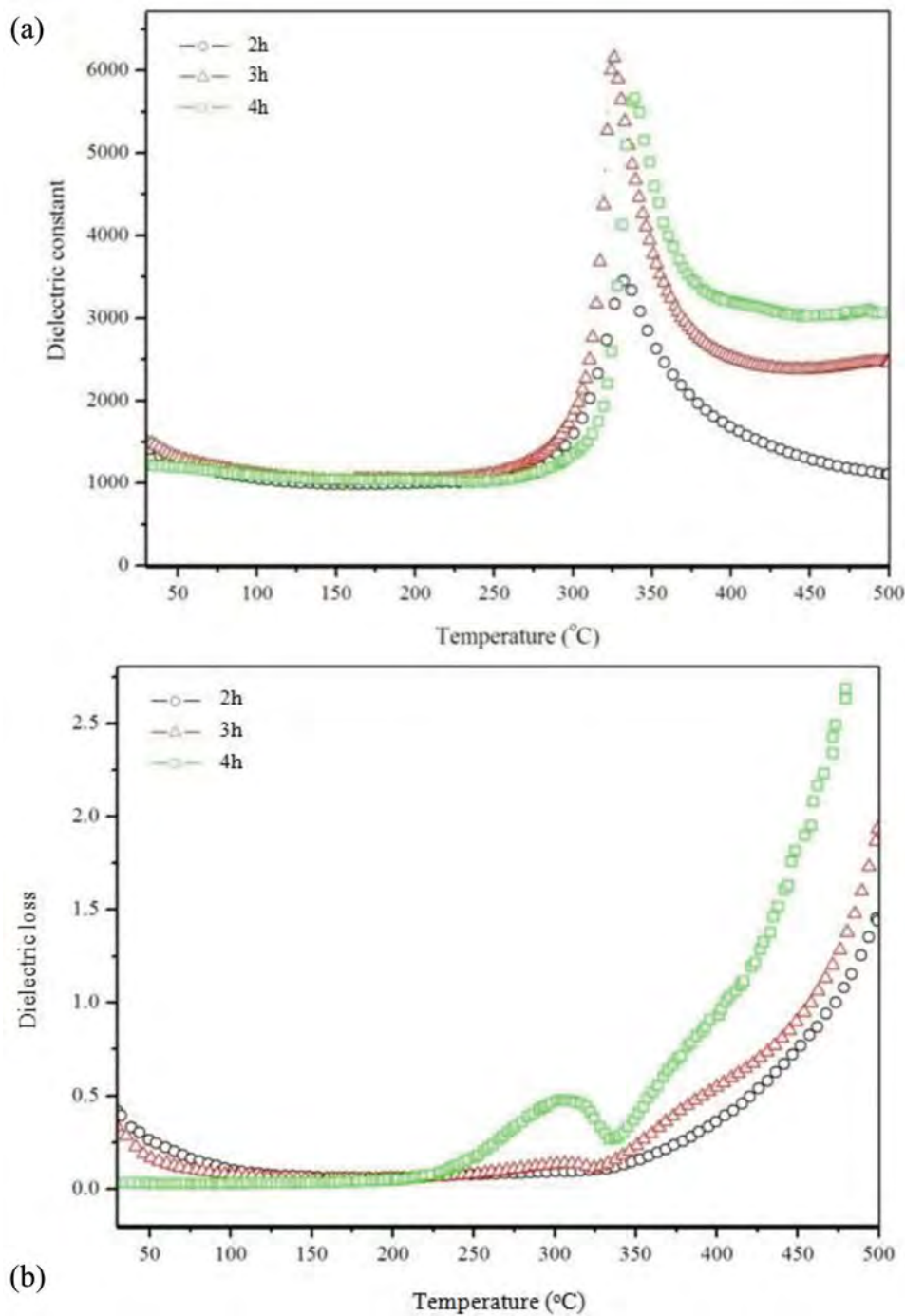


**Figure 5.** (a) the dielectric constant and (b) dielectric loss at 1 kHz for KNN-LS-BF ceramics sintered at 1075°C. (Color figure available online.)



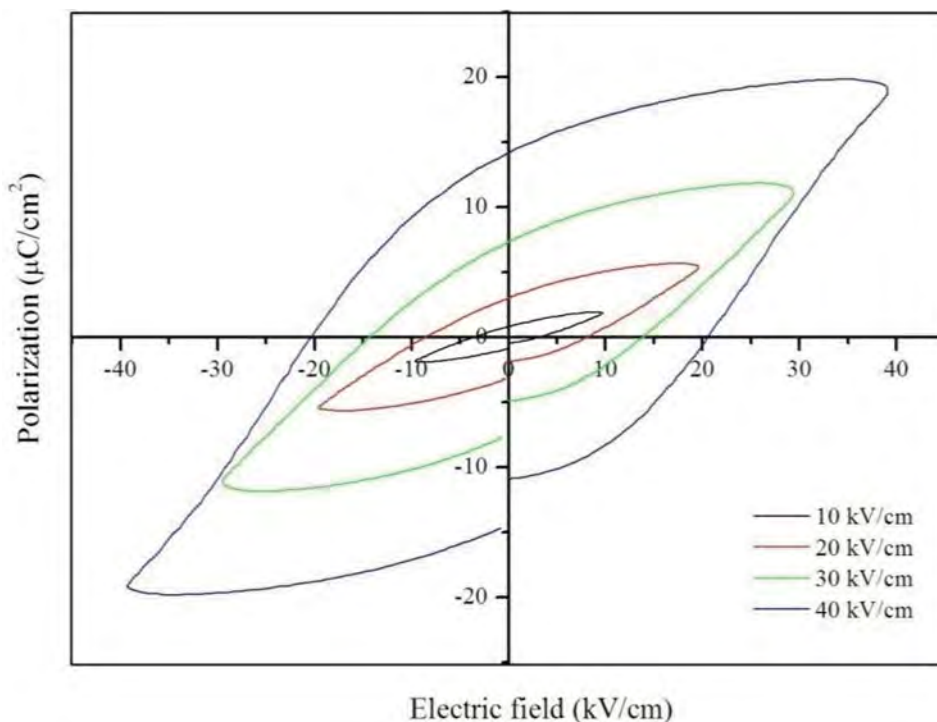


**Figure 6.** The ferroelectric polarization-electric field (P-E) loop of KNN-LS-BF densest ceramic.

SEM photographs of KNN-LS-BF ceramics sintered at 1075°C with heating/cooling rate of 10°C/min, for 2–4 h are shown in Fig. 4. The grains have mostly rectangle morphology. This result was similar to that of the previous work [10]. The grain size increased with the increasing of dwell time (Table 3). At the 4 h of dwell time, the grain melted together and large amount of the liquid phase produced a larger grains.

The % of linear shrinkage and % of theoretical density of KNN-LS-BF samples sintered at 1075°C for 0.5–4 h are presented in Table 3. The % linear shrinkage increased between 15.8% and 17.5 % as the dwell time increased. The theoretical density increased up to 98.4% for the sample sintered for 3 h and then decreased with the rising of dwell time (Table 3). This may happen due to the expanding of gas in pores and the evaporation of Na<sub>2</sub>O and K<sub>2</sub>O due to the large dwell time. The density was in agreement with the SEM micrograph result.

The temperature dependence of the dielectric properties at 1 kHz for KNN-LS-BF ceramics sintered at 1075°C for different dwell times is shown in Fig. 5. The dielectric constant peak was found at temperature approximately 330°C. This peak can be attributed to the phase transition from ferroelectric tetragonal to paraelectric cubic. The Curie temperature ( $T_c$ ) was between 325 and 341°C (Table 3). The largest dielectric constant and smallest dielectric loss at  $T_c$  were 6180 and 0.11, respectively, obtained for the sample sintered at 1075°C for 3 h (Table 3). These results are in accordance with the density and microstructure results. The dielectric properties of KNN-LS-BF ceramic prepared by combustion technique were higher than those produced by conventional method [7]. The results

prove that the good quality KNN-LS-BF ceramics can be fabricated by the combustion method.

The ferroelectric polarization-electric field (P-E) loop of the KNN-LS-BF densest ceramic is shown in Fig. 6. It was found that the shape of the hysteresis loops differed for the different electric field strengths. At the lower electric fields (10–20 kV/cm), a loop pinching was observed, which is linked to a preferred orientation of defect dipole in the materials [4]. At the electric fields higher 30 kV/cm, a well formed symmetric loops were observed. At the maximum electric fields of 40 kV/cm, the coercive field ( $E_c$ ) and remnant polarization ( $P_r$ ) of 20.68 kV/cm and 14.30  $\mu\text{C}/\text{cm}^2$  were obtained

## Conclusions

The firing conditions for (KNN-LS-BF) ceramics have a strong influence on phase formation, microstructure, density and electrical properties. The pure perovskite phase was obtained from the sample sintered at 1075°C for 2–4 h. As the dwell time increased, the grain size became larger. The largest dielectric constant of 6180, the smallest dielectric loss of 0.1 at  $T_c$ , the coercive field ( $E_c$ ) 20.68 kV/cm of and remnant polarization ( $P_r$ ) 14.30  $\mu\text{C}/\text{cm}^2$  were found for the densest sample (98.4% TD) sintered at 1075°C for 3 h. These evidenced that high-density KNN-LS-BF ceramics could be produce via the combustion method.

## Acknowledgments

This work was financially supported by the Thailand Research Fund (TRF). Thanks also to Department of Physics, Faculty of Science, Naresuan University for supporting facilities. Acknowledgments to Prof. Galina Popovici, for helpful comments and corrections of the manuscript.

## References

1. Y. Saito, H. Takao, T. Tani, T. Nonoyama, K. Takatori, T. Homma, T. Nagaya, and M. Nagamura, Lead-free piezoceramics. *Nature*. **432**, 84 (2004).
2. E. Ringgaard and T. Wurlitzer, Lead-free piezoceramics based on alkali niobates. *J. Eur. Ceram. Soc.* **25**, 2701 (2005).
3. W.W. Wolny, European approach to development of new environmentally sustainable electroceramics. *Ceram. Int.* **30**, 1079 (2004).
4. H. Birol, D. Damjanovic, and N. Setter, Preparation and characterization of  $(\text{K}_{0.5}\text{Na}_{0.5})\text{NbO}_3$  ceramics. *J. Eur. Ceram. Soc.* **26**, 861 (2006).
5. M.D. Maeder, D. Damjanovic, and N. Setter, Lead free piezoelectric materials. *J. Electroceram.* **13**, 385 (2004).
6. S. Zhang, R. Xia, T.R. Shrout, G. Zang, and J. Wang, Piezoelectric properties in perovskite  $0.948(\text{K}_{0.5}\text{Na}_{0.5})\text{NbO}_3\text{--}0.052\text{LiSbO}_3$  lead-free ceramics. *J. Appl. Phys.* **100**, 104 (2006).
7. M. Jiang, X. Liu, and G. Chen, Phase structures and electrical properties of new lead-free  $\text{Na}_{0.5}\text{K}_{0.5}\text{NbO}_3\text{--LiSbO}_3\text{--BiFeO}_3$  ceramics. *Scripta Materialia*. **60**, 909 (2009).
8. A. Thongtha and T. Bongkarn, Phase formation and microstructure of barium zirconate ceramics prepared using the combustion technique, *Ferroelectrics*. **383**, 33 (2009).
9. N. Phungjit, P. Panya, and T. Bongkarn, The structural phase and microstructure of perovskite  $\text{Ba}(\text{Ti}_{1-x}\text{Zr}_x)\text{O}_3$  ceramics using the combustion route. *Func. Matter. Lett.* **4**, 169 (2009).
10. H. Du, F. Tang, Z. Li, W. Zhou, S. Qu, and Z. Pei, Effect of poling condition on piezoelectric properties of  $(\text{K}_{0.5}\text{Na}_{0.5})\text{NbO}_3$  ceramics. *Tran. Nonferrous. Soc. China*. **16**, s462 (2006).



## Ferroelectrics

Publication details, including instructions for authors and subscription information:

<http://www.tandfonline.com/loi/gfer20>

### Effect of Firing Conditions on Phase Formation, Microstructure and Dielectric Properties of KNN-LS-BN Ceramics Fabricated by Combustion Technique

Peerapong Panya<sup>a</sup>, Chakkaphan Wattanawikkam<sup>a b</sup>, Suphornphun Chootin<sup>a b</sup> & Theerachai Bongkarn<sup>a b</sup>

<sup>a</sup> Department of Physics, Faculty of Science, Naresuan University, Phitsanulok, 65000, Thailand

<sup>b</sup> Research Center for Academic Excellence in the Petroleum, Petrochemicals and Advanced Materials, Naresuan University, Phitsanulok, 65000, Thailand

Published online: 09 Dec 2013.

To cite this article: Peerapong Panya, Chakkaphan Wattanawikkam, Suphornphun Chootin & Theerachai Bongkarn (2013) Effect of Firing Conditions on Phase Formation, Microstructure and Dielectric Properties of KNN-LS-BN Ceramics Fabricated by Combustion Technique, *Ferroelectrics*, 454:1, 119-128

To link to this article: <http://dx.doi.org/10.1080/00150193.2013.842852>

PLEASE SCROLL DOWN FOR ARTICLE

Taylor & Francis makes every effort to ensure the accuracy of all the information (the "Content") contained in the publications on our platform. However, Taylor & Francis, our agents, and our licensors make no representations or warranties whatsoever as to the accuracy, completeness, or suitability for any purpose of the Content. Any opinions and views expressed in this publication are the opinions and views of the authors, and are not the views of or endorsed by Taylor & Francis. The accuracy of the Content should not be relied upon and should be independently verified with primary sources of information. Taylor and Francis shall not be liable for any losses, actions, claims, proceedings, demands, costs, expenses, damages, and other liabilities whatsoever or howsoever caused arising directly or indirectly in connection with, in relation to or arising out of the use of the Content.

This article may be used for research, teaching, and private study purposes. Any substantial or systematic reproduction, redistribution, reselling, loan, sub-licensing, systematic supply, or distribution in any form to anyone is expressly forbidden. Terms &



# Effect of Firing Conditions on Phase Formation, Microstructure and Dielectric Properties of KNN-LS-BN Ceramics Fabricated by Combustion Technique

PEERAPONG PANYA,<sup>1</sup> CHAKKAPHAN  
WATTANAWIKKAM,<sup>1,2</sup> SUPHORNPHUN CHOOTIN,<sup>1,2</sup>  
AND THEERACHAI BONGKARN<sup>1,2,\*</sup>

<sup>1</sup>Department of Physics, Faculty of Science, Naresuan University, Phitsanulok, 65000, Thailand

<sup>2</sup>Research Center for Academic Excellence in the Petroleum, Petrochemicals and Advanced Materials, Naresuan University, Phitsanulok, 65000, Thailand

*The 0.998[0.95(K<sub>0.5</sub>Na<sub>0.5</sub>NbO<sub>3</sub>–0.05LiSbO<sub>3</sub>)]–0.002BiNiO<sub>3</sub>; KNN-LS-BN ceramics has been prepared by the combustion technique using glycine as a fuel. A pure orthorhombic phase was obtained in the powder calcined at 750°C for 0.5 h. For the sintered pellets, a pure tetragonal structure was found in the ceramic sintered at 1100°C for 1–3 h using heating and cooling rate of 15°C/min. The average grain size and linear shrinkage were increased with the increasing of dwell time. The highest density, maximum dielectric constant and lowest dielectric loss at T<sub>c</sub> with a value of 98.4%, 4872 and 0.1 were found in the sample sintered at 1100°C for 2 h using heating and cooling rate of 15°C/min.*

**Keywords** KNN-LS-BN ceramics; dielectric constant; combustion method; ferroelectric

## Introduction

Due to their excellent piezoelectric properties, lead titanate zirconate (PZT) ceramics have been widely used in resonators, actuators, transducers and filters and so on, since 1950s [1–3]. However, the high toxicity of the lead raises environmental concerns. Therefore, it is necessary to rapidly develop lead-free piezoelectric ceramics with excellent electrical properties for replacing the lead-based ceramics. Over the past few years, considerable attentions for lead-free piezoelectric ceramics have been given to the sodium potassium niobate (KNN) ceramics for their good properties, such as high Curie temperature (T<sub>c</sub> = 420°C), and good ferroelectric properties (P<sub>r</sub> = 33 μC/cm<sup>2</sup>) [2, 4]. However, the major drawback for pure KNN ceramic is the difficulty of obtaining high density. Therefore, in order to solve the above problems, many recent researches have shown that different additives in KNN materials, such as LiBO<sub>3</sub> (B = Nb, Ta, Sb), ATiO<sub>3</sub> (A = Ba, Sr, Ca, Bi<sub>0.5</sub>Na<sub>0.5</sub>), BiMeO<sub>3</sub> (Me = Fe, Sc, Al) and Ag(Ta, Sb)O<sub>3</sub>, prepared by the conventional

---

Received December 11, 2012; in final form March 16, 2013.

\*Corresponding author. E-mail: researchcmu@yahoo.com

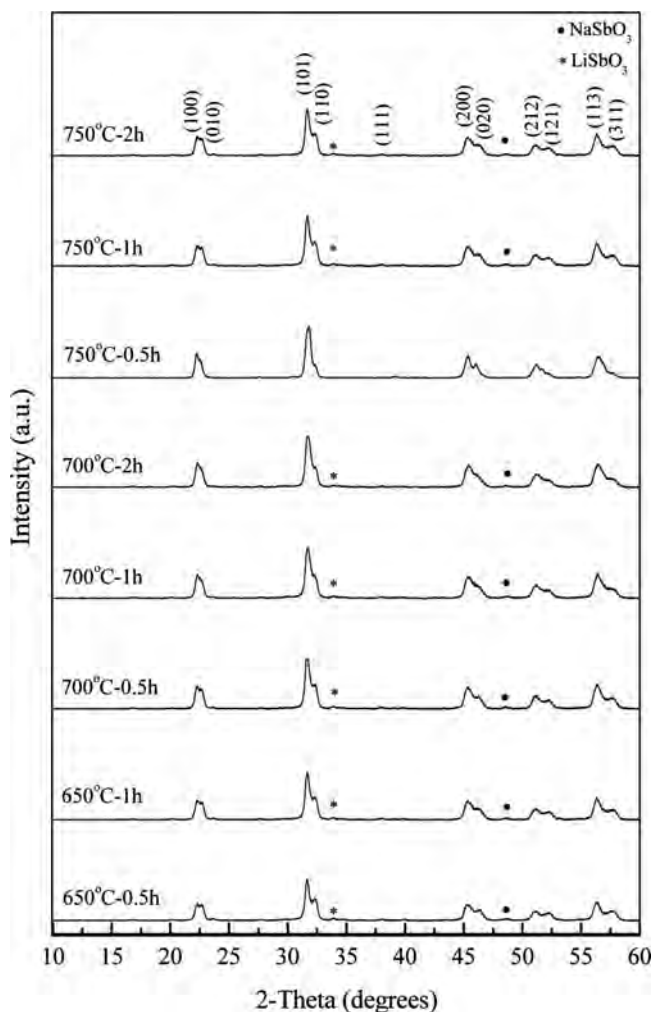


**Figure 1.** The XRD patterns of KNN-LS-BN powders calcined at various temperatures (650–750°C) with 0.5–2 h of dwell time and heating/cooling rate of 5°C/min.

solid-state reaction, can improve the sintering behavior of KNN, which enhance the piezoelectric and dielectric properties comparing with the pure KNN [2, 5–8]. Liu *et al.* [9], fabricated the  $(0.94-x)\text{K}_{0.5}\text{Na}_{0.5}\text{NbO}_3-0.06\text{LiSbO}_3-x\text{BiNiO}_3$  ceramics by the mixed oxide method using the calcination temperature of 850°C for 6 h. The morphotropic phase boundary (MPB) was found at  $x = 0.002$  which exhibits the highest piezoelectric properties ( $d_{33} = 240 \text{ pC/N}$ ,  $k_p = 0.42$ ). However, the conventional solid-state route which involves prolonged firing at high temperatures with intermediate grindings, yielding large coarse grained micron sized powders and the evaporation of  $\text{Na}^+$ ,  $\text{K}^+$ ,  $\text{Bi}^{3+}$  and  $\text{Ni}^{2+}$  are obtained.

Recently, the combustion technique has successfully prepared lead-free ferroelectric ceramics such as,  $\text{BaTiO}_3$ ,  $\text{BaZrO}_3$ ,  $\text{K}_{0.5}\text{Na}_{0.5}\text{NbO}_3$  and  $\text{KNN-LiSbO}_3\text{-BiScO}_3$  ceramics [10–12]. It has an uncomplicated, very cheap and it produces a high ultra-fine powder. It can also fabricate good ceramics with a high density and excellent electrical properties,

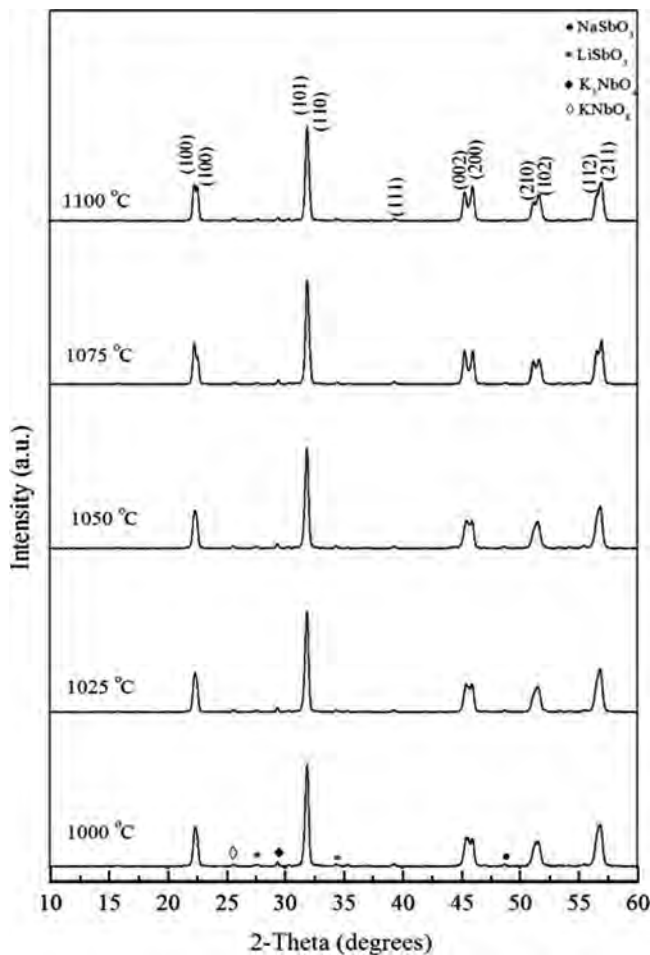


**Figure 2.** The XRD patterns of KNN-LS-BN ceramics sintered at various temperatures (1000–1100°C) with 2 h of dwell time and heating/cooling rate of 5°C/min.

**Table 1**

The % perovskite phase of KNN-LS-BN powders calcined at various temperatures and dwell time

Calcination temperature (°C)	Dwell time (h)	% perovskite phase
650	0.5	87.6
	1	88.3
	0.5	91.2
700	1	90.1
	2	90.1
	0.5	100.0
750	1	92.3
	2	91.5

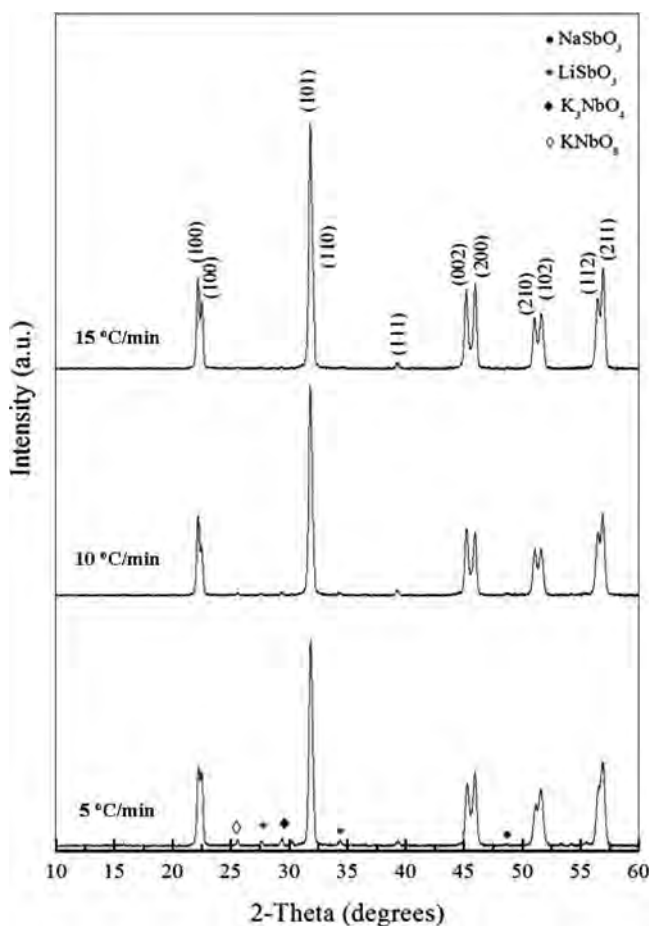


**Figure 3.** The XRD patterns of KNN-LS-BN ceramics sintered at 1100°C with various heating/cooling rates for 2 h of dwell time.

which use a lower firing temperature and soak time compared to the conventional method [11, 13].

Therefore, in the present work, the  $0.998(0.95\text{K}_{0.5}\text{Na}_{0.5}\text{NbO}_3-0.05\text{LiSbO}_3)-0.002\text{BiNiO}_3$ ; KNN-LS-BN ceramics were prepared by the combustion method using glycine as a fuel. The effect of firing conditions on phase formation, microstructure and dielectric properties of the ceramic systems were closely observed.

## Experimental Procedure

The KNN-LS-BN ceramics were prepared by the combustion method using glycine as a fuel. The mixtures of  $\text{K}_2\text{CO}_3$ ,  $\text{NaCO}_3$ ,  $\text{Nb}_2\text{O}_5$ ,  $\text{LiCO}_3$ ,  $\text{Sb}_2\text{O}_3$ ,  $\text{Bi}_2\text{O}_3$  and  $\text{Ni}_2\text{O}_3$  powders were ball milling (zirconia milling media under ethanol for 24 h) and drying was carried out at 120°C. After sieving, the powders and glycine in the ratio of 1:2 were mixed in agate mortar. Then, the mixture was calcined at various temperatures ranging from 650 to 750°C, dwell time 0.5–2 h and heating/cooling rate of 5°C/min. The calcined powders were then pressed



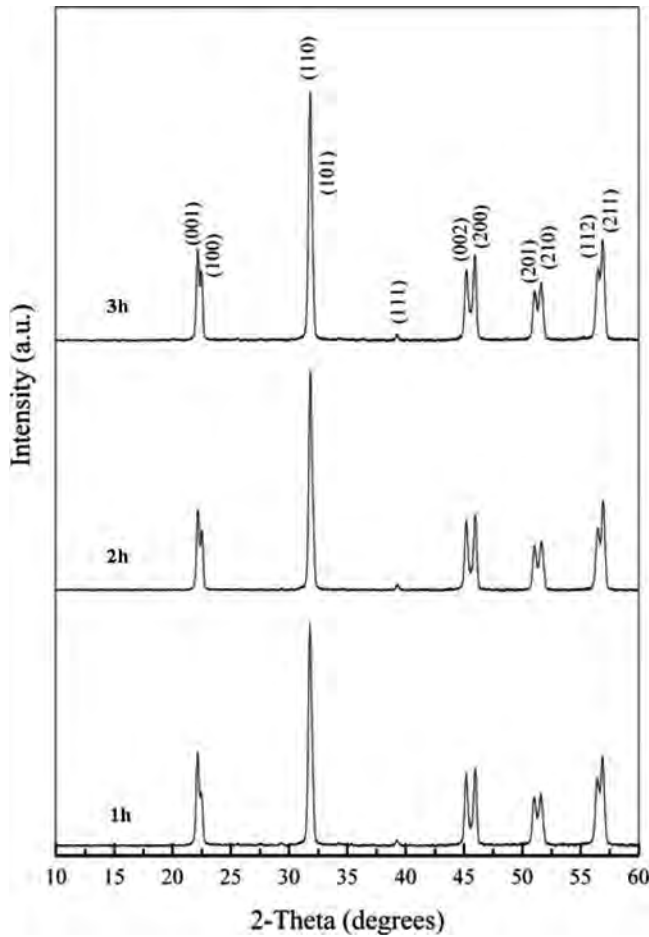
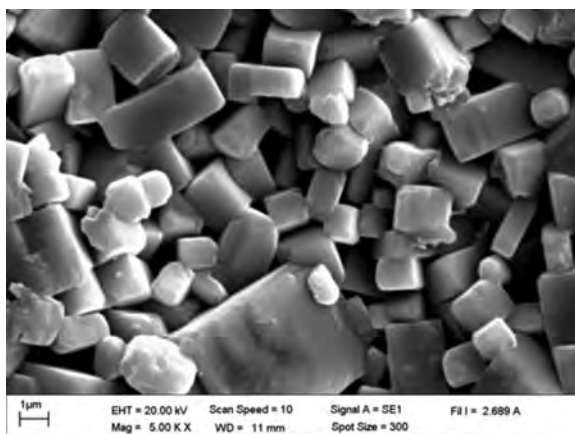


**Figure 4.** The XRD patterns of KNN-LS-BN ceramics sintered at 1100°C using heating/cooling rate of 15°C/min with various dwell times.

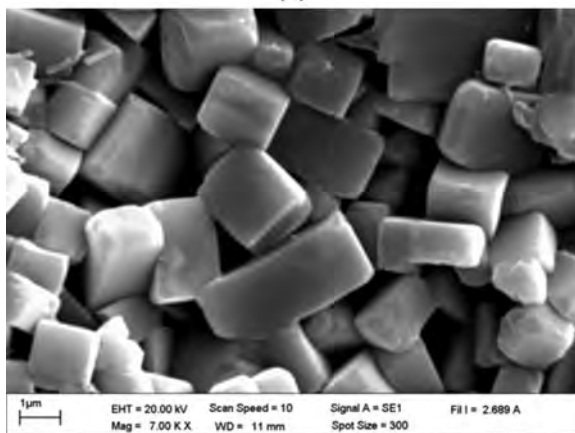
into disks with a diameter of 15 mm at a pressure of 80 MPa. The pellets were sintered from 1000 to 1100°C for 0.5–3 h with heating/cooling rate of 5–15°C/min. To identify the phase formed and optimum firing temperatures of KNN-LS-BF powders and ceramics, the samples were examined by room temperature X-ray diffraction (XRD). The sintered ceramics morphologies were directly imaged using scanning electron microscopy (SEM). Densities of sintered ceramics were measured by Archimedes method and the average grain size was determined by using a mean linear intercept method. The capacitance was measured with a LCR meter. The dielectric constant ( $\epsilon_r$ ) was calculated using the geometric area and thickness of the discs.

## Results and Discussion

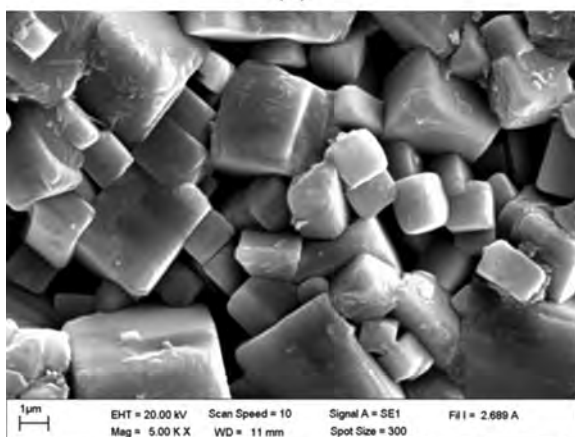
The XRD patterns of KNN-LS-BN powders calcined at various temperatures (650–750°C) with 0.5–2 h dwell time using heating/cooling rate of 5°C/min are shown in Fig. 1. At calcination temperatures below 750°C, second phases such as  $\text{NaSbO}_3$  and  $\text{LiSbO}_3$  were



(a)



(b)



(c)

**Figure 5.** SEM photographs of KNN-LS-BN ceramics sintered at 1100°C using heating /cooling rate of 15°C/min for (a) 1 h, (b) 2 h and (c) 3 h.

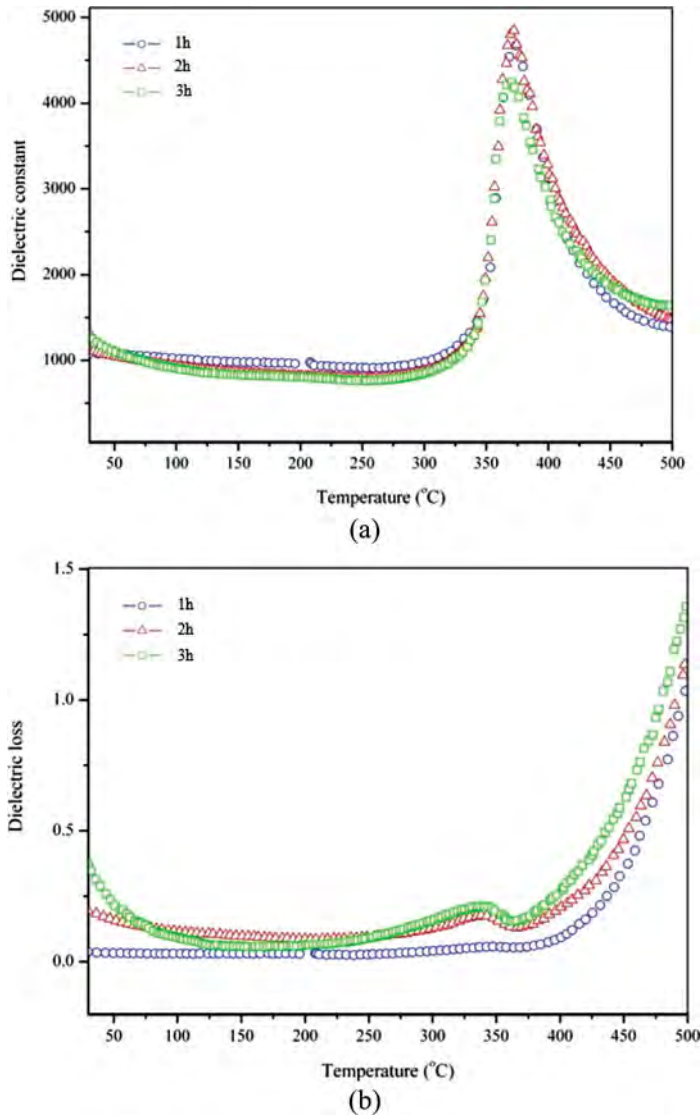


**Figure 6.** (a) the dielectric constant and (b) dielectric loss at 1 kHz of KNN-LS-BN ceramics sintered at 1100°C using heating/cooling rate of 15°C/min with various dwell time. (Color figure available online.)

formed due to the temperature is too low. The 100% orthorhombic perovskite phase of KNN-LS-BN powder was obtained from the sample calcined only at 750°C for 0.5 h dwell time using heating/cooling rate of 5°C/min (Table 1). With longer than 0.5 h of dwell time, the minor phases appear again. The combustion technique, compared with mixed oxide method, can reduce the calcination temperature by about 100°C and decreases the dwell time by approximately 5.5 h [9]. The lower firing temperature and shorter dwell time on calcination process could be explained by the decomposition of glycine (fuel). The energy released from decomposition reaction of fuel speeds up the chemical reaction of

**Table 2**

The % perovskite phase of KNN-LS-BN ceramics sintered at various conditions

Sintering temperature (°C)	Heating/cooling rate (°C)	Dwell time (h)	% perovskite phase
1000	5	2	89.2
1025	5	2	90.2
1050	5	2	90.9
1075	5	2	91.1
1100	5	2	92.9
1100	5	2	92.9
1100	10	2	95.7
1100	15	2	100.0
1100	15	1	100.0
1100	15	2	100.0
1100	15	3	100.0

raw materials which reduces the amount of external energy needed to supply to systems. Moreover, the liquid phase caused from melting of fuel (melting point of glycine  $\sim 260^\circ\text{C}$ ) availed the chemical reaction of raw materials easier [14].

The KNN-LS-BN powder calcined at  $750^\circ\text{C}$  for 0.5 h with heating/cooling rate of  $5^\circ\text{C}/\text{min}$  were pressed and sintered at various temperatures ( $1000$ – $1100^\circ\text{C}$ ) for 2 h with heating/cooling rate of  $5^\circ\text{C}/\text{min}$ . The XRD patterns of KNN-LS-BN ceramics are shown in Fig. 2 Unfortunately, minor phases of  $\text{NaSbO}_3$ ,  $\text{LiSbO}_3$ ,  $\text{K}_3\text{NbO}_4$  and  $\text{KNbO}_8$  and were obtained in all samples. The percentage of perovskite phase was increased with the increasing of the sintering temperatures (Table 2). The maximum% of perovskite phase of 92.9% was found in the sample sintered at  $1100^\circ\text{C}$ . Above  $1100^\circ\text{C}$  of sintering temperatures, the pellets were distorted and began melting. The sintering temperature of  $1100^\circ\text{C}$  was then chosen for more investigation. Fig. 3 shows the XRD pattern of KNN-LS-BN ceramics sintered at  $1100^\circ\text{C}$  with various heating/cooling rate ( $5$ – $15^\circ\text{C}/\text{min}$ ), for 2 h. When the heating/cooling rate increases, the percentages of perovskite phase are increased (Table 2). The pure orthorhombic phase is obtained in sample calcined at  $1100^\circ\text{C}$  for 2 h with heating/cooling rate of  $15^\circ\text{C}/\text{min}$ . So, the sintering temperature of  $1100^\circ\text{C}$  with

**Table 3**The average grain size, linear shrinkage, density,  $T_c$  and dielectric properties of KNN-LS-BN ceramics sintered at  $1100^\circ\text{C}$  with various dwell time

Dwell time (h)	Average grain size ( $\mu\text{m}$ )	Linear shrinkage (%)	Density $\text{g}/\text{cm}^3$	$T_c$ ( $^\circ\text{C}$ )	Dielectric properties at $T_c$	
					$\varepsilon_r$	$\tan \delta$
1	1.42	17.9	4.40	373	4726	0.11
2	1.62	18.0	4.44	370	4872	0.10
3	1.68	19.9	4.41	368	4249	0.16

heating/cooling rate of 15°C/min was selected to investigate the optimum dwell time. The XRD patterns of samples sintered at 1100°C with heating/cooling rate of 15°C/min at different dwell time (1–3 h) are illustrated in Fig. 4. It can be seen that all samples were free from impurity phase and the pure orthorhombic was discovered (Table 2).

SEM photographs of KNN-LS-BN ceramics sintered at 1100°C with heating /cooling rate of 15°C/min, for 1–3 h are shown in Fig. 5. It is clearly seen that the grains exhibit most rectangular morphology in all samples. This result was similar to the previous work [9,13]. At the 3 h of dwell time, the grain boundaries began to melt and the small grains merge together to produce a larger grain (Fig. 5(c)). The grain size increases with the increasing of dwell time (Table 3).

The % linear shrinkage and density of KNN-LS-BN samples sintered at 1100°C with 15°C/min of heating/cooling rate for 1–3 h are shown in Table 3. The % linear shrinkage increases with the increasing of dwell time. The highest density of 4.44 g/cm<sup>3</sup> was found in sample sintered for 2 h (Table 3). At 3 h of dwell time, the sample obtained 4.41 g/cm<sup>3</sup> of density. This may be ascribed to the melting of grain boundary due to the extreme of dwell time.

The dwell time dependence of the dielectric properties at 1 kHz for KNN-LS-BN ceramics sintered at 1100°C with 15°C/min of heating cooling rate for 1–3 h is shown in Fig. 6. The maximum dielectric constant peak exists at temperature of approximately 370°C. This peak can be attributed to the phase transition from tetragonal ferroelectric to cubic paraelectric. The Curie temperature ( $T_c$ ) slightly decreased from 373 to 368°C when the dwell time increased (Table 3). The maximum dielectric constant and minimum dielectric loss at  $T_c$  were respectively 4872 and 0.10 obtained from sample sintered at 1100°C for 2 h (Table 3). The dielectric result corresponded to the density and microstructure of ceramics results.

## Conclusions

The pure perovskite phase was obtained from the sample calcined at 750°C for 0.5 h which has lower temperatures and shorter dwell time than those synthesized by mixed oxide method. The effect of sintering conditions has a strong influence on phase formation, microstructure, density and dielectric properties. The grain size increased as the dwell time increased. The densest of 4.44 g/cm<sup>3</sup>, the maximum dielectric constant of 4872 and minimum dielectric loss of 0.10 at  $T_c$  were obtained in the sample sintered at 1100°C for 2 h using heating/cooling rate of 15°C/min. These evidenced that high quality KNN-LS-BN ceramics could be produced via the combustion method.

## Acknowledgments

This work was financially supported by the Thailand Research Fund (TRF). Thanks also to Department of Physics, Faculty of Science, Naresuan University for supporting facilities.

## References

1. Y. Saito, H. Takao, T. Tani, T. Nonoyama, K. Takatori, T. Homma, T. Nagaya and M. Nagamura, Lead-free piezoceramics. *Nature*. **432**, 84 (2004).
2. X. Y. Sun, J. Chen, R. B. Yu, C. Sun, G. R. Liu, X. R. Xing and L. J. Qiao, BiScO<sub>3</sub> doped Na<sub>0.5</sub>K<sub>0.5</sub>NbO<sub>3</sub> lead-free piezoelectric ceramics. *J. Am. Ceram. Soc.* **92**, 130 (2009).

3. R. C. Chang, S. Y. Chu, Y. F. Lin, C. S. Hong, P. C. Kao, and C. H. Lu, The effects of sintering temperature on the properties of  $(\text{Na}_{0.5}\text{K}_{0.5})\text{NbO}_3\text{--CaTiO}_3$  based lead-free ceramics. *Sens. Actuators A*. **138**, 355 (2007).
4. D. M. Lin, K. W. Kwok, and H. L. Chan, Structure, dielectric, and piezoelectric properties of CuO-doped  $\text{K}_{0.5}\text{Na}_{0.5}\text{NbO}_3\text{--BaTiO}_3$  lead-free ceramics. *J. Appl. Phys.* **102**, 74113 (2007).
5. Y. Guo, K. Kakimoto, and H. Ohsato, Phase transitional behavior and piezoelectric properties of  $(\text{Na}_{0.5}\text{K}_{0.5})\text{NbO}_3\text{--LiNbO}_3$  ceramics. *Appl. Phys. Lett.* **85**, 4121 (2004).
6. Y. Guo, K. I. Kakimoto, and H. Ohsato,  $(\text{Na}_{0.5}\text{K}_{0.5})\text{NbO}_3\text{--LiTaO}_3$  lead-free piezoelectric ceramics. *Mater. Lett.* **59**, 241 (2005).
7. G. Z. Zang, J. F. Wang, H. C. Chen, W. B. Su, C. M. Wang, P. Qi, B. Q. Ming, J. Du, L. M. Zheng, S. Zhang, and T. R. Shrout, Perovskite  $(\text{Na}_{0.5}\text{K}_{0.5})_{1-x}(\text{LiSb})_x\text{Nb}_{1-x}\text{O}_3$  lead-free piezoceramics. *Appl. Phys. Lett.* **88**, 212908 (2006).
8. R. Wang, R. J. Xie, K. Hanada, K. Matsusaki, H. Bando, T. Sekiya, and M. Itoh, Phase diagram of the  $\text{Na}_{0.5}\text{K}_{0.5}\text{NbO}_3\text{--ATiO}_3$  solid solution. *Ferroelectrics*. **336**, 39 (2006).
9. C. Liu, X. Liu, M. Jiang and J. Ma, Microstructure and piezoelectric properties of  $\text{Na}_{0.5}\text{K}_{0.5}\text{NbO}_3\text{--BiNiO}_3\text{--LiSbO}_3$  lead-free ceramics. *J Alloys Comp.* **503**, 209 (2010).
10. P. Panya and T. Bongkarn, Fabrication of perovskite barium titanate ceramics using the combustion route. *Ferroelectrics*. **383**, 102 (2009).
11. A. Thongtha and T. Bongkarn, Phase formation and microstructure of barium zirconate ceramics prepared using the combustion technique, *Ferroelectrics*. **383**, 33 (2009).
12. C. Wattanawikkam, N. Vittayakorn, and T. Bongkarn, Low temperature fabrication of lead-free KNN-LS-BS ceramics via the combustion method. *Ceram. Int.* **39**, S399 (2013).
13. N. Phungjit, P. Panya, and T. Bongkarn, The structural phase and microstructure of perovskite  $\text{Ba}(\text{Ti}_{1-x}\text{Zr}_x)\text{O}_3$  ceramics using the combustion route. *Func. Matter. Lett.* **4**, 169 (2009).
14. C. Hwang, T. Wu, J. Wan, and J. Tsai, Development of a novel combustion synthesis method for synthesizing of ceramic oxide powders. *Matter. Sci. Eng.* **B111**, 49 (2004).

This article was downloaded by: [Theerachai Bongkarn]

On: 09 December 2013, At: 21:16

Publisher: Taylor & Francis

Informa Ltd Registered in England and Wales Registered Number: 1072954 Registered office: Mortimer House, 37-41 Mortimer Street, London W1T 3JH, UK



## Ferroelectrics

Publication details, including instructions for authors and subscription information:

<http://www.tandfonline.com/loi/gfer20>

### The Effects of Firing Temperatures and Dwell Time on Phase and Morphology Evolution of $\text{LaNi}_{0.6}\text{Fe}_{0.4}\text{O}_3$ Ceramics Prepared via the Combustion Technique

Phongthorn Julphunthong<sup>a</sup>, Sujiphat Janaun<sup>a</sup> & Theerachai Bongkarn<sup>a b</sup>

<sup>a</sup> Department of Physics, Faculty of Science, Naresuan University, Phitsanulok, 65000, Thailand

<sup>b</sup> Research Center for Academic Excellence in Petroleum, Petrochemicals and Advanced Materials, Naresuan University, Phitsanulok, 65000, Thailand

Published online: 09 Dec 2013.

To cite this article: Phongthorn Julphunthong, Sujiphat Janaun & Theerachai Bongkarn (2013) The Effects of Firing Temperatures and Dwell Time on Phase and Morphology Evolution of  $\text{LaNi}_{0.6}\text{Fe}_{0.4}\text{O}_3$  Ceramics Prepared via the Combustion Technique, *Ferroelectrics*, 454:1, 135-144

To link to this article: <http://dx.doi.org/10.1080/00150193.2013.842881>

PLEASE SCROLL DOWN FOR ARTICLE

Taylor & Francis makes every effort to ensure the accuracy of all the information (the "Content") contained in the publications on our platform. However, Taylor & Francis, our agents, and our licensors make no representations or warranties whatsoever as to the accuracy, completeness, or suitability for any purpose of the Content. Any opinions and views expressed in this publication are the opinions and views of the authors, and are not the views of or endorsed by Taylor & Francis. The accuracy of the Content should not be relied upon and should be independently verified with primary sources of information. Taylor and Francis shall not be liable for any losses, actions, claims, proceedings, demands, costs, expenses, damages, and other liabilities whatsoever or howsoever caused arising directly or indirectly in connection with, in relation to or arising out of the use of the Content.

This article may be used for research, teaching, and private study purposes. Any substantial or systematic reproduction, redistribution, reselling, loan, sub-licensing, systematic supply, or distribution in any form to anyone is expressly forbidden. Terms &





# The Effects of Firing Temperatures and Dwell Time on Phase and Morphology Evolution of $\text{LaNi}_{0.6}\text{Fe}_{0.4}\text{O}_3$ Ceramics Prepared via the Combustion Technique

PHONGTHORN JULPHUNTHONG,<sup>1</sup> SUJIPHAT JANAUN,<sup>1</sup>  
AND THEERACHAI BONGKARN<sup>1,2,\*</sup>

<sup>1</sup>Department of Physics, Faculty of Science, Naresuan University, Phitsanulok 65000, Thailand

<sup>2</sup>Research Center for Academic Excellence in Petroleum, Petrochemicals and Advanced Materials, Naresuan University, Phitsanulok 65000, Thailand

*The optimization of the preparation condition of single phase  $\text{LaNi}_{0.6}\text{Fe}_{0.4}\text{O}_3$  or LNF by the combustion technique was examined. The phase formation and the crystal structure were investigated using X-ray diffraction pattern. The highest percent of the perovskite phase at 93.5% was exhibited in the sample calcined at 1000°C for 4 h and repeatedly calcined again at 1200°C for 4 h. A higher than optimum calcination temperature lead to an occurrence of a secondary phase which included a tiny amount of  $\text{La}_4\text{Ni}_3\text{O}_{10}$ . After being sintered between 1250–1450°C for 2 h, the pure perovskite phase was obtained from the samples sintered in the range of 1250 to 1350°C while a higher sintering temperature induced a tiny amount  $\text{La}_4\text{Ni}_3\text{O}_{10}$ . Moreover, increasing the sintering temperature affected the crystal structure which changed from rhombohedral to orthorhombic. The SEM observation revealed that the grain boundaries of sintered ceramics melted when the sintering temperature was higher than 1300°C. From the SEM and density investigation, the results proved that the optimum sintering condition is 1300°C for 2 h. Using the combustion technique, both firing temperature and soaked time is lower than the conventional method preparation.*

**Keywords** Combustion technique; lanthanum nickel iron; perovskite phase; lattice parameter

## Introduction

The perovskite  $\text{LaNi}_{0.6}\text{Fe}_{0.4}\text{O}_3$  (LNF) is considered a candidate cathode and interconnect coating material for various intermediate temperature solid oxide fuel cell (IT-SOFC) systems [1]. Chiba *et al.* [2] was the first group to investigate  $\text{LaNi}_x\text{Fe}_{1-x}\text{O}_3$  ( $x = 0.0 - 1.0$ ) and  $\text{LaNi}_{1-x}\text{M}_x\text{O}_{3-\delta}$  ( $\text{M} = \text{Al}, \text{Cr}, \text{Mn}, \text{Fe}, \text{Co}, \text{and Ga}$ ) as cathode materials for IT-SOFC. The results revealed that  $\text{LaNi}_{0.6}\text{Fe}_{0.4}\text{O}_3$  exhibits the greatest electronic conductivity over three times greater than the conventional cathode material of  $\text{La}_{0.8}\text{Sr}_{0.2}\text{MnO}_3$ . Moreover, its thermal expansion coefficient is closer to Ytria-Stabilized Zirconia (YSZ) which is widely

---

Received December 11, 2012; in final form March 16, 2013.

\*Corresponding author's. E-mail: researchcmu@yahoo.com

applied to electrolyte materials [3]. So,  $\text{LaNi}_{0.6}\text{Fe}_{0.4}\text{O}_3$  is a promising candidate for the cathode material of solid oxide fuel cells.

The synthesis methods of preparing LNF perovskite have been investigated and reported by several groups [1–6]. T. Ohzeki *et al.* [6] investigated the optimization of preparation conditions of single phase  $\text{LaNi}_x\text{Fe}_{1-x}\text{O}_3$  using the solid state reaction method. First, the raw materials were heated between 150 to 1000°C for more than 12 h in air to remove impurities. Then, they were mixed and calcined at 1100°C for 8 h, then pulverized and calcined again at 1200°C for 24 h. After being fabricated into a disc shape, the pellets were sintered at 1400°C for 24 h and annealed at 1400°C for 24 h. After being characterized by XRD, almost all the diffraction reflections could be indexed as  $\text{LaAlO}_3$ -type rhombohedral distorted perovskite. However, minor peaks, which could be indexed as  $\text{La}_4\text{Ni}_3\text{O}_{10}$  or NiO were observed. The report demonstrates that the impurities could be eliminated by prepared under an  $\text{O}_2$  flow during both the calcining and sintering processes. M. Bevilacqua *et al.* [3] examined the effects of three preparation routes on the properties of the prepared LNF: the glycine–nitrate process (GN), the gel–citrate complexation route (GC) and the co-precipitation route (CP). The study results suggest that a single perovskite structure with a low calcination temperature was obtained by the CP route. This preparation procedure leads to a sample that easily sinters and leads to a fully dense material already at 1200°C. Although the GC route can produce homogenous powders but the desirable sintering temperature is higher than that of the CP route, while the GN process leads to non homogeneous materials and needs a high temperature to reach an acceptable phase purity and porosity.

As mention above, LNF can be produced by the solid state reaction route under an  $\text{O}_2$  flow, but high energy consumption and low quality products are the main problems of this technique. Whereas the wet chemical route, such as CP, can produce high quality products with low energy consumption, but these methods require a longer processing time, require special equipment, and have a complex procedure including a low production rate.

Recently, the combustion technique has become an attractive technique to prepare perovskite ceramics [7–16]. It is an uncomplicated technique which provides high quality ceramics. The combustion reaction provides heat that can be effectively applied to the raw materials. This energy speeds up the chemical reaction of raw materials which reduces the amount of external energy needed to supply to systems. Moreover, this released energy obtained high quality products with high homogeneity [11], pure nanocrystalline powders [12], a high density [13, 14] and good electrical properties [15, 16]. Moreover, firing temperature highly influences on the phase formation and the microstructure of electroceramics materials. Therefore, the purpose of this study was to synthesize LNF ceramics via the combustion route. The effect of firing temperature and dwell time on phase formation, morphology and density of LNF ceramics were also investigated.

## Experimental

$\text{LaNi}_{0.6}\text{Fe}_{0.4}\text{O}_3$  ceramics were prepared via the combustion technique using urea as a fuel. High purity of  $\text{La}_2\text{O}_3$ , NiO and  $\text{Fe}_2\text{O}_3$  were stoichiometrically weighed and then mixed by the ball-milling method for 24 h using ethanol as the milling media. After being dried and pulverized, urea ( $\text{CH}_4\text{N}_2\text{O}$ ) was added to the mixed raw materials and then the mixed powders were ground and sieved into a fine powder. The mixed powders were calcined at various calcination conditions such as: 1000°C for 4 h or 8 h, 1100°C for 4 h or 8 h, including being repeatedly calcined at 1200°C for 4 h. The calcined powder with most appropriate calcined condition was selected to fabricate pellets of 15 mm in diameter. The green pellets were subsequently sintered between 1250 and 1450°C with a dwell time of

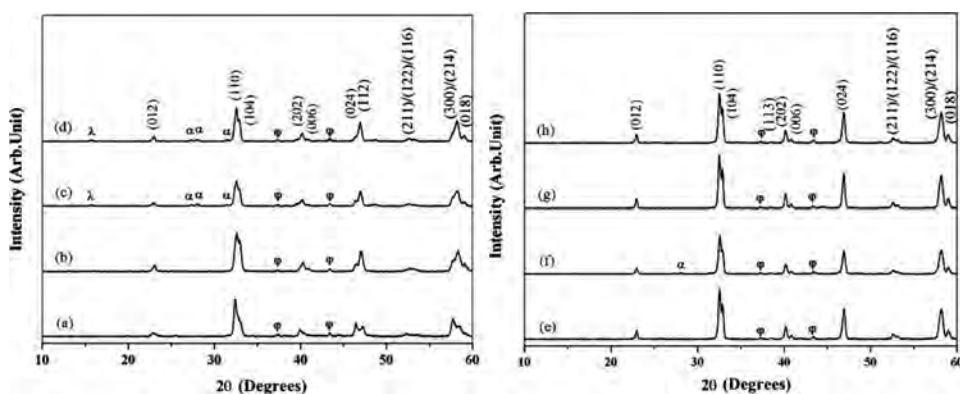


**Figure 1.** XRD patterns of LaNi<sub>0.6</sub>Fe<sub>0.4</sub>O<sub>3</sub> powders calcined at various conditions: (a) 1000°C for 4 h, (b) 1000°C for 8 h, (c) 1100°C for 4 h, (d) 1100°C for 8 h, (e) 1000°C for 4 h and repeated again at 1200°C for 4 h, (f) 1100°C for 4 h and repeated again at 1200°C for 4 h, (g) 1000°C for 4 h and repeated again at 1200°C for 8 h and (h) 1100°C for 4 h and repeated again at 1200°C for 8 h. (Note: (φ) NiO, (α) La<sub>4</sub>Ni<sub>3</sub>O<sub>10</sub> and (λ) La<sub>2</sub>O<sub>2</sub>CO<sub>3</sub>).

2 h. The crystal structure, phase formation behavior, and optimum preparation condition of the calcined powders and sintered ceramics were investigated using X-ray diffraction (XRD). SEM photographs were used to observe morphology, the particle size of powders, and the grain size of the ceramics. The morphologies of the calcined powders were also studied by transmission electron microscopy (TEM). The sintered ceramics bulk densities were determined by the Archimedes method.

## Results and Discussion

Figure 1(a)–(d) shows the XRD patterns of powders calcined at various temperatures and times. It was found that the LNF perovskite initially formed in the sample calcined at 1000°C for 4 h (Fig. 1(a)) (refer to JCPDS file no. 33-711). The impurity NiO (JCPDS file no.47-1049) was detected. Moreover, the splitting patterns of the (024)/(122) and (300)/(214)/(018) peaks resembled the diffraction peak of LaNiO<sub>3</sub> materials (JCPDS file no. 33-0711). These results showed that there was insufficient energy diffuse the Fe-ion into the LNF system. This was because the ionic radius of Fe<sup>3+</sup> (79 pm) is larger than that of Ni<sup>3+</sup> (74 pm). By increasing soaked time to 8 h, the peak intensities of (024)/(122) and (300)/(214)/(018) diffraction peaks were switched (Fig. 1(b)). This demonstrated that an increase of LNF perovskite was formed. However, tiny amounts of impurities of NiO still remained and the percent perovskite phase, which was indicated the relative amounts of perovskite and impurity phases, slightly increased from 90.4 to 90.6% as listed in Table 1. Although the calcination temperature was increased up to 1100°C, the impurities of NiO still appeared. Furthermore, the secondary phases of La<sub>4</sub>Ni<sub>3</sub>O<sub>10</sub> (JCPDS file no. 35-1242) and La<sub>2</sub>O<sub>2</sub>CO<sub>3</sub> (JCPDS file no. 23-0322) emerged in both samples which had been fired for 4 and 8 h (Fig1(c) and (d)). A perovskite percentage of 73.8 and 82.4% were exhibited in the samples calcined at 1100°C for 4 h and 8 h, respectively (Table 1).

The powders calcined at 1000°C for 4 h and 1100°C for 4 h were selected to ground and repeat calcined again in air at 1200°C for 4 or 8 h. The diffraction patterns are shown in Fig. 1(e)–(h). The splitting of (110/104) peaks and an appearance of a non-splitting (024)

**Table 1**The percent perovskite phase and average particle size of  $\text{LaNi}_{0.6}\text{Fe}_{0.4}\text{O}_3$  powders

Calcination condition	Repeated calcination condition	% perovskite phase	Average particle size (nm)
1000°C (4 h)	—	90.4	330
1000°C (8 h)	—	90.6	370
1100°C (4 h)	—	73.8	390
1100°C (8 h)	—	82.4	480
1000°C (4 h)	1200°C (4 h)	93.5	560
1000°C (4 h)	1200°C (8 h)	91.5	570
1100°C (4 h)	1200°C (4 h)	88.4	590
1100°C (4 h)	1200°C (8 h)	92.3	670

peak could be explained as a  $\text{LaAlO}_3$ -type rhombohedral distorted perovskite (JCPDS file no. 33-711) [6]. The small impurity phase of  $\text{La}_2\text{O}_2\text{CO}_3$  was disappeared due to it was decomposed to  $\text{La}_2\text{O}_3$  and  $\text{CO}_2$  at high temperature [17]. However, a tiny impurity of  $\text{NiO}$  was detected in all calcined powders. Even though the impurities remained in twice calcined powders in this work, these impurities are much lower than the LNF ceramics prepared through the solid state reaction method [6]. The percent perovskite phase has been calculated and is listed in Table 1. The highest percent perovskite phase of 93.5% was exhibited in the sample which was calcined at 1000°C for 4 h and calcined again at 1200°C for 4 h. This prepared condition was selected to be the representative of calcined powders and were sintered later.

The SEM photographs of LNF calcined powders are shown in Fig. 2. The powders calcined at 1000°C for 4 h Fig. 2(a), exhibited a spherical particle shape with a porous agglomerated form. A narrow particle size distribution was observed. When increasing the calcination temperature to 1100°C, the particles lost their spherical morphology and the narrow particle size distribution (Fig. 2(b)). This can be attributed by the partially melted of powders and joined together to nearby particles. The combination of nearby particles with non symmetry character caused the prepared powders showed an irregular shape with wide range in a particle size distribution. The morphology of powders calcined at 1000°C for 4 h and calcined again at 1200°C for 4 h is shown in Fig. 2(c). The photograph reveals that repeated calcination affects the powders as is exhibited in their irregular shape and the rapid increase in particle size. The powders calcined at 1100°C for 4 h and calcined again at 1200°C for 4 h exhibited non-spherical shape and a lot of particles melted and merged into the grain (Fig. 2(d)). The average particle size of the calcined powders was observed from the SEM results and is listed in Table 1. The results demonstrated that increasing calcination temperature, soaked time and an increased number of calcination brought about an increase of average particle size from 330–670 nm. Fig. 3 shows the comparative TEM images of powders calcined at 1000°C for 4 h (Fig. 3(a)) and the calcined powders which were calcined again at 1200°C for 4 h (Fig. 3(b)). In the single calcined image, many fine particles smaller than 100 nm can be seen. This is unagreeable with the average particle size observed from SEM photographs. The calcined powders exhibited an agglomerated form and the agglomerated size was around 400 nm. Which is similar to the average particle size observed from the SEM results. This observation shows an agglomeration of many fine

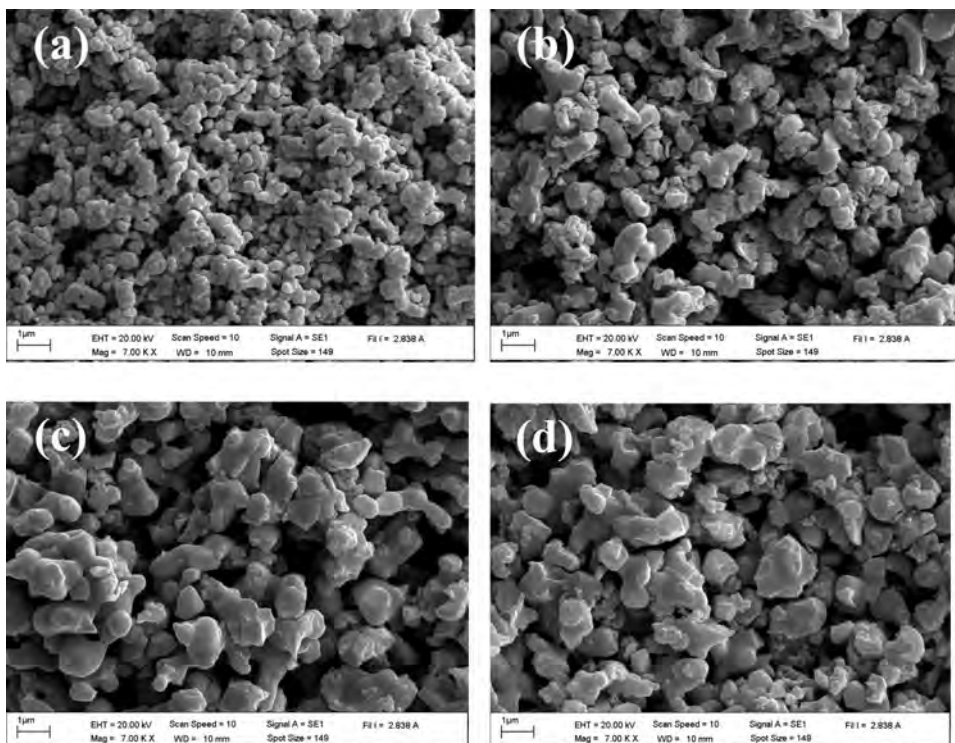


**Figure 2.** The SEM morphology of synthesized LaNi<sub>0.6</sub>Fe<sub>0.4</sub>O<sub>3</sub> powders prepared with different conditions: (a) 1000°C for 4 h, (b) 1100°C for 4 h, (c) 1000°C for 4 h and repeated again at 1200°C for 4 h and (d) 1100°C for 4 h and repeated again at 1200°C for 4 h.

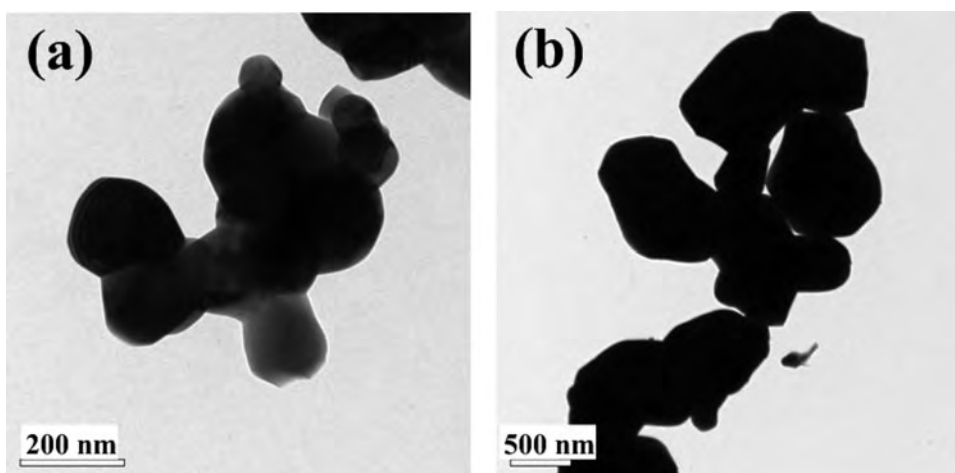


**Figure 3.** TEM micrographs of LaNi<sub>0.6</sub>Fe<sub>0.4</sub>O<sub>3</sub> powders prepared with different conditions: (a) calcined at 1000°C for 4 h and (b) calcined at 1000°C for 4 h and repeated again at 1200°C for 4 h.

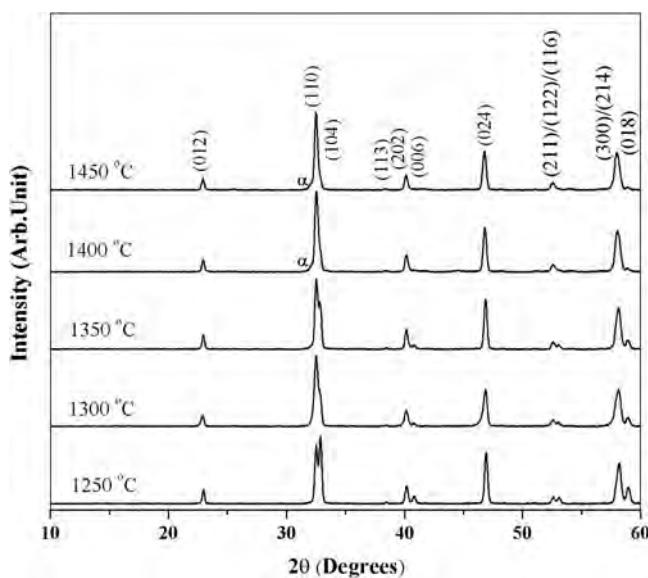


**Figure 4.** X-ray diffraction patterns of  $\text{LaNi}_{0.6}\text{Fe}_{0.4}\text{O}_3$  ceramics sintered at various temperatures for 2 h; ( $\alpha$ )  $\text{La}_4\text{Ni}_3\text{O}_{10}$ .

particles effects on average particle size which was observed from SEM photographs. In the case of the powders which were calcined twice (Fig. 3(b)), A dark zone appeared which indicate that electron cannot transmitted through the multilayer of the sample. This result exhibited in all of samples which were twice calcined. This demonstrated twice calcined process effect an agglomeration increase.

The phase formation of LNF ceramics which were sintered at various sintering temperatures was studied using XRD patterns as shown in Fig. 4. The results indicated that a pure perovskite phase was exhibited in all sintered samples. Moreover, it was observed that the phase formation of the sintered ceramics formed two major groups. The first group exhibited in samples sintered below  $1400^\circ\text{C}$ , the splitting of (110)/(104), (202)/(006) and

**Table 2**

Average grain size, lattice parameters and density of  $\text{LaNi}_{0.6}\text{Fe}_{0.4}\text{O}_3$  ceramics

Sintering temperature ( $^\circ\text{C}$ )	Lattice parameters			Average grain size (nm)	Density ( $\text{g}/\text{cm}^3$ )
	$a$ ( $\text{\AA}$ )	$b$ ( $\text{\AA}$ )	$c$ ( $\text{\AA}$ )		
1250	5.505	—	6.633	620	4.19
1300	5.512	—	6.637	660	4.61
1350	5.511	—	6.633	910	4.25
1400	5.741	7.850	5.213	1130	4.17
1450	5.698	7.884	5.314	1700	4.04

*Note:* Hexagonal phase lattice constants are used to express the rhombohedral phase.

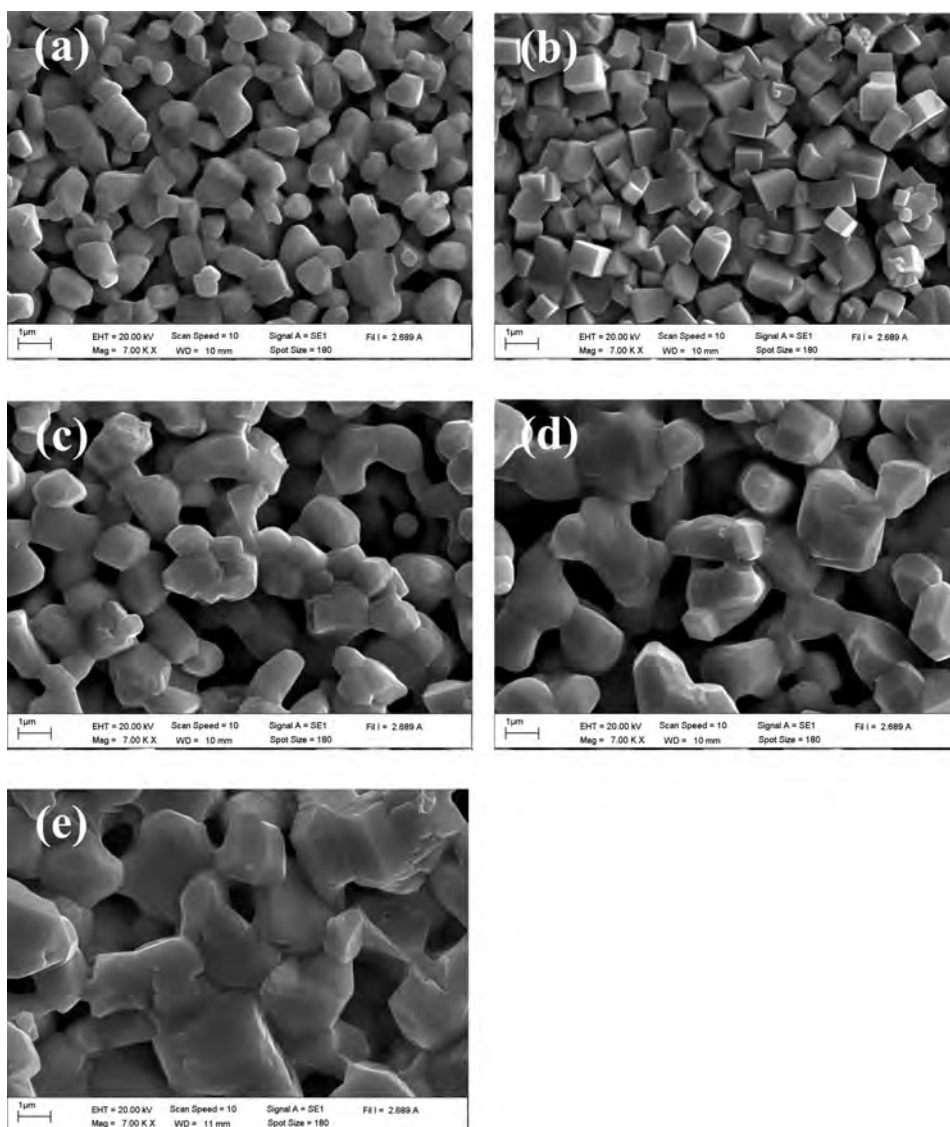


**Figure 5.** SEM photographs of surface  $\text{LaNi}_{0.6}\text{Fe}_{0.4}\text{O}_3$  ceramics sintered at; (a) 1250°C, (b) 1300°C, (c) 1350°C, (d) 1400°C and (e) 1450°C.

(300)/(214)/(018) diffraction peaks. This illustrates that the crystal structure is in the rhombohedral phase. This exhibited phase is the same as that of  $\text{LaNiO}_3$ . Moreover, increasing sintering temperature caused an observable separation of splitting peaks to decrease. This can be explained as the rhombohedral phase decreased and the orthorhombic phase slightly enhanced. The next group is the samples sintered between 1400 to 1450°C, in which the splitting of diffraction peaks disappeared. This indicates the samples exhibited an orthorhombic phase like  $\text{LaFeO}_3$ . These observations suggest a higher energy requirement to diffuse the Fe ion into the LNF system because the Fe ion radius is larger than that of the Ni. A slight increase of sintering temperature greatly affects which phase is formed

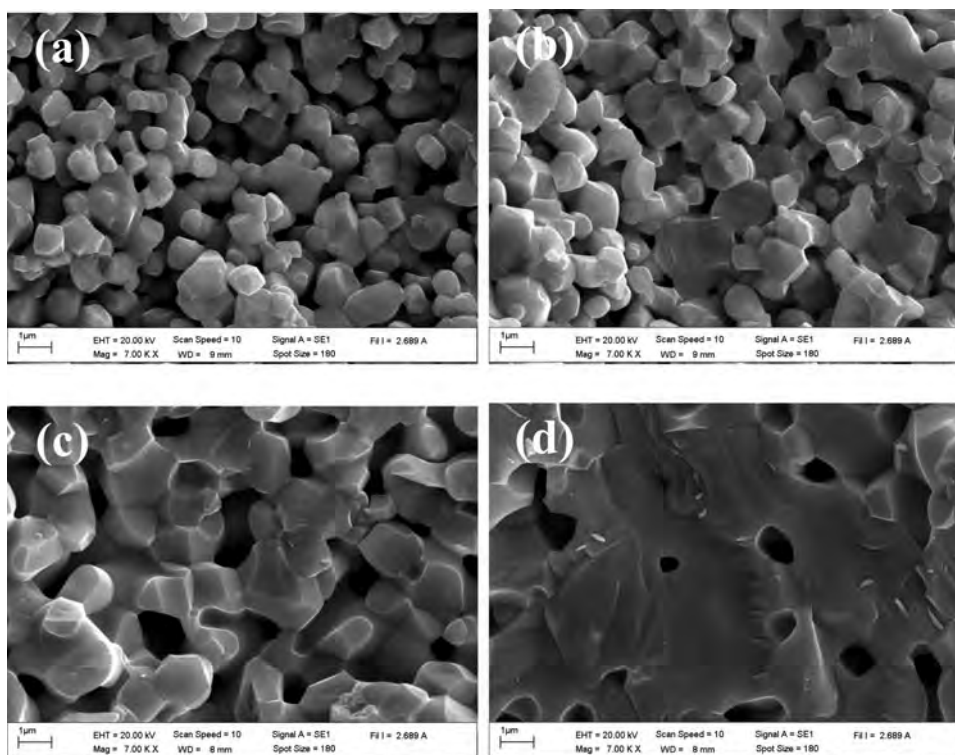


**Figure 6.** SEM photographs of fracture  $\text{LaNi}_{0.6}\text{Fe}_{0.4}\text{O}_3$  ceramics sintered at; (a) 1250°C, (b) 1300°C, (c) 1350°C and (d) 1400°C.

in sintered ceramics but it is the small effects on the lattice parameters which are calculated and listed in Table 2. Moreover, the high sintering temperature also induced a tiny amount  $\text{La}_4\text{Ni}_3\text{O}_{10}$ .

Figure 5 shows the SEM micrographs of the natural surface of LNF samples fired at different temperatures and these results were used to calculate average grain size as listed in Table 2. At low sintering temperature (Fig. 5(a)), the sample presents nearby cube shape with an average grain size of 620 nm. However, the grain description demonstrates an incomplete grain because there was insufficient energy supplied. Fig. 5(b) shows the morphology of a sample in which the sintered temperature was increased up to 1300°C. A cube shapes with an average grain size of 660 nm were exhibited. Although increasing sintering temperature effected average grain size slight increase but the sharp grain boundary, which indicates nearly complete grain growth, was exhibited. The grain boundaries were initially melted and the fusion in the grains was initially begun when the sintering temperature was increased to 1350°C (Fig. 5(c)). Moreover, the average grain size was greatly increased to 910 nm. When the sintering temperature was increased up to 1400°C, many small grains merged to form larger grains and the average grain size increased to 1,130 nm (Fig. 5(d)). This indicated the large amount of liquid phase was occurred in the samples (melting point of  $\text{LaNi}_{0.6}\text{Fe}_{0.4}\text{O}_3$  around 1360°C [18]). This phenomenon produced many large pores. Fig. 5(e) demonstrates how excess energy destroyed the grain boundaries. A lot of grains melted and platelike grains were exhibited.



Figure 6 shows SEM microstructures of the fracture surfaces of samples sintered at various temperatures. Low sintered temperatures brought about an inadequate energy supply to the sample. Thus the sample grains were weakened and transgranular fractures were exhibited (Fig. 6(a)). By increasing the sintered temperature up to 1300°C, many intergranular fractures were observed as shown in Fig. 6(b). This shows that the grains are sturdier than the grain boundaries. The intergranular fractures were distinctly observed when the sintering temperature was increased to 1350°C (Fig. 6(c)). However, a lot of large pores were observed. Fig. 6(d) demonstrates how an excessive sintered temperature has melted the grain and resulted in a porous sample.

The measured densities with a variation in sintering temperatures are listed in Table 2. The density of the ceramics was increased from 4.19 to 4.61 g/cm<sup>3</sup> when the sintering temperatures increased from 1250 to 1300°C, respectively. Thereafter, increasing sintering temperature decreased density. The density results corresponded with microstructure investigation which was observed by SEM results. From SEM and density investigation, the results show that the optimum sintering condition is 1300°C for 2 h. This is a lower firing temperature with a much shorter soaked time than that required by the solid state reaction method [6]. Moreover, the pure perovskite phase was exhibited even though the prepared processes were not under an oxidative atmosphere. These investigations show that the combustion route is an effective technique to prepared LNF ceramics.

## Conclusion

Single phase LaNi<sub>0.6</sub>Fe<sub>0.4</sub>O<sub>3</sub> (LNF) ceramics were successfully synthesized using the combustion route. The X-ray diffraction pattern indicated that a higher than optimum firing temperature and soak time brought about the secondary phases of La<sub>4</sub>Ni<sub>3</sub>O<sub>10</sub>. In the calcined process, a highest percent perovskite phase of 93.5% was exhibited in the sample calcined at 1000°C for 4 h and calcined again at 1200°C for 4 h. High sintering temperatures created a small impurity phase and transformed the crystal structure from a rhombohedral to an orthorhombic phase. The single phase of LNF was obtained when sintering between 1250–1350°C for 2 h. The results of morphology and density were consistent with each other and suggested that the optimum sintering condition is 1300°C for 2 h. The lower energy supplied and non-oxidative atmosphere in preparation processes demonstrated the combustion is more economical and more convenient technique compared with the solid state reaction technique.

## Acknowledgments

This work was financially supported by the Thailand Research Fund (TRF) and Commission on Higher Education (CHE). Thanks also to Department of Physics, Faculty of Science, Naresuan University for supporting facilities. Acknowledgments also to Mr. Don Hindle for helpful comments and corrections of the manuscript.

## References

1. S. Lee, M. Bevilacqua, P. Fornasier, J. M. Vohsa and R. J. Gorte, Solid oxide fuel cell cathodes prepared by infiltration of LaNi<sub>0.6</sub>Fe<sub>0.4</sub>O<sub>3</sub> and La<sub>0.91</sub>Sr<sub>0.09</sub>Ni<sub>0.6</sub>Fe<sub>0.4</sub>O<sub>3</sub> in porous yttria-stabilized zirconia. *J. Power. Sources.* **193**, 747 (2009).
2. R. Chiba, F. Yoshimura and Y. Sakurai, An investigation of LaNi<sub>1-x</sub>Fe<sub>x</sub>O<sub>3</sub> as a cathode material for solid oxide fuel cells. *Solid State Ionics* **124**, 281 (1999).

3. M. Bevilacqua, T. Montini, C. Tavagnacco, G. Vicario, P. Fornasiero and M. Graziani, Influence of synthesis route on morphology and electrical properties of  $\text{LaNi}_{0.6}\text{Fe}_{0.4}\text{O}_3$ . *Solid State Ionics* **177**, 2957 (2006).
4. N. Sukpirom, S. Iamsaard, S. Charojrochkul and J. Yeyongchaiwat, Synthesis and properties of  $\text{LaNi}_{1-x}\text{Fe}_x\text{O}_{3-\delta}$  as cathode materials in SOFC. *J. Mater. Sci.* **46**, 6500 (2011).
5. H. Falcon, A. E. Goeta, G. Punte and R. E. Carbonio, Crystal Structure Refinement and Stability of  $\text{LaNi}_{1-x}\text{Fe}_x\text{O}_3$  Solid Solutions. *J. Solid State. Chem.* **133**, 379 (1997).
6. T. Ohzeki, T. Hashimoto, K. Shozugawa and M. Matsuo, Preparation of  $\text{LaNi}_{1-x}\text{Fe}_x\text{O}_3$  single phase and characterization of their phase transition behaviors. *Solid State Ionics* **181**, 1771 (2010).
7. C. C. Hwang, T. Y. Wu, J. Wan and J. S. Tsai, Development of a novel combustion synthesis method for synthesizing of ceramics oxide powders. *Mat. Sci. Eng. B-Solid* **111**, 49 (2004).
8. R. V. Mangalaraja, J. Mouzon, P. Hedstrom, I. Kero, K. V. S. Ramam, C. P. Camurri and M. Oden, Combustion synthesis of  $\text{Y}_2\text{O}_3$  and  $\text{Yb-Y}_2\text{O}_3$ . *J. Mater. Process. Tech.* **208**, 415 (2008).
9. A. Thongtha and T. Bongkarn, Phase formation and microstructure of barium zirconate ceramics prepared using the combustion technique. *Ferroelectrics* **383**, 33 (2009).
10. P. Panya and T. Bongkarn, Fabrication of perovskite barium titanate ceramics using combustion route. *Ferroelectrics* **383**, 102 (2009).
11. N. Chaiyo, R. Muanghlua, S. Niemcharoen, B. Boonchom and N. Vittayakorn, Solution combustion synthesis and characterization of lead-free piezoelectric sodium niobate ( $\text{NaNbO}_3$ ) powders. *J. Alloy. Compd.* **509**, 2445 (2011).
12. P. Julphunthong and T. Bongkarn, Phase formation, microstructure and dielectric properties of  $\text{Ba}(\text{Zr}_{0.1}\text{Ti}_{0.9})\text{O}_3$  ceramics prepared via the combustion technique. *Curr. Appl. Phys.* **11**, S60 (2011).
13. Q. Feng, X. H. Ma, Q. Z. Yan and C. C. Ge, Preparation of soft-agglomerated nanosized ceramic powders by sol-gel combustion process. *Mat. Sci. Eng. B-Solid* **162**, 53 (2009).
14. A. Thongtha and T. Bongkarn, Fabrication and characterization of perovskite  $\text{SrZrO}_3$  ceramics through a combustion technique. *Key Eng. Mater.* **421**, 223 (2010).
15. N. Phungjitt, P. Panya, T. Bongkarn and N. Vittayakorn, The structure phase and microstructures of perovskite  $\text{Ba}(\text{Ti}_{1-x}\text{Zr}_x)\text{O}_3$  ceramics using the combustion route. *Func. Matter. Lett.* **4**, 169 (2009).
16. Z. Tian, L. Lin, F. Meng and W. Huang, Combustion synthesis and characterization of nanocrystalline  $\text{Ba}(\text{Mg}_{1/3}\text{Nb}_{2/3})\text{O}_3$  powders. *Mat. Sci. Eng. B-Solid* **158**, 188 (2009).
17. A. N. Shirsat, M. Ali, K. N. G. Kaimal, S. R. Bharadwaj and D. Das, Thermochemistry of  $\text{La}_2\text{O}_2\text{CO}_3$  decomposition. *Thermochim. Acta* **399**, 167 (2003).
18. E. A. Kiselev and V. A. Cherepanov,  $p(\text{O}_2)$ -stability of  $\text{LaFe}_{1-x}\text{Ni}_x\text{O}_{3-\delta}$  solid solutions at 1100°C. *J. Solid State Chem.* **183**, 1992 (2010).



## Ferroelectrics

Publication details, including instructions for authors and subscription information:

<http://www.tandfonline.com/loi/gfer20>

### Fabrication of 0.62[0.75PMN-0.25PYbN]-0.38PT Ceramics Using One Step Calcination via Combustion Technique

Chittakorn Kornphom<sup>a b</sup>, Pamornnarumol Bhupaijit<sup>a b</sup>, Naratip Vittayakorn<sup>c</sup> & Theerachai Bongkarn<sup>a b</sup>

<sup>a</sup> Department of Physics, Faculty of Science, Naresuan University, Phitsanulok, 65000, Thailand

<sup>b</sup> Research Center for Academic Excellence in Applied Physics, Naresuan University, Phitsanulok, 65000, Thailand

<sup>c</sup> Materials Science Research Unit, Department of Chemistry, Faculty of Science, King Mongkut's Institute of Technology Ladkrabang, Bangkok, 10520, Thailand

Published online: 09 Dec 2013.

To cite this article: Chittakorn Kornphom, Pamornnarumol Bhupaijit, Naratip Vittayakorn & Theerachai Bongkarn (2013) Fabrication of 0.62[0.75PMN-0.25PYbN]-0.38PT Ceramics Using One Step Calcination via Combustion Technique, *Ferroelectrics*, 456:1, 89-97, DOI: [10.1080/00150193.2013.846639](https://doi.org/10.1080/00150193.2013.846639)

To link to this article: <http://dx.doi.org/10.1080/00150193.2013.846639>

PLEASE SCROLL DOWN FOR ARTICLE

Taylor & Francis makes every effort to ensure the accuracy of all the information (the "Content") contained in the publications on our platform. However, Taylor & Francis, our agents, and our licensors make no representations or warranties whatsoever as to the accuracy, completeness, or suitability for any purpose of the Content. Any opinions and views expressed in this publication are the opinions and views of the authors, and are not the views of or endorsed by Taylor & Francis. The accuracy of the Content should not be relied upon and should be independently verified with primary sources of information. Taylor and Francis shall not be liable for any losses, actions, claims, proceedings, demands, costs, expenses, damages, and other liabilities whatsoever or howsoever caused arising directly or indirectly in connection with, in relation to or arising out of the use of the Content.

This article may be used for research, teaching, and private study purposes. Any substantial or systematic reproduction, redistribution, reselling, loan, sub-licensing,

systematic supply, or distribution in any form to anyone is expressly forbidden. Terms & Conditions of access and use can be found at <http://www.tandfonline.com/page/terms-and-conditions>

# Fabrication of 0.62[0.75PMN-0.25PYbN]-0.38PT Ceramics Using One Step Calcination via Combustion Technique

CHITTAKORN KORNPOM,<sup>1,2</sup> PAMORNNARUMOL  
BHUPAIJIT,<sup>1,2</sup> NARATIP VITTAYAKORN,<sup>3</sup>  
AND THEERACHAI BONGKARN<sup>1,2,\*</sup>

<sup>1</sup>Department of Physics, Faculty of Science, Naresuan University, Phitsanulok 65000, Thailand

<sup>2</sup>Research Center for Academic Excellence in Applied Physics, Naresuan University, Phitsanulok 65000, Thailand

<sup>3</sup>Materials Science Research Unit, Department of Chemistry, Faculty of Science, King Mongkut's Institute of Technology Ladkrabang, Bangkok 10520, Thailand

*The fabrication of 0.62[0.75Pb(Mg<sub>1/3</sub>Nb<sub>2/3</sub>)O<sub>3</sub>-0.25Pb(Yb<sub>1/2</sub>Nb<sub>1/2</sub>)O<sub>3</sub>]-0.38PbTiO<sub>3</sub> ceramics (abbreviated PMN-PYbN-PT) by combustion technique using one step calcination was studied. Glycine was used as fuel to reduce the reaction temperature. The phase formation, microstructure, density and dielectric properties were investigated. It was shown that calcination method is more effective than conventional solid state reaction. The crystal structure of PMN-PYbN-PT ceramics exhibited a single rhombohedral perovskite phase in samples sintered at temperature  $T < 1200^\circ\text{C}$ . The pyrochlore phase was found in the samples sintered at  $1200^\circ\text{C}$ . The average grain size of the ceramics increases with increasing sintering temperature. The density and the maximum dielectric constant increases with increasing sintering temperatures up to  $1150^\circ\text{C}$ , and then decreases at higher temperatures. The maximum density ( $8.04\text{ g/cm}^3$ ), highest dielectric constant (19000) and excellent ferroelectric properties ( $P_r \sim 41.05\text{ }\mu\text{C/cm}^2$  and  $E_c \sim 8.1\text{ kV/cm}$ ) were obtained for the sample sintered at  $1150^\circ\text{C}$ .*

**Keywords** Combustion technique; phase formation; perovskite structure; dielectric properties; ferroelectric properties

## Introduction

Pb(Mg<sub>1/3</sub>Nb<sub>2/3</sub>)O<sub>3</sub>-based piezoelectric materials attracted considerable attention due to their high dielectric constant, good ferroelectric properties, and excellent piezoelectric properties. [1–3]. However, it is difficult to fabricate pyrochlore-free phase PMN-based ceramic because of the impurity phase of pyrochlore is easily formed in this system. The formation of pyrochlore phase leads to the deterioration of electrical properties in this ceramics [4–6].

---

Received December 11, 2012; in final form March 16, 2013.

\*Corresponding author. E-mail: researchcmu@yahoo.com

To eliminate the pyrochlore phase and improve the electrical properties, E. Akc et al. [7] investigated the  $(1-x)[\text{Pb}(\text{Mg}_{1/3}\text{Nb}_{2/3})\text{O}_3\text{-Pb}(\text{Yb}_{1/2}\text{Nb}_{1/2})\text{O}_3]\text{-xPbTiO}_3$  system. They found that  $0.62[0.75\text{Pb}(\text{Mg}_{1/3}\text{Nb}_{2/3})\text{O}_3\text{-}0.25\text{Pb}(\text{Yb}_{1/2}\text{Nb}_{1/2})\text{O}_3]\text{-}0.38\text{PbTiO}_3$  (PMN-PYbN-PT) ceramics display a high Curie temperature ( $T_c \sim 200^\circ\text{C}$ ) and remarkable electrical properties, such as good dielectric constant (1500), excellent ferroelectric properties ( $P_r = 36 \mu\text{C}/\text{cm}^2$ ,  $E_c = 10 \text{ kV}/\text{cm}$ ) and high piezoelectric  $d_{33}$  (560 pC/N) [7]. This ceramic is a good candidate for applications in microelectronic and micro electromechanical devices [8–10]. The pyrochlore free phase, PMN-PYbN-PT ceramic, however, was prepared via conventional method using 6 steps calcination. The synthesis of  $\text{MgNb}_2\text{O}_6$  (MN),  $\text{YbNbO}_4$  (YbN) and  $\text{PbTiO}_3$  (PT) powders was initially performed at  $1150^\circ\text{C}$  for 4 h, at  $1200^\circ\text{C}$  for 4 h and  $800^\circ\text{C}$  for 2 h, respectively. After that, the  $\text{Pb}(\text{Yb}_{1/2}\text{Nb}_{1/2})\text{O}_3\text{-PbTiO}_3$  (PYbN-PT) powder and  $\text{Pb}(\text{Mg}_{1/3}\text{Nb}_{2/3})\text{O}_3\text{-PbTiO}_3$  (PMN-PT) powder were obtained from the mixture of YbN powder with PT powder (calcined at  $900^\circ\text{C}$  for 2 h) and the mixture of MN powder with PT powder (calcined at  $875^\circ\text{C}$  for 4 h), respectively. Finally, in order to fabricate pure PMN-PYN-PT ceramic, the PYbN-PT powder and PMN-PT powder were mixed and sintered at  $1000^\circ\text{C}$  for 4 h. This method was complicated and required a lot of time and energy.

In recent year, we have successfully fabricated pure oxides ceramics such as:  $\text{Pb}(\text{MgNb})\text{O}_3\text{-PbTiO}_3$  [6],  $\text{PbZrO}_3$  [11],  $(\text{Pb Ba})\text{ZrO}_3$  [11],  $\text{BaTiO}_3$  [12],  $\text{Ba}(\text{Ti Zr})\text{O}_3$  [13] and  $(\text{Ba Sr})(\text{Zr Ti})\text{O}_3$  [15] by combustion technique. It is simple, low cost and produces high quality fine powders. This technique involves a self-sustained reaction between the reactant materials and the fuel (e.g., glycine), which supplies a liquid medium at the beginning of reaction. The reaction can advance easily because the diffusion coefficients are higher in the liquid than in solid medium [15]. The combustion technique can usually result in products with the desired structure and composition, high density and good electrical properties [15]. Therefore, in this work, the pyrochlore free PMN-PYbN-PT ceramics were synthesized by combustion technique using one-step calcination. The effect of the firing temperatures on the crystal structure, microstructure, physical and electrical properties was investigated.

## Experimental

In the present work,  $0.62[0.75\text{Pb}(\text{Mg}_{1/3}\text{Nb}_{2/3})\text{O}_3\text{-}0.25\text{Pb}(\text{Yb}_{1/2}\text{Nb}_{1/2})]\text{O}_3\text{-}0.38\text{PbTiO}_3$  (PMN-PYbN-PT) ceramics were prepared via combustion technique. Starting materials,  $\text{PbO}$  (99%),  $\text{MgNO}_3 \cdot 6\text{H}_2\text{O}$  (99%),  $\text{Nb}_2\text{O}_5$  (99%),  $\text{Yb}_2\text{O}_3$  (99%) and  $\text{TiO}_2$  (99%) were weighed according to the stoichiometric proportion with excess of 3 wt% of  $\text{PbO}$  and ball milled in ethanol for 24 h, using yttrium stabilized zirconia balls in a plastic container, then dried at  $120^\circ\text{C}$ . The powders were mixed with glycine ( $\text{C}_2\text{H}_5\text{NO}_2$ ) in the ratio of 1:2. The mixed powders were calcined at various temperatures between  $800^\circ\text{C}$  and  $1050^\circ\text{C}$  for 2 h. Thereafter, the PMN-PYbN-PT perovskite powder was milled with 3 wt% of polyvinyl alcohol (PVA) for 12 h.

After milling, the slurry was dried at room temperature and then the calcined powders were pressed into pellets 15 mm in diameter at a pressure of 80 MPa. Subsequently, the pellets were sintered at temperatures from  $1050^\circ\text{C}$  to  $1200^\circ\text{C}$  with a dwell time of 2 h in air. The crystalline structure of calcined and sintered samples was examined by X-ray diffraction (XRD) with  $\text{Cu-K}\alpha$  radiation. The microstructure of the powders and surface of the ceramic pellets were observed by scanning electron microscopy (SEM). The density of the sintered ceramics was measured by the Archimedes method. The average particle size and the average grain size were determined by mean linear intercept method. The

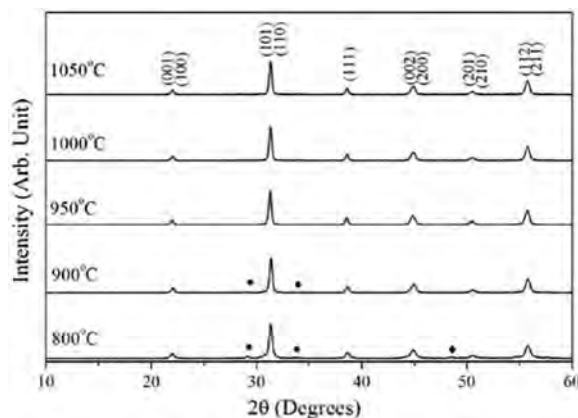


**Figure 1.** XRD patterns of PMN-PYbN-PT powders calcined at various temperatures for 2 h; (●) pyrochlore phase (◆) MgO.

dielectric constant was measured by a LCR meter. The ferroelectric hysteresis ( $P$ - $E$ ) loop was measured by a computer controlled modified Sawyer-Tower circuit.

## Results and Discussion

Figure 1 presents the X-ray diffraction (XRD) patterns of the PMN-PYbN-PT powders calcined between 800°C and 1050°C for 2 h. The diffraction patterns of the samples indexed on the basis of a rhombohedral structure are consistent with the previous works [7]. The impurities of MgO and pyrochlore phase were found at the calcination temperature below 950°C. The single rhombohedral perovskite phase was observed in the powders, which calcined at a temperature higher than 950°C. The relative amounts of perovskite phase were determined by measuring the major XRD peak intensities. The percentage of the perovskite phase was estimated using the equation:

$$\% \text{ Perovskite phase} = \frac{I_{\text{perov}}}{I_{\text{perov}} + I_{\text{pyrochlore}} + I_{\text{MgO}}} \times 100 \quad (1)$$

where  $I_{\text{perov}}$ ,  $I_{\text{pyrochlore}}$  and  $I_{\text{MgO}}$  refer to the intensity of the (110) perovskite peak and the intensities of the major impurity peaks, respectively. Equation (1) is well-known and widely employed in the characterization of complex perovskite materials [11–14]. The percent of perovskite phase of the PMN-PYbN-PT calcined powders increases with increasing calcined temperatures, as listed in Table 1. The 100% the perovskite phase was obtained for the specimen calcined at the temperature of 950°C. The results suggest that the synthesis of the pure perovskite phase PMN-PYbN-PT powders by combustion technique using one step calcination at 950°C for 2 h is more convenient, and it is safer than prepared by the conventional solid state reaction [7]. A lower calcination temperature and the absence of pyrochlore phase in combustion technique is due to the additional combustion energy and the liquid phase that is produced by the melting and decomposing of fuel during combustion process [6, 15].

The pure PMN-PYbN-PT powders obtained by calcination at 950°C for 2 h were pressed into pellets and sintered at temperatures between 1050°C and 1200°C for 2 h. The XRD patterns of the obtained ceramics are shown in Fig. 2, indicating that a single perovskite

**Table 1**  
Percentage of perovskite and the average particle size of PMN-PYbN-PT powders

Calcination temperature (°C)	% perovskite phase	Average particle size (μm)
800	94.7	0.33 ± 0.11
900	98.2	0.36 ± 0.13
950	100	0.64 ± 0.21
1000	100	1.04 ± 0.25
1050	100	1.18 ± 0.36

phase was obtained at sintered temperatures from 1050°C to 1150°C. Pyrochlore phase, however, was observed at sintered temperatures higher than 1150°C. The formation of the pyrochlore phase was most probably due to the evaporation of PbO [6, 11]. XRD patterns also showed a phase change from a rhombohedral to tetragonal phase, as the sintering temperature increases. The transformation between these two structures can be seen in Fig. 2(b), which was obtained at a low scanning rate. As the sintering temperatures increases from 1050°C to 1200°C, the peak (200)<sub>R</sub> separates into two peaks of (002)<sub>T</sub>/(200)<sub>T</sub>. The peaks slightly shift toward low angles, indicating an increase in tetragonality.

The SEM photographs of the PMN-PYbN-PT powders calcined at various temperatures are shown in Fig. 3(a)–(d). The morphology of PMN-PYbN-PT powders exhibit an almost spherical shape and a porous agglomerated structure. The average particle size of the PMN-PYbN-PT powders increase with increasing calcination temperatures, as listed in Table 1.

The microstructure of the PMN-PYbN-PT sintered pellets is shown in Fig. 4(a)–(d). The grain morphology is non-uniform for all samples. At a low sintering temperature (1050°C), many pores can be seen (Fig. 4(a)). An increase in grain size and a decrease in

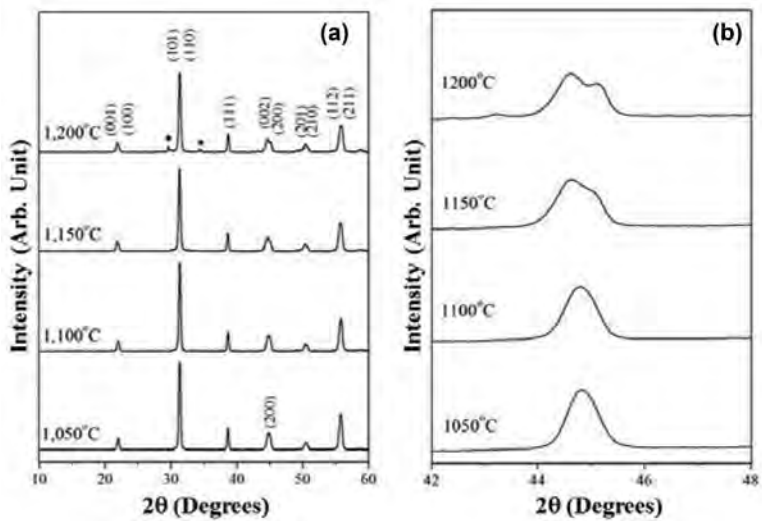


**Figure 2.** XRD patterns of PMN-PYbN-PT ceramics sintered between 1050°C and 1200°C for 2 h: (●) pyrochlore phase (a) at high scanning rate and (b) at very low scanning rate.



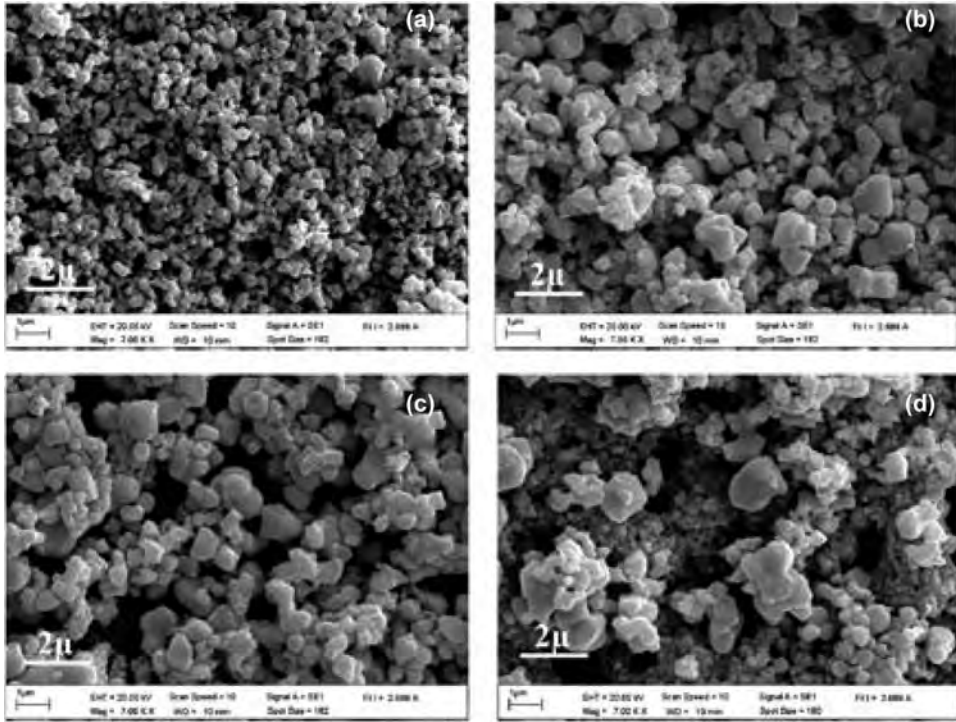


**Figure 3.** The SEM micrographs of PMN-PYbN-PT powders calcined at (a) 800°C, (b) 900°C, (c) 950°C and (d) 1000°C for 2 h.

porosity were observed when the ceramic was sintered at 1100°C and 1150°C, as shown in Fig. 4(b) and (c). At the sintering temperature of 1200°C, the ceramic exhibited a rugged surface, a low porosity and a large grain (Fig. 4(d)). A rugged surface and an increase in porosity indicate that the grains began to melt as a result of the evaporation of PbO at high sintering temperatures [6, 7, 11]. The average grain size increases, as the sintering temperature increases from 1050°C to 1200°C, as listed in Table 2.

**Table 2**  
Average grain size, linear shrinkage, density,  $T_c$ , and dielectric properties of PMN-PYbN-PT ceramics

Sintering temperature (°C)	Average grain size (μm)	Linear shrinkage (%)	Density (g/cm <sup>3</sup> )	$T_c$ (°C)	$\epsilon_r$ at $T_{room}$	$\tan \delta$ at $T_{room}$	$\epsilon_r$ at $T_c$	$\tan \delta$ at $T_c$
1050	$2.88 \pm 1.17$	8.2	$7.79 \pm 0.08$	194.2	2082	0.070	8997	0.018
1100	$3.75 \pm 0.60$	11.9	$7.86 \pm 0.04$	191.3	2728	0.035	15357	0.016
1150	$3.87 \pm 148$	13.1	$8.04 \pm 0.05$	188.6	3165	0.014	19325	0.013
1200	$3.42 \pm 0.84$	14.3	$7.88 \pm 0.07$	186.4	2899	0.032	15357	0.020

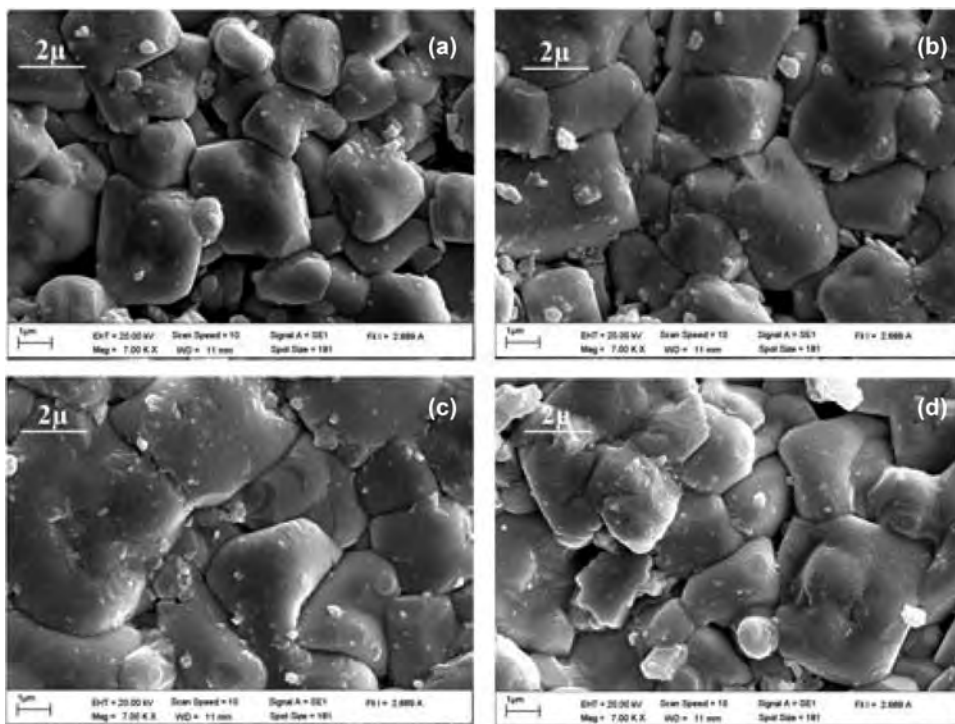


**Figure 4.** SEM surface micrographs of PMN-PYbN-PT ceramics with different sintering temperature; (a) 1050°C, (b) 1100°C, (c) 1150°C and (d) 1200°C for 2 h.

The measured linear shrinkage and density of PMN-PYbN-PT samples sintered at various temperatures are listed in Table 2. The linear shrinkage increases successively from 8.2 to 14.3%, as the sintered temperature increases. The density of the PMN-PYbN-PT ceramics increases from 7.79 to 8.04 g/cm<sup>3</sup> with increasing sintering temperature from 1050°C to 1150°C, and then decreases to 7.88 g/cm<sup>3</sup> at 1200°C. This may be due to the distension of trapped gas in the pores [16]. The highest density of 97.5% (theoretical density) was obtained for the sample sintered at 1150°C. The density measurements were confirmed by the microstructure results. The density of PMN-PYbN-PT ceramic prepared via the combustion technique was higher than that of samples prepared via the solid state reaction [7].

Figure 5 shows the dielectric constant ( $\epsilon_r$ ) of the ceramics measured at 1 kHz as a function of temperature for the samples obtained at different sintering temperatures. The temperature dependence of  $\epsilon_r$  shows a phase transition from tetragonal ferroelectric phase to cubic paraelectric phase at the Curie temperature ( $T_c$ ) between  $\sim 186^\circ\text{C}$  and  $\sim 194^\circ\text{C}$ . The  $T_c$  value shifts to a lower temperature, as the sintered temperature increases from 1050°C to 1200°C (Table 2). Both the  $\epsilon_r$  measured at  $T_c$  and  $T_{\text{room}}$  of PMN-PYbN-PT ceramics increases with increasing sintering temperatures from 1050°C to 1150°C. Upon further increasing the sintering temperature from 1150°C to 1200°C, the  $\epsilon_r$  values decreases (Table 2). The value of dielectric loss ( $\tan \delta$ ) at  $T_{\text{room}}$ , however, showed an opposite trend (Table 2). The decrease of the dielectric constant in the samples that sintered at high temperatures was due to a large porosity and the presence of pyrochlore impurity. The dielectric properties are consistent with the density, the microstructure and the XRD

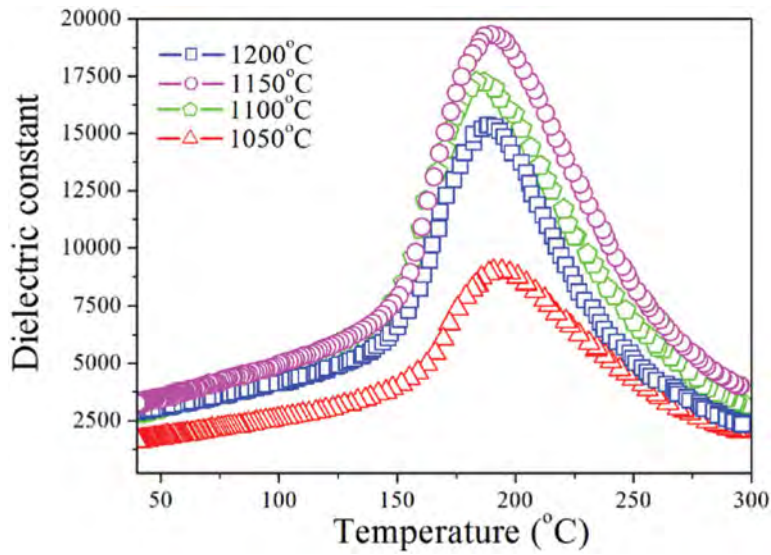


**Figure 5.** Temperature dependence of dielectric constant for PMN-PYbN-PT ceramics sintered at various temperatures and measured at 1 kHz. (Color figure available online.)

results. The maximum  $\varepsilon_r$  at  $T_{\text{room}}$  and at  $T_c$  of the sample sintered temperature at  $1150^\circ\text{C}$  was higher than that of the samples prepared by the solid-state reaction method ( $\varepsilon_r$  at  $T_{\text{room}} \cong 2500$  and  $\varepsilon_r$  at  $T_c \cong 16500$ ).

Figure 6 shows the  $P$ - $E$  loops of the highest density PMN-PYbN-PT ceramics sintered at  $1150^\circ\text{C}$ , measured at  $30\text{ kV/cm}$  at room temperature. A slim  $P$ - $E$  loop with a coercive field of  $E_c \sim 8.1\text{ kV/cm}$  and a high remanent polarization of  $P_r \sim 41.05\text{ }\mu\text{C/cm}^2$  is obtained. E. Akc and C. Duran [7] reported lower  $P_r$  ( $36\text{ }\mu\text{C/cm}^2$ ) and higher  $E_c$  ( $10\text{ kV/cm}$ ) at

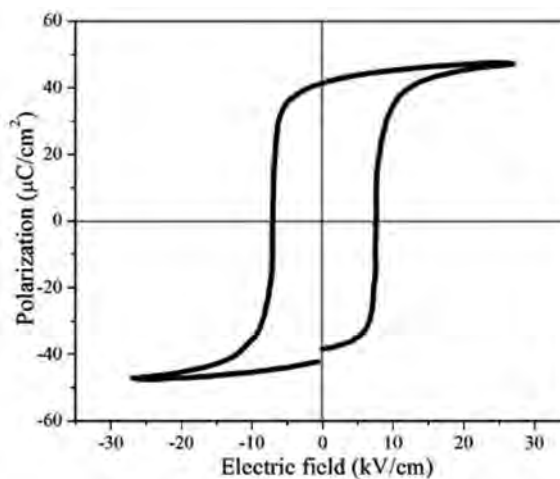


**Figure 6.** Polarization versus electric field at room temperature for the PMN-PYbN-PT ceramics sintered at  $1150^\circ\text{C}$  for 2 h.

the electric field of 30 kV/cm of PMN-PYbN-PT ceramics synthesized by the solid state reaction method.

## Conclusions

High quality PMN-PYbN-PT ceramics were obtained successfully by the combustion method. The firing conditions affect the phase formation, morphology and dielectric properties of the ceramics. A single rhombohedral phase of PMN-PYbN-PT powder was obtained at the calcination temperature of 900°C for 2 h. The XRD results evidenced a change from the rhombohedral to tetragonal phase in the PMN-PYbN-PT ceramics. The content of tetragonal phase increased as sintering temperature increase. The ceramics sintered at 1150°C for 2 h exhibited the highest density, the highest dielectric constant, the lowest dielectric loss and excellent ferroelectric properties: 8.04 g/cm<sup>3</sup>, 19325, 0.013, 41.05  $\mu\text{C}/\text{cm}^2$  and 8.1 kV/cm, respectively. These results confirm that the combustion technique is a convenient and economical method of preparing ferroelectric PMN-based ceramics.

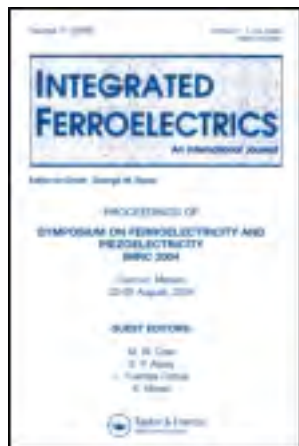
## Acknowledgments

This work was financially supported by the Thailand Research Fund (TRF) and Commission on Higher Education (CHE). Thanks also to the Department of Physics, Faculty of Science, Naresuan University for supporting facilities. Acknowledgements to Prof. Dr. Galina Popovici for helpful comments and corrections of the manuscript.

## References

1. L. E. Cross, Relaxor ferroelectrics. *Ferroelectrics*. **76**, 241 (1987).
2. Y. H. Chen, K. Uchino, and D. Viehland, Substituent effects in 0.65Pb(Mg<sub>1/3</sub>Nb<sub>2/3</sub>)O<sub>3</sub>-0.35PbTiO<sub>3</sub> piezoelectric ceramics. *J. Electroceram.* **6**(1), 13 (2001).
3. G. A. Smolenskii and A. I. Agranovskaya, Dielectric polarization of a number of complex compounds. *Sov. Phys. Solid State*. **1**, 14297 (1959).
4. S. L. Swartz and T. R. Shrout, Fabrications of perovskite lead magnesium niobate. *Mater. Res. Bull.* **17**, 1245 (1982).
5. T. R. Shrout, Z. P. Chang, N. Kim, and S. Markgraf, Dielectric behavior of single crystals near the (1-x)Pb(Mg<sub>1/3</sub>Nb<sub>2/3</sub>)O<sub>3</sub>-x PbTiO<sub>3</sub> morphotropic phase boundary. *Ferroelectrics lett.* **12**, 63 (1990).
6. C. Kornphom and T. Bongkarn, Fabrication and characterization of 0.67Pb(Mg<sub>1/3</sub>Nb<sub>2/3</sub>)O<sub>3</sub>-0.33PbTiO<sub>3</sub> ceramics prepared via combustion technique. *Adv. Sci. Lett.* **19**, 686 (2013).
7. E. Akc and C. Duran, Fabrication and characterization of (Pb(Mg<sub>1/3</sub>Nb<sub>2/3</sub>)O<sub>3</sub>, Pb(Yb<sub>1/2</sub>Nb<sub>1/2</sub>)O<sub>3</sub>-PbTiO<sub>3</sub> ternary system ceramics. *Ceram. Int.* **37**, 2135 (2011).
8. V. A. Bokov and I. E. Myl'nikova, Piezoelectric properties of new compound single crystals with perovskite structure. *Fiz. Tverd. Tela* **2**, 2728 (1960).
9. S. E. Park and T. R. Shrout, Ultrahigh strain and piezoelectric behavior in relaxor based ferroelectric single crystals. *J. Appl. Phys.* **82**, 1804 (1997).
10. G. H. Haertling, Ferroelectric ceramics: history and technology. *J. Am. Ceram. Soc.* **82**, 797 (1999).
11. W. Tangkawsakul and T. Bongkarn, Low temperature preparation of antiferroelectric PZ and PBZ powders using the combustion technique. *Ferroelectrics*. **383**, 50 (2009).
12. P. Panya and T. Bongkarn, Fabrication of perovskite barium titanate ceramics via combustion route. *Ferroelectrics*. **383**, 102 (2009).

13. N. Phungjitt, P. Panya, T. Bongkarn, and N. Vittayakorn, The structural phase and microstructure of perovskite  $\text{Ba}(\text{Ti}_{1-x}\text{Zr}_x)\text{O}_3$  ceramics using the combustion route. *Funct. Mater. Lett.* **2**(4), 169 (2009).
14. A. Thongtha, K. Angsukased, and T. Bongkarn, Fabrication of  $(\text{Ba}_{1-x}\text{Sr}_x)(\text{Zr}_x\text{Ti}_{1-x})\text{O}_3$  ceramics using the combustion technique. *Smart Mater. Struct.* **19**, 1 (2010).
15. K. C. Patil, S. T. Aruna, and S. Ekambaram, Combustion synthesis. *Curr. Opin. Solid. St. M.* **2**, 156 (1997).
16. J. Minhong, D. Manjiao, H. Lu, S. Wang, and X. Lui, Piezoelectric and dielectric properties of  $\text{K}_{0.5}\text{Na}_{0.5}\text{NbO}_3\text{--LiSbO}_3\text{--BiScO}_3$  lead-free piezoceramics. *Mater. Sci. Eng. A.* **176**, 167 (2011).



## Integrated Ferroelectrics: An International Journal

Publication details, including instructions for authors and subscription information:

<http://www.tandfonline.com/loi/ginf20>

### Influence of Firing Temperatures on Crystal Structure and Microstructure of LiNbO<sub>3</sub> Ceramics

Rattiphorn Sumang<sup>a b</sup>, Fuangfa Sutamma<sup>a</sup>, Suphornphun Chootin<sup>a</sup>  
& Theerachai Bongkarn<sup>a b</sup>

<sup>a</sup> Department of Physics, Faculty of Science, Naresuan University, Phitsanulok, 65000, Thailand

<sup>b</sup> Research Center for Academic Excellence in Applied Physics, Naresuan University, Phitsanulok, 65000, Thailand

Published online: 07 Dec 2013.

To cite this article: Rattiphorn Sumang, Fuangfa Sutamma, Suphornphun Chootin & Theerachai Bongkarn (2013) Influence of Firing Temperatures on Crystal Structure and Microstructure of LiNbO<sub>3</sub> Ceramics, Integrated Ferroelectrics: An International Journal, 149:1, 1-8, DOI: [10.1080/10584587.2013.852879](https://doi.org/10.1080/10584587.2013.852879)

To link to this article: <http://dx.doi.org/10.1080/10584587.2013.852879>

PLEASE SCROLL DOWN FOR ARTICLE

Taylor & Francis makes every effort to ensure the accuracy of all the information (the "Content") contained in the publications on our platform. However, Taylor & Francis, our agents, and our licensors make no representations or warranties whatsoever as to the accuracy, completeness, or suitability for any purpose of the Content. Any opinions and views expressed in this publication are the opinions and views of the authors, and are not the views of or endorsed by Taylor & Francis. The accuracy of the Content should not be relied upon and should be independently verified with primary sources of information. Taylor and Francis shall not be liable for any losses, actions, claims, proceedings, demands, costs, expenses, damages, and other liabilities whatsoever or howsoever caused arising directly or indirectly in connection with, in relation to or arising out of the use of the Content.

This article may be used for research, teaching, and private study purposes. Any substantial or systematic reproduction, redistribution, reselling, loan, sub-licensing, systematic supply, or distribution in any form to anyone is expressly forbidden. Terms &



# Influence of Firing Temperatures on Crystal Structure and Microstructure of $\text{LiNbO}_3$ Ceramics

RATTIPHORN SUMANG,<sup>1,2</sup> FUANGFA SUTAMMA,<sup>1</sup>  
SUPHORNPHUN CHOOTIN,<sup>1,2</sup> AND  
THEERACHAI BONGKARN<sup>1,2,\*</sup>

<sup>1</sup>Department of Physics, Faculty of Science, Naresuan University, Phitsanulok, 65000, Thailand

<sup>2</sup>Research Center for Academic Excellence in Applied Physics, Naresuan University, Phitsanulok, 65000, Thailand

*The effects of calcination temperature (500–800°C for 2 h) and sintering temperature (900–1025°C for 2 h) on the crystal structure and microstructure of perovskite lithium niobate (LN) ceramics were investigated. The LN ceramics were synthesized using the solid-state reaction method. The phase formation and microstructure of samples were examined using X-ray diffraction (XRD) and scanning electron microscopy (SEM), respectively. The XRD results showed a single phase of LN powders which was successfully obtained using a calcination temperature of 600°C for 2 h with a heating/cooling rate of 5°C/min. With increased firing temperatures, the lattice parameter  $a$  of the calcined powders and sintered ceramics increased from 5.4912 to 5.4945 Å and 5.4952 to 5.5086 Å, respectively. The SEM result showed that the average particle size (0.31–0.39  $\mu\text{m}$ ) and the average grain size (0.63–2.81  $\mu\text{m}$ ) increased with the increase of calcination and sintering temperatures, respectively. The maximum density and dielectric constant (4.46  $\text{g}/\text{cm}^3$  and 754) were obtained from the sample sintered at 1000°C for 2 h.*

**Keywords** Microstructure; crystal structure;  $\text{LiNbO}_3$ ; perovskite; ferroelectric

## Introduction

Lithium niobate [ $\text{LiNbO}_3$ ; LN] is well known as an important ferroelectric material with a high Curie temperature ( $T_c = 1210^\circ\text{C}$ ). It has a rhombohedral symmetry and space group  $R3c$  at room temperature [1, 2]. This material possesses a large number of interesting characteristics such as: ferroelectric and piezoelectric devices [3–5].

Various techniques such as sol–gel and co-precipitation methods have been used for preparing LN ceramics [6, 7]. In the recent years, the sol–gel process and the co-precipitation method have become popular for producing ceramic material with improved compositional homogeneity and a lower sintering temperature. However, the sol–gel process utilizes expensive precursors and depends on a critical drying process, whereas the co-precipitation method is limited by cation solutions with similar solubility constants [8]. On the other hand, the solid-state reaction method is relatively simple, has a low product cost and is a suitable method for industries [9–11]. Moreover, from the literature, LN ceramics prepared

---

Received December 9, 2012; in final form August 25, 2013.

\*Corresponding author. E-mail: researchcmu@yahoo.com



by solid-state reaction have not been studied. Thus, in this work,  $\text{LiNbO}_3$  ceramics were prepared by the solid-state reaction method. The effects of calcination and sintering temperatures on the phase formation, microstructure, and dielectric properties of ceramics were investigated.

## Experimental

Lithium niobate [ $\text{LiNbO}_3$ ; LN] powders were synthesized using the solid state reaction method. The raw materials of  $\text{Li}_2\text{CO}_3$  (99%) and  $\text{Nb}_2\text{O}_5$  (99.5%) were weighed. A thoroughly ground mixture of raw materials was ground by a ball milling procedure (zirconia milling media under ethanol for 24 h). Drying was carried out at  $120^\circ\text{C}$ . LN was calcined between  $500^\circ\text{C}$  and  $800^\circ\text{C}$  with a dwell time of 2 h and a heating/cooling rate of  $5^\circ\text{C}/\text{min}$ . The calcined powders of LN were weighed and mixed with a 2 wt.% binder solution and reground by ball milling for 24 h. The mixed calcined powders were then pressed into disks with a diameter of 15 mm at a pressure of 80 MPa. The pellets were sintered between  $900^\circ\text{C}$  and  $1025^\circ\text{C}$  for 2 h and cooled in a furnace. X-ray diffraction (XRD) was employed to identify the phase formed and the optimum temperature for the optimum formation of the LN ceramics. The morphological features of the product were imaged using scanning electron microscopy (SEM). The density of the sintered ceramics was measured by the Archimedes method. The average grain sizes were determined by using the mean linear intercept method. The raw data were obtained by measuring the grain sizes over 300 grains. Silver paste was coated on the discs and fired at  $550^\circ\text{C}$  for 5 min to form electrodes. The dielectric property at room temperature was also observed using a LCR impedance analyzer (Agilent 4263B).

## Results and Discussion

The XRD patterns of LN powders calcined at various temperatures from  $500^\circ\text{C}$  to  $800^\circ\text{C}$  are shown in Fig. 1. The crystal structure belonged to a rhombohedral phase (JCPDS file number 20–0631 [12]). At the calcinations temperature of  $500^\circ\text{C}$ , X-ray peaks of raw materials exhibited the impurity phase of  $\text{Li}_5\text{CO}_3$  at the diffraction angles of  $22.61^\circ$  and  $28.23^\circ$ . When there was an increase of calcination temperatures from  $500^\circ\text{C}$  to  $550^\circ\text{C}$ , the impurity phase of  $\text{Li}_5\text{CO}_3$  disappeared but the  $\text{Nb}_2\text{O}_5$  impurity phase appeared at the  $2\theta$  range of  $30.30^\circ$ . Above  $550^\circ\text{C}$ , the sample showed a pure perovskite phase. The percent perovskite phase of LN increased with increased calcination temperature and a hundred percent of the perovskite phase was found above the calcination temperature of  $550^\circ\text{C}$  (Table 1). The lattice parameter was calculated first by indexing the diffractogram according to hexagonal unit cell and the resulting parameters were then converted to the rhombohedral. The lattice parameter  $a$  of all the calcined powders increased from  $5.4912 \text{ \AA}$  to  $5.4945 \text{ \AA}$  with increased calcination temperatures as listed in Table 1. Fig. 2 shows the XRD diffraction pattern of LN ceramics sintered at various temperatures from  $900^\circ\text{C}$  to  $1025^\circ\text{C}$ . The LN ceramics showed a single-phase perovskite structure in all samples. All the peaks of the solid solution system were indexed by pattern matching based on JCPDS file number 20–0631. The lattice parameter  $a$  of all the sintered ceramics increased from  $5.4952 \text{ \AA}$  to  $5.5086 \text{ \AA}$  with increase of sintering temperatures as listed in Table 1. The increase of lattice parameter  $a$  existed in a more strain formed within the atomic entities in non-equilibrium positions at low calcining temperatures, which relaxed to equilibrium

**Table 1**  
Percent perovskite phase, lattice parameter *a*, average particle size, average grain size, density and dielectric constant of LN samples

Calcination Temperature (°C)	Calcined powder			Sintered ceramic					
	Perovskite phase (%)	Lattice parameter <i>a</i> (Å)	Average particle size (nm)	Sintering Temperature (°C)	Lattice parameter <i>a</i> (Å)	Average grain size (μm)	Measured density (g/cm <sup>3</sup> )	Relative density (%)	Dielectric constant at <i>T</i> <sub>Room</sub>
500	93.9	5.4912	310 ± 0.07	900	5.4952	0.63 ± 0.28	4.32	93.3	187
550	96.0	5.4915	310 ± 0.11	925	5.4988	0.85 ± 0.15	4.38	94.6	237
600	100	5.4922	310 ± 0.09	950	5.5008	1.09 ± 0.16	4.42	95.4	363
650	100	5.4927	320 ± 0.10	975	5.5029	1.22 ± 0.07	4.45	96.1	404
700	100	5.4930	320 ± 0.09	1000	5.5042	1.82 ± 0.06	4.46	96.3	754
750	100	5.4937	370 ± 0.12	1025	5.5086	2.81 ± 0.07	4.40	95.0	507
800	100	5.4945	390 ± 0.10						

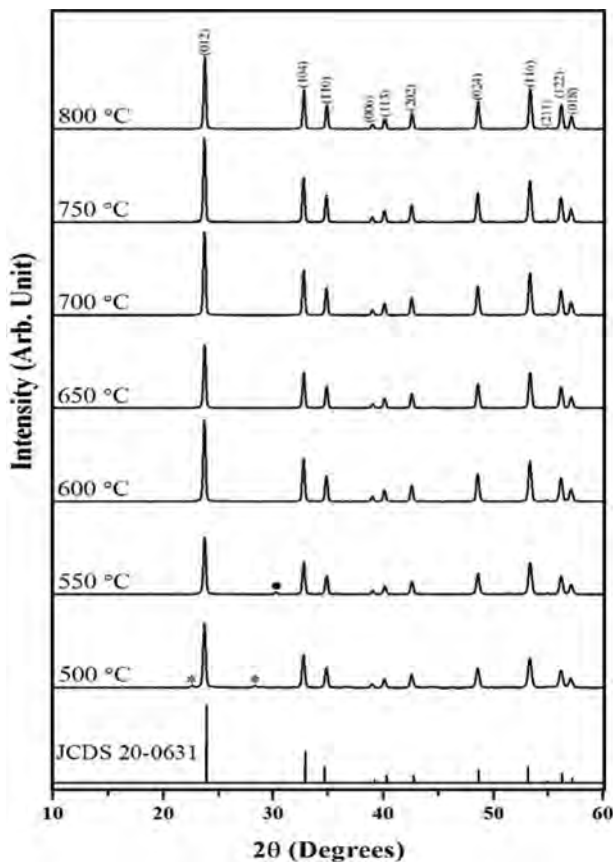


**Figure 1.** X-ray diffraction patterns of LN powders calcined at various temperatures: (●  $\text{Nb}_2\text{O}_5$ ) and (\*  $\text{Li}_5\text{CO}_3$ ).

positions at higher temperatures. Another possible reason may be that the domain mobility is restricted due to pinning of the domain boundaries by crystal defects [13].

Figure 3(a–d) illustrates the SEM photographs of LN powders calcined at different temperatures. All the particles consisted of an agglomerated spherical shape and dispersed spherical shape depending on the calcination temperature. At a low calcination temperature of 500°C, the particles are agglomerated and had a spherical morphology shape. With an increase of calcination temperature from 500°C to 800°C, the particles began to lose their spherical shape. The average particle size increased from 310 nm to 390 nm with an increase of calcination temperature from 500°C to 800°C and is listed in Table 1. Fig. 4(a–c) exhibits surface morphology micrographs of the LN ceramics sintered at various temperatures. In general, the grain size has a spherical morphology shape. At a low sintering temperature (950°C), a number of voids and small flaws existed in the specimen, due to a loose connection between the LN grains, as seen in Fig. 4(a). These voids and small flaws were reduced greatly when increasing sintering temperatures from 900°C to 1025°C, indicating a better connection between the LN grains (Fig. 4(b) and (c)). However, when the sample was sintered at 1025°C a slump occurred on the grain surface. To investigate the slump of the sample sinter at high temperature, the cross-sectional micrographs of the LN

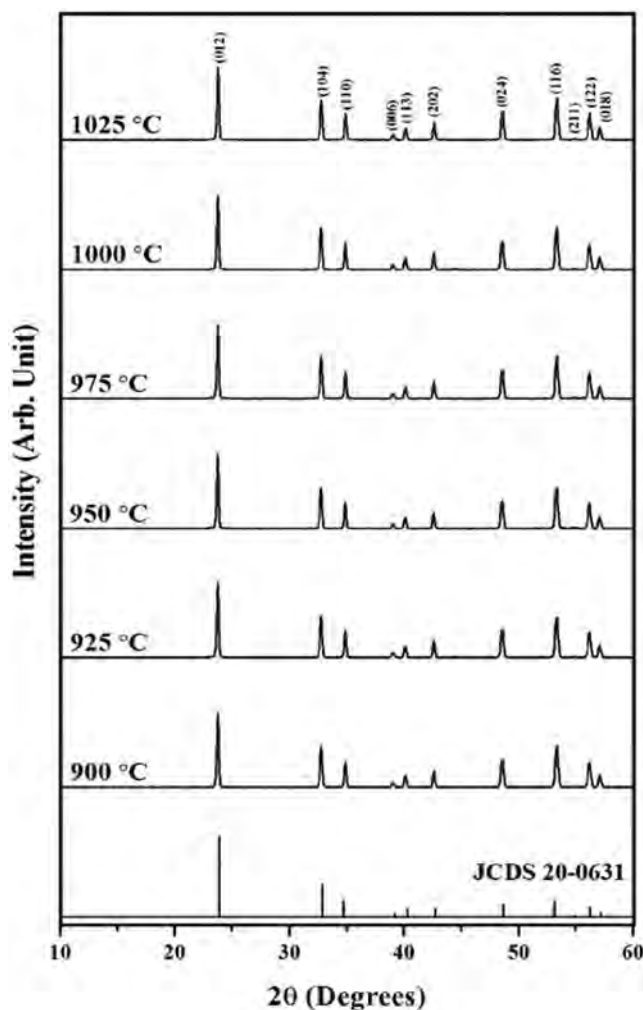


**Figure 2.** X-ray diffraction patterns of LN ceramics sintered at various temperatures.

were also studied, as shown in Fig. 4(d). The sample was mixing types of fractures, both inter-granular and intra-granular. At the connection of the grain boundaries, the nucleation of cavities was observed. This may have been caused by evaporation of Li<sub>2</sub>O during sintering at high temperature [1] (Fig. 4(d)). The average grain size increased from 0.63 to 2.81  $\mu\text{m}$  with the increase of sintering temperature as listed in Table 1.

The density of LN ceramics with sintering temperature between 900°C and 1025°C can be also seen in Table 1. The density and shrinkage increased with increasing sintering temperatures from 900°C to 1000°C reached a maximum value of 4.46 g/cm<sup>3</sup> (96.3% of theoretical density) at 1000°C, and decreased after further sintering at a higher temperature (1025°C). The density results corresponded to the SEM results. The densification mechanisms during treatment in the sintering process related to the grain growth, especially at the final stage of sintering. The density decreases when the sintering temperature is higher

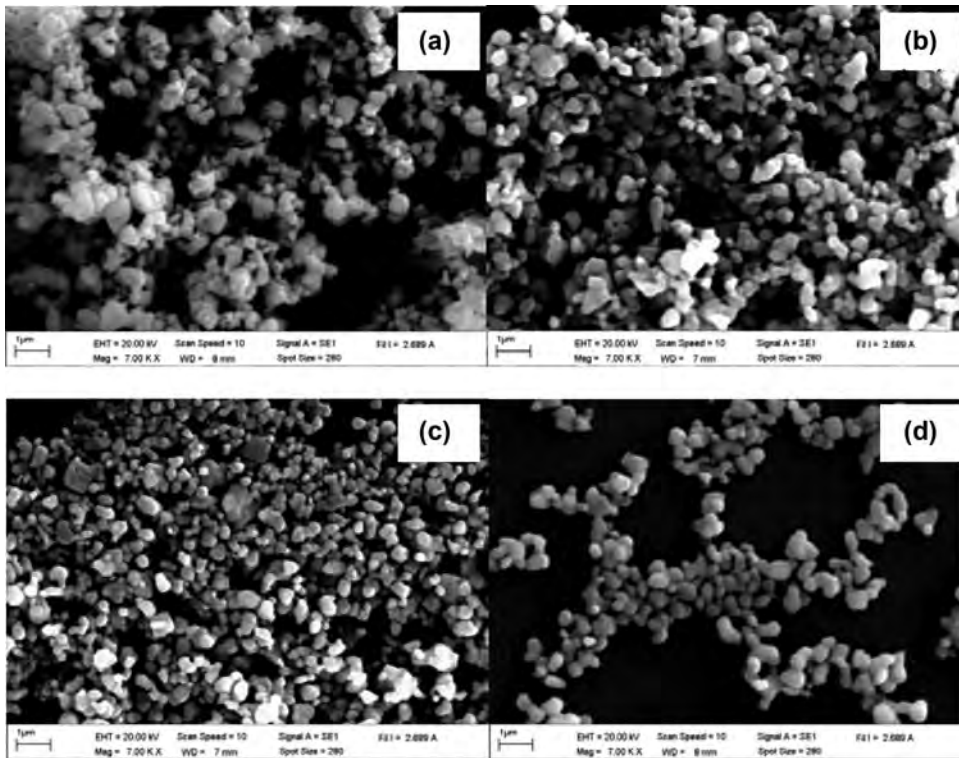


**Figure 3.** Microstructure images of LN powders calcined at various temperatures (a) 500°C (b) 600°C (c) 700°C and (d) 800°C.

than the optimal temperature. This may be caused by enlarging of the trapped gas in the pores. The gas-filled pores combined and grew because of the grain growth [14,15].

The dielectric constant ( $\epsilon_r$ ) at room temperature ( $T_{\text{Room}}$ ), as a function of the sintering temperatures, is listed in Table 1. The values of dielectric constant with the sintering temperature is similar to that of the result of density, while the average grain size slightly increased with increasing sintering temperatures. The result corresponds with the results of R. Yimnirun et al. [16] which investigated the effect of sintering temperature on densification and dielectric properties of  $\text{Pb}(\text{Zr}_{0.44}\text{Ti}_{0.56})\text{O}_3$ ; PZT ceramics prepared by solid state reaction method. They explain that the increased of dielectric constant of PZT ceramics depend on the increase of grain size. The increasing grain size results in a reduction in the volume fraction of grain boundaries, which makes domain reorientation more difficult and severely constrains the domain wall motion. This translates to an increase in the domain wall mobility corresponding to an increase in the dielectric constant. In this study, the increasing dielectric constant from 187 to 754 in sintering temperatures up to 1000°C can be related to the increasing grain size as shown in Table 1. Although the grain size in the sample sintered at 1025°C also increased, the values of dielectric constant exhibited a decrease from 754 to 507. This may be due to the evaporation of the  $\text{Li}_2\text{O}$  during sintering at high temperature [1] which presents the cavities in the SEM results as seen in Fig. 4(d).

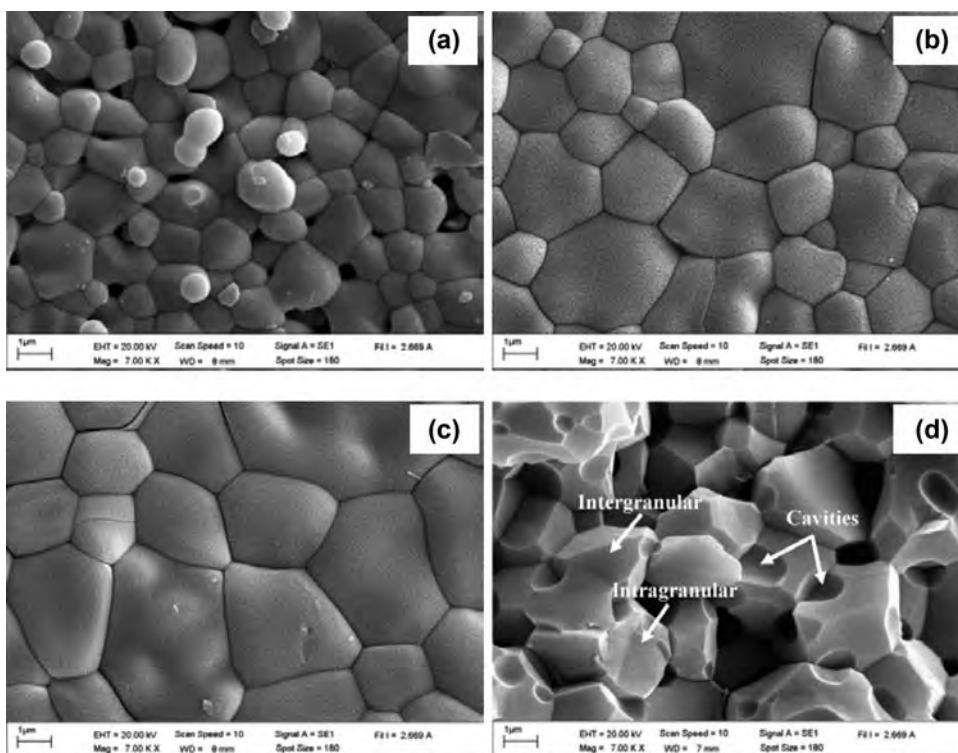


**Figure 4.** Surface morphologies of the LN ceramics sintered at (a) 950°C, (b) 1000°C (c) 1025°C and (d) cross-sectional micrographs of LN ceramics sintered at 1025°C.

## Conclusions

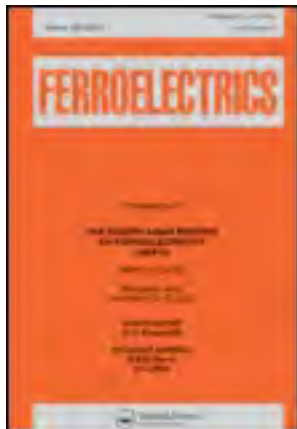
Lead free LN ceramics were synthesized by the solid state reaction method. The optimal calcination and sintering conditions were found to be 600°C for 2 h and 1000°C for 2 h, respectively. The calcination and sintering temperatures directly affected the phase formation, microstructure, density and dielectric properties. The lattice parameter  $a$  increased with increasing calcination and sintering temperatures. The average particle size and average grain size increased with the increase of calcination and sintering temperatures. The maximum density ( $\rho = 4.46 \text{ g/cm}^3$ ) and dielectric constant at room temperature ( $\epsilon_r = 754$ ) were obtained from the sample sintered at 1000°C.

## Acknowledgments

This work was financially supported by the Thailand Research Fund (TRF), Commission on Higher Education (CHE). The authors wish to thanks the Science Lab Center, Faculty of Sciences, Naresuan University. Thanks are also given to Mr. Don Hindle for his help in editing the manuscript.

## References

1. A. Z. Simoes, A. H. M. Gonzalez, A. A. Cavaleiro, M. A. Zaghete, B. D. Stojanovic, and J. A. Varela, Effect of magnesium on structure and properties of  $\text{LiNbO}_3$  prepared from polymeric precursors. *Ceram. Int.* **28**, 265–270 (2002).
2. P. Prapitpongwanich, K. Pengpat, and C. Russel, Phase separation and crystallization in  $\text{LiNbO}_3/\text{SiO}_2$  glasses. *Mater. Chem. Phys.* **113**, 913–918 (2009).
3. M. P. F. Graca, M. A. Valente, and M. G. Ferreira da Silva, Electrical properties of lithium niobium silicate glasses. *J. Non-crystalline Solids.* **325**, 267–274 (2003).
4. J. E. Kim, S. J. Kim, Ken-ichi Ohshima, Y. H. Hwang, and Y. S. Yang, Crystallization and dielectric properties of  $4\text{LiNbO}_3\text{-SiO}_2$  glass. *Mater. Sci. Eng. A* **375**, 1255–1258 (2004).
5. D. Xue, and K. Kitamura, Crystallographic medications of physical properties of lithium niobate crystals by the cation location. *J. Cry. Growth* **249**, 507–513 (2003).
6. P. K. Gallagher, and F. Schrey, The thermal decomposition of freeze-dried tantalum and mixed lithium-niobium oxalate. *Thermochim. Acta* **1**, 465–476 (1970).
7. S. Hirano, and K. Kato, Synthesis of  $\text{LiNbO}_3$  by hydrolysis of metal alkoxides. *Adv. Ceram. Mater.* **2**, 142–145 (1987).
8. A. Z. Simoes, A. Ries, C. S. Riccardi, A. H. Gonzalez, M. A. Zaghete, B. D. Stojanovic, M. Cilense, and J. A. Varela, Potassium niobate thin films prepared through polymeric precursor method. *Mater. Lett.* **58**, 2537–2540 (2004).
9. S. Kongtaweelert, D. C. Sinclair, and S. Panichphant, Phase and morphology investigation of  $\text{Ba}_x\text{Sr}_{1-x}\text{TiO}_3$  ( $x = 0.6, 0.7$  and  $0.8$ ) powders. *Curr. Appl. Phys.* **6**, 474–477 (2006).
10. R. Sumang, and T. Bongkarn, Effect of sintering temperature on the crystal structure, microstructure and phase transition of  $(\text{Pb}_{1-x}\text{Sr}_x)\text{TiO}_3$  ceramics. *Func. Mater. Lett.* **2**, 193–197 (2009).
11. R. Sumang, and T. Bongkarn, The Effect of Calcination Temperatures on the Phase Formation and Microstructure of  $(\text{Pb}_{1-x}\text{Sr}_x)\text{TiO}_3$  Powders. *Key Eng. Mater.* **421**, 243–246 (2010).
12. Powder Diffraction File No. 20-0631, International Center for Diffraction Data. Newton Square, PA, 2003.
13. S. Kongtaweelert, D. C. Sinclair, and S. Panichphant, Phase and morphology investigation of  $\text{Ba}_x\text{Sr}_{1-x}\text{TiO}_3$  ( $x = 0.6, 0.7$  and  $0.8$ ) powders. *Curr. Appl. Phys.* **6**, 474–477 (2006).
14. R. M. German, *Sintering Theory and Practice*. John Wiley & Sons, New York, 1996.
15. A. Thongtha, and T. Bongkarn, Optimum Sintering Temperature for Fabrication of  $0.8\text{Bi}_{0.5}\text{Na}_{0.5}\text{TiO}_3\text{-}0.2\text{Bi}_{0.5}\text{K}_{0.5}\text{TiO}_3$  Lead-Free Ceramics by Combustion Technique. *Key Eng. Mater.* **474**, 1754–1759 (2011).
16. R. Yimnirun, R. Tipakontitukul, and S. Ananta, Effect of sintering temperature on densification and dielectric properties of  $\text{Pb}(\text{Zr}_{0.44}\text{Ti}_{0.56})\text{O}_3$  ceramics. *Inter. J. Modern Phys. B* **20**, 2415–2424 (2006).



## Ferroelectrics

Publication details, including instructions for authors and subscription information:

<http://www.tandfonline.com/loi/gfer20>

### The Effect of Excess PbO on Crystal Structure, Microstructure and Dielectric Properties of $(\text{Pb}_{0.50}\text{Sr}_{0.50})\text{TiO}_3$ Ceramics

Rattiphorn Sumang<sup>a b</sup>, Naratip Vittayakorn<sup>c</sup> & Theerachai Bongkarn<sup>a b</sup>

<sup>a</sup> Department of Physics, Faculty of Science, Naresuan University, Phitsanulok, 65000, Thailand

<sup>b</sup> Research Center for Academic Excellence in Advanced Physics, Naresuan University, Phitsanulok, 65000, Thailand

<sup>c</sup> Department of Chemistry, Faculty of Science, King Mongkut's Institute of Technology Ladkrabang, Ladkrabang, Bangkok, 10520, Thailand

Published online: 09 Dec 2013.

To cite this article: Rattiphorn Sumang, Naratip Vittayakorn & Theerachai Bongkarn (2013) The Effect of Excess PbO on Crystal Structure, Microstructure and Dielectric Properties of  $(\text{Pb}_{0.50}\text{Sr}_{0.50})\text{TiO}_3$  Ceramics, *Ferroelectrics*, 456:1, 98-106, DOI: [10.1080/00150193.2013.846651](https://doi.org/10.1080/00150193.2013.846651)

To link to this article: <http://dx.doi.org/10.1080/00150193.2013.846651>

PLEASE SCROLL DOWN FOR ARTICLE

Taylor & Francis makes every effort to ensure the accuracy of all the information (the "Content") contained in the publications on our platform. However, Taylor & Francis, our agents, and our licensors make no representations or warranties whatsoever as to the accuracy, completeness, or suitability for any purpose of the Content. Any opinions and views expressed in this publication are the opinions and views of the authors, and are not the views of or endorsed by Taylor & Francis. The accuracy of the Content should not be relied upon and should be independently verified with primary sources of information. Taylor and Francis shall not be liable for any losses, actions, claims, proceedings, demands, costs, expenses, damages, and other liabilities whatsoever or howsoever caused arising directly or indirectly in connection with, in relation to or arising out of the use of the Content.

This article may be used for research, teaching, and private study purposes. Any substantial or systematic reproduction, redistribution, reselling, loan, sub-licensing, systematic supply, or distribution in any form to anyone is expressly forbidden. Terms &





# The Effect of Excess PbO on Crystal Structure, Microstructure and Dielectric Properties of $(\text{Pb}_{0.50}\text{Sr}_{0.50})\text{TiO}_3$ Ceramics

RATTIPHORN SUMANG,<sup>1,2</sup> NARATIP VITTAYAKORN,<sup>3</sup>  
AND THEERACHAI BONGKARN<sup>1,2,\*</sup>

<sup>1</sup>Department of Physics, Faculty of Science, Naresuan University, Phitsanulok 65000, Thailand

<sup>2</sup>Research Center for Academic Excellence in Advanced Physics, Naresuan University, Phitsanulok 65000, Thailand

<sup>3</sup>Department of Chemistry, Faculty of Science, King Mongkut's Institute of Technology Ladkrabang, Ladkrabang, Bangkok 10520, Thailand

*Lead strontium titanate  $[(\text{Pb}_{50}\text{Sr}_{50})\text{TiO}_3]$  PST ceramics were fabricated by the conventional solid state reaction method using calcination and sintering temperatures of 950°C and 1250°C. To prevent PbO evaporation during the firing processes, excess PbO was added to the samples in varying amounts from 0–10 wt.%. It was found that PST powders indexed in a tetragonal structure. Impurity phases were detected in the calcined powders which had excess PbO higher than 3 wt%. A pure perovskite phase was obtained from all ceramic samples. The lattice parameters  $a$ ,  $c$  and the  $c/a$  ratio decreased with an increasing excess of PbO. The average particle size and the average grain size increased with the increase of PbO. The porous microstructure slightly decreased with an increasing amount of PbO, up to 1 wt.%, then slightly increased with higher excess PbO. The density can be improved by adding 1 wt.% of excess PbO. The dielectric constant increased from 7500 for the 0 wt.% sample to 8300 for the 1 wt.%. This was followed by reductions for 3, 5 and 10wt.%. The Curie temperature and transition enthalpy slightly increased with an increase amount of PbO until 1 wt.%, then slightly decreased, for the higher excess PbO.*

**Keywords** Excess PbO; tetragonality; lead strontium titanate; dielectric properties

## Introduction

Lead titanate,  $\text{PbTiO}_3$  (PT), is one of the perovskite-type ferroelectric materials having useful, unique, properties such as: a high transition temperature ( $\sim 490^\circ\text{C}$ ), an excellent pyroelectric coefficient and a large spontaneous polarization [1, 2]. However, pure lead titanate ceramics are difficult to sinter because of their large lattice anisotropy ( $c/a = 1.064$ ), which makes them break during cooling. By substitution of isovalent ( $\text{Sr}^{2+}$ ,  $\text{Ca}^{2+}$ ,  $\text{Ba}^{2+}$ ,  $\text{Cd}^{2+}$  . . . etc.) or off-valent ( $\text{Sm}^{3+}$ ,  $\text{Gd}^{3+}$ ,  $\text{Y}^{3+}$  . . . etc.) ions into the  $\text{Pb}^{2+}$  sites, the lattice anisotropy is reduced, and the sample becomes more dense [3, 4].

---

Received December 11, 2012; in final form March 16, 2013.

\*Corresponding author. E-mail: researchcmu@yahoo.com

Many researchers have reported that  $(\text{Pb}_{1-x}\text{Sr}_x)\text{TiO}_3$  is an excellent material for use in microelectric technology, particularly, resonators, filters, and dynamic random access memory (DRAM) capacitors [5, 6, 7].  $(\text{Pb}_{0.50}\text{Sr}_{0.50})\text{TiO}_3$ ; PST ceramics was successfully prepared by various techniques such as: complex polymerization [8], coprecipitation [9] and solid state reaction [10]. The high composition accuracy and homogeneity of PST nano powders were obtained from the complex polymerization method using a low calcination temperature of  $700^\circ\text{C}$  for 4 h [8]. Lead acetate trihydrate and strontium carbonate were dissolved in a titanium citrate solution. The mixed citrate polymerization was promoted by adding ethylene glycol (mass ratio of the citric acid: ethylene glycol = 60:40) to the mixed solution. PST nano-powders ( $\sim 10$  nm) were successfully obtained by the coprecipitation method which had a reaction temperature of  $600^\circ\text{C}$  for 1 h. The solution of lead nitrate, strontium nitrate (with an excess of 25 mol%) and distilled water was dripped into an oxalotitanic acid solution with constant stirring for 15 min. The microemulsion-derived precursor was obtained by adding aqueous ammonia to the mixed solution thereby adjusting the acidity to  $\text{pH} = 1$ . When preparing PST by solid-state reaction, the calcinations temperature is about  $850$ – $950^\circ\text{C}$  for 3–5 h [10, 11]. An average particle size of approximately 300 nm was obtained. The ceramics exhibited a maximum density and maximum dielectric constant of 94% and 3250.

It is well known that, ceramics which are synthesized by chemical process methodologies mostly use raw materials which are costly and entail a complex procedure [12, 13]. The solid state reaction method is simple, has a relatively low cost and provides more products. However, preparing PST ceramics by conventional methods uses high calcinations temperatures above  $850^\circ\text{C}$ . This temperature is higher than the melting point of PbO. The vaporization of PbO causes lead deficiency which may produce large pores in the microstructure and have a subsequent effect on densification. The addition of excess PbO is one of the techniques developed to counteract this problem. For example, the optimum density of PLZST [12], PBT [14], PBZ [15], PZT [16] ceramics can be improved by the addition of excess PbO. From a survey of the literature, the effect of excess PbO on PST ceramics prepared via the solid-state reaction method had not been observed yet. Therefore, in this work, PST ceramic was prepared by the solid state reaction method. The effect of excess PbO on the crystal structure, microstructure and dielectric properties of PST was investigated.

## Experimental

$(\text{Pb}_{0.5}\text{Sr}_{0.5})\text{TiO}_3$  ceramics were prepared by a conventional solid state reaction method [10]. Commercially available PbO (99%),  $\text{SrCO}_3$  (98+%) and  $\text{TiO}_2$  (99%) were used as raw materials. The powders were weighed and mixed well in alcohol using stabilized zirconia balls for 24 h. An excess of PbO, equivalent to 1, 3, 5 and 10 wt.% was added prior to ball milling. The calcination was then conducted at  $950^\circ\text{C}$  for 2 h. The obtained powders were pressed at 80 MPa into disks with a diameter of 15.0 mm and thickness of 1.5 mm. Then, the disks were sintered at  $1250^\circ\text{C}$  for 2 h.

The crystallite structure of the samples was examined using an X-ray diffractometer (XRD). The microstructure was observed using a scanning electron microscope (SEM). The average particle size and average grain size of the powders and ceramics were determined using the mean linear method. The dielectric constant and the dielectric loss of the ceramics were measured using an LCR meter (Agilent 4263B). The measuring frequency was 1 kHz. The Curie temperature was determined by using a differential scanning calorimeter (DSC). The apparent density of the samples was measured by the Archimedes method.

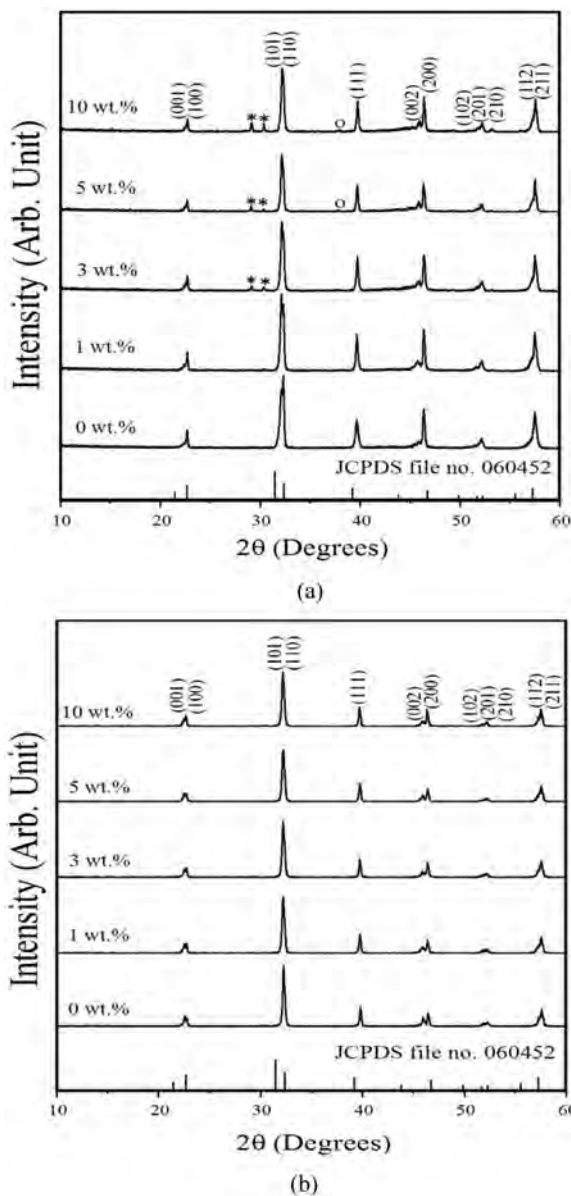


**Figure 1.** XRD patterns of PST (a) calcined powders and (b) sintered ceramics made from starting powders containing different amounts of excess  $\text{PbO}$ : (\*)  $\text{PbO}$ , (o)  $\text{PbO}_2$ .

## Results and Discussion

The X-ray diffraction patterns of the PST calcined powders are shown in Fig. 1(a). The PST had a tetragonal structure, which could be matched with the JCPDS file number 06-0452 [17] and earlier reports [5, 18]. A pure perovskite structure was obtained in the powders containing 0 and 1 wt.% excess  $\text{PbO}$ . On the other hand, when the excess of  $\text{PbO}$  was greater than 3 wt.%, the  $\text{PbO}$  and  $\text{PbO}_2$  phases were observed. Figure 1(b) shows the XRD patterns of PST sintered ceramics. In these patterns, no second phase could be found. This

**Table 1**  
Lattice parameters  $a$ ,  $c$ ,  $c/a$  ratio, average particle size, average grain size, density, and dielectric properties of the PST

Excess PbO (wt%)	Calcined powder				Sintered ceramic					
	Lattice parameters (Å)			Average particle size ( $\mu\text{m}$ )	Lattice parameters (Å)		Average grain size ( $\mu\text{m}$ )	Density ( $\text{g}/\text{cm}^3$ )	Dielectric constant at $T_c$	Dielectric loss at $T_c$
	$a$	$c$	$c/a$ ratio		$a$	$c$				
0	3.9191	3.9546	1.0099	$0.38 \pm 0.14$	3.9151	3.9489	$0.91 \pm 0.22$	6.61	7,500	0.03
1	3.9167	3.9538	1.0097	$0.58 \pm 0.25$	3.9135	3.9481	$1.15 \pm 0.31$	6.67	8,300	0.01
3	3.9151	3.9530	1.0095	$0.78 \pm 0.29$	3.9127	3.9473	$1.20 \pm 0.30$	6.62	3,000	0.01
5	3.9143	3.9522	1.0094	$0.94 \pm 0.36$	3.9119	3.9424	$1.32 \pm 0.37$	6.59	3,100	0.02
10	3.9135	3.9505	1.0091	$1.02 \pm 0.39$	3.9111	3.9400	$1.55 \pm 0.64$	6.55	2,100	0.02

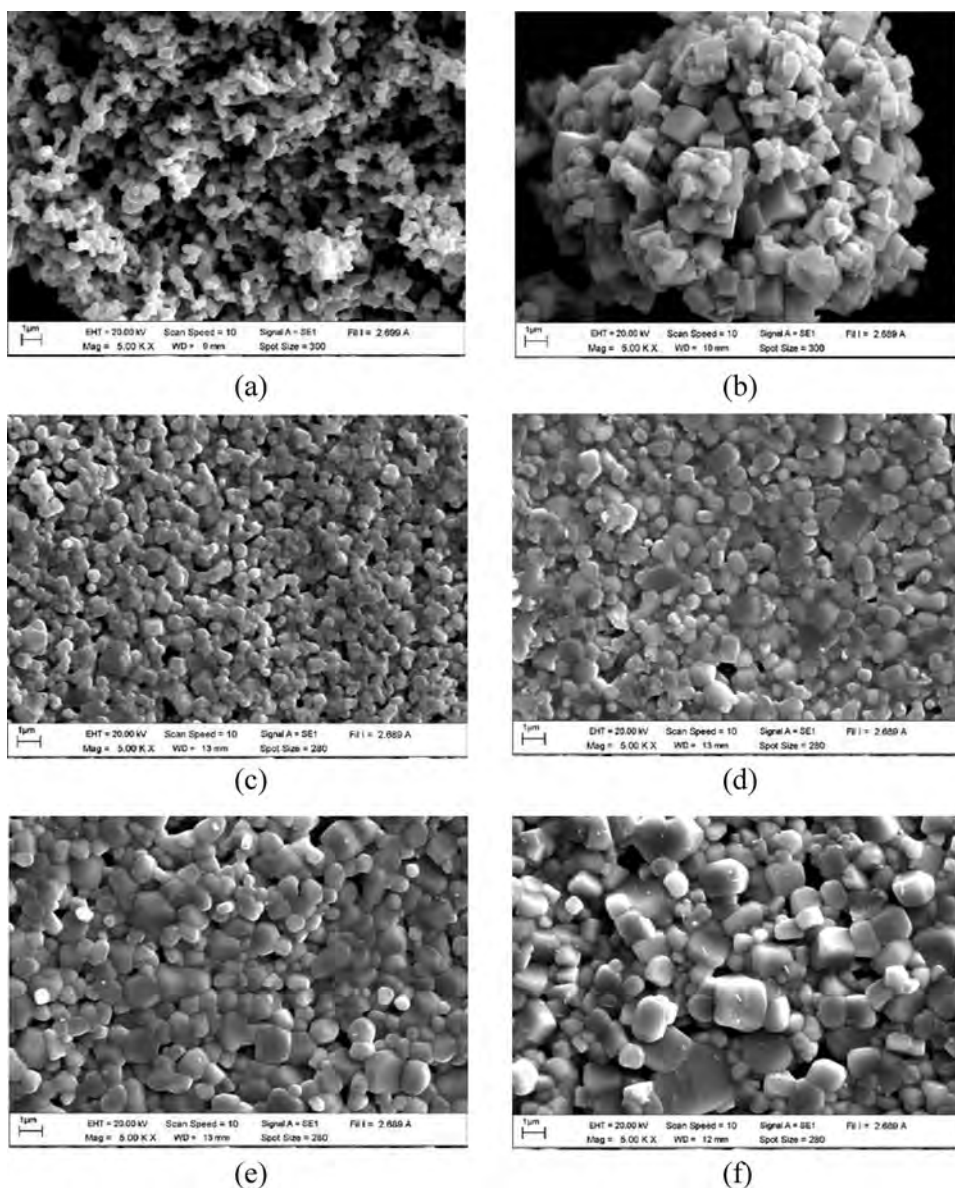


**Figure 2.** SEM photomicrographs of the PST calcined powders with excess PbO (a) 0 wt.% (b) 10 wt.% and the PST sintered surfaces of the ceramics with excess PbO (c) 0 wt.% (d) 1 wt.% (e) 5 wt.% (f) 10 wt.%.

indicated that the PbO and PbO<sub>2</sub> phases (impurity phase) that had been formed in the high excess PbO PST powders were eliminated from the samples by volatilization during sintering at 1250°C. All of the peaks shifted slightly to a higher angel when compared to specimens with no excess of PbO, and the shifts are proportional to the amount of the PbO content. The lattice parameters  $a$ ,  $c$  and the  $c/a$  ratio of the PST calcined powders and sintered ceramics tended to decrease with an increase of excess PbO content as shown in

Table 1. This result indicated that the addition of PbO caused a phase transformation from a tetragonal to a cubic phase. The decrease of the tetragonality affected by excess PbO was similar to our previous work on PBT ceramics with excess lead [19, 20].

The microstructure of PST calcined powders, investigated by SEM, is shown in Fig. 2(a) and (b). The powders without excess PbO (0 wt.%) exhibited an almost spherical morphology and a narrow size distribution. The powder changed from a spherical morphology to a nearly cubic shape and was more agglomerated with increased PbO content. The average particle sizes increased from 0.38 to 1.02  $\mu\text{m}$  with increased PbO content from 0 wt.% to 10 wt.% and are listed in Table 1. Figure 2(c)-(f) reveals the SEM photomicrograph of PST sintered pellets. It can be seen that the grain exhibits an almost spherical morphology. The average grain size increased from 0.91  $\mu\text{m}$  to 1.55  $\mu\text{m}$  when increasing excess PbO from 0 wt.% to 10 wt.% (Table 1). The additional excess PbO combined in the grain boundary and formed a grain boundary layer, which hindered the grain growth. A porous microstructure was found on the surface in the samples without PbO content. The porosity decreased with increasing excess PbO 1 wt.% and increased with further excess PbO higher than 1 wt.%.

The densities of the PST ceramics are listed in Table 1. The density increases with an increased amount of PbO. It reaches a maximum value at 1 wt.% excess PbO, and slightly decreases with >1 wt.% excess PbO. The increases and decreases in the densities of the PST ceramics are due to the decrease and increase in porosity. The rearrangement of the particles begins most probably at the melting temperature of PbO (890°C) and takes place rapidly [14]. This process becomes more intense if a sufficient liquid phase is present to allow an easy rearrangement of the grains. Consequently, the densification should be proportional to the amount of liquid PbO [13]. In this study, the amount of liquid PbO was not enough to fill the pores of the sample without excess PbO (0 wt.%), thus forming the porous microstructure on the surface as shown in Fig. 2(c). The higher densification of 1 wt.% excess PbO decreased the porosity (Fig. 2(d)). However, a large amount of the PbO liquid phase produced an initial rapid densification but a lower final density as a result of void formation due to the PbO evaporation. As a consequence, the porosity of the pellet increases, as shown in Fig. 2(e) and (f).

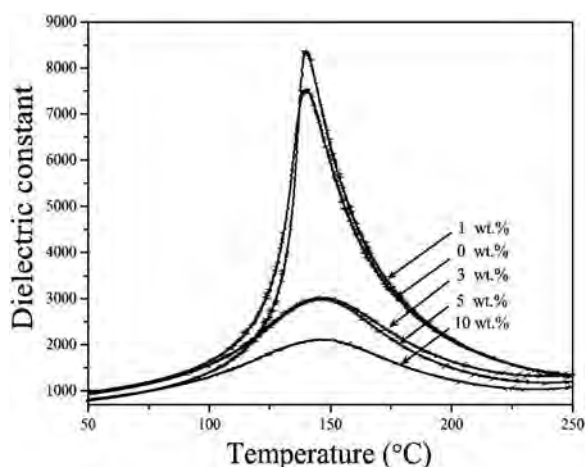


**Figure 3.** Dielectric constant versus temperature for PST sintered ceramics with different amounts of excess PbO.

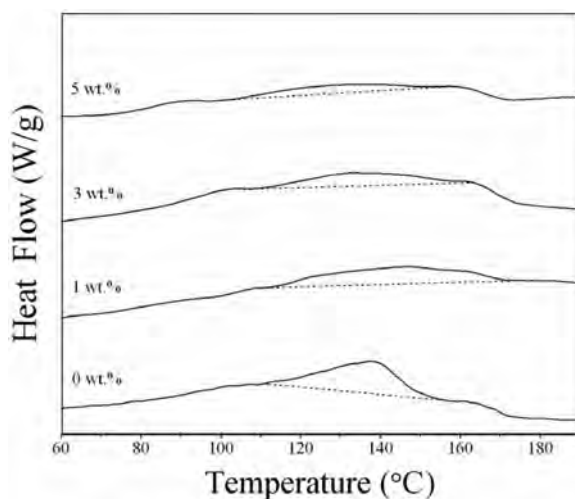


**Figure 4.** DSC plots showing the heating of PST grounded pellet samples with different amounts of excess PbO.

Dielectric constants (1 kHz) vs temperature is shown in Fig. 3. The dielectric properties of the PST ceramics depend on the excess PbO content. As listed in Table 1, the maximum value of the dielectric constant ( $\epsilon_r$ , max) measured at  $T_c$  increases from 7500 to 8300 as the excess PbO increases from 0 wt.% to 1 wt.%. A further increase in excess PbO, to 10 wt.%, resulted in a drop in the values of  $\epsilon_r$ , max to 2100. The opposing trend is observed in the values of the dielectric loss ( $\tan \delta$ ), which are listed in Table 1. It is well known that, increased density and decreased porosity are the dominant factors controlling the dielectric constant [14, 21]. So, the dielectric constant decreased in the sample excess PbO > 1 wt.% with increasing porosity and decreasing density.

The enthalpy transfer at Curie temperature of the PST ceramics was studied using DSC measurement, as shown in Fig. 4. The Curie temperature of PST ceramics undergoes a phase transition from a tetragonal ferroelectric phase (FE) to a cubic paraelectric phase (PE). It was found that the samples with excess PbO 0 wt.% transformed at 137°C with a related enthalpy of 0.682 J/g. When the PbO excess was raised to 1 wt.%, the Curie temperature and the transition enthalpy increased up to a maximum of 145°C and 0.697 J/g. The Curie temperature and the transition enthalpy decreased from 145°C to 130°C and 0.697 J/g to 0.252 J/g, respectively, with increasing excess PbO from 1 to 10 wt.%. This indicated that the samples with added excess PbO > 1 wt.% preferred the PE phase. This result was different from excess PbO in PBT ceramics [19, 20], which preferred the FE phase when excess PbO was increased from 0 wt.% to 10 wt.%. The structural reason for this is uncertain at this stage.

## Conclusions

The excess of PbO affected phase formation, microstructure, density, porosity, dielectric constant, and phase transition of the PST ceramics. The addition of PbO caused phase transformation from a tetragonal to a cubic phase. The particle size and average grain size increased with an increase of excess PbO. The Curie point and transition enthalpy increased



with excess PbO 1 wt.%. With  $\geq 3$  wt.% of excess PbO samples, they dropped in the values. The highest density and maximum dielectric constant was found in excess PbO 1 wt.%.

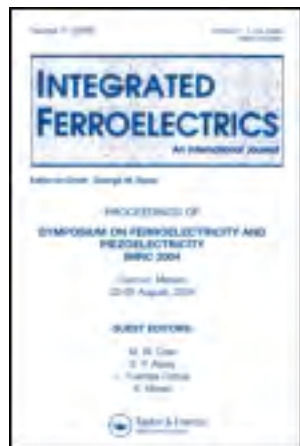
## Acknowledgments

This work was financially supported by the Thailand Research Fund (TRF) and the Commission on Higher Education (CHE). The authors wish to thanks the Science Lab Center, Faculty of Science, Naresuan University for supporting facilities. Thanks are given to Mr. Don Hindle for his help in editing the manuscript.

## References

1. R. Wongmaneeruag, R. Yimnirun, and S. Ananta, Effect of vibro-milling time on phase formation and particle size of lead titanate nanopowders. *Mater. Lett.* **60**, 1447–1452 (2006).
2. S. Y. Chu and T. Y. Chen, Strontium doping effects on the characteristics of Sm-modified PbTiO<sub>3</sub> ceramics. *Sensor Actuat. A-Phys.* **107**, 75–79 (2003).
3. P. R. Arya, P. Jha, G. N. Subbanna, and A. K. Ganguli, Polymeric citrate precursor route to the synthesis of nano-sized barium lead titanates. *Mater. Res. Bull.* **38**, 617–628 (2003).
4. M. Jain, S. B. Majumder, R. Guo, A. S. Bhalla, and R. S. Katiyar, Synthesis and characterization of lead strontium titanate thin films by sol-gel technique. *Mater. Lett.* **56**, 692–697 (2002).
5. I. Rivera, A. Kumar, F. Mendoza, and R. S. Katiyar, Investigation of dielectric, electrical and optical properties of Pb<sub>0.5</sub>Sr<sub>0.5</sub>TiO<sub>3</sub> ceramic. *Physica. B.* **403**, 2423–2430 (2008).
6. M. Jain, Y. I. Yuzyuk, R. S. Katiyar, Y. Somiya, and A. S. Bhalla, Local symmetrybreaking in Pb<sub>x</sub>Sr<sub>1-x</sub>TiO<sub>3</sub> ceramics and composites studied by Raman spectroscopy. *J. Appl. Phys.* **98**, 024116 (2005).
7. X. T. Li, P. Y. Du, L. Zhu, C. L. Mak, and K. H. Wong, Structure and dielectric properties of highly (100)-oriented PST thin-films deposited on MgO substrates. *Thin. Solid. Films.* **516**, 5296–5299 (2008).
8. S. H. Leal, M. T. Escote, F. M. Pontes, E. R. Leite, M. R. Joya, P. S. Pizani, E. Longo, and J. A. Varela, Structure transition on Pb<sub>1-x</sub>Sr<sub>x</sub>TiO<sub>3</sub> produced by chemical method. *J. Alloys. Compd.* **475**, 940–945 (2009).
9. F. Zhang, T. Karaki, and M. Adachi, Synthesis of nanosized (Pb,Sr)TiO<sub>3</sub> perovskite powders by coprecipitation processing. *Powder. Tech.* **159**, 13–16 (2005).
10. S. Subrahmanyam and E. Goo, Nucleation of the ferroelectric phase in the (Pb<sub>x</sub>Sr<sub>1-x</sub>)TiO<sub>3</sub> system. *Acta. mater.* **46**, 817–822 (1998).
11. R. Sumang and T. Bongkarn, The effect of calcination temperature on the phase formation and microstructure of (Pb<sub>1-x</sub>Sr<sub>x</sub>)TiO<sub>3</sub> Powders. *Key. Eng. Mater.* **421**, 243–246 (2010).
12. L. Zhou, A. Zimmermann, Y. P. Zeng, and F. Aldinger, Effects of PbO content on the sintering behavior, microstructure, and properties of La-doped PZST antiferroelectric ceramics. *J. Mater. Sci: Mater Electron.* **15**, 145–151 (2004).
13. L. B. Kong, J. Ma, H. Huang, and R. F. Zhang, Effect of excess PbO on microstructure and electrical properties of PLZT7/60/40 ceramics derived from a high-energy ball milling process. *J. Alloy. Compd.* **345**, 238–245 (2002).
14. L. Amaranda, C. Miclea, and C. Tanasoiu, Effect of excess PbO on the structure and piezoelectric properties of Bi-modified PbTiO<sub>3</sub> ceramics. *J. Eur. Ceram. Soc.* **22**, 1269–1275 (2002).
15. T. Bongkarn and G. Rujijanagul, Effect of excess PbO on microstructure and mechanical properties of (Pb<sub>0.975</sub>Ba<sub>0.025</sub>)ZrO<sub>3</sub> ceramics. *Curr. Appl. Phys.* **6**, 319–322 (2006).
16. C. Miclea, C. Tanasoiu, C. F. Miclea, L. Amarande, A. Gheorghiu, I. Spanulescu, C. Plavitu, C. T. Miclea, M. C. Cioangher, L. Trupina, and A. Iuga, Effect of lead content on the structure and piezoelectric properties of hard type lead titanate-zirconate ceramics. *J. Euro. Ceram. Soc.* **27**, 4055–4059 (2007).

17. Powder Diffraction File No. 06-0452, *International Center for Diffraction Data*, Newton Square, PA, 2003.
18. F. M. Pontes, S. H. Leal, S. H. Leal, E. Longo, P. S. Pizani, A. J. Chiquito, and J. A. Verela, Investigation of phase transition in ferroelectric  $\text{Pb}_{0.70}\text{Sr}_{0.30}\text{TiO}_3$  thin films. *J. Appl. Phys.* **96**, 1192–1196 (2004).
19. T. Bongkarn and R. Sumang, The effect of excess PbO on crystal structure and microstructure of  $(\text{Pb}_{0.925}\text{Ba}_{0.075})\text{TiO}_3$  ceramics. *Adv. Mater. Res.* **55**, 177–180 (2008).
20. R. Sumang and T. Bongkarn, Phase formation, microstructure and phase transition of lead barium titanate ceramics: effect of PbO content. *Ferroelectrics*. **383**, 57–64 (2009).
21. T. Zeng, X. Dong, C. Mao, Z. Zhou, and H. Yang, Effects of pore shape and porosity on the properties of porous PZT 95/5 ceramics. *J. Euro. Ceram. Soc.* **27**, 2025–2029 (2007).



## Integrated Ferroelectrics: An International Journal

Publication details, including instructions for authors and subscription information:

<http://www.tandfonline.com/loi/ginf20>

### Influences of Excess $\text{Bi}_2\text{O}_3$ and $\text{K}_2\text{CO}_3$ on Crystal Structure, Microstructure and Dielectric Properties of Bismuth Potassium Titanate Ceramics

Chamaiporn Wicheanrat <sup>a b</sup>, Artid Laowanidwatana <sup>a b</sup> & Theerachai Bongkarn <sup>a b</sup>

<sup>a</sup> Department of Physics, Faculty of Science, Naresuan University, Phitsanulok, 65000, Thailand

<sup>b</sup> Research Center for Academic Excellence in Applied Physics, Naresuan University, Phitsanulok, 65000, Thailand

Published online: 07 Dec 2013.

To cite this article: Chamaiporn Wicheanrat, Artid Laowanidwatana & Theerachai Bongkarn (2013) Influences of Excess  $\text{Bi}_2\text{O}_3$  and  $\text{K}_2\text{CO}_3$  on Crystal Structure, Microstructure and Dielectric Properties of Bismuth Potassium Titanate Ceramics, Integrated Ferroelectrics: An International Journal, 149:1, 9-17, DOI: [10.1080/10584587.2013.852891](https://doi.org/10.1080/10584587.2013.852891)

To link to this article: <http://dx.doi.org/10.1080/10584587.2013.852891>

PLEASE SCROLL DOWN FOR ARTICLE

Taylor & Francis makes every effort to ensure the accuracy of all the information (the "Content") contained in the publications on our platform. However, Taylor & Francis, our agents, and our licensors make no representations or warranties whatsoever as to the accuracy, completeness, or suitability for any purpose of the Content. Any opinions and views expressed in this publication are the opinions and views of the authors, and are not the views of or endorsed by Taylor & Francis. The accuracy of the Content should not be relied upon and should be independently verified with primary sources of information. Taylor and Francis shall not be liable for any losses, actions, claims, proceedings, demands, costs, expenses, damages, and other liabilities whatsoever or howsoever caused arising directly or indirectly in connection with, in relation to or arising out of the use of the Content.

This article may be used for research, teaching, and private study purposes. Any substantial or systematic reproduction, redistribution, reselling, loan, sub-licensing, systematic supply, or distribution in any form to anyone is expressly forbidden. Terms &



# Influences of Excess $\text{Bi}_2\text{O}_3$ and $\text{K}_2\text{CO}_3$ on Crystal Structure, Microstructure and Dielectric Properties of Bismuth Potassium Titanate Ceramics

CHAMAIPORN WICHEANRAT,<sup>1,2</sup>  
ARTID LAOWANIDWATANA,<sup>1,2</sup>  
AND THEERACHAI BONGKARN<sup>1,2,\*</sup>

<sup>1</sup>Department of Physics, Faculty of Science, Naresuan University, Phitsanulok, 65000, Thailand

<sup>2</sup>Research Center for Academic Excellence in Applied Physics, Naresuan University, Phitsanulok, 65000, Thailand

*Bismuth potassium titanate  $[(\text{Bi}_{0.5}\text{K}_{0.5})\text{TiO}_3]$  BKT ceramics were fabricated by the solid state reaction method using calcination and sintering temperatures of  $800^\circ\text{C}$  and  $1030^\circ\text{C}$ . To prevent  $\text{Bi}_2\text{O}_3$  and  $\text{K}_2\text{CO}_3$  evaporation during the firing process, excess  $\text{Bi}_2\text{O}_3$  and  $\text{K}_2\text{CO}_3$  in the ratio of 1:1 were added to the samples in varying amounts from 0–10 mol%. The XRD results of all samples were indexed in a tetragonal structure. The lattice parameters  $a$ ,  $c$  and the  $c/a$  ratio tended to decrease with increasing excess  $\text{Bi}_2\text{O}_3$  and  $\text{K}_2\text{CO}_3$ . The average particle size increased while the average grain size decreased with increasing amounts of  $\text{Bi}_2\text{O}_3$  and  $\text{K}_2\text{CO}_3$ . The porous microstructure slightly decreased with an increasing amount of  $\text{Bi}_2\text{O}_3$  and  $\text{K}_2\text{CO}_3$ , up to 1 wt.%, and then slightly increased with higher amount of excess  $\text{Bi}_2\text{O}_3$  and  $\text{K}_2\text{CO}_3$ . The density ( $\rho = 5.75 \text{ g/cm}^3$ ), dielectric constant ( $\epsilon_r = 5,584$ ) and dielectric loss ( $\tan\delta = 0.76$ ) can be improved by adding 1 wt.% of excess  $\text{Bi}_2\text{O}_3$  and  $\text{K}_2\text{CO}_3$ .*

**Keywords** Bismuth potassium titanate; dielectric constant; excess  $\text{Bi}_2\text{O}_3$ ; excess  $\text{K}_2\text{CO}_3$

## Introduction

Considering environmental problems, many researchers have focused on lead-free ceramics.  $\text{Bi}_{0.5}\text{K}_{0.5}\text{TiO}_3$  (BKT) is one of the most interesting lead-free ferroelectrics. BKT was first determined by Smolenskii *et al.* [1–2] in 1961. It has a perovskite-type ferroelectric structure belonging to a tetragonal crystal system at room temperature and a relatively high Curie temperature ( $T_c = 380^\circ\text{C}$ ). Ivanova *et al.* [3, 4] reported that the lattice parameters of BKT ceramics are  $a = 0.3913 \text{ nm}$ ,  $c = 0.3993 \text{ nm}$ . It showed uniform spherical particles with diameters ranging from 100 to 200 nm [5]. The remnant polarization, coercive field and piezoelectric properties of BKT ceramics are  $22.2 \mu\text{C/cm}^2$ ,  $52.5 \text{ kV/cm}$  and  $69.8 \text{ pC/N}$ , respectively [4, 6].

Various fabrication techniques such as sol-gel [5], sol-gel-hydrothermal [7] and molten salt [8] have been used to study BKT ceramics. Hou *et al.* [5] fabricated dense BKT ceramics

---

Received December 9, 2012; in final form August 25, 2013.

\*Corresponding author. E-mail: researchcmu@yahoo.com

[193]/9

by a sol-gel method. For preparing dry gel, the sol was heated at 70°C for 2 h. A relative density of more than 90% was obtained from the sample sintered at 1050°C for 2 h. To improve densification, BKT ceramics were prepared by the sol-gel-hydrothermal method. The solution of sol-gel-hydrothermal method was selected at 200°C for 48 h in 6 M KOH. A relative density of 95% was found in the sample sintered at 1050°C for 2 h. However, the compound also contained very small quantities of  $K_4Ti_3O_8$  impurity [7]. Recently, BKT ceramics were successfully prepared with a relative density above 98% for the sample sintered at 1070°C for 2 h using the molten salt synthetic method in a KCl medium. It is well known that chemical synthesis can provide high purity nanosized powders at lower reaction temperatures. Unfortunately, they have high material costs and are complicated to prepare [9–12]. The most fundamental, practical, routine technique which provides more product is the solid state reaction method. Using the solid state reaction method, the maximum density (96% of the theoretical density) was obtained from the sample sintered at 1030°C for 20 h. However, secondary-phase formation of  $K_2Ti_6O_{13}$  and a new Bi-rich ternary phase due to volatilization during the synthesis of BKT, were observed [6, 13]. The change in stoichiometry of  $Bi_2O_3$  and  $K_2CO_3$  change the properties of the ceramics. Therefore, in this work some excess  $Bi_2O_3$  and  $K_2CO_3$  were added during the batch preparation to compensate for the  $Bi_2O_3$  and  $K_2CO_3$  loss in the samples, which were prepared by the solid-state reaction method. The effect of the amount of excess  $Bi_2O_3$  and  $K_2CO_3$  on the crystal structure, microstructure and dielectric properties of BKT was also studied.

## Experimental

Ceramic compositions of  $Bi_{0.5}K_{0.5}TiO_3$  were prepared by the solid-state reaction method. Potassium carbonate (99%  $K_2CO_3$ ), bismuth oxide (99%  $Bi_2O_3$ ) and titanium oxide (99%  $TiO_2$ ) powders were used as starting materials. Stoichiometric amount of starting powders was weighed and ball-milled using a zirconia milling media for 24 h in ethanol. After the drying process, the mixed powders were calcined from 650°C to 900°C for 2 h to discover the optimum calcination temperature. The calcined powders were mixed with 4 wt% PVA binder and then ball-milled again in ethanol for 24 h. Subsequently, the calcined powders were pressed into disks with a diameter of 15 mm at a pressure of 80 MPa. The disk samples were then sintered from 1000°C to 1040°C for 2 h to discover the optimum sintering temperature. In order to compensate for the  $Bi_2O_3$  and  $K_2CO_3$  loss during the process of calcination and sintering, excess  $Bi_2O_3$  and  $K_2CO_3$  in the ratio of 1:1 were added. The excess  $Bi_2O_3$  and  $K_2CO_3$  were subdivided into 0, 1, 2, 3, 4, 5 and 10 wt.% at calcination and sintering temperatures of 800°C and 1030°C for 2 h. respectively.

The crystalline phase structure of the BKT was analyzed by X-ray diffraction (XRD). Scanning electron microscopy (SEM) was used to examine the surface morphologies. Lattice parameters  $c$ ,  $a$  and  $c/a$  ratio were determined from the (001)/(100) and (002)/(200) diffraction planes obtained by XRD peaks. The average particle size and average grain size of samples were determined by using the linear interception method. The apparent density of the samples was measured by the Archimedes method. Dielectric measurements were performed using an LCR meter (Agilent 4263B).

## Results and Discussion

The XRD patterns of BKT powders calcined at 650°C–900°C for 2 h are shown in Fig. 1(a). The phase structure in all samples is a tetragonal structure, which could be matched

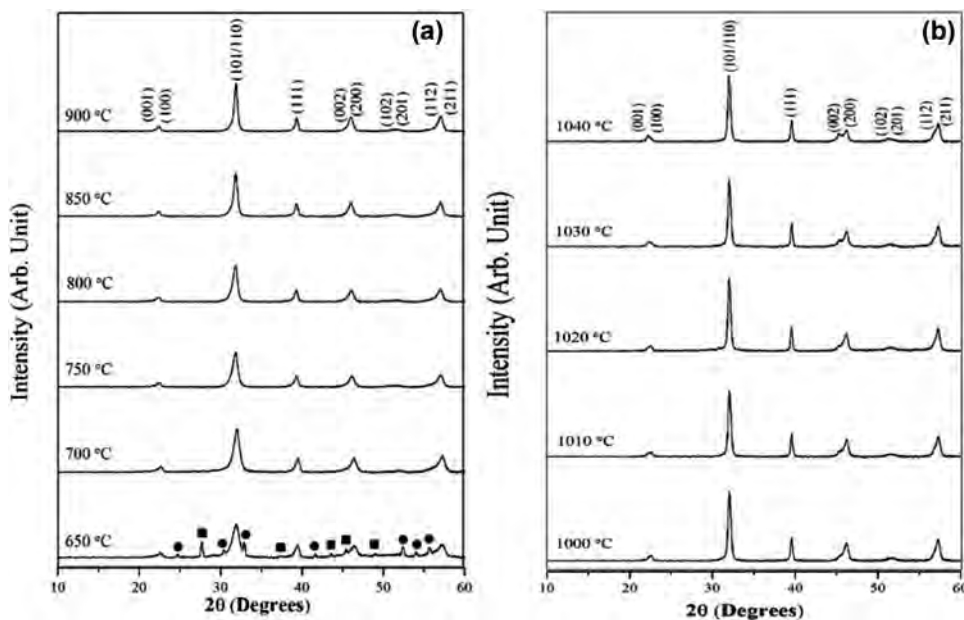


**Figure 1.** X-ray diffraction patterns of BKT (a) calcined powders and (b) sintered ceramic at various temperatures: (■  $\text{K}_2\text{Ti}_6\text{O}_{13}$ ) and (● Bi-rich phase).

with JCPDS file number 36-0339 [14]. At calcination temperatures below  $800^\circ\text{C}$ , the impurity phase of  $\text{K}_2\text{Ti}_6\text{O}_{13}$  and Bi-rich were found. When the calcination temperatures were increased above  $800^\circ\text{C}$ , the impurity phases disappeared and the samples showed pure perovskite phase. The percent of the perovskite phase in the sample increased with increasing calcination temperatures and reached a hundred percent of the perovskite phase when the calcination temperature was above  $800^\circ\text{C}$ . Fig. 1(b) shows the XRD patterns of the BKT sintered ceramics at different sintering temperatures between  $1000^\circ\text{C}$  and  $1040^\circ\text{C}$  for 2 h. The sintered pellets showed a pure perovskite phase. The diffraction patterns of BKT could be indexed with respect to a tetragonal structure. The lattice parameters  $a$  and  $c$  of the BKT ceramics were calculated by the following equation:

$$\frac{1}{d_{hkl}^2} = \frac{h^2 + k^2}{a^2} + \frac{l^2}{c^2} \quad (1)$$

The lattice parameters in which  $a$  and  $c$  decreased while the  $c/a$  increased with increasing sintering temperatures, are listed in Table 1. The density and dielectric constant at  $T_c$  increased with increasing sintering temperatures from  $1000^\circ\text{C}$  to  $1030^\circ\text{C}$  and decreased after being further sintered at a higher temperature ( $1040^\circ\text{C}$ ). The behavior of the dielectric loss is opposite to the dielectric constant. The highest densities ( $\rho = 5.57 \text{ g/cm}^3$ ), maximum dielectric constant ( $\epsilon_r = 5,113$ ), and lowest dielectric loss ( $\tan\delta = 1.30$ ) were obtained from the sample sintered at  $800^\circ\text{C}$  and  $1030^\circ\text{C}$ , respectively for 2 h were used for the preparation of the BKT ceramics.

The X-ray diffraction patterns of BKT calcined powders and sintered ceramics, containing differing amounts of  $\text{Bi}_2\text{O}_3$  and  $\text{K}_2\text{CO}_3$ , are shown in Fig. 2(a) and 2(b). The crystal

**Table 1**  
Lattice parameters  $a$ ,  $c$  and  $c/a$ , density and dielectric properties of BKT ceramics at various temperatures

Sintering temperature (°C)	Lattice parameters (Å)			Measured density (g/cm <sup>3</sup> )	$\epsilon_r$ at $T_c$	$\tan\delta$ at $T_c$
	$a$	$c$	$c/a$			
1000	4.0080	3.9320	1.0193	5.22	1000	1.35
1010	4.0080	3.9311	1.0195	5.44	1500	1.31
1020	4.0029	3.9262	1.0195	5.52	2250	1.30
1030	4.0029	3.9234	1.0202	5.57	5113	1.30
1040	3.9959	3.9157	1.0225	5.48	4000	2.74

structure of the BKT powder and ceramic samples was a tetragonal phase, which could be matched with the JCPDS file number 36–0339 [14]. The pure perovskite phase of the BKT calcined powders and sintered ceramics were obtained in all samples, except for the sintered ceramic sample with an excess of  $\text{Bi}_2\text{O}_3$  and  $\text{K}_2\text{CO}_3$  10 wt.%. The impurity phases of  $\text{K}_2\text{Ti}_6\text{O}_{13}$  and Bi-rich were found in this sample. The lattice parameters  $a$ ,  $c$  and  $c/a$  of the sintered ceramic samples tended to decrease with the increase of excess  $\text{Bi}_2\text{O}_3$  and  $\text{K}_2\text{CO}_3$  content, as listed in Table 2. These indicated that the increase of excess  $\text{Bi}_2\text{O}_3$  and  $\text{K}_2\text{CO}_3$  contents affected the crystal structure.

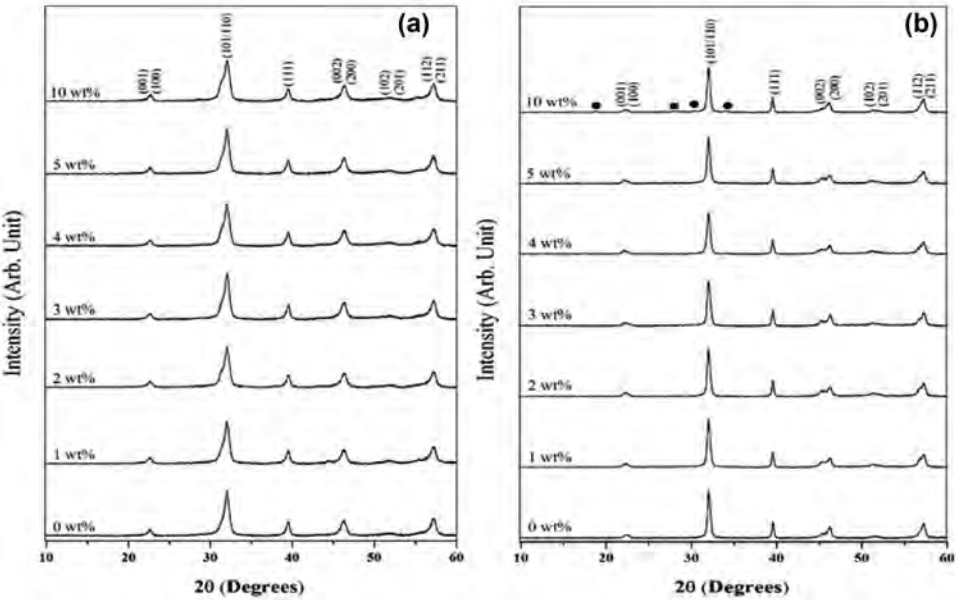


**Figure 2.** X-ray diffraction patterns of BKT (a) calcined powder and (b) sintered ceramics made from starting powders containing different amounts of excess  $\text{Bi}_2\text{O}_3$  and  $\text{K}_2\text{CO}_3$ : (• Bi-rich phase).



**Table 2**  
Lattice parameters, average particle size, average grain size, density, shrinkage, dielectric properties and Curie temperature of BKT with different amounts of excess Bi<sub>2</sub>O<sub>3</sub> and K<sub>2</sub>CO<sub>3</sub>

Excess of Bi <sub>2</sub> O <sub>3</sub> and K <sub>2</sub> CO <sub>3</sub> (wt.%)	Calcined powders		Sintered ceramics							
	Average particle size (μm)	Lattice parameter <i>c</i> (Å)	Lattice parameter <i>a</i> (Å)	<i>c/a</i>	Average grain size (μm)	Density (g/cm <sup>3</sup> )	Relative Density (%)	ε <sub>r</sub> (at <i>T</i> <sub>c</sub> )	tan δ (at <i>T</i> <sub>c</sub> )	<i>T</i> <sub>c</sub>
0	0.23	4.0029	3.9234	1.0202	0.43	5.57	93.9	5113	1.30	312
1	0.24	4.0009	3.9224	1.0200	0.42	5.75	96.9	5584	0.76	340
2	0.25	4.0009	3.9224	1.0200	0.42	5.71	96.2	4870	1.15	356
3	0.25	4.0009	3.9224	1.0200	0.41	5.65	95.3	4924	1.21	395
4	0.26	3.9989	3.9214	1.0197	0.39	5.64	95.0	5156	1.74	413
5	0.28	3.9979	3.9214	1.0195	0.39	5.61	94.6	4800	1.10	422
10	0.29	3.9949	3.9195	1.0192	0.38	5.43	91.5	—	—	—

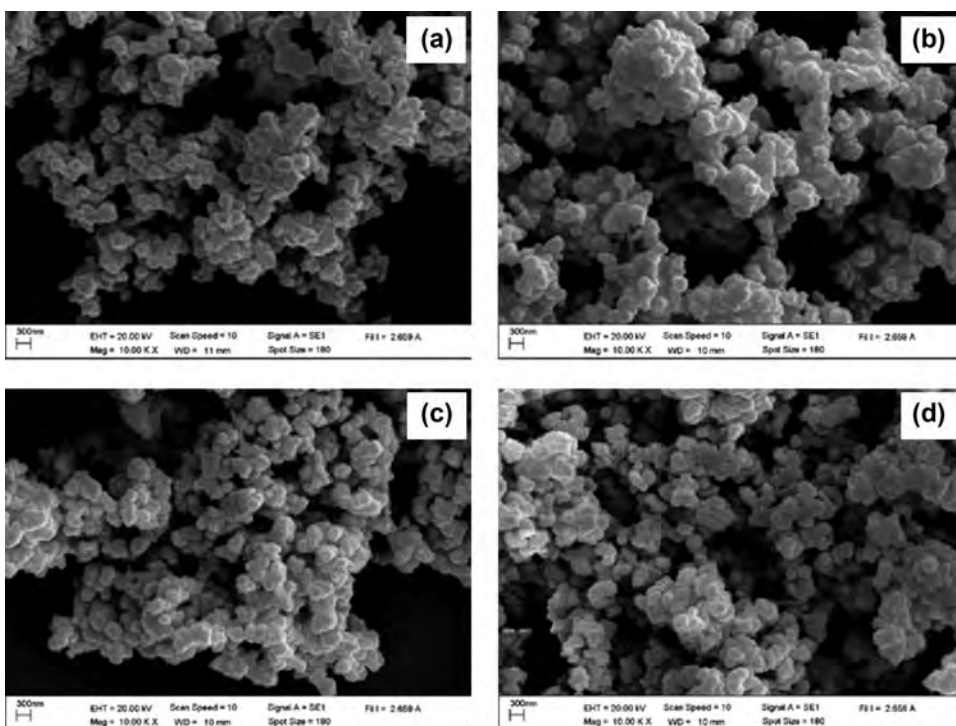


**Figure 3.** SEM photomicrographs of BKT made from starting with different excess  $\text{Bi}_2\text{O}_3$  and  $\text{K}_2\text{CO}_3$  contents: (a) 0 wt.%, (b) 1 wt.%, (c) 3 wt.% and (d) 5 wt.% of calcined powders.

The SEM photographs of BKT calcined powders with various excess  $\text{Bi}_2\text{O}_3$  and  $\text{K}_2\text{CO}_3$  contents are shown in Fig. 3(a–d). These powders exhibited an almost spherical morphology and have a porous agglomerated form. The average particle size increased from 0.23 to 0.29  $\mu\text{m}$  with a slight increase of excess  $\text{Bi}_2\text{O}_3$  and  $\text{K}_2\text{CO}_3$  (Table 2). Fig. 4 shows the SEM photographs of BKT sintered ceramics with various excess  $\text{Bi}_2\text{O}_3$  and  $\text{K}_2\text{CO}_3$  contents. The grain growth exhibited an almost irregular shape. The average grain size, which decreased from 0.43 to 0.38  $\mu\text{m}$  with an increase of  $\text{Bi}_2\text{O}_3$  and  $\text{K}_2\text{CO}_3$  content, are listed in Table 2. A porous microstructure was also found on the surface of the samples without (0 wt.%) excess of  $\text{Bi}_2\text{O}_3$  and  $\text{K}_2\text{CO}_3$  contents. With the addition of 1 wt.% excess  $\text{Bi}_2\text{O}_3$  and  $\text{K}_2\text{CO}_3$ , the porosity decreased, due to a liquid phase which formed between the perovskite grains. The porosity increased with an increase of  $\text{Bi}_2\text{O}_3$  and  $\text{K}_2\text{CO}_3$  higher than 1 wt.%. This could be caused by the loss of  $\text{Bi}_2\text{O}_3$  and  $\text{K}_2\text{CO}_3$  from the compact pellet which increased its porosity.

The density of BKT sintered ceramics with various excess  $\text{Bi}_2\text{O}_3$  and  $\text{K}_2\text{CO}_3$  contents is listed in Table 2. The addition of excess  $\text{Bi}_2\text{O}_3$  and  $\text{K}_2\text{CO}_3$  contents (1 wt.%) caused the density reaching a maximum value of 5.75  $\text{g}/\text{cm}^3$  (96.9% of theoretical density), which was higher than that prepared by the molten salt, sol-gel hydrothermal and sol-gel method [5, 7, 8]. For samples with an excess of bismuth and potassium >1 wt.%, the density decreased, indicating that the system had over the solubility limit of excess of  $\text{Bi}_2\text{O}_3$  and  $\text{K}_2\text{CO}_3$  in the matrix, as seen in Table 2.

Figure 5 shows the temperature dependence of the dielectric constant ( $\epsilon_r$ ) of BKT ceramics at different excess  $\text{Bi}_2\text{O}_3$  and  $\text{K}_2\text{CO}_3$  contents (measured at 1 kHz). The phase

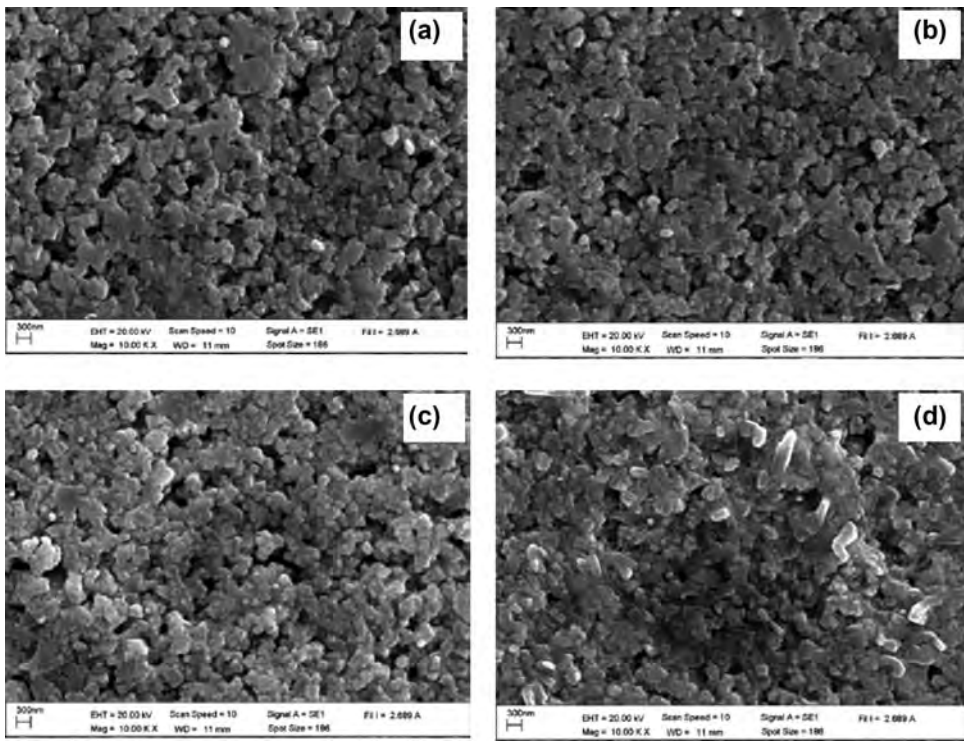


**Figure 4.** SEM photomicrographs of BKT made from starting with different excess  $\text{Bi}_2\text{O}_3$  and  $\text{K}_2\text{CO}_3$  contents: (a) 0 wt.%, (b) 1 wt.%, (c) 3 wt.% and (d) 10 wt.% of sintered ceramics.

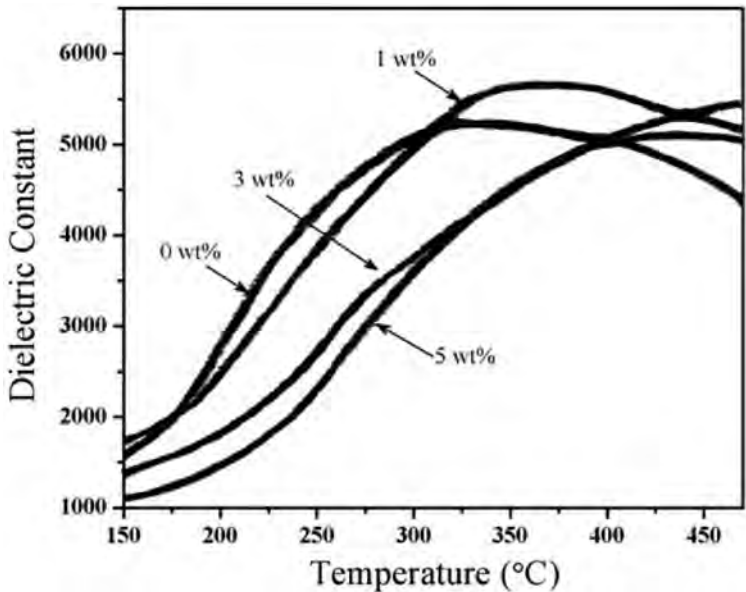


**Figure 5.** Dielectric constant of BKT ceramics sintered at different amounts of excess  $\text{Bi}_2\text{O}_3$  and  $\text{K}_2\text{CO}_3$ .

transition temperature is related to the transition from a tetragonal ferroelectric phase (FE) to a cubic paraelectric phase (PE). At 0 wt.% of excess  $\text{Bi}_2\text{O}_3$  and  $\text{K}_2\text{CO}_3$  contents, the FE to PE phase transition occurs at  $312^\circ\text{C}$ . The phase transition shifted at a temperature of  $422^\circ\text{C}$  when there was the increase of contents of excess  $\text{Bi}_2\text{O}_3$  and  $\text{K}_2\text{CO}_3$  (Table 2). The dielectric constant at the transition temperature increased with increasing excess  $\text{Bi}_2\text{O}_3$  and  $\text{K}_2\text{CO}_3$  contents. It reached a maximum value of 5,584 at 1 wt.% and then dropped in value when excess  $\text{Bi}_2\text{O}_3$  and  $\text{K}_2\text{CO}_3$  contents were higher than 1 wt.% as listed in Table 2. The dielectric loss at the transition temperature tended to decrease from 1.30 to 0.76 with increased  $\text{Bi}_2\text{O}_3$  and  $\text{K}_2\text{CO}_3$  until 1 wt.% and then increased with higher excess  $\text{Bi}_2\text{O}_3$  and  $\text{K}_2\text{CO}_3$ . When compared dielectric properties of the sample with excess 1 wt.% of excess  $\text{Bi}_2\text{O}_3$  and  $\text{K}_2\text{CO}_3$  in this study with the sample without excess  $\text{Bi}_2\text{O}_3$  and  $\text{K}_2\text{CO}_3$  of the previous works [5, 7, 8], it confirmed that the dielectric properties can be improved by excess of  $\text{Bi}_2\text{O}_3$  and  $\text{K}_2\text{CO}_3$  1 wt.%. The result of dielectric properties corresponded with the result from XRD, SEM and density.

## Conclusions

Lead free BKT ceramics were synthesized using the solid state method with calcination and sintering temperature at  $800^\circ\text{C}$  and  $1030^\circ\text{C}$ , respectively. The excess of  $\text{Bi}_2\text{O}_3$  and  $\text{K}_2\text{CO}_3$  affected phase formation, microstructure, density, dielectric properties and Curie temperature. The lattice parameter  $a$ ,  $c$  and  $c/a$  decreased with an increase of excess  $\text{Bi}_2\text{O}_3$  and  $\text{K}_2\text{CO}_3$  contents. The average particle size increased while the average grain size decreased with the increase of  $\text{Bi}_2\text{O}_3$  and  $\text{K}_2\text{CO}_3$  contents. The phase transition shifted at a high temperature when there was an increase in the contents of excess  $\text{Bi}_2\text{O}_3$  and  $\text{K}_2\text{CO}_3$ . The porous microstructure slightly decreased with an increased amount of  $\text{Bi}_2\text{O}_3$  and  $\text{K}_2\text{CO}_3$  up to 1 wt.% then slightly increased with the higher excess  $\text{Bi}_2\text{O}_3$  and  $\text{K}_2\text{CO}_3$ . The highest density ( $\rho = 5.75 \text{ g/cm}^3$  or 96.9% of relative density) and dielectric properties at  $T_c$  ( $\epsilon_r = 5,584$  and  $\tan\delta = 0.76$ ) were obtained from the sample 1 wt.% excess of  $\text{Bi}_2\text{O}_3$  and  $\text{K}_2\text{CO}_3$  contents.

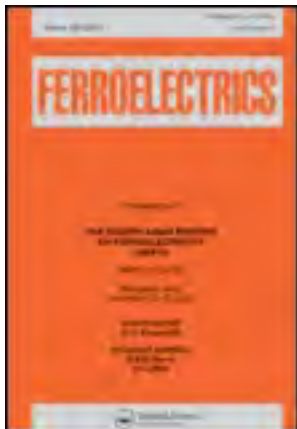
## Acknowledgments

This work was financially supported by the Thailand Research Fund (TRF), Commission on Higher Education (CHE). The authors wish to thanks the Science Lab Center Faculty. Thanks are also given to Mr. Don Hindle for his help in editing the manuscript.

## References

1. G. A. Smolenskii, Dielectric polarization of number of complex compounds. *Sov. Phys. Solid State* **1**, 1562–1573 (1959).
2. P. Vijaya Bhaskar Rao, and T. Bhima Sankaram, Impedance spectroscopy studies of  $\text{K}_{0.5}\text{Bi}_{0.5}\text{TiO}_3$ . *J. Electroceramics* **25**, 60–69 (2010).
3. V. V. Ivanova, A. G. Kapyshv, Y. N. Venetsev, and V. S. Zhdanov, X-ray determination of the symmetry of elementary cells of the ferroelectric materials  $\text{K}_{0.5}\text{Bi}_{0.5}\text{TiO}_3$  and  $\text{Na}_{0.5}\text{Bi}_{0.5}\text{TiO}_3$  and of high temperature phase transition in  $\text{K}_{0.5}\text{Bi}_{0.5}\text{TiO}_3$ . *Izv Akad Nauk SSSR Ser Fiz* **26**, 354–356 (1962).
4. Y. Hiruma, K. Marumo, R. Aoyagi, H. Nagata, and T. Takenaka, Ferroelectric and piezoelectric properties of  $(\text{Bi}_{1/2}\text{K}_{1/2})\text{TiO}_3$  ceramics fabricated by hot-pressing method. *J. Electroceramics* **21**, 296–299 (2008).

5. Y. Hou, M. Zhu, L. Hou, J. Liu, J. Tang, H. Wang, and H. Yan, Synthesis and characterization of lead-free  $\text{K}_{0.5}\text{Bi}_{0.5}\text{TiO}_3$  ferroelectrics by sol-gel technique. *J. Crys. Growth* **273**, 500–503 (2005).
6. Y. Hiruma, R. Aoyagi, H. Nagata, and T. Takennaka, Ferroelectric and piezoelectric properties of  $(\text{Bi}_{1/2}\text{K}_{1/2})\text{TiO}_3$  ceramics. *Jpn. J. Appl. Phys.* **44**, 5040–5044 (2005).
7. L. Hou, Y. D. Hou, X. M. Song, M. K. Zhu, H. Wang, and H. Yan, Sol-gel-hydrothermal synthesis and sintering of  $\text{K}_{0.5}\text{Bi}_{0.5}\text{TiO}_3$  nanowires. *Mater. Res. Bull.* **41**, 1330–1336 (2006).
8. J. Yang, Y. Hou, C. Wang, M. Zhu, and H. Yan, Relaxor behavior of  $(\text{K}_{0.5}\text{Bi}_{0.5})\text{TiO}_3$  ceramics derived from molten salt synthesized single-crystalline nanowires. *Appl. Phys. Lett.* **91**, 023118 (2007).
9. R. Sumang, and T. Bongkarn, The influences of firing temperatures and excess PbO on the crystal structure and microstructure of  $(\text{Pb}_{0.25}\text{Sr}_{0.75})\text{TiO}_3$  ceramics. *J. Mater. Sci.* **46**, 6823–6829 (2011).
10. A. Thongtha, K. Angsukased, and T. Bongkarn, Fabrication of  $(\text{Ba}_{1-x}\text{Sr}_x)(\text{Zr}_x\text{Ti}_{1-x})\text{O}_3$  ceramics prepared using the combustion technique. *Smart Mater. Struc.* **19**, 12400 (2010).
11. N. Phungjitt, P. Panya, and T. Bongkarn, The Structure phase and microstructures of perovskite  $\text{Ba}(\text{Ti}_{1-x}\text{Zr}_x)\text{O}_3$  ceramics using the combustion route. *Funct. Mater. Lett.* **4**, 169–174 (2009).
12. U. Chaimongkon, A. Thongtha, and T. Bongkarn, The effects of firing temperatures and barium content on phase formation, microstructure and dielectric properties of lead barium titanate ceramics prepared via the combustion technique. *Curr. Appl. Phys.* **11**, 70–76 (2011).
13. J. Konig, M. Spreitzer, B. Jancar, D. Suvorov, Z. Samardzija, and A. Popovic, The thermal decomposition of  $\text{K}_{0.5}\text{Bi}_{0.5}\text{TiO}_3$  ceramics. *J. Euro. Ceram. Soc.* **29**, 1695–1701 (2009).
14. Powder Diffraction File No. 36–0339, International Center for Diffraction Data. Newton Square, PA, 2003.



## Ferroelectrics

Publication details, including instructions for authors and subscription information:

<http://www.tandfonline.com/loi/gfer20>

## Combustion Synthesis and Characterization of Perovskite $(\text{Pb}_{0.75}\text{Ca}_{0.13}\text{Sm}_{0.08})(\text{Ti}_{0.98}\text{Mn}_{0.02})\text{O}_3$ Ceramics

Atthakorn Thongtha<sup>a</sup>, Sariya Tupmongkol<sup>a</sup>, Artid Laowanidwatana<sup>a b</sup> & Theerachai Bongkarn<sup>a b</sup>

<sup>a</sup> Department of Physics, Faculty of Science, Naresuan University, Phitsanulok, 65000, Thailand

<sup>b</sup> Research Center for Academic Excellence in Petroleum, Petrochemicals and Advanced Materials, Naresuan University, Phitsanulok, 65000, Thailand

Published online: 10 Dec 2013.

To cite this article: Atthakorn Thongtha, Sariya Tupmongkol, Artid Laowanidwatana & Theerachai Bongkarn (2013) Combustion Synthesis and Characterization of Perovskite  $(\text{Pb}_{0.75}\text{Ca}_{0.13}\text{Sm}_{0.08})(\text{Ti}_{0.98}\text{Mn}_{0.02})\text{O}_3$  Ceramics, *Ferroelectrics*, 455:1, 6-14, DOI: [10.1080/00150193.2013.843402](http://dx.doi.org/10.1080/00150193.2013.843402)

To link to this article: <http://dx.doi.org/10.1080/00150193.2013.843402>

PLEASE SCROLL DOWN FOR ARTICLE

Taylor & Francis makes every effort to ensure the accuracy of all the information (the "Content") contained in the publications on our platform. However, Taylor & Francis, our agents, and our licensors make no representations or warranties whatsoever as to the accuracy, completeness, or suitability for any purpose of the Content. Any opinions and views expressed in this publication are the opinions and views of the authors, and are not the views of or endorsed by Taylor & Francis. The accuracy of the Content should not be relied upon and should be independently verified with primary sources of information. Taylor and Francis shall not be liable for any losses, actions, claims, proceedings, demands, costs, expenses, damages, and other liabilities whatsoever or howsoever caused arising directly or indirectly in connection with, in relation to or arising out of the use of the Content.

This article may be used for research, teaching, and private study purposes. Any substantial or systematic reproduction, redistribution, reselling, loan, sub-licensing, systematic supply, or distribution in any form to anyone is expressly forbidden. Terms &



# Combustion Synthesis and Characterization of Perovskite ( $\text{Pb}_{0.75}\text{Ca}_{0.13}\text{Sm}_{0.08}$ ) ( $\text{Ti}_{0.98}\text{Mn}_{0.02}$ ) $\text{O}_3$ Ceramics

ATTHAKORN THONGTHA,<sup>1</sup> SARIYA TUPMONGKOL,<sup>1</sup>  
ARTID LAOWANIDWATANA,<sup>1,2</sup>  
AND THEERACHAI BONGKARN<sup>1,2,\*</sup>

<sup>1</sup>Department of Physics, Faculty of Science, Naresuan University, Phitsanulok,  
65000, Thailand

<sup>2</sup>Research Center for Academic Excellence in Petroleum, Petrochemicals and  
Advanced Materials, Naresuan University, Phitsanulok, 65000, Thailand

*The effects of calcination temperature (600–900°C) and sintering temperature (1100–1225°C) on the phase evolution, microstructure and dielectric properties of ( $\text{Pb}_{0.75}\text{Ca}_{0.13}\text{Sm}_{0.08}$ )( $\text{Ti}_{0.98}\text{Mn}_{0.02}$ ) $\text{O}_3$ : PCSTM ceramics were investigated. PCSTM powders were synthesized by the combustion technique. The combustion fuel (glycine) carried out an important role in reducing the firing temperatures and improving the density and dielectric properties. The pure tetragonal perovskite phase of PCSTM powders was detected above the calcination temperature of 750°C for all calcined powders. The tetragonality of PCSTM powders and ceramics tended to decrease with increasing of firing temperatures, while average particle size and average grain size increased. The maximum density around 7.43 g/cm<sup>3</sup> was obtained for the sample sintered at 1150°C for 2 h. This sample also exhibited the maximum dielectric constant of 7290 and low dielectric loss about 0.0657 at the Curie temperature.*

**Keywords** ( $\text{Pb}_{0.75}\text{Ca}_{0.13}\text{Sm}_{0.08}$ )( $\text{Ti}_{0.98}\text{Mn}_{0.02}$ ) $\text{O}_3$ ; microstructure; combustion technique; dielectric properties

## Introduction

Lead titanate ( $\text{PbTiO}_3$ ) ceramics have attracted attention because of their high Curie temperature of 490°C. They are considered to be good candidates for high-temperature and high-frequency transducer applications [1, 2]. However, the sintering difficulties may exist because of the ceramic large lattice anisotropy ( $c/a = 1.064$ ). To prepare the samples with high density, the isovalent ( $\text{Ca}^{2+}$ ,  $\text{Ba}^{2+}$ ,  $\text{Cd}^{2+}$ ) or off-valent ( $\text{Sm}^{3+}$ ,  $\text{Gd}^{3+}$ ,  $\text{Y}^{3+}$ ) ions were placed into the  $\text{Pb}^{2+}$  sites in order to reduce the lattice anisotropy [3–7]. Such ceramics ( $\text{Pb}_{0.88-x}\text{Ca}_x\text{Sm}_{0.08}$ )( $\text{Ti}_{0.98}\text{Mn}_{0.02}$ ) $\text{O}_3$  were studied by the solid state reaction method. They were fabricated at the calcination temperature of 900°C and sintering temperature of 1200°C for 2 h. Particularly, in the ratio of  $x = 0.13$ , the ceramic showed high density

---

Received December 11, 2012; in final form March 16, 2013.

\*Corresponding author. E-mail: researchcmu@yahoo.com



( $\sim 7.21 \text{ g/cm}^3$ ), good dielectric constant ( $\sim 5000$  at  $T_c$ ), relatively large electromechanical coupling coefficient ( $\sim 0.574$ ) and good piezoelectric properties ( $\sim 80 \text{ pC/N}$ ) [8].

In our recent work, the ferroelectric ceramics such as:  $\text{CaZrO}_3$  [9],  $0.8(\text{Bi}_{0.5}\text{Na}_{0.5})\text{TiO}_3$ – $0.2(\text{Bi}_{0.5}\text{K}_{0.5})\text{TiO}_3$  [10],  $(\text{Pb}_{1-x}\text{Ba}_x)\text{TiO}_3$  [11],  $\text{SrZrO}_3$  [12],  $\text{Ba}(\text{Ti}_{1-x}\text{Zr}_x)\text{O}_3$  [13],  $(\text{Ba}_{1-x}\text{Sr}_x)(\text{Zr}_x\text{Ti}_{1-x})\text{O}_3$  [14] has been successfully fabricated using the combustion technique. This technique involves a self-sustained reaction between the reactant materials and the fuel (e.g., urea and/or glycine) which supplies a liquid medium at the start of the reaction. The reaction occurs more easily in the liquid system due to larger diffusion coefficient in liquid than in solid. Moreover, the system receives a supplemental energy from the fuel combustion [14, 15]. The obtained ceramics have a high density and good electrical properties with a low firing temperatures [14–16]. The detailed study of the synthesis and characterization of  $(\text{Pb}_{0.75}\text{Ca}_{0.13}\text{Sm}_{0.08})(\text{Ti}_{0.98}\text{Mn}_{0.02})\text{O}_3$  ceramics by the combustion technique have rarely been reported in the literature. Therefore, in this work, preparation of  $(\text{Pb}_{0.75}\text{Ca}_{0.13}\text{Sm}_{0.08})(\text{Ti}_{0.98}\text{Mn}_{0.02})\text{O}_3$  ceramics using the combustion technique was studied. Effects of the calcination and sintering temperatures on the crystal structure, microstructure and dielectric properties of  $(\text{Pb}_{0.75}\text{Ca}_{0.13}\text{Sm}_{0.08})(\text{Ti}_{0.98}\text{Mn}_{0.02})\text{O}_3$  ceramics were investigated and compared with previous work.

## Experimental

The starting materials were commercially available:  $\text{PbO}$  (99%),  $\text{CaCO}_3$  (99%),  $\text{Sm}_2\text{O}_3$  (99%),  $\text{TiO}_2$  (99%) and  $\text{MnO}_2$  (99%).  $(\text{Pb}_{0.75}\text{Ca}_{0.13}\text{Sm}_{0.08})(\text{Ti}_{0.98}\text{Mn}_{0.02})\text{O}_3$  (PCSTM) powder was prepared using the combustion technique. The mixture of the raw materials was thoroughly grinded by the ball milling procedure (zirconia milling media under ethanol for 24 h). Drying was carried out at  $120^\circ\text{C}$  for 4 h. After sieving, the powders were well-mixed with the fuel (glycine) in the agate mortar. The mixed powders were calcined at temperatures ranging from  $600$  to  $900^\circ\text{C}$ , with a dwell time of 1 h and a heating/cooling rate of  $5^\circ\text{C/min}$ . The calcined powders were then pressed at the pressure of 80 MPa into disks with the diameter of 15 mm. The pellets were sintered at  $1100$  to  $1225^\circ\text{C}$  for 2 h and cooled at the rate of  $5^\circ\text{C/min}$  to room temperature. X-ray diffraction was employed to identify the crystal structure and to find the optimum temperature for preparation of the PCSTM powder and ceramics. The calcined powders and sintered ceramics morphologies were imaged using scanning electron microscopy. The density of the sintered ceramics was measured using the Archimedes method. The average particle size and the average grain size were determined by the mean linear intercept method by measuring over 300 particles and 300 grains. A coat of silver paste, fired at  $600^\circ\text{C}$  for 5 min formed the electrodes. The dielectric properties as a function of the ceramic sintering temperature were measured by a LCR impedance analyzer.

## Results and Discussion

XRD patterns of PCSTM powder calcined at various temperatures are shown in Fig. 1. The diffraction lines were indexed on the basis of a tetragonal structure matched with JCPDS file number 43-0303 and corresponded to the previous work [8]. The impurity phases of  $\text{PbO}$ ,  $\text{CaCO}_3$  and  $\text{TiO}_2$  existed at calcination temperatures below  $750^\circ\text{C}$ . The pure tetragonal perovskite phase was found above a calcined temperature of  $750^\circ\text{C}$ . The percentage of the

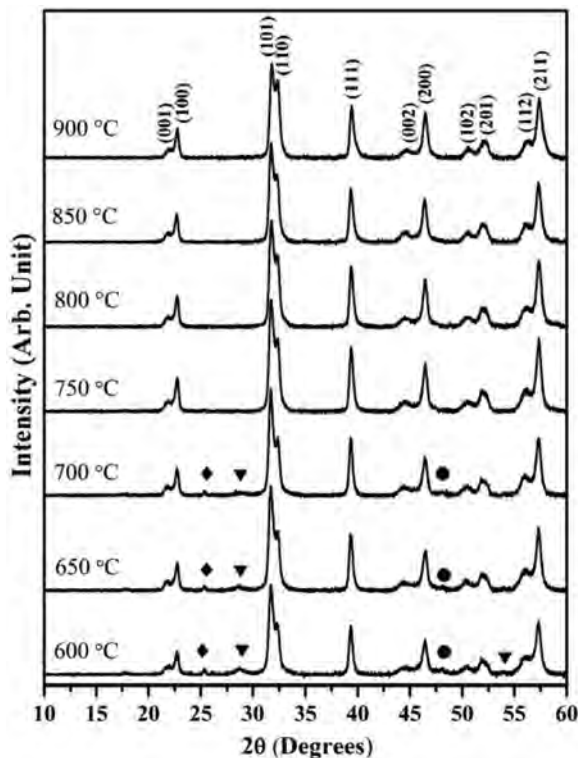


**Figure 1.** XRD patterns of PCSTM powders at various calcination temperatures for 1 h: (♦)  $\text{TiO}_2$ ; (●)  $\text{CaCO}_3$ ; (▼)  $\text{PbO}$ .

perovskite phase can be calculated by the following equation (1):

$$\% \text{ perovskite phase} = \left( \frac{I_{\text{perov}}}{I_{\text{perov}} + I_{\text{PbO}} + I_{\text{CaCO}_3} + I_{\text{TiO}_2}} \right) \times 100 \quad (1)$$

This equation is a well-known equation widely employed in the preparation of complex perovskite structure materials [17–19]. Here  $I_{\text{perov}}$ ,  $I_{\text{PbO}}$ ,  $I_{\text{CaCO}_3}$  and  $I_{\text{TiO}_2}$  refer to the intensity of the (101) perovskite peak, and the intensities of the highest  $\text{PbO}$ ,  $\text{CaCO}_3$  and  $\text{TiO}_2$  peaks, respectively. The percent of the perovskite phase of PCSTM calcined powders is shown in Table 1. There was an increase of the phase purity with the increase of the calcination temperature. The calcination temperature in the combustion method was lower by approximately  $150^\circ\text{C}$  than in the solid-state reaction technique [8]. This suggests that the combustion technique is an advantageous and efficient method for producing pure powders and can be considered as an alternative way. The lattice parameter  $a$  and  $c$  of PCSTM calcined powders was calculated by the following equation (2):

$$\frac{I}{d_{hkl}^2} = \frac{h^2 + k^2}{a^2} + \frac{l^2}{c^2} \quad (2)$$

The data were obtained from the (100), (001), (200) and (002) XRD peaks. The tetragonality,  $c/a$  ratio, has a tendency to decrease as the calcination temperature increases (see Table 1).

**Table 1**

The percent perovskite phase, lattice parameters, *c/a* ratio, average particle size of PCSTM powder

Calcination temperature (°C)	% perovskite phase	Lattice parameters (Å)			Average particle size (nm)
		<i>a</i>	<i>c</i>	<i>c/a</i> ratio	
600	69.2	3.9191	4.1214	1.0516	150 ± 14
650	88.9	3.9109	4.1056	1.0498	199 ± 18
700	98.8	3.9109	4.0989	1.0481	231 ± 24
750	100	3.9109	4.0966	1.0475	310 ± 20
800	100	3.9089	4.0855	1.0452	338 ± 12
850	100	3.9088	4.0810	1.0441	454 ± 18
900	100	3.9047	4.0744	1.0435	812 ± 97

The change of the firing temperatures alters the lattice strain producing the change in the lattice parameters and *d* spacing [14].

Figure 2(a)–(c) shows the SEM photographs of PCSTM powders at various calcination temperatures. The powders exhibit an almost similar spherical morphology. The average particle size of PCSTM powder increases from 150 to 812 nm with the increase of the calcined temperatures from 600 to 900°C as shown in Table 1.

The powder calcined at 750°C was pressed into pellets and sintered at temperatures from 1100 to 1225°C for 2 h. The XRD patterns of the obtained PCSTM ceramics at different sintering temperatures are shown in Fig. 3. All ceramic samples showed a single perovskite tetragonal phase. The lattice parameters *a* and *c* as a function of sintering temperatures are presented in Table 2. The tetragonality of the ceramics tends to decrease with the increase of sintering temperatures. This result is similar to the calcined powder XRD results. The XRD reflection peaks become sharper at higher sintering temperatures, indicating larger crystallization.

The morphological changes of the ceramics as a function of sintered temperatures are shown in Fig. 2(d–f). The increasing of sintered temperature from 1100 to 1150°C caused no obvious change in the microstructure except for an increase in the grain size. When the sintering temperature increased higher than 1150°C, the grain growth became increasingly active and led to an obvious change in the features of the grains. The grains exhibited the rectangular morphology, as shown in Fig. 2(f). The average grain sizes increased from 0.79 to 1.76 μm when the sintering temperatures increased from 1100 to 1225°C, as shown in Table 2.

The measured density with a variation of the sintering temperatures is shown in Table 2. The density increased with increase sintering temperatures, reached the maximum at 1150°C and dropped at higher temperatures. The maximum density was around 7.43 g/cm<sup>3</sup> for the sample sintered at 1150°C for 2 h. The microstructure is related to the density because the grain growth correlates with the densification mechanisms during the treatment, particularly during the final stage of sintering [20, 21]. The expansion of trapped gases in the pores, assembled and grew because of grain growth [20, 21].

The percentage of linear shrinkage in PCSTM samples is listed in Table 2. The tendency of linear shrinkage as a function of sintering temperature is similar to that of density.

**Table 2**  
Lattice parameters,  $c/a$  ratio, density, shrinkage, average grain size, Curie temperature ( $T_c$ ), and dielectric properties of PCSTM ceramics at various sintering temperature

Sintering temperature (°C)	Lattice parameters (Å)		Average grain size (nm)	Density (g/cm <sup>3</sup> )	Linear shrinkage (%)	$T_c$ (°C)	$\epsilon_r$ (at $T_c$ )	$\tan \delta$ (at $T_c$ )
	$a$	$c$						
1100	3.8935	4.0304	$0.79 \pm 0.21$	7.08	11.0	236	5795	0.0616
1125	3.8953	4.0409	$0.83 \pm 0.29$	7.11	18.7	237	7043	0.0872
1150	3.9029	4.0382	$1.05 \pm 0.22$	7.43	20.0	241	7290	0.0657
1175	3.8984	4.0337	$1.08 \pm 0.27$	7.02	19.3	243	6202	0.0961
1200	3.9007	4.0342	$1.14 \pm 0.21$	6.88	18.7	245	4021	0.0885
1225	3.9014	4.0290	$1.76 \pm 0.26$	6.53	13.3	248	3297	0.0702

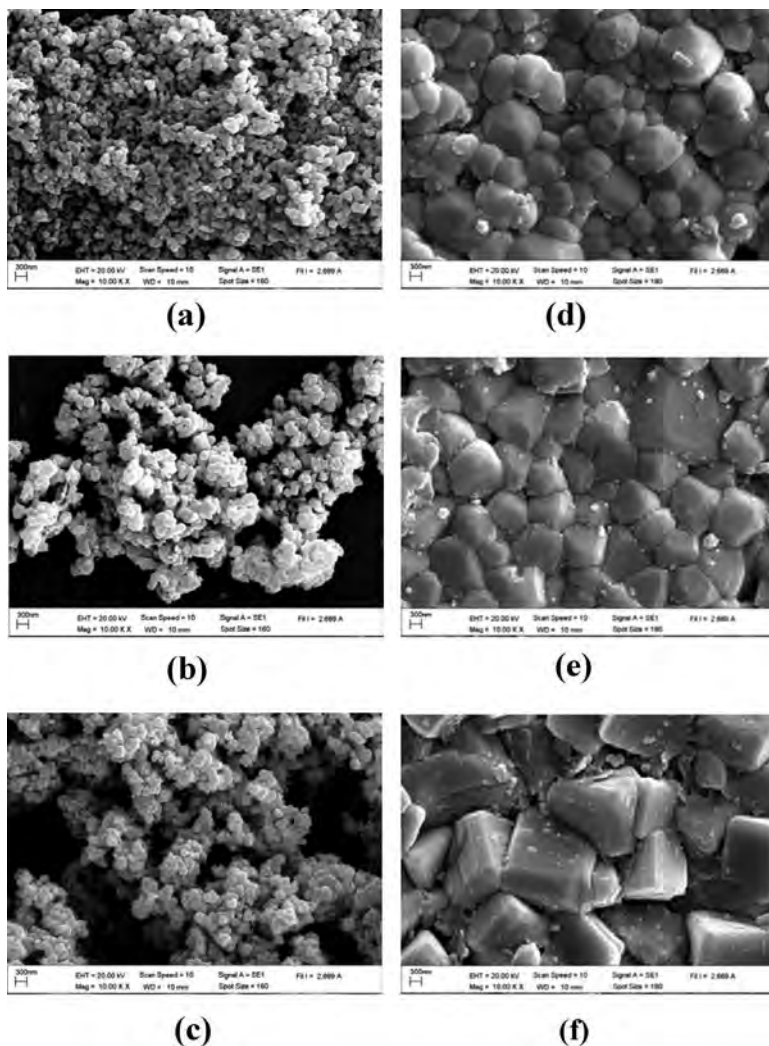


**Figure 2.** SEM photomicrographs of the powders calcined at: (a) 850°C, (b) 950°C and (c) 1000°C for 1 h and the pellet surface sintered at: (d) 1100°C, (e) 1150°C and (f) 1200°C, for 2 h.

The linear shrinkage increased and reached its maximum at 1150°C and decreased above 1150°C.

Figure 4 shows the temperature dependence of the dielectric constant ( $\epsilon_r$ ) of PCSTM ceramics measured at 1 kHz. The dielectric constant curve exhibited a peak between 236 and 248°C as listed in Table 2. This peak can be attributed to the transition from the tetragonal ferroelectric (FE) to the cubic paraelectric (PE) phase characterized by the Curie temperature ( $T_c$ ). At the Curie temperature, the maximum dielectric constant increased from 5795 to 7290 with the increase of sintering temperatures up to 1150°C. Above the optimal sintering temperature, the dielectric constant decreased. The dielectric loss at  $T_c$  is shown in Table 2. The dielectric properties are correlated with the density. The samples, which were sintered at 1150°C for 2 h using the combustion technique, exhibited a high density of about 7.43 g/cm<sup>3</sup> and a high dielectric constant at  $T_c$  around 7290. The dielectric constant at  $T_c$  in

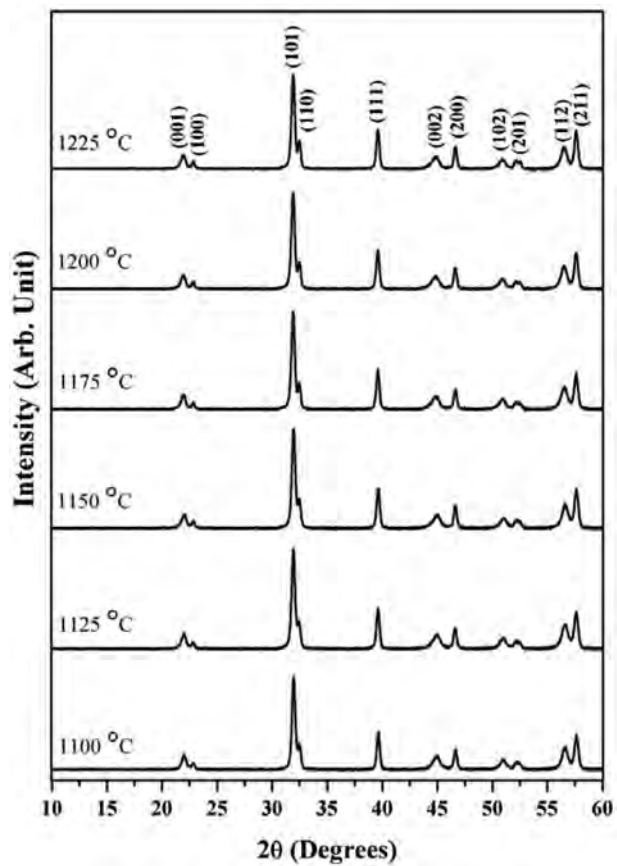


**Figure 3.** X-ray patterns of PCSTM ceramic sintered between 1100 and 1225°C for 2 h.

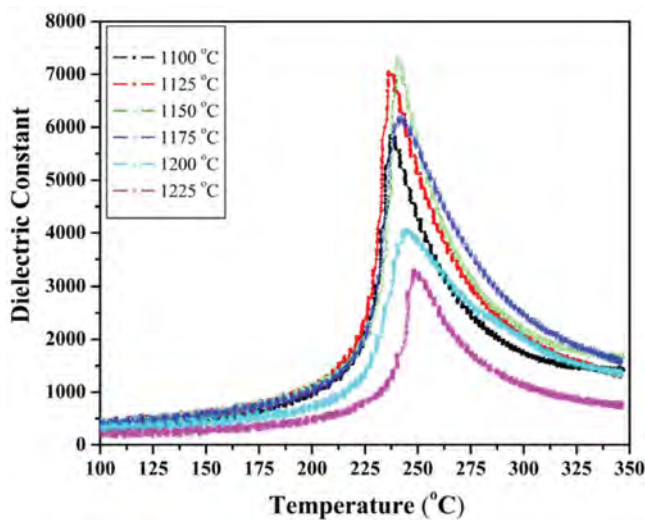


**Figure 4.** Temperature dependence of the dielectric constant of PCSTM ceramics measured at 1 kHz.

this study was higher than that of the samples prepared by the solid state reaction method [8]. Furthermore, the energy needed for the sintering process of the combustion technique (1150°C) was lower than that of the solid-state reaction method by approximately 50°C. This indicated that a liquid medium and the high surface energy produced in the combustion process resulted in high quality PCSTM ceramics.

## Conclusions

PCSTM powders can be successfully prepared by the combustion technique. The pure tetragonal perovskite phase was obtained at a calcination temperature of 750°C for 1 h. The PCSTM powders had a porous agglomerated form and spherical morphology. The maximum density (7.43 g/cm<sup>3</sup>) and the highest dielectric constant (7290) at 1 kHz were obtained for the samples sintered at 1150°C for 2 h. The molten-glycine and the combustion of glycine play an important role in the process. The calcination and sintering temperatures have a strong influence on the crystal structure, lattice parameters, microstructure and dielectric properties of the PCSTM samples.

## Acknowledgments

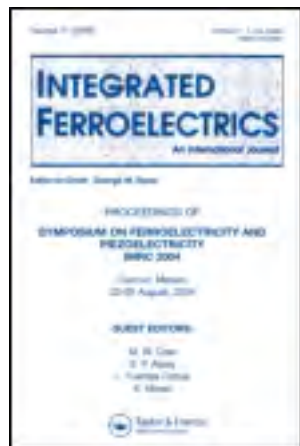
This work was supported financially by the Thailand Research Fund (TRF), Faculty of Science, Naresuan University. Thanks to the Science Lab Center, Faculty of Science, Naresuan University for support facilities. Thanks are also given to Prof. Galina Popovici for her help in editing the manuscript.

## References

1. S. Ikegami, I. Ueda, and T. Nagata, Electromechanical properties of PbTiO<sub>3</sub> ceramics containing La and Mn. *J. Acoust. Soc. Am.* **50**, 1060–1066 (1971).
2. T. Takahashi, Lead titanate ceramics with large piezoelectric anisotropy and their application. *Ceram. Bull.* **69**, 691–695 (1990).
3. H. Takeuchi, S. Jyomura, E. Yamamoto, and Y. Ito, Electromechanical properties of (Pb,Ln)(Ti,Mn)O<sub>3</sub> ceramics. *J. Acoust. Soc. Am.* **72**, 1114–1120 (1982).
4. K. Takeuchi, D. Damjanovic, T. R. Gururaja, S. J. Jang, and L. E. Cross, Electromechanical properties of calcium-modified lead titanate ceramics. *Proc. of the Sixth ISAF IEEE*. 402–405 (1986).
5. J. Shenglin, Z. Xuli, W. Xiaozhen, and W. Xianghong, Investigation on anisotropy in piezoelectric properties of modified PbTiO<sub>3</sub> ceramics. *Piezoelect Acoust.* **17**, 26–29. (1995).
6. I. Ueda and S. Ikegami, Piezoelectric properties of modified PbTiO<sub>3</sub> ceramics. *Jpn. J. Appl. Phys.* **7**, 236–242. (1968).
7. Y. Yamashita, K. Yokoyama, H. Honda, and T. Takahashi, (Pb,Ca)[(Co<sub>1/2</sub>W<sub>1/2</sub>),Ti]O<sub>3</sub> piezoelectric ceramics and their applications. *Jpn. J. Appl. Phys.* **20**, 183–187 (1981).
8. T. Y. Chen and S. Y. Chu, The piezoelectric and dielectric properties of Ca-additive Sm-modified PbTiO<sub>3</sub> ceramics intended for surface acoustic wave devices. *J. Euro. Ceram. Soc.* **23**, 2171–2176 (2003).
9. A. Thongtha and T. Bongkarn, Effect of firing temperatures on phase and morphology evolution of CaZrO<sub>3</sub> ceramics synthesized using the combustion technique. *Ferroelectrics*. **403**, 3–10 (2010).
10. A. Thongtha and T. Bongkarn, Optimum sintering temperature for fabrication of 0.8Bi<sub>0.5</sub>Na<sub>0.5</sub>TiO<sub>3</sub>-0.2Bi<sub>0.5</sub>K<sub>0.5</sub>TiO<sub>3</sub> lead-free ceramics by combustion technique. *Key. Eng. Mater.* **474–476**, 1754–1759 (2011).

11. U. Chaimongkon, A. Thongtha, and T. Bongkarn, The effects of firing temperatures and barium content on phase formation, microstructure and dielectric properties of lead barium titanate ceramics prepared via the combustion technique. *Curr. Appl. Phys.* **11**, S70–S76 (2011).
12. A. Thongtha and T. Bongkarn, Fabrication and characterization of perovskite  $\text{SrZrO}_3$  ceramics through a combustion technique. *Key. Eng. Mater.* **421–422**, 223–226 (2011).
13. P. Julphunthong and T. Bongkarn, Phase formation, microstructure and dielectric properties of  $\text{Ba}(\text{Zr}_{0.1}\text{Ti}_{0.9})\text{O}_3$  ceramics prepared via the combustion technique. *Curr. Appl. Phys.* **11**, S60–S65 (2011).
14. A. Thongtha, K. Angsukased, and T. Bongkarn, Fabrication of  $(\text{Ba}_{1-x}\text{Sr}_x)(\text{Ti}_{1-x}\text{Zr}_x)\text{O}_3$  ceramics prepared using the combustion technique. *Smart. Mater. Struct.* **19**, 124001 (2010).
15. D. Xue, J. Xu, and C. Yan, Chemical synthesis of  $\text{NaTaO}_3$  powder at low-temperature. *Mater. Lett.* **59**, 2920–2922 (2005).
16. K. C. Patil, S. T. Aruna, S. Ekambaram, Combustion synthesis. *Curr. Opin. Solid State Mater Sci.* **2**, 156–165 (1997).
17. A. Thongtha, K. Angsukased, and T. Bongkarn, Influences of firing temperatures on phase and morphology evolution of  $(\text{Ba}_{0.25}\text{Sr}_{0.75})(\text{Zr}_{0.75}\text{Ti}_{0.25})\text{O}_3$  ceramics synthesized via solid-state reaction method. *Key. Eng. Mat.* **421–422**, 247–250 (2010).
18. A. Thongtha, K. Angsukased, and T. Bongkarn, Preparation of  $(\text{Ba}_{1-x}\text{Sr}_x)(\text{Zr}_x\text{Ti}_{1-x})\text{O}_3$  ceramics via the solid state reaction method. *Ferroelectrics*. **403**, 68–75 (2010).
19. A. Thongtha and T. Bongkarn, Phase formation and microstructure of barium zirconate ceramics prepared using the combustion technique. *Ferroelectrics*. **383**, 33–39 (2009).
20. R. M. German, Sintering Theory and Practice. *New York. Wiley.* (1996).
21. B. Guillaume, F. Boschini, I. C. Cano, A. Rulmont, R. Cloots, and M. Ausloos, Optimization of  $\text{BaZrO}_3$  sintering by control of the initial powder size distribution; a factorial design statistical analysis. *J. Eur. Ceram. Soc.* **25**, 3593–3604 (2005).





## Integrated Ferroelectrics: An International Journal

Publication details, including instructions for authors and subscription information:

<http://www.tandfonline.com/loi/ginf20>

### Phase Formation, Microstructure and Dielectric Properties of Bismuth Potassium Titanate Ceramic Fabricated Using the Combustion Technique

Atthakorn Thongtha<sup>a b</sup>, Artid Laowanidwatana<sup>a b</sup> & Theerachai Bongkarn<sup>a b</sup>

<sup>a</sup> Department of Physics, Faculty of Science, Naresuan University, Phitsanulok, 65000, Thailand

<sup>b</sup> Research Center for Academic Excellence in Applied Physics, Naresuan University, Phitsanulok, 65000, Thailand

Published online: 07 Dec 2013.

To cite this article: Atthakorn Thongtha, Artid Laowanidwatana & Theerachai Bongkarn (2013) Phase Formation, Microstructure and Dielectric Properties of Bismuth Potassium Titanate Ceramic Fabricated Using the Combustion Technique, Integrated Ferroelectrics: An International Journal, 149:1, 32-38, DOI: [10.1080/10584587.2013.852921](https://doi.org/10.1080/10584587.2013.852921)

To link to this article: <http://dx.doi.org/10.1080/10584587.2013.852921>

PLEASE SCROLL DOWN FOR ARTICLE

Taylor & Francis makes every effort to ensure the accuracy of all the information (the "Content") contained in the publications on our platform. However, Taylor & Francis, our agents, and our licensors make no representations or warranties whatsoever as to the accuracy, completeness, or suitability for any purpose of the Content. Any opinions and views expressed in this publication are the opinions and views of the authors, and are not the views of or endorsed by Taylor & Francis. The accuracy of the Content should not be relied upon and should be independently verified with primary sources of information. Taylor and Francis shall not be liable for any losses, actions, claims, proceedings, demands, costs, expenses, damages, and other liabilities whatsoever or howsoever caused arising directly or indirectly in connection with, in relation to or arising out of the use of the Content.

This article may be used for research, teaching, and private study purposes. Any substantial or systematic reproduction, redistribution, reselling, loan, sub-licensing, systematic supply, or distribution in any form to anyone is expressly forbidden. Terms &



# Phase Formation, Microstructure and Dielectric Properties of Bismuth Potassium Titanate Ceramic Fabricated Using the Combustion Technique

ATTHAKORN THONGTHA,<sup>1,2</sup> ARTID LAOWANIDWATANA,<sup>1,2</sup>  
AND THEERACHAI BONGKARN<sup>1,2,\*</sup>

<sup>1</sup>Department of Physics, Faculty of Science, Naresuan University, Phitsanulok, 65000, Thailand

<sup>2</sup>Research Center for Academic Excellence in Applied Physics, Naresuan University, Phitsanulok, 65000, Thailand

*The effect of sintering temperature (975–1025°C) on crystal structure, microstructure and dielectric properties of perovskite bismuth potassium titanate (BKT) ceramics was investigated. The pure BKT ceramics were firstly prepared using the combustion technique. The phase purity, crystal structure and microstructure of samples were examined using X-ray diffraction (XRD) and scanning electron microscopy (SEM). The purity phase of BKT samples, which has a tetragonal structure, was observed in all samples. The lattice parameters  $a$ ,  $c$  and the tetragonality tended to decrease with increased sintering temperature. The SEM result showed the average grain size increased (0.37–0.58  $\mu\text{m}$ ) with the increase of sintering temperature (975–1025°C). The shrinkage of the ceramics increased when the sintering temperature increased. The maximum density and dielectric constant at Curie temperature were around 5.71 g/cm<sup>3</sup> and 3850, and were obtained from the sample sintered at 1020°C for 2 h. Importantly, the preparation using the combustion technique can improve the density and dielectric properties of BKT ceramics.*

**Keyword** Combustion technique; bismuth potassium titanate; phase formation; dielectric properties

## Introduction

Lead-free materials have attracted considerable attention because of environmental concerns.  $\text{Bi}_{0.5}\text{Na}_{0.5}\text{TiO}_3$ -based multi-component solid solution systems have been widely studied [1, 2], while research on  $\text{Bi}_{0.5}\text{K}_{0.5}\text{TiO}_3$  (BKT) has rarely been reported [3]. This is possibly because it is difficult to fabricate high density BKT ceramics due to the high volatility of the bismuth component at high sintering temperature [4–5]. BKT was first described by Smolenskii *et al.* [6] in 1959. It is a perovskite type ferroelectric structure with a tetragonal crystal system at room temperature. The obtained lattice parameters were  $a = 3.913 \text{ \AA}$  and  $c = 3.993 \text{ \AA}$  [7]. It undergoes a phase transition ( $T_c$ ) at about 380°C. Previous works have reported that BKT ceramics are considered to be a good candidate for

---

Received December 9, 2012; in final form August 25, 2013.

\*Corresponding author. E-mail: researchcmu@yahoo.com

device applications such as piezoelectric filters, resonators and micro-electro-mechanical systems [8, 9].

From a survey of the literature, the BKT ceramics have been prepared by the solid state reaction method [10, 11], the sol-gel method [8, 12] and the sol-gel-hydrothermal method [5]. Using the solid state reaction method, the maximum density (96% of the theoretical density) was obtained from the sample sintered at 1030°C for 20–80 h [11]. To reduce the dwell time, BKT ceramics were fabricated by the sol-gel method [8, 12] and the sol-gel-hydrothermal method using a sintering temperature of 1050°C for 2 h [5], which obtained a sintered density of ~95% of theoretical density and a dielectric constant at Curie temperature ~1100 (at 10 kHz). However, chemical synthesis has high material costs, and is intricate and complicated to prepare [13–15]. Thus, a technique which has low material costs and is simple to prepare was required for BKT ceramics fabrication.

Recently, our previous work has successfully fabricated different oxides ceramics such as: BaZrO<sub>3</sub> [16], SrZrO<sub>3</sub> [17], BaTiO<sub>3</sub> [18], CaZrO<sub>3</sub> [19], Ba(Ti<sub>1-x</sub>Zr<sub>x</sub>)O<sub>3</sub> [20], (Ba<sub>1-x</sub>Sr<sub>x</sub>)(Zr<sub>x</sub>Ti<sub>1-x</sub>)O<sub>3</sub> [21] using the combustion technique. This technique involves a self-sustained reaction between the reactive materials and the fuel which supplies a liquid medium at the start of the reaction. The reaction can react easily in a liquid system because the diffusion coefficient is higher than in a solid medium [16, 22]. The combustion technique can reduce the dwell time, obtain a high density and has good electrical properties [16–23]. Moreover, a detailed study of the preparation and characterization of BKT ceramics via the combustion technique has not been reported in the literature. Therefore, in this work, Bi<sub>0.5</sub>K<sub>0.5</sub>TiO<sub>3</sub> (BKT) ceramics were firstly prepared via the combustion technique. The effect of sintering temperature on the crystal structure, microstructure and dielectric properties of BKT ceramics was investigated and also compared with previous work.

## Experimental

The starting materials were commercially available: K<sub>2</sub>CO<sub>3</sub> (99%), Bi<sub>2</sub>O<sub>3</sub> (99%) and TiO<sub>2</sub> (99%). Bi<sub>0.5</sub>K<sub>0.5</sub>TiO<sub>3</sub> (BKT) powders were prepared using the combustion technique, by thoroughly grinding mixtures of the raw materials by a ball milling procedure (zirconia milling media under ethanol for 24 h). Drying was carried out at 120°C for 4 h. After sieving, the mixture of raw materials and the fuel, glycine, was well-mixed before the calcination step. The mixed powders were calcined at 850°C, with a dwell time of 2 h and a heating/cooling rate of 5°C/min. To compensate for the bismuth oxide loss during the sintering process, excess Bi<sub>2</sub>O<sub>3</sub> content (0.2 weight%) was added prior to ball milling. The calcined powders were then pressed into disks with a diameter of 15 mm at a pressure of 80 MPa. The pellets were sintered at 975 to 1025°C for 2 h and cooled in a furnace. X-ray diffraction was employed to identify the crystal structure and the optimum temperature to prepare the BKT ceramics. The sintered ceramics morphologies were imaged using scanning electron microscopy. The density of the sintered ceramics was measured using the Archimedes method. The average particle size and the average grain size were determined by using a mean linear intercept method. Dielectric constants were also measured by a LCR meter.

## Results and Discussion

The crystal structure of the sintered ceramics was revealed using the XRD technique as seen in Fig. 1. The diffraction synthesis lines could be indexed on the basis of a tetragonal

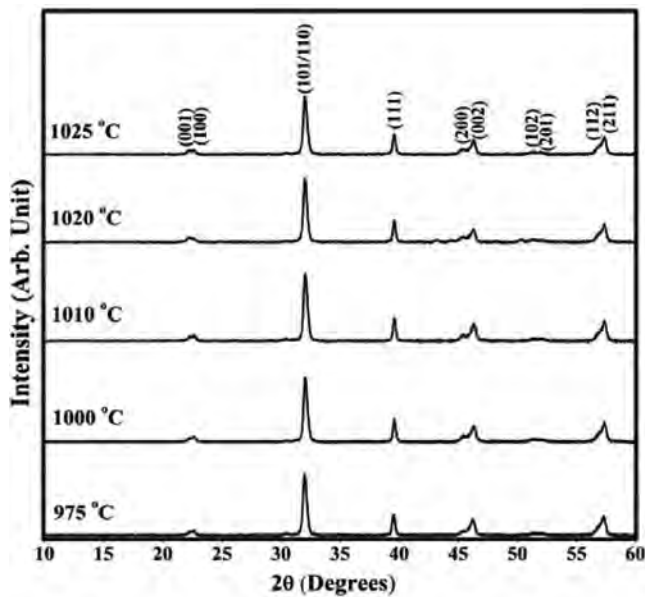


**Figure 1.** XRD patterns of BKT ceramics sintered between 975 and 1025°C.

structure matched with JCPDS file number 36–0339. The BKT ceramics were identified as having a single phase in all samples. The lattice parameters  $a$  and  $c$  of the BKT ceramics were calculated by the following equation:

$$\frac{1}{d_{hkl}^2} = \frac{h^2 + k^2}{a^2} + \frac{l^2}{c^2} \tag{1}$$

The data for calculation were received from (200) and (002) XRD peaks. The lattice parameters  $c$ ,  $a$  and  $c/a$  tended to decrease with the increasing sintering temperatures as seen in Table 1. The change of sintering temperature affected the lattice strain, which is determined as the change in the  $d$  spacing and the lattice parameters of the samples [24]. This indicated that the sintering temperature affected the crystal structure.

**Table 1**

Lattice parameters,  $c/a$  ratio, average grain size, density and shrinkage of BKT ceramics

Sintered temperature (°C)	Lattice parameters (Å)		<i>c/a</i> ratio	Average grain size (μm)	Shrinkage (%)	Density	
	<i>c</i>	<i>a</i>				Measured (g/cm <sup>3</sup> )	Theoretical (%)
975	4.0081	3.9298	1.0199	0.37	16.5	5.62	94.8
1000	4.0043	3.9286	1.0192	0.40	16.8	5.65	95.3
1010	3.9997	3.9271	1.0184	0.42	17.0	5.70	96.1
1020	3.9981	3.9258	1.0184	0.47	24.2	5.71	96.3
1025	3.9968	3.9231	1.0188	0.58	25.0	5.50	92.8

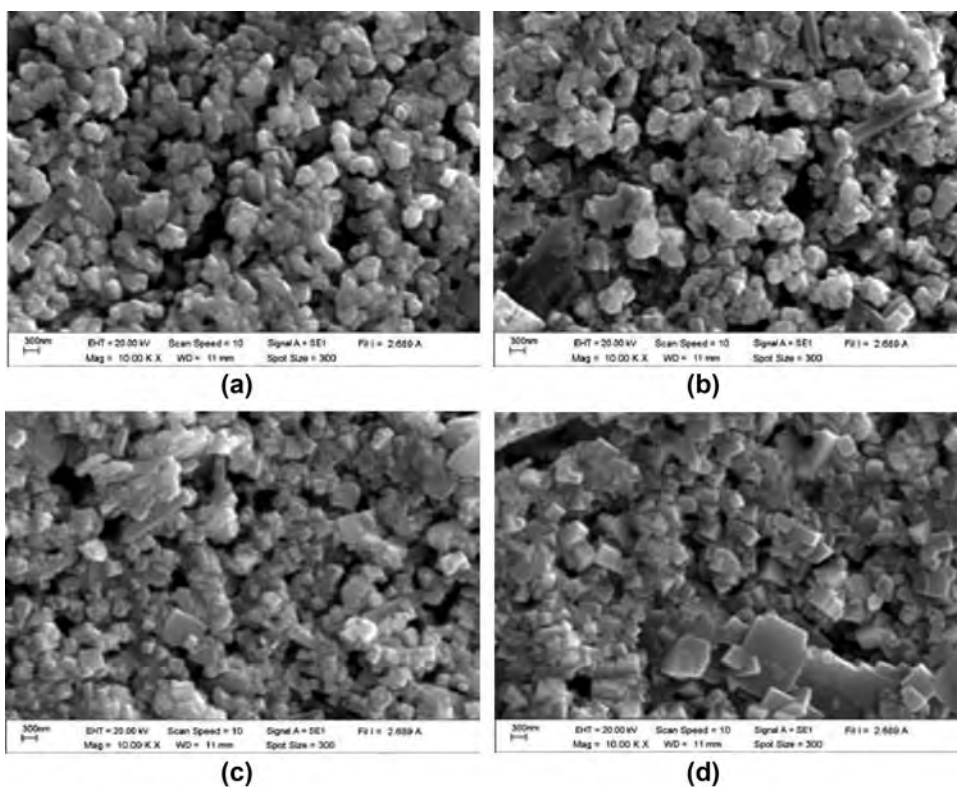


**Figure 2.** SEM photographs of BKT ceramics sintered at; (a) 975°C, (b) 1000°C, (c) 1010°C and (d) 1020°C.

The morphological changes in the BKT surface of the sintered ceramics as a function of sintering temperature are shown in Fig. 2. The contact points between particles grew into necks which showed the primary state of sintering at the sintering temperature  $\leq 1000^\circ\text{C}$ , as shown in Fig. 2(a). Increasing the sintering temperature up to  $1000^\circ\text{C}$  caused little change in the microstructure except for a slight increase in the grain size. When the sintering temperature increased above  $1000^\circ\text{C}$  and reached its highest at  $1020^\circ\text{C}$ , the grain growth was still slight. At the same time, it was evident that the porosity was also decreased and led to an obvious change in the features of the grain size. The grain growth exhibited an almost rectangular morphology, as shown in Fig. 2(c)-(d). The average grain sizes increased from  $0.37$  to  $0.58\ \mu\text{m}$  when the sintering temperatures were increased from  $975$  to  $1025^\circ\text{C}$ , as shown in Table 1.

The percent of shrinkage of the pellet samples increased with the increase of sintering temperature as shown in Table 1. The measured density with a variation of the sintering temperature is shown in Table 1. The density first increased and reached its highest at  $1020^\circ\text{C}$  then dropped in value when the sintering temperature was higher than  $1020^\circ\text{C}$ . The maximum density was around  $5.71\ \text{g/cm}^3$  or  $\sim 96.3\%$  of the theoretical density of the sintered sample at  $1020^\circ\text{C}$  for 2 h. The microstructure corresponded to the density because the grain growth correlated with the densification mechanisms during treatment, particularly during the final stage of sintering [25, 26]. The expansion of trapped gases in the pores assembled and grew because of grain growth [25, 26].

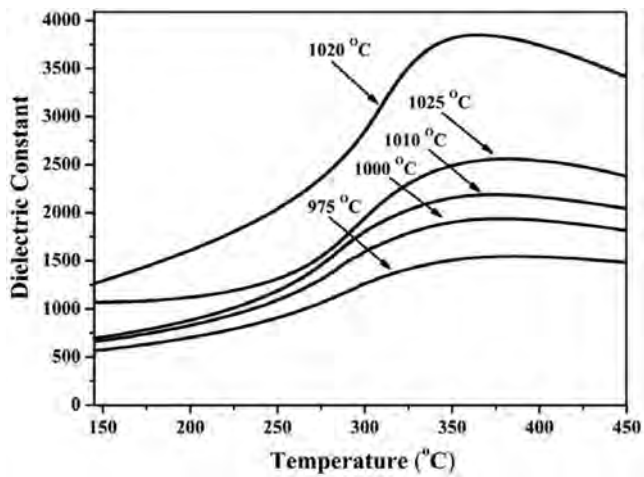


**Figure 3.** Temperature dependence of the dielectric constant of BKT ceramics measured at 10 kHz.

Figure 3 shows the temperature dependence of the dielectric constant ( $\epsilon_r$ ) of BKT ceramics which were measured at 10 kHz. The dielectric constant curve exhibited a broadened peak between 358 and 377°C, which listed in Table 2. This peak can be attributed to the Curie temperature ( $T_c$ ) – the transition temperature from the ferroelectric (FE) to the paraelectric (PE) phase. The different sintering temperatures had the effect on the change in  $T_c$ . It was probable cause by the small change in the lattice parameters and composition. At Curie temperature, the maximum dielectric constant increased from 1546 to 3850 with the increase of sintering temperatures up 1020°C. Above the proper sintering temperature, the dielectric constant decreased as listed in Table 2. The dielectric loss at  $T_c$  is also shown in Table 2. The dielectric properties correspond to the density. The excellent samples, which were sintered at 1020°C for 2 h using the combustion technique, exhibited a high density about 96.3% of the theoretical density and a high dielectric constant at  $T_c$  around 3850. This indicates that a shorter dwell time during the sintering process was obtained using the combustion technique when compared to the solid-state reaction method, which used the dwell time for 20 h to prepare the samples with the highest density [11]. Furthermore, the dielectric properties at  $T_c$  in this study were higher than the previous works, which were prepared by the sol-gel method [8, 12] and sol-gel hydrothermal method [5]. This

**Table 2**

Curie temperature ( $T_c$ ), dielectric constant ( $\epsilon_r$ ), and loss tangent ( $\tan \delta$ ) of BKT ceramics

Sintered temperature (°C)	$T_c$ (°C)	$\epsilon_r$ (at $T_c$ )	$\tan \delta$ (at $T_c$ )
975	377	1546	0.0548
1000	371	1938	0.0521
1010	362	2189	0.0456
1020	358	3850	0.0545
1025	376	2560	0.0829

demonstrated that a liquid medium and high surface energy in the calcinations process [21] resulted in the high quality BKT ceramics.

## Conclusions

Pure BKT ceramics with a high density and a high dielectric constant can be obtained successfully using the combustion method. The sintering temperatures directly affect crystal structure, microstructure, density, and dielectric properties of the sintered ceramics. BKT ceramics were identified as a single phase with a tetragonal perovskite structure in all sintered samples. The average grain size increased with the increase of sintering temperatures. The maximum densities  $\sim 96.3\%$  of the theoretical density and the maximum dielectric constant of 3850 at  $T_c$  were received when the ceramics sintered at the optimal temperature of 1020°C for 2 h.

## Acknowledgments

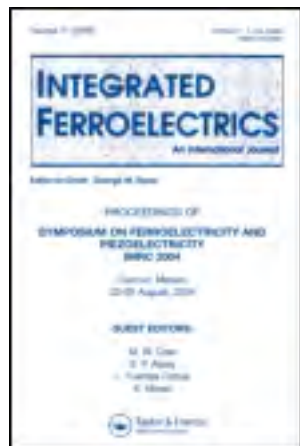
This work was supported financially by the Thailand Research Fund (TRF), Commission on Higher Education (CHE), Faculty of Science, Naresuan University. Thanks also to the Science Lab Center, Faculty of Science, Naresuan University for support facilities.

## References

1. S. Kuharuangrong, Effect of La and K on the microstructure and dielectric properties of  $\text{Bi}_{0.5}\text{Na}_{0.5}\text{TiO}_3\text{--PbTiO}_3$ . *J. Mater. Sci.* **36**, 1727–1733 (2001).
2. Y. Hosono, K. Harada, and Y. Yamashita, Crystal growth and electrical properties of lead free piezoelectric material  $(\text{Na}_{1/2}\text{Bi}_{1/2})\text{TiO}_3\text{--BaTiO}_3$ . *Jpn. J. Appl. Phys.* **40**, 5722–5726 (2001).
3. T. Wada, A. Fukui, and Y. Matsuo, Preparation of  $(\text{K}_{0.5}\text{Bi}_{0.5})\text{TiO}_3$  ceramics by polymerized complex method and their properties. *Jpn. J. Appl. Phys.* **41**(11B), 7025–7028 (2002).
4. Z. F. Li, C. L. Wang, W. L. Zhong, J. C. Li, and M. L. Zhao, Dielectric relaxor properties of  $\text{K}_{0.5}\text{Bi}_{0.5}\text{TiO}_3$  ferroelectrics prepared by sol–gel method. *J. Appl. Phys.* **94**(4), 2548–2552 (2003).
5. L. Hou, Y. D. Hou, X. M. Song, M. K. Zhu, H. Wang, and H. Yan, Sol–gel hydrothermal synthesis and sintering of  $\text{K}_{0.5}\text{Bi}_{0.5}\text{TiO}_3$  nanowires. *Mater. Res. Bull.* **41**, 1330–1336 (2006).
6. G. A. Smolenskii, Dielectric polarization of a number of complex compounds. *Sov. Phys. Solid State.* **1**, 1562–1573 (1959).
7. V. V. Ivanova, A. G. Kapyshev, Y. N. Venetsev, and V. S. Zhdanov, X-ray determination of the symmetry of elementary cells of the ferroelectric materials  $\text{K}_{0.5}\text{Bi}_{0.5}\text{TiO}_3$  and  $\text{Na}_{0.5}\text{Bi}_{0.5}\text{TiO}_3$  and of high temperature phase transition in  $\text{K}_{0.5}\text{Bi}_{0.5}\text{TiO}_3$ . *Izv. Akad. Nauk SSSR. Ser. Fiz.* **26**, 354–356 (1962).
8. M. Zhu, L. Hou, Y. Hou, J. Liu, H. Wang, and H. Yan, Lead-free  $(\text{K}_{0.5}\text{Bi}_{0.5})\text{TiO}_3$  powders and ceramics prepared by a sol–gel method. *Mater. Chem. Phys.* **99**, 329–332 (2006).
9. C. H. Yang, Z. Wang, H. Y. Xu, Z. H. Sun, F. Y. Jiang, J. P. Zh, and J. R. Han, Preparation and main characteristics of lead-free  $\text{K}_{0.5}\text{Bi}_{0.5}\text{TiO}_3$  ferroelectric thin films. *J. Crystal Growth.* **262**, 304–307 (2004).
10. T. Zaremba, Application of thermal analysis to study of the synthesis of  $\text{K}_{0.5}\text{Bi}_{0.5}\text{TiO}_3$  ferroelectric. *J. Therm. Anal. Calorim.* **74**, 653–658 (2003).
11. J. König, M. Spreitzer, B. Jancar, D. Suvorov, Z. Samardzija, and A. Popovic, The thermal decomposition of  $\text{K}_{0.5}\text{Bi}_{0.5}\text{TiO}_3$  ceramics. *J. Eur. Ceram. Soc.* **29**, 1695–1701 (2009).
12. Y. Hou, M. Zhu, L. Hou, J. Liu, J. Tang, H. Wang, and H. Yan, Synthesis and characterization of lead-free  $\text{K}_{0.5}\text{Bi}_{0.5}\text{TiO}_3$  ferroelectrics by sol–gel technique. *J. Crystal Growth.* **273**, 500–503 (2005).



13. O. Z. Yanchevskii, O. I. V. Yunov, and A. G. Belooous, Fabrication and properties of semiconducting barium lead titanate ceramics containing low-melting glass additions. *Inorg. Mater.* **39**, 645–651 (2003).
14. P. R. Arya, P. Jha, G. N. Subbanna, and A. K. Ganguli, Polymeric citrate precursor route to the synthesis of nano-sized barium lead titanates. *Mater. Res. Bull.* **38**, 617–628 (2003).
15. R. E. Vold, R. Biederman, G. A. Rossetti, and A. Sacco, Hydrothermal synthesis of lead doped barium titanate. *J. Mater. Sci.* **36**, 2019–2026 (2001).
16. A. Thongtha, and T. Bongkarn, Phase formation and microstructure of barium zirconate ceramics prepared using the combustion technique. *Ferroelectrics* **383**, 33–39 (2009).
17. A. Thongtha, and T. Bongkarn, Fabrication and characterization of perovskite  $\text{SrZrO}_3$  ceramics through a combustion technique. *Key. Eng. Mater.* **421–422**, 223–226 (2010).
18. P. Panya, and T. Bongkarn, Fabrication of perovskite barium titanate ceramics using combustion route. *Ferroelectrics* **383**, 102–110 (2009).
19. A. Thongtha, and T. Bongkarn, Effect of firing temperatures on phase and morphology evolution of  $\text{CaZrO}_3$  ceramics synthesized using the combustion technique. *Ferroelectrics* **403**, 3–10 (2010).
20. P. Julphunthong, and T. Bongkarn, Phase formation, microstructure and dielectric properties of  $\text{Ba}(\text{Zr}_{0.1}\text{Ti}_{0.9})\text{O}_3$  ceramics prepared via the combustion technique. *Curr. Appl. Phys.* **11**, S60–S65 (2011).
21. A. Thongtha, K. Angsukased, and T. Bongkarn, Fabrication of  $(\text{Ba}_{1-x}\text{Sr}_x)(\text{Ti}_{1-x}\text{Zr}_x)\text{O}_3$  ceramics prepared using the combustion technique. *Smart. Mater. Struct.* **19**, 124001 (2010).
22. D. Xue, J. Xu and C. Yan, Chemical synthesis of  $\text{NaTaO}_3$  powder at low-temperature. *Mater. Lett.* **59**, 2920–2922 (2005).
23. K. C. Patil, S. T. Aruna, and S. Ekambaram, Combustion synthesis. *Curr. Opin. Solid State Mater. Sci.* **2**, 156–165 (1997).
24. S. Eitssayeam, U. Intatha, K. Pengpat, G. Rujjanagul, K. J. D. MacKanzie, and T. Tunkasiri, Effect of the solid-state synthesis parameters on the physical and electronic properties of perovskite-type  $\text{Ba}(\text{Fe,Nb})_{0.5}\text{O}_3$  ceramics. *Curr. Appl. Phys.* **9**, 993–996 (2009).
25. R. M. German, Sintering Theory and Practice. *New York. Wiley.* (1996).
26. B. Guillaume, F. Boschini, I. C. Cano, A. Rulmont, R. Cloots, and M. Ausloos, Optimization of  $\text{BaZrO}_3$  sintering by control of the initial powder size distribution; a factorial design statistical analysis. *J. Eur. Ceram. Soc.* **25**, 3593–3604 (2005).



## Integrated Ferroelectrics: An International Journal

Publication details, including instructions for authors and subscription information:

<http://www.tandfonline.com/loi/ginf20>

### The Effect of Firing Temperatures on $(\text{Pb}_{0.75}\text{Ba}_{0.25})(\text{Zr}_{0.70}\text{Ti}_{0.30})\text{O}_3$ Ceramics Prepared via the Combustion Technique

Panadda Sittiketkorn<sup>a b</sup>, Pongkiti Wongtey<sup>a</sup>, Naratip Vittayakorn<sup>c</sup> & Theerachai Bongkarn<sup>a b</sup>

<sup>a</sup> Department of Physics, Faculty of Science, Naresuan University, Phitsanulok, 65000, Thailand

<sup>b</sup> Research Center for Academic Excellence in Applied Physics, Naresuan University, Phitsanulok, 65000, Thailand

<sup>c</sup> Materials Science Research Unit, Department of Chemistry, Faculty of Science, King Mongkut's Institute of Technology Ladkrabang, Bangkok, 10520, Thailand

Published online: 07 Dec 2013.

To cite this article: Panadda Sittiketkorn, Pongkiti Wongtey, Naratip Vittayakorn & Theerachai Bongkarn (2013) The Effect of Firing Temperatures on  $(\text{Pb}_{0.75}\text{Ba}_{0.25})(\text{Zr}_{0.70}\text{Ti}_{0.30})\text{O}_3$  Ceramics Prepared via the Combustion Technique, Integrated Ferroelectrics: An International Journal, 149:1, 39-48, DOI: [10.1080/10584587.2013.852925](https://doi.org/10.1080/10584587.2013.852925)

To link to this article: <http://dx.doi.org/10.1080/10584587.2013.852925>

PLEASE SCROLL DOWN FOR ARTICLE

Taylor & Francis makes every effort to ensure the accuracy of all the information (the "Content") contained in the publications on our platform. However, Taylor & Francis, our agents, and our licensors make no representations or warranties whatsoever as to the accuracy, completeness, or suitability for any purpose of the Content. Any opinions and views expressed in this publication are the opinions and views of the authors, and are not the views of or endorsed by Taylor & Francis. The accuracy of the Content should not be relied upon and should be independently verified with primary sources of information. Taylor and Francis shall not be liable for any losses, actions, claims, proceedings, demands, costs, expenses, damages, and other liabilities whatsoever or howsoever caused arising directly or indirectly in connection with, in relation to or arising out of the use of the Content.

This article may be used for research, teaching, and private study purposes. Any substantial or systematic reproduction, redistribution, reselling, loan, sub-licensing,

systematic supply, or distribution in any form to anyone is expressly forbidden. Terms & Conditions of access and use can be found at <http://www.tandfonline.com/page/terms-and-conditions>

# The Effect of Firing Temperatures on $(\text{Pb}_{0.75}\text{Ba}_{0.25})(\text{Zr}_{0.70}\text{Ti}_{0.30})\text{O}_3$ Ceramics Prepared via the Combustion Technique

PANADDA SITTIKETKORN,<sup>1,2</sup> PONGKITI WONGTEY,<sup>1</sup>  
NARATIP VITTAYAKORN,<sup>3</sup> AND  
THEERACHAI BONGKARN<sup>1,2,\*</sup>

<sup>1</sup>Department of Physics, Faculty of Science, Naresuan University, Phitsanulok,  
65000, Thailand

<sup>2</sup>Research Center for Academic Excellence in Applied Physics, Naresuan  
University, Phitsanulok, 65000, Thailand

<sup>3</sup>Materials Science Research Unit, Department of Chemistry, Faculty of Science,  
King Mongkut's Institute of Technology Ladkrabang, Bangkok 10520, Thailand

*The  $(\text{Pb}_{0.75}\text{Ba}_{0.25})(\text{Zr}_{0.70}\text{Ti}_{0.30})\text{O}_3$  (PBZT) ceramics were prepared via the combustion technique.  $(\text{CO}(\text{NH}_2)_2)$  was used as a fuel. The effect of firing temperature on PBZT's phase formation, microstructure and electrical properties were investigated. The calcination and sintering temperatures were  $600^\circ\text{C}$ – $1000^\circ\text{C}$  and  $1100^\circ\text{C}$ – $1300^\circ\text{C}$ . The pure rhombohedral perovskite was obtained from the powders calcined at  $850^\circ\text{C}$ . The average particle size tended to increase with increased calcination temperatures. A pure rhombohedral perovskite phase was found in all pellet samples. The average grain size and linear shrinkage tended to increase from  $0.57$  to  $2.15\ \mu\text{m}$  and from  $6.8$  to  $15.8\%$  with increased sintering temperatures. The dielectric results indicated the relaxer behavior of PBZT ceramics. The Curie temperature tended to decrease with increasing sintering temperatures. The highest density ( $\sim 7.39\ \text{g/cm}^3$ ) and highest dielectric constant ( $\sim 8620$ ) were obtained by using the combustion technique which was higher than the conventional mixed oxide method.*

**Keywords** Lead barium zirconate titanate; phase formation; microstructure; electrical properties; combustion technique

## Introduction

Lead barium zirconate titanate perovskite ferroelectric ceramics are widely applied in multilayer capacitors and sensors because of their excellent electrical properties. The structural phase transitions occurring in these ceramics and their dielectric properties are strongly dependent on both the Zr/Ti ratio and Ba contents [1, 2]. The dielectric properties of  $(\text{Pb}_{0.75}\text{Ba}_{0.25})(\text{Zr}_{0.70}\text{Ti}_{0.30})\text{O}_3$  (PBZT) ceramics have been broadly investigated and these ceramics exhibit relaxer ferroelectrics behavior [3, 4].

In previous works,  $(\text{Pb}_{0.75}\text{Ba}_{0.25})(\text{Zr}_{0.70}\text{Ti}_{0.30})\text{O}_3$  ceramics were successfully prepared by the conventional mixed oxides method using a calcination temperature of  $925^\circ\text{C}$  for 2 h

Received December 9, 2012; in final form August 25, 2013.

\*Corresponding author. E-mail: researchcmu@yahoo.com

and two sintering temperatures of 1250°C and 1300°C [3–6]. This creates problems with the vaporization of the PbO during firing because of the low melting point of PbO which is about 850°C, and possible lead deficiency which may cause large pores from the microstructure and have a subsequent effect on densification. The combustion method has much interest; at present, it helps to decrease the temperature in the preparation and has a small particle size [7–9]. The combustion technique also has interesting characteristics such as: its simplicity, its relatively low cost and the fact that it usually results in products with the desired structure and composition [10]. Thus, in this work,  $(\text{Pb}_{0.75}\text{Ba}_{0.25})(\text{Zr}_{0.70}\text{Ti}_{0.30})\text{O}_3$  (PBZT) ceramics were prepared via the combustion technique. The effect of firing temperatures on its phase formation, microstructure, ferroelectric and dielectric properties was investigated.

## Experimental

$(\text{Pb}_{0.75}\text{Ba}_{0.25})(\text{Zr}_{0.70}\text{Ti}_{0.30})\text{O}_3$  (PBZT) was fabricated using the combustion technique. PbO, BaCO<sub>3</sub>, ZrO<sub>2</sub> and TiO<sub>2</sub> powders were used as starting materials. The powders were mixed by ball milling for 24 h with ethanol as a solution media. The mixed powders were dried at 120°C for 6 h. Prior to sieving, the powders and urea were mixed and crushed in an agate mortar, then calcined between 600°C and 1000°C for 2 h. The calcined powders were reground by wet ball milling with 2 wt% binder for 24 h. The obtained powders were pressed into pellets with a diameter of 15 mm prior to sintering between 1100°C and 1300°C for 2 h. The reaction of uncalcined PBZT powders and urea fuel taking place during heat treatment were investigated by thermogravimetric (TG) and differential thermogravimetric (DTG). X-ray diffraction (XRD) was performed to examine the phase constitution of the specimens at room temperature. The microstructures of the PBZT samples were examined using scanning electron microscopy (SEM). The densities of the sintered ceramics were measured by the Archimedes's method and the average grain size was determined by using a mean linear intercept method. The polarization–electric field ( $P$ – $E$ ) hysteresis loop, under 35 kV/cm was obtained using a Radiant Technologies (Version: 4.1.1). Dielectric measurements were performed using an LCR meter (Agilent 4263B), and the measuring frequency was 1, 10, 100 and 500 kHz.

## Results and Discussion

The TG-DTG curves of the uncalcined powders of PBZT and urea are illustrated in Fig. 1. From the curve of thermogravimetric analysis, three-stage weight losses were observed. The first weight loss occurred between 150 and 200°C, corresponding to the endothermic peak at 181°C in the DTG curve. This phenomenon related to the decomposition reaction of urea to ammonia, vapor and gasses as shown in the Formula (1) (decomposition temperature of urea is 135°C [11]). The second weight loss occurred between 300 and 500°C which corresponds to the endothermic peak at 320, 385, 446°C in the DTG curve. These can be attributed to the vaporization of water and gas caused by the oxidation-reduction reaction between ammonia and NO as exhibited in the Formula (2) [10, 12]. The energy was released from the combustion reaction in these two steps, supplied and accelerated the chemical reaction of raw materials. The third weight loss occurred above 600°C and corresponded to the endothermic peak at 800°C in the DTG curve, which is associated with the chemical reaction between PbO, BaCO<sub>3</sub>, ZrO<sub>2</sub> and TiO<sub>2</sub>. As temperature reached up to 850°C, its weight loss was reduced to 32.25% of its original weight. This confirms the decomposition processes of urea (66.66%) following the Formula (1) and (2) and CO<sub>2</sub> (1.08%), which

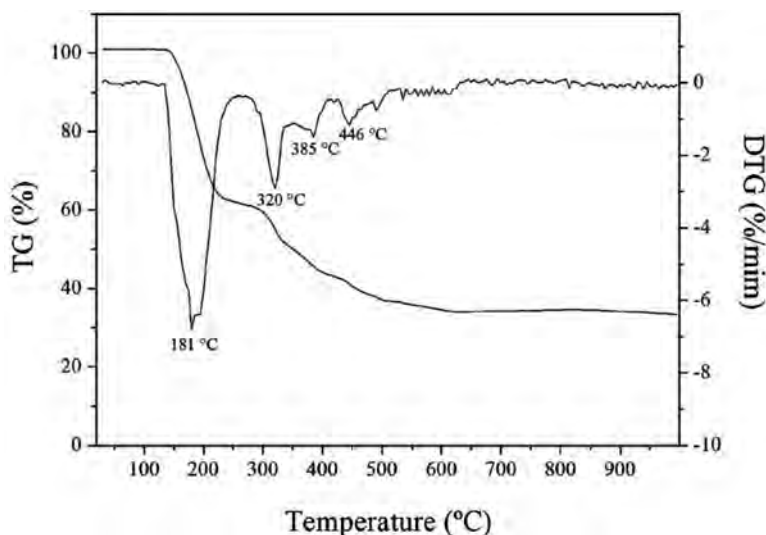
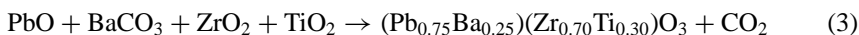
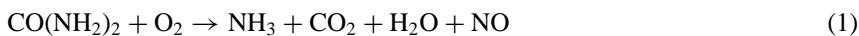


**Figure 1.** The TG-DTG curves of the uncalcined powders of PBZT and urea.

produced from the chemical reaction of raw materials following the Formula (3) were existed. These results were used to estimate the calcinations temperature started at 850°C.



The XRD pattern of the PBZT powders at various calcined temperatures are given in Fig. 2. It was found that the PBZT powders indexed in a rhombohedral structure, which could be matched with JCPDS file number 73-2022 [13]. The samples calcined below 850°C impurity phases of PbO, PbO<sub>2</sub>, TiO, ZrO, ZrO<sub>2</sub> and BaTiO<sub>3</sub> were detected (Fig. 2). The pure rhombohedral perovskite was obtained from the powders calcined at 850°C. The relative percentage in the perovskite and impurity phases were determined by measuring the major XRD peak intensities of the perovskite and impurity phases. The XRD results corresponded with the TG-DTG results. The percentage of the perovskite phase was estimated by the following equation:

$$\% \text{ perovskite phase} = \left( \frac{I_{\text{perov}}}{I_{\text{perov}} + I_{\text{PbO}} + I_{\text{PbO}_2} + I_{\text{TiO}} + I_{\text{ZrO}} + I_{\text{ZrO}_2} + I_{\text{BaTiO}_3}} \right) \times 100 \quad (4)$$

This equation is a well-known equation which is widely employed in the preparation of complex perovskite structure materials [14]. Here  $I_{\text{perov}}$ ,  $I_{\text{PbO}}$ ,  $I_{\text{PbO}_2}$ ,  $I_{\text{TiO}}$ ,  $I_{\text{ZrO}}$ ,  $I_{\text{ZrO}_2}$  and  $I_{\text{BaTiO}_3}$  refer to the intensity of the (110) perovskite peak, and the highest intensities of PbO, PbO<sub>2</sub>, TiO, ZrO, ZrO<sub>2</sub> and BaTiO<sub>3</sub>. The percent perovskite phase increased with an increase of the calcining temperature as seen in Fig. 3. It was clearly seen that urea played an important role in reducing calcination

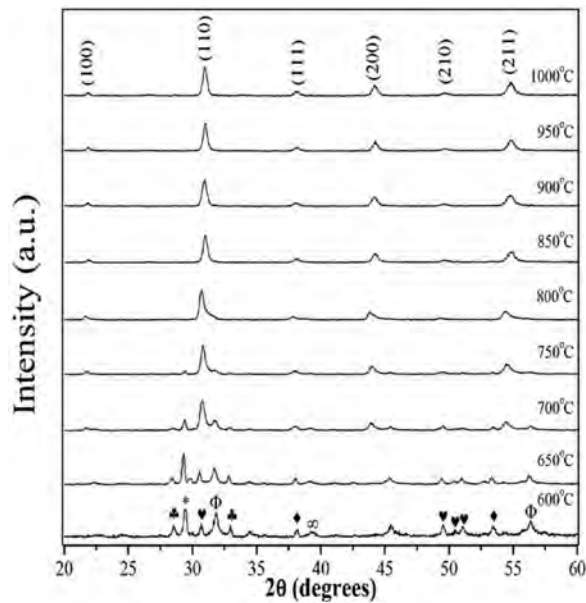


**Figure 2.** XRD patterns of PBZT powders at various calcinations temperatures; (\*) PbO, (♣) PbO<sub>2</sub>, (♦) TiO, (∞) ZrO, (♥) ZrO<sub>2</sub> and (Φ) BaTiO<sub>3</sub>.

temperatures. The calcination temperature of PBZT powders synthesized via the combustion technique, using urea as a fuel was lower than the conventional mixed oxide method by around 75°C, which is nearly the melting point of PbO. This decreased PbO evaporation [15]. The SEM photomicrographs of PBZT powders calcined at various temperatures are

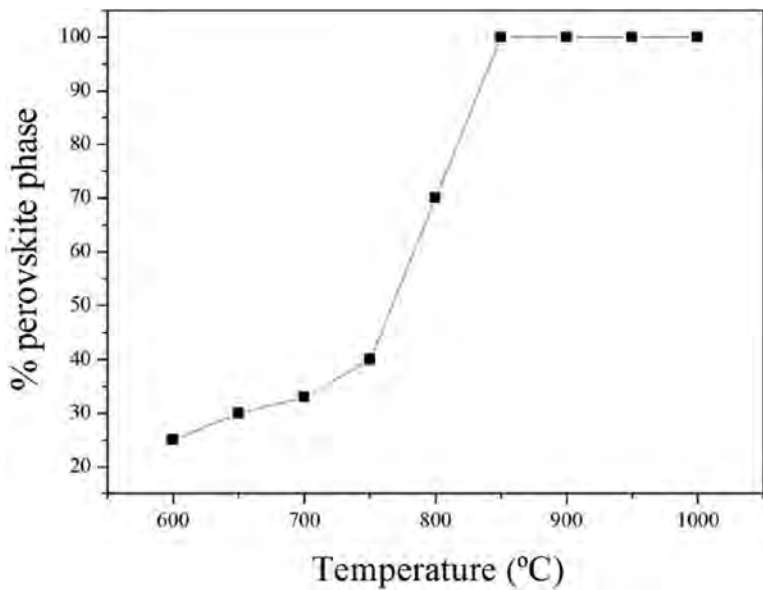


**Figure 3.** The percent perovskite phase of PBZT powders at various calcination temperatures.

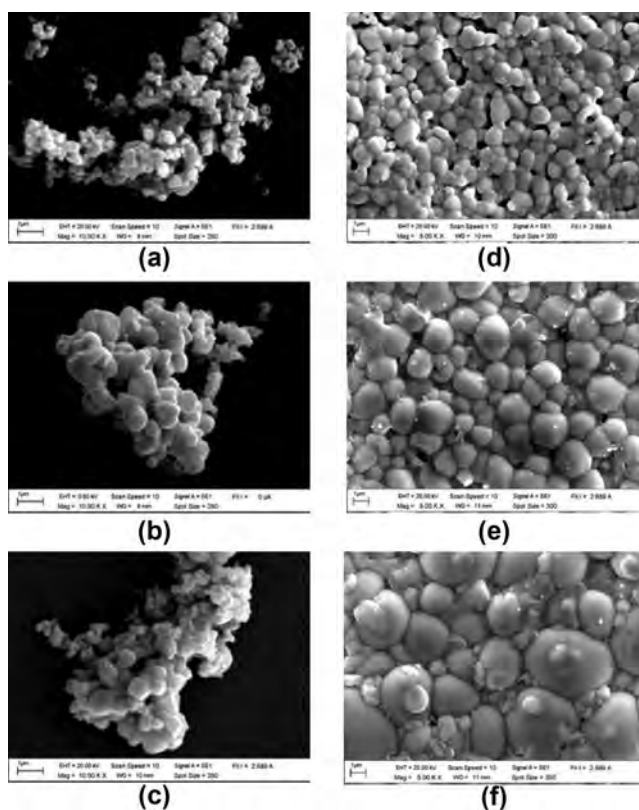


**Figure 4.** SEM morphology of PBZT powders calcined at (a) 750°C, (b) 850°C, (c) 950°C and ceramics sintered at (d) 1150°C, (e) 1250°C and (f) 1300°C.

illustrated in Fig. 4(a), (b) and (c). These powders exhibited an almost spherical morphology and have a porous agglomerate. The particle size, which is calculated from the cutting lines in SEM, ranging from 0.25 to 0.58  $\mu\text{m}$ . The average particle size tended to increase with an increased calcination temperatures.

The PBZT powders, using urea as a fuel, calcined at 850°C were pressed into pellets and sintered between 1100 and 1300°C. Fig. 5 shows the XRD patterns of PBZT ceramics at various sintering temperatures. A pure rhombohedral perovskite phase was found in all pellet samples. Fig. 4(d)–(f) shows the microstructure of ceramics at various sintering temperatures. The grains were nearly spherical in shape. It was found that increasing sintering temperatures helped grain size grow. The average grain sizes increased from 0.57 to 2.15  $\mu\text{m}$  (Table 1). A porous microstructure with small grain size was observed in the PBZT sintered at 1100°C and 1150°C. The increase of sintering temperature significantly promoted the grain growth and microstructure densification. However, at the sintering temperature above 1300°C, the grain uniformity decreased and small grains at the conjunction of the grain boundary began to melt.

The shrinkage and density of PBZT sintered ceramics are listed in Table 1. The shrinkage increased with an increase in sintering temperatures. The density increased with increasing sintering temperatures, reached a maximum value at 1300°C and decreased after increasing the sintering temperature. The low density occurring in low sintered temperature



**Table 1**  
The average grain size, shrinkage, density, ferroelectric properties,  $T_c$  and dielectric properties of PBZT ceramics

Sintered temperature (°C)	Average grain size (μm)	Shrinkage (%)	Density (g/cm <sup>3</sup> )	Ferroelectric properties			Loop squareness ( <i>R</i> <sub>sq</sub> )	Curie temperature (°C)	Dielectric constant at <i>T</i> <sub>c</sub>	Loss factor at <i>T</i> <sub>c</sub>
				<i>P</i> <sub>r</sub> (μC cm <sup>-2</sup> )	<i>P</i> <sub>s</sub> (μC cm <sup>-2</sup> )	<i>E</i> <sub>c</sub> (kV cm <sup>-1</sup> )				
1100	0.57	6.8	7.22	—	—	—	—	160	2110	0.058
1150	0.76	11.9	7.25	—	—	—	—	156	4220	0.096
1200	1.14	15.6	7.27	8.2	20.4	7	0.64	131	7880	0.011
1250	1.61	15.7	7.36	11.8	24.1	7.8	0.72	132	7940	0.005
1300	2.15	15.8	7.39	16.1	26.9	7.4	0.82	132	8620	0.064

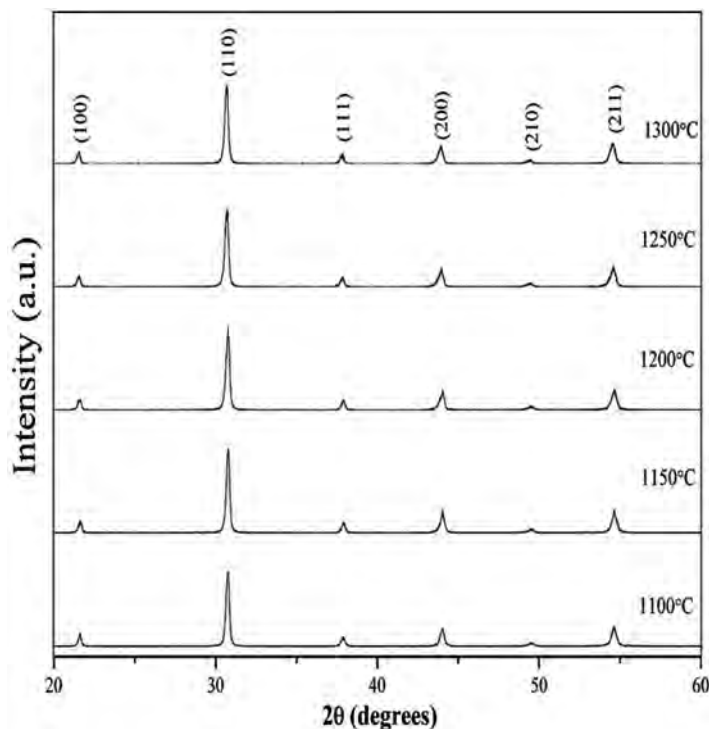


**Figure 5.** XRD patterns of PBZT ceramics using urea as fuel at various sintering temperatures.

samples was due to the preexisting porosity as seen in Fig. 4(d). The evaporation of PbO caused the low density in the high sintering temperature samples which related to the grains melting.

The relationships between polarization and electric field for PBZT ceramics samples sintered at different temperatures are demonstrated in Fig. 6. A slim-loop characteristic was found for these samples. The value of  $P_r$  (the polarization) increased with increasing sintering temperatures (Table 1). While the value of  $E_c$  (the coercive field) increased with sintering temperatures up to 1250°C. The value of  $E_c$  was reduced when sintering temperature increased. The hysteresis loop of the ceramics sintered at a low temperature was immeasurable, which was due to the low resistivity of the samples.

Figure 7 shows the dielectric constant of PBZT ceramics sintered at 1300°C, when the measuring frequency was 1, 10, 100 and 500 kHz. The dielectric constant decreased with increasing frequency. The results indicated the relaxor behaviour of PBZT ceramics. The dielectric constant of PBZT ceramics at various sintering temperature, measured at 1 kHz is shown Fig. 8. The dielectric constant curve of PBZT ceramics is broad at low sintering temperatures and sharper at higher sintering temperatures. The Curie temperature ( $T_c$ ) tended to decrease with increasing sintering temperatures as listed in Table 1. A similar result has been reported by in PZT, PZ and PBZ ceramics [8,15]. The maximum dielectric constant increased with increasing sintering temperatures (Table 1). The loss factor at  $T_c$  tended to decreased with increased sintering temperatures up to 1250°C. and increased after further sintering at a higher temperature (1300°C). However, when the sintering temperature was over 1300°C, the PBZT ceramics became very fragile. The highest density, a high

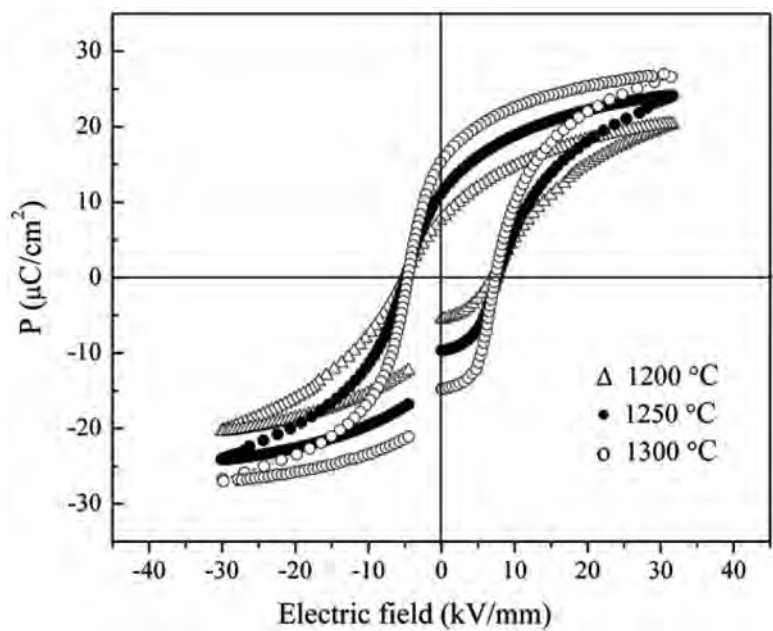


**Figure 6.**  $P$ - $E$  hysteresis loop of PBZT ceramics at various sintering temperatures, measured at an electric field of 35 kV/cm.

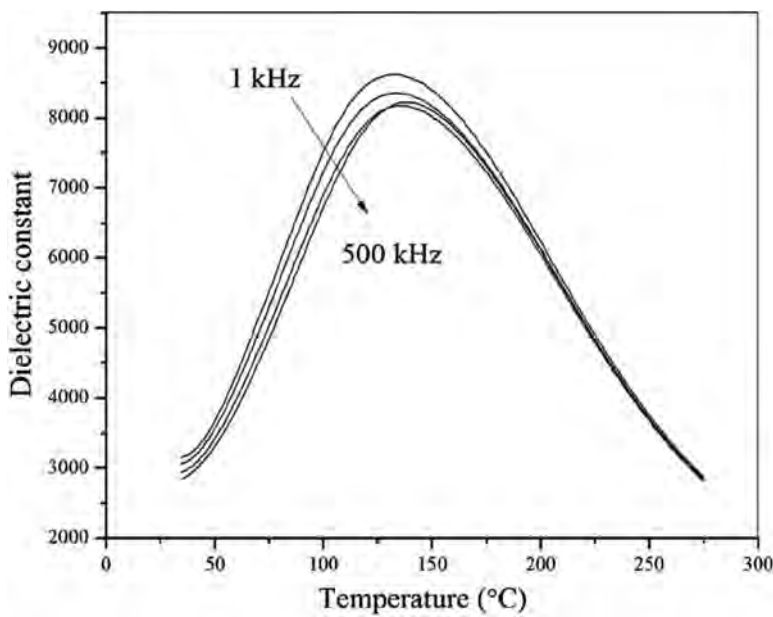


**Figure 7.** Dielectric constant of PBZT ceramics sintered at 1300 °C as a function of temperatures at frequencies of 1, 10, 100 and 500 kHz.

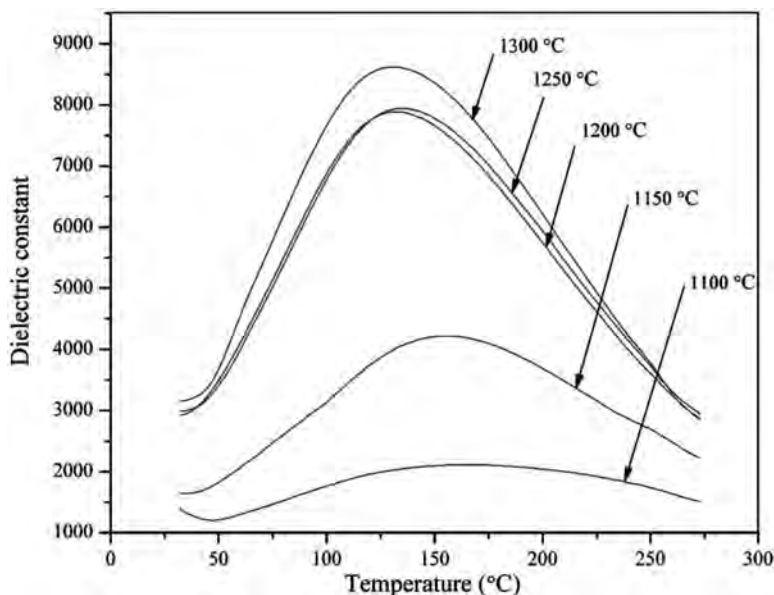


**Figure 8.** Dielectric constant of PBZT ceramics at various sintering temperatures, measured at 1 kHz.

dielectric constant and the lowest loss factor of the PBZT ceramics obtained by using urea as fuel, at calcinations temperature of 850°C and sintering temperatures of 1300°C, should be the proper condition using for the combustion technique. The conventional mixed oxide method uses higher firing temperatures (calcinations at 925°C and two sintering temperatures at 1250°C and 1300°C), but achieves a lower density (6.8 g/cm<sup>3</sup>) and lower dielectric properties (the dielectric constant ~5500 and loss factor ~0.080) [3]. These confirmed that the combustion technique is simple and inexpensive for fabricating high quality ferroelectric PBZT ceramics.

## Conclusions

The high quality PBZT ceramics were successfully prepared by the combustion technique using urea as a fuel. The optimum calcination and sintering temperatures were 850°C and 1300°C. They were lower than the conventional mixed oxide method and had a higher density and greater dielectric properties. The firing temperatures directly affected the phase formation, microstructure, density, ferroelectric and dielectric properties.

## Acknowledgments

This work was financially supported by the Thailand Research Fund (TRF), Commission on Higher Education (CHE). The authors wish to thanks the Science Lab Center, Faculty of Science, Naresuan University for supporting facilities. Thanks are also given to Mr. Don Hindle for his help in editing the manuscript.

## References

1. W. Chaisan, R. Yimnirun, S. Ananta, and D. P. Cann, Phase development and dielectric properties of  $(1-x)\text{Pb}(\text{Zr}_{0.52}\text{Ti}_{0.48})\text{O}_3$ - $x\text{BaTiO}_3$  ceramics. *Mater. Sci. Eng. B*. **132**, 300–306 (2006).
2. W. Chaisan, R. Yimnirun, S. Ananta, and D. P. Cann, Dielectric and ferroelectric properties of lead zirconate titanate-barium titanate ceramics prepared by a modified mixed-oxide method. *Mater. Chem. Phys.* **104**, 113–118 (2007).
3. M. Adamczyk, Z. Ujama, L. Szymczak, and A. Sozynski, Influence of external electric field on relaxor behaviour of  $(\text{Pb}_{0.75}\text{Ba}_{0.25})(\text{Zr}_{0.52}\text{Ti}_{0.48})\text{O}_3$  ceramics. *Ceram. Int.* **32**, 877–881 (2006).
4. M. Adamczyk, Influence of lanthanum and niobium doping on the relaxor behaviour of  $(\text{Pb}_{0.75}\text{Ba}_{0.25})(\text{Zr}_{0.52}\text{Ti}_{0.48})\text{O}_3$  ceramics. *Ceram. Int.* **32**, 923–928 (2006).
5. M. Adamczyk, Z. Ujama, L. Szymczak, and I. Gruszka, Influence Effect of Nb doping on the relaxor behaviour of  $(\text{Pb}_{0.75}\text{Ba}_{0.25})(\text{Zr}_{0.52}\text{Ti}_{0.48})\text{O}_3$  ceramics. *J. Eur. Ceram. Soc.* **26**, 331–336 (2006).
6. M. Adamczyk, Z. Ujama, L. Szymczak, and J. Koperski, Influence of post-sintering annealing on the relaxor behaviour of  $(\text{Pb}_{0.75}\text{Ba}_{0.25})(\text{Zr}_{0.52}\text{Ti}_{0.48})\text{O}_3$  ceramics. *Ceram. Int.* **31**, 791–794 (2005).
7. A. Thongtha, and T. Bongkarn, Phase formation and microstructure of barium zirconate ceramics prepared using the combustion technique. *Ferroelectrics*. **383**, 33–39 (2009).
8. T. Bongkarn, and W. Tangkawsakul, Low temperature preparation of antiferroelectric PZ and PBZ powders using the combustion technique. *Ferroelectrics*. **383**, 50–56 (2009).
9. P. Panya, and T. Bongkarn, Fabrication of perovskite barium titanate ceramics using the combustion route. *Ferroelectrics*. **383**, 102–110 (2009).
10. A. Thongtha, and T. Bongkarn, Fabrication and characterization of perovskite  $\text{SrZrO}_3$  ceramics through a combustion technique. *Key Eng Mater.* **421–422**, 233–226 (2010).
11. D. Xue, J. Xu, and C. Yan, Chemical synthesis of  $\text{NaTaO}_3$  powder at low temperature. *Mater. Lett.* **59**, 2920–2922 (2005).
12. C. C. Hwang, T. Y. Wu, J. Wan, and J. S. Tsai, Development of a novel combustion synthesis method for synthesizing of ceramic oxide powders. *Mater. Sci. Eng. B* **111**, 49–56 (2004).
13. Powders diffraction File no.73–2022, International Center Diffraction Data. Newton Square, PA, 2003.
14. A. Thongtha, A. Angsukased, and T. Bongkarn, Influences of firing temperature on phase and morphology evolution of  $(\text{Ba}_{0.5}\text{Sr}_{0.5})(\text{Zr}_{0.75}\text{Ti}_{0.25})\text{O}_3$  ceramics synthesized via solid-state reaction method. *Key Eng Mater.* **421–422**, 247–250 (2010).
15. R. Sumang, and T. Bongkarn, Effect of sintering temperature on the crystal structure, microstructure and phase transition of  $(\text{Pb}_{1-x}\text{Sr}_x)\text{TiO}_3$  ceramics. *Func. Mater. Lett.* **4**, 193–197 (2009).
16. R. Yimnirun, R. Tipakontitkul, and S. Ananta, Effect of sintering temperature on densification and dielectric properties of  $\text{Pb}(\text{Zr}_{0.44}\text{Ti}_{0.56})\text{O}_3$  ceramics. *Int. J. Modern. Phys. B* **17**, 2415–2424 (2006).



## Ferroelectrics

Publication details, including instructions for authors and subscription information:

<http://www.tandfonline.com/loi/gfer20>

### Phase Evolution, Microstructure and Dielectric Properties of $\text{CaCu}_3\text{Ti}_4\text{O}_{12}$ Ceramics Fabricated by Combustion Technique

Atthakorn Thongtha<sup>a</sup>, Artid Laowanidwatana<sup>a</sup> & Theerachai Bongkarn<sup>a</sup>

<sup>a</sup> Department of Physics, Faculty of Science, Naresuan University, Phitsanulok, 65000, Thailand; and Research Center for Academic Excellence in Applied Physics, Naresuan University, Phitsanulok, 65000, Thailand

Published online: 09 Dec 2013.

To cite this article: Atthakorn Thongtha, Artid Laowanidwatana & Theerachai Bongkarn (2013) Phase Evolution, Microstructure and Dielectric Properties of  $\text{CaCu}_3\text{Ti}_4\text{O}_{12}$  Ceramics Fabricated by Combustion Technique, *Ferroelectrics*, 457:1, 23-29, DOI: [10.1080/00150193.2013.846757](https://doi.org/10.1080/00150193.2013.846757)

To link to this article: <http://dx.doi.org/10.1080/00150193.2013.846757>

PLEASE SCROLL DOWN FOR ARTICLE

Taylor & Francis makes every effort to ensure the accuracy of all the information (the "Content") contained in the publications on our platform. However, Taylor & Francis, our agents, and our licensors make no representations or warranties whatsoever as to the accuracy, completeness, or suitability for any purpose of the Content. Any opinions and views expressed in this publication are the opinions and views of the authors, and are not the views of or endorsed by Taylor & Francis. The accuracy of the Content should not be relied upon and should be independently verified with primary sources of information. Taylor and Francis shall not be liable for any losses, actions, claims, proceedings, demands, costs, expenses, damages, and other liabilities whatsoever or howsoever caused arising directly or indirectly in connection with, in relation to or arising out of the use of the Content.

This article may be used for research, teaching, and private study purposes. Any substantial or systematic reproduction, redistribution, reselling, loan, sub-licensing, systematic supply, or distribution in any form to anyone is expressly forbidden. Terms &



# Phase Evolution, Microstructure and Dielectric Properties of $\text{CaCu}_3\text{Ti}_4\text{O}_{12}$ Ceramics Fabricated by Combustion Technique

ATTHAKORN THONGTHA, ARTID LAOWANIDWATANA,  
AND THEERACHAI BONGKARN\*

Department of Physics, Faculty of Science, Naresuan University, Phitsanulok, 65000, Thailand; and Research Center for Academic Excellence in Applied Physics, Naresuan University, Phitsanulok, 65000, Thailand

*The effects of calcination temperature (750–1000 °C) and sintering temperature (1000–1125°C) on phase evolution, microstructure and the dielectric properties of  $\text{CaCu}_3\text{Ti}_4\text{O}_{12}$  (CCTO) ceramics were investigated. CCTO powders were synthesized by the combustion technique. The pure cubic perovskite phase of CCTO powders was detected above a calcination temperature of 950°C and it was also obtained from the ceramics sintered below 1125°C. The lattice parameter  $a$  of CCTO powder (7.3829–7.3870 Å) and ceramic (7.3721–7.3857 Å) increased with the higher firing temperatures. The increasing of the average particle size and the average grain size of samples was caused by the increase of firing temperatures. The highest density was ~96% of the theoretical density, and was obtained from the sample sintered at 1100°C for 2 h. This sample also exhibited a maximum dielectric constant of approximately 29664 and a low dielectric loss of about 0.0925. Most importantly, the combustion fuel (glycine) carried out an important role by reducing the dwell time and improving the density and dielectric properties.*

**Keywords**  $\text{CaCu}_3\text{Ti}_4\text{O}_{12}$ ; combustion technique; giant dielectric

## Introduction

$\text{CaCu}_3\text{Ti}_4\text{O}_{12}$  (CCTO) [1,2] is a material with a large dielectric constant, a low loss tangent, and belongs to a family of the type,  $\text{ACu}_3\text{Ti}_4\text{O}_{12}$  (where A=Ca or Cd). CCTO was first reported by Deschanvres et al. in 1967 [2]. It is a non-ferroelectric ceramic with a body-centered cubic structure at room temperature [3] and exhibits an anomalous high dielectric constant (~10,000) at 1 kHz [1]. This makes this ceramic an interesting candidate for technological applications such as: capacitors, resonators, and filters.

CCTO preparation is cumbersome and it is difficult to obtain a high chemical homogeneity. CCTO is generally prepared by the conventional solid-state method [4–6]. It is calcined at a high temperature for long periods (typically 1000–1050°C for 24–48 h) with repeated intermediate grindings. To reduce the calcination temperature and the dwell time,

---

Received December 11, 2012; in final form March 16, 2013.

\*Corresponding author: Tel.: +66-5596-3528, Fax: +66-5596-3501. E-mail: researchcmu@yahoo.com



CCTO powders were fabricated by the coprecipitation method [7], which used a calcination temperature of 900°C for 10 h. Unfortunately, impurity phases were found from both early reported methods.

To obtain high chemical homogeneity, various methods such as: the conventional solid-state reaction method [8–10], the microwave synthesis [10], the molten salts method [11] and the sol-gel method [12–14] have been developed to fabricate CCTO samples. Using the solid state reaction method, the powder is calcined at 1000°C for 24 h. This procedure is repeated three times and then the samples that exhibit the dielectric constant ( $\epsilon_r$ )  $\sim 10240$  at 1 kHz are sintered at the specific temperatures of 1100°C for 3 h [10]. For the microwave synthesis, the raw materials are calcined at 750°C for 30 min and 800°C (further repeated three times) for 30 min. Afterward, the samples are sintered at 1100°C for 3 h to obtain  $\epsilon_r \sim 21400$  at 1 kHz. Using the molten salts method, the samples are calcined at 1000°C for 2 h and sintered at 1060°C for 4 h to obtain  $\epsilon_r \sim 22000$  at 1 kHz [11]. For the sol-gel method, the powder is calcined between 800 and 930°C for 1–6 h and sintered between 1000 and 1050°C for 4–10 h. These samples show a dielectric constant  $\sim 20000$ – $23000$  at 1 kHz [12–14]. Although, these initial methods can produce samples with a high chemical homogeneity [8–14], their procedures are very cumbersome because of either the preparation at high temperature for long durations (the solid-state reaction method) or complicated fabrication (the chemical synthesis). Hence, a technique which is simple and uses low temperatures with a short soaking time was required for CCTO ceramics fabrication.

Our recent work has successfully fabricated ferroelectric ceramics using the combustion technique [15–18]. This technique involves a self-sustained reaction between the reactive materials and the fuel (e.g., urea and glycine) which supplies a liquid medium at the start of the reaction. The reaction can occur easily in a liquid system because the diffusion coefficient is higher than in a solid medium [17–18]. The obtained ceramics have a high density and excellent electrical properties with a low firing temperature and a short soaking time [15–18]. Furthermore, the preparation and characterization of  $\text{CaCu}_3\text{Ti}_4\text{O}_{12}$  (CCTO) ceramics, using the combustion technique, have not been reported in the literature. Therefore, CCTO ceramic was prepared using the combustion technique. The effect of firing temperatures on the crystal structure, homogeneity, microstructure, and dielectric properties of the CCTO ceramics was investigated and compared with previous works.

## Materials and Methods

$\text{CaCu}_3\text{Ti}_4\text{O}_{12}$  powder (CCTO) was synthesized using the combustion technique. To prepare the CCTO powder, the raw materials of  $\text{CaCO}_3$  (99%),  $\text{CuO}$  (99%), and  $\text{TiO}_2$  (99%) were first weighed. The mixtures of raw materials were ground by a ball milling procedure (zirconia milling media under ethanol for 24 h). Drying was carried out at 120°C for 4 h. The raw material powders were well-mixed with the fuel (glycine) in the ratio of 1:2 by weight before the calcination step. Then, the uncalcined CCTO was calcined at temperatures ranging between 750 and 1000°C for 2 h and a heating/cooling rate of 5°C/min. The calcined powders were then pressed into disks with a diameter of 15 mm at a pressure of 80 MPa. The pellets were sintered at 1000 to 1125°C for 2 h and cooled at a rate of 5°C/min to room temperature in a furnace. X-ray diffraction was employed to identify the crystal structure and to discover the optimum temperature to prepare the CCTO powder and ceramics. The morphological features of the samples were imaged using scanning electron microscopy. The density of the sintered ceramics was measured by the Archimedes method. The average

grain sizes were determined by using the mean linear intercept method. The raw data was obtained by measuring the grain sizes over 300 grains. Silver paste was coated on the surface of the ceramics, fired at 600°C for 5 min to form electrodes. The dielectric properties at room temperature were also observed by a LCR impedance analyzer.

## Results and Discussion

XRD patterns of the calcined powders between 750 and 1000°C for 2 h are given in Fig. 1(a). The diffraction lines were indexed on the basis of a cubic structure which matched with JCPDS file number 21-0140 and corresponded to previous works [4–14]. The crystalline phase of CCTO was accompanied with TiO<sub>2</sub>, CuO and CaTiO<sub>3</sub> as separate phases below 950°C. The pure cubic perovskite phase was observed in the powders calcined at a temperature higher than 950°C. The percent phase purity of the CCTO calcined powders is listed in Table 1. There was an increase of percent phase purity as a result of an increase of calcination temperature. This calcination temperature and dwell time were lower and much shorter than those of the solid-state reaction technique, around 50–100°C and 22–70 h [4–6, 8–10]. Moreover, the calcination temperature and the dwell time of this technique were closed to that of the coprecipitation method [7], the microwave synthesis [10], the molten salts method [11] and the sol-gel method [12–14]. This indicated that the combustion technique has the ability to produce very pure powders and can be considered an alternative way to save energy and time. The tendency of lattice parameter *a* slightly increased on account of an increase of calcination temperatures as listed in Table 1. These obtained lattice parameters were similar to the literature values (7.373–7.391 Å) [1, 12,

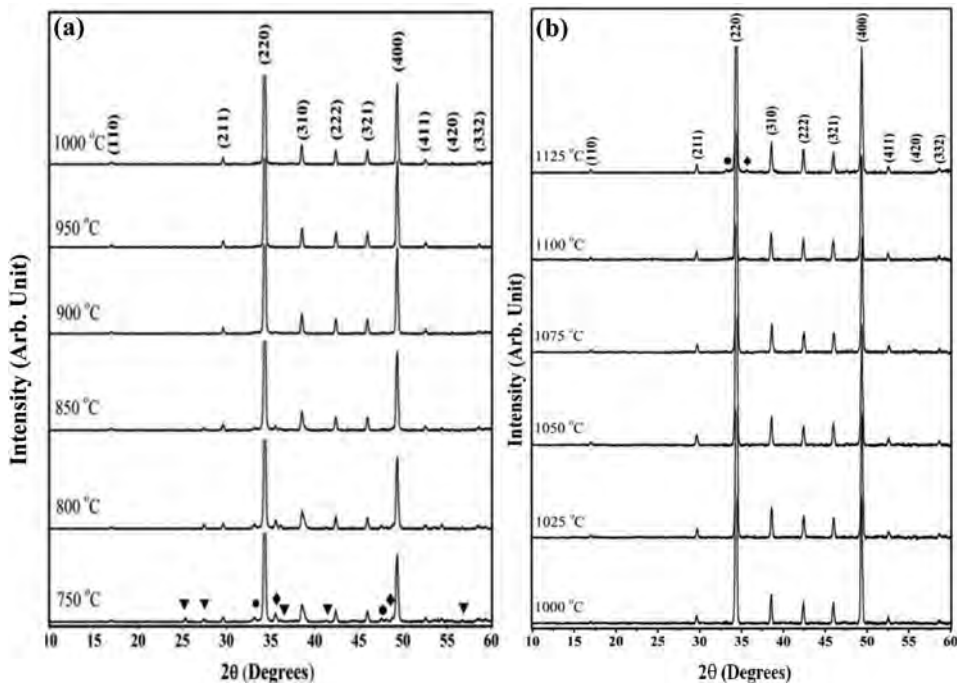


**Figure 1.** XRD patterns of CCTO (a) powder and (b) ceramic for 2 h; (▼) TiO<sub>2</sub>; (◆) CuO and (●) CaTiO<sub>3</sub>.

**Table 1**  
The percent perovskite phase, lattice parameter *a* and average particle size of CCTO powder

Calcination temperature (°C)	% perovskite phase	Lattice parameter <i>a</i> (Å)	Average particle size (μm)
750	83.2	7.3829	0.19 ± 0.05
800	83.4	7.3843	0.24 ± 0.07
850	93.9	7.3846	0.28 ± 0.12
900	98.8	7.3852	0.37 ± 0.14
950	100	7.3853	0.73 ± 0.30
1000	100	7.3868	1.13 ± 0.37

19]. The changing of firing temperatures affected the lattice strain that defined the change in the d spacing and the lattice parameters of the samples [17]. This demonstrated that the calcination temperatures had an influence on the crystal structure and the phase formation.

Fig. 2(a)–(c) are SEM photographs illustrating morphological changes in the calcined CCTO powders as a result of calcination temperatures. The particles showed a porous agglomerated form and similar spherical morphology with a difference in particle size. The average particle size increased from 0.19 to 1.13 μm with an increase of calcination temperature from 750 to 1000°C, as listed in Table 1.

The powder which was calcined at 950°C was pressed into pellets and sintered from 1000 to 1125°C for 2 h. Fig. 1(b) shows the XRD patterns of CCTO ceramics at different sintering temperatures. The ceramics that sintered below 1125°C were identified as having a single phase with a cubic perovskite structure. The peaks of CaTiO<sub>3</sub> and CuO were

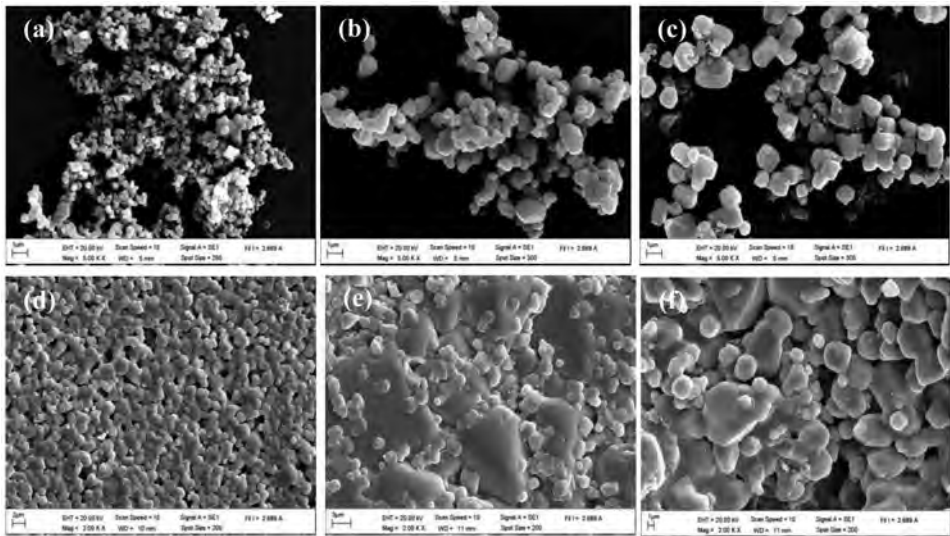


**Figure 2.** SEM photographs of the powders calcined at: (a) 850°C, (b) 950°C and (c) 1000°C for 2 h and the pellet surface sintered at: (d) 1000°C, (e) 1100°C and (f) 1125°C, for 2 h.

**Table 2**

The percent perovskite phase, lattice parameter  $a$ , average grain size, shrinkage and density of CCTO ceramic

Sintering Temperature (°C)	% perovskite phase	Lattice parameter $a$ (Å)	Average grain size ( $\mu\text{m}$ )	% Shrinkage	Density (g/cm <sup>3</sup> )	Relative density (%)
1000	100	7.3721	1.16 ± 0.11	15.02	4.63	91.3
1025	100	7.3757	1.25 ± 0.12	18.67	4.66	91.8
1050	100	7.3807	1.58 ± 0.23	18.67	4.71	92.9
1075	100	7.3848	1.67 ± 0.20	18.64	4.79	94.6
1100	100	7.3849	2.89 ± 0.42	18.19	4.88	96.2
1125	97.6	7.3857	3.48 ± 0.53	16.67	4.78	94.3

detected at 1125°C. This may have been caused by the partiality of Ca—O to bonding with Ti—O, while leaving some of the Cu—O alone at this temperature. It related to the complete forming temperature of pure CaTiO<sub>3</sub> which appeared at around 1155°C [20]. The percentage of the pure perovskite phase in the sintered samples is listed in Table 2. The lattice parameter  $a$ , as a function of sintering temperatures, is exhibited in Table 2. These lattice parameters agreed with the values of previous works (7.373–7.391 Å) [1, 12, 19]. An increase in value of the lattice parameter  $a$  may be due to the changing of the lattice strain, which explained in the part of the calcined powders. This was similar to the XRD result of the calcined powders [17]. With the increasing of sintering temperatures, the reflection peaks, which indicated larger crystallization, were sharper.

The morphological changes in the CCTO ceramic surfaces, as a function of sintered temperatures, are illustrated in Fig. 2(d)–(f). It was observed that the increasing of the sintering temperatures from 1000 to 1100°C led to a decrease in the porosity, while the porosity of samples sintered higher than 1100°C increased as shown in Fig. 2(f). The average grain sizes increased from 1.16 to 3.48  $\mu\text{m}$  when the sintering temperature increased from 1000 to 1125°C, as listed in Table 2.

The percent shrinkage and density of the pellet samples as a function of the different sintering temperatures are shown in Table 2. The maximum density, which was obtained from the sample sintered at the optimum temperature (1100°C), was around 4.88 g/cm<sup>3</sup> or ~96.2% of the theoretical density. The densification mechanisms during treatment corresponded to the grain growth, especially during the final stage of sintering. The expansion of trapped gases in the pores assembled and grew as a result of the grain growth [15, 17]. This result agreed with the microstructure and XRD result of the ceramic and proved that high density of CCTO ceramics could be prepared by the combustion technique.

Table 3 illustrates the frequency dependence of the dielectric constant ( $\epsilon_r$ ) and the dielectric loss ( $\tan \delta$ ) of CCTO ceramics, which had been sintered a various temperatures, at room temperature. At the same sintering temperature, the dielectric constant decreased due to an increase of frequency, as listed in Table 3. At the same frequency of 100 Hz, 1kHz, 10 kHz and 100 kHz, the dielectric constant first increased and reached its highest at 1100°C. Next, it reduced in value when the sintering temperature was higher than 1100°C, as shown in Table 3. This result correlated with the density results. The dielectric loss at room temperature is also shown in Table 3. The frequency and sintering temperature influenced the dielectric properties. The dielectric properties corresponded to the density

**Table 3**The dielectric constant ( $\epsilon_r$ ), and loss tangent ( $\tan \delta$ ) of CCTO ceramic at room temperature

Sintering Temperature ( $^{\circ}\text{C}$ )	100 Hz		1 kHz		10 kHz		100 kHz	
	$\epsilon_r$	$\tan \delta$	$\epsilon_r$	$\tan \delta$	$\epsilon_r$	$\tan \delta$	$\epsilon_r$	$\tan \delta$
1000	5719	0.6605	3884	0.3498	2296	0.3343	1588	0.2234
1025	7782	0.3603	6486	0.1180	5610	0.1233	4799	0.1178
1050	21489	0.2658	17944	0.1172	15290	0.1357	12673	0.1695
1075	28507	0.3360	25433	0.0887	22381	0.1168	18988	0.1436
1100	32819	0.1117	29664	0.0925	24736	0.1607	19015	0.1937
1125	31905	0.1624	26100	0.1515	19920	0.2271	13565	0.2822

and the microstructure results. Furthermore, the highest dielectric constant at 1 kHz, when using the combustion technique, was approximately 29664. This value at 1 kHz was higher than that obtained when using the coprecipitation method ( $\epsilon_r \sim 24000$ ) [7], the solid-state reaction technique ( $\epsilon_r \sim 9600$ –23600) [8–10], the microwave synthesis ( $\epsilon_r \sim 21400$ ) [10], the molten salts method ( $\epsilon_r \sim 22000$ ) [11] and the sol-gel method ( $\epsilon_r \sim 20000$ –23000) [12–14]. This demonstrated the ability of the combustion technique to produce very pure and dense CCTO ceramics with a high dielectric constant. Hence, this technique could be considered as an alternative way for CCTO fabrication.

## Conclusions

CCTO powders can be successfully synthesized using the combustion technique. The pure cubic perovskite phase was obtained at a calcination temperature of  $950^{\circ}\text{C}$  for 2 h. The CCTO powders had a porous agglomerated form and similar spherical morphology. The maximum densities ( $4.88 \text{ g/cm}^3$ ) and the highest dielectric constant (29664) at 1 kHz were received from the ceramics sintered at  $1100^{\circ}\text{C}$  for 2 h. The molten-glycine and the combustion of glycine play an important role in the complete process and the calcination and sintering temperatures have a strong influence on the crystal structure, lattice parameter, and the homogeneity, microstructure and dielectric properties of the CCTO samples.

## Acknowledgments

This work was supported financially by the Thailand Research Fund (TRF), Faculty of Science, Naresuan University. Thanks to the Science Lab Center, Faculty of Science, Naresuan University for support facilities. Acknowledgments also go to Mr. Don Hindle, for his helpful correction of the manuscript.

## References

1. M. A. Subramanian, D. Li, N. Duan, B. A. Reisner, and A. W. Sleight, High dielectric constant in  $\text{ACu}_3\text{Ti}_4\text{O}_{12}$  and  $\text{ACu}_3\text{Ti}_3\text{FeO}_{12}$  phases, *J. Solid State Chem.* **151**(2), 323–325 (2000).
2. A. Deschanvres, B. Raveau, and F. Tollemer, Substitution of copper for a divalent metal in perovskite-type titanates, *Bull. Soc. Chim. Fr.* **11**, 4077–4078 (1967).
3. C. C. Homes, T. Vogt, and S. M. Shapiro, Charge transfer in the high dielectric constant materials  $\text{CaCu}_3\text{Ti}_4\text{O}_{12}$  and  $\text{CdCu}_3\text{Ti}_4\text{O}_{12}$ , *Phys. Rev. B.* **67**, 092106 (2003).

4. T. B. Adams, D. C. Sinclair, and A. R. West, Giant barrier capacitance effects in CaCu<sub>3</sub>Ti<sub>4</sub>O<sub>12</sub> ceramics, *Adv. Mater.* **14**, 1321–1323 (2002).
5. B. A. Bender, and M. J. Pan, The effect of processing on the giant dielectric properties of CaCu<sub>3</sub>Ti<sub>4</sub>O<sub>12</sub>, *Mater. Sci. Eng. B* **117**, 339–347 (2005).
6. D. C. Sinclair, T. B. Adams, F. D. Morrison, and A. R. West, CaCu<sub>3</sub>Ti<sub>4</sub>O<sub>12</sub>: one-step internal barrier layer capacitor, *Appl. Phys. Lett.* **80**, 2153–2155 (2002).
7. S. G. Fritsch, T. Lebey, M. Boulos, and B. Durand, Dielectric properties of CaCu<sub>3</sub>Ti<sub>4</sub>O<sub>12</sub> based multiphased ceramics, *J. Euro. Ceram. Soc.* **26**, 1245–1257 (2006).
8. T. Li, R. Xue, J. Hao, Y. Xue, and Z. Chen, The effect of calcining temperatures on the phase purity and electric properties of CaCu<sub>3</sub>Ti<sub>4</sub>O<sub>12</sub> ceramics, *J. Alloys Compd.* **509**, 1025–1028 (2011).
9. T. Li, K. Fang, J. Hao, Y. Xue, and Z. Chen, The effect of Ca-rich on the electric properties of Ca<sub>1+x</sub>Cu<sub>3-x</sub>Ti<sub>4</sub>O<sub>12</sub> polycrystalline system, *Mater. Sci. Eng. B* **176**, 171–176 (2011).
10. H. Yu, H. Liu, D. Luo, and M. Cao, Microwave synthesis of high dielectric constant CaCu<sub>3</sub>Ti<sub>4</sub>O<sub>12</sub>, *J. Mater. Process. Tech.* **208**, 145–148 (2008).
11. K. P. Chen, and X. W. Zhang, Synthesis of calcium copper titanate ceramics via the molten salts method, *Ceram. Int.* **36**, 1523–1527 (2010).
12. D. L. Sun, A. Y. Wu, and S. T. Yin, Structure, properties, and impedance spectroscopy of CaCu<sub>3</sub>Ti<sub>4</sub>O<sub>12</sub> ceramics prepared by sol–gel process, *J. Am. Ceram. Soc.* **91**, 169–173 (2008).
13. S. Jesurani, S. Kanagesan, R. Velmurugan, C. Thirupathi, M. Sivakumar, and T. Kalaivani, Nanoparticles of the giant dielectric material, calcium copper titanate from a sol–gel technique, *Mater. Lett.* **65**, 3305–3308 (2011).
14. Z. Li, and H. Fan, Structure and electric properties of sol–gel derived CaCu<sub>3</sub>Ti<sub>4</sub>O<sub>12</sub> ceramics as a pyroelectric sensor, *Solid State Ionics.* **192**, 682–687 (2011).
15. A. Thongtha, and T. Bongkarn, Effect of firing temperatures on phase and morphology evolution of CaZrO<sub>3</sub> ceramics synthesized using the combustion technique, *Ferroelectrics* **403**, 3–10 (2010).
16. U. Chaimongkon, A. Thongtha, and T. Bongkarn, The effects of firing temperatures and barium content on phase formation, microstructure and dielectric properties of lead barium titanate ceramics prepared via the combustion technique, *Curr. Appl. Phys.* **11**, S70–S76 (2011).
17. A. Thongtha, K. Angsukased, and T. Bongkarn, Fabrication of (Ba<sub>1-x</sub>Sr<sub>x</sub>)(Ti<sub>1-x</sub>Zr<sub>x</sub>)O<sub>3</sub> ceramics prepared using the combustion technique, *Smart Mater. Struct.* **19**, 124001 (2010).
18. D. Xue, J. Xu, and C. Yan, Chemical synthesis of NaTaO<sub>3</sub> powder at low-temperature, *Mater. Lett.* **59**, 2920–2922 (2005).
19. R. N. P. Choudhary, and U. Bhunia, Structural, dielectric and electrical properties of ACu<sub>3</sub>Ti<sub>4</sub>O<sub>12</sub> (A=Ca, Sr and Ba), *J. Mater. Sci.* **37**, 5177–5182 (2002).
20. V. V. Lemanov, A. V. Sotnikov, E. P. Smirnova, M. Weihnacht, and R. Kunze, Perovskite CaTiO<sub>3</sub> as an incipient ferroelectric, *Solid State Commun* **110**, 611–614 (1999).



## Ferroelectrics

Publication details, including instructions for authors and  
subscription information:

<http://www.tandfonline.com/loi/gfer20>

### Influence of Sintering Temperature on Phase Formation, Microstructure and Dielectric Properties of Calcium and Strontium Doped BNT Ceramics Prepared via Combustion Technique

Panadda Sittiketkorn<sup>a b</sup>, Artid Laowanidwatana<sup>a b</sup>, Naratip  
Vittayakorn<sup>c</sup> & Theerachai Bongkarn<sup>a b</sup>

<sup>a</sup> Department of Physics, Faculty of Science, Naresuan University,  
Phitsanulok, 65000, Thailand

<sup>b</sup> Research Center for Academic Excellence in Petroleum,  
Petrochemicals and Advanced Materials, Naresuan University,  
Phitsanulok, 65000, Thailand

<sup>c</sup> Materials Science Research Unit, Department of Chemistry, Faculty  
of Science, King Mongkut's Institute of Technology Ladkrabang,  
Bangkok, 10520, Thailand

Published online: 10 Dec 2013.

To cite this article: Panadda Sittiketkorn, Artid Laowanidwatana, Naratip Vittayakorn & Theerachai Bongkarn (2013) Influence of Sintering Temperature on Phase Formation, Microstructure and Dielectric Properties of Calcium and Strontium Doped BNT Ceramics Prepared via Combustion Technique, *Ferroelectrics*, 455:1, 54-61, DOI: [10.1080/00150193.2013.843425](https://doi.org/10.1080/00150193.2013.843425)

To link to this article: <http://dx.doi.org/10.1080/00150193.2013.843425>

PLEASE SCROLL DOWN FOR ARTICLE

Taylor & Francis makes every effort to ensure the accuracy of all the information (the "Content") contained in the publications on our platform. However, Taylor & Francis, our agents, and our licensors make no representations or warranties whatsoever as to the accuracy, completeness, or suitability for any purpose of the Content. Any opinions and views expressed in this publication are the opinions and views of the authors, and are not the views of or endorsed by Taylor & Francis. The accuracy of the Content should not be relied upon and should be independently verified with primary sources of information. Taylor and Francis shall not be liable for any losses, actions, claims, proceedings, demands, costs, expenses, damages, and other liabilities whatsoever or howsoever caused arising directly or indirectly in connection with, in relation to or arising out of the use of the Content.

This article may be used for research, teaching, and private study purposes. Any substantial or systematic reproduction, redistribution, reselling, loan, sub-licensing, systematic supply, or distribution in any form to anyone is expressly forbidden. Terms & Conditions of access and use can be found at <http://www.tandfonline.com/page/terms-and-conditions>



# Influence of Sintering Temperature on Phase Formation, Microstructure and Dielectric Properties of Calcium and Strontium Doped BNT Ceramics Prepared via Combustion Technique

PANADDA SITTIKETKORN,<sup>1,2</sup> ARTID  
LAOWANIDWATANA,<sup>1,2</sup> NARATIP VITTAYAKORN,<sup>3</sup>  
AND THEERACHAI BONGKARN<sup>1,2,\*</sup>

<sup>1</sup>Department of Physics, Faculty of Science, Naresuan University, Phitsanulok, 65000, Thailand

<sup>2</sup>Research Center for Academic Excellence in Petroleum, Petrochemicals and Advanced Materials, Naresuan University, Phitsanulok, 65000, Thailand

<sup>3</sup>Materials Science Research Unit, Department of Chemistry, Faculty of Science, King Mongkut's Institute of Technology Ladkrabang, Bangkok 10520, Thailand

*Influence of sintering temperature on phase formation, microstructure and dielectric properties of calcium and strontium doped BNT ceramics (BNTST20 and BNTCT2) were investigated. The BNTST20 and BNTCT2 ceramics were prepared using the combustion technique. The structural phase of the BNTST20 ceramics indexed in a cubic phase, while the BNTCT2 ceramics indexed in a rhombohedral phase. The average grain size tended to increase with increasing sintering temperature. The density and the dielectric constant at Curie temperatures increased with increasing sintering temperature up to 1200°C and 1150°C, thereafter they decreased for BNTST20 and BNTCT2 ceramics, respectively. Moreover, the highest density (5.59 and 5.57 g/cm<sup>3</sup>) ceramics exhibited the highest dielectric constant at Curie temperatures (~4733 and ~3218) for BNTST20 and BNTCT2, respectively. The ferroelectric properties were also investigated.*

**Keywords** Bismuth sodium titanate; phase formation; dielectric constant; hysteresis loop

## Introduction

Bismuth sodium titanate [(Bi<sub>0.5</sub>Na<sub>0.5</sub>)TiO<sub>3</sub>; BNT] is a kind of perovskite ferroelectric type, which has been considered to be a good candidate for lead-free ceramics because of its relatively large remnant polarization ( $P_r = 38 \mu\text{C}/\text{cm}^2$ ) at room temperature, high Curie temperature ( $T_c = 320^\circ\text{C}$ ) and high coercive field ( $E_c = 7.3 \text{ kV}/\text{mm}$ ) [1]. It has been reported that BNT experiences two phases transition: from a ferroelectric rhombohedral phase to an antiferroelectric tetragonal phase and from an antiferroelectric tetragonal phase to a paraelectric cubic phase, resulting in a maximum dielectric constant. To improve its properties, several solid solutions of BNT with BaTiO<sub>3</sub> (BT), SrTiO<sub>3</sub> (ST), and CaTiO<sub>3</sub> (CT) etc,

---

Received December 11, 2012; in final form March 16, 2013.

\*Corresponding author. E-mail: researchcmu@yahoo.com

have been investigated [2, 3]. In the case of  $(1-x)(\text{Bi}_{0.5}\text{Na}_{0.5})\text{TiO}_3-x\text{SrTiO}_3$  (BNTST100 $x$ ) ceramics, the crystal structure is indexed as the mixed phase between rhombohedral and pseudocubic (tetragonal) phases. The composition of  $0.80(\text{Bi}_{0.5}\text{Na}_{0.5})\text{TiO}_3-0.20\text{SrTiO}_3$  (BNTST20) exhibits good piezoelectric properties and the dielectric constant at Curie temperatures with a maximum value of 2258 [2, 3]. For  $(1-x)(\text{Bi}_{0.5}\text{Na}_{0.5})\text{TiO}_3-x\text{CaTiO}_3$  (BNTCT100 $x$ ) ceramics, the crystal structure is indexed as the rhombohedral phase in all the samples. The composition of  $0.98(\text{Bi}_{0.5}\text{Na}_{0.5})\text{TiO}_3-0.02\text{CaTiO}_3$  (BNTCT2) demonstrates the dielectric constant at room temperatures with a maximum value of 775 [3, 4].

Recently, the combustion method is popular for preparing ferroelectric ceramics. It is an uncomplicated method, with produces ultra-fine particle size, high density, and a excellent electric properties and the desired structure and composition [6–8]. In addition, the influence of sintering temperature on properties of BNTST20 and BNTCT2 ceramics has not been reported in the literature. Thus, in this work,  $0.80(\text{Bi}_{0.5}\text{Na}_{0.5})\text{TiO}_3-0.20\text{SrTiO}_3$  (BNTST20) and  $0.98(\text{Bi}_{0.5}\text{Na}_{0.5})\text{TiO}_3-0.02\text{CaTiO}_3$  (BNTCT2) ceramics were prepared via the combustion technique. The influence of sintering temperature on phase formation, microstructure and electrical properties of Calcium and Strontium doped BNT ceramics (BNTST20 and BNTCT2) were investigated.

## Experimental

$0.80(\text{Bi}_{0.5}\text{Na}_{0.5})\text{TiO}_3-0.20\text{SrTiO}_3$  (BNTST20) and  $0.98(\text{Bi}_{0.5}\text{Na}_{0.5})\text{TiO}_3-0.02\text{CaTiO}_3$  (BNTCT2) ceramics were synthesized by the combustion method. Reagent-grade oxide and carbonate powders of  $\text{Bi}_2\text{O}_3$ ,  $\text{NaCO}_3$ ,  $\text{TiO}_2$ ,  $\text{SrCO}_3$  and  $\text{CaCO}_3$  were used as starting materials. The powders were prepared separately and then blended together. To prepare the BNT powders,  $\text{Bi}_2\text{O}_3$ ,  $\text{NaCO}_3$  and  $\text{TiO}_2$  were weighed and mixed by ball-milling in ethanol for 24 h. After drying, the powders were mixed with glycine as a fuel, and then calcined at  $650^\circ\text{C}$  for 2 h.  $\text{SrTiO}_3$  (ST) powders were also prepared from raw materials of  $\text{SrCO}_3$  and  $\text{TiO}_2$  under the same procedure then mixed with urea as a fuel. The mixed powders were calcined at  $1200^\circ\text{C}$  for 4 h.  $\text{CaTiO}_3$  (CT) powders were also prepared from raw materials of  $\text{CaCO}_3$  and  $\text{TiO}_2$  under the same route then mixed with glycine as a fuel. The mixed powders were calcined at  $1000^\circ\text{C}$  for 2 h. After weighing according to the formula BNTST20 and BNTCT2, the calcined powders were ball-milled in ethanol for 24 h and dried. The blended powders were die-pressed into discs of 15 mm in diameter and 1–2 mm in thickness. The small disc samples were sintered at  $1050-1250^\circ\text{C}$  for 2 h. The crystalline phase of the calcined and sintered samples was identified by X-ray diffractometer (XRD). The microstructure evolution was observed using a scanning electron microscope (SEM). Density was measured by the Archimedes method with distilled water. Dielectric properties were investigated using an LCR meter. The measurement of ferroelectric hysteresis loops was conducted with different electric field strengths by using a ferroelectric tester.

## Results and Discussion

Figure 1(a) shows the XRD patterns of the BNTST20 ceramics at different sintering temperatures ( $1050-1250^\circ\text{C}$ ). The structural phase of the pure BNT calcined powder indexed in a rhombohedral phase, while the pure ST calcined powder indexed in a cubic phase. This matched with JCPDS file number 36-0340 and 05-0634, respectively. Generally, the rhombohedral symmetry is characterized by a (003)/(021) peak splitting between  $38^\circ$  and  $42^\circ$ . The cubic symmetry is identified by a single (111) peak between  $38^\circ$  and  $42^\circ$ . In the

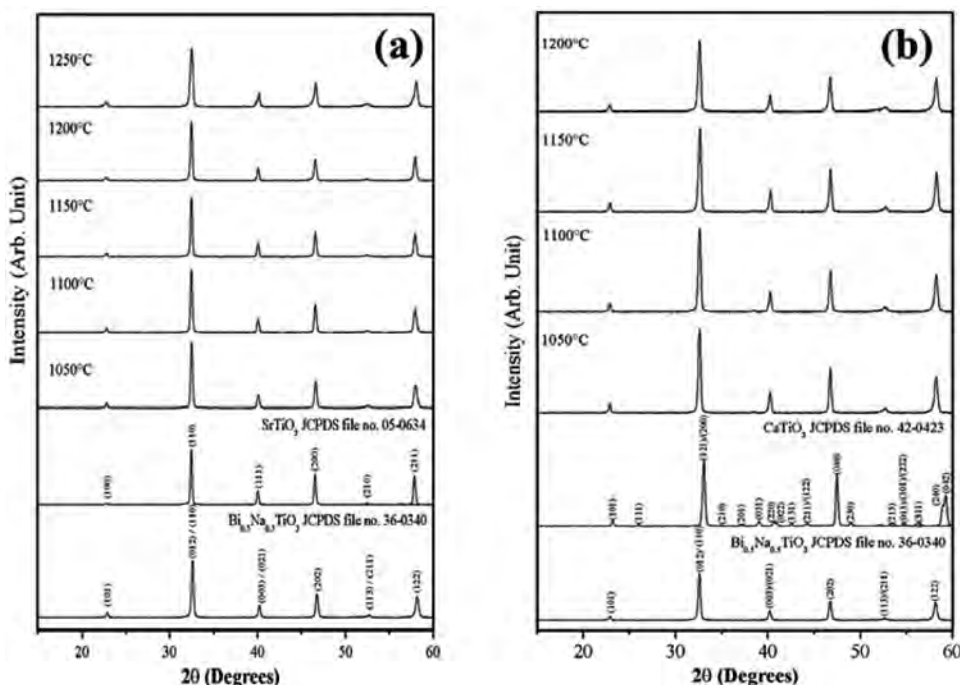


**Figure 1.** XRD patterns of (a) BNTST20 and (b) BNTCT2 ceramics sintered at different temperatures.

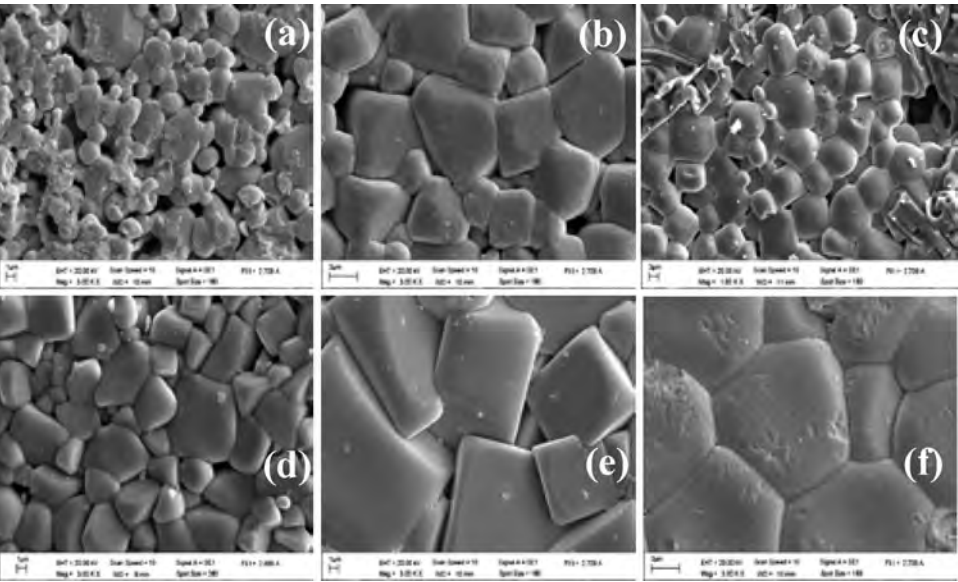
case of this work, the peak splitting of (003)/(021) between  $38^\circ$  and  $42^\circ$  did not distinctively appear at the sintering temperatures. This result indicates that the structural phase of BNTST20 ceramics has a cubic phase and corresponds to previous work [2, 3]. The purity of the perovskite phase was found in all samples as seen in Fig. 1(a). The lattice parameter  $a$  of sintered BNTST20 ceramics with various temperatures ( $1050$ – $1250^\circ\text{C}$ ) is shown in Table 1. The tendency of lattice parameters  $a$  slightly increased on account of an increase in sintering temperatures (Table 1). It is demonstrated that the sintering temperatures has an influence on the crystal structure.

Figure 2(a–c) show the SEM micrographs of BNTST20 ceramics at various sintered temperatures ( $1050$ – $1250^\circ\text{C}$ ). These ceramics exhibited a spherical or rectangular shape. At low sintering temperature, many distinct pores occurred in the samples (Fig. 2(a)). When the sintering temperature increased up to  $1200^\circ\text{C}$  (Fig. 2(b)), the porosity markedly decreased, while the average grain size slightly increased. The increase of sintering temperature significantly promoted the grain growth and microstructure densification. However, at a sintering temperature above  $1250^\circ\text{C}$ , the grain uniform decreased and began to melt (Fig. 2(c)). The average grain size determined with the linear intercept method is summarized in Table 1. The average grain size increased from  $1.14$  to  $5.42\ \mu\text{m}$  when the sintering temperature increased from  $1050$  to  $1200^\circ\text{C}$  (Table 1).

The linear shrinkage and density of the pellet samples as a function of different sintering temperatures are shown in Table 1. The density increased with an increase in sintering temperatures (Table 1). The maximum density, which was obtained from the sample sintered at the optimum temperature ( $1200^\circ\text{C}$ ), was around  $5.59\ \text{g/cm}^3$ . However,

**Table 1**  
The lattice parameter  $a$ , average grain size, density, shrinkage  $T_d$ ,  $T_m$  and dielectric properties of BNTST20 and BNTCT2 ceramics

	Sintering temperature (°C)	Lattice parameter $a$ (Å)	Average grain size (μm)	Density (g/cm <sup>3</sup> )	Linear shrinkage (%)	$T_d$ (°C)	$T_m$ (°C)	$\epsilon_r$ at $T_m$	$\tan \delta$ at $T_m$	$\epsilon_r$ at $T_r$	$\tan \delta$ at $T_r$
BNTST20	1050	3.8941	1.14	4.90	12.7	111	222	1269	0.040	1118	0.070
	1100	3.8944	2.85	5.14	13.1	112	216	2230	0.055	1774	0.077
	1150	3.8959	4.85	5.45	13.4	122	211	3883	0.059	2092	0.084
	1200	3.8971	5.42	5.59	13.7	127	215	4733	0.062	2848	0.091
	1250	3.9011	—	—	—	—	—	—	—	—	—
BNTCT2	1050	3.8782	2.43	5.19	12.7	280	392	2002	0.030	600	0.003
	1100	3.8777	4.28	5.37	12.9	282	391	2079	0.045	682	0.004
	1150	3.8776	6.71	5.57	13.0	288	429	3218	0.056	800	0.005
	1200	3.8765	8.28	5.45	13.4	284	382	2780	0.062	750	0.005



**Figure 2.** SEM photomicrographs of the BNTST20 ceramics sintered at: (a) 1100°C, (b) 1200°C and (c) 1250°C and the BNTCT2 ceramics sintered at: (d) 1100°C, (e) 1150°C and (f) 1200°C.

the density of the pellet sintered at 1250°C could not be reported due to its fragility, corresponding to the SEM result.

Figure 3(a) shows the dielectric constant of BNTST20 ceramics at various sintered temperatures, measured at 1 kHz. At 1200°C sintering temperature, the ceramics exhibited two dielectric anomalies: the lower dielectric peaks  $T_d$  (127°C) and the higher dielectric peaks  $T_m$  (215°C) (Table 1).  $T_d$  is the depolarization temperature which corresponds to the transition from a ferroelectric state to a so-called “anti-ferroelectric” state, while  $T_m$  is the maximum temperature at which  $\epsilon_r$  reaches a maximum value and corresponds to a transition

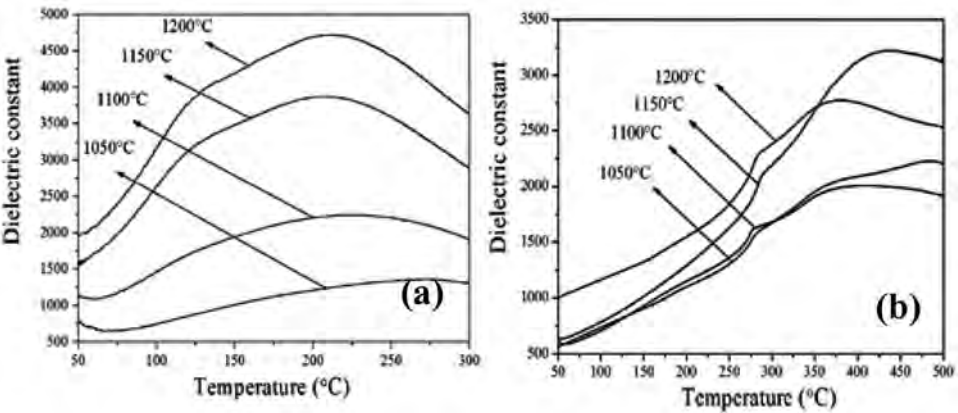


**Figure 3.** Dielectric constant of (a) BNTST20 and (b) BNTCT2 ceramics with various sintering temperatures, measured at 1 kHz.

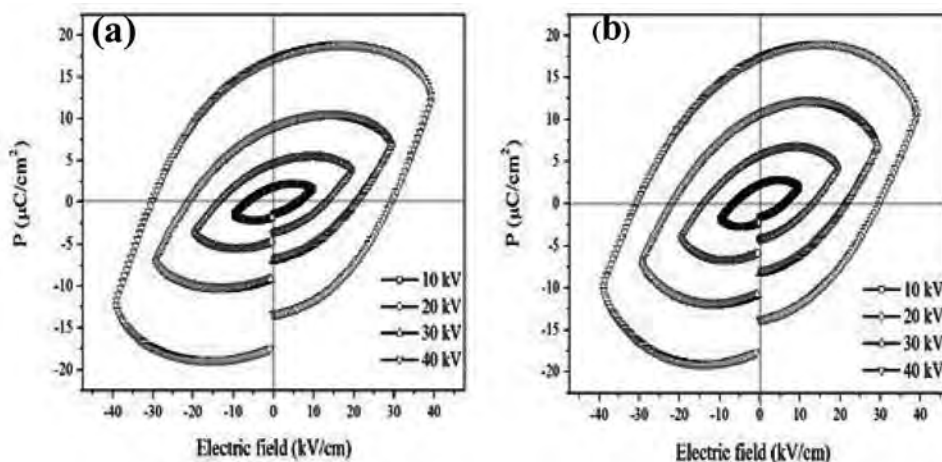


**Figure 4.**  $P$ - $E$  hysteresis loop of dense (a) BNTST20 and (b) BNTCT2 ceramics with different electric fields strengths.

from an “anti-ferroelectric state” to a paraelectric state [9]. At a lower sintering temperature, the dielectric curves broadened even more and the  $T_d$  peaks gradually disappeared. At room temperature ( $T_r$ ), the dielectric constant and loss factor of the BNTST20 ceramics increased with increased sintering temperature (Table 1). The pellets sintered at 1250°C could not have its dielectric properties measured due to its fragility. The highest dielectric constant of the BNTST20 ceramics were obtained from the sample sintered at 1200°C, which should be the proper condition when using the combustion technique. It should be noted that the dielectric constant at  $T_m$  of the BNTST20 ceramics (Table 1) obtained by using the combustion technique ( $\sim 4733$ ) was higher than a sol-gel method ( $\sim 2258$ ) [2]. These results confirm that the combustion technique is a simple method for fabricating high quality BNTST20 ceramics.

The ferroelectric polarization-electric field ( $P$ - $E$ ) loops of BNTST20 ceramic sintered at 1200°C with different electric field strengths are seen in Fig. 4(a). It is noted that the shape of hysteresis varies greatly with electric fields strength. A pinching of  $P$ - $E$  hysteresis loops were observed at 10 kV/cm electrical field strength. This result is due to the fact that the electric field is not large enough to switch any domains. In the increase of electrical field strength, the shapes of  $P$ - $E$  hysteresis loops are improved in both regions of positive and negative. These due to the electrical field strength is enough energy to constrain realignment of some domains in the direction of applied fielded. The measured remnant polarization ( $P_r$ ) and coercive field ( $E_c$ ) at 40 kV/cm are 17.19  $\mu\text{C}/\text{cm}^2$  and 29.61 kV/cm.

Figure 1(b) shows the XRD patterns of the BNTCT2 ceramics at different sintering temperatures (1050–1200°C). The structural phase of the pure BNT calcined powder indexed in a rhombohedral phase, while the pure CT calcined powder indexed in a orthorhombic phase. This matched with JCPDS file number 36-0340 and 42-0423, respectively. In this work, the structural phase of BNTCT2 ceramics indexed as the rhombohedral phase and corresponded to previous work [3, 4]. The purity of the perovskite phase was found in all samples as seen in Fig. 1(b). The lattice parameter  $a$  of BNTCT2 sintered at various temperatures (1050–1200°C) is seen in Table 1. The lattice parameters  $a$  of the BNTCT2 decreased with the increasing of sintering temperatures.

Figure 2(d–f) show the SEM micrographs of BNTCT2 ceramics at various sintered temperatures (1050–1200°C). It can be seen that the grain exhibits an almost spherical or rectangular morphology. The porosity in the ceramics decreased with an increase in sintering temperature. The average grain size increased with an increase of sintering temperature. By using the intercept method, the average grain size increased from 2.43 to 8.28  $\mu\text{m}$  when the sintering temperature increased from 1050–1200°C as listed in Table 1.

The measured density and linear shrinkage with various sintering temperatures are shown in Table 1. The density increased with an increase in sintering temperature, up to 1150°C and dropped in value at higher sintering temperature. This result was due to the evaporation of the  $\text{Bi}^{2+}$  and  $\text{Na}^+$  in the A-site position at high sintering temperatures [9]. The maximum density, which was obtained from the sample sintered at the optimum temperature (1150°C), was around 5.57  $\text{g}/\text{cm}^3$ .

The temperature dependence of dielectric permittivity ( $\epsilon_r$ ) of the BNTCT2 ceramics at different sintering temperatures at 1 kHz is shown in Fig. 3(b). The  $T_d$ ,  $T_m$  and  $\epsilon_r$  at  $T_m$  increased with increasing sintering temperature, up to 1150°C and then decreased with higher sintering temperatures (Table 1). The highest dielectric constant of the BNTCT2 ceramics were obtained from the sample sintered at 1150°C, which should be the proper condition when using the combustion technique.

The  $P$ - $E$  hysteresis loops of the BNTCT20 are shown in Fig. 4(b). It can be seen that the shape of hysteresis loops correspond to the electric field strength. At low electrical field strength a pinching of  $P$ - $E$  hysteresis loops were observed. The shape of  $P$ - $E$  hysteresis loops are improved in both regions of positive and negative by increasing of electric fields strength. The largest of hysteresis loops were observed in 40  $\text{kV}/\text{cm}$  of electrical field strength, with a  $P_r$  of 17.4  $\mu\text{C}/\text{cm}^2$  and  $E_c$  of 30.1  $\text{kV}/\text{cm}$ . This is the first time that ferroelectric properties of BNTCT2 ceramics were revealed.

## Conclusion

High density BNTST20 and BNTCT2 ceramics were successfully prepared via the combustion technique. The sintering temperature has an influence on phase structure, microstructure, density, dielectric properties and ferroelectric properties of BNTST20 and BNTCT2 ceramics. The lattice parameter  $a$  of BNTST20 and BNTCT2 tended to increase, and then decrease, with increasing sintering temperatures. The average grain size tended to increase with increasing sintering temperature. The highest density and dielectric constant of the BNTST20 and BNTCT2 ceramics were obtained from the sample sintered at 1200°C and 1150°C, respectively, which indicates the recommended condition when using the combustion technique.

## Acknowledgments

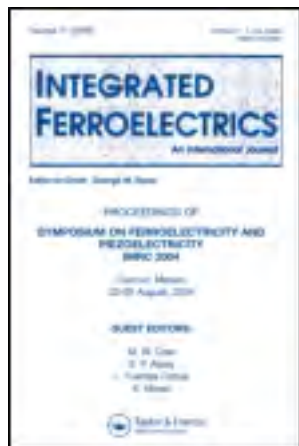
This work was financially supported by the Thailand Research Fund (TRF) and Naresuan University. The authors wish to thank the Science Lab Center, Faculty Thanks are also given to Dr. Antony Harfield for his help in editing the manuscript.

## References

1. C. S. Chou, R. Y. Yang, J. H. Chen, and S.W. Chou, The optimum conditions for preparing the lead-free piezoelectric ceramic of  $\text{Bi}_{0.5}\text{Na}_{0.5}\text{TiO}_3$  using the Taguchi method. *Powder Technol.* **199**, 264–271 (2010).

2. Z. Fu, R. Zhu, D. Wu, and A. Li, Preparation of  $(1-x\%)(\text{Na}_{0.5}\text{Bi}_{0.5})\text{TiO}_3$ - $x\%\text{SrTiO}_3$  thin films by a sol-gel method for dielectric tunable applications. *J. Sol-Gel Sci. Technol.* **49**, 29–34 (2009).
3. Y. Watanabe, Y. Hiruma, H. Nagata, and T. Takenaka, Phase transition temperatures and electrical properties of divalent ions ( $\text{Ca}^{2+}$ ,  $\text{Sr}^{2+}$  and  $\text{Ba}^{2+}$ ) substituted  $(\text{Bi}_{1/2}\text{Na}_{1/2})\text{TiO}_3$  ceramics. *Ceram. Int.* **34**, 761–764 (2008).
4. Y. Yuan, E. Z. Li, B. Li, B. Tang, and X. H. Zhou, Effects of Ca and Mn additions on the microstructure and dielectric properties of  $(\text{Bi}_{0.5}\text{Na}_{0.5})\text{TiO}_3$  ceramics. *J. Electro. Mater.* **40**, 2234–2239 (2011).
5. C. Wattanawikkam and T. Bongkarn, The influence of calcinations temperature on phase and morphology of BST powders synthesis via solid state reaction method and combustion technique. *Ferroelectrics* **282**, 42–48 (2009).
6. P. Sittiketkorn, S. Ramaneeepikool, and T. Bongkarn, The effects of firing temperatures on phase formation and microstructure of  $\text{Pb}_{0.975}\text{Sr}_{0.025}\text{TiO}_3$  ceramics synthesized via the combustion technique. *Ferroelectrics* **403**, 158–165 (2010).
7. P. Panya and T. Bongkarn, Fabrication of perovskite barium titanate ceramics using combustion route. *Ferroelectrics* **383**, 102–110 (2009).
8. A. Thongtha, A. Laowanidwatana, and T. Bongkarn, Effect of firing temperatures on phase and morphology evolution of  $\text{CaZrO}_3$  ceramics synthesized using the combustion technique. *Ferroelectrics* **403**, 3–10 (2010).
9. T. Takenaka, H. Nagata, and Y. Hiruma, Current developments and prospective of lead-free piezoelectric ceramics. *Jpn. J. Appl. Phys.* **47**, 3787–38001 (2008).





## Integrated Ferroelectrics: An International Journal

Publication details, including instructions for authors and subscription information:

<http://www.tandfonline.com/loi/qinf20>

# Influence of Firing Temperatures on Phase Formation and Microstructure of $\text{La}_{0.92}\text{Mg}_{0.18}\text{Fe}_{0.90}\text{O}_3$ Ceramics Synthesized via the Combustion Route

Phongthorn Julphunthong <sup>a b</sup>, Suphornpun Chootin <sup>a b</sup>, Benjawan Suansawan <sup>a</sup> & Theerachai Bongkarn <sup>a b</sup>

<sup>a</sup> Department of Physics, Faculty of Science , Naresuan University ,  
Phitsanulok , 65000 , Thailand

<sup>b</sup> Research Center for Academic Excellence in Applied Physics ,  
Naresuan University , Phitsanulok , 65000 , Thailand

Published online: 07 Dec 2013.

To cite this article: Phongthorn Julphunthong , Suphornpun Chootin , Benjawan Suansawan & Theerachai Bongkarn (2013) Influence of Firing Temperatures on Phase Formation and Microstructure of  $\text{La}_{0.92}\text{Mg}_{0.18}\text{Fe}_{0.90}\text{O}_3$  Ceramics Synthesized via the Combustion Route, Integrated Ferroelectrics: An International Journal, 148:1, 116-123. DOI: [10.1080/10584587.2013.852049](https://doi.org/10.1080/10584587.2013.852049)

To link to this article: <http://dx.doi.org/10.1080/10584587.2013.852049>

PLEASE SCROLL DOWN FOR ARTICLE

Taylor & Francis makes every effort to ensure the accuracy of all the information (the "Content") contained in the publications on our platform. However, Taylor & Francis, our agents, and our licensors make no representations or warranties whatsoever as to the accuracy, completeness, or suitability for any purpose of the Content. Any opinions and views expressed in this publication are the opinions and views of the authors, and are not the views of or endorsed by Taylor & Francis. The accuracy of the Content should not be relied upon and should be independently verified with primary sources of information. Taylor and Francis shall not be liable for any losses, actions, claims, proceedings, demands, costs, expenses, damages, and other liabilities whatsoever or howsoever caused arising directly or indirectly in connection with, in relation to or arising out of the use of the Content.

This article may be used for research, teaching, and private study purposes. Any substantial or systematic reproduction, redistribution, reselling, loan, sub-licensing, systematic supply, or distribution in any form to anyone is expressly forbidden. Terms &



# Influence of Firing Temperatures on Phase Formation and Microstructure of $\text{La}_{0.92}\text{Mg}_{0.18}\text{Fe}_{0.90}\text{O}_3$ Ceramics Synthesized via the Combustion Route

PHONGTHORN JULPHUNTHONG,<sup>1,2</sup>  
SUPHORNPNUN CHOOTIN,<sup>1,2</sup> BENJAWAN SUANSAWAN,<sup>1</sup>  
AND THEERACHAI BONGKARN<sup>1,2,\*</sup>

<sup>1</sup>Department of Physics, Faculty of Science, Naresuan University, Phitsanulok, 65000, Thailand

<sup>2</sup>Research Center for Academic Excellence in Applied Physics, Naresuan University, Phitsanulok, 65000, Thailand

*A novel combustion technique has been developed to synthesize  $\text{La}_{0.92}\text{Mg}_{0.18}\text{Fe}_{0.90}\text{O}_3$  or LMF ceramics. The  $\text{NH}_2\text{CH}_2\text{COOH}$  was used as the fuel to accelerate the chemical reaction of raw materials. Thermogravimetric TG and differential thermal analysis DTA were used to estimate the calcination temperature in the range from 800 to 1000°C. The pure perovskite phase was obtained for the samples calcined at 900°C for 2 h. This calcination temperature was selected for the pellets sintered between 1000°C and 1200°C for 2 h. The effect of calcination and sintering temperatures on the phase and morphology evolution of perovskite LMF was investigated. The XRD patterns indicated that LMF exhibited orthorhombic perovskite structure. With increasing the firing temperatures, the lattice parameters and the unit cell volume changed only slightly; the average particle size and the average grain size tended to increase from 133 to 227 nm and 0.40 to 0.92  $\mu\text{m}$ , respectively. The density of sintered ceramics changed between 3.19 and 3.37  $\text{g}/\text{cm}^3$  depending on the sintering temperature.*

**Keywords** Lanthanum magnesium iron; combustion route; perovskite structure; gas sensing

## Introduction

A gas sensor presents the property of changing the resistivity of the sensing material when it is exposed to different gas atmospheres. The perovskite type ( $\text{ABO}_3$ )  $\text{LaFeO}_3$  has received considerable interest for ethanol-gas sensing applications due to its response to ethanol gas and selectivity [1, 2]. However, its gas-sensing properties such as response to ethanol, selectivity and operating conditions are still unsatisfactory. X. Liu *et al.* [3, 4] attempted to improve ethanol sensing properties of  $\text{LaFeO}_3$  by substituting  $\text{Mg}^{2+}$  to A-site ( $\text{La}^{3+}$ ) and B-site ( $\text{Fe}^{4+}$ ) of  $\text{LaFeO}_3$ .

---

Received December 9, 2012; in final form August 25, 2013.

\*Corresponding author. E-mail: researchcmu@yahoo.com

In case of  $\text{La}_{1-x}\text{Mg}_x\text{FeO}_3$  system (A-site substituted), the results demonstrated that increased Mg content enhanced the ethanol response. The highest response of 93.93 was obtained for  $\text{La}_{0.92}\text{Mg}_{0.08}\text{FeO}_3$  while the highest response of  $\text{LaFeO}_3$  was only 15 [3]. For B-site substituted system, the highest response of 128 was obtained from the  $\text{LaMg}_{0.1}\text{Fe}_{0.9}\text{O}_3$  ceramics. Moreover, the response to other gases, such as gasoline, formaldehyde and ammonia, was low i.e. 1.80, 3.10 and 1.37, respectively [4]. These results showed that Mg substitution in  $\text{LaFeO}_3$  at the A-site of 0.08 and the B-site of 0.10 composition may be an attractive considerable for a new type of ethanol sensing materials.

$\text{LaMg}_x\text{Fe}_{1-x}\text{O}_3$  powders can be prepared by wet-chemical methods such as sol-gel [4], citrate method [5] and co-precipitation method [6]. For instance, Porta *et al.* [6] prepared  $\text{LaMg}_x\text{Fe}_{1-x}\text{O}_3$  powders from the citrate precursors. A concentrated solution of metal nitrates was mixed with an aqueous solution of citric acid, by fixing at unity the molar ratio of citric acid to the total metal cations. After evaporation, the gel was heated overnight at  $110^\circ\text{C}$ . The dried gel was slowly calcined for 5 h at  $800^\circ\text{C}$ . The investigation results revealed orthorhombic perovskite with the lattice parameters of 5.556, 7.859 and 5.560 Å for *a*, *b* and *c*, respectively. The average crystallite dimension was 36.4 nm.

Although  $\text{LaMg}_x\text{Fe}_{1-x}\text{O}_3$  powders have been successfully synthesized through the wet chemical methods, these synthesizing techniques are not preferred because they have a complex procedure, require special equipment and have a longer processing time and low production rate. Recently, the combustion technique is increasingly used for the preparation of perovskite ceramics because of their uncomplicated [7–13]. The liquid phase and energy released which are produced by the melting and decomposition fuel effectively speeds up the chemical reaction of raw materials.

As mentioned,  $\text{Mg}^{2+}$  substitution into A-site and B-site for 0.08 and 0.10 of perovskite  $\text{LaFeO}_3$  composition effectively improve ethanol sensing properties of materials. Moreover, the combustion technique may effectively simplify the complicated procedures of the preparation processes. Therefore, the  $\text{La}_{0.92}\text{Mg}_{0.18}\text{Fe}_{0.90}\text{O}_3$  ceramics (abbreviated LMF) were fabricated through the combustion route in this work. The effect of firing temperatures on phase formation and microstructure of LMF was also investigated.

## Experimental Procedure

High purity powders of lanthanum oxide ( $\text{La}_2\text{O}_3$ ), magnesium carbonate ( $\text{MgCO}_3$ ), and iron oxide ( $\text{Fe}_2\text{O}_3$ ) were used as starting materials for producing  $\text{La}_{0.92}\text{Mg}_{0.18}\text{Fe}_{0.90}\text{O}_3$  or LMF ceramics. The above raw materials mixed in the stoichiometric ratio were ball-milled in ethanol for 24 h. After drying, the powder and glycine were mixed in the ratio of 1:2. After grounding and sieving, the reactions of uncalcined LMF powders mixed with glycine were investigated by thermogravimetric and differential thermal analysis (TG-DTA) using a heating rate of  $10^\circ\text{C}/\text{min}$  in air from room temperature to  $1000^\circ\text{C}$ . The various calcined temperatures in the range of 800 to  $1000^\circ\text{C}$  for 2 h were used in order to investigate the formation behavior of synthesized powders. The calcined powders with the optimum calcined conditions were mixed thoroughly with the PVA binder solution. After drying, disk pellets of 15 mm in diameter were fabricated. PVA was burned out in the electric furnace at  $600^\circ\text{C}$ . The disk samples were finally sintered at different temperatures from 1000 to  $1200^\circ\text{C}$  for 2 h in air. The phase content and the crystal structure of prepared samples were characterized by X-ray diffraction. SEM photographs were used to observe morphology, the particle size of powders and grain size of the ceramics. The morphology of calcined

powders was also studied by transmission electron microscopy (TEM). Density of sintered ceramics was measured by the Archimedes method.

## Results and Discussion

The TG-DTA data measured in the interval from the room temperature to 1000°C of  $\text{La}_2\text{O}_3$ ,  $\text{MgCO}_3$ ,  $\text{Fe}_2\text{O}_3$  and glycine are shown in Fig. 1. The decomposition of the organic fuel and the chemical reaction of raw materials were marked by three distinct weight losses. The first weight loss occurred in the temperature range from 170 to 290°C which corresponded to the distinct endothermic peaks at 180 and 215°C. This could be attributed to the decomposition reaction of glycine to ammonia, methanoic acid and carbon dioxide as shown in Formula (1) (decomposition temperature of glycine is 262°C [14]). The second weight loss occurred between 380 and 720°C corresponding to the broad exothermic DTA peak at 390°C. This could be attributed to the vaporization of water and gas caused by the decomposition of methanoic acid as shown in Formula (2) [15]. The energy from the combustion reactions was released in these processes and accelerated the chemical reactions. The third weight loss occurred above 750°C and corresponded to two endothermic peaks at 785 and 810°C seen in the DTA curve. These phenomena were associated with the chemical reaction between  $\text{La}_2\text{O}_3$ ,  $\text{MgCO}_3$  and  $\text{Fe}_2\text{O}_3$ . As temperature reached 1000°C, the weight loss was reduced to 28% of its original weight. It could be inferred that the decomposition processes of glycine and the chemical reaction of raw materials were complete because their weight loss was close to the weight of glycine (66.66%) and the weight of  $\text{CO}_2$  (3.34%) produced by the chemical reaction of raw materials. These results were used to estimate the starting

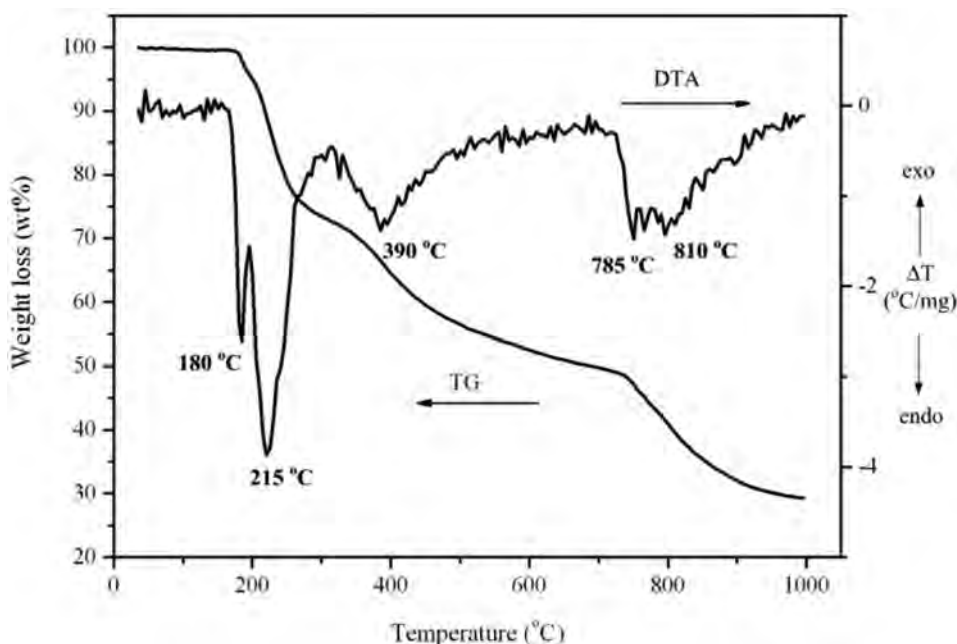


**Figure 1.** TG-DTA curves of the calcinations process of the raw materials mixed with glycine.

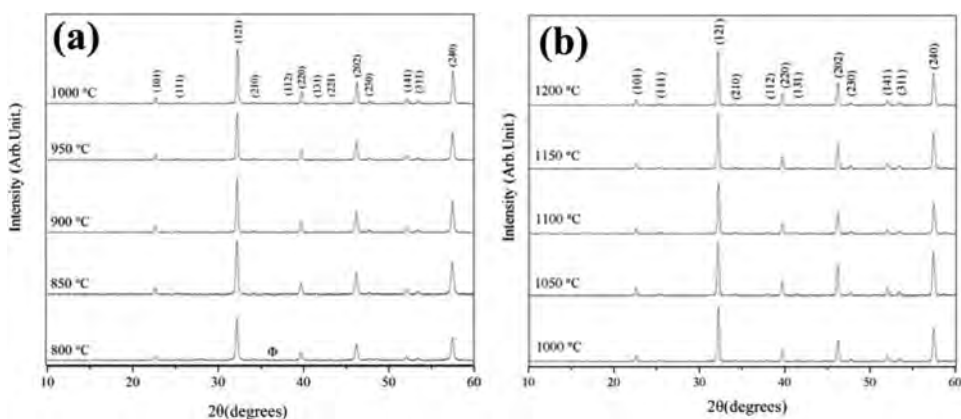
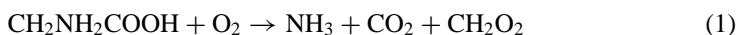


**Figure 2.** X-ray diffraction patterns of LMF; (a) powders calcined at various temperatures for 2 h; ( $\Phi$ )  $\text{La}_2\text{O}_3$  and (b) ceramics sintered at various temperatures for 2 h.

temperature of the calcination process ( $800^\circ\text{C}$ ).



The X-ray diffraction patterns of the calcined powders measured at room temperature displayed the perovskite phase (Fig. 2(a)). The  $\text{La}_2\text{O}_3$  (JCPDS file number 02–0688) was observed at low calcination temperature and was absent at high calcination temperature. The pure perovskite with orthorhombic structure (JCPDS file number 37–1493) existed in the calcined powders with calcination temperature higher than  $850^\circ\text{C}$ . This was consistent with the TG-DTA results. Therefore, in order to obtain the complete reaction and high purity, the optimal calcination temperature of  $900^\circ\text{C}$  was chosen to subsequently produce LMF powder. The percentage of the perovskite phase obtained at various calcination temperatures is listed in Table 1. The lattice parameters and the unit cell volume changed slightly with increasing calcining temperature (Table 1).

Fig. 3 shows the TEM images of LMF powders calcined at  $900^\circ\text{C}$ . A soft agglomeration with narrow particle size distribution was observed (Fig. 3(a)). At higher magnification (Fig. 3(b)), the image showed many fine particles with particle size lower than 100 nm. This confirmed that LMF nano-powders could be produced using the combustion technique.

The calcined powders obtained at  $900^\circ\text{C}$  for 2 h were pressed into pellets and sintered at temperatures in the range from  $1000$  to  $1200^\circ\text{C}$  (step  $50^\circ\text{C}$ ). Fig. 2(b) shows the XRD patterns of the samples sintered at various temperatures. The pure orthorhombic perovskite phase was exhibited in all samples. Table 1 shows the dependence of the unit cell parameters on sintering temperatures. It was found that the firing temperature slightly affected the lattice parameter which was similar to the results of the calcination process.

The SEM micrographs of the ceramics are presented in Fig 4(a–f). The average grain size was determined using the linear interception method. As shown in Fig. 4(a)–(c) and Table 1, the average grain sizes increased with the increase of sintering temperature. Samples sintered at  $1050^\circ\text{C}$  showed comparatively smaller grains than the samples sintered at higher temperatures. The microstructure of the sample sintered at  $1050^\circ\text{C}$  (Fig. 4(a)) showed that the particles became joined together at the contact points. By increasing the

**Table 1**  
Percent perovskite phase, lattice parameters, unit cell volume, average grain size, linear shrinkage and density of LMF

Calcination temperature (°C)	Percent perovskite phase (%)	Lattice parameters (Å)			Unit cell volume (Å <sup>3</sup> )	Sintering temperature (°C)	Lattice parameters (Å)			Unit cell volume (Å <sup>3</sup> )	Average grain size (nm)	Linear shrinkage (%)	Density (g/cm <sup>3</sup> )	Theoretical density %
		a	b	c			a	b	c					
800	95	5.541	7.869	5.562	242.8	1000	5.567	7.979	5.537	245.5	400	0.99	3.37	61.5
850	96	5.555	7.855	5.533	241.5	1050	5.565	7.988	5.532	245.8	450	2.31	3.31	60.4
900	100	5.553	7.857	5.537	241.5	1100	5.553	7.984	5.536	245.5	530	4.29	3.31	60.4
950	100	5.558	7.857	5.534	241.7	1150	5.576	7.983	5.533	246.2	700	4.95	3.26	59.5
1000	100	5.557	7.848	5.521	240.7	1200	5.554	7.991	5.541	246.0	900	6.39	3.19	58.2

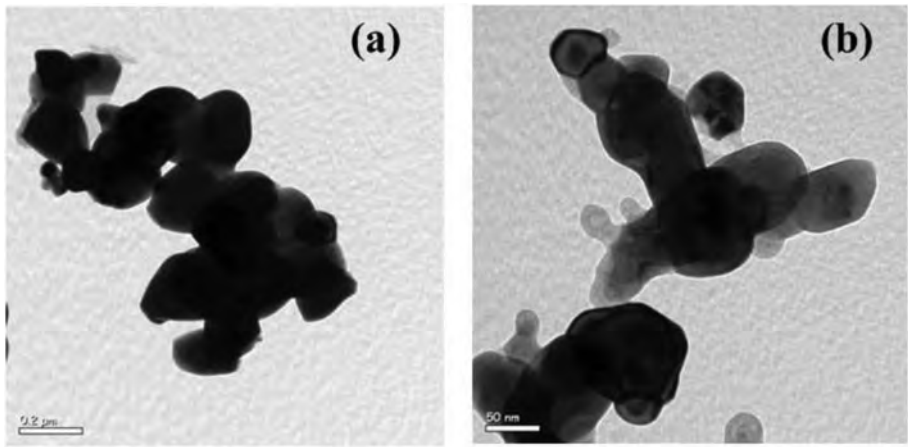


**Figure 3.** TEM micrographs of LMF powders calcined at 900°C for 2 h; (a) original magnification  $\times 37,000$  and (b) original magnification  $\times 135,000$ .

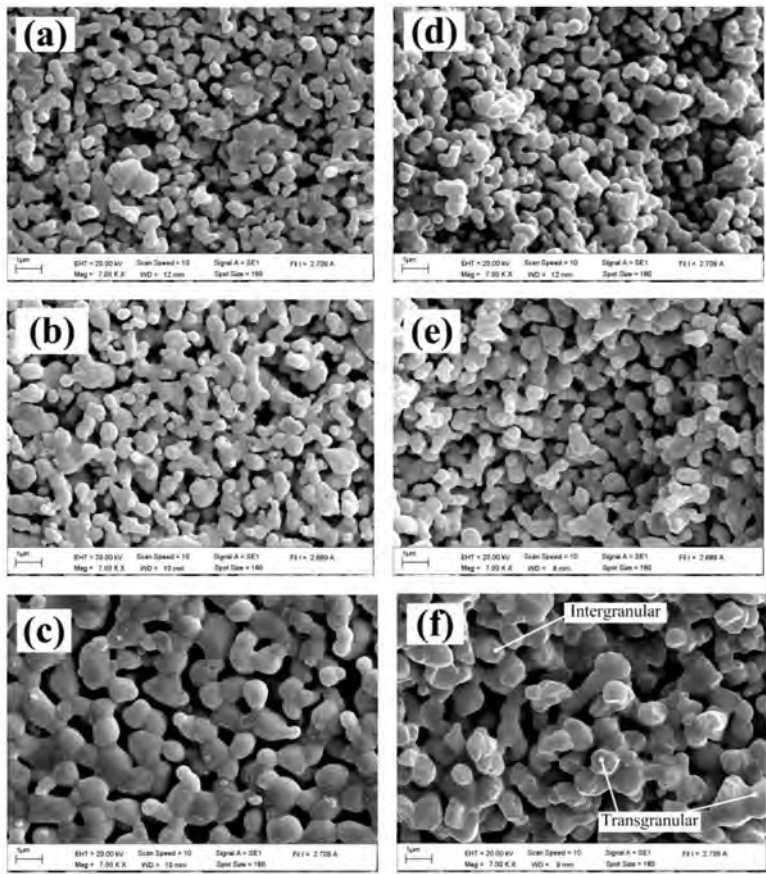


**Figure 4.** SEM photographs of LMF ceramics; (a) surface sintered at 1050°C, (b) surface sintered at 1100°C, (c) surface sintered at 1200°C, (d) fracture sintered at 1050°C, (e) fracture sintered at 1100°C and (f) fracture sintered at 1200°C.



sintering temperature to 1100°C (Fig. 4(b)), the point contacts between particles grew into necks and the grain growth became increasingly active. However, the grain boundaries did not completely form. There was a combination of the neck and grain boundaries. At higher sintering temperature (Fig. 4(c)), the grain growth increased dramatically. The small grains merged and large grain boundaries began to emerge. However, increasing sintering temperature caused the increase of the grain size accompanied with an occurrence of a large pore size. This can be attributed to the coarsening process reduces the driving force for densification [16].

Fig. 4(d)–(f) display the SEM image of the fracture cross section for the LMF sample sintered at 1050, 1100 and 1200°C, respectively. The fracture surface exhibited mostly the transgranular fracture which was characteristic to the weak grains. Increasing the sintering temperature to 1100°C led to significant reduction in pore number and pore size and the increase in the grain size. The transgranular fracture was dominant indicating the weakness in grain still remained. For the pellet sintered at 1200°C, the image showed a mixture of transgranular and intergranular fractures, although the transgranular fracture was dominant. As the grains did not carry any internal strain caused by lattice distortion, a high shear stress might be concentrated at the grain boundaries, leading to intergranular fractures. The increase of intergranular fracture in the samples sintered at high temperature demonstrated the decrease of the defects in ceramics [17].

The measured linear shrinkage, density and theoretical density with a variation in sintering temperatures are listed in Table 1. With increasing sintering temperature, the linear shrinkage and the average grain size tended to increase while the density slightly decreased. This could be explained by the increasing in pore size, observed at the SEM photographs.

## Conclusions

The influence of the firing temperature on the properties of LMF ceramics was studied. The XRD results indicated the pure orthorhombic perovskite structure when the calcination temperature was higher than 900°C. The firing temperature slightly affected the changing of lattice parameters and unit cell volume of the samples. The average agglomerated particle size increased from 133 to 267 nm with the increase of calcination temperature while many fine individual particles with the size lower than 100 nm existed. When the sintered temperature increased, the average grain size tended to increase from 400 to 900 nm. The linear shrinkage increased while the density slightly decreased.

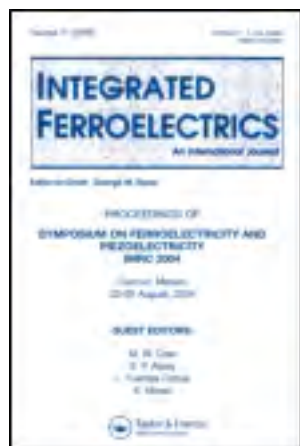
## Acknowledgments

This work was financially supported by the Thailand Research Fund (TRF) and Commission on Higher Education (CHE). Thanks also to Department of Physics, Faculty of Science, Naresuan University for supporting facilities. Acknowledgments also to Prof. Dr. Galina Popovici for helpful comments and corrections of the manuscript.

## References

1. J. Mizusaki, M. Yoshihiro, S. Yamauchi, and K. Fueki, Thermodynamic quantities and defect equilibrium in the perovskite-type oxide solid solution  $\text{La}_{1-x}\text{FeO}_{3-\delta}$ . *J. Solid State Chem.* **67**, 1 (1987).

2. X. Liu, H. Ji, Y. Gu, and M. Xu, Preparation and acetone sensitive characteristics of nano-LaFeO<sub>3</sub> semiconductor thin films by polymerization complex method. *Mater. Sci. Eng. B* **133**, 98 (2006).
3. X. Liu, B. Cheng, H. Qin, P. Song, S. Huang, R. Zhang, J. Hu, and M. Jiang, Preparation, electrical and gas-sensing properties of perovskite-type La<sub>1-x</sub>Mg<sub>x</sub>FeO<sub>3</sub> semiconductor materials. *J. Phys. Chem. Solids*. **68**, 511 (2007).
4. X. Liu, B. Cheng, J. Hu, H. Qin, and M. Jiang, Semiconducting gas sensor for ethanol based on LaMg<sub>x</sub>Fe<sub>1-x</sub>O<sub>3</sub> nanocrystals. *Sensor. Actuat. B* **129**, 53 (2008).
5. P. Ciambelli, S. Cimino, S. De Rossi, L. Lisi, G. Minelli, P. Porta, and G. Russo, AFeO<sub>3</sub> (A = La, Nd, Sm) and LaFe<sub>1-x</sub>Mg<sub>x</sub>O<sub>3</sub> perovskites as methane combustion and CO oxidation catalysts: structural, redox and catalytic properties. *Appl. Catal. B-Environ.* **29**, 239 (2001).
6. P. Porta, S. Cimino, S. Rossi, M. Faticanti, G. Minelli, and I. Pettiti, AFeO<sub>3</sub> (A = La, Nd, Sm) and LaFe<sub>1-x</sub>Mg<sub>x</sub>O<sub>3</sub> perovskites: structural and redox properties. *Mater. Chem. Phys.* **71**, 165 (2001).
7. A. Thongtha and T. Bongkarn, Phase formation and microstructure of barium zirconate ceramics prepared using the combustion technique. *Ferroelectrics*. **383**, 33 (2009).
8. P. Panya and T. Bongkarn, Fabrication of perovskite barium titanate ceramics using combustion route. *Ferroelectrics*. **383**, 102 (2009).
9. N. Chaiyo, R. Muanghlua, S. Niemcharoen, B. Boonchom, and N. Vittayakorn, Solution combustion synthesis and characterization of lead-free piezoelectric sodium niobate (NaNbO<sub>3</sub>) powders. *J. Alloy. Compd.* **509**, 2445 (2011).
10. P. Julphunthong and T. Bongkarn, Phase formation, microstructure and dielectric properties of Ba(Zr<sub>0.1</sub>Ti<sub>0.9</sub>)O<sub>3</sub> ceramics prepared via the combustion technique. *Curr. Appl. Phys.* **11**, S60 (2011).
11. Q. Feng, X. H. Ma, Q. Z. Yan, and C. C. Ge, Preparation of soft-agglomerated nanosized ceramic powders by sol-gel combustion process. *Mat. Sci. Eng. B-Solid*. **162**, 53 (2009).
12. A. Thongtha and T. Bongkarn, Fabrication and characterization of perovskite SrZrO<sub>3</sub> ceramics through a combustion technique. *Key Eng. Mater.* **421**, 223 (2010).
13. N. Phungjitt, P. Panya, T. Bongkarn, and N. Vittayakorn, The structure phase and microstructures of perovskite Ba(Ti<sub>1-x</sub>Zr<sub>x</sub>)O<sub>3</sub> ceramics using the combustion route. *Func. Matter. Lett.* **4**, 169 (2009).
14. C. C. Hwang, T. Y. Wu, J. Wan, and J. S. Tsai, Development of a novel combustion synthesis method for synthesizing of ceramic oxide powders. *Mater. Sci. Eng. B* **111**, 49 (2004).
15. N. Sato, A. T. Quitain, K. Kang, H. Daimon, and K. Fujie, Reaction kinetics of amino acid decomposition in high-temperature and high-pressure water. *Ind. Eng. Chem. Res.* **43**, 3217 (2004).
16. M. N. Rahaman, Ceramic Processing. New York: Taylor and Francis, 2007
17. J. Tong, D. Clark, M. Hoban, and R. O. Hayre, Cost-effective solid-state reactive sintering method for high conductivity proton conducting yttrium-doped barium zirconium ceramics. *Solid State Ionics* **181**, 496 (2010).



## Integrated Ferroelectrics: An International Journal

Publication details, including instructions for authors and subscription information:

<http://www.tandfonline.com/loi/ginf20>

### Low Temperature Fabrication of Dense Calcium Titanate Ceramics via Combustion Technique

Phongthorn Julphunthong<sup>a</sup>, Boonyaphas Phengraek<sup>a</sup>, Artid Laowanidwatana<sup>a</sup> & Theerachai Bongkarn<sup>a b</sup>

<sup>a</sup> Department of Physics, Faculty of Science, Naresuan University, Phitsanulok, 65000, Thailand

<sup>b</sup> Research Center for Academic Excellence in Applied Physics, Naresuan University, Phitsanulok, 65000, Thailand

Published online: 25 Feb 2014.

To cite this article: Phongthorn Julphunthong, Boonyaphas Phengraek, Artid Laowanidwatana & Theerachai Bongkarn (2014) Low Temperature Fabrication of Dense Calcium Titanate Ceramics via Combustion Technique, Integrated Ferroelectrics: An International Journal, 150:1, 107-115, DOI: [10.1080/10584587.2014.874826](https://doi.org/10.1080/10584587.2014.874826)

To link to this article: <http://dx.doi.org/10.1080/10584587.2014.874826>

PLEASE SCROLL DOWN FOR ARTICLE

Taylor & Francis makes every effort to ensure the accuracy of all the information (the "Content") contained in the publications on our platform. However, Taylor & Francis, our agents, and our licensors make no representations or warranties whatsoever as to the accuracy, completeness, or suitability for any purpose of the Content. Any opinions and views expressed in this publication are the opinions and views of the authors, and are not the views of or endorsed by Taylor & Francis. The accuracy of the Content should not be relied upon and should be independently verified with primary sources of information. Taylor and Francis shall not be liable for any losses, actions, claims, proceedings, demands, costs, expenses, damages, and other liabilities whatsoever or howsoever caused arising directly or indirectly in connection with, in relation to or arising out of the use of the Content.

This article may be used for research, teaching, and private study purposes. Any substantial or systematic reproduction, redistribution, reselling, loan, sub-licensing, systematic supply, or distribution in any form to anyone is expressly forbidden. Terms &



# Low Temperature Fabrication of Dense Calcium Titanate Ceramics via Combustion Technique

PHONGTHORN JULPHUNTHONG,<sup>1</sup> BOONYAPHAS  
PHENGRAEK,<sup>1</sup> ARTID LAOWANIDWATANA,<sup>1</sup>  
AND THEERACHAI BONGKARN<sup>1,2,\*</sup>

<sup>1</sup>Department of Physics, Faculty of Science, Naresuan University, Phitsanulok 65000, Thailand

<sup>2</sup>Research Center for Academic Excellence in Applied Physics, Naresuan University, Phitsanulok 65000, Thailand

*In this work, dense calcium titanate ferroelectric ceramics were successfully synthesized using the combustion technique. Urea, glycine and the mixture of urea-glycine were selected as fuels and added to the mixed powders to accelerate the chemical reaction of raw materials. The mixtures were calcined and sintered from 600 to 1150°C and 1150 to 1450°C, respectively. The effects of firing temperatures on the phase formation, crystal structure, microstructure, density and dielectric properties of the prepared samples were investigated. The X-ray diffraction patterns exhibited a pure perovskite structure which was identified for the glycine and urea-glycine mixed samples calcined at 1000°C for 2 h. The calcined powders exhibited an irregular shape and a wide range of particle size distribution at a low calcination temperature. By increasing the calcination temperature, the average particle size tended to increase and the samples expressed a more spherical shape which decreased the particle size distribution. The microstructure, density and dielectric properties results demonstrated that the optimum sintering temperature was 1400°C. The ceramic sintered at this temperature showed dielectric constant and loss of 194 and 0.004, respectively.*

**Keywords** Calcium titanate; combustion technique; phase formation; perovskite phase

## 1. Introduction

Calcium titanate ( $\text{CaTiO}_3$ ) is a perovskite ferroelectric discovered by Gustav Rose in 1839 [1]. Below 1107°C, this material exhibits an orthorhombic structure with space group  $Pbnm$ . Between 1107 to 1227°C, a phase transition occurs and changes the space group to  $Cmcm$ . At 1227°C, the orthorhombic structure transforms to a tetragonal structure with a space group  $I4/mcm$  and it changes to a cubic structure at 1307°C [1].  $\text{CaTiO}_3$  has been widely used in electronic devices and it is a key component of Synroc (a type of synthetic rock used to store nuclear waste) [1]. In addition, it's also used as a thermally-sensitive resistor element due to its negative temperature coefficient [2]. Calcium titanate ceramics are conventionally prepared based on a solid solution of  $\text{CaCO}_3$  and  $\text{TiO}_2$  at a temperature

---

Received in final form August 10, 2013.

\*Corresponding author. E-mail: researchcmu@yahoo.com

of approximately 1465°C, the density of 92–95% of theoretical and the dielectric constant at room temperature of 168 were obtained [2]. This method is relatively simple, yet it is time-consuming and energy intensive while low quality powders are obtained. Recently, a variety of wet-chemical methods such as the sol-gel technique [3], the water-stabilized plasma spray system [4] and the hydrothermal-electrochemical method [5] have also been reported to be effective in generating ultrafine and more homogeneous powders. However, complex schedules and low production rates are the common problems of these wet-chemical methods.

The researchers thus eliminated the drawbacks of the methods mention above by using the combustion synthesis method [6–9]. The basic principle of this method consists of several steps in which the molten organic compound such as urea, glycine, alanine and citric acid provide a liquid medium at the beginning of the reaction. The organic compound combusts quickly within the mixture, which gives out heat that can be effectively supplied to the raw powder in the mixture [10]. Various advantages such as; low processing cost, energy efficiency and high production rate are among the benefits of the combustion synthesis method [11]. In this work, we investigated the synthesis of  $\text{CaTiO}_3$  by the combustion of redox mixtures containing different fuels (urea, glycine and the mixture of urea-glycine). The effects of calcination temperature, sintering temperature and fuel type on phase, morphology and dielectric properties of perovskite  $\text{CaTiO}_3$  were investigated.

## 2. Experimental Procedure

$\text{CaTiO}_3$  powders were synthesized by the combustion technique using urea, glycine and a mixture of urea-glycine as fuels. The raw material composition was prepared from calcium carbonate ( $\text{CaCO}_3$ ) and titanium dioxide ( $\text{TiO}_2$ ) which were weighed and mixed by the ball-milling method for 24 h. The raw materials were dried and ground until fine powders were obtained. The three types of selected fuels, urea, glycine and the mixture of urea-glycine, were added to these powders with a weight ratio of 2:1. After sieving, all mixtures were calcined at various calcinations temperatures ranging from 600 to 1150°C for 2 h. X-ray diffractometry was used to determine the quantitative composition of the phases formed during the calcination process. The selected mixtures were fabricated into disc-shaped specimens, 15 mm in diameter, using a hydraulic press. The pellets were sintered in air atmosphere, at different temperatures from 1150 to 1450°C, for 2 h. The phase formation, crystallographic structure and lattice parameter were examined by X-ray diffraction (XRD). The microstructure of the surface was examined by scanning electron microscopy (SEM). The density of the sintered samples was measured using the Archimedes' method. The dielectric constant ( $\epsilon_r$ ) and the dielectric loss ( $\tan \delta$ ) at room temperature of the ceramics were measured by an LCR meter.

## 3. Results and Discussion

Figure 1(a)–(c) shows the X-ray diffraction (XRD) patterns of the calcined powders which were prepared using three types of fuel. After calcining at 800°C, an orthorhombic perovskite structure was detected together with a tiny amount of a  $\text{CaCO}_2$  and  $\text{TiO}_2$  impurity phase. The relative percentage of the perovskite phase was determined by measuring the major peak intensities of the perovskite phase (the best fit is JCPDS 42-0423) using the



Downloaded by [Naresuan University], [Theerachai Bongkarn] at 20:37 25 February 2014

following equation:

$$\% \text{perovskite phase} = \left( \frac{I_{\text{perov}}}{I_{\text{perov}} + I_{\text{impurities}}} \right) \times 100 \quad (1)$$

This is a well-known equation widely employed in connection with the preparation of complex perovskite structure materials [12]. Here  $I_{\text{perov}}$  and  $I_{\text{impurities}}$  refer to the intensity of the (121) perovskite peak, and the intensities of the highest impurities peaks such as  $\text{CaCO}_3$  or  $\text{TiO}_2$ , respectively. For the samples calcined lower than  $1000^\circ\text{C}$ , the percent of the perovskite phase increased with increasing calcination temperatures. This was exhibited in all fuel mixed powders. However, the percent perovskite phase in the glycine mixed powders was higher than the glycine-urea mixed or the urea mixed powders (Fig. 2). The pure perovskite phase was found in the powder mixed with glycine and urea-glycine when calcined at a temperature higher than  $1000^\circ\text{C}$ . For the urea mixed calcined powders, the pure perovskite phase could not be found and the percent perovskite tended to be unabated at 85% although the calcination temperature was increased up to  $1250^\circ\text{C}$ . These may have been caused by the combustion heat supplied by the urea (10.5 kJ/g) which is lower than glycine (13.0 kJ/g) [7]. From this, it can be inferred that glycine is an appropriate type of fuel for synthesizing calcium titanate via the combustion technique [7]. In addition, the decomposition of glycine effectively supplied sufficient heat to the raw powder in the mixture. The energy supplied in this way speed ups the chemical reaction of the raw powder [10]. This makes the calcination temperature and dwell time, of the combustion technique

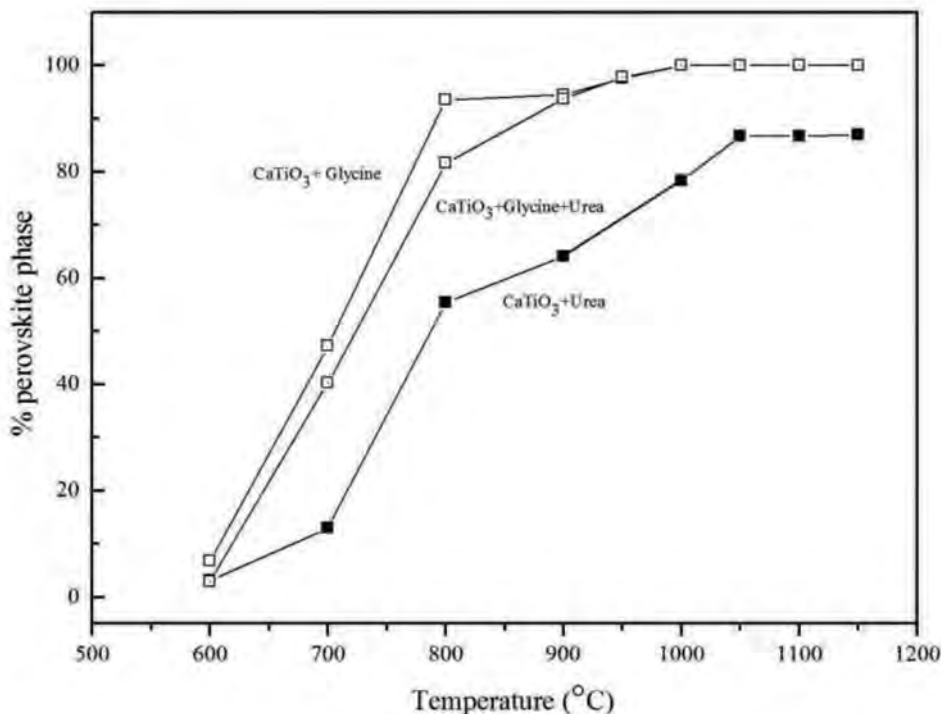


**Figure 2.** The percent perovskite phase of  $\text{CaTiO}_3$  powders calcined at various temperatures.



**Table 1**

Lattice parameter, unit cell volume and average particle size of  $\text{CaTiO}_3$  calcined powders using glycine as a fuel

Calcined temperature (°C)	Lattice parameter <i>a</i> (Å)	Lattice parameter <i>b</i> (Å)	Lattice parameter <i>c</i> (Å)	Unit cell volume (Å <sup>3</sup> )	Average particle size (μm)
600	—	—	—	—	0.31
700	—	—	—	—	0.32
800	—	—	—	—	0.37
900	—	—	—	—	0.37
950	5.417	7.640	5.369	222.2	0.38
1000	5.418	7.641	5.372	222.3	0.47
1050	5.420	7.643	5.373	222.6	0.54
1100	5.423	7.646	5.376	222.9	0.60
1150	5.426	7.648	5.379	223.2	0.64

lower than that of solid state reaction [11, 12] around 115–200°C and 10–19 h, respectively [2, 13].

The lattice parameters of calcined powders were calculated by the least square fitted method. The lattice parameter and the unit cell volume of the glycine mixed samples tended to slightly increase with increased calcining temperatures (Table 1). This result also appeared in the urea and glycine-urea mixed samples. The variation of lattice parameters can probably be associated with the presence of defects due to the structural disorder in the  $\text{CaTiO}_3$  lattice [1].

Figure 3(a)–(d) shows the SEM images of the glycine mixed calcined powders calcined at different temperatures. The samples calcined at 800°C exhibited an irregular shape and a wide range of particle size distribution (Fig. 3(a)). A higher narrow range of particle size distribution and spherical shape appeared when the calcination temperature increased up to 900°C (Fig. 3(b)). Increasing the calcining temperature to 1000°C brought about an increase of the particle size and an agglomerate effect (Fig. 3(c)). When the calcination temperature reached 1150°C, the samples began sintering characteristic particles (Fig. 3(d)). For the glycine mixed calcined powders, the average particle size tended to increase in a range of 0.31–0.64 μm with increasing calcination temperatures as listed in Table 1. The trend of morphology character and an increasing of average particle size of the urea and glycine-urea mixed calcined powders were similar.

The sintered properties of the mixture of raw materials and glycine were investigated. The calcined mixture obtained from the material heated at 1000°C for 2 h was pressed into discs. The green bodies were sintered from 1150–1450°C for 2 h. The XRD patterns of the mixed glycine  $\text{CaTiO}_3$  ceramics sintered at various sintering temperatures is shown in Fig. 1(d). All diffraction peaks, in all sintered samples, were identified as having a pure perovskite structure (Table 2). The lattice parameters and unit cell volume slightly changed with increase of sintered temperatures which was similar to the trend revealed in calcined powders.

The surface microstructural photographs of  $\text{CaTiO}_3$  sintering at different sintering temperature are shown in Fig. 4(a)–(d). The porosity decreased and the uniformity of grain increased with increasing sintering temperature. A uniform grain with low porosity

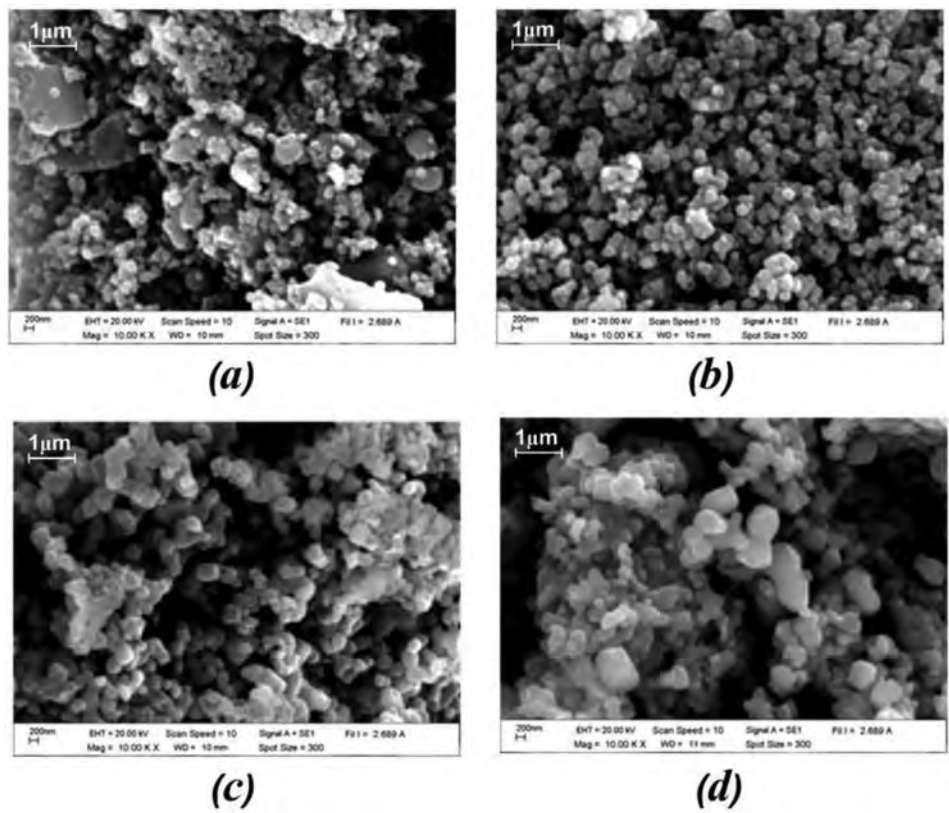


**Figure 3.** SEM photographs of  $\text{CaTiO}_3$  mixed with glycine calcined at various temperatures; (a) calcined at  $800^\circ\text{C}$ , (b) calcined at  $900^\circ\text{C}$ , (c) calcined at  $1000^\circ\text{C}$  and (d) calcined at  $1150^\circ\text{C}$ .

was achieved at  $1400^\circ\text{C}$  (Fig. 4(c)). However, the higher sintering temperature photograph exhibited an unobvious grain which was caused by the melting of the grain boundary (Fig. 4(d)). The increasing of grain size when the sintering temperature was increased can be described by the common grain-growth law [14]. However, at high sintering temperatures

**Table 2**  
Percent perovskite, average grain size, theoretical density, dielectric constant and dielectric loss of  $\text{CaTiO}_3$  ceramics using glycine as a fuel

Sintered temperature ( $^\circ\text{C}$ )	Percent perovskite (%)	Average grain size ( $\mu\text{m}$ )	Theoretical density (%)	Dielectric constant $T_r$	Dielectric loss at $T_r$
1150	100	0.31	87.6	230	19.789
1200	100	0.46	90.2	280	10.031
1250	100	0.52	92.9	703	7.614
1300	100	0.94	93.4	431	1.432
1350	100	1.28	94.6	203	0.031
1400	100	1.39	95.9	194	0.004
1450	100	1.57	91.5	101	0.012

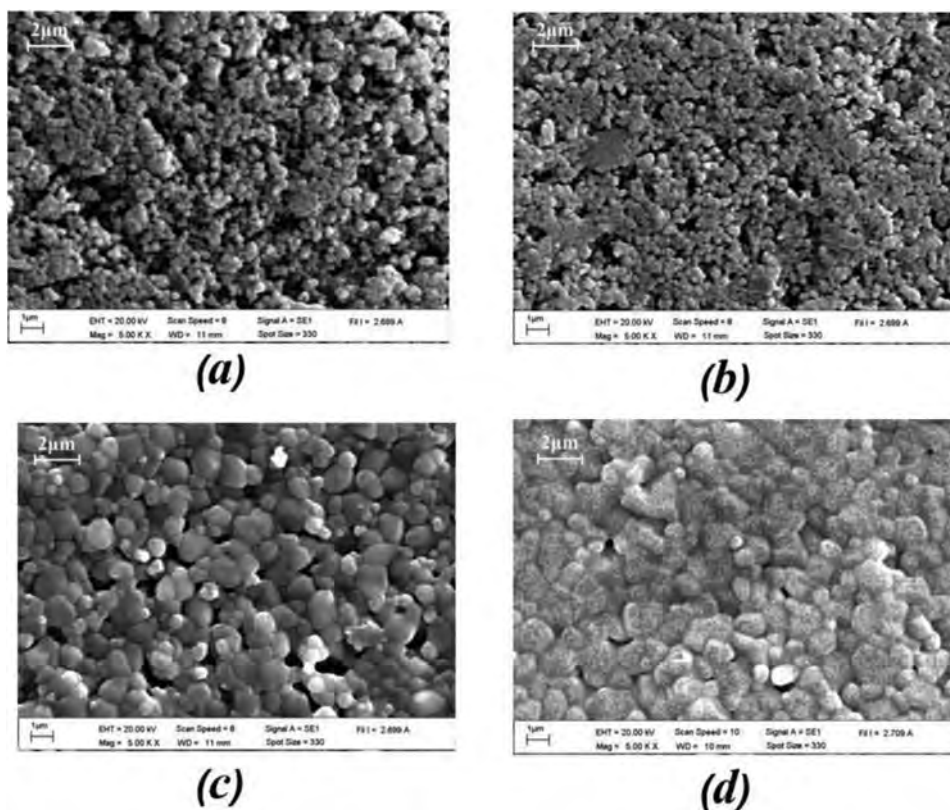


**Figure 4.** SEM photographs of  $\text{CaTiO}_3$  ceramics using glycine as a fuel sintered at various temperatures; (a) sintered at  $1200^\circ\text{C}$ , (b) sintered at  $1300^\circ\text{C}$ , (c) sintered at  $1400^\circ\text{C}$  and (d) sintered at  $1450^\circ\text{C}$ .

( $1450^\circ\text{C}$ ), the increasing of sintering temperature increased the amount of the liquid phase which influenced the diffusion and melting of the grain boundary [15].

The measured density, at various sintering temperatures, is listed in Table 2. The density of the ceramics increased when the sintering temperatures increased and reached its highest density at  $1400^\circ\text{C}$ . The density decreased when the sintering temperature was higher than  $1400^\circ\text{C}$ . These results corresponded with the researcher's microstructure investigation.

The dielectric constant and dielectric loss at room temperature ( $T_r$ ) are listed in Table 2. The dielectric constant at  $T_r$  of the ceramics was increased when sintering temperatures increased and reached its highest at  $1250^\circ\text{C}$ . The dielectric constant decreased when the sintering temperature was higher than  $1250^\circ\text{C}$ . The dielectric loss decreased when sintering temperatures increased and were lowest at  $1400^\circ\text{C}$ . At sintering temperature above  $1400^\circ\text{C}$  the dielectric loss increased. Although the ceramic sintered at  $1250^\circ\text{C}$  exhibited the highest dielectric constant, the high porosity still remained and this brought about a high dielectric loss. This result corresponded to the density result. Due to the decreasing porosity and the increasing density, the ceramics sintered at  $1400^\circ\text{C}$  showed the lowest dielectric loss. The dielectric constant of these sintered ceramics was 194. This value was higher than the ceramics prepared via the solid state route around 15% [2]. The optimum sintering temperature for calcium titanate ceramics prepared via the combustion technique was

1400°C. The ceramics had higher density and dielectric constant, even though the sintering temperatures were lower than those used in the solid state reaction method [2]. This indicates that the combustion technique is an effective way to produce high quality calcium titanate ceramics.

#### 4. Conclusions

High quality calcium titanate ceramics were prepared at a low firing temperature using the combustion technique. The firing temperatures influenced the phase formation, microstructure and dielectric properties of the ceramics. A pure perovskite phase was found in the samples which had been mixed with glycine and urea-glycine calcined at 1000°C. This result was not obtained in the urea mixed sample at any calcination temperatures. The dielectric results demonstrated that the optimum sintering temperature was 1400°C with lowest dielectric loss. The results of the morphology and density investigation supported this conclusion.

#### Acknowledgments

Thanks are also given to Department of Physics, Faculty of Science, Naresuan University for supporting facilities. Acknowledgment also goes to Mr. Don Hindle, for helpful comments and corrections of manuscript.

#### Funding

This work was financially supported by the Thailand Research Fund (TRF) and Commission on Higher Education (CHE).

#### References

1. L. S. Cavalcantea, V. S. Marquesb, J. C. Sczancoski, M. T. Escotec, M. R. Joyaa, J. A. Varelad, M. R. M. C. Santosb, P. S. Pizani, and E. Longo, Synthesis, structural refinement and optical behavior of CaTiO<sub>3</sub> powders: A comparative study of processing in different furnaces. *Chem. Eng. J.* **143**, 299–307 (2008).
2. V. V. Lemanova, A. V. Sotnikova, E. P. Smirnova, M. Weihnacht, and R. Kunze, Perovskite CaTiO<sub>3</sub> as an incipient ferroelectric. *Solid State Commun.* **110**, 611–614 (1999).
3. S. Kaciulis, G. Mattognoa, A. Napoli, E. Bemporad, F. Ferrari, A. Monteneroc, and G. Gnappi, Surface analysis of biocompatible coatings on titanium. *J. Electron. Spectrosc.* **95**, 61–69 (1998).
4. K. Neufussa, and A. Rudajevova, Thermal properties of the plasma-sprayed MgTiO<sub>3</sub>–CaTiO<sub>3</sub> and CaTiO<sub>3</sub>. *Ceram. Int.* **28**, 93–97 (2002).
5. J. P. Wiff, V. M. Fuenzalida, J. L. Arias, and M. S. Fernandez, Hydrothermal–electrochemical CaTiO<sub>3</sub> coatings as precursor of a biomimetic calcium phosphate layer. *Mater. Lett.* **61**, 2739–2743 (2007).
6. T. Bongkarn, and W. Tangkawsakul, Low temperature preparation of antiferroelectric PZ and PBZ powders using the combustion technique. *Ferroelectrics* **383**, 50–56 (2009).
7. C. C. Hwang, T. Y. Wu, J. Wan, and J. S. Tsai, Development of a novel combustion synthesis method for synthesizing of ceramic oxide powders. *Mater. Sci. Eng. B* **111**, 49–56 (2004).
8. P. Julphunthong, and T. Bongkarn, Phase formation, microstructure and dielectric properties of Ba(Zr<sub>0.1</sub>Ti<sub>0.9</sub>)O<sub>3</sub> ceramics prepared via the combustion technique. *Curr. Appl. Phys.* **11**, s60–s65 (2011).

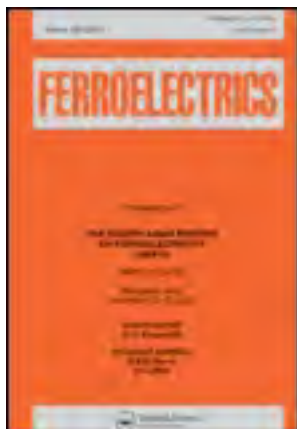
9. P. Sittiketkorn, S. Ramaneeepikool, and T. Bongkarn, The effects of firing temperatures on phase formation and microstructure of  $\text{Pb}_{0.975}\text{Sr}_{0.025}\text{TiO}_3$  ceramics synthesized via the combustion technique, *Ferroelectrics* **403**, 158–165 (2010).
10. J. Xu, D. Xue, and C. Yan, Chemical synthesis of  $\text{NaTaO}_3$  powder at low-temperature. *Mater. Lett.* **59**, 2920–2924 (2005).
11. P. Panya, and T. Bongkarn, Fabrication of perovskite barium titanate ceramics using combustion route. *Ferroelectrics* **383**, 102–110 (2009).
12. R. Sumang, and T. Bongkarn, The effect of calcinations temperatures on the phase formation and microstructure of  $(\text{Pb}_{1-x}\text{Sr}_x)\text{TiO}_3$  powders. *Key. Eng. Mater.* **421–442**, 243–246 (2010).
13. M. Yashima, and R. Ali, Structural phase transition and octahedral tilting in the calcium titanate perovskite  $\text{CaTiO}_3$ . *Solid state ionics* **180**, 120–126 (2009).
14. S. Wagner, D. Kahraman, H. Kungl, and M. J. Hoffmann, Effect of temperature on grain size, phase composition, and electrical properties in the relaxor-ferroelectric-system  $\text{Pb}(\text{Ni}_{1/3}\text{Nb}_{2/3})\text{O}_3\text{-Pb}(\text{Zr,Ti})\text{O}_3$ . *J. Appl. Phys.* **98**, 024102 (2005).
15. M. N. Rahaman, Ceramics processing. *Taylor & Francis*, New York (2007).

This article was downloaded by: [Theerachai Bongkarn]

On: 18 January 2014, At: 08:58

Publisher: Taylor & Francis

Informa Ltd Registered in England and Wales Registered Number: 1072954 Registered office: Mortimer House, 37-41 Mortimer Street, London W1T 3JH, UK



## Ferroelectrics

Publication details, including instructions for authors and subscription information:

<http://www.tandfonline.com/loi/gfer20>

### Low Temperature Fabrication of Lead-Free KNN-BNT Ceramics via the Combustion Technique

Krailas Mathrmool<sup>a b</sup>, Aniruj Akkarapongtrakul<sup>a b</sup>, Supattra Sukkum<sup>a</sup> & Theerachai Bongkarn<sup>a b</sup>

<sup>a</sup> Department of Physics, Faculty of Science, Naresuan University, Phitsanulok, 65000, Thailand

<sup>b</sup> Research Center for Academic Excellence in Applied Physics, Naresuan University, Phitsanulok, 65000, Thailand

Published online: 17 Jan 2014.

To cite this article: Krailas Mathrmool, Aniruj Akkarapongtrakul, Supattra Sukkum & Theerachai Bongkarn (2014) Low Temperature Fabrication of Lead-Free KNN-BNT Ceramics via the Combustion Technique, *Ferroelectrics*, 458:1, 136-145, DOI: [10.1080/00150193.2013.850351](https://doi.org/10.1080/00150193.2013.850351)

To link to this article: <http://dx.doi.org/10.1080/00150193.2013.850351>

PLEASE SCROLL DOWN FOR ARTICLE

Taylor & Francis makes every effort to ensure the accuracy of all the information (the "Content") contained in the publications on our platform. However, Taylor & Francis, our agents, and our licensors make no representations or warranties whatsoever as to the accuracy, completeness, or suitability for any purpose of the Content. Any opinions and views expressed in this publication are the opinions and views of the authors, and are not the views of or endorsed by Taylor & Francis. The accuracy of the Content should not be relied upon and should be independently verified with primary sources of information. Taylor and Francis shall not be liable for any losses, actions, claims, proceedings, demands, costs, expenses, damages, and other liabilities whatsoever or howsoever caused arising directly or indirectly in connection with, in relation to or arising out of the use of the Content.

This article may be used for research, teaching, and private study purposes. Any substantial or systematic reproduction, redistribution, reselling, loan, sub-licensing, systematic supply, or distribution in any form to anyone is expressly forbidden. Terms & Conditions of access and use can be found at <http://www.tandfonline.com/page/terms-and-conditions>

# Low Temperature Fabrication of Lead-Free KNN-BNT Ceramics via the Combustion Technique

KRAILAS MATHRMOOL,<sup>1,2</sup>  
ANIRUJ AKKARAPONGTRAKUL,<sup>1,2</sup> SUPATTRA SUKKUM,<sup>1</sup>  
AND THEERACHAI BONGKARN<sup>1,2,\*</sup>

<sup>1</sup>Department of Physics, Faculty of Science, Naresuan University, Phitsanulok, 65000, Thailand

<sup>2</sup>Research Center for Academic Excellence in Applied Physics, Naresuan University, Phitsanulok, 65000, Thailand

*A lead-free 0.97(K<sub>0.5</sub>Na<sub>0.5</sub>NbO<sub>3</sub>)-0.03(Bi<sub>0.5</sub>Na<sub>0.5</sub>TiO<sub>3</sub>); KNN-BNT ceramic has been fabricated by the combustion technique using urea as a fuel. The precursors were calcined at 600–900°C for 3 h and then sintered at 1000–1100°C for 2 h of dwell time. A pure perovskite phase was found in the powders calcined above 700°C which is lower than the calcination temperature of the solid state reaction method ~200°C. The pellets sintered below 1050°C illustrated a 100% of perovskite phase. The microstructure demonstrated a square and rectangular shape of grains. The average grain size and linear shrinkage increased with the increasing of sintering temperatures. The densest ceramic was discovered in the sample sintered at 1050°C. The DSC result indicated that the Curie point significantly changed with various sintering temperatures.*

**Keywords** KNN-BNT ceramics; combustion method; phase transition

## Introduction

Sodium Potassium Niobate (K<sub>0.5</sub>Na<sub>0.5</sub>)NbO<sub>3</sub> (KNN) is one of the important lead-free piezoelectric materials with a perovskite structure. KNN ceramics have been reported to possess a high Curie temperature ( $T_C \approx 420^\circ\text{C}$ ), a large piezoelectric constant ( $d_{33} \approx 160$  pC/N), high remanent polarization ( $P_r \approx 33$   $\mu\text{C}/\text{cm}^2$ ) and a high electromechanical coupling coefficient ( $k_p \approx 45\%$ ) [1–3]. Unfortunately, pure KNN-ceramics have difficulty becoming fully dense using ordinary sintering methods. This is because the Na<sub>2</sub>O and K<sub>2</sub>O easily disappear at high temperatures [4]. Recently, an efficient solution to this problem was achieved by adding ZnO, BaTiO<sub>3</sub>, SrTiO<sub>3</sub>, CaTiO<sub>3</sub>, Ba(SnTiO<sub>3</sub>) and (BiNa)TiO<sub>3</sub> to the KNN ceramics [5–12]. Among these binary systems, 0.97(K<sub>0.5</sub>Na<sub>0.5</sub>NbO<sub>3</sub>)-0.03(Bi<sub>0.5</sub>Na<sub>0.5</sub>TiO<sub>3</sub>) (KNN-BNT) exhibited a high density ( $\rho = 96\%$ ), high planar coupling coefficient ( $k_p = 43\%$ ) and high piezoelectric properties ( $d_{33} = 195$  pC/N) [12].

The KNN-BNT which has been prepared by the solid state reaction method has consisted of calcined powder and sintered ceramic at 900°C for 5 h and 1100°C for 2 h, respectively [12]. It is well known that ceramics synthesized by the solid state reaction method provide a simple preparation process but they also require high temperatures,

---

Received December 11, 2012; in final form March 16, 2013.

\*Corresponding author. E-mail: researchcmu@yahoo.com

are time consuming and the resulting powders exhibit many undesirable characteristics [13]. Recently, interest has been shown in using the combustion method in the preparation of ferroelectric ceramics because it decreases the temperature in the preparation and results in an ultra-fine particle size [14–18]. The combustion reaction method also has interesting characteristics such as: its simplicity, its relatively low cost, and the fact that it usually results in products with the desired structure and composition [14–18]. Furthermore, a detailed study of KNN-BNT ceramics fabrication using the combustion method has not been reported in the literature. Therefore, in this work, the preparation of  $0.97(\text{K}_{0.5}\text{Na}_{0.5}\text{NbO}_3)-0.03(\text{Bi}_{0.5}\text{Na}_{0.5}\text{TiO}_3)$ ; KNN-BNT via the combustion method using urea as a fuel was studied. The effects of calcination and sintering temperatures on phase formation, microstructure, density and phase transition were investigated and compared to previous works.

## Experimental

The starting materials were commercially available:  $\text{K}_2\text{CO}_3$  (99%),  $\text{Nb}_2\text{O}_5$  (99%),  $\text{Na}_2\text{CO}_3$  (99%),  $\text{Bi}_2\text{O}_3$  (99%) and  $\text{TiO}_2$  (99%). KNN-BNT powders were prepared, using the combustion technique, by thoroughly grinding mixtures of the raw materials by a ball milling procedure (zirconia milling media under ethanol for 24 h). Drying was carried out at  $120^\circ\text{C}$  for 4 h. After sieving, the reaction of the uncalcined powders with well-mixed urea taking place during heat treatment was investigated by thermogravimetric analysis (TGA) using a heating rate of  $10^\circ\text{C}/\text{min}$ , in air, from room temperature up to  $1000^\circ\text{C}$ . The mixed powders were calcined at temperature ranging from 600 to  $900^\circ\text{C}$ , with a dwell time of 3 h and a heating/cooling rate of  $5^\circ\text{C}/\text{min}$ . The calcined powders were then pressed into disks with a diameter of 15 mm at a pressure of 80 MPa. The pellets were sintered at 1000 to  $1100^\circ\text{C}$  for 2 h and cooled in a furnace. X-ray diffraction was employed to identify the phase formed and the optimum temperature to prepare the KNN-BNT powders and ceramics. The calcined powders and sintered ceramics morphologies were imaged using scanning electron microscopy. The density of the sintered ceramics was measured using the Archimedes method. The average particles size and the average grains size were determined by using a mean linear intercept method. The transition temperature was determined by using a Differential Scanning Calorimeter (DSC).

## Results and Discussion

Figure 1 demonstrates the TGA plot of the mixed powders of raw materials and fuel (urea) with a ratio of 1:2. From observations of the TGA curve, there appeared to be three-stages of weight loss from room temperature to  $1000^\circ\text{C}$ . The first immediate weight loss occurred between 140 and  $210^\circ\text{C}$ . This observations related to the reaction when urea melts into a liquid phase (melting point of urea is  $135^\circ\text{C}$ ) and decomposes to produce ammonia isocyanic acid ( $\text{HNCO}$ ) as shown in Formula (1) [19]. The second weight loss occurred rapidly (the slope of weight loss–temperature curve is very steep) between 320 and  $380^\circ\text{C}$ . This can be attributed to the rapid vaporization of ammonia and gas caused by the hydrolysis reaction of isocyanic acid as exhibited in Formula (2) [19]. The energy from the combustion reactions accelerated the chemical reactions and energy was released in these processes [20]. The third weight loss which consisted of a chemical reaction of the raw materials occurred gradually between 360 and  $680^\circ\text{C}$ . Above this temperature the TGA curve basically stabilized. The overall weight loss was found to be about 73%, which



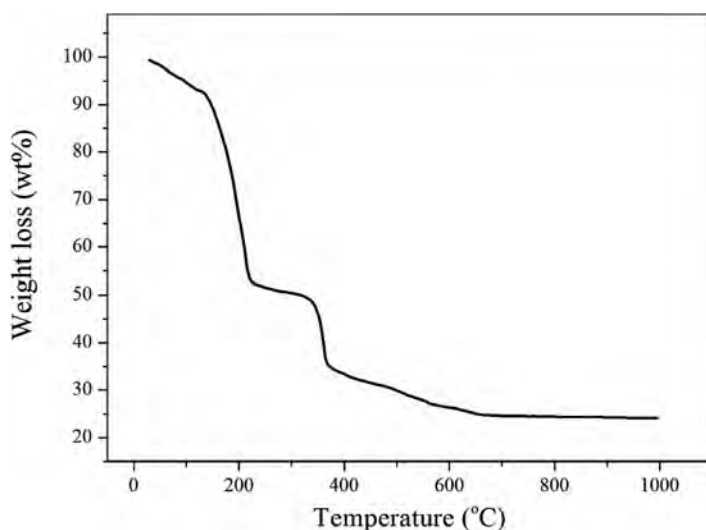


**Figure 1.** TGA curve for the mixture of raw materials and urea.

is close to the value of completely decomposed urea weight and the  $\text{CO}_{2(g)}$  produced from the chemical reaction of the raw materials. Therefore, a temperature of  $600^{\circ}\text{C}$  was selected as the starting calcining temperature in this work.



The XRD patterns of KNN-BNT powders at different calcination temperatures are shown in Fig. 2. The diffraction lines were indexed on the basis of a tetragonal corresponded by ICDD no. 31-1059. The impurity phase of  $\text{K}_2\text{Nb}_4\text{O}_{11}$  was discovered at calcination temperatures below  $700^{\circ}\text{C}$ . The relative amounts of the perovskite phase were determined by measuring the major XRD peak intensities of the perovskite phase. The percentage of the perovskite phase can be calculated by the following equation:

$$\% \text{ perovskite} = \left( \frac{I_{\text{perovskite}}}{I_{\text{perovskite}} + I_{\text{K}_2\text{Nb}_4\text{O}_{11}}} \right) \times 100$$

This equation is well-known and widely employed in the preparation of complex perovskite structure materials [21]. Here  $I_{\text{perovskite}}$ ,  $I_{\text{K}_2\text{Nb}_4\text{O}_{11}}$  and refer to the intensity of the (110) perovskite peak and the intensities of the highest  $\text{K}_2\text{Nb}_4\text{O}_{11}$  peak, respectively. The percentage of the perovskite phase of the KNN-BNT powders calcined for 3 h at temperatures ranging from  $600^{\circ}\text{C}$  to  $900^{\circ}\text{C}$  is shown in Table 1. The increase of phase purity with increasing calcination temperatures is evident. The XRD results corresponded to the TGA investigation. A pure perovskite phase was found in the powders calcined at  $700^{\circ}\text{C}$  which is lower than the calcinations temperature of the solid state reaction method  $\sim 200^{\circ}\text{C}$ .

Figure 3 exhibits SEM photomicrographs of KNN-BNT powders, which were calcined between  $600$  and  $900^{\circ}\text{C}$  for 3 h. These powders exhibited a similar, almost cubic morphology with a variation in size and a porous agglomerated from. The average particle size of the KNN-BNT powders tended to increased with the increase of calcination temperatures. The

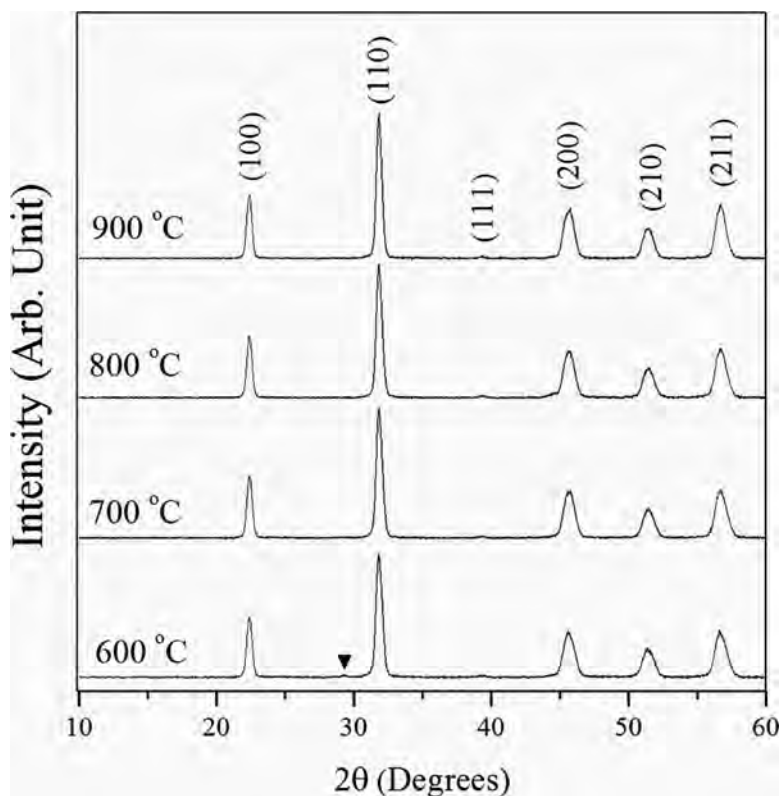


**Figure 2.** XRD patterns of KNN-BNT powders calcined at various temperatures for 3 h: (▼)  $\text{K}_2\text{Nb}_4\text{O}_{11}$ .

linear intercept method gave an average particle size which increased from  $0.43 \mu\text{m}$  to  $0.87 \mu\text{m}$  when the calcination temperatures increased from  $600^\circ\text{C}$  to  $900^\circ\text{C}$  (Table 1).

Calcined powders obtained at  $700^\circ\text{C}$  were pressed into pellets and sintered from  $1000$  to  $1100^\circ\text{C}$  (step up  $25^\circ\text{C}$ ) for 2 h. Figure 4 shows the XRD patterns of KNN-BNT sintered ceramics. The KNN-BNT ceramics were identified as a single phase of a perovskite tetragonal structure in the sample sintered below  $1075^\circ\text{C}$ . The peak of  $\text{K}_4\text{Nb}_6\text{O}_{17}$  (ICDD

**Table 1**

The percent of perovskite phase and average particle size of KNN-BNT powders

Calcined temperature ( $^\circ\text{C}$ )	Percent perovskite phase (%)	Average particle size ( $\mu\text{m}$ )
600	98.2	0.43
650	98.8	0.79
700	100	0.67
750	100	0.75
800	100	0.82
850	100	0.84
900	100	0.87

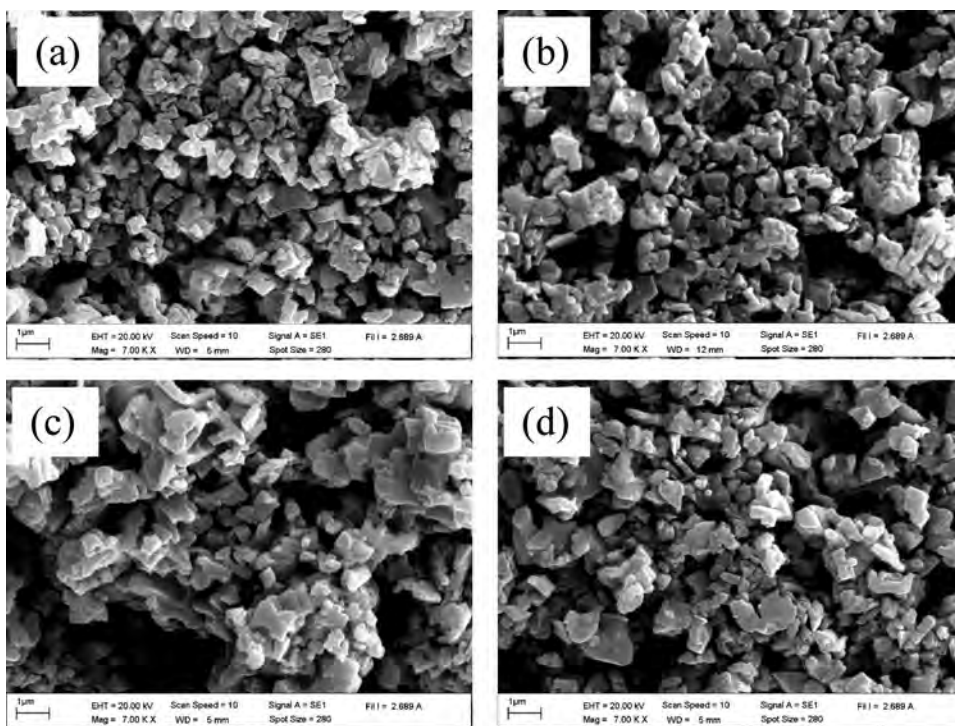


**Figure 3.** SEM photographs of KNN-BNT powders calcined for 3 h at (a) 600°C, (b) 700°C, (c) 800°C and (d) 900°C.

no. 31-1064) was detected at 1075 and 1100°C. This may be due to the vaporization of  $\text{Na}_2$  and  $\text{K}_2\text{O}$  at high temperature [4]. The % perovskite phase of KNN-BNT ceramics at various sintering temperatures exhibits in Table 2. The lattice parameter  $a$  of the KNN-BNT ceramics tended to decreased, while the lattice parameter  $c$  and the lattice anisotropy ( $c/a$ ) of the KNN-BNT ceramics tended to increase when sintering temperature increased as seen in Table 2.

Figure 5 shows the SEM micrograph of the KNN-BNT ceramics sintered between 1000 and 1100°C for 2 h. These ceramics exhibited a square or rectangular shape. When the sintering temperature increased grain size was increased. The average value of the grain size, as measured by the linear intercept method, increased from 0.76 to 1.28  $\mu\text{m}$  with increasing sintering temperature from 1000 to 1100°C (Table 2). At a low sintering temperature (Fig. 5(a) and (b)), many distinct pores and wide grain size distribution were observed. When the sintering temperature was increased to 1050°C (Fig. 5(c)), the porosity decreased significantly and a narrow grain size distribution was obtained. At a high sintering temperature of 1100°C (Fig. 5(d)), the melting of the grain boundaries and an increased porosity were found.

The percentage shrinkage of the pellet samples increased with the increase of sintering temperatures, as shown in Table 2. The highest relative density of 96% (4.37  $\text{g}/\text{cm}^3$ ), is the same level as the previous work [12]. The density of the KNN-BNT ceramics increased when the sintered temperatures increased from 1000°C to 1050°C; thereafter, it decreased when the sintering temperatures increased (Fig. 6). The density results corresponded to the SEM investigation of KNN-BNT ceramics. High dense KNN-BNT ceramics can be

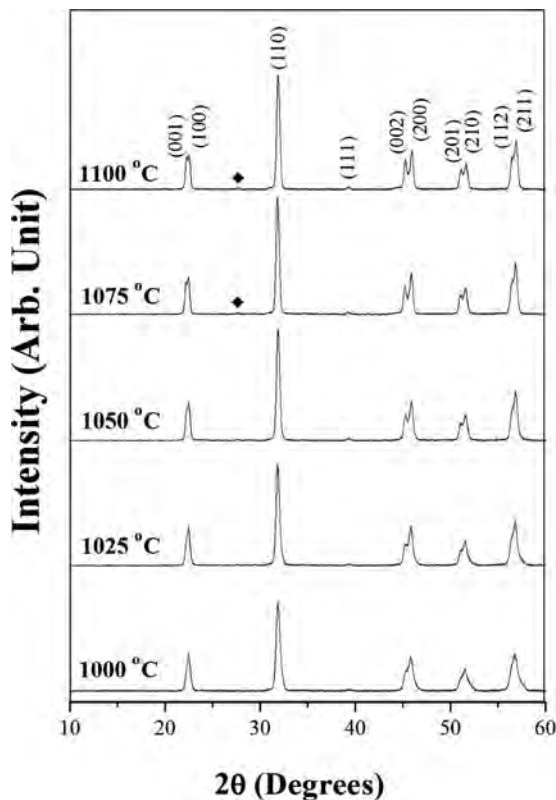


**Figure 4.** XRD patterns of KNN-BNT ceramics sintered for 2 h at various sintering temperatures: (◆)  $\text{K}_4\text{Nb}_6\text{O}_{17}$ .

successfully fabricated by the combustion method using sintering temperature of 1050°C which is lower than the sintering temperature of the solid state reaction method ~40°C.

The DSC thermographs with different sintering temperatures are demonstrated in Fig. 7. On the heating cycle, the endothermic peak was observed in Fig. 7 (a) and (c). This peak is associated with the Curie temperature ( $T_c$ ). The  $T_c$  of all samples exhibits in Table 2.

**Table 2**

The percent perovskite phase, lattice parameters  $a$ ,  $c$ ,  $c/a$ , average grain size and  $T_c$  of KNN-BNT ceramics

Sintering temperature (°C)	% perovskite phase	Lattice Parameter $a$ (Å)	Lattice parameter $c$ (Å)	$c/a$ ratio	Average grain size (μm)	Shrinkage (%)	$T_c$ (°C)
1000	100	3.9578	2.8218	0.7130	$0.76 \pm 2.73$	5.62	314.1
1025	100	3.9518	2.8270	0.7154	$0.77 \pm 2.02$	7.23	274.8
1050	100	3.9508	2.8284	0.7159	$0.81 \pm 2.12$	10.93	312.3
1075	98.07	3.9498	2.8321	0.7170	$1.18 \pm 2.08$	13.53	347.6
1100	97.42	3.9426	2.8298	0.7178	$1.28 \pm 1.93$	15.71	273.9

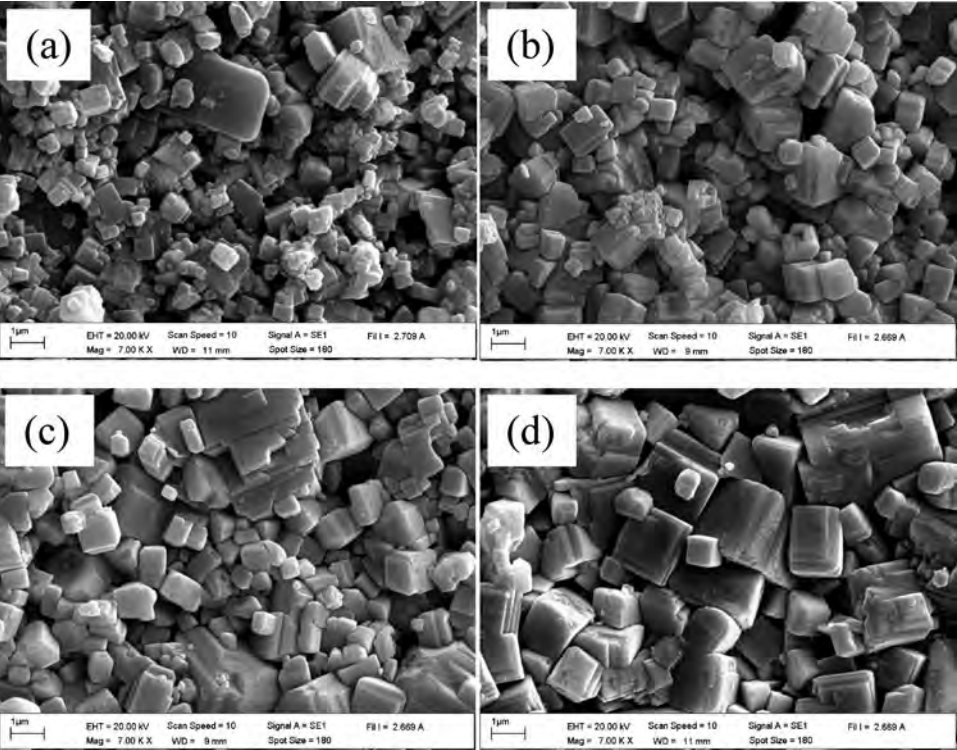


**Figure 5.** SEM photographs of KNN-BNT ceramics sintered for 2 h at (a) 1000°C, (b) 1025°C, (c) 1050°C and (d) 1100°C.

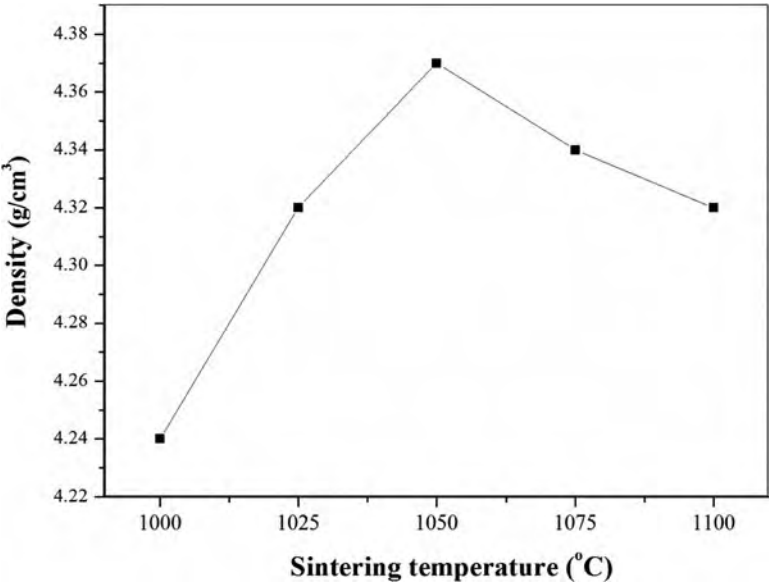


**Figure 6.** Density of KNN-BNT ceramics sintered at various temperatures.

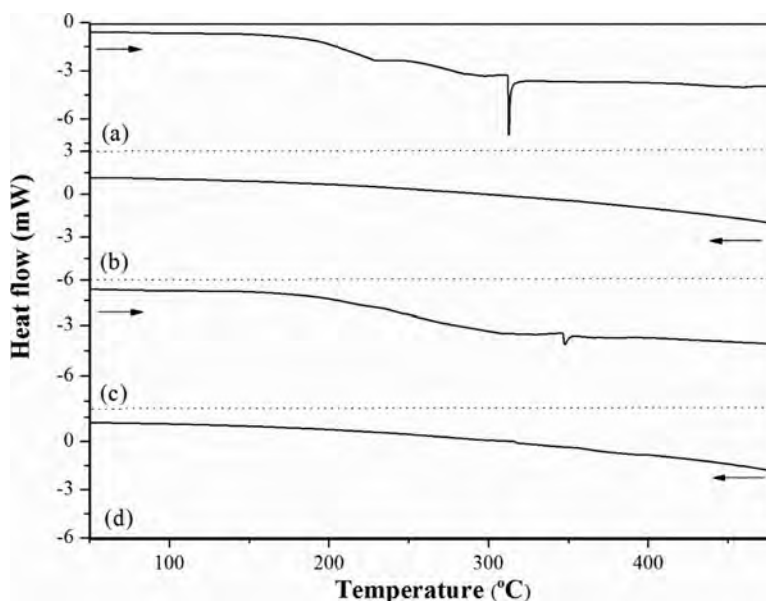


**Figure 7.** DSC plots showing heating and cooling cycles of KNN-BNT ceramics sintered at (a) and (b) 1050°C, (c) and (d) 1075°C.

There was an obvious change in  $T_c$  when the sintering temperature changed. This indicated that the sintering temperature strongly affects the stoichiometric of KNN-based ceramics. During the cooling cycle, the transformation from a paraelectric cubic to a ferroelectric rhombohedral phase was not observed in any samples as shown in Fig. 7(b) and (d). This result is similar to the phase transition from a ferroelectric rhombohedral to antiferroelectric orthorhombic phase of  $(\text{Pb}_{0.90}\text{Ba}_{0.10})\text{ZrO}_3$  ceramics, as reported by B.P. Pokharel and D. Pandey [22, 23]. They proposed that the irreversible cause from transformation of strain during heating-cooling cycles.

## Conclusion

KNN-BNT ceramics were successfully prepared by the combustion method using urea as a fuel. A pure perovskite phase was found in the powders calcined above 700°C for 3 h. and in the pellets sintered at 1050°C for 2 h. These temperatures are lower than KNN-BNT prepared by the solid state reaction method. The XRD results correspond to the TGA results. The average grain size increased with increased sintering temperature. The maximum density was found in the sample sinter at 1050°C. The sintering temperature strongly affected the Curie point of KNN-based ceramics.

## Acknowledgments

This work was financially supported by the Thailand Research Fund (TRF), Commission on Higher Education (CHE). The authors wish to thank the Department of Physics, Faculty of Science, Naresuan University for support facilities. Thanks are also

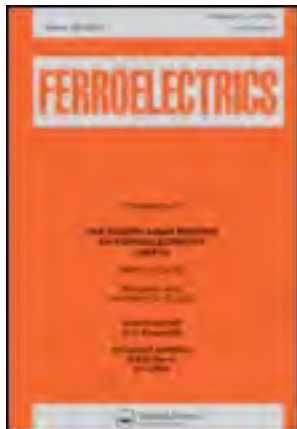
given to Prof. Galina Popovici and Mr. Don Hindle, for their helpful correcting of the manuscript.

## References

1. G. Shirane, R. Newnham, and R. Pepinsky, Dielectric properties and phase transitions of  $\text{NaNbO}_3$  and  $(\text{Na,K})\text{NbO}_3$ . *Phys. Rev.* **96**, 581 (1954).
2. L. Egerton and D. M. Dillon, Piezoelectric and dielectric properties of ceramics in the system potassium-sodium niobate. *J. Am. Ceram. Soc.* **42**, 438 (1959).
3. R. E. Jaeger and L. Egerton, Hot pressing of potassium-sodium niobates, *J. Am. Ceram. Soc.* **45**, 209 (1962).
4. C. Wattanawikkam, S. Chootin, and T. Bongkarn, Crystal structure, microstructure, dielectric and piezoelectric properties of lead-free KNN ceramics fabricated via the combustion method, *Ferroelectrics* (inpress).
5. S. H. Park, C. W. Ahn, S. Nahm, and J. S. Song, Microstructure and piezoelectric properties of ZnO-added  $(\text{Na}_{0.5}\text{K}_{0.5})\text{NbO}_3$ , *Jpn. J. Appl. Phys.* **43**, L1072 (2004).
6. Y. Guo, K. Kakimoto, and H. Ohsato, Structure and electrical properties of lead-free  $(\text{Na}_{0.5}\text{K}_{0.5})\text{NbO}_3$ - $\text{BaTiO}_3$  ceramics. *Jpn. J. Appl. Phys.* **43**, L6662 (2004).
7. M. Kosec, V. Bobnar, M. Hrovat, J. Bernard, B. Malic, and J. Holc, New lead-free relaxors based on the  $\text{K}_{0.5}\text{Na}_{0.5}\text{NbO}_3$ - $\text{SrTiO}_3$  solid solution. *J. Mater. Res.* **19**, 1849 (2004).
8. Y. Guo, K. Kakimoto, and H. Ohsato, Dielectric and piezoelectric properties of lead-free  $(\text{Na}_{0.5}\text{K}_{0.5})\text{NbO}_3$ - $\text{SrTiO}_3$  ceramics, *Solid State Commun.* **129**, 279 (2004).
9. R. C. Chang, S. Y. Chu, Y. F. Lin, C. S. Hong, and Y. P. Wong, An investigate of  $(\text{Na}_{0.5}\text{K}_{0.5})\text{NbO}_3$ - $\text{CaTiO}_3$  base lead-free ceramics and surface acoustic wave devices, *J. Eur. Ceram. Soc.* **27**, 4453 (2007).
10. R. C. Chang, S. Y. Chu, Y. F. Lin, C. S. Hong, P. C. Kao, and C. H. Lu, The effects of sintering temperature on the properties of  $(\text{Na}_{0.5}\text{K}_{0.5})\text{NbO}_3$ - $\text{CaTiO}_3$  base lead-free ceramics, *Sensor Actuat A-phys.* **138**, 355 (2007).
11. C. Wang and J. Wang, Structural and electrical properties of lead-free  $\text{Ba}(\text{Sn,Ti})\text{O}_3$ - $(\text{Na}_{0.5}\text{K}_{0.5})\text{NbO}_3$  ceramics, *Jpn. J. Appl. Phys.* **48**, (2009).
12. R. Zuo, X. Fang, and C. Ye, Phase structures and electric properties of new lead  $(\text{Na}_{0.5}\text{K}_{0.5})\text{NbO}_3$ - $(\text{Bi}_{0.5}\text{Na}_{0.5})\text{TiO}_3$  ceramics, *Appl. Phys. Lett.* **90**, (2007).
13. P. Sittiketkorn, S. Ramaneeepikool, and T. Bongkarn, The effects of firing temperature on phase formation and microstructure of  $\text{Pb}_{0.975}\text{Sr}_{0.025}\text{TiO}_3$  ceramics synthesized via the combustion technique, *Ferroelectrics*, **403**, 158–165 (2010).
14. P. Panya and T. Bongkarn, Fabrication of perovskite barium titanate ceramics using combustion route. *Ferroelectrics*, **383**, 102–110 (2009).
15. C. Wattanawikkam and T. Bongkarn, The influence of calcinations temperature on phase and morphology of BST powders synthesis via solid state reaction method and combustion technique. *Ferroelectrics*. **382**, 42–48 (2009).
16. A. Thongtha, A. Laowanidwatana, and T. Bongkarn, Effect of firing temperatures on phase and morphology evolution of  $\text{CaZrO}_3$  ceramics synthesized using the combustion technique. *Ferroelectrics*. **403**, 3–10 (2010).
17. A. Thongtha and T. Bongkarn, Phase formation and microstructure of barium zirconate ceramic prepared using the combustion technique. *Ferroelectrics*. **383**, 33–39 (2009).
18. N. Phungjit, P. Panya, T. Bongkarn, and N. Vittayakarn, The structure phase and microstructure of perovskite  $\text{Ba}(\text{Ti}_{1-x}\text{Zr}_x)\text{O}_3$  ceramics using a combustion route. *Func. Metter. Lett.* **4**, 169–174 (2009).
19. E. Seker, N. Yasyerli, E. Gulari, C. Lambert, and R. H. Hammerle,  $\text{NO}_x$  reduction by urea under lean conditions oversingle step sol–gel Pt/alumina catalyst. *Appl. Catal. B-environ.* **37**, 27–35 (2002).

20. T. Bongkarn and P. Julphunthong, Phase formation, microstructure and dielectric properties of  $\text{Ba}(\text{Zr}_{0.1}\text{Ti}_{0.9})\text{O}_3$  ceramics prepared via the combustion technique. *Curr. Appl. Phys.* **11**, S60–S65 (2011).
21. R. Zuo, X. Fang, and C. Ye, Phase structures and electrical properties of new lead-free  $(\text{Na}_{0.5}\text{K}_{0.5})\text{NbO}_3-(\text{Bi}_{0.5}\text{Na}_{0.5})\text{TiO}_3$  ceramics. *Appl. Phys. Lett.* **90**, 092904 (2007).
22. B. P. Pokharel and D. Pandey, Irreversibility of the antiferroelectric to ferroelectric phase transition in  $(\text{Pb}_{0.90}\text{Ba}_{0.10})\text{ZrO}_3$  ceramics, *J. Appl. Phys.* **86**, 3327 (1999).
23. B. P. Pokharel and D. Pandey, Dielectric studies of phase transition in  $(\text{Pb}_{1-x}\text{Ba}_x)\text{ZrO}_3$ . *J. Appl. Phys.* **88**, 5364 (2000).





## Ferroelectrics

Publication details, including instructions for authors and  
subscription information:

<http://www.tandfonline.com/loi/gfer20>

### Phase Formation, Microstructure and Electrical Properties of KNN-BZT Ceramics Fabricated via Combustion Technique

Chittakorn Kornphom<sup>a b</sup>, Saranporn Paowsawat<sup>a</sup> & Theerachai  
Bongkarn<sup>a b</sup>

<sup>a</sup> Department of Physics, Faculty of Science, Naresuan University,  
Phitsanulok, 65000, Thailand

<sup>b</sup> Research Center for Academic Excellence in Applied Physics,  
Naresuan University, Phitsanulok, 65000, Thailand

Published online: 17 Jan 2014.

To cite this article: Chittakorn Kornphom, Saranporn Paowsawat & Theerachai Bongkarn (2014) Phase Formation, Microstructure and Electrical Properties of KNN-BZT Ceramics Fabricated via Combustion Technique, *Ferroelectrics*, 458:1, 127-135, DOI: [10.1080/00150193.2013.850342](https://doi.org/10.1080/00150193.2013.850342)

To link to this article: <http://dx.doi.org/10.1080/00150193.2013.850342>

PLEASE SCROLL DOWN FOR ARTICLE

Taylor & Francis makes every effort to ensure the accuracy of all the information (the "Content") contained in the publications on our platform. However, Taylor & Francis, our agents, and our licensors make no representations or warranties whatsoever as to the accuracy, completeness, or suitability for any purpose of the Content. Any opinions and views expressed in this publication are the opinions and views of the authors, and are not the views of or endorsed by Taylor & Francis. The accuracy of the Content should not be relied upon and should be independently verified with primary sources of information. Taylor and Francis shall not be liable for any losses, actions, claims, proceedings, demands, costs, expenses, damages, and other liabilities whatsoever or howsoever caused arising directly or indirectly in connection with, in relation to or arising out of the use of the Content.

This article may be used for research, teaching, and private study purposes. Any substantial or systematic reproduction, redistribution, reselling, loan, sub-licensing, systematic supply, or distribution in any form to anyone is expressly forbidden. Terms &



# Phase Formation, Microstructure and Electrical Properties of KNN-BZT Ceramics Fabricated via Combustion Technique

CHITTAKORN KORNPOM,<sup>1,2</sup> SARANPORN PAOWSAWAT,<sup>1</sup>  
AND THEERACHAI BONGKARN<sup>1,2,\*</sup>

<sup>1</sup>Department of Physics, Faculty of Science, Naresuan University, Phitsanulok, 65000, Thailand

<sup>2</sup>Research Center for Academic Excellence in Applied Physics, Naresuan University, Phitsanulok, 65000, Thailand

*In this work, the effects of calcination temperature in the range of 550–800°C for 2 h and sintering temperature in the range of 1000–1100°C for 2 h on phase formation, microstructure and dielectric properties of the potassium sodium niobate-bismuth zinc titanate  $[0.995(\text{K}_{0.5}\text{Na}_{0.5})\text{NbO}_3-0.005\text{Bi}(\text{Zn}_{0.5}\text{Ti}_{0.5})\text{O}_3]$  (KNN-BZT) ceramics prepared via combustion technique were investigated. Glycine was used as fuel to reduce the reaction temperature. It was found that a single orthorhombic perovskite phase of KNN-BZT powders was observed from the sample calcined at 650°C for 2 h, which was lower than the conventional mixed oxide route  $\sim 200^\circ\text{C}$ . The single orthorhombic perovskite phase was detected in the sample sintered at the temperature lower than 1075°C. The secondary phase of  $\text{Bi}_2\text{Ti}_2\text{O}_7$  was found in the sample sintered at 1100°C. The microstructure of the KNN-BZT powders exhibited an almost-spherical morphology and a highly agglomerated form. The particle size was ranging from 0.2–0.3  $\mu\text{m}$  and the average grain size of the ceramics increased as sintering temperature increased. The optimum condition of sintering was obtained for the sample sintered at 1075°C for 2 h. This sample exhibited maximum density (97%), highest dielectric constant (6400) and excellent ferroelectric properties ( $P_r = 20.5 \mu\text{C}/\text{cm}^2$  and  $E_c = 9.7 \text{ kV}/\text{cm}$ ).*

**Keywords** KNN-BZT ceramic; combustion technique; crystal structure; dielectric properties; ferroelectric properties

## Introduction

The developments of lead-free ferroelectric materials have attracted great attention as a technological problem and environmental impact due to limited use of baneful lead-based materials in electronic devices [1–3]. Significant attention has been paid to  $(\text{K}_{0.5}\text{Na}_{0.5})\text{NbO}_3$  (KNN) materials because of its high piezoelectric properties ( $d_{33} \sim 160 \text{ pC}/\text{N}$ ), good ferroelectric properties ( $P_r = 33 \mu\text{C}/\text{cm}^2$ ), high Curie temperature ( $T_c$ ) (above 420°C) and environmental friendly nature [4–6]. However, it is very difficult to obtain dense KNN

---

Received December 11, 2012; in final form March 16, 2013.

\*Corresponding author. E-mail: researchcmu@yahoo.com

ceramics because of the high volatility of alkaline elements at high temperatures and the easy reaction of potassium carbonate and water vapors in air [7].

To improve the densification and the dielectric properties of KNN ceramics, the system of  $(1-x)(\text{K}_{0.5}\text{Na}_{0.5})\text{NbO}_3-x\text{Bi}(\text{Zn}_{0.5}\text{Ti}_{0.5})\text{O}_3$  ceramics at a composition of around  $0 \leq x \leq 0.3$  was suggested by M. Sutapun *et al.* [8]. At  $x = 0.005$ , this ceramic exhibited an orthorhombic perovskite structure, high density ( $\sim 94\%$ ), high dielectric constant ( $\sim 5900$ ) and high Curie temperature ( $\sim 412^\circ\text{C}$ ). However, the  $0.995(\text{K}_{0.5}\text{Na}_{0.5})\text{NbO}_3-0.005\text{Bi}(\text{Zn}_{0.5}\text{Ti}_{0.5})\text{O}_3$  (KNN-BZT) powders prepared by mixed oxide method using high calcinations temperature ( $850-900^\circ\text{C}$ ) and long dwell time (4 h). Furthermore, for the fabrication of high dense KNN-BZT ceramic, sintering temperatures between  $1000$  and  $1100^\circ\text{C}$  for 2 h must be used [8].

Recently, the high dense ferroelectric ceramics such as  $[(\text{KNaNb})\text{O}_3-(\text{LiSb})\text{O}_3]-(\text{BiSc})\text{O}_3$  [9],  $(\text{Bi Na La Ti})\text{O}_3-(\text{Ba Zr Ti})\text{O}_3$  [10],  $\text{Ba}(\text{Ti}_{1-x}\text{Zr}_x)\text{O}_3$  [11],  $(\text{Ba}_{1-x}\text{Sr}_x)(\text{Zr}_x\text{Ti}_{1-x})\text{O}_3$  [12] were successfully fabricated by the combustion technique using low firing temperature and short dwell time. This technique involves a self-sustained reaction between the reactive materials and the fuel (e.g., urea or glycine) which supplies a liquid medium at the start of the reaction. The reaction can occurrence easily in the liquid medium because the diffusion coefficient is higher than in the solid medium [13]. Moreover, from the literature survey, the preparation of KNN-BZT ceramic by the combustion technique and the ferroelectric properties of KNN-BZT ceramics have not been studied. Therefore, the purposes of this research were to synthesise KNN-BZT ceramics via the combustion technique and to investigate the effect of firing temperatures on phase structure, microstructure, density and electrical properties of this ceramics.

## Experimental

KNN-BZT ceramics with chemical formula of  $(0.995)(\text{K}_{0.5}\text{Na}_{0.5})\text{NbO}_3-0.005\text{Bi}(\text{Zn}_{0.5}\text{Ti}_{0.5})\text{O}_3$  was synthesized by the combustion technique. Raw materials of  $\text{K}_2\text{CO}_3$  (99.0%),  $\text{Na}_2\text{CO}_3$  (99.5%),  $\text{Nb}_2\text{O}_5$  (99.9%),  $\text{Bi}_2\text{O}_3$  (99.97%),  $\text{ZnO}$  (99.9%) and  $\text{TiO}_2$  (99.9%) were dried at  $110^\circ\text{C}$  for 24 h and weighed in chemical stoichiometric proportion. Then, they were mixed and ball milled in ethanol for 24 h by a planetary ball mill with  $\text{YbZrO}_2$  ball media. The suspensions were dried and the powders were ground and sieved. The mixed powders and fuel (glycine ( $\text{C}_2\text{H}_5\text{NO}_2$ )) were mixed with a ratio of 1:2 in the agate mortar. The mixed powders were calcined at various calcination temperatures from  $550^\circ\text{C}$  to  $800^\circ\text{C}$  for 2 h. The KNN-BZT ceramics were fabricated by pure KNN-BZT calcined powders mixed with 3 wt% polyvinyl alcohol (PVA) bond, and uniaxially pressed under 80 MPa into pellets of 15 mm in diameter. After that, the KNN-BZT pellets were sintered in the range of  $1000-1100^\circ\text{C}$  in air for 2 h with a heating rate of  $5^\circ\text{C}/\text{min}$  and cooling down naturally. The phase structures of these sintered pellets were analyzed by X-ray diffraction (XRD) with  $\text{CuK}\alpha$  radiation. Scanning electron microscopy (SEM) was used to examine the surface morphology micrographs. The average particle size and average grain size of the samples were determined by using the linear interception method. The apparent density of the samples was measured by the Archimedes method. Dielectric measurements were performed using an LCR meter at the frequency of 1 kHz. The polarization versus electric field ( $P-E$ ) hysteresis loops of the ceramics were measured using a computer controlled modified Sawyer-Tower circuit.

## Results and Discussion

The X-ray diffraction patterns of the KNN-BZT powder calcined between  $550^\circ\text{C}$  and  $800^\circ\text{C}$  for 2 h are shown in Fig. 1. All peaks showed an orthorhombic perovskite

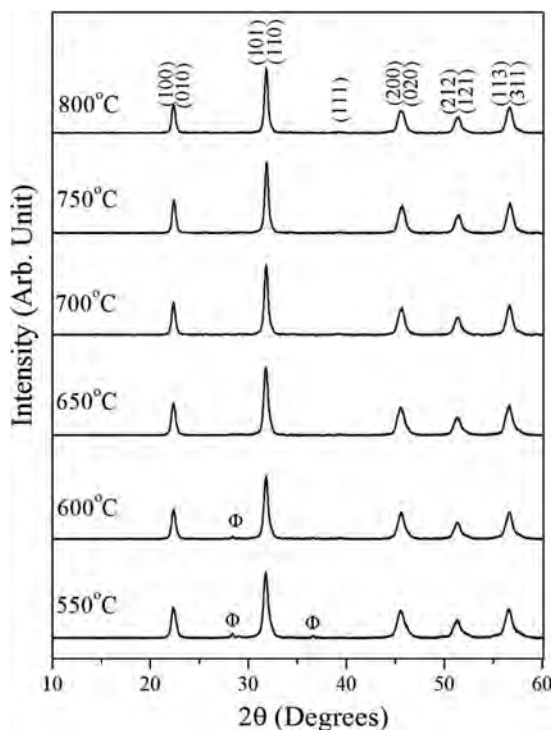


**Figure 1.** X-ray diffraction patterns of the KNN-BZT powders calcined at various temperature; ( $\Phi$ )  $\text{Bi}_2\text{Ti}_2\text{O}_7$ .

structure [8]. However, a weak peak appeared in the calcined powders at  $2\theta$  of  $29^\circ$ , that suggested the existence of the impurity phase identified as  $\text{Bi}_2\text{Ti}_2\text{O}_7$  in the samples calcined at 550 and  $600^\circ\text{C}$ . In order to evaluate the relative amounts of perovskite and impurity phase at each calcined temperature, the following approximation was employed:

$$\% \text{ perovskite phase} = \left( \frac{I_{\text{perov}}}{I_{\text{perov}} + I_{\text{impurity}}} \right) \times 100 \quad (1)$$

This equation is a well-known equation widely employed in connection with the preparation of complex perovskite structure materials [9–12]. Here  $I_{\text{perov}}$  and  $I_{\text{impurity}}$  refer to the intensity of the (110) perovskite peak, and the intensity of the highest  $\text{Bi}_2\text{Ti}_2\text{O}_7$  peak. The percentage of the perovskite phase of KNN-BZT powders increased with increasing calcined temperature (Table 1). The maximum percentage of the perovskite phase in the KNN-BZT powders was 100% obtained by the sample calcined above  $650^\circ\text{C}$  for 2 h. The fabrication of pure KNN-BZT powder via combustion technique was accomplished using lower calcined temperature and shorter dwell time than by using the solid state reaction method (about  $200^\circ\text{C}$  and 2 h, respectively). The reducing calcined temperature by using combustion technique was due to the discharge of the combustion energy and the medium liquid phase which were obtained from the melting and decomposing of fuel in the combustion process [13].

The single phase KNN-BZT powder calcined at  $650^\circ\text{C}$  were pressed into pellets and sintered from 1000 to  $1100^\circ\text{C}$  for 2 h. X-ray diffraction patterns of KNN-BZT sintered

**Table 1**  
Percentage perovskite and the average particle size of KNN-BZT powders

Calcination temperature (°C)	% perovskite phase	Average particle size (μm)
550	93.8	0.21
600	97.6	0.25
650	100	0.27
700	100	0.28
750	100	0.29
800	100	0.30

ceramics are shown in Fig. 2. The ceramics sintered below 1075°C exhibited the single orthorhombic perovskite phase. While the second phase of  $\text{Bi}_2\text{Ti}_2\text{O}_7$  appeared in the ceramic sintered at 1100°C. This result was possibly caused by the evaporations of  $\text{Na}_2\text{O}$ , and  $\text{K}_2\text{O}$  which have low melting point [9].

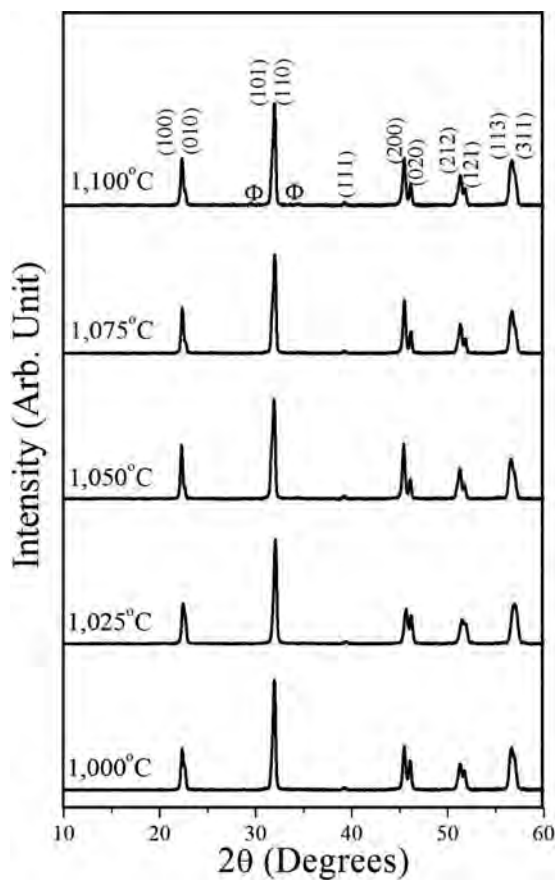


**Figure 2.** X-ray diffraction patterns of the KNN-BZT ceramics sintered at various temperature; (Φ)  $\text{Bi}_2\text{Ti}_2\text{O}_7$ .

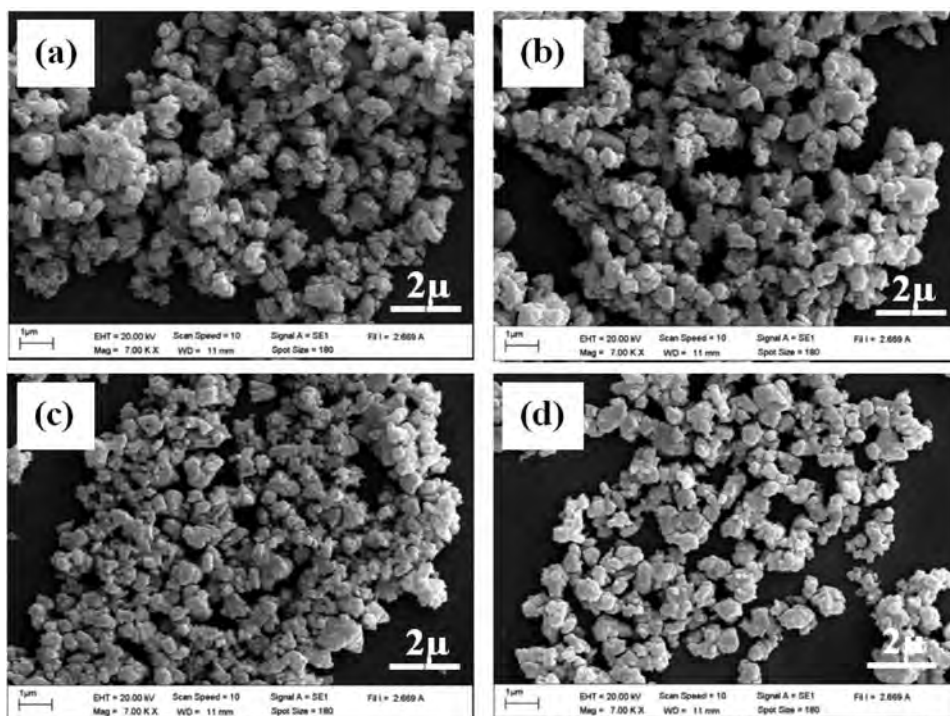


**Figure 3.** The SEM micrographs of KNN-BZT powders calcined at (a) 550°C, (b) 650°C, (c) 750°C and (d) 800°C for 2 h.

The SEM photographs of KNN-BZT powder exhibited an almost spherical morphology and a very agglomerated form (Fig. 3 (a)–(d)). The average particle size of the KNN-BZT powders slightly increased with increasing calcination temperatures as listed in Table 1.

SEM micrographs of as sintered surface of KNN-BZT ceramic sintered at 1000–1100°C for 2 h are presented in Fig 4. The ceramic grain exhibited the polygonal shape in all samples. At a low sintering temperature of 1025–1050°C (Fig 4(a) and (b)), the ceramic exhibited small grain and uniform distribution, with many porosity. The grain grew greatly and the porosity decreased with increased sintering temperature up to 1075°C, in Fig 4(c). When the sintering temperature increased to 1100°C, the ceramic grain have indistinct grain boundaries and increased porosity caused by the grain melt (Fig 4(d)). The average grain size of KNN-BZT ceramics increased from 0.4 to 4.2  $\mu\text{m}$  when sintering temperature increased from 1000 to 1075°C. At the sintering temperatures higher than 1075°C, the average grain size of KNN-BZT decreased as shown in Table 2.

The linear shrinkage, measured density and theoretical density (%T.D.) of KNN-BZT ceramics with the various sintering temperatures are listed in Table 2. The linear shrinkage of ceramics increased from 13.7 to 18.0% when the sintered temperature increased. The density of the ceramics was in the range of 4.05–4.32  $\text{g}/\text{cm}^3$ . They increased with increasing sintering temperature up to 1075°C and then drop in value. The highest density was 95% of the theoretical density and was higher than of the samples prepared via the solid-state reaction method (93%) [8]. The density agree with the microstructure results. Generally, the increase and decrease in density depend on the porosity and the degree of the liquid phase. In our case, the melting temperatures of alkali elements and in the KNN system are low

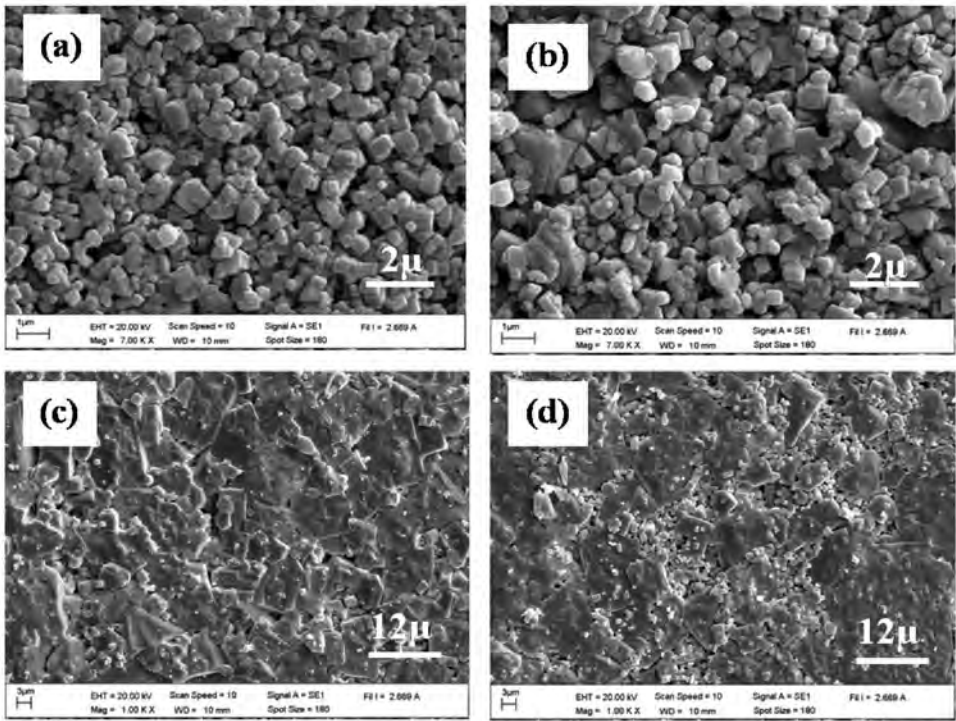


**Figure 4.** The SEM micrographs of KNN-BZT ceramics sintered at (a) 1025°C, (b) 1050°C, (c) 1075°C and (d) 1100°C for 2 h.

[8, 9, 14]. So, the high sintering temperature beget liquid phase and evaporation in KNN-based ceramics.

The dielectric constant ( $\epsilon_r$ ) and dielectric loss ( $\tan \delta$ ) of the KNN-BZT ceramics as a function of temperature measured at the frequency of 1 kHz, are shown in Fig. 5. It was found that, the peak of dielectric constant curve exhibited two dielectric anomalies at  $T_p$  ( $T_p$  is the transition temperature from orthorhombic ferroelectric to tetragonal ferroelectric) and  $T_c$  ( $T_c$  is Curie temperature and relates to the transition from tetragonal ferroelectric to cubic paraelectric) [14, 15]. The  $T_p$  and  $T_c$  of KNN-BZT samples tend to decrease when the sintering increased up to 1050°C and thereafter values of  $T_p$  and  $T_c$  increased as shown

**Table 2**  
Average grain size, linear shrinkage, density, phase transition, and dielectric properties of KNN-BZT ceramics

Sintering temperature (°C)	Average grain size (μm)	Linear shrinkage (%)	Density (g/cm <sup>3</sup> )	%T.D.	$T_p$ (°C)	$T_c$ (°C)	$\epsilon_r$ at $T_c$	$\tan \delta$ at $T_c$
1000	0.41	13.7	4.05 ± 0.03	89.44	159.9	378.6	2704	0.112
1025	0.45	13.9	4.20 ± 0.05	92.76	137.2	383.7	5378	0.122
1050	0.53	16.5	4.22 ± 0.02	93.33	135.8	377.4	6365	0.120
1075	4.22	16.7	4.32 ± 0.07	95.27	137.5	383.2	6400	0.082
1100	2.01	18.0	4.15 ± 0.04	91.67	138.5	379.1	3295	0.121



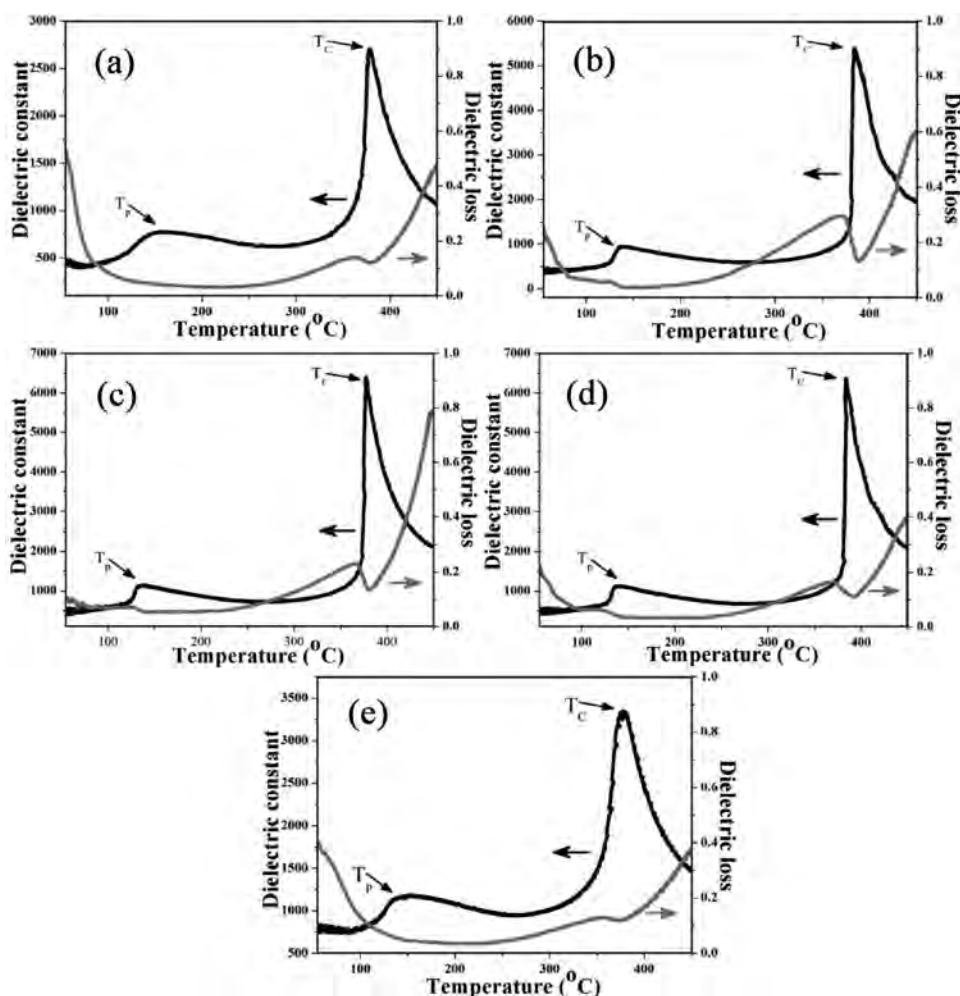


**Figure 5.** Temperature dependence of dielectric constant and dielectric loss of KNN-BZT ceramics sintered at: (a) 1000 °C (b) 1025 °C, (c) 1050 °C, (d) 1075 °C and (e) 1100 °C for 2 h.

in Table 2. From the previous works, The value of  $T_p$  and  $T_c$  of the KNN-BZT ceramics prepared via the solid-state reaction method, which were reported about 118 °C and 412 °C, respectively [8]. In this work, the value of  $T_p$  was in the range of 135–159 °C and  $T_c$  in the range of 377–384 °C, which  $T_p$  was higher while  $T_c$  was lower than the solid-state reaction method. In other words, this specimen exhibited tetragonal phase in the narrow range.

The dielectric constant ( $\epsilon_r$ ) at  $T_c$  of KNN-BZT ceramics increased when sintering temperatures increase up to 1075 °C and thereafter drop to values (Table 2). The value of dielectric loss ( $\tan\delta$ ) at  $T_c$  of KNN-BZT ceramics was exhibited in opposite trend (Table 2). The decrease of the dielectric constant in the samples sintered at high temperatures was due to high porosity which caused a high space charge in the samples. The dielectric properties corresponded with the density, the microstructure and the XRD results. The highest dielectric constant at  $T_c$  of 6,400 was accompanied with a dielectric loss of 0.082, which was obtained in the sample sintered at 1075 °C for 2 h. The maximum dielectric

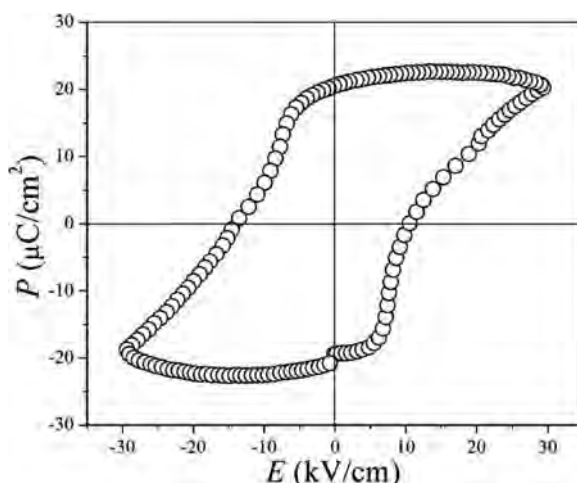


**Figure 6.** The ferroelectric hysteresis of KNN-BZT ceramic sintered at 1075°C for 2 h.

constant prepared via the combustion method was higher than the samples prepared by the solid-state reaction method ( $\sim 5900$ ) [8]. This indicated that the combustion technique is the expedient and the high efficiency method to synthesis high quality of KNN-BZT ceramics.

The polarization ( $P$ – $E$ ) hysteresis loop of the KNN-BZT ceramic sintered at 1075°C which exhibit highest density and measured at a maximum electric field of 30 kV/cm as illustrated in Fig. 6. It is evident that the shape of the  $P$ – $E$  loops exhibited square loop. The remnant polarization ( $P_r$ ) and the coercive field ( $E_c$ ) are determined to be 20.5  $\mu\text{C}/\text{cm}^2$  and 9.7 kV/cm, respectively. This result indicated that the KNN-BZT ceramic are suitably for applied as an micro-actuator and a transducer.

## Conclusions

In conclusion, solid solution KNN-BZT ceramics with a relatively high density was obtained through a combustion technique. The effect of calcination and sintering conditions on phase structure, microstructure, physical properties, dielectric properties and ferroelectric properties were investigated. The single orthorhombic perovskite phase of the KNN-BZT calcined powders was discover in the specimen calcined at 650°C for 2 h. The KNN-BZT could be exhibited the pure orthorhombic structure when sintered below 1075°C. The microstructure and physical properties of the KNN-BZT ceramics has changed for the better when sintering increased up to 1075°C. The maximum density (4.32 g/cm<sup>3</sup>) and the highest dielectric properties at  $T_C$  ( $\epsilon_r = 6400$  and  $\tan \delta = 0.082$ ) were obtained from the specimen sintered at 1075°C for 2 h. The highest dense specimen has good ferroelectric properties ( $P_r = 20.5 \mu\text{C}/\text{cm}^2$  and  $E_c = 9.7 \text{ kV}/\text{cm}$ ).

## Acknowledgments

This work was financially supported by the Thailand Research Fund (TRF) and Commission on Higher Education (CHE). Thanks also to Department of Physics, Faculty of

Science, Naresuan University for supporting facilities. Acknowledgements to Prof. Dr. Galina Popovici, for helpful comments and corrections of the manuscript.

## References

1. B. Jaffe, *Piezoelectric ceramics*. Academic, India, 1971.
2. K. Uchino, *Ferroelectric device*. Marcel Dekker, New York, 2000.
3. T. R. Shrout and S. Zhang, Lead-free piezoelectric ceramics: Alternatives for PZT. *J. Electroceram.* **19**, 113 (2007).
4. J. Tellier, B. Malic, B. Dkhil, D. Jenko, J. Cilensek, and M. Kosec, Crystal structure and phase transitions of sodium potassium niobate perovskites. *Solid State Sci.* **11**, 320 (2009).
5. H. Birol, D. Damjanovic, and N. Setter, Preparation and characterization of  $(K_{0.5}Na_{0.5})NbO_3$  ceramics. *J. Eur. Ceram. Soc.* **26**, 861 (2006).
6. S. Wongsanmai, S. Ananta, and R. Yimnirun, Effect of Li addition on phase formation behavior and electrical properties of  $(K_{0.5}Na_{0.5})NbO_3$  lead free ceramics. *Ceram. Int.* **38**, 147 (2012).
7. W. W. Wolny, European approach to development of new mentally sustainable electroceramics. *Ceram. Int.* **30**, 1079 (2004).
8. M. Sutapuna, C. C. Huang, D. P. Cann, and N. Vittayakorn, Phase transitional behavior and dielectric properties of lead free  $(1-x)(K_{0.5}Na_{0.5})NbO_3-xBi(Zn_{0.5}Ti_{0.5})O_3$  ceramics. *J. All. Comp.* **479**, 462 (2009).
9. C. Wattanawikkam, N. Vittayakorn, and T. Bongkarn, Low temperature fabrication of lead-free KNN-LS-BS ceramics via the combustion method. *Ceram. Int.* **39**, S399 (2013).
10. C. Kornphom, A. Laowanidwatana and T. Bongkarn, The effects of sintering temperature and content of x on phase formation, microstructure and dielectric properties of  $(1-x)(Bi_{0.4871}Na_{0.4871}La_{0.0172}TiO_3)-x(BaZr_{0.05}Ti_{0.95}O_3)$  ceramics prepared via the combustion technique. *Ceram. Int.* **39**, S421 (2013).
11. N. Phungjitt, P. Panya, T. Bongkarn, and N. Vittayakorn, The structural phase and microstructure of perovskite  $Ba(Ti_{1-x}Zr_x)O_3$  ceramics using the combustion route. *Funct. Mater. Lett.* **2**(4), 169 (2009).
12. A. Thongtha, K. Angsukased, and T. Bongkarn, Fabrication of  $(Ba_{1-x}Sr_x)(Zr_xTi_{1-x})O_3$  ceramics using the combustion technique. *Smart Mater. Struct.* **19**, 1 (2010).
13. K. C. Patil, S. T. Aruna, and S. Ekambaram. Combustion synthesis. *Curr. Opin. Solid. St. M.* **2**, 156 (1997).
14. L. Zhengfa, L. Yongxiangand, and Z. Jiwei, Grain growth and piezoelectric property of KNN-based lead-free ceramics. *Curr. Appl. Phys.* **11**, S2 (2011).
15. J. Minhong, D. Manjiao, H. Lu, S. Wang, and X. Lui, Piezoelectric and dielectric properties of  $K_{0.5}Na_{0.5}NbO_3-LiSbO_3-BiScO_3$  lead-free piezoceramics. *Mater. Sci. Eng. A.* **176**, 167 (2011).

# Phase formation and piezoelectric properties of $(\text{Pb}_{0.95}\text{Ba}_{0.05})(\text{Zr}_{1-x}\text{Ti}_x)\text{O}_3$ ceramics fabricated by solid state reaction technique

C. Kornphom, C. Panich and T. Bongkarn\*

This work studied the crystal structure, microstructure and piezoelectric properties of Lead Barium Zirconate Titanate  $[(\text{Pb}_{0.95}\text{Ba}_{0.05})(\text{Zr}_{1-x}\text{Ti}_x)\text{O}_3]$  (PBZT) ceramics with  $0 \leq x \leq 0.50$  step 0.05 prepared by the solid state reaction method. PBZT samples were calcined in the range of 900–1000°C for 1 h and sintered at 1200°C for 3 h. The crystal structure, microstructure and piezoelectric properties were analysed by an X-ray diffractometer (XRD), scanning electron microscope (SEM) and  $d_{33}$  meter. It was found that the PBZT ceramics are indexed in the orthorhombic structure for  $x=0$ , the rhombohedral structure for  $0.05 \leq x \leq 0.30$ , the coexisting of rhombohedral and tetragonal structure for  $0.35 \leq x \leq 0.45$  and the tetragonal structure for  $x=0.50$ . The average grain size and the density are around  $1.20\text{--}2.59\text{ }\mu\text{m}$  and  $7.52\text{--}7.67\text{ g cm}^{-3}$  respectively. The highest piezoelectric coefficient is 129 pC/N obtained by  $x=0.40$ .

**Keywords:** PBZT, Phase formation, Microstructure, Piezoelectric properties, Solid state reaction technique

## Introduction

Lead barium zirconate  $(\text{Pb}_{0.95}\text{Ba}_{0.05})\text{ZrO}_3$  (PBZ) is one of the most widely studied lead based ferroelectric materials. The PBZ shows an anti-ferroelectric orthorhombic phase at room temperature and changes to a rhombohedral ferroelectric phase at high temperature.<sup>1–4</sup> During the phase transition, the PBZ ceramics exhibit high expansion, making it an attractive candidate as a micro actuator in electronic devices.<sup>3,7</sup> In addition, the PBZ ceramic exhibits a cubic paraelectric phase at Curie temperature ( $\sim 210^\circ\text{C}$ ) and its maximum dielectric constant is  $\sim 10\,000$ .<sup>5,6</sup>

Lead barium titanate  $(\text{Pb}_{0.95}\text{Ba}_{0.05})\text{TiO}_3$  (PBT) is an important ferroelectric material because it exhibits a tetragonal ferroelectric phase at room temperature,<sup>8–11</sup> which turns into a cubic paraelectric phase at the Curie point of  $\sim 460^\circ\text{C}$ .<sup>11</sup> The PBT ceramic exhibits a dielectric constant of 3151 at a room temperature. The high Curie temperature of PBT ceramics makes it attractive in the applications of high temperature electric and optical devices.<sup>11</sup>

Lead barium zirconate titanate  $(\text{Pb}_{0.95}\text{Ba}_{0.05})(\text{Zr}_{1-x}\text{Ti}_x)\text{O}_3$  (PBZT) ceramic is a solid system composed of orthorhombic anti-ferroelectric PBZ and tetragonal ferroelectric PBT.<sup>6,11</sup> It can be seen from the phase formation investigation that PBZT ceramic is best applied in the electronic devices using high temperature.<sup>7</sup>

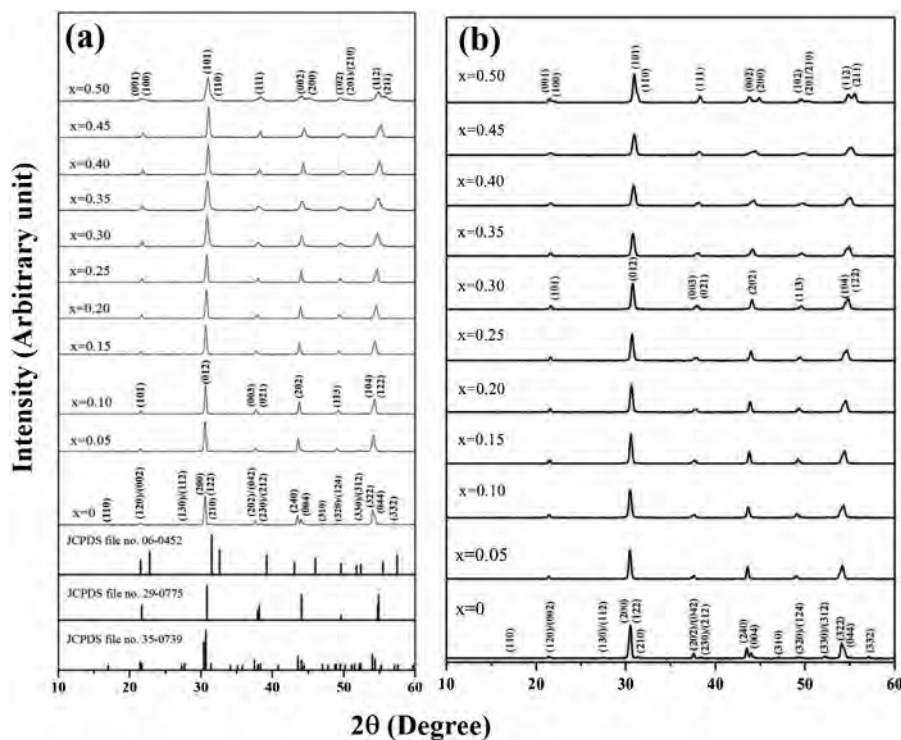
However, its piezoelectric properties are still unknown. Therefore, in this paper, PBZT ceramics with a composition of  $0 \leq x \leq 0.5$  (mole step 0.05 was performed) were prepared by the solid state reaction technique to investigate the influence of the  $x$  content on the phase formation, microstructure, dielectric and piezoelectric properties.

## Experimental

PBZT ceramics with  $0 \leq x \leq 0.50$  step 0.05 were prepared by the solid state reaction method. The raw materials of  $\text{PbO}$ ,  $\text{BaCO}_3$ ,  $\text{ZrO}_2$  and  $\text{TiO}_2$  were weighed and mixed by ball milling for 24 h in ethanol. After being dried, sieved and calcined between 900 and 1000°C for 1 h, the calcined powder was reground and mixed with 2 wt-% binder by ball milling for 24 h. After drying and sieving, the powder was pressed into 15 mm diameter pellets at 80 MPa and sintered at 1200°C for 3 h. During sintering,  $\text{PbZrO}_3$  was used as the spacer powder to minimise the loss of lead due to vaporisation. The crystal structure and microstructure were studied by X-ray diffraction (XRD) and scanning electron microscope (SEM). The average particle size and the average grain size of the samples were determined by using the linear interception method. The density of the sintered ceramics was measured by the Archimedes method using distilled water as a medium. The porosity of the sintered ceramic was measured optically. Dielectric properties measurements were performed using an LCR meter (Agilent 4263B). The measuring frequency was 1 kHz at room temperature. Piezoelectric properties were evaluated after a polling process was carried out in a silicone oil bath at  $150^\circ\text{C}$  under a DC electric field of

Department of Physics, Faculty of Science, Naresuan University, Phitsanulok 65000, Thailand  
Research Center for Academic Excellent in Applied Physics, Naresuan University, Phitsanulok, 65000, Thailand

\*Corresponding author, email researchcmu@yahoo.com



1 XRD patterns of PBZT *a* powders and *b* ceramics with composition of  $0 \leq x \leq 0.50$

30 kV cm<sup>-1</sup> for 30 min. The piezoelectric constant  $d_{33}$  was measured using a piezo- $d_{33}$  meter.

## Results and discussion

The XRD patterns of the PBZT powder with a composition of  $0 \leq x \leq 0.05$  are shown in Fig. 1a. All peaks showed a single phase of the perovskite structure which matched the JCPDS file numbers 35-0739,<sup>12</sup> 29-0775<sup>13</sup> and 06-0452.<sup>14</sup> The SEM photographs of PBZT powder at various compositions exhibited an almost spherical morphology and a porous agglomerated form (Fig. 2a–d). The average particle size of PBZT powders at various compositions was about 0.36–0.52  $\mu\text{m}$  as listed in Table 1.

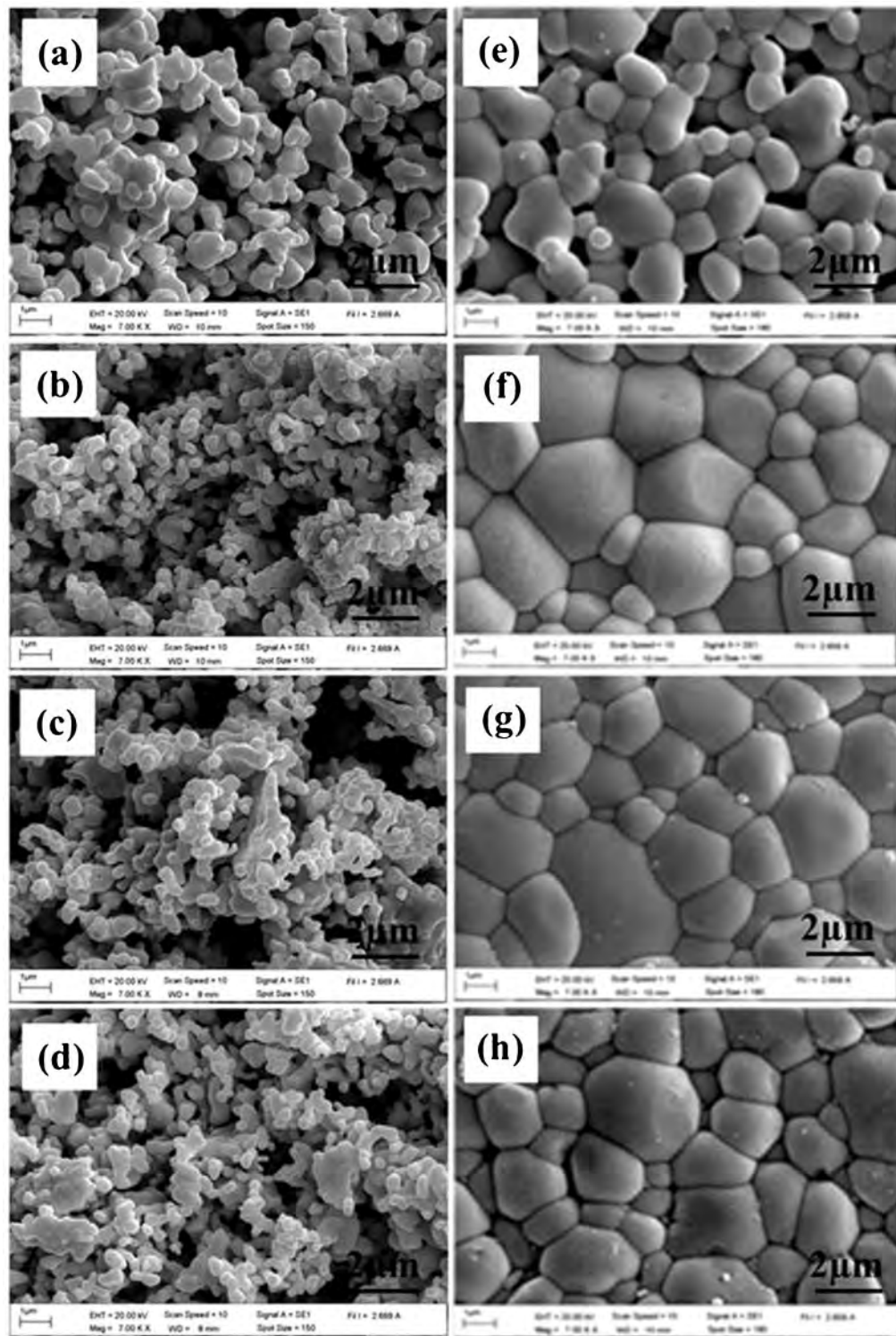
Figure 1b shows the XRD diffraction patterns of PBZT ceramics with  $0 \leq x \leq 0.50$ . The pure perovskite phase was found in all compositions. The XRD patterns at a very low scanning speed, showed the phase change seen in Fig. 3a–c. The theoretic XRD pattern of the orthorhombic structure exhibited a large number of superlattice phases of  $(130)/(112)_O$ ,  $(210)_O$  and  $(230)/(212)_O$ .<sup>6</sup> At  $2\theta$  around  $38^\circ$ , the orthorhombic structure

exhibited doublet peaks of  $(202)_O$  and  $(230)/(212)_O$  whereas the rhombohedral structure and tetragonal structure changed to peaks of  $(003)/(021)_R$  and  $(111)_T$  in the XRD patterns<sup>6</sup> respectively. At  $2\theta$  around  $45^\circ$ , the orthorhombic structure showed double peaks of  $(240)_O$  and  $(004)_O$ , while they unified into a single peak of  $(202)_R$  in the rhombohedral structure, which then split into double peaks of  $(002)_T$  and  $(200)_T$  in a tetragonal structure. The structure of PBZT at a composition of  $x=0$  exhibited an orthorhombic perovskite structure, while the crystal structure was rhombohedral at  $0.05 \leq x \leq 0.30$ , during which the peaks of  $(202)_R$  and  $(003/021)_R$  shifted slightly toward high angles, indicating that the value of the lattice parameter of the rhombohedral structure decreased. The XRD pattern of the PBZT ceramic with  $x$  content being 0.50 indicated a tetragonal structure. However, when  $0.30 \leq x \leq 0.45$ , the diffraction peak of  $(012)_R$  at  $2\theta$  around  $30^\circ$ , and the peak of  $(202)_R$  at  $2\theta$  around  $44^\circ$  changed from symmetry to non-symmetry. Moreover, the peaks of  $(012)_R$  and  $(202)_R$  skewed to the right and the left direction respectively with the increase of the  $x$  content (Fig. 3a and c). The peak of  $(003)/(021)_R$  at  $2\theta$  around  $38^\circ$  started to merge into a single peak of  $(111)_T$ , as seen in (Fig. 3b). However, the peaks of  $(012)_R$  and  $(202)_R$  still exhibited the unclear splitting into doublet peaks of  $(101)/(110)_T$  and  $(002)/(200)_T$  respectively while the peaks of  $(003)/(021)_R$  were still merging and the obvious single peaks of  $(111)_T$  could not be seen. The PBZT ceramics with a composition between 0.30 and 0.45 exhibited the coexisting phases of the rhombohedral and tetragonal structure and the tetragonality increased with the increasing  $x$  content.

The SEM image of the surface of the PBZT ceramics with a composition of  $0 \leq x \leq 0.50$ , sintered at 1200°C for 3 h is shown in Fig. 2e–h. The grain of the PBZT ceramic exhibited a polygonal shape in all samples. At

**Table 1** Average particle size and dielectric properties at  $T_{\text{room}}$  of PBZT samples

$x$	Average particle size/ $\mu\text{m}$	$\varepsilon_r$	$\tan \delta$
0	$0.36 \pm 0.012$	173	0.05
0.05	$0.42 \pm 0.020$	419	0.07
0.10	$0.52 \pm 0.018$	372	0.02
0.15	$0.46 \pm 0.016$	583	0.01
0.20	$0.42 \pm 0.008$	565	0.01
0.25	$0.43 \pm 0.013$	631	0.01
0.30	$0.39 \pm 0.012$	675	0.02
0.35	$0.41 \pm 0.013$	644	0.01
0.40	$0.40 \pm 0.017$	656	0.02
0.45	$0.40 \pm 0.014$	939	0.01
0.50	$0.38 \pm 0.014$	916	0.01

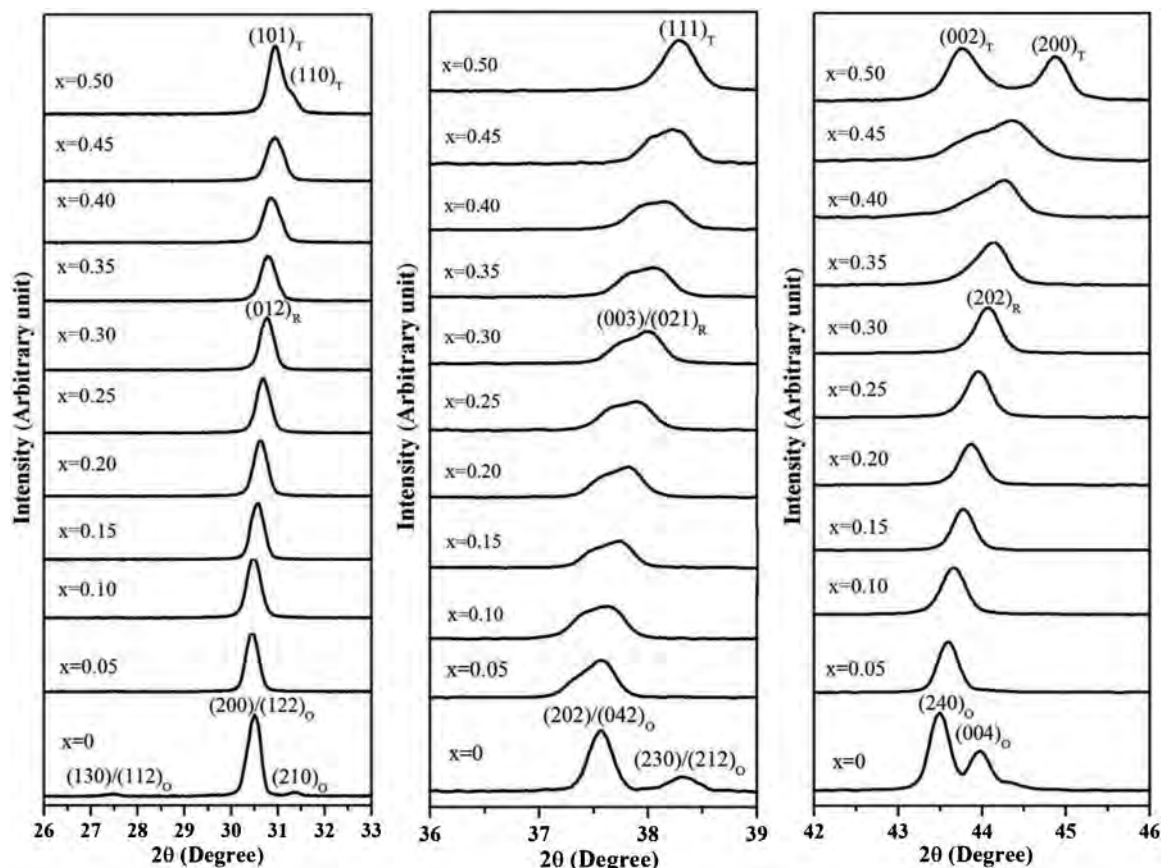


**2 Images (SEM) of PBZT powders with *a*  $x=0.10$ , *b*  $x=0.30$ , *c*  $x=0.40$ , *d*  $x=0.50$  and PBZT ceramics with *e*  $x=0.05$ , *f*  $x=0.15$ , *g*  $x=0.25$  and *h*  $x=0.35$**

$x=0.05$  (Fig. 2e), this ceramic exhibited small grains and a uniform distribution, with much porosity. The grain grew greatly and the porosity decreased with the  $x$  content between 0.15 and 0.25 as shown in Fig. 2f and g. When the  $x$  content exceeded 0.35, the ceramics grain was reduced, but its porosity increased (Fig. 2h). The average grain size of the PBZT ceramics was around 1.2 to 2.7  $\mu\text{m}$ . The density and the theoretical density of these ceramics were about 7.52–7.67  $\text{g cm}^{-3}$  and 94.0–95.9% respectively.

The dielectric constant ( $\epsilon_r$ ) and the dielectric loss ( $\tan \delta$ ) at room temperature of the PBZT ceramic at  $0 \leq x \leq 0.05$  are shown in Table 1. The value of  $\epsilon_r$  tended to increase with the increasing  $x$  content, whereas the value of  $\tan \delta$  are free from the  $x$  content, between 0.01 and 0.07 (see Table 1).

Piezoelectric properties ( $d_{33}$ ) as a function of the  $x$  content are shown in Fig. 4. The  $d_{33}$  tended to increase with  $x$  content going up to 0.40 and then decreased rapidly when  $x$  exceeded 0.40. The highest  $d_{33}$  value



**3** X-ray diffraction pattern of PBZT ceramics with compositions of  $0 \leq x \leq 0.50$  at very low scanning rate: *a* at  $2\theta$  around  $30^\circ$ ; *b* at  $2\theta$  around  $36^\circ$ ; *c* at  $2\theta$  around  $44^\circ$

of 129.4 pC/N was obtained at  $x=0.40$ . The piezoelectric coefficient measurements verified the superior piezoelectric properties at a ratio of  $x=0.40$ . At this ratio, the ceramic exhibits coexisting phases between the rhombohedral and the tetragonal. It should be noted that this composition of PBZT ceramic (Zr/Ti=60:40) is close to the MPB of PZT ceramic (Zr/Ti=52:48).<sup>15</sup>

## Conclusions

The amount of  $Zr^{4+}$  and  $Ti^{4+}$  ions has significant effects on the phase formation, microstructure, and piezoelectric properties of PBZT ceramics. The structure

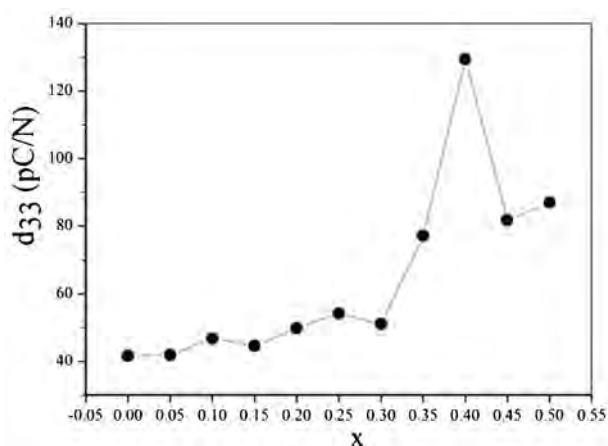
of the PBZT ceramics are orthorhombic for  $x=0$ , rhombohedral for  $0.05 \leq x \leq 0.30$ , both rhombohedral and tetragonal for  $0.35 \leq x \leq 0.45$  and tetragonal for  $x=0.50$ . The highest piezoelectric coefficient is 129.4 pC/N obtained at  $x=0.40$ .

## Acknowledgement

This study was financially supported by the Thailand Research Fund (TRF), and the Commission on Higher Education (CHE). The authors sincerely thank the Department of Physics, Faculty of Science, Naresuan University for supporting facilities. Thanks also go to Dr Antony Harfield and Mr Don Hindle for their help in editing the manuscript.

## References

1. S. Roberts: 'Dielectric properties of lead zirconate and barium-lead zirconate', *J. Am. Ceram. Soc.*, 1950, **33**, 63–66.
2. S. Roberts: 'Piezoelectric effect in lead zirconate', *Phys. Rev.*, 1951, **83**, 1078.
3. G. Rujijanagul and T. Bongkarn: 'Phase transition and linear thermal expansion of  $(Pb_{1-x}Ba_x)ZrO_3$  ceramics', *Phase Trans.*, 2007, **80**, 209–215.
4. T. Bongkarn and G. Rujijanagul: 'Properties of perovskite lead barium zirconate ceramics', *Ferroelectrics*, 2007, **358**, 67–73.
5. B. P. Pokharel and D. Pandey: 'Dielectric studies of phase transitions in  $(Pb_{1-x}Ba_x)ZrO_3$ ', *J. Appl. Phys.*, 2000, **88**, 5364–5373.
6. N. Vittayakorn, T. Bongkarn and G. Rujijanagul: 'Phase transition, mechanical, dielectric and piezoelectric properties of perovskite  $(Pb_{1-x}Ba_x)ZrO_3$  ceramics', *Phys. B*, 2007, **387B**, 415–420.
7. A. Thongtha, C. Wattanawikkam and T. Bongkarn: 'Phase formation and dielectric properties of  $(Pb_{0.925}Ba_{0.075})(Zr_{1-x}Ti_x)O_3$  ceramics prepared by the solid-state reaction method', *Phase Trans.*, 2011, **84**, 952–959.



**4** Piezoelectric coefficient of PBZT ceramics at various compositions

8. T. Bongkarn and P. Panya: 'Fabrication of lead barium titanate ceramics via conventional solid-state mixed oxide technique', *Adv. Mater. Res.*, 2008, **55-57**, 209–212.
9. X. Xing, J. Deng, Z. Zhu and G. Liu: 'Solid solution Ba<sub>1-x</sub>Pb<sub>x</sub>TiO<sub>3</sub> and its thermal expansion', *J. Alloy Comp.*, 2003, **353**, 1–4.
10. R. Sumang and T. Bongkarn: 'Phase formation, microstructure and phase transition of lead barium titanate ceramics: effect of PbO content', *Ferroelectrics*, 2009, **313**, 57–64.
11. P. Panya, S. Ramaneeepikool and T. Bongkarn: 'Dependence of firing temperatures on phase formation, microstructure and phase transition of (Pb<sub>1-x</sub>Ba<sub>x</sub>)TiO<sub>3</sub> ceramics', *Ferroelectrics*, 2010, **403**, 204–212.
12. Powder Diffraction File No. 35-0739, International Centre for Diffraction Data, Newton Square, PA, 2000.
13. Powder Diffraction File No. 29-0775, International Centre for Diffraction Data, Newton Square, PA, 2000.
14. Powder Diffraction File No. 06-0452, International Centre for Diffraction Data, Newton Square, PA, 2000.
15. C. Wang, Q. F. Fang and Z. G. Zhu: 'Internal friction study of Pb(Zr,Ti)O<sub>3</sub> ceramics with various Zr/Ti ratios and dopants', *J. Phys. D: Appl. Phys.*, 2002, **35**, 1545.



# Phase formation, microstructure and dielectric properties of $\text{Bi}_{0.5}(\text{Na}_{0.74}\text{K}_{0.16}\text{Li}_{0.10})_{0.5}\text{TiO}_3-x\text{Ba}(\text{Zr}_{0.5}\text{Ti}_{0.95})\text{O}_3$ ceramics prepared via combustion technique

P. Julphunthong and T. Bongkarn\*

Binary lead free electroceramics with the composition of  $(1-x)\text{Bi}_{0.5}(\text{Na}_{0.74}\text{K}_{0.16}\text{Li}_{0.10})_{0.5}\text{TiO}_3-x\text{Ba}(\text{Zr}_{0.5}\text{Ti}_{0.95})\text{O}_3$  or BNKLT–100xBZT with  $0.025 \leq x \leq 0.150$  were synthesised via the combustion technique. The results showed how BZT content affects typical properties of a BNKLT–100xBZT system such as phase formation and dielectric properties. The XRD investigation revealed that BNKLT–100xBZT exhibits the coexistence of rhombohedral and tetragonal phases. By adding BZT, the rhombohedral phase decreases and tetragonal phase increases. From a dielectric properties investigation, BNKLT–100xBZT shows two dielectric loss peaks at  $\sim 190$  and  $\sim 320^\circ\text{C}$  defined as  $T_d$  and  $T_m$  respectively. Increasing the BZT fraction makes  $T_m$  shift to a lower temperature but has no effect on the  $T_d$  shifting. The maximum  $\epsilon_r$  and  $\epsilon_{\max}$  with their respective values of 1380 and 4050 are observed from the sample with the composition BNKLT–5BZT, which can be attributed to its location near the MPB region.

**Keywords:** BNT, Combustion technique, Core–shell structure, Dielectric properties

## Introduction

It is well known that BNT is a ferroelectric ceramic with strong ferroelectricity.<sup>1</sup> However, its application to electronic devices is limited by such problems as its high coercive field, low piezoelectricity and low dielectric constant.<sup>2</sup> Therefore, other compositions or some cation additives are added into BNT to improve its properties.<sup>3,4</sup>

Yang *et al.*<sup>5</sup> modified BNT by substituting  $\text{Na}^+$  by  $\text{K}^+$  for 10–20 mol.-%. The result demonstrated that K substitution induced the MPB region between the rhombohedral and tetragonal phases at 18 mol.-% of K. This composition is very promising for lead free piezoelectric materials because it shows the optimum values of  $d_{33}$ ,  $K_p$ ,  $\epsilon_r$  and  $\tan \delta$  of 144 pC/N, 0.29, 893 and 0.037 respectively. Lu *et al.*<sup>6</sup> investigated the  $\text{Bi}(\text{Na}_{1-x-y}\text{K}_x\text{Li}_y)_{0.5}\text{TiO}_3$  system by replacing the  $\text{Na}^{1+}$  ion with  $\text{K}^{1+}$  and  $\text{Li}^{1+}$  ion additives, which suggested that the  $\text{Bi}_{0.5}(\text{Na}_{0.74}\text{K}_{0.16}\text{Li}_{0.10})_{0.5}\text{TiO}_3$  composition showed the coexistence of rhombohedral and tetragonal structures which is the MPB composition. The MPB composition led to a great enhancement in electrical properties compared with BNT, increasing  $d_{33}$  from 78 to 160 pC/N,  $K_p$  from 0.16 to 0.35 and  $\epsilon_r$  from 420 to 1080. In addition, using different approaches,

many researchers have reported BNT improvement by introducing the BNT binary or ternary system chemical compositions such as BNT–BZT,<sup>7,8</sup> BNT–KNN<sup>9</sup> or BNT–BKT–BF.<sup>10,11</sup> For example, Parija *et al.*<sup>2</sup> demonstrated that 5 mol.-%BZT doped BNT increases the  $\epsilon_m$  from 1020 to 3533,  $d_{33}$  from 41 to 131 pC/N and  $P_r$  from 2.5 to 12  $\mu\text{C cm}^{-2}$  for BZT doped.

Recently, the idea of combining cation additives with the binary system of BNT based solid solution to improve BNT properties has generated interest. Jarupoom *et al.*<sup>12</sup> produced a system of  $(1-x)\text{BNLT}-x\text{BT}$  where 1.7 mol.-% $\text{La}^{3+}$  was doped to BNT with  $0 \leq x \leq 0.10$ . By the addition of the BT fraction, the  $\epsilon_r$  and  $\epsilon_{\max}$  values of the BNLT–BT system increased but  $T_c$  lowered the  $\tan \delta$  of the ceramics was reduced at high temperature. Moreover, the  $\epsilon_r$  and  $\epsilon_{\max}$  obtained their maximum value of 1615 and 4250 respectively from the BNLT with an addition of 10 mol.-%BZT.

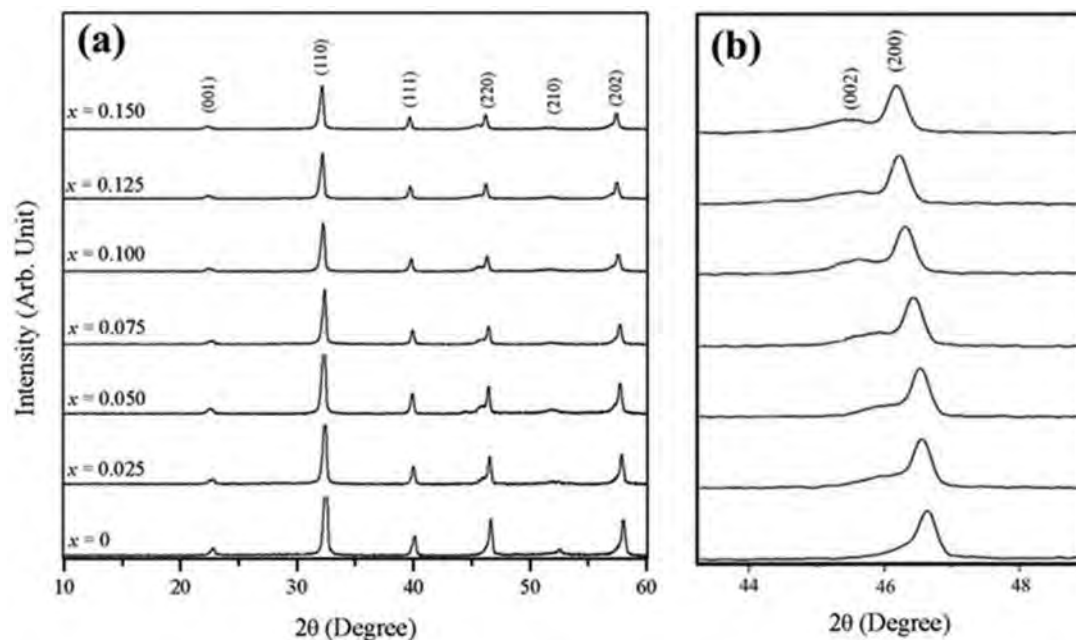
The objective of this study was to investigate the possibilities of improving BNT properties by producing a new system of  $(1-x)\text{Bi}_{0.5}(\text{Na}_{0.74}\text{K}_{0.16}\text{Li}_{0.10})_{0.5}\text{TiO}_3-x\text{Ba}(\text{Zr}_{0.5}\text{Ti}_{0.95})\text{O}_3$  or BNKLT–100xBZT ceramics. The effects of BZT fraction on phase formation, morphology and dielectric properties were also investigated. The samples were synthesised through the combustion technique since this has been shown to be an effective way to improve BNT and BZT properties.<sup>13–15</sup>

## Experimental procedure

The  $(1-x)\text{Bi}_{0.5}(\text{Na}_{0.74}\text{K}_{0.16}\text{Li}_{0.10})_{0.5}\text{TiO}_3-x\text{Ba}(\text{Zr}_{0.5}\text{Ti}_{0.95})\text{O}_3$  ( $0.025 \leq x \leq 0.15$ , step=0.025) ceramics were synthesised

Department of Physics, Faculty of Science, Naresuan University, Phitsanulok 65000, Thailand and Research Center for Academic Excellent in Applied Physics, Faculty of Science, Naresuan University, Phitsanulok, 65000, Thailand

\*Corresponding author, email researchcmu@yahoo.com



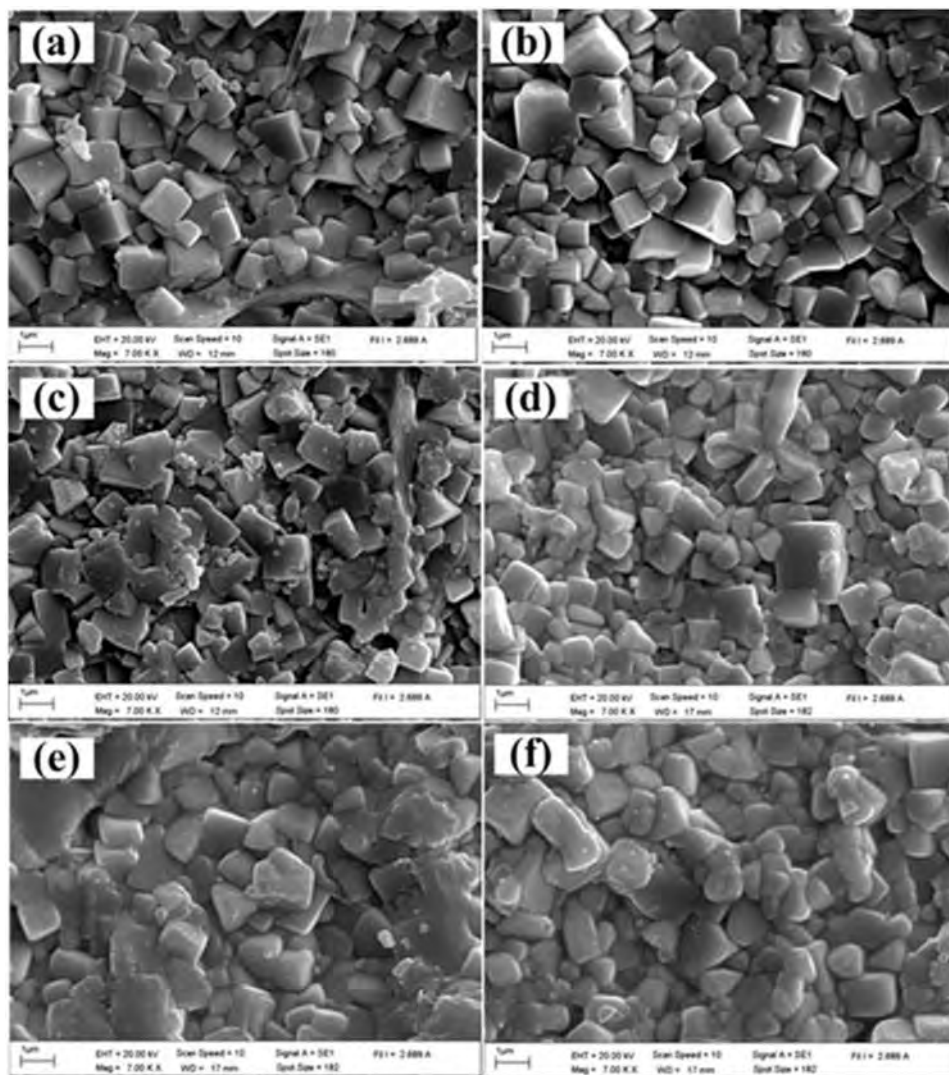
**1** XRD patterns of BNKLT–100xBZT ceramics with  $0 \leq x \leq 0.15$ : **a** at  $2\theta$  between  $10^\circ$  and  $60^\circ$ ; **b** at a very low scanning rate of  $2\theta$  between  $44^\circ$  and  $48^\circ$

using the combustion technique. Highly pure bismuth oxide ( $\text{Bi}_2\text{O}_3$ ), sodium carbonate ( $\text{Na}_2\text{CO}_3$ ), potassium carbonate ( $\text{K}_2\text{CO}_3$ ), lithium carbonate ( $\text{Li}_2\text{CO}_3$ ), titanium oxide ( $\text{TiO}_2$ ), barium carbonate ( $\text{BaCO}_3$ ) and zirconium oxide ( $\text{ZrO}_2$ ) were used as the starting materials. First, the raw materials were weighed according to the designed chemical formulae and were ball milled in an ethanol medium for 24 h. After being mixed with  $\text{CH}_4\text{N}_2\text{O}$  (fuel), the  $\text{Bi}_{0.5}(\text{Na}_{0.74}\text{K}_{0.16}\text{Li}_{0.10})_{0.5}\text{TiO}_3$  (BNKLT) and  $\text{Ba}(\text{Zr}_{0.05}\text{Ti}_{0.95})\text{O}_3$  (BZT) were synthesised at  $750^\circ\text{C}$  for 2 h and  $1000^\circ\text{C}$  for 5 h respectively. After calcination, the two synthesised powders were mixed with different values of  $x$ , milled once again, dried and granulated by adding polyvinyl alcohol. The granulated powders were pressed into discs of 15 mm in diameter using a uniaxial pressure of 80 MPa, then sintered in air at  $1100^\circ\text{C}$  for 2 h. The crystal structures of the ceramics were characterised by an X-ray diffractometer (XRD). In addition, the scanning electron microscopy (SEM) was employed to examine the microstructure of the sintered ceramics. The sintered discs were polished and silver paste was applied to both surfaces to measure their electrical properties. After applying the silver, the discs were fired at  $600^\circ\text{C}$  for 5 min and the temperature dependences of the dielectric properties were measured using a LCR meter.

## Results and discussion

The XRD patterns of the BNKLT–100xBZT ceramics with  $0 \leq x \leq 0.15$  are shown in Fig. 1. All BNKLT–100xBZT samples showed a pure perovskite phase, which indicated that the BZT had completely diffused into a lattice to form a solid solution. Moreover, the diffraction peaks at  $2\theta$  of  $44\text{--}48^\circ$  at a very low scanning rate (step size  $0.00116^\circ$ , time/ $\theta$  7.42 s and scan speed  $0.05152^\circ \text{ s}^{-1}$ ) showed interesting characteristics due to a significant change in the composition (Fig. 1b). The investigation demonstrated that there were two features of the diffraction patterns which were of interest. First, the diffraction peaks shifted to a lower angle when the BZT content increased. This suggested that the unit cell

was stretched, which may be because the larger size  $\text{Ba}^{2+}$  (161 pm) occupies the A-site lattice by replacing  $\text{Bi}^{3+}$  (130 pm) and/or because the  $\text{Na}^{1+}$  (139 pm) and  $\text{Zr}^{4+}$  (72 pm) ion replace the  $\text{Ti}^{4+}$  (61 pm) ion at the B site lattice. The other feature is the splitting of the (002) and (200) peaks. Lu *et al.*<sup>6</sup> demonstrated that BNKLT shows the coexistence of rhombohedral and tetragonal phases with the former in a dominant position. Additional BZT into BNKLT for BNKLT–2.5BZT induced the occurrence of a small hump at the left side of the (200) peak, indicating that the crystal structure was initially transformed to a tetragonal phase. The asymmetrical feature was distinctly observed when the BZT content increased to 5 mol.-%. For the BNKLT–7.5BZT composition, the diffraction peak split into (200) and (002) peaks. The splitting characteristic was observed clearly with the increase of the BZT content, indicating that the tetragonality tended to increase. To understand the variation of the unit cell volume due to a change in composition, the lattice parameters were also investigated. The BNKLT was assumed as a rhombohedral structure, and the lattice parameter  $a$  was calculated. For the BNKLT–100xBZT structure, the splitting of (002) and (200) peaks at  $2\theta$  of  $44\text{--}48^\circ$  was observed in the system containing over 5 mol.-%BZT. Therefore, the crystal structure of BNKLT–100xBZT was assumed to be a rhombohedral and tetragonal structure with  $x \leq 5$  mol.-% and  $x > 5$  mol.-% respectively. The lattice parameters, unit cell volume and  $c/a$  ratio were calculated as listed in Table 1. The calculation for the lattice parameters was based on different structures. The calculated lattice parameter  $a$  changed dramatically between BNKLT–5BZT (assumed as rhombohedral structure) and BNKLT–7.5BZT (assumed as tetragonal structure). However, it can be noted that the lattice parameter  $a$ , lattice parameter  $c$ , unit cell volume and the  $c/a$  ratio also increase with increasing BZT fraction. This observation supports the previous comment that more BNT doped leads to the enlargement of crystal unit cell volume.



**2 SEM photographs of surface of BNKLT-100xBZT ceramics: a  $x=0.025$ ; b  $x=0.050$ ; c  $x=0.075$ ; d  $x=0.100$ ; e  $x=0.125$ ; f  $x=0.150$**

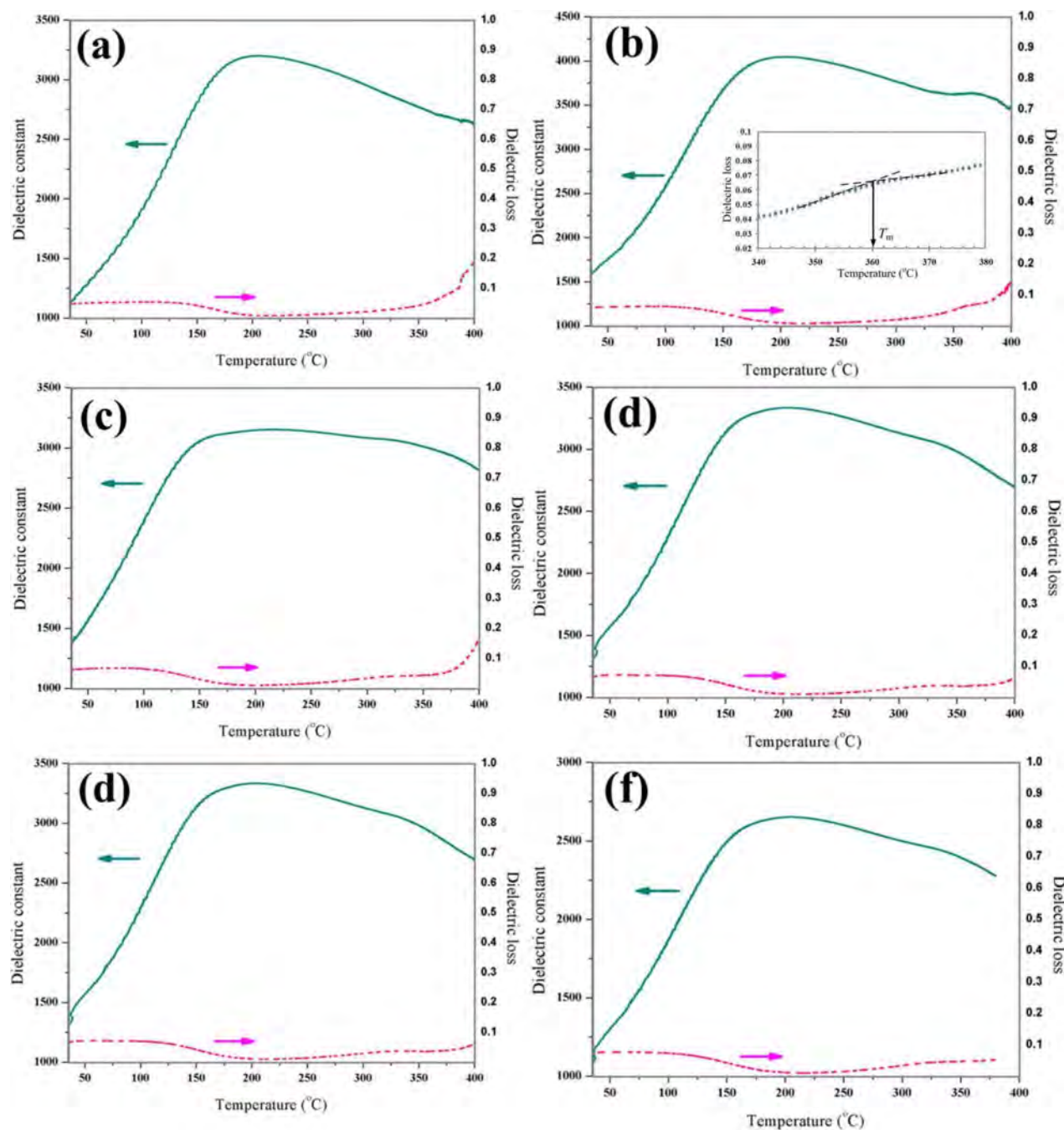
The surface morphologies of BNKLT-100xBZT ceramics were investigated, and the results are shown in Fig. 2. Generally, pure BNT exhibits a cube shaped grain.<sup>5</sup> Therefore, a characteristic of quasicubic morphology can be seen from the samples with a small amount of BZT in a BNKLT-100xBZT system (Fig. 2a–c). In the case of over 7.5 mol.-%BZT, the addition of BZT into the BNKLT matrix caused the cubic grain shape to change to a spherical grain gradually (Fig. 2d–f). The variation of average grain

size due to its changing composition is listed in Table 1. The addition of BZT fraction on a BNKLT system affected the value of average grain size in the range of 1.43–1.89  $\mu\text{m}$ .

The measured density with a variation in BZT content of BNKLT-100xBZTBZT is listed in Table 2. The density of the ceramics was in the range of 5.79–5.87  $\text{g cm}^{-3}$  with the highest obtained by BNKLT-12.5BZT. It can be observed that high density ceramics were obtained by the samples with high BZT content. In

**Table 1 Lattice parameters  $a$  and  $c$ , unit cell volume,  $c/a$  ratio and average grain size of BNKLT-100xBZT ceramics**

Samples	Lattice parameters		Unit cell volume	$c/a$ ratio	Average grain size
	$a$	$c$			
	$\text{\AA}$	$\text{\AA}$	$\text{\AA}^3$		$\mu\text{m}$
BNKLT	3.432	...	...	...	1.72
BNKLT-2.5BZT	3.438	...	...	...	1.64
BNKLT-5.0BZT	3.449	...	...	...	1.89
BNKLT-7.5BZT	3.916	3.971	61.740	1.014	1.70
BNKLT-10.0BZT	3.926	3.986	62.368	1.015	1.43
BNKLT-12.5BZT	3.928	3.988	62.453	1.015	1.59
BNKLT-15.0BZT	3.927	3.991	62.560	1.016	1.44



3 Temperature dependence of dielectric constant and dielectric loss of BNKLT–xBZT ceramics: *a*  $x=0.025$ ; *b*  $x=0.050$ ; *c*  $x=0.075$ ; *d*  $x=0.100$ ; *e*  $x=0.125$ ; *f*  $x=0.150$

the previous work, the results indicated Bi and/or K and/or Na ions evaporate from the BNT system during the sintering process, resulting in lower density samples.<sup>16</sup> By the addition of BZT, evaporated ions can be substituted by more stable ions such as Na, and the

volatility is reduced.<sup>15</sup> Therefore, the relative density is enhanced.

The dielectric constant and loss as a function of temperature for BNKLT–100xBZT ceramics are illustrated in Fig. 3. For the sample with 2.5 mol.-%BZT

Table 2 Density,  $T_d$ ,  $T_m$ ,  $\epsilon_r$ ,  $\epsilon_{max}$  and  $\tan \delta$  of BNKLT–100xBZT ceramics

Samples	Density g cm <sup>-3</sup>	$T_d$ °C	$T_m$ °C	$\epsilon_r$	$\epsilon_{max}$	$\tan \delta$
BNKLT–2.5BZT	5.81	190	>400	1020	3200	0.045
BNKLT–5.0BZT	5.83	193	360	1380	4050	0.051
BNKLT–7.5BZT	5.79	191	330	1340	3150	0.061
BNKLT–10.0BZT	5.82	189	325	1260	3330	0.065
BNKLT–12.5BZT	5.87	190	320	1260	3390	0.068
BNKLT–15.0BZT	5.84	188	310	1050	2650	0.070

(Fig. 3a), the distinct dielectric peak with the maximum value of dielectric constant occurs at  $\sim 200^\circ\text{C}$ . This point is referred to as the dielectric peak in which the phase transition from a ferroelectric to an antiferroelectric phase at a temperature called  $T_d$ .<sup>6</sup> Similarly, the dielectric loss curve shows an initial occurrence of another dielectric peak at a higher temperature is called  $T_m$ .<sup>6</sup> By increasing BZT content to 5 mol.-%, the dielectric loss peak at  $T_m$  is more obvious and shifted to a lower temperature (the inset in Fig. 3b). The dielectric loss peak at  $T_m$  tends to move toward a lower temperature as the BZT content increases (Fig. 3c–f). However, an increase in the BZT content only slightly affects the dielectric loss peak at  $T_d$ . The dielectric constant and dielectric loss, however, could not be measured at high temperatures for BNKLT with 12.5 and 15 mol.-%BZT (Fig. 3e–f). This indicated that the materials exhibit high conductivity at high temperature, because the structure changes to paraelectric above Curie temperature.<sup>12</sup> The  $T_d$  and  $T_m$  are listed in Table 2. It can be noted that, an increased BZT content causes the shifting of  $T_m$  to a lower temperature, because the BZT has a lower value of paraelectric phase transition temperature ( $\sim 100^\circ\text{C}$ )<sup>17</sup> compared with that of BNKLT ( $\sim 335^\circ\text{C}$ ).<sup>6</sup> In term of dielectric constant, the maximum value is exhibited at the dielectric peak near  $T_d$  for all samples. This phenomenon shows the contrary behaviour of the dielectric curve of BNT as reported in the literature<sup>18,19</sup> in which the dielectric peak shows its higher altitude at  $T_m$  and its lower altitude at  $T_d$ . Yuan *et al.*<sup>20</sup> suggested that the altitude of the dielectric constant peak at Curie temperatures and lower temperature is correlated with the grain core and grain shell, respectively, which is exhibited in the core–shell structure materials. The core–shell structure, which can be formed in ferroelectric ceramics such as BT and BNT with some cation additives, consists of relatively pure composition grain cores embedded in and surrounded by a second impurity phase grain shell.<sup>21</sup> In this study, the dielectric constant peak at  $T_m$  was indistinct while the dielectric constant peak at  $T_d$  dominated for all samples. This suggests that the core–shell structure is formed in the system, but the influence of the grain shell is higher than that of the grain core, thus the dielectric constant peak at  $T_d$  is more dominate than that at  $T_m$ .

The variation of maximum dielectric constant ( $\epsilon_{\text{max}}$ ), dielectric constant at room temperature ( $\epsilon_r$ ) and dielectric loss at room temperature ( $\tan \delta$ ) for various BZT contents are presented in Table 2. An increase of the BZT content could enhance both  $\epsilon_r$  and  $\epsilon_{\text{max}}$ , which obtained the maximum at 5 mol.-%BZT. Thereafter,  $\epsilon_{\text{max}}$  dropped suddenly, and then increased with BZT content going up to 12.5%, then decreased again. Chu *et al.*<sup>22</sup> reported that the MPB composition of BNT–BT is 6 mol.-%BT. Therefore, the highest values of  $\epsilon_r$  and  $\epsilon_{\text{max}}$  obtained by BNKLT–5BZT may be attributed to this composition being near the MPB region of the BNKLT–100xBZT system. At the MPB region, the polarisation vector can easily switch between all the allowed polarisation orientations. Therefore, the dielectric properties increased.<sup>23</sup> After dropping,  $\epsilon_{\text{max}}$  tended to increase with increasing BZT content from 7.5 to 12.5 mol.-%, which corresponds with the literature<sup>24</sup> suggesting that the dielectric constant of BNT–BT increases when the composition is near the tetragonal

side of the MPB region. However, the cause of the reduction of  $\epsilon_r$  and  $\epsilon_{\text{max}}$  in BNKLT–15BZT sample is ambiguous.

## Conclusions

The effect of BZT content on the phase formation, morphology and dielectric properties of BNKLT–100xBZT was studied. The XRD results demonstrated that the coexistence of the rhombohedral–tetragonal phase exists for all samples. The addition of BZT content leads to the increase of the tetragonal phase and decrease of the rhombohedral phase. Moreover, the increase of BZT content cause the increase of lattice parameters, unit cell volume and  $c/a$  ratio. The SEM results suggest that the average grain size is slightly affected by the addition of BZT. However, the relative density increases with increasing BZT fraction. After dielectric properties characterisation is employed, BZT adding is observed to able to shift  $T_m$  to a lower temperature while little impacts are found on  $T_d$ . The appearance of the dielectric constant peak at  $T_d$  rather than at  $T_m$  is apparent for all compositions, indicating that the grain shell has higher influences than grain core in a BNKLT–100xBZT system. The maximum  $\epsilon_r$  and  $\epsilon_{\text{max}}$  with respective values of 1380 and 4050 are observed from the sample with the composition BNKLT–5BZT, which can be attributed to the fact that this composition is located near the MPB region.

## Acknowledgements

This work was financially supported by the Thailand Research Fund (TRF). Thanks also go to Department of Physics, Faculty of Science, Naresuan University for supporting facilities. Acknowledgements go to Mr D. Hindle for helpful comments and corrections of the manuscript.

## References

1. R. Zuo, S. Su, Y. Wu, J. Fu, M. Wang and L. Li: 'Influence of A-site nonstoichiometry on sintering, microstructure and electrical properties of  $(\text{Bi}_{0.5}\text{Na}_{0.5})\text{TiO}_3$  ceramics', *Mater. Chem. Phys.*, 2008, **110**, 311–315.
2. B. Parija, T. Badapanda, S. K. Rout, L. S. Cavalcante, S. Panigrahi and E. Longo: 'Morphotropic phase boundary and electrical properties of  $1-x[\text{Bi}_{0.5}\text{Na}_{0.5}]\text{TiO}_3-x\text{Ba}[\text{Zr}_{0.25}\text{Ti}_{0.75}]\text{O}_3$  lead-free piezoelectric ceramics', *Ceram. Int.*, 2013, **39**, 4877–4886.
3. Y. Zhang, X. Zheng and T. Zhang: 'Characterization and humidity sensing properties of  $\text{Bi}_{0.5}\text{Na}_{0.5}\text{TiO}_3$ – $\text{Bi}_{0.5}\text{K}_{0.5}\text{TiO}_3$  powder synthesized by metal–organic decomposition', *Sensor Actuat. B*, 2011, **156B**, 887–892.
4. Y. Liao, D. Xiao, D. Lin, J. Zhu, P. Yu and L. Wu: 'Synthesis and properties of  $\text{Bi}_{0.5}(\text{Na}_{1-x-y}\text{K}_x\text{Ag}_y)_{0.5}\text{TiO}_3$  lead-free piezoelectric ceramics', *Ceram. Int.*, 2007, **33**, 1445–1448.
5. Z. Yang, B. Liu, L. Wei and Y. Hou: 'Structure and electrical properties of  $(1-x)\text{Bi}_{0.5}\text{Na}_{0.5}\text{TiO}_3-x\text{Bi}_{0.5}\text{K}_{0.5}\text{TiO}_3$  ceramics near morphotropic phase boundary', *Mater. Res. Bull.*, 2008, **43**, 81–89.
6. W. Lu, Y. Wang, G. Fan, X. Wang and F. Liang: 'The structural and electric properties of Li- and K-substituted  $\text{Bi}_{0.5}\text{Na}_{0.5}\text{TiO}_3$  ferroelectric ceramics', *J. Alloys Compd.*, 2011, **509**, 2738–2744.
7. P. Du, L. Luo, W. Li, Y. Zhang and H. Chen: 'Photoluminescence and piezoelectric properties of Pr-doped NBT– $x$ BZT ceramics: Sensitive to structure transition', *J. Alloys Compd.*, 2013, **559**, 92–96.
8. W. Lee, M. Lee, C. Tseng, Y. Huang and C. Wu: 'Crystal structure and ferroelectric properties of  $(\text{Bi}_{0.5}\text{Na}_{0.5})\text{TiO}_3$ – $\text{Ba}(\text{Zr}_{0.05}\text{Ti}_{0.95})\text{O}_3$  piezoelectric ceramics', *J. Am. Ceram. Soc.*, 2009, **92**, 1069–1073.
9. P. Laoratanakul, R. Yimnirun and S. Wongsanmai: 'Phase formation and dielectric properties of bismuth sodium

- titanate–potassium sodium niobate ceramics’, *Curr. Appl. Phys.*, 2011, **11**, S161–S166.
10. C. Zhou, X. Liu, W. Li and C. Yuan: ‘Structure and piezoelectric properties of  $\text{Bi}_{0.5}\text{Na}_{0.5}\text{TiO}_3\text{--Bi}_{0.5}\text{K}_{0.5}\text{TiO}_3\text{--BiFeO}_3$  lead-free piezoelectric ceramics’, *Mater. Chem. Phys.*, 2009, **114**, 832–836.
11. M. Zou, H. Fan, L. Chen and W. Yang: ‘Microstructure and electrical properties of  $(1-x)[0.82\text{Bi}_{0.5}\text{Na}_{0.5}\text{TiO}_3\text{--}0.18\text{Bi}_{0.5}\text{K}_{0.5}\text{TiO}_3]\text{--}x\text{BiFeO}_3$  lead-free piezoelectric ceramics’, *J. Alloys Compd.*, 2010, **495**, 280–283.
12. P. Kantha, K. Pengpat, P. Jarupoom, U. Intatha, G. Rujijanagul and T. Tunkasiri: ‘Phase formation and electrical properties of BNLT–BZT lead-free piezoelectric ceramic system’, *Curr. Appl. Phys.*, 2009, **9**, 460–466.
13. F. Moura, A. Z. Simões, B. D. Stojanovic, M. A. Zaghe, E. Longo and J. A. Varela: ‘Dielectric and ferroelectric characteristics of barium zirconate titanate ceramics prepared from mixed oxide method’, *J. Alloys Compd.*, 2008, **462**, 129–134.
14. R. Sumang, N. Vittayakorn and T. Bongkarn: ‘Crystal structure, microstructure and electrical properties of  $(1-x-y)\text{Bi}_{0.5}\text{Na}_{0.5}\text{TiO}_3\text{--}x\text{Bi}_{0.5}\text{K}_{0.5}\text{TiO}_3\text{--}y\text{BiFeO}_3$  ceramics near MPB prepared via the combustion technique’, *Ceram. Int.*, 2013, **39**, (1), S409–S413.
15. K. A. Razak, C. J. Yip and S. Sreekantan: ‘Synthesis of  $(\text{Bi}_{0.5}\text{Na}_{0.5})\text{TiO}_3$  (BNT) and Pr doped BNT using the soft combustion technique and its properties’, *J. Alloys Compd.*, 2011, **509**, 2936–2941.
16. M. Naderer, D. Schütz, T. Kainz, K. Reichmann and F. Mittermayr: ‘The formation of secondary phases in  $\text{Bi}_{0.5}\text{Na}_{0.375}\text{K}_{0.125}\text{TiO}_3$  ceramics’, *J. Eur. Ceram. Soc.*, 2012, **32**, (10), 2399–2404.
17. P. Julphunthong, S. Chootin and T. Bongkarn: ‘Phase formation and electrical properties of  $\text{Ba}(\text{Zr}_x\text{Ti}_{1-x})\text{O}_3$  ceramics synthesized through a novel combustion technique’, *Ceram. Int.*, 2013, **39**, (1), S415–S419.
18. R. Zuo, S. Su, Y. Wu, J. Fu, M. Wang and L. Li: ‘Influence of A-site nonstoichiometry on sintering, microstructure and electrical properties of  $(\text{Bi}_{0.5}\text{Na}_{0.5})\text{TiO}_3$  ceramics’, *Mater. Chem. Phys.*, 2008, **110**, 311–315.
19. D. Lin, K. W. Kwok and H. L. W. Chan: ‘Structure and electrical properties of  $\text{Bi}_{0.5}\text{Na}_{0.5}\text{TiO}_3\text{--BaTiO}_3\text{--Bi}_{0.5}\text{Li}_{0.5}\text{TiO}_3$  lead-free piezoelectric ceramics’, *Solid State Ionics*, 2008, **178**, 1930–1937.
20. Y. Yuan, S. R. Zhang, X. H. Zhou, B. Tang and B. Li: ‘High-temperature capacitor materials based on modified  $\text{BaTiO}_3$ ’, *J. Electron. Mater.*, 2009, **38**, 706–710.
21. N. Wada, T. Hiramatsu, T. Tamura and Y. Sakabe: ‘Investigation of grain boundaries influence on dielectric properties in fine-grained  $\text{BaTiO}_3$  ceramics without the core–shell structure’, *Ceram. Int.*, 2008, **34**, 933–937.
22. B.-J. Chu, D.-R. Chen, G.-R. Li and Q.-R. Yin: ‘Electrical properties of  $\text{Na}_{1/2}\text{Bi}_{1/2}\text{TiO}_3\text{--BaTiO}_3$  ceramics’, *J. Eur. Ceram. Soc.*, 2002, **22**, 2115–2121.
23. Y. Tian, L. Wei, X. Chao, Z. Liu and Z. Yang: ‘Phase transition behavior and large piezoelectricity near the morphotropic phase boundary of lead-free  $(\text{Ba}_{0.85}\text{Ca}_{0.15})(\text{Zr}_{0.1}\text{Ti}_{0.9})\text{O}_3$ ’, *J. Am. Ceram. Soc.*, 2013, **96**, 496–502.
24. J. Shieh, K. C. Wu and C. S. Chen: ‘Switching characteristics of MPB compositions of  $(\text{Bi}_{0.5}\text{Na}_{0.5})\text{TiO}_3\text{--BaTiO}_3\text{--}(\text{Bi}_{0.5}\text{K}_{0.5})\text{TiO}_3$  lead-free ferroelectric ceramics’, *Acta Mater.*, 2007, **55**, 3081–3087.